UNIVERSITY OF OSLO

Approaching the pygmy dipole resonance in Sn isotopes with the Oslo method

Thesis submitted in partial fulfillment of the requirements
for the degree of Phlosophiae Doctor

Maria Markova

Department of Physics
Faculty of Mathematics and Natural Sciences

May, 2024

To Alexei Navalny

Частица твоей души живёт в нас,
оттуда её им достать уже не удастся.
Спасибо тебе за надежду!

16.02.2024

1976 - ∞

Abstract

Collective resonance phenomena in atomic nuclei are historically one of the first and most plentiful sources of unique information on the intricate nuclear structure and properties of nuclear matter. One of them, the pygmy dipole resonance, still remains one of the least understood features of the nuclear response to an external excitation, despite great experimental efforts to study its properties in the past two decades. Within numerous theoretical frameworks, it is recognized as a potential key to the description of dense neutron-rich matter, thus bridging the gap between the neutron skin in heavy nuclei and massive astrophysical objects, such as neutron stars. In this regard, systematic experimental studies of the pygmy dipole resonance in different chains of isotopes are highly desired to guide future improvements in the theoretical description of its underlying mechanisms.

This dissertation sheds new light on the evolution of the low-lying electric dipole strength in Sn isotopes, commonly interpreted as the pygmy dipole resonance, based on a systematic analysis of particle-γ coincidence data for eleven nuclei, from unstable ^{111}Sn to the heaviest stable ^{124}Sn, using the Oslo method. Three central questions form the basis for this study. Firstly, how do the bulk properties of the low-lying electric dipole strength evolve with increasing proton-neutron asymmetry and whether this information can aid with the interpretation of the observed features as the pygmy dipole resonance? Secondly, can the Brink-Axel hypothesis be considered a reliable assumption in the energy range of the pygmy dipole resonance? And, finally, what impact do the extracted results have on statistical-model calculations of radiative neutron-capture rates of interest for the heavy-element nucleosynthesis in the universe?

Sammendrag

Resonansfenomener i atomkjerner er historisk sett en av hovedkildene til kunnskap om deres struktur og egenskaper. Pygme-dipolresonansen er et slikt fenomen, som fortsatt vekker en rekke spørsmål om dens opprinnelse og egenskaper, til tross for stor eksperimentell oppmerksomhet i de siste to tiårene. En større forståelse av oppførelsen til pygme-dipolresonansen ville gitt bedre innsikt i egenskapene til nøytronrik materie, som er funnet både i tunge kjerners ytre nøytronlag og nøytronstjerner. Et systematisk eksperimentelt studie av pygme-dipolresonans i forskjellige isotoper er defor nødvendig for å forbedre den teoretiske beskrivelsen av de underliggende mekanismer i atomkjerner.

Denne avhandlingen kaster et nytt lys på utviklingen av lavenergi-dipol-styrke i tinnisotoper, ofte betraktet som en pygme-dipolresonans. Resultatene er baset på en systematisk analyse av partikkel-γ-koinsidensdata for elleve kjerner, fra ustabil ^{111}Sn til den tyngste stabile ^{124}Sn, ved å anvende Oslo-metoden. Tre sentrale spørsmål danner grunnlaget for denne avhandlingen: Hvordan utvikler lavenergi-dipol-styrkens egenskaper seg under økende proton-nøytron asymmetri, og hvordan kan denne informasjonen brukes for å betrakte den observerte styrken som en pygme-dipolresonans? Er Brink-Axel hypothesen en god antakelse i energiregionen relevant for pygme-dipolresonansen? Og til slutt, hvordan kan disse resultatene påvirke statistiskmodellberegningene av nøytroninnfagningsratene viktige for studiet om dannelsen av de tunge grunnstoffene i universet?

Acknowledgment

I wish I could say that my PhD years have been the most fantastic time of my life, but, unfortunately, the war split the lives of everyone dear to me and my own into "before" and "after". In the incessant flow of devastating news and constant fear, the work on this project has been a true joy, a source of light and hope. Of course, this journey could not have been possible without the immense support of my family and my colleagues.

First and foremost, I would like to thank my main supervisor, Ann-Cecilie Larsen, for making this academic journey and the work on this fascinating project possible, for the help with the experiments, for the exciting scientific discussions, for our shifts together, for the freedom to choose my own path, for sharing the passion for Doctor Who, Star Wars, and Amorphis, and, of course, for the incredible amount of support and encouragement throughout all these years. You have already long ago become so much more than a supervisor to me; you have motivated and inspired so many students, and I am proud of being among them.

My co-advisors, Andreas Görgen and Frank Leonel Bello Garrote, thank you so much for this incredible journey and being there for me, for making me understand the nuclear structure and the data analysis better, and encouraging me to keep learning new things. Thank you, Magne Guttormsen, for all the fantastic discussions we have had, I have learned so much from you. I would also like to thank Peter von Neumann-Cosel, who has always been encouraging and supporting me in our studies. Thank you, Sunniva Siem, for being a fantastic group leader, who makes everyone feel like an important and appreciated member of our nuclear physics group. Pawel Sobas and Victor Modamio, thank you for all your magic to make the cyclotron work and make all our projects come true. Thank you, Francesco, for all the fantastic trips we have had, for your help and exciting conversations. Thanks to everyone in our group, you make the university feel like home.

My infinitely supportive family, thank you so much for believing in me, for being there for me every single day, for being there for each other, and for making my Norwegian dream come true. I promise, one day, we will watch that ballet together. Thank you, Jan, for showing me the hidden treasures of Norway, for spontaneous road trips, for cheering me up, and for supporting me no matter what. Thank you, Sasha, for being the best friend one could ever dream of. Your friendship has always been one of the very few constants in my life that I will treasure forever. And, yes, answering your question, I will of course read Futu.re. Some day)

Maria Markova,
Oslo, May, 2024

Contents

Chapter 1

Introduction

After more than a century of elaborate theoretical and experimental investigations, atomic nuclei remain a wellspring of exciting new questions on the structure of nuclear matter and its properties. How do the bound constituents, namely protons and neutrons, of these complex many-body systems interact? What processes are induced in a nucleus through interactions with other nuclei and particles under different conditions? What are the properties of nuclei in different excited states? How does the complexity of a nucleus increase with increasing number of nucleons and excitation energy? These are just a few of the many questions that keep inciting the development of new experimental techniques and more advanced theories to seek answers to even more fundamental questions, such as, for example, the origin of isotopes of different chemical elements in the universe.

Naturally, the experimental way to approach the structural properties and different excitation mechanisms inside the nucleus is to study its response to an external perturbation. Early on, at the dawn of experimental and theoretical nuclear physics, the probabilities, or the cross sections, of induced reactions as functions of transferred energy and angular momentum were realized to be a unique source of information on nuclear properties. In particular, the first experimental observation of an enhanced photodissociation cross section for ^{63}Cu by Bothe and Gentner in 1937 [1] suggested the presence of a resonance effect in the nuclear response. The first theoretical description of this phenomenon in terms of quantum collective modes of excitation was suggested by Migdal in 1944 [2]. The potential resonance excitation was suggested to be due to the dipole oscillation of interpenetrating compressible proton and neutron "liquids". A large, Lorentzian-shaped resonance was indeed observed soon after by Baldwin and Klaiber in photofission cross sections for several heavy nuclei [3] and photodissociation cross section of lighter nuclei [4]. This groundbreaking work started a new era of giant resonance studies in nuclei across the whole nuclear chart.

The collectivity, i.e. the degree of involvement of nucleons in such oscillations, inspired a rather simple classification of these giant resonance phenomena according to the type of collective motion and attributed changes in the multipolarity (L), spin S, and isospin T induced by an external perturbation. In particular, the large resonance observed by Baldwin and Klaiber corresponds to the mode with $\Delta S = 0$ (electric, no spin flip involved), $\Delta T = 1$ (isovector, out-of-phase oscillations of protons against neutrons), $\Delta L = 1$ (dipole), and in the following it will be referred to as the isovector (IV) giant dipole resonance (IVGDR). By analogy, an excitation accompanied by the spin flip ($\Delta S = 1$) is of magnetic type, and in-phase

oscillations of protons and neutrons are characteristic for the so-called isoscalar (IS) modes with $\Delta T = 0$.

The conceptual approach of Migdal to the description of the IVGDR appeared to be quite successful and provided the foundation for the future development of macroscopic models for the resonance phenomena. In particular, the macroscopic frameworks of Goldhaber and Teller [5] and Steinwedel and Jensen [6] contributed to the interpretation of the IVGDR in terms of a bulk out-of-phase motion of protons and neutrons in the nucleus. In the literature, it is commonly viewed as a high-frequency, nearly harmonic, damped vibration of nuclear density/shape, manifested as a broad peak in photoabsorption cross sections of nuclei [7].

In the early 1960s, a series of thermal neutron-capture experiments by Bartholomew *et al.* revealed the first hints of a new feature in the electric dipole response besides the IVGDR: an additional enhancement in the reduced transition probability, commonly referred to as the transition strength distribution at relatively low energies (5 – 7 MeV) in several neutron-rich nuclei with mass numbers $A \approx 130 - 200$ [8]. Subsequent statistical-model calculations of neutron-capture cross sections between neutron energies of 1 and 8 MeV were found to underestimate the experimental values considerably, unless a newly observed bump in experimental γ-ray spectra was accounted for [9]. The potential importance of this feature, named the pygmy dipole resonance (PDR) in the work of Brzosko *et al.* [10], was one of the reasons for a gradually increased interest in experimental studies in the vicinity of the neutron separation energy (S_n) in the past several decades.

The collectivity of the giant resonance modes is commonly expressed in terms of the sum rules, quantifying the transition strength between the ground state and the collective state, and estimated using the corresponding multipole transition operator. It can also be viewed as a certain limit for the excitation probability of a resonance mode, distributed over many nuclear states. Most of the strength of the IVGDR is known be concentrated in the vicinity of its peak, where it exhausts nearly 100% of the energy-weighted sum rule (EWSR) for isovector electric dipole transitions [7]. This limit is also commonly referred to as the classical Thomas-Reiche-Kuhn (TRK) sum rule, expressed as [7, 11–13]:

$$\int_0^\infty \sigma_\gamma^{\text{abs}}(E_\gamma)dE_\gamma \approx 60\frac{NZ}{A}(1+\kappa) \text{ MeV·mb},\tag{1.1}$$

where $\sigma_\gamma^{\text{abs}}$ is the photoabsorption cross section, E_γ is the energy of the absorbed photon, N, Z, A are the neutron, proton, and mass numbers, respectively. A correction κ is due to meson-exchange effects and usually considered negligible. From the early experiments of Bartholomew *et al.*, it was clear that the PDR exhausts at most a few percent of the TRK rule [14], thus raising further questions regarding its collectivity [15]. The present-day understanding of the origin and properties of the PDR remains quite limited, leaving plenty of room for new studies, including the one presented in this thesis.

1.1 Brief introduction to the pygmy dipole resonance

The observations of the PDR in the vicinity of the neutron separation energy, or threshold, in neutron-rich nuclei naturally suggested that its emergence might be linked to the neutron excess in these nuclei. The macroscopic pictures of the IVGDR, quite successful in describing
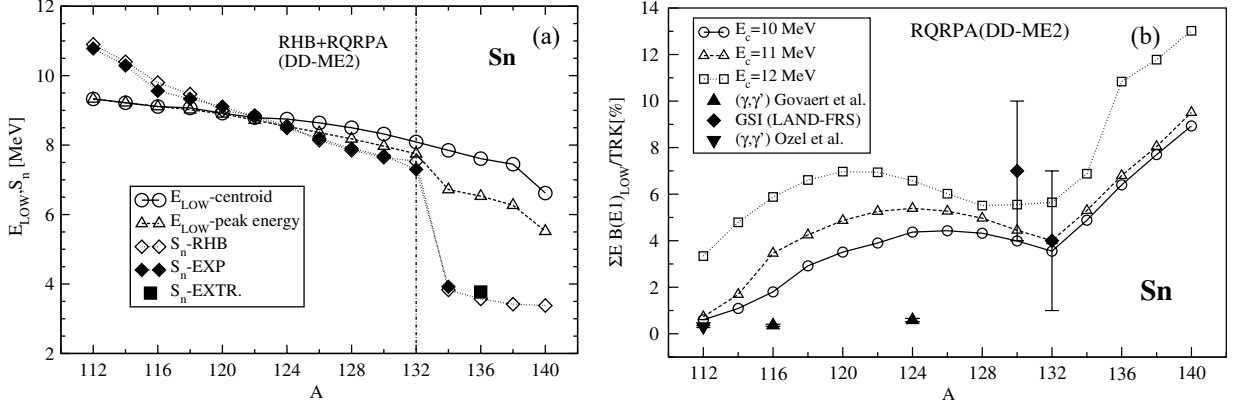
Figure 1.1: (a) Calculated peak and centroid energies of the PDR in Sn isotopes as functions of the mass number calculated within the RHB+RQRPA approach with the DD-ME2 type of effective interaction. (b) The RHB+RQRPA energy-weighted dipole strength, integrated up to the cutoff energies $E_c = 10, 11, 12$ MeV and shown as fractions of the TRK sum rule. Figures are taken from Ref. [19].

its bulk properties, formed the basis for a macroscopic description of the PDR as well. In particular, the hydrodynamical model of Steinwedel and Jensen [6], combining two types of compressible irrotational liquids (protons and neutrons) in an incompressible total liquid, was expanded by Mohan *et al.* [16] to include three types of liquid: the liquids of protons and neutrons occupying the same orbitals in the core and the neutron excess liquid. Within this approach, both the IVGDR and the PDR can be reproduced. To further reduce the number of parameters required for the description of a vibrational motion between these three components, nucleons in the core were suggested to be combined into the corresponding core liquid [17]. This model, its adaptation according to the Goldhaber-Teller picture of the IVGDR, and a comparatively new elastodynamic model [18] share the same idea of the mechanism for the PDR generation; it is described as emerging due to the oscillations of the neutron excess (skin) versus the isospin-saturated core. Despite its quite poor predictive power, this picture of the PDR is an excellent tool for a crude, approximate description of this mode, which partly makes it the most commonly appearing in the literature.

A more detailed description of the electric dipole strength distribution in medium- and heavy-mass nuclei is provided within the microscopic self-consistent mean field (MF) approaches, relying on different types of effective interactions. The earliest attempts to approach the PDR region with microscopic calculations were performed using the Hartree-Fock (HF) plus Random Phase Approximation (RPA) with Skyrme interactions, further expanded by taking the pairing correlations into account within the Hartree–Fock–Bogoliubov (HFB) plus Quasiparticle RPA (QRPA) [15]. A fairly good description of the low-lying electric dipole ($E1$) strength in open-shell nuclei was achieved using the Relativistic QRPA (RQRPA), where the interaction between nucleons is mediated by virtual mesons and photons [15]. An example of relativistic Hartree–Bogoliubov (RHB) plus RQRPA calculations for Sn isotopes by Paar [19] is shown in Fig. 1.1. Approaches beyond the RPA allow for a more accurate description of the spreading width in the strength distribution by taking into account the coupling of one-particle–one-hole (1p–1h) configurations to more complex ones. The Quasi-particle Phonon

Model (QPM) (see [15] and references therein) is one of the approaches of this kind, exploiting the solutions of the QRPA to span a one-phonon basis and build up more complex two- and three-phonon states. A self-consistent alternative of the QPM is the Relativistic Quasi-particle Time Blocking Approximation (RQTBA), which also includes the quasi-particle–phonon coupling for the description of the strength. Among other methods, solving the Vlasov equation in the semi-classical limit of the Time Dependent Hartree Fock (TDHF) approach has also been actively and quite successfully used for the description of the PDR (see e.g. [20, 21]). A comprehensive overview of these and other existing microscopic models with their advantages and drawbacks has been previously presented in Ref. [19] and recently recapped and updated in Ref. [15].

Considering the characteristics of the PDR (or, rather, the low-lying $E1$ strength), the vast majority of these microscopic approaches reveal several common trends [14, 19]. Firstly, its energy centroid shifts gradually towards lower energies with increasing neutron number. Secondly, there is a net increase of the total integrated strength below the neutron threshold with increasing proton-neutron asymmetry, often expressed as $\alpha = (N - Z)/A$, also accompanied by abrupt changes in the close proximity to a shell closure. Some of these observations have indeed been confirmed in experimental studies. Photonuclear reactions and, specifically, high-resolution photon scattering (γ, γ') or Nuclear Resonance Fluorescence (NRF) experiments are one of the most plentiful sources of systematic information on the low-lying $E1$ strength strength below the neutron threshold [14, 22]. The photon probe is fully absorbed by a target nucleus and interacts with it as a whole, thus being highly selective with respect to dipole excitations of the isovector type. High-purity Ge detectors employed in such analyses allow for a high-energy resolution spectroscopic study of various fine structures and the fragmentation of the strength within the PDR region. The state-to-state analysis of resolved transitions can be used to extract the reduced transition probabilities $B(E1)$ in a completely model-independent way (see e.g. [23]). For example, the NRF experiments on several Ca isotopes have revealed a somewhat non-linear evolution of the $E1$ strength with neutron number, rather than an intuitively expected monotonous increase according to the neutron-skin oscillation picture [24].

The NRF method, however, suffers from some limitations, which might be critical for the PDR studies. Most importantly, certain assumptions need to be made to account for unresolved transitions due to the experimental sensitivity limit and branching ratios of high-lying states. In NRF experiments using bremsstrahlung beams, e.g. at the γELBE facility at the Helmholtz-Zentrum Dresden-Rossendorf [25], the latter problem can be solved with a statistical-model analysis of the continuous spectrum (see e.g. [23]). Alternatively, information on final populated states can be extracted provided a priori known energies of incident bremsstrahlung photons in tagged-photon experiments. In this case, the energy of the electrons coincident with the absorbed photons is also measured (see e.g. the NEPTUN setup at TU Darmstadt [26]). Moreover, NRF with high-intensity quasi-monoenergetic photon beams from the High Intensity γ-ray Source (HIγS) facility [27] produced via Compton back-scattering at the Duke Free Electron Laser Laboratory is the most recent modification of this method, which is specifically designed to avoid the above-mentioned problems of NRF studies with bremsstrahlung beams.

The need for introducing additional corrections to the state-to-state NRF results is especially evident from their comparison with the strength distributions from relativistic proton

scattering in extreme forward angles. The Coulomb excitation in such kinematic conditions is the dominant interaction mechanism, and both the $E1$ and $M1$ components of the strength can be obtained with a multipole decomposition analysis (MDA) (see e.g. [28]). Extraction of the total strength over a wide energy range is an advantage of this method, despite some model dependence introduced through the MDA. Such experiments on relatively light-to heavy-mass nuclei have been successfully performed at the Research Center for Nuclear Physics (RCNP) [29] and iThemba LABS [30]. Coulomb excitation is also employed in experiments in inverse kinematics using radioactive ion beams, produced through fragmentation of a primary beam (e.g. ^{238}U [31]) in a collision with a light-nucleus target. These experiments allow for the study of unstable, neutron-rich nuclei away from the valley of stability, thus providing unique constraints for theoretical calculations. However, a certain fraction of the PDR strength below the neutron threshold remains unobserved, which makes a comparison with e.g. NRF results on stable targets quite challenging.

Another way to approach the $E1$ strength below the neutron threshold in stable nuclei and nuclei close to the valley of stability is the Oslo method [33–35], which is the main method applied in this thesis. The statistical properties, such as the nuclear level density and γ-ray strength function introduced in the following chapter, are extracted from particle-γ coincidence data and normalized to auxiliary experimental data. The details of this technique in application to Sn isotopes are presented in Sec. 3.3. A certain advantage of the Oslo method is the ability to extract to the dipole strength distribution down to low γ energies; this part of the dipole response includes not only the main concentration of the PDR strength, but also the so-called scissors $M1$ mode (see e.g. [36]) and an additional low-energy enhancement (at $\approx 1-2$ MeV), presumably of $M1$ nature (see e.g.[37]), commonly referred to as an upbend. Due to the dependence of the Oslo method on additional experimental and theoretical inputs for the normalization of the data, any additional experimental constraints below the neutron threshold are highly desired to benchmark the Oslo method results.

An important property of the $E1$ strength in the PDR region has been discovered using complementary (α, α'), $(^{17}$O, ^{17}O$'\gamma)$, and $(p, p'\gamma)$ hadron probes in addition to the NRF results. Such multi-messenger experiments on ^{140}Ce, ^{138}Ba, ^{124}Sn, ^{90,94}Zr [38–41] revealed a mixed isoscalar-isovector nature of the low-lying strength. The observed distributions of 1^- states can be split into two groups: lower-lying states of mixed nature populated through both isoscalar $((\alpha, \alpha')$, $(^{17}$O, ^{17}O$'\gamma)$, $(p, p'\gamma)$ in [32]) and isovector $((\gamma, \gamma')$, (p, p') in [42]) probes and a higher-lying group of states suppressed in the isoscalar response. Two distinct groups of 1^- states are clearly seen in the (α, α'), (p, p'), and (γ, γ') results for ^{140}Ce in Fig. 1.2. This splitting is also a well-known feature from theoretical calculations (see e.g. [21]), predicting a considerable neutron contribution in transition densities close to the nuclear surface. The suppression of the isoscalar and the presence of the isovector response at higher energies is interpreted as a predominant contribution of the tail of the IVGDR. These experimental observations and the accompanying theoretical descriptions are well in line with the neutron-skin picture of the PDR. The isoscalar-isovector splitting can be viewed as one of the key criteria for the theoretical definition of the PDR [15].

This splitting is closely related to a still unanswered question on the collectivity of the low-lying $E1$ strength, i.e. whether it stems from a coherent nucleon motion or consists of uncorrelated 1p–1h contributions. No consensus has been reached within theory so far; some of the approaches, such as, e.g., RQRPA and RQTBA [19, 40], strongly suggest a certain
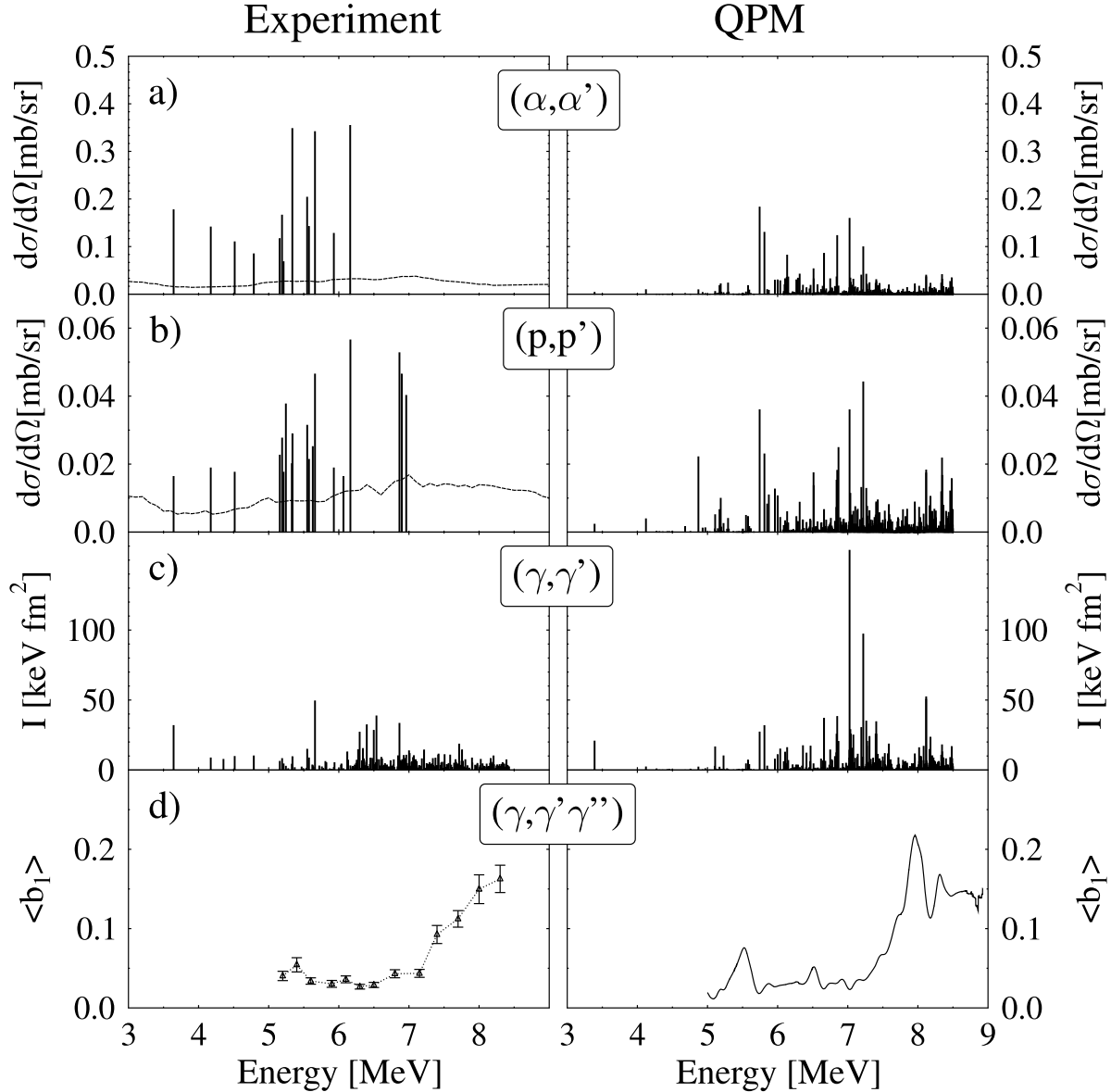
Figure 1.2: The experimental strength distributions extracted in (a) (α,α'), (b) $(p,p'\gamma)$, and (c) (γ,γ') reactions on ^{140}Ce. The right column shows the corresponding QPM calculations. In (d) the averaged branching ratio to the first excited state is shown. Figures are taken from Ref. [32].

degree of collectivity, while in other works it has not been confirmed (as in e.g. [43]). The present status of the theoretical and experimental studies suggests, however, the collective nature of the isoscalar component of the PDR and a non-collective nature of the isovector part [15]. Experiments using the one-nucleon transfer reaction (d,p) have recently been shown to yield new information on the microscopic 1p–1h structure of the strength in the PDR region [44].

Among the unsolved questions, first formulated in Ref. [45] and recently summarized in

Ref. [15], a further investigation of the collectivity and isospin properties of the low-lying $E1$ strength comprise only a small fraction of possible avenues of the PDR studies. Characteristics of the PDR in deformed nuclei and its coexistence with other "pygmy" modes of other multipolarities are currently two completely open questions. The neutron-skin picture of this strength has also been questioned in several earlier works, suggesting that it might rather be a manifestation of the dipole toroidal mode [46, 47]. Despite the fact that experimental studies have already been performed for some neutron-rich, unstable nuclei, the evolution of the PDR in stable isotopes of different elements is far from being completely understood and remains a subject for further investigations. In this regard, the Oslo method is our technique of choice to extract the full dipole strength below the neutron threshold.

1.2   Implications of the PDR: neutron skins, equation of state, nucleosynthesis

The potential connection of the PDR to the neutron excess within the macroscopic picture, combined with the first experimental observations of the enhanced low-lying $E1$ strength in neutron-rich nuclei, inspired a series of exciting studies on several far-reaching implications of this puzzling mode. In particular, correlations between the low-lying $E1$ strength, the neutron skin thickness[1], and the symmetry energy in the equation of state (EoS) of neutron-rich matter have been the focus of a large number of publications since the early 2000s. Besides a general interest for the nuclear structure studies and benchmarking of theoretical approaches, the neutron skin thickness in heavy nuclei, specifically in ^{208}Pb, has been identified as a perfect observable to place a stringent experimental constraint on the density dependence of the EoS [48]. Experimental information on neutron radii remains rather scarce, and the most accurate estimates so far have been extracted in the parity radius experiment (PREX) at the Jefferson Laboratory for ^{208}Pb in parity violating electron scattering [49] (despite some technical issues affecting the statistical accuracy) and, quite recently, in the updated experiment PREX-2 [50]. The far-reaching objective of these studies was to exploit similarities of the composition (neutron-rich matter) and conditions (density, pressure) established in the neutron skin and the crust of a neutron star to determine the properties of the latter, such as radii and transition density from a solid crust to a liquid mantle [49]. The thicker the neutron skin, the higher the pressure analogous to the one counteracting gravitational forces in neutron stars, leading to larger neutron star radii. Correspondingly, the thicker the neutron skin, the thinner the solid neutron star crust. Further attempts to optimize the theoretical apparatus, including the error and correlation analyses, for such studies have been performed in Refs. [52, 53]. On the other hand, the first observation of gravitational waves from a binary neutron star merger GW170817 with the Advanced LIGO and Virgo detectors [54] in 2017 has been recently discussed in view of its potential to provide a new puzzle piece in the complex interplay between nuclei and neutron stars based on the mass-radius relation for the observed neutron star merger [55].

  Assuming that a measurement of the neutron radius in a single heavy nucleus can provide

---

[1]The neutron skin thickness is commonly defined as the difference of the root-mean-square neutron and proton radii in a nucleus.
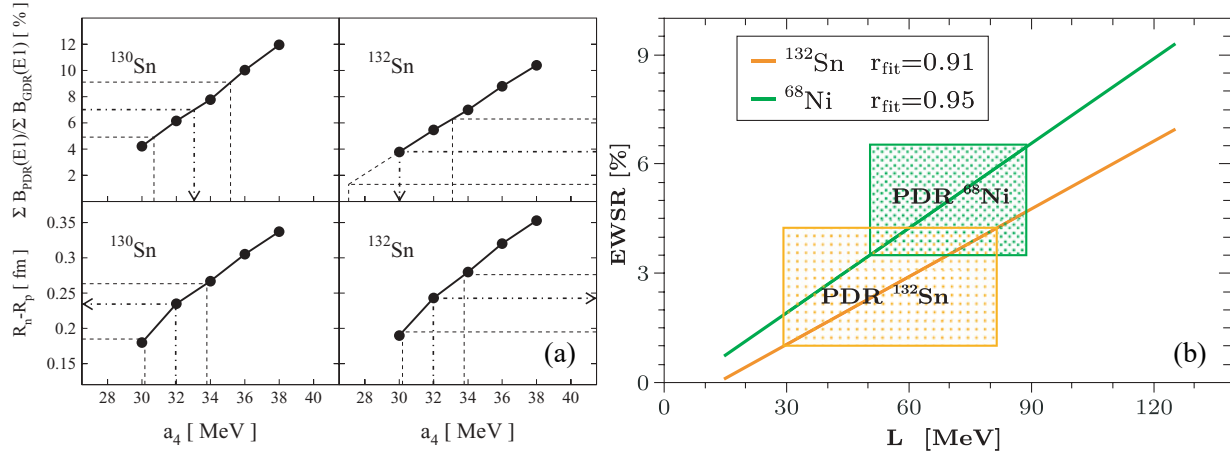
Figure 1.3: (a) Ratio of the PDR and IVGDR strength and the neutron skin thickness $R_n - R_p$ for ^{130,132}Sn versus the symmetry energy parameter J (a_4) extracted within the QRPA approach. The dot-dashed and dashed lines correspond to the experimental values and the respective uncertainties [61]. (b) The correlation between the fraction of the EWSR exhausted by the PDR in ^{68}Ni and ^{132}Sn and the symmetry energy parameter L shown together with the experimental constraints (dotted boxes) and the correlation coefficients r [62].

a constraint on neutron radii in other nuclei, the correlation between the neutron skin in Sn isotopes and the fraction of the EWSR within the PDR region (5-10 MeV) relative to that in the IVGDR region (10-25 MeV) has been studied by Piekarewicz [56] using MF plus RPA calculations. This correlation was indeed found, at least up to ^{120}Sn, where a strong correlation turns abruptly into an anti-correlation attributed to the filling of the neutron $1h_{11/2}$ orbital. Based on the subsequent correlation analysis of different observables using the self-consistent energy density functional of the Skyrme type, Reinhard and Nazarewicz suggested that an alternative, more robust constraint for the neutron skin thickness is provided by the dipole polarizability [43, 57], corresponding to the inverse energy-weighted photoabsorption cross section σ_γ [58]:

$$\alpha_D = \frac{\hbar c}{2\pi^2 e^2} \int \frac{\sigma_\gamma}{E_\gamma^2} dE_\gamma. \tag{1.2}$$

This quantity weighs the PDR contribution to the total strength more than the strength in the IVGDR region, thus being potentially more sensitive to the variations of the neutron skin. Even though one of the main claims in this study, namely a weak correlation of the skin thickness and the low-lying $E1$ strength, was confronted in the follow-up work by Piekarewicz [59], the dipole polarizability is still considered to be a more promising candidate for the extraction of the EoS parameters (see e. g.[60]).

In asymmetric nuclear matter, the EoS is commonly approached by considering the lowest terms in a Taylor expansion of the energy of a nuclear system as a function of its total density and the proton-neutron asymmetry $\delta = (\rho_n - \rho_p)/\rho$ ($\rho_{p,n}$ are the proton and neutron densities) [63]:

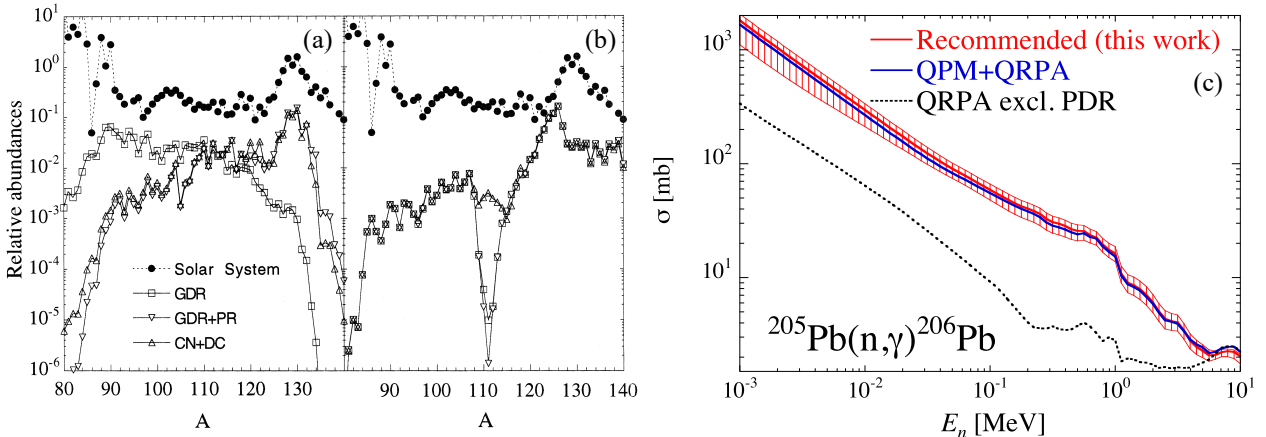$$E(\rho, \delta) = E(\rho, \delta = 0) + S(\rho)\delta^2 + \mathcal{O}(\delta^4), \tag{1.3}$$

Figure 1.4: (a) Calculated r-process abundances for the temperature $T = 10^9$ K, irradiation time τ_{irr} = 2.4 s, and neutron density 10^{20} cm^{-3} using the standard IVGDR component, the combined IVGDR and the PDR response, and the damped statistical (CN) plus direct capture contribution. (b) Same as (a) for $T = 1.5 \times 10^9$ K, irradiation time τ_{irr} = 2.4 s, and neutron density 10^{28} cm^{-3} [64]. (c) Radiative neutron-capture cross section ^{205}Pb$(n,\gamma)^{206}$Pb obtained using the experimental $(\tilde{\gamma}, \tilde{\gamma}')$ data from the HIγS facility shown together with the calculations based on the energy density functional (EDF) plus QPM with and without the PDR contribution [65].

where the first term represents the energy of symmetric matter, and the second is commonly referred to as the symmetry energy. The latter can be approximated by the first two terms of the expansion as:

$$S(\rho) = J + L\frac{\rho - \rho_0}{3\rho_0}(\rho - \rho_0) + \mathcal{O}(\delta^2). \tag{1.4}$$

Here, ρ_0 is the saturation density, J (or a_4) is the symmetry energy in pure neutron matter (at saturation $\rho = \rho_0$), and the slope L can be linked to the symmetry energy pressure. The first attempt to constrain the symmetry energy parameter J using the experimental low-lying $E1$ strength distributions was done by Klimkiewicz *et al.* for ^{130,132}Sn [61]. The analysis employed the relativistic Hartree-Bogoliubov (RHB) plus RQRPA model in order to set the correspondence between the experimental $B(E1)$ strength integrated up to 11 MeV relative to the IVGDR strength, J, and the neutron skin thickness. Analogously, the PDR data on ^{68}Ni and ^{132}Sn were used in the work of Carbone *et al.*, where almost linear relations between the PDR EWSR and J and between J and L were extracted based on different RPA models [62]. The most relevant results of the above-mentioned publications are shown in Fig. 1.3.

The presence of the PDR in the nuclear response in the vicinity of the neutron threshold, especially in neutron-rich nuclei, has also been shown to have a potential impact on the radiative neutron-capture rates relevant for the astrophysical rapid (r) neutron-capture process, responsible for about 50% of the elements heavier than Fe produced in the universe [64, 66, 67]. These rates are commonly calculated within the statistical model approach of Hauser and Feshbach[2] [68, 69], assuming that the reaction proceeds through the formation of

---

[2]In some works it is also referred to as the Wolfenstein-Hauser-Feshbach formaliam.

a compound nucleus. This matter will be discussed in more detail in the following chapters. Using a rather simplistic non-equilibrium canonical model, Goriely demonstrated in Ref. [64] an "accelerating" effect of the PDR on the neutron-capture process, leading to an increased production and abundances of elements with mass numbers of $A \sim 130$ (see Fig. 1.4). A direct impact of the PDR on the neutron-capture cross sections has been studied in, e.g., Ref. [70] using the experimental Oslo data on ^{195,196}Pt. Excluding the features identified as the PDR on top of the tail of the IVGDR from the $E1$ response reduced the neutron-capture rates by a factor of ≈ 2 for incident neutron energies up to ≈ 1 MeV. A much larger impact was observed in the work by Tonchev *et al.* [65] using experimental $E1$ and $M1$ data on ^{206}Pb and the energy density functional plus QPM, as shown in Fig. 1.4. In this case, an increase of up to five times was observed in the calculations using the total low-lying $E1$ strength as compared to those using the strength without the PDR contribution. The question of how the PDR might affect the r-process abundances from astrophysical large-scale network calculations is far from being settled, partly due to the lack of experimental constraints for the theoretical approaches used to model the low-lying $E1$ response. In terms of the amount of strength and its distribution with respect to the neutron threshold, the theoretical predictions (for example, the RQTBA calculations from Ref. [67]) are still far from reproducing the experimentally observed results, leading to a potential underestimation or overestimation of the neutron-capture rates for more neutron-rich nuclei.

1.3   PDR in Sn isotopes: current status

Throughout the history of the PDR studies, the Sn isotopic chain has always been considered an ideal candidate for a systematic investigation of the PDR evolution with gradually increasing neutron excess. Indeed, it offers the largest number of stable isotopes (10 nuclei) with the closed proton shell $Z = 50$ and little structural change between the neighboring nuclei, in addition to a perfect opportunity to study potential structural effects when approaching the $N = 82$ neutron shell closure in doubly-magic ^{132}Sn. Currently, the Sn isotopes can be considered one of the best studied chains of isotopes, from both the experimental and theoretical points of view. With experimental data available up to ^{132}Sn [31], it provides an excellent case for benchmarking various theoretical approaches. Systematic studies of the PDR strength are currently available within a large variety of theoretical frameworks, such as, for example, the relativistic RPA by Piekarewicz [56], RQRPA by Paar [19], QRPA and QTBA by Avdeenkov *et al.* [71], RQRPA and RQTBA by Litvinova *et al.*[72], QPM by Tsoneva and Lenske [73], reviewed in detail in Refs. [15, 19].

The first experimental attempts to approach the PDR region in ^{116,124}Sn have been performed with NRF measurements using bremsstrahlung by Govaert *et al.* [74], following the earlier tagged-photon scattering experiments on a natural Sn sample (with the most abundant isotopes ^{116,118,120}Sn) [75]. A pronounced maximum of the elastic photon scattering cross section at ≈ 6.5 MeV was observed in all the measurements and identified as the PDR. Later bremsstrahlung experiments at the Darmstadt High-Intensity Photon Setup (DHIPS) on ^{112,120}Sn [76] also revealed signs of resonance-like structures in both nuclei at $6 - 7$ MeV, although quite fragmented for ^{120}Sn. The summed $B(E1)$ strength for this isotope was found to fall out of the trend of increasing summed strength with increasing neutron number, set by

^{112,116,124}Sn. However, a large number of previously unobserved dipole transitions were identified in a recent high-sensitivity bremsstrahlung experiment on ^{120}Sn at the γELBE facility, yielding a value of the summed strength enhanced by a factor of $\approx 2-3$ as compared to the previous result [23]. Based on these and other NRF data alone, the total $E1$ strength indeed appears to increase with increasing neutron number.

The same isotope, ^{120}Sn, has been studied through relativistic Coulomb excitation in inelastic proton scattering at extreme forward angles at the RCNP [77]. The comparison of the summed $E1$ strength in the resolved states from the recent (γ, γ') experiment with that from the (p, p') measurements clearly demonstrated the need for an additional correction for the unknown ground state branching ratios using the statistical model analysis, which is especially relevant for transitions above ≈ 6.5 MeV. The latter brought the results of these two experiments into a much more reasonable comparison, as was shown in Ref. [23]. Moreover, a new NRF experiment on ^{120}Sn using a quasi-monoenergetic photon beam at HIγS is currently being analyzed[3] and is expected to resolve the inherent problem of the missing strength in the above-mentioned bremsstrahlung experiments. A series of similar Coulomb excitation (p, p') experiments on even-even ^{112,114,116,118,120,124}Sn at the RCNP provided unique experimental information for a systematic study of the $E1$ and $M1$ strength distributions (and, thus, the dipole polarizability) below and above the neutron threshold, including the PDR region down to excitation energies of ≈ 6 MeV and the IVGDR region up to $\approx 20-22$ MeV [42]. In all of the studied cases, a bump-like concentration of the $E1$ strength at $\approx 8-10$ MeV was observed.

The first experimental evidence of the potential PDR strength in neutron-rich, unstable nuclei was obtained in Coulomb dissociation of secondary Sn beams at the LAND-FRS facility at GSI [31]. In this pioneering work, a resonance-like feature was identified at excitation energies of ≈ 10 MeV in both ^{130}Sn and doubly-magic ^{132}Sn and was found to exhaust 7(3)% and 4(3)% of the TRK sum rule in these nuclei, respectively. The extracted strengths were limited to energies above the neutron threshold in these nuclei, which somewhat complicates a direct comparison with experimental data obtained with different techniques (e. g. the NRF data below and photoabsorption (γ, n) data above the neutron separation energy in stable Sn isotopes).

In the past decade, the heaviest stable ^{124}Sn isotope has been in particular focus of complementary studies of the low-lying $E1$ strength with probes of different isospin nature. The first study of this kind involved a direct comparison of the $E1$ strength distribution from the NRF measurements (Ref. [74] and an additional NRF experiment at the Superconducting Darmstadt Linear Accelerator (S-DALINAC)) with the strength from the α-γ coincidence experiment $(\alpha, \alpha'\gamma)$ with a 136-MeV α beam using the Big-Bite Spectrometer at the Kernfysisch Versneller Instituut in Groningen [39, 40]. An abrupt change of the $E1$ response with the α probe was observed: at excitation energies below ≈ 6.8 MeV, the strength is present in both the (γ, γ') and $(\alpha, \alpha'\gamma)$ data, whereas at higher energies the latter is practically absent (considering the sensitivity limit). This effect is clearly seen in Fig. 1.5. The interpretation of transition densities for protons and neutrons within the RQTBA approach suggested a considerable contribution of neutrons close to the nuclear surface for the lower-lying states, similar to the one expected within the neutron-skin oscillation picture of the PDR (see Fig. 1.5). The higher-lying states, on the contrary, demonstrate an out-of-phase distribution of neu-

---
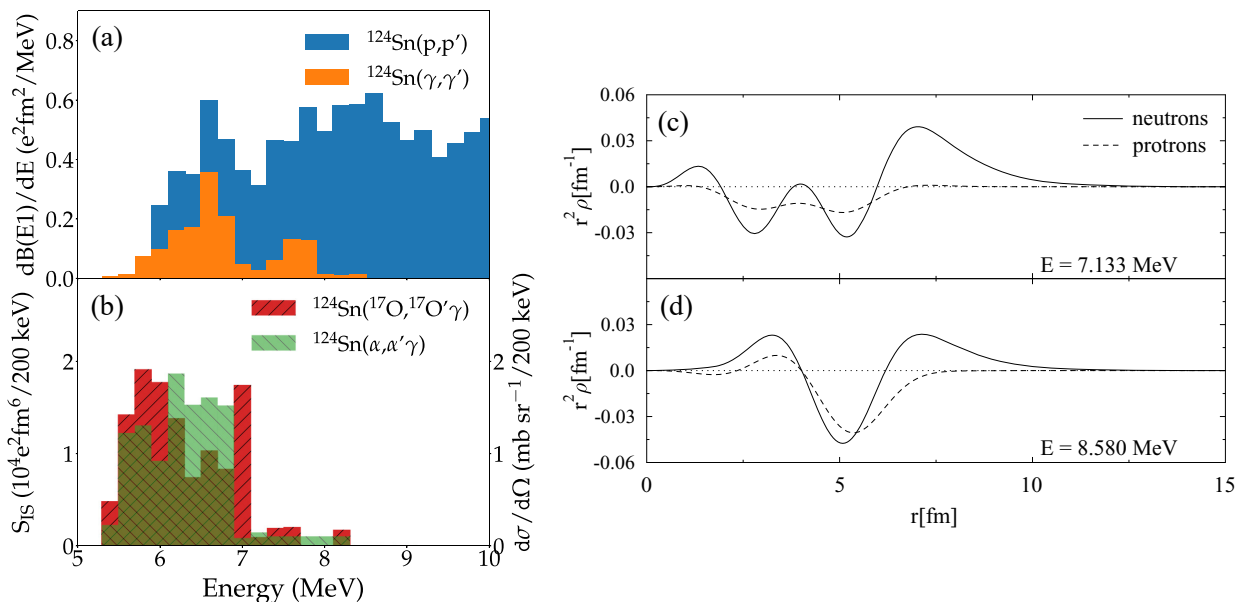
[3]J. Isaak, private communication.

Figure 1.5: Left panel: (a) Electric dipole strength distributions for ^{124}Sn extracted with the NRF and (p, p') experiments and (b) the isoscalar $E1$ strength distributions from the $(\alpha, \alpha'\gamma)$ and $(^{17}O, ^{17}O'\gamma)$ experiments [42]. Right panel: RQTBA transition densities for protons and neutrons for two states at (c) 7.133 MeV and (d) 8.580 MeV in ^{124}Sn [40].

trons and protons, more typical for the IVGDR. Combined with the earlier observations for ^{140}Ce and ^{138}Ba [38, 39], this study was the next step towards confirming the mixed isospin nature of the low-lying $E1$ response, accessible through both isovector (γ) and isoscalar (α) probes. An important further confirmation of this splitting was provided by the isoscalar strength extracted in the $(^{17}O, ^{17}O'\gamma)$ experiment [78], which was found to be concentrated at $\approx 5.5 - 7$ MeV, well in agreement with the $(\alpha, \alpha'\gamma)$ data. Finally, the recent (p, p') experiment, inducing predominantly isovector transitions by analogy with (γ, γ'), pointed at the presence of the isovector response below and above ≈ 7 MeV. The differential cross sections from the $(^{17}O, ^{17}O'\gamma)$ experiment and the $B(E1)$ strength distribution from (p, p') are also shown in Fig. 1.5.

A combined analysis of the $E1$ strength distribution from the ^{119}Sn$(d, p\gamma)^{120}$Sn experiment and the energy density functional plus QPM calculations has been recently used to provide a deeper insight into the particle-hole composition of the low-lying $E1$ strength in ^{120}Sn [79]. Several 1p–1h configurations strongly contributing between 6 and 7 MeV have been identified. On the other hand, the role of more complex complex 2-phonon+3-phonon configurations was shown to increase towards higher energies.

Finally, a series of Oslo method particle-γ coincidence experiments on Sn isotopes have been performed in order to investigate the low-lying dipole $(E1 + M1)$ strength below the neutron threshold. The ^{117,119,122}Sn and ^{116,118,121}Sn isotopes were studied in $(^3He, ^3He'\gamma)$ and $(^3He, \alpha'\gamma)$ reactions, respectively, at the Oslo Cyclotron Laboratory (OCL) with the results published in Refs. [80–83]. A peak-like structure associated with the PDR was identified in all the studied isotopes, and its bulk characteristics (energy centroid, fraction of the TRK

sum rule) were reported in Ref. [83]. In contrast to the microscopic QPM [73], RQRPA, and RQTBA [72] calculations and macroscopic estimates by Van Isacker [84], the strength of the identified feature appeared to remain essentially constant with increasing proton-neutron asymmetry. Moreover, the position of the energy centroid was shown to shift towards higher energies with increasing asymmetry at variance with the theoretical predictions [72, 73]. It is important to note that no experimental information on the low-lying strength in these isotopes, except for the NRF data on ^{116}Sn, was available to provide benchmarks for the normalization of the Oslo data at the time of this publication.

1.4 Main objectives of the work

This work is to a large extent inspired by the previous measurements on $^{116-119,121,122}$Sn at the OCL [80–83] and the recent series of (p,p') experiments on even-even ^{112,114,116,118,120,124}Sn by Bassauer *et al.* [42]. The principal goal is to shed more light on the low-lying electric dipole response and, potentially, the PDR in Sn isotopes through a consistent analysis. Due to the wide range of covered energies, the new (p,p') data can serve as an excellent benchmark for the normalization of the Oslo method γ-ray strength functions close to the neutron threshold. Moreover, the combined Oslo and (p,p') data provide the total dipole strength from ≈ 2 MeV up to ≈ 20 MeV, which can further be used for a model-based extraction of the bulk characteristics of the low-lying electric dipole strength and observing their evolution with gradually increasing proton-neutron asymmetry. This study involves several recently performed experiments on ^{117,119,120,124}Sn, analyses of the earlier collected and previously unpublished data on $^{111-113}$Sn, and a complete re-analysis of the earlier published results on $^{116-119,121,122}$Sn using updated experimental inputs for the normalization of the data.

Two additional objectives relevant for the overarching subject of this work, the evolution of the low-lying electric dipole strength in the Sn isotopes from ^{111}Sn to ^{124}Sn, are considered here: the test of the validity of the generalized Brink-Axel hypothesis [85, 86] in the PDR region and the extraction of new constraints for radiative neutron-capture cross sections of relevance for astrophysical neutron-capture processes. The Brink-Axel hypothesis, introduced in more detail in Sec. 2.2.2, is one of the key assumptions underlying the Oslo method and is also commonly adopted in statistical-model calculations. Moreover, the related question on the excitation-energy dependence of the observed strength below the neutron threshold remains a matter of ongoing debates (see Sec. 2.2.2). Finally, the statistical properties of excited nuclei obtained with the Oslo method are often found to be useful for providing indirect experimental constraints on radiative neutron-capture cross sections and rates, used as input for reaction-network simulations of heavy-element nucleosynthesis. The studied Sn isotopes are no exception in this regard, especially given that some of the heaviest stable Sn isotopes have been recently shown to be of potential interest for the so-called intermediate neutron-capture process [87].

This thesis is organized as follows. Chapter 2 provides an introduction to the statistical properties of excited nuclei studied with the Oslo method, theoretical models for their description, experimental techniques for their extraction, the Brink-Axel hypothesis, Porter-Thomas fluctuations, and statistical-model calculations. In Chapter 3 all the details regarding the performed experiments and the application of the Oslo method are presented. Chapter 4 pro-

vides the most relevant results of testing the Brink-Axel hypothesis in ^{120,124}Sn, which form the basis for Papers I and II. The evolution of the low-lying dipole strength and astrophysical implications are discussed in Chapters 5 and 6, which also include some of the discussions relevant for Papers III, IV, and V. The main findings and perspectives for future studies are summarized in Chapter 7.

Chapter 2

Statistical approach to the γ decay within the quasi-continuum regime

In this thesis, the low-lying dipole strength is studied using the γ-ray strength function (GSF), which describes the average photoexcitation and γ-decay properties of nuclei in a similar way as the average cross sections. Together with the nuclear level density (NLD), the GSF is one of the key statistical nuclear characteristics employed in the statistical model approach, formulated by Hauser and Feshbach in 1952 [68] in an attempt to estimate cross sections of inelastic neutron scattering proceeding through the formation of a compound nucleus.

The latter is the central concept of the statistical model, introduced by Bohr in his seminal work on the nuclear structure and the neutron-capture process in 1936 [88]. It applies to the description of binary reactions of type:

$$a + X \rightarrow C \rightarrow b + Y, \tag{2.1}$$

where C denotes a compound system of a projectile a plus a target nucleus X. Depending on the reaction time scale, one can distinguish between different reaction mechanisms. If it is comparable with the time needed for a projectile particle to pass through the nucleus without any interactions, a direct reaction takes place. On the other hand, the interaction of a particle with many nucleons within the nucleus, and thus the redistribution of its energy among a large number of degrees of freedom, takes a longer time and leads to the formation of a complex system, which is commonly referred to as the compound nucleus. This process is accompanied by strong configuration mixing, in the sense that different possible configurations are strongly coupled with each other and their properties are distributed over excited states lying within the same energy region. This picture implies that the decay channel of the compound nucleus into the particle b and the residual nucleus Y is no longer coupled to its initial formation channel, or, in other words, the compound nucleus "forgets" the way it was formed. In this case, the cross-section of the above-mentioned reaction can be written as [89, 90]:

$$\sigma(\alpha, \beta) = \sigma_C(\alpha) G_C(\beta), \tag{2.2}$$

where $\sigma_C(\alpha)$ is a cross section of forming the compound nucleus through a certain entrance channel α in the $a + X$ process, and $G_C(\beta)$ is the decay probability of the compound nucleus through an exit channel β, leaving the residual nucleus Y and the emitted particle b. For an

intermediate, pre-equilibrium process, the exit channel remains somewhat correlated with the entrance channel, but not as strongly as under the direct reaction mechanism.

The formation of a compound nucleus happens at relatively high excitation energies, where different excited states are closely spaced. Within a rather crude semi-classical picture [90], the level spacing D can be associated with the period of nucleon motion ($P \sim 1/D$), resulting in a repetition of "the same" configuration. For a compound state to exist, it is essential that this period is significantly smaller than its decay lifetime[1]. This is one of the key assumptions underlying the particle evaporation studies and the Oslo method, discussed in the following sections.

In this work, the analysis is limited to the excited states below the neutron threshold, for which γ decay is the only decay channel we are going to consider. Here, the average level spacing D and the average γ-decay width Γ_γ, related to the lifetime τ_γ of excited states through $\Gamma_\gamma = \hbar/\tau_\gamma$, can be used to separate between the so-called discrete ($D \gg \Gamma_\gamma$), quasi-continuum ($D \geq \Gamma_\gamma$), and continuum ($D \leq \Gamma_\gamma$) regimes. The Oslo method, employed in this work, operates within the quasi-continuum energy range with decays of closely spaced excited states. Here, the experimental energy resolution, even in high-resolution studies, becomes too large to distinguish between individual states, which should rather be treated in terms of average quantities.

Two of them, the NLD and the GSF, will be introduced in the following sections, which also include a discussion of various theoretical approaches and experimental techniques used to extract them. Furthermore, the connection between these two functions and the radiative neutron-capture cross sections within the Hauser-Feshbach approach is discussed at the end of this chapter.

2.1   The nuclear level density

Besides the connection in the classical sense to the period of the intranuclear motion, the average level spacing D also determines one more characteristic of the nuclear structure: the nuclear level density (NLD)

$$\rho = \frac{1}{D(E, J, \pi)} = \frac{\Delta N(E, J, \pi)}{\Delta E}, \tag{2.3}$$

defined as a number of levels $\Delta N(E, J, \pi)$ of a certain spin J and parity π per excitation energy unit ΔE. At sufficiently high excitation energies, equal positive and negative parity contributions are often assumed, and the parity dependence is reduced to a factor of 1/2 in Eq. (2.3). The NLD dependent on spin and excitation energy is often referred to as the *partial* NLD, whereas the *total* NLD is obtained by summing over all possible contributing spins and both parities. It is also important to emphasize that the nuclear *state* density is determined by all possible magnetic substates for each level of spin J:

$$\rho^{st}(E_x) = \sum_J (2J + 1)\rho(E_x, J). \tag{2.4}$$

---

[1]It is important to note that this simplistic consideration implies the average spacing between levels of equal spin and parity [90].

On par with the optical model potential, the NLD is a key ingredient for modeling scattering reactions [91]. In general, it enters any statistical-model calculations, and thus appropriate theoretical models with wide applicability ranges, preferably over the whole nuclear chart, are required in addition to available experimental data for isotopes close to and within the valley of stability.

2.1.1 Theoretical NLD models

The first pivotal theoretical expression for the NLD was derived in 1936 by Bethe [92] by treating a nucleus as a group of $A = N + Z$ non-interacting fermions (ideal Fermi gas) with an equally spaced single-particle spectrum. The state density within this approach can be written as [93, 94]:

$$\rho_{FG}^{st}(E_x) = \frac{\sqrt{\pi}2^{1/4}e^{\tilde{a}\sqrt{2E_x}}}{12\sqrt{\tilde{a}}E_x^{5/4}}, \tag{2.5}$$

where E_x denotes the excitation energy above the zero point energy of the Fermi gas, and $\tilde{a}$ is determined by the average Fermi energy of protons and neutrons ϵ_f as $\tilde{a} = \pi\sqrt{A/2\epsilon_f}$. Using this relation as a starting point, the Gaussian distribution of different projections of the total angular momentum at a given E_x can be further considered to derive the partial density of nuclear levels as [95–97]:

$$\rho_{FG}(E_x, J) \simeq \frac{\sqrt{\pi}e^{2\sqrt{aE_x}}}{12\sqrt{2\pi}\sigma a^{1/4}E_x^{5/4}} \frac{(2J+1)}{2\sigma^2} \exp\left(-\frac{(J+1/2)^2}{2\sigma^2}\right). \tag{2.6}$$

Here, $a = \frac{1}{6}\pi^2(g_p + g_n)$ is commonly referred to as the level density parameter and determined by the sum g of proton and neutron single-particle level densities g_p and g_n, respectively. The parameter σ, or the spin-cutoff parameter, corresponds to the dispersion of the above-mentioned Gaussian distribution and can be expressed through the mean-square magnetic quantum number for single-particle states $\langle m^2 \rangle$ and thermodynamic temperature T:

$$\sigma^2 = g\langle m^2 \rangle T. \tag{2.7}$$

Moreover, this parameter explicitly enters what can be considered a definition of the moment of inertia of a heated nucleus $\mathcal{I} = \hbar^2 g\langle m^2 \rangle$ [98] (in some sources $\hbar = 1$ is assumed [91]). It should also be noted that σ is a parameter dependent on the excitation energy through T.

Finally, the temperature within the Fermi gas approach is linked to the excitation energy E_x through a rather simple relation:

$$E_x = aT^2. \tag{2.8}$$

This NLD model, established in the pioneering work of Bethe and commonly referred to as the Fermi gas (FG) model, provides an overall correct energy dependence of the level density over a wide energy range below and above the neutron separation energy. However, due to the inherent simplicity of the Fermi gas approach, it does not account for several important nuclear structure effects. Most notably, it disregards shell and collective effects and does not include any treatment of pairing correlations. The latter issue can be explicitly revealed in a comparison of observed NLDs of even-even, even-odd, and odd-odd nuclei with different mass numbers when attempting to describe them with the FG model. These nuclei appear

to fall into three different groups with respect to the level density parameter a [99]. To effectively account for the extra energy required to break Cooper pairs of coupled nucleons, the excitation energy in Eq. (2.6) should be redefined by correcting for proton and/or neutron pairing energies Δ, as was first suggested in Ref. [100]:

$$E'_x = \begin{cases} E_x - \Delta_n - \Delta_p, & \text{for even-even nuclei} \\ E_x - \Delta_p \text{ or } E_x - \Delta_n, & \text{for odd nuclei} \\ E_x, & \text{for odd-odd nuclei.} \end{cases} \tag{2.9}$$

The pairing energies can be estimated based on mass differences of neighboring nuclei or, e.g., adopted to be $12/\sqrt{A}$ as suggested in Ref. [91]. This "backshift" assumes that all corrections due to shell and collective effects should be then introduced in a. In an attempt to redistribute these corrections between both of these parameters, an additional correction δ is usually subtracted from the corrected energies E'_x in Eq. (2.9) [101].

Several phenomenological models for the level density parameter have been proposed in the literature to effectively introduce the damping of shell and collective effects with excitation energy [102]. In general, it is quite challenging to disentangle corrections due to both of these effects in the level density parameter and the energy backshift. Therefore, for the majority of practical applications, both of these parameters are determined from the fit to experimental data. In this thesis, we are going to exploit the back-shifted Fermi gas (BSFG) as presented in Ref. [103]:

$$\rho_{BSFG}(E_x) = \frac{e^{2\sqrt{a(E_x - E_1)}}}{12\sqrt{2}\sigma a^{1/4}(E_x - E_1)^{5/4}}, \tag{2.10}$$

where the level density and the backshift parameters a and E_1 ($E'_x = E_x - E_1$) are found from fitting low-lying discrete states and $\rho(S_n)$ values obtained from s-wave neutron resonance spacings in 310 nuclei between ^{18}F and ^{251}Cf.

The spin-cutoff parameter σ is an additional source of uncertainty of NLD values obtained with the BSFG model, which may differ significantly depending on the approach used to estimate σ. Among the commonly used expressions is the one proposed in Refs. [97, 104] and based on the mean-square magnetic quantum number $\langle m^2 \rangle$ by Jensen and Luttinger [105]:

$$\sigma^2(E'_x) = 0.0888aTA^{2/3} = 0.0888a\sqrt{E'_x/a}A^{2/3}, \tag{2.11}$$

which suggests a rather slow variation of σ^2 with excitation energy. By treating a nucleus as a sphere having a rigid body moment of inertia, the spin-cutoff parameter takes the following form [106]:

$$\sigma^2(E'_x) = 0.0145\sqrt{E'_x/a}A^{5/3}, \tag{2.12}$$

The rigid-body approach is also commonly used with a slightly modified expression for the temperature, $E'_x = aT^2 - T$, as suggested by Dilg *et al.* [107], which was found to be quite reasonable at relatively low energies [103]:

$$\sigma^2(E'_x) = 0.0146\frac{1 + \sqrt{1 + 4aE'_x}}{2a}A^{5/3}. \tag{2.13}$$

Several other parametrizations have also been proposed in Refs. [104, 108] as possible alternatives to the above-mentioned expressions.

Another frequently used model for the NLD was first suggested by Ericson in 1959 [96], who observed that the logarithm of a cumulative number of levels $\log N(E_x)$ in medium-mass nuclei is a linear function of excitation energy up to ≈ 10 MeV, and the slope can be associated with the constant nuclear temperature T. The NLD in this constant-temperature (CT) approach is thus given by:

$$\rho_{CT}(E_x) = \frac{dN(E_x)}{dE_x} = \frac{N(E_x)}{T} = \frac{1}{T}e^{\frac{E_x-E_0}{T}}, \tag{2.14}$$

where T and E_0 are commonly treated as free parameters when fitting experimental data.

The constant-temperature regime can often be observed in Oslo method NLDs to be valid up to the neutron separation energy [109]. It can be interpreted in terms of a first-order phase transition at a certain constant temperature, characterized by a gradual breaking of Cooper pairs of nucleons, which become available for forming new configurations. This process continues up to energies around or above the neutron threshold, where the temperature starts to increase, and the Fermi gas description becomes more appropriate (see [109] and references therein). To combine both of these models for a description of NLDs over large energy ranges, a composite formula was suggested by Gilbert and Cameron in Ref. [97]. Within this approach, a continuous NLD is presented by the CT model up to a point of tangency with the BSFG trend at relatively high excitation energies.

A more rigorous attempt to incorporate shell effects as well as superfluid and collective effects driven by the residual interaction was suggested by Ignatyuk within the so-called generalized superfluid model (GSM) [110]. It accounts for these complex effects almost as efficiently as microscopic approaches, while still being a relatively simple phenomenological model. The NLD is factorized into a contribution due to quasi-particle excitations, treated within the superconductivity theory, and enhancement factors due to vibrations and rotations. This model is somewhat similar to the composite formula by Gilbert and Cameron in the sense that it describes a phase transition between the superfluid state with a strong influence of pairing correlations on creation of possible nucleon configurations at relatively low energies and a more Fermi-gas-like behavior at higher energies. Even though this model provides the next step towards more realistic microscopic calculations, there is still a set of parameters to be adjusted to achieve a better fit to experimental data.

The microscopic approaches to the NLD are expected to have an improved predictive power away from the valley of stability as compared to the above-mentioned phenomenological models, generally based on numerous simplifications and adjustments to available experimental data for stable nuclei. One of two most commonly used statistical methods is the microscopic version of the generalized superfluid model (see [91] and references therein), which estimates the NLD from realistic single-particle level schemes and accounts for collective effects similarly to how it is done within the phenomenological version of this model. Statistical calculations by Goriely from Ref. [118] employed ground-state properties based on the extended Thomas–Fermi plus Strutinsky integral (ETFSI) and provided the first global microscopic NLD with shell and pairing effects included explicitly. The latter modification of this approach used HF plus Bardeen–Cooper–Schrieffer (BCS) predictions of the ground-state properties and also included deformation effects in single-particle spectra and vibrational collective excitations [111, 119].
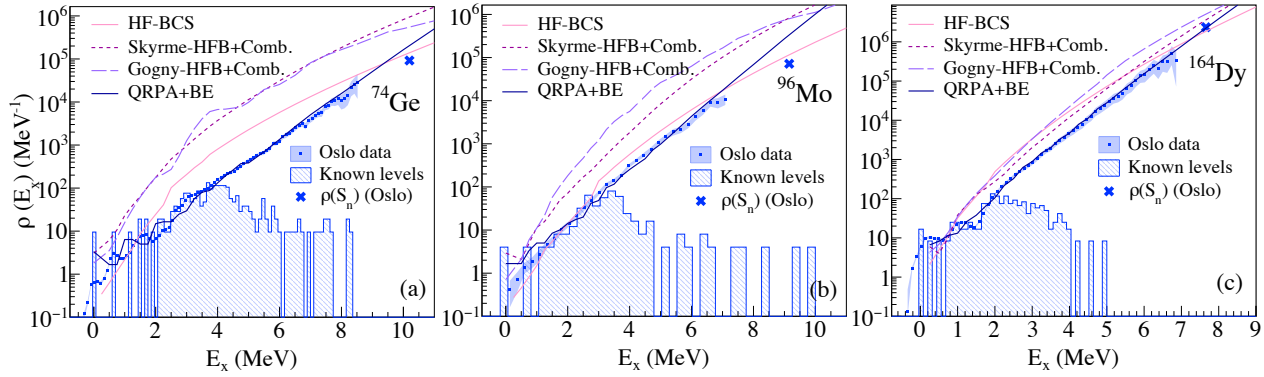
Figure 2.1: Comparison of the experimental NLDs extracted with the Oslo method with the microscopic HF+BCS [111], Skyrme+HFB+combinatorial (Comb.) [112], temperature-dependent Gogny+HFB+combinatorial [113], and QRPA+boson expansion (BE) [114] calculations for (a) ^{74}Ge, (b) ^{96}Mo, (c) ^{164}Dy. The Oslo data were taken from Refs. [115–117].

On the other hand, combinatorial approaches provide access to the low-energy NLD by effectively including non-statistical effects, which can not be treated within statistical methods. In calculations by Hilaire *et al.* [120], the combinatorial approach was implemented based on single-particle level schemes obtained within the HFB approach with the D1S Gogny effective interaction to extract spin- and parity-dependent NLDs in nuclei with $26 \leq A \leq 250$. Later on, vibrational effects due to phonon excitations were included to improve the performance of this model, but this time using a Skyrme-type effective interaction [112]. The refined calculations with single-particle levels and collective properties described with the updated D1M-type of the Gogny interaction were presented in Ref. [113]. A conceptually new approach to global calculations of NLDs has recently been proposed by Hilaire *et al.* [114] based on the boson expansion of QRPA excitations, significantly improving the reproduction of experimental results compared to all present statistical and combinatorial approaches. In particular, it demonstrates an excellent agreement with Oslo method results as well as s-wave resonance spacings for medium to heavy nuclei. A comparison of some of the above-mentioned microscopic calculations with the Oslo method data is shown in Figure 2.1.

Finally, the configuration interaction shell model approach to level densities can provide access to correlations beyond the mean field theory. It is known to be quite computationally demanding for the majority of medium-mass and all heavy nuclei due to increasingly large model spaces required to solve the eigenvalue problem of the shell-model Hamiltonian matrix. For example, the application of quantum Monte Carlo methods [121] in such cases allows to work with significantly larger model spaces than the conventional Lanczos diagonalization method can handle. Recent advances in this shell model Monte-Carlo (SMMC) approach allowed to estimate NLDs of odd nuclei and achieve an excellent agreement with discrete low-lying tabulated levels and neutron resonance data in spherical and deformed nuclei up to relatively heavy Sm, Nd, and Dy isotopes [122, 123]. Furthermore, numerous codes have been recently developed to exploit the power of massively parallel computation and perform shell-model calculations with the conventional Lanczos method (e.g. KSHELL [124]).

2.1.2 Experimental approaches to the extraction of the NLD

The parameters in phenomenological approaches are derived from available experimental data, which are also used to test microscopic models. Several methods have been proposed to extract total and, in some cases, partial NLDs as function of excitation energy up to several tens of MeV. The most straightforward approach to obtaining NLDs at low excitation energies, well below the particle threshold, is to rely on spectroscopic data from, e.g., inelastic proton, neutron, alpha scattering, and various transfer reactions and simply count tabulated levels collected in, e.g., the Evaluated Nuclear Structure Data Files (ENSDF) [125]. The main advantages of this approach are its absolute model independence and access to information on spins and parities, which can further be used to estimate the spin-cutoff value. Moreover, these data are available for a large number of exotic nuclei, and they thus become the only available source of experimental information away from the stability. The NLDs obtained in this manner are, however, limited to low excitation energies ($1-3$ MeV). Above these energies, the level spacing decreases, the experimental resolution is no longer sufficient to distinguish between individual states, and the level schemes can no longer be considered complete.

At higher excitation energies, resonance capture of low-energy s- or p-wave neutrons yields information on the NLD in the immediate vicinity of the neutron threshold. For example, capture of thermal neutrons with angular momentum $l = 0$ populates only resonance states with spins $J_t + 1/2$ and $J_t - 1/2$ in the compound nucleus, determined by the ground state spin of the target J_t. Even though this method allows for resolving states with certain parity and spin among all closely overlapping states, some assumptions need to be made regarding the parity ratio and the spin distribution at these energies to estimate the total NLD. Moreover, the low energies of incident neutrons limit the extracted information to only one NLD data point close to S_n. Despite these limitations, a wealth of neutron resonance data collected in the Reference Input Parameter Library (RIPL-3) [91] or the Atlas of Neutron Resonances by Mughabghab [126] provides crucial benchmarks for NLD values at relatively high excitation energies.

Historically, the first method used to access the NLD over a relatively wide energy range, well above and below the particle threshold, was particle evaporation studies in compound-nucleus reactions (see e.g. [127]). This method exploits the fact that the energy spectrum of emitted (evaporated) particles from a compound nucleus is expected to be proportional to the level density in the residual nucleus [89]. The spectra of evaporated protons, neutrons, and alpha particles are usually studied in light-ion-induced reactions (p and α) or in reactions with relatively heavy ions (^{11}B, ^{12}C, ^{16}O, ^{19}F, ^{28}Si) [102]. Using heavier ions ensures that the reaction proceeds through a compound nucleus formation and that the contribution due to pre-equilibrium mechanisms is negligible [128]. The latter is crucial for statistical-model calculations used for the extraction of the total NLD. Such reactions also enable the population of wide excitation energy and spin ranges, which can further be used to extract information on the spin dependence of the NLD. In such studies, one should take into account that evaporation spectra are, in general, due to multi-step decays, which might complicate the analysis. Moreover, the method is essentially model-dependent and relies on adopted optical model parameters used to calculate particle transmission coefficients [102] and some model calculations and/or experimental data to normalize the total NLD.

At even higher energies, where multi-step decays complicate the analysis of evaporation
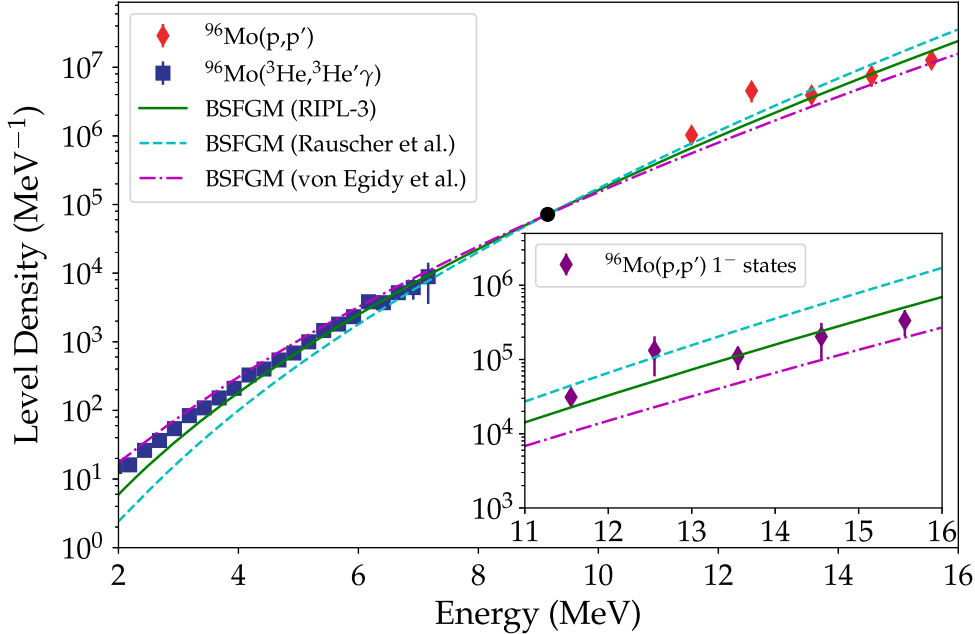
Figure 2.2: Total NLD of ^{96}Mo deduced from the fine structure of the (p, p') data in the IVGDR region (red diamonds). The Oslo method results are shown as blue squares together with several parametrizations of the BSFG model [91, 108, 129]. The Inlet shows the density of 1^- states. Figure is reprinted with permission from Ref. [130].

spectra, another method involving the compound-nucleus mechanism is the Ericson fluctuation analysis. Within the statistical theory, Ericson demonstrated that not only average cross-sections but also variances in the energy dependence of cross sections can be estimated for reactions proceeding through a compound nucleus [131]. The latter can be used to extract the NLD. Alternatively, the NLD can be obtained from exit channel transmission coefficients and partial decay widths. These methods have been successfully applied to total and partial neutron cross sections of light- and medium-mass nuclei in Refs. [132–134]. As the NLD increases, Ericson fluctuations become smaller and can no longer be used to produce reliable results. For this reason, the applicability of this analysis was limited up to ≈ 25 MeV in the above-mentioned works.

A somewhat similar technique was proposed by Kalmykov *et al.* in Ref. [135] to extract the density of 1^+ states based on the fine structure of the Gamow-Teller resonance in ^{90}Nb, studied in the high-energy (^{3}He, t) reaction under scattering angles close to $0°$. It has also been applied to extract the density of $2^\pm$ states from fluctuations of cross sections in the energy ranges corresponding to the $M2$ and $E2$ giant resonances in ^{58}Ni and ^{90}Zr, studied in the (e, e') and (p, p') reactions [136]. Moreover, the density of 1^- states in ^{208}Pb and ^{96}Mo has been obtained from fluctuations of the cross section in the IVGDR region from the (p, p') reaction under extreme forward angles [130, 137]. In the latter two cases, the deduced total NLDs were combined with the corresponding Oslo method results in Refs. [130, 138], where both experiments were shown to agree quite well with respect to the same BSFG model. An example of such a comparison for the ^{96}Mo isotope is shown in Fig. 2.2.

Finally, the Oslo method is currently the most plentiful source of NLDs below the neutron threshold in numerous medium- to heavy-mass nuclei [109]. In general, the Oslo data reproduce the low-lying states quite well and agree fairly well with available particle evaporation NLDs (see e.g. [139]). The Oslo NLDs rely on several assumptions, models, and auxiliary experimental data for the normalization. This matter will be discussed in more detail in Sec. 3.3.4. In particular, the NLDs at the neutron threshold obtained from neutron resonance studies are crucial for constraining the slopes of the exponentially growing Oslo method level densities above excitation energies, where level schemes are no longer complete. Moreover, the Oslo results provide important input for Hauser-Feshbach calculations of radiative neutron-capture cross sections (see e.g. [140]). In this regard, the modifications of the Oslo method, such as the β-Oslo method [141] and the Oslo method in inverse kinematics [142], are a promising step forward in estimating neutron-capture rates relevant for the astrophysical r process, involving unstable nuclei.

2.2 The γ-ray strength function

At relatively high excitation energies, where it becomes more convenient to refer to ensembles of closely grouped states in terms of the NLD rather than individual states, the concept of individual transition widths is commonly substituted by the γ-ray strength function (GSF). It characterizes the average γ-decay pattern and can be defined as the average reduced partial radiative width per unit energy interval. Historically, there has been no unified approach to the definition of the GSF up until the 1970s. In this thesis, we are going to adopt the definition as suggested by Bartholomew in Ref. [143], most commonly used in modern publications and nuclear reaction codes (e.g. TALYS). For photon emissions from a group of initial excited states with spin J_i in the vicinity of E_i to a lower-lying state (or states) f, the GSF can can be defined as:

$$\overleftarrow{f}_{XL}(i \to f) = \frac{\langle \Gamma_{\gamma XL}(i \to f) \rangle \rho(J_i, E_i, \pi_i)}{E_\gamma^{2L+1}}, \tag{2.15}$$

where the partial radiative widths $\langle \Gamma_{\gamma XL}(i \to f) \rangle$ are assumed to be averaged in the vicinity of E_i, $\rho(J_i, E_i, \pi_i)$ is the level density at the initial excitation energy, and $E_\gamma = E_i - E_f$ is the energy of the emitted photon. Equation (2.15) does not imply any a priori adopted model to characterize the γ-decay pattern. The type X (E for electric and M for magnetic) and multipolarity are also specified. By analogy, a similar definition can be written for the inverse process, namely the photoabsorption on an initial state i (usually the ground state) leading to the population of a group of final states f, by swapping the corresponding indices in the level density in Eq. (2.15). As was shown by Axel in Ref. [144], it can further be linked to the average ground-state photoabsorption cross section $\langle \sigma_{XL}(g.s. \to f) \rangle$ as:

$$\overrightarrow{f}_{XL}(E_\gamma) = \frac{1}{(2L+1)(\pi \hbar c)^2} \frac{\langle \sigma_{XL}(E_\gamma) \rangle}{E_\gamma^{2L-1}}. \tag{2.16}$$

Here, the dependence on initial and final excitation energies, spin, and parity has been omitted in line with the so-called Brink-Axel hypothesis [85, 86], discussed in more detail in Sec. 2.2.2. In the literature, the photoabsorption $\overrightarrow{f}$ and the γ-decay $\overleftarrow{f}$ strengths are often referred to as the *upward* and *downward* GSFs, respectively [145].

It is also convenient to establish a link between the γ-ray transmission coefficient $\mathcal{T}$, commonly used to express the γ-emission rate of a multipole type XL in compound-nucleus calculations, and the GSF as functions of γ-ray energy [146]:

$$\mathcal{T}_{XL}(E_\gamma) = 2\pi E_\gamma^{2L+1} f_{XL}(E_\gamma). \qquad (2.17)$$

Experimental and theoretical information on these functions in stable and exotic nuclei is a crucial ingredient for any calculations involving electromagnetic emission and absorption processes, e.g., for calculations of photon production spectra, radiative neutron-capture cross sections, evaluating the relative contribution of the photon decay in comparison to the competing particle emission channels, and many more. To further understand the structure of the GSF and adapt it to statistical-model calculations, it is important to introduce the concept of Porter-Thomas fluctuations of individual partial widths, entering its definition, and the Brink-Axel hypothesis, generalizing the definition of the GSF and setting the correspondence between strength distributions from photoabsorption and decay experiments.

2.2.1 Porter-Thomas fluctuations

The averages and deviations from averages of GSFs and cross sections from reactions involving formation of a compound nucleus are closely related to the distribution of nuclear reaction widths and their fluctuations. The latter can be especially prominent in strength functions for the decay from states within the quasi-continuum down to a limited number of final states or a single isolated final state. Compilations of data from the earlier works suggest the distribution of partial γ-decay widths to follow a χ^2 distribution with $\nu = 1$ degree of freedom, commonly referred to as the Porter-Thomas distribution.

In their original work from 1956 [147], Porter and Thomas performed a maximum-likelihood analysis of reduced neutron widths[2] Γ_n^0 from the resonance region of total neutron cross sections in medium and heavy nuclei in an attempt to find the shape of their distribution. Two alternative exponential-like distribution forms, $x^{-1/2}\exp(-x/2)$ and $\exp(-x)$ with $x = \Gamma_n^0/\langle\Gamma_n^0\rangle$, have been revealed based on the earlier data in the study by Hughes and Harvey [148]. The former distribution with $\nu = 1$ for the neutron reduced widths and $\nu \approx 2.5$ for fission widths has been indeed confirmed in Ref. [147]; moreover, Porter and Thomas were the first to suggest a theoretical explanation of this fact within the compound nuclear picture. The strong nuclear interaction and the configuration mixing leading to the formation of complex wave functions of compound nuclear states result in an approximately Gaussian distribution with a zero mean of reduced width amplitudes ($\propto x^{1/2}$) when sampling many states, according to the central limit theorem. For the same reason, the distribution of amplitudes determining partial radiative capture widths can also be expected to follow the same Gaussian distribution. On the other hand, the total radiative capture width for a state with a certain spin should be assumed to follow a rather narrow χ^2 distribution, with the number of degrees of freedom ν and the variance inversely proportional to the number of independently contributing partial widths.

---

[2]The velocity-independent reduced neutron width Γ_n^0 is related to the width as $\Gamma_n^0 = \Gamma_n/E_0^{1/2}$, where E_0 is the resonance energy.

The work of Porter and Thomas was mainly focused on the distribution of neutron widths of s-wave resonances and was followed by a series of studies of widths in elastic scattering, fission, and radiative capture. An experimental confirmation of the χ^2 distribution with $\nu = 1$ of the partial widths for γ transitions from compound states of certain spins and parities following resonance neutron capture was presented in an extensive work by Bollinger *et al.* [149]. By the 1970s, sufficient experimental evidence was collected, confirming that the Porter-Thomas (PT) distribution can also be applied to the partial radiative widths $\Gamma_{\gamma i}$ [150]:

$$P\left(\frac{\Gamma_{\gamma i}}{\overline{\Gamma}_{\gamma i}}\right) = \left(\frac{2\pi\Gamma_{\gamma i}}{\overline{\Gamma}_{\gamma i}}\right)^{-1/2} \exp\left(-\Gamma_{\gamma i}/2\overline{\Gamma}_{\gamma i}\right). \tag{2.18}$$

With the Oslo method, such fluctuations are clearly manifested in dipole GSFs extracted for different narrow initial and final excitation energy ranges, resulting in the following deviations from the GSF averaged over a large number of involved transitions [143]:

$$\Delta f(E_\gamma) \approx f(E_\gamma)\sqrt{2/N}, \tag{2.19}$$

where N is a sufficiently large number of sample states. The standard Oslo method implies averaging over a large number of states and transitions, mainly due to relatively high densities of initial states within the quasi-continuum and final states in the quasi-continuum and the discrete region. The contribution of PT fluctuations to the total uncertainty band of the Oslo method GSF is expected to be smaller than typical statistical uncertainties, especially for heavy nuclei with high NLDs.

2.2.2 Important simplification: the Brink-Axel hypothesis

At excitation energies where the statistical treatment of γ-decay properties is justified, the dependence of the GSF on the properties of initial and final states introduces an additional degree of complexity in any calculations involving excited nuclei and thus needs to be tackled. This is especially relevant for reactions on excited nuclei within different astrophysical scenarios involving finite temperatures. For example, by analogy with the NLD, the GSF is one of main ingredients for Hauser-Feshbach calculations of astrophysical radiative neutron-capture rates and modeling of s- and r-process nucleosynthesis beyond the Fe abundance peak (see e.g. [64, 152]).

An important simplification in such calculations is provided by the Brink-Axel hypothesis, suggesting that the GSF (or the photoabsorption cross section) is independent of the detailed structure of initial and final states and depends only on the energy of the emitted (or absorbed) photons. In the original form formulated and introduced by Brink in 1955 in his doctoral thesis [85], the energy dependence of the photoabsorption cross section was assumed to be independent of the detailed structure of the initial state, and thus the IVGDR built on an excited state would have the same Lorentzian shape as the one observed in the ground-state photoabsorption process. This is in accordance with the macroscopic picture of the IVGDR, implying a collective vibrational movement of all protons and neutrons in a nucleus, which would be essentially insensitive to the initial state it was excited from. This assumption can be further generalized by applying the principle of the detailed balance to include the photon emission process on an equal footing [143] and allowing independence[3] of spins of initial and

---

[3]Selection rules for multipole transitions still apply in this case.

final states. An important conclusion from this formulation is the equivalence of the upward
and downward GSFs:

$$\overrightarrow{f}_{XL} \approx \overleftarrow{f}_{XL}. \tag{2.20}$$

In the literature, it is sometimes referred to as the generalized Brink-Axel (BA) hypothesis
(see e.g. [153]). It is commonly used in statistical-model calculations, for example, with
nuclear reaction codes TALYS [154] and EMPIRE [155]. Moreover, this hypothesis plays an
important role in the Oslo method, being one of the key assumptions for the decomposition
of photon emission spectra at different excitation energies into the NLD and the GSF. It has
also been tested and used for estimating Gamow-Teller transition strengths of interest for
stellar electron capture rates in Refs. [156, 157].

Even though this hypothesis was initially formulated for the IVGDR and not too high tem-
peratures and spins [158], it is often applied to low-lying $M1$ and $E1$ strengths distributions
in the PDR region. Whether the applicability range of the BA hypothesis can be extended
down to such low energies is a question still far from being completely settled. The major-
ity of experimental studies explicitly testing this hypothesis are either inconclusive, indicate
some deviations from it, or suggest further modifications for it to be applicable. Among some
works supporting its validity below the neutron threshold, the experimental results by Martin
et al. demonstrate a good correspondence between photoabsorption and emission strengths
through a comparison of Coulomb excitation (p, p') and Oslo data for ^{96}Mo, already mentioned
in Sec. 2.1.2. A similar comparison for ^{208}Pb by Bassauer *et al.* [138] was, however, found
to be less informative due to large fluctuations of the (p, p') GSFs, related to the compara-
tively low NLD in this nucleus. Strength functions of ^{64,66}Zn from radiative proton capture
on ^{64,66}Cu have recently been shown to be approximately the same at different excitation
energies in Ref. [159]. Moreover, the BA hypothesis appears to hold relatively well for the
$M1$ scissors mode in deformed ^{163}Dy [160].

Numerous tests have been performed by the Oslo group to reveal any dependence of the
extracted strengths on the initial and final excitation energies and thus test the BA hypothesis
as one of the underlying assumptions of the Oslo method. An excellent agreement of GSFs
extracted by gating on different initial and final excitation energy bins with each other and the
"averaged" standard Oslo method strength was found in the case of ^{238}Np [153] (see Fig. 2.3).
Similar tests have been performed for the lighter ^{46}Ti [161], ^{64,65}Ni [162], and ^{92}Zr [163] nuclei.
In all these cases, a fairly good agreement between GSFs for different initial excitation energy
bins was found; they tend to fluctuate in the vicinity of the standard Oslo method results
within the uncertainty bands. For the cases including transitions to a few isolated final states,
the GSFs demonstrate quite large fluctuations as a consequence of significantly increased PT
fluctuations. The contribution of quadrupole transitions has also been considered as one of
potential reasons for the observed deviations. In general, the independence of initial and
final excitation energies in these nuclei is more difficult to conclude as compared to the ^{238}Np
case, chiefly due to significantly lower NLDs below the neutron threshold. The validity of
the BA hypothesis in these cases can only be established approximately, within the expected
systematic uncertainty bands, which is sufficient for the Oslo method to produce reliable
NLDs and GSFs. However, for isotopes of heavy elements with sufficiently high NLDs, the
BA hypothesis is expected to be a reliable approximation due to the smearing of potential
individual variations of transition strengths over numerous contributing excited states (see
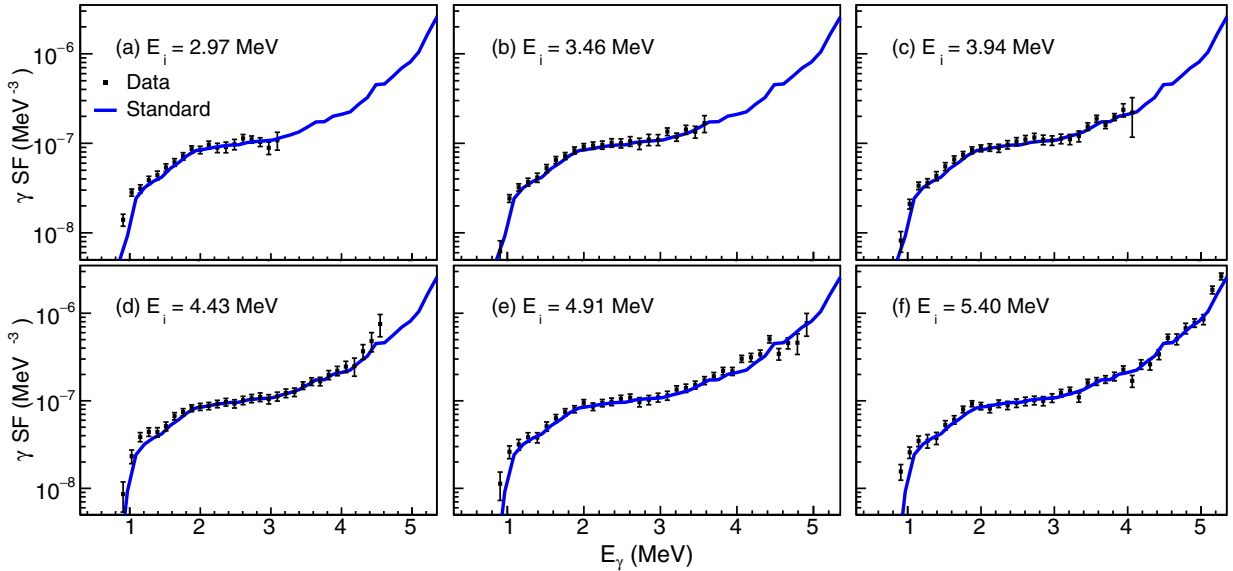
Figure 2.3: The GSFs of ^{238}Np as functions of the initial excitation energies below the neutron threshold. The blue solid line corresponds to the standard Oslo method result. The excitation energy bin width is 121 keV. Figure is reprinted with permission from Ref. [153].

also [143] and references therein).

On the other hand, experimental evidence suggesting deviations from the BA hypothesis is far more plentiful. One of the first observations of its violation was provided by a comparison of experimental average ground-state branching ratios from NRF data on ^{142}Nd with statistical-model calculations [164]. Similar subsequent studies on ^{94}Mo [165] and ^{130}Te [166] revealed that ground-state decay branching ratios in these nuclei can no longer be reproduced within the statistical model below certain excitation energies, but can rather be explained by a strong preferential decay to the ground state. Furthermore, disagreements between photoabsorption strengths and a decay strength obtained within the Hauser-Feshbach model from partial cross sections of the ^{89}Y$(p, \gamma)^{90}$Zr reaction have been observed in Ref. [167]. A recent result on ^{128}Te from the combined NRF and γ-γ coincidence spectroscopy [168], shown in Fig. 2.4(a), also demonstrates deviations of the GSF from the photoabsorption data (blue triangles) from the downward decay strength (red band), which can not be explained by PT fluctuations. This and other above-mentioned observations are in contradiction with the equivalence of the upward and downward strengths, following from the BA hypothesis.

Similarly, the majority of theoretical attempts to test the BA hypothesis reveal its violations. For example, thermally unblocked QRPA [170] and the phonon damping model [171] calculations point at an explicit dependence of the low-lying $E1$ strength (as well as $M1$ and $E2$ in [171]) on the nuclear temperature. Shell-model calculations for ^{44}Sc also suggest a strongly varying shape of the low-energy part of the $E1$ strength distribution, depending on the initial excitation energy window [172]. In this work, the observed non-zero $E_\gamma \to 0$ limit in the $E1$ and $M1$ downward strengths, similar to the upbend seen in the Oslo method data, points towards at a violation of the equivalence of the upward and downward strengths at very low γ-ray energies. Indeed, no counterpart of the upbend can be observed in ground-
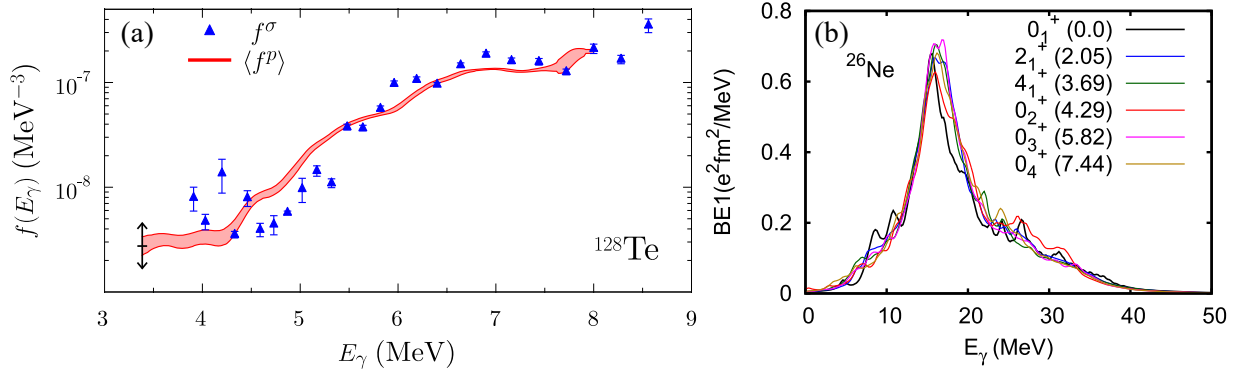
Figure 2.4:   (a) Comparison of the GSF derived independently from the photoabsorption cross section data (f^σ) and the γ-ray emission with the ratio method ($\langle f^p \rangle$) for ^{128}Te from Ref. [168]. (b) $E1$ dipole strength distributions computed within the shell model on the ground and several excited states with different excitation energies and spins. Figure is reprinted with permission from Ref. [169].

state photobabsorption experiments due to an energy gap determined by excitation energies of the first accessible states. The potential importance of this violation for Hauser-Feshbach calculations for r-process nuclei has been studied on the basis of $M1$ transitions in Fe isotopes in Ref. [173]. The cross-sections of radiative neutron-capture reactions can be significantly affected by using the ground-state upward strength in such calculations due to underestimating the contribution of the non-zero low-energy tail. Recent shell-model calculations also revealed deviations from the BA hypothesis for light nuclei. An example of the $E1$ strengths for states with different excitation energies and spins in ^{26}Ne [169] is shown in Fig. 2.4(b). The $B(E1)$ distributions for different excited states are somewhat similar, whereas the ground-state distribution demonstrates a larger concentration of the strength at $\approx 7 - 9$ MeV, typical for the PDR. The latter, however, does not contribute to the radiative neutron-capture cross section on ^{25}Ne due to the low neutron separation energy in ^{26}Ne. On the other hand, non-energy-weighted isovector $E1$ sum rules for other light isotopes obtained within the shell model by Johnson in Ref. [174] seem to be relatively constant up to quite high initial excitation energies of ≈ 20 MeV.

Even though the observations made regarding the $E1$ and $M1$ strengths in the PDR region within the shell model approach are exceptionally relevant for astrophysical calculations, they apply to relatively light nuclei, and it is not quite clear how they can further be extrapolated to heavier s- and r-process nuclei. The Oslo strengths relying on the BA hypothesis are often used in such calculations, and it is thus advisable to verify at least an approximate validity of the hypothesis in the mass range where the Oslo method is applied.

2.2.3   Theoretical approach to the dipole GSF

The first indirect attempts to provide a model for the GSF were performed in 1951 by Weisskopf [175] and later on by Blatt and Weisskopf [90] in "*Theoretical Nuclear Physics*" by deriving single-particle estimates of electric and magnetic multipole transition rates. Cal-

culations were performed assuming independent particles interacting only through a mean field, and the transition being caused by a single independently moving proton. Within this approach, reduced widths are distributed randomly, and the GSF appears to be energy independent. Even though the single-particle model was soon shown to be overly simplified (see e.g. [176]), it has been used in numerous later publications for modeling the $M2$, $E3$, and $M3$ radiation contributions [146].

The link between the strength function and photoabsorption data [85, 144] suggested a more realistic energy dependence of the GSF, determined by the dominant feature in the observed experimental cross sections, namely the IVGDR. This model, commonly referred to as the Standard Lorentzian (SLO), adopts the Lorentzian shape of the IVGDR under the Brink-Axel hypothesis assumption, allowing to exclude the excitation energy, spin, and parity dependence from consideration:

$$f_{\text{SLO}}(E_\gamma) = \frac{1}{3\pi^2\hbar^2c^2}\frac{\sigma_0\Gamma_0^2 E_\gamma}{(E_\gamma^2 - E_0^2)^2 + \Gamma_0^2 E_\gamma^2}. \tag{2.21}$$

Here, σ_0, Γ_0, and E_0 are the peak cross section, energy independent damping width, and centroid of the resonance, respectively. The constant width is consistent with the fragmentation of the strength, assuming that no nucleon-nucleon collisions take place, and nucleons interact only with the nuclear surface. A single or several Lorentzian peaks indeed reproduce the general shape of photoabsorption cross sections in the immediate vicinity of the IVGDR peak quite well for the majority of medium to heavy spherical and deformed nuclei [91]. However, it fails to simultaneously fit the IVGDR peak and reproduce the experimental (n,γ) cross sections close to the neutron threshold, which also affects calculations of capture cross sections and γ-ray spectra [145, 146]. Moreover, it tends to underestimate the experimental strength distribution below $\approx$ 1-2 MeV ([91] and references therein). Despite these limitations in its application to the $E1$ strength, the SLO is commonly used for the description of the $M1$ and $E2$ components of the total decay strength (see e.g.[91, 154]).

These shortcomings were further mitigated within the Fermi-liquid theory in the work by Kadmenskij, Markushev, and Furman (KMF)[177], who suggested the following energy-dependent form of the resonance width:

$$\Gamma_{\text{KMF}}(E_\gamma, T_f) = \frac{\Gamma_0}{E_0^2}(E_\gamma^2 + 4\pi^2 T_f^2), \tag{2.22}$$

which also depends on the temperature of the final states T_f. Here, Γ_0 is the IVGDR width for cold nuclei ($T = 0$ MeV). The last term in Eq. (2.22) is thus related to collisions between quasi-particles, while the first one is determined by the spreading of particle-hole excitations over more complex configurations. The final derived GSF takes the following form within the KMF approach:

$$f_{\text{KMF}}(E_\gamma, T_f) = \frac{1}{3\pi^2\hbar^2c^2}\frac{0.7\sigma_0\Gamma_0^2(E_\gamma^2 + 4\pi^2 T_f^2)}{E_0(E_\gamma^2 - E_0^2)^2}. \tag{2.23}$$

Including the γ energy and temperature dependence of the width, and therefore a non-zero strength at the $E_\gamma \to 0$ limit, allowed for a more accurate description of experimental strength functions at relatively low energies. However, the main drawback of the original KMF formula [91, 177] limiting the energy range of its applicability is a singularity at the resonance energy

E_0. To take advantage of both the KMF model and the SLO, a new formula, the so-called Generalized Lorentzian (GLO), was proposed by Kopecky and Chrien, who combined the standard Lorentzian shape with the KMF energy-dependent width and the $E_\gamma = 0$ limit of the KMF strength [178]:

$$f_{\text{GLO}}(E_\gamma, T_f) = \frac{\sigma_0 \Gamma_0}{3\pi^2 \hbar^2 c^2} \left(\frac{E_\gamma \Gamma_{\text{KMF}}(E_\gamma, T_f)}{(E_\gamma^2 - E_0^2)^2 + E_\gamma^2 \Gamma_{\text{KMF}}^2(E_\gamma, T_f)} + \frac{0.7 \Gamma_{KMF}(E_\gamma = 0, T_f)}{E_0^3} \right). \quad (2.24)$$

As was shown in Refs. [146], a more reasonable simultaneous description of $E1$ strengths from average resonance capture data and (n, γ) cross sections in spherical and several transitional nuclei was finally achieved with this approach. To adjust the GLO for the application to a wider range of nuclei, including deformed ones, an empirical correction to the KMF width was introduced [179]:

$$\Gamma(E_\gamma, T_f)^{\text{EGLO}} = \left(\kappa + (1 - \kappa) \frac{E_\gamma - \epsilon_0}{E_0 - \epsilon_0} \right) \frac{\Gamma_0}{E_0^2} (E_\gamma^2 + 4\pi^2 T_f^2), \quad (2.25)$$

where $\epsilon_0 = 4.5$ MeV, and κ is an empirical factor, dependent on the mass number and the adopted NLD model. The GLO strength with the enhanced width from Eq. (2.25) presents the Enhanced Generalized Lorentzian model (EGLO).

Despite a reasonable reproduction of the strength distribution with GLO and EGLO, the width employed in these models accounts for the two-body collisional damping mechanism within the Fermi liquid approach and disregards completely an almost temperature-independent fragmentation (one-body) damping, identified with the width in the SLO model. Moreover, the shapes of the above-mentioned strengths are in contradiction with the imaginary part of the nuclear response function in the electromagnetic field in the form of a Lorentzian shape with an energy-dependent width (see [180] and references therein). These shortcomings called for further improvements of these models. One of them, the thermodynamic pole approach formulated in [181–184], accounts for a temperature-dependent enhancement of the standard Lorentzian shape due to the average number of excited particle-hole states in a heated system in an external electromagnetic field. The energy- and temperature-dependent width within this model effectively accounts for both the fragmentation and collisional contributions and can be determined with different semi-empirical expressions [91]. Similarly, the so-called Generalized Fermi Liquid (GFL) model [185] preserves the Lorentzian shape and allows for combining the collisional and fragmentation damping due to the dipole-quadrupole interaction.

Finally, another noteworthy approach, the so-called hybrid formula providing a good simultaneous description of the low-energy tail and the peak of the IVGDR, was suggested by Goriely in Ref. [64]:

$$f_{\text{Hyb}}(E_\gamma, T_f) = \frac{\sigma_0 \Gamma_0}{3\pi^2 \hbar^2 c^2} \left(\frac{E_\gamma \Gamma_h(E_\gamma, T_f)}{(E_\gamma^2 - E_0^2)^2 + E_\gamma^2 \Gamma_h(E_\gamma, T_f) \Gamma_0} \right). \quad (2.26)$$

with the width defined as:

$$\Gamma_{\text{Hyb}}(E_\gamma, T_f) = K_{\text{Hyb}} \frac{\Gamma_0}{E_0 E_\gamma} (E_\gamma^2 + 4\pi^2 T_f^2), \quad (2.27)$$

where K_{Hyb} is determined by Migdal constants in the Fermi liquid theory and adopted to be 0.63 within this approach. It combines some features of the KMF and the SLO models, avoiding the singularity at the IVGDR peak and preserving the non-zero $E_\gamma = 0$ limit. The strength distribution predicted by this model closely resembles the one obtained with the (E)GLO. Both of these models have been previously shown to provide good alternatives for the description of the Oslo method strengths [186, 187].

All of the above-mentioned models (except for the SLO) share a certain dependence on the temperature of the final states, which evidently leads to the breakdown of the Brink-Axel hypothesis. As was mentioned earlier, the $E_\gamma \to 0$ limit predicted by these models is tailored to the description of the non-zero low-energy tail in the decay strength, which is not observed in the photoabsorption data. Despite that, the Lorentzian functions are widely implemented in different databases (e.g. RIPL-3 [91], JENDL-5 [188], IAEA Evaluated Photonuclear Data Library [145]) and astrophysical calculations [154] and provide quite flexible alternatives for the description of photonuclear data. The parameters in these models to a large extent rely on fits to existing experimental data for stable isotopes and/or droplet-model estimates. Similarly to the phenomenological NLD models, the predictive power of these approaches is thus limited to nuclei not too far from the stability valley. Moreover, the need to account for such low-lying dipole features as the PDR, scissors mode, and upbend calls for alternative ways to estimate GSFs.

At relatively low energies[4], the microscopic shell model approach provides an excellent framework to extract strength functions by averaging over a large number of electromagnetic transitions. It has first been applied to Mo and Zr isotopes with $A \sim 90$ by Schwengner *et al.* [190] to study the $M1$ strength function below the neutron threshold. The calculations confirmed a steep increase of the strength (upbend) towards the zero transition energy, observed also with the Oslo method. Similar shell-model calculations for the $E1$ strength are, however, more computationally demanding due to the need to include sufficiently large model spaces. Up until recently, no consistent calculations of both the $M1$ and the $E1$ components within the same theoretical framework have been performed. The first calculations of this kind for ^{44}Sc have been presented by Sieja in Ref. [172], revealing an upbend of $M1$ nature and a non-vanishing tail of the $E1$ strength, in accordance with experimental observations and the majority of empirical models. Calculations of this kind have also been presented for the case of ^{51}Ti in Ref. [191].

At present, large scale shell-model calculations are still limited to light- and medium-mass nuclei and predominantly $M1$ strength distributions. Large scale (Q)RPA calculations remain the only microscopic (or rather semi-microscopic[5]) approach with a predictive power sufficient to provide $E1$ strength distributions over the whole nuclear chart. Such calculations have been performed by Goriely and Khan for nuclei with $8 \leq Z \leq 110$ in [192]. The calculations were restricted to excited states calculated with QRPA on top of HF plus BCS ground states for different Skyrme-types of effective nucleon interaction. The obtained strengths, broadened by folding with the Lorentzian function, provide a reasonable description of the IVGDR region

---

[4]There are, however, several examples of photoabsorption cross section calculations in the IVGDR region using an extension of the Monte Carlo shell model [189].

[5]For a practical use in statistical model codes, calculations of (Q)RPA type are usually adjusted to be more compatible with experimental results by an additional broadening, energy shift, and scaling. Corrections are also introduced in deformed nuclei to account for the splitting of the IVGDR.

for the vast majority of stable nuclei [145]. The reliability of the HF plus BCS and QRPA calculations was further improved by treating the pairing correlations in the ground state within the HFB approach in [66] and introducing finite-range Gogny forces [193, 194]. Taking into account more complex configurations in the form of coupling of single-particle degrees of freedom with phonon degrees within QPM [195] and QTBA [196] has been the next step towards a more realistic description of both the IVGDR and the PDR.

Despite an improved predictive power of microscopic approaches, there are still no means to test them far from the valley of stability (except for very few cases, see e.g. [71]). Evidently, microscopic and semi-microscopic calculations, as well as the empirical models described above, need to be verified against available experimental strength functions.

2.2.4 GSFs from experiments

Considering the importance of assessing the quality of theoretical approaches and the extensive use of GSFs as inputs for reaction modeling, a coordinated effort supported by the International Atomic Energy Agency (IAEA) has been recently made to collect all available sources of experimental information on GSFs of different types and multipolarities and within different energy ranges in a reference data library in 2019 [197]. Even though all of the included experimental techniques have been presented in the review paper by Goriely *et. al.* [145], it is still instructive to provide a brief overview here.

Below the neutron threshold, one of the main sources of upward strength functions deduced from absolute measurements of photoabsorption cross sections is NRF studies, introduced in the previous chapter. In these experiments, ground-state decay widths are extracted from measured ground-state transition intensities by assuming that no branching transitions take place and all excited states decay directly to the ground state. To account for the missing strength and be able to compare NRF results with other experimental strengths closer to the neutron threshold, corrections for weak unresolved transitions and branching ratios are usually performed. In experiments at the γELBE facility [25] and the S-DALINAC electron accelerator facility at TU Darmstadt [198] with broad ranges of bremsstrahlung photons up to certain end-point energies, one should also account for the feeding of excited states from higher-lying states, contributing to the total measured decay intensities. This is partly resolved by performing experiments with different bremsstrahlung end-point energies. Intensities of branching transitions and ground-state branching ratios for populated states can be obtained from statistical model simulations (see e.g. [23]), which inevitably introduce a model dependence in the analysis. In the experiments with quasi-monoenergetic, fully polarized photons at the HIγS facility [27], this is overcome by studying intensities of both ground state transitions and transitions cascading via certain low-lying states, which serve as collectors of inelastic transitions. The angular distribution study and the use of polarized beams or Compton polarimeters in such experiments allows to determine spins of excited states and discriminate between $M1$ and $E1$ transitions.

Within the PDR region, the Oslo method applied to particle-γ coincidence spectra from light-ion-induced reactions is an alternative approach to extract GSFs, which can be explicitly compared with available NRF data. The details of the extraction of the GSF with this method will be outlined in Sec. 3.3.5. In a large number of cases where both types of experiments have been performed, some disagreements in both shape and absolute values between the extracted
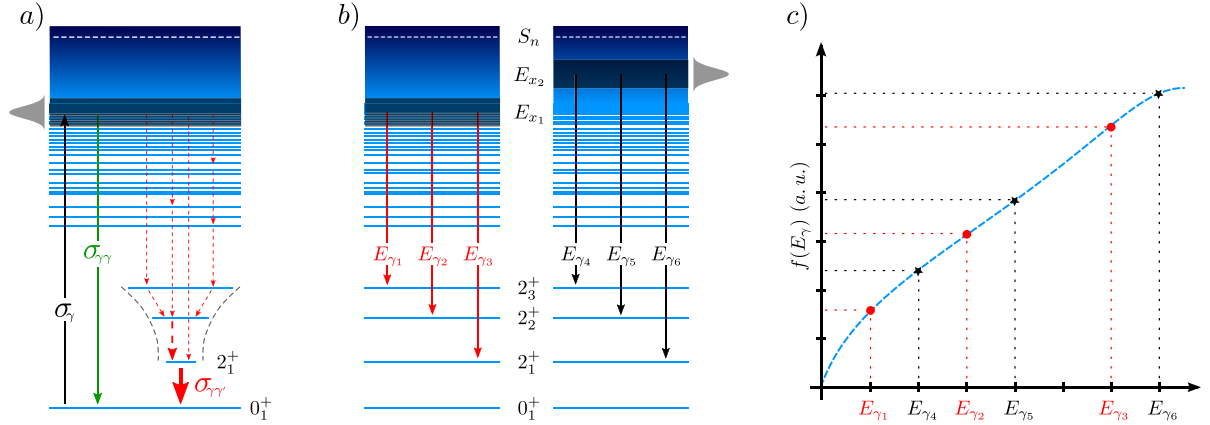
Figure 2.5: Schematic representation of the experimental method using quasi-monochromatic photon beams at the HIγS facility. (a) Extraction of photoabsorption cross sections, (b)-(c) extraction of the shape of the GSF from primary γ transitions to low-lying excited states. Figure is reprinted with permission from Ref. [198].

GSFs have been observed [145]. Prior to testing the applicability of the BA hypothesis based on the comparison of such strengths, one should consider relatively large systematic uncertainties of the Oslo method, as well as systematic uncertainties due to statistical model corrections and the atomic background subtraction and statistical uncertainties in the NRF data. Despite some disagreements in shapes, the GSFs overlap within rather broad uncertainty bands in some cases [145], and no clear conclusions on potential violations of the BA hypothesis can be drawn.

A more promising test of the correspondence between the downward and upward strengths can be performed with the ratio method developed by Wiedeking *et al.* and presented in Ref [199]. In this work, the shape of the downward GSF was extracted in a model-independent way using this method. In general, it can further be compared with both an upward NRF strength and a model-dependent downward Oslo method strength. One of such tests, mentioned in the previous section and shown in Fig. 2.4(a), was done using a quasi-monochromatic photon beam and a high-efficiency γ-ray detection setup at HIγS, allowing to perform both a standard NRF analysis and γ-γ coincidence spectroscopy for ^{128}Te [168]. Both the upward NRF and the downward decay strengths have been extracted from the same data set. A schematic outline of this procedure is shown in Fig. 2.5. The ratio method is based on estimating relative intensities of primary transitions from the same excitation energy window to low-lying excited states of the same spin and parity. The latter condition allows to avoid introducing a model dependence through assuming a certain form of the spin distribution. This method is, however, limited to extracting only the shape of the GSF, and an absolute normalization of the strength has to rely on some auxiliary experimental data.

The GSF over wide energy ranges above the neutron threshold are available from a plethora of photoneutron cross sections, currently collected in the EXFOR database [200]. The experiments usually employ bremsstrahlung beams, mono-energetic beams from in-flight annihilation of positrons, and laser-induced Compton backscattering. The cross-sections are extracted from either high-efficiency neutron counting or offline γ-ray spectroscopy. In the same energy

41

range and even below the neutron threshold, the GSFs can also be extracted with inelastic proton scattering experiments with polarized and unpolarized relativistic proton beams at the the Research Center for Nuclear Physics (RCNP), yielding both the $M1$ and $E1$ components via the multipole decomposition analysis or studying polarization of scattered particles with a polarimeter. For the cases of ^{208}Pb [138] and ^{96}Mo [130], where a comparison of (p, p') data with the Oslo method results has been performed (see also Sec. 2.2.2), the strengths agree quite well within the uncertainties.

The GSF within rather narrow energy ranges below the neutron threshold can be extracted from intensities of primary γ transitions following resonant neutron capture [176, 201, 202]. The partial radiative widths can be obtained for capture on individual resonances by means of the Time-of-Flight (TOF) spectroscopy (Discrete Resonance Capture (DRC)). The effect of PT fluctuations in such data is quite strong, and averaging over measured resonances is required in the analysis to reduce their impact. Alternatively, the average resonance capture (ARC) exploits filtered neutrons with broader incident energy ranges. The dipole GSF from such experiments is obtained in arbitrary units and needs to be normalized to DRC data. Knowledge of spins of initial and final states for individual resonances allows for discrimination between the $E1$ and $M1$ components of the total strength. Relative intensities of primary photons following thermal neutron capture can serve as one more source of information on the GSF [203]. This method is similar to the DRC, with the exception of larger PT fluctuations due to averaging over only the final states but not the initial resonances. Radiative proton capture experiments have also been included in the database [145], even though their applicability is limited to medium-mass nuclei with relatively low proton separation energies of product nuclei. Moreover, average total radiative widths obtained for resolved s and p neutron resonances are important ingredients for the absolute normalization of the Oslo method strength. In general, the systematics of available DRC data for GSF values between $\approx 4 - 6$MeV are in fairly good agreement with those based on the Oslo data for nuclei with $A > 130$. For the lighter nuclei, the Oslo method tends to provide lower values than the DRC [204].

Several methods have also been proposed to test various GSF models. For example, a reproduction of unfolded singles photon spectra from thermal neutron capture (n, γ) reactions with a statistical model code can be used to verify the γ-decay pattern predicted by a chosen GSF model, as was shown in Ref. [205]. Furthermore, a similar test can be performed by measuring spectra of the so-called two-step cascades (TSC) following thermal neutron capture with high-resolution Ge detectors (see [206] and references therein). Such cascades proceed between populated compound states and fixed low-lying states of certain spins and parities and can be measured by selecting pairs of coincident events yielding a fixed sum energy equal to the energy difference between the initial and final states. The measured spectra for all possible cascades have been shown to be quite sensitive to the expressions for the $E1$ and $M1$ components of the GSF and the NLD model in Monte-Carlo simulations in [206]. In the work by Krtička et $al.$ [160], this method was used to confirm the presence of scissors resonances built on excited states in ^{163}Dy, in line with the Brink-Axel hypothesis. Moreover, the TSC method with the NLD extracted independently from neutron evaporation data has been applied to spectra from the $(p, 2\gamma)$ reaction on ^{59}Co [207], which allowed to suppress PT fluctuations and achieve better precision than in neutron-capture reactions. This experiment has revealed a presence of an $M1$ upbend, also observed in the corresponding Oslo data.

A later modification of this method, developed at Los Alamos National Laboratory, expanded the TSC method to measurements of multi-step γ cascades (MSC) for different multiplicities following neutron capture on isolated resonances with the highly-segmented, high-efficiency detector array DANCE [208]. These studies continued the investigation of the $M1$ scissors mode and the upbend in Dy isotopes [209] and were recently used test the HFB plus QRPA with the D1M Gogny interaction [210], inciting further theoretical attempts to reproduce and include the upbend in semi-microscopic models.

2.3 Statistical calculations of radiative neutron-capture cross sections

Astrophysical radiative neutron capture on the nuclei studied in this thesis is expected to proceed through the compound-nucleus mechanism, and can thus be treated within the statistical model, sometimes referred to as the Hauser-Feshbach formalism [68]. In their pioneering work, Hauser and Feshbach used the compound nucleus as initially defined by Bohr as a starting point to derive the reaction cross section through statistical nuclear characteristics by taking into account the conservation of angular momentum and parity in the reaction[6]. Following their derivation, Eq. (2.2) from the beginning of this chapter can be rewritten as:

$$\sigma(\alpha, \beta) = \sigma_{\alpha C} G_C(\beta) = \sum_{J\pi} \sigma_{\alpha C}^{J\pi} \frac{P^{J\pi}(\beta)}{\sum_\beta P^{J\pi}(\beta)} = \sum_{J\pi} \sigma_{\alpha C}^{J\pi} \frac{\langle \Gamma^{J\pi}(\beta) \rangle}{\sum_\beta \langle \Gamma^{J\pi}(\beta) \rangle}. \tag{2.28}$$

Here, we introduced the spin J and parity π of the compound state. The decay probability of the compound nucleus $G_C(\beta)$ through the channel β can be written explicitly using a normalized decay probability $P^{J\pi}(\beta)$, which is proportional to the average decay width $\langle \Gamma^{J\pi}(\beta) \rangle$. The cross section for the formation of the compound state with energy E_C and spin-parity J^π can be expressed in terms of the transmission coefficient for an incident particle $\mathcal{T}(\alpha)$ and the wave number of its relative motion k as [211]:

$$\sigma_{\alpha C} = \sum_{J\pi} \sigma_{\alpha C}^{J\pi} = \frac{\pi}{k_\alpha^2} \sum_{J\pi} \frac{2J+1}{(2J_t+1)(2J_p+1)} \sum_{sl} \mathcal{T}_l(\alpha). \tag{2.29}$$

In this relation, the transmission coefficients have been weighted with probabilities that unpolarized projectiles with spin J_p and orbital angular momentum l and target nuclei with spin J_t form the compound nucleus with spin J, as well as the number of projections of the angular momentum l. The transmission coefficients are summed over spins s of the entrance channels $(\vec{s} = \vec{J}_p + \vec{J}_t)$ and the angular momentum l $(\vec{l} + \vec{s} = \vec{J})$. Taking further into account that the average decay widths can be linked to the transmission coefficients for the exit channel β, the total cross section of the reaction can be written as:

$$\sigma(\alpha, \beta) = \frac{\pi}{k_\alpha^2} \sum_{J\pi} \frac{2J+1}{(2J_t+1)(2J_p+1)} \frac{\sum_{sl} \mathcal{T}_l(\alpha) \sum_{s'l'} \mathcal{T}_{l'}(\beta)}{\sum_\beta \sum_{s''l''} \mathcal{T}_{l''}(\beta)}. \tag{2.30}$$

---

[6]This publication continues the work by Wolfenstein [69], who was the first one to introduce the conservation of total angular momentum, z-component of angular momentum, and parity into the description of a compound nucleus decay.

This is, however, a general expression for the unspecified entrance and exit channels α and β. In the radiative capture process in astrophysical environments, the entrance channel becomes neutron capture, whereas the exit channel corresponds to photon emission, allowing us to introduce the corresponding transmission coefficients $\mathcal{T}_n$ and $\mathcal{T}_\gamma$ in the previous relation. Provided that the maximum energy of captured neutrons in astrophysical scenarios should not exceed ~ 1 MeV, the decay channels of the compound nucleus in the denominator of Eq. (2.30) are usually dominated by neutron and γ emission, so that:

$$\sigma(n,\gamma) = \frac{\pi}{k_n^2} \sum_{J\pi} \frac{2J+1}{(2J_t+1)(2J_p+1)} \frac{\mathcal{T}_n(E_C,J,\pi)\mathcal{T}_\gamma(E_C,J,\pi)}{\mathcal{T}_n(E_C,J,\pi) + \mathcal{T}_\gamma(E_C,J,\pi)}. \tag{2.31}$$

The neutron transmission coefficient can be estimated with the optical model potential of the target nucleus. The γ-ray transmission coefficient includes decays with photons of all possible types XL to the final states $J_f^{\pi_f}$ accessible from the initial state of the compound nucleus J^π after applying all appropriate selection rules:

$$\mathcal{T}_\gamma(E_C,J,\pi) = \sum_{XL} \sum_{J_f=|J-L|}^{J+L} \sum_{\pi_f} \int_0^{E_C} \mathcal{T}_{\gamma XL}(E_\gamma)\rho(E_C - E_\gamma, J_f, \pi_f)dE_\gamma. \tag{2.32}$$

Thus, the experimental γ-ray transmission coefficient $\mathcal{T}_{\gamma XL}(E_\gamma)$ and the NLD $\rho(E_x, J, \pi)$ of the compound nucleus can be combined with an appropriate optical model potential to calculate the radiative neutron-capture cross section. This provides an additional experimental alternative to direct (n,γ) measurements and the surrogate method using the $(d,p\gamma)$ reaction to provide reaction cross sections and rates of interest for astrophysical simulations.

Chapter 3

Experiments at the OCL and the Oslo method

To lay the foundation for a systematic study of the low-lying $E1$ strength in the Sn isotopic chain, experimental data on eleven Sn nuclei were collected at the Oclo Cyclotron Laboratory (OCL) of the University of Oslo. The following chapter provides the most important experimental details and procedures applied to extract their NLDs and GSFs. As mentioned earlier, the Oslo method, yielding simultaneously both of these statistical characteristics of excited nuclei, is the central method exploited in this thesis. It is a complex procedure involving such steps as unfolding of experimental spectra for selected particle-γ events, extraction of primary photons for excitation energies below the neutron threshold, decomposition of two-dimensional primary spectra into the NLDs and GSFs, and, finally, their normalization to auxiliary experimental data. These steps are outlined in detail in Sec. 3.3. Furthermore, the ^{120,124}Sn isotopes have been analyzed with the shape method (Sec. 3.4), providing additional information on downward GSFs from a selective decay into the ground and the first excited states in these nuclei. These two methods, combined with the results of other experimental techniques, allow for a thorough test of the assumptions underlying the Oslo method and benchmarking the obtained strength distributions. In this chapter, we are going to use the ^{120}Sn case to illustrate some of the key steps of the analysis.

3.1 Experimental setup

Since the first experimental setup was put into use at the OCL in the 1990s, the Oslo group has been actively involved in experimental nuclear structure research with the main focus on statistical properties of nuclei within the quasi-continuum excitation regime. The latter is attained in studied nuclei via light-ion-induced transfer or inelastic scattering reactions. All experiments were carried out with the MC-35 Scanditronix cyclotron, providing pulsed beams of protons, deuterons, ^{3}He, and α with energies up to several tens MeV (up to ≈ 47 MeV for a ^{3}He beam). On the way through the experimental hall, the beam can be delivered with two switching magnets to several stations for the production of medical isotopes, irradiation of cancer cells, and radiation hardness testing of electronics. The beam is bent by an analyzing magnet by 90° and redirected from the cyclotron vault towards the experimental hall. The
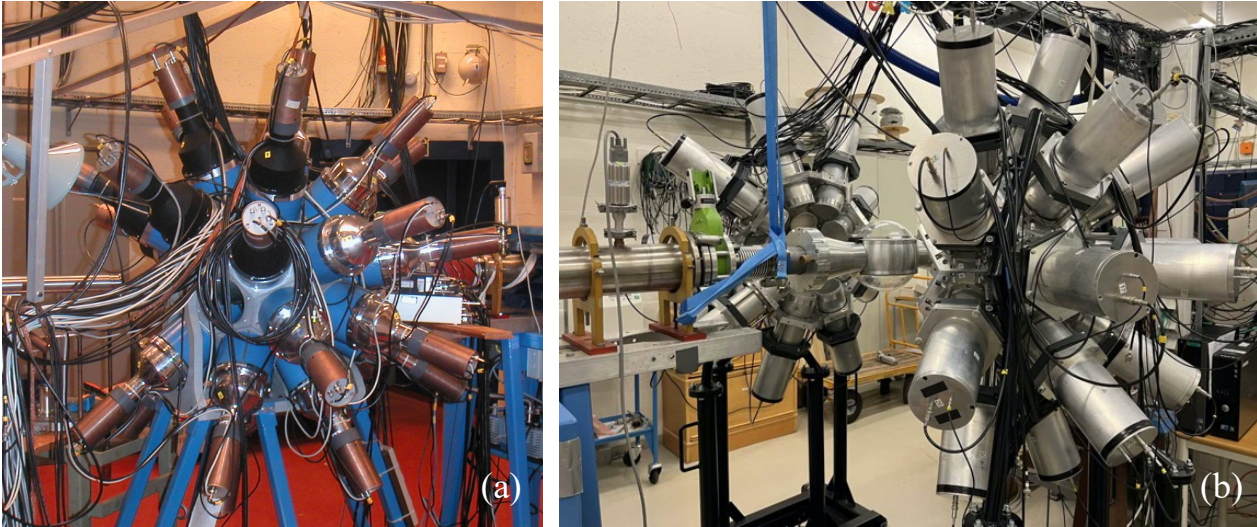
Figure 3.1: (a) The CACTUS NaI(Tl) scintillator detector array used to perform experiments to study $^{111-113,116-119,121,122}$Sn. The photograph supplied courtesy of Prof. M. Guttormsen. (b) The OSCAR LaBr$_3$(Ce) scintillator detector array, installed in 2018 to replace CACTUS. The array was used to study the ^{117,119,120,124}Sn isotopes. The target chamber can be seen in the center of the open frame of OSCAR.

principal experimental station comprises the target chamber with target holders on a wheel, surrounded by an array of scintillator detectors, and a particle telescope system placed inside the chamber. This configuration ensures efficient detection of particle and photon events following an excitation of a studied nucleus with an impinging beam of light ions.

Before 2018, the CACTUS array [212] (see Fig. 3.1(a)), consisting of 28 spherically distributed 5″×5″ NaI(Tl) γ detectors, was used in all experiments. Placed at a distance of 22 cm from the target center, the detectors covered a solid angle of $\approx 18\%$ of 4π, considering additional lead collimators (thickness of 10 cm, $\varnothing 7$ cm) and 2 mm copper absorbers, used to suppress the crosstalk between the detectors and X-rays, respectively. The total efficiency and energy resolution at E_γ = 1332 keV were estimated to be 15.2(1)% and $\approx 6.8\%$ with a ^{60}Co source. In some of the earliest experiments, CACTUS was combined with one (see e.g. Ref. [80]) or two 60% Ge detectors to estimate the populated spin range and to monitor potential contaminants in the spectra. In 2018, this system was replaced by the new Oslo SCintillator ARray (OSCAR) [213], consisting of 30 large volume $\varnothing 3.5″×8″$ LaBr$_3$(Ce) detectors mounted in a truncated icosahedron-shaped frame. Figure 3.1(b) shows OSCAR with the open frame and the target chamber located in the center. All detectors are confined in aluminium housings and coupled to Hamamatsu R10233-100 photomultiplier tubes (PMT) combined with LABRVD active voltage dividers [214]. The latter were specifically designed for large volume LaBr$_3$(Ce) detectors to ensure PMT gain stability in case of high event count rates. Overall, the new scintillator array provided a number of significant advancements as compared to CACTUS, such as improved energy resolution, efficiency, stability of the emitted light with temperature, and excellent intrinsic time under 1 ns [215]. The latter is especially crucial for the selection of particle-γ coincidence events for the further analysis with the Oslo method. The time resolution was reduced to $\approx 4-5$ ns Full Width at Half Maximum (FWHM)
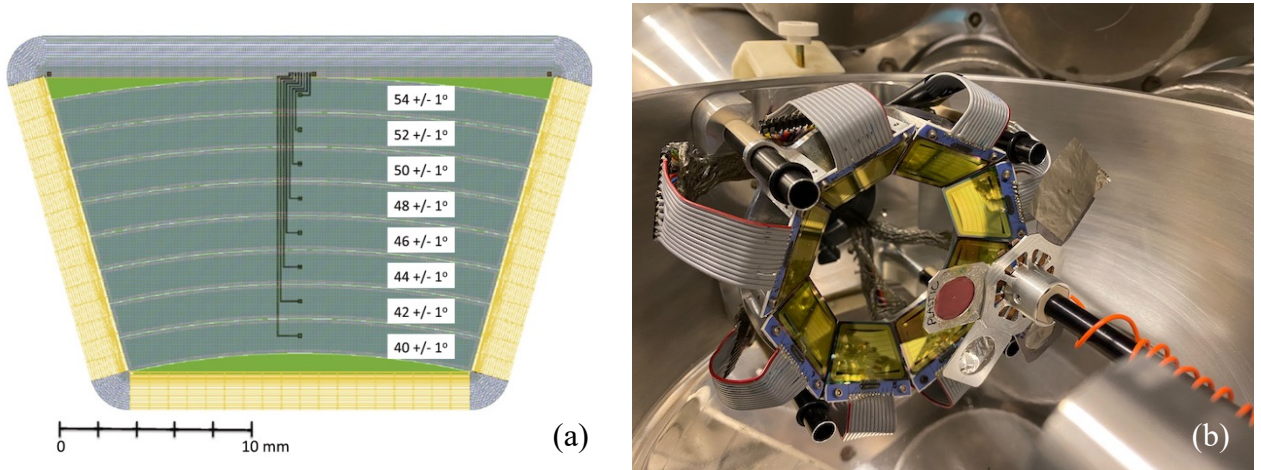
Figure 3.2: (a) The layout of the front ΔE pads of the particle telescope SiRi. The illustration is reprinted with permission from Ref. [216]. (b) The photograph of SiRi placed inside the target chamber (supplied courtesy of Prof. A.-C. Larsen).

of the prompt peak for such events, compared to $\approx 10-15$ ns FWHM for CACTUS, and it is mainly limited by the timing properties of the particle detection system and electronics. With OSCAR placed at a distance of ≈16 cm from the chamber center, the solid angle coverage was increased to $\approx 57\%$ of 4π (no additional collimators are used). The total efficiency and energy resolution with the ^{60}Co source for the $E_\gamma = 1332$ keV transition were estimated to be $\approx 40\%$ and 2.2%, respectively.

An accurate estimation of the excitation energy of a nucleus prior to γ-ray emission relies on an accurate measurement of scattering angles and energies of ejectiles, provided a known beam energy and a Q-value of the reaction. The currently used particle detection system is presented by a custom-designed silicon ring (SiRi) [216], consisting of 8 trapezoidal-shaped 1550-μm-thick E detector pads and the corresponding 130-μm-thick ΔE layers. The center of each pad is placed at a distance of 5 cm from the target. The implemented E-ΔE technique allows for an efficient separation between reaction channels with ejectiles of different mass and charge. This can be easily understood based on the energy loss mechanism for charged particles traveling though a medium. Provided charged particles move at higher speed ($\beta = v/c$) than typical velocities of orbital electrons, the energy loss per unit path length (stopping power) for ions can be expressed by a simplified Bethe-Bloch formula [92, 217]:

$$\Delta E = \left| -\frac{dE}{dx} \right| \sim \frac{z^2}{\beta^2} \sim \frac{mz^2}{E}, \tag{3.1}$$

where z, m and E are the charge, mass, and energy of the charged particles, respectively. The energy loss of a particle along its trajectory and, thus, in the ΔE and E layers as a function of energy depends also on its charge and mass. Experimentally measured two-dimensional spectra of registered ejectiles, plotted as functions of energies deposited in the thin ΔE Si layer versus the thick E detector, reveal several (if kinematically allowed and if recorded statistics are sufficient) clearly separated reaction channels, which can be easily separated by applying energy-dependent graphical gates.

The range of covered particle scattering angles is either from 40° to 54° or from 126° to 140°, depending on whether SiRi is placed in a backward or a forward position with respect to the beam direction. The ΔE layers are additionally segmented into 8 curved pads (see Fig. 3.2(a)), corresponding to 2° polar angles each, to provide more accurate estimation of the excitation energy prior to γ-ray emission and to avoid pile-up events. In total, this segmentation provides 64 combinations of E-ΔE detectors. The SiRi array placed in the backward position in the target chamber with the target holder wheel is shown in Fig. 3.2(b). To moderate a high-voltage operation required for a complete depletion of the thick Si E wafers, the ΔE and E detectors share the same system of 18 guard rings, covering the edges of active areas in all detector segments. With an approximately 6% of 4π solid angle coverage, SiRi has significantly improved detection efficiency (≈ 10 times) compared to the telescope system in use before its installation in 2011. The previous detector was presented by 8 standard, commercial E-ΔE Si telescopes, with E and ΔE counters of 1500 μm and $\sim 140 - 150$ μm thickness. The detectors were not segmented and thus had to be collimated to reduce the scattering angle uncertainty, at the expense of detection efficiency. In all experiments before 2011, the telescopes were placed at $\approx 45°$ with respect to the beam direction, covering a 5° window of scattering angles. In addition, a 10.5-μm- or a 15-μm-thick Al foil was used to cover the ΔE counters in these experiments to stop high-energy δ electrons produced in the target material.

With the present configuration of the setup (OSCAR and SiRi), signals are processed with Digital Gamma Finder (DGF) Pixie-16 modules manufactured by XiA [218]. Each module is a 16-channel all-digital waveform acquisition and spectrometer card, digitizing signals with a 14-bit analog-to-digital converter, running at 500 MHz for signals from the 30 OSCAR channels and at 250 MHz for signals from the 72 ΔE and E detector channels after passing through the SiRi preamplifiers. Continuously sampled signals are written in list mode and available both in real time for an online monitoring, diagnostics, control of triggering, energy and time filtering, and for an offline analysis after writing to disc. Since some particles might be stopped by the ΔE layer without being registered in the backward E detector, such events are rejected at the online in-beam data collection stage. To single out particle-γ coincidence events, signals (time stamps) from E detectors are considered the time start point, while the stop points are attributed individually to each LaBr$_3$(Ce) or NaI(Tl) detector signal. In contrast to the constant fraction discrimination in Pixie-16, the leading-edge timing implemented in the earlier used (before 2018) Mesytec STM-16 modules [216] required an amplitude-dependent time "walk" correction. This correction was performed in all experiments carried out before the installation of XiA electronics in 2018. Finally, all recorded and saved data are grouped into larger events within a 1 μs time frame with respect to recorded ΔE signals, chosen as reference points in the offline analysis due to an overall better time resolution.

3.2 Experiments on Sn isotopes

Eleven Sn isotopes, $^{111-113,116-122,124}$Sn, were studied in nine experimental campaigns at the OCL in the period of time from 2003 to 2022. The first experiments were aiming at studying the pair breaking process in NLDs and enhancement in GSFs of ^{116,117}Sn with a 38-MeV beam of ^{3}He in the ^{117}Sn(^{3}He,$\alpha\gamma$)^{116}Sn and ^{117}Sn(^{3}He,^{3}He$'\gamma$)^{117}Sn reactions. The used ^{117}Sn target was self-supporting and had a thickness of 2.1 mg/cm^2 and an enrichment of 92%.

These experiments were followed by the investigation of ^{118,119}Sn with the same beam energy in the ^{119}Sn(^{3}He,$\alpha\gamma$)^{118}Sn and ^{119}Sn(^{3}He,^{3}He$'\gamma$)^{119}Sn reactions on a 1.6-mg/cm²-thick ^{119}Sn target with a 93.2% enrichment. All of the above-mentioned experiments were performed with the older configuration of the setup, including CACTUS and eight standard, commercial Si telescopes. To reduce the uncertainty in the scattering angle, the latter were equipped with collimators with either a circular (^{117}Sn) or a squared (^{119}Sn) opening, limiting the solid angle coverage to $\approx 0.72\%$ and $\approx 1.5\%$ of 4π, respectively. The Si detectors were placed at 45° with respect to the beam direction to provide sufficiently high cross sections of the reactions of interest, while still having reasonably low relative contribution of elastic events.

After installation of SiRi, the ^{122}Sn(^{3}He,$\alpha\gamma$)^{121}Sn and ^{122}Sn(^{3}He,^{3}He$'\gamma$)^{122}Sn reactions with a 38-MeV ^{3}He beam impinging on ^{122}Sn (1.43-mg/cm²-thick, 94% enrichment) were performed. With SiRi, the excitation energy resolution was significantly improved as compared to the earlier experiments. Further, the ^{112}Sn target (4-mg/cm²-thick, 99.8% enrichment) was used to collect the data in the ^{112}Sn($p,d\gamma$)^{111}Sn, ^{112}Sn($p,p'\gamma$)^{112}Sn, and ^{112}Sn($d,p\gamma$)^{112}Sn reactions with a proton beam of 25 MeV and 16 MeV and a 11.5-MeV beam of deuterons, respectively. In all of the first experiments with SiRi, the telescope was placed in the forward position, covering polar angles between 40° and 54°.

The most recent experiments on ^{120,124}Sn were carried out with OSCAR and SiRi, with the latter placed in backward angles to suppress the contribution of elastic scattering events. They were among the first in the series of experiments with OSCAR performed after 2018. Both nuclei were studied in the $(p,p'\gamma)$ reactions with 16 MeV protons impinging on ^{120,124}Sn targets (thicknesses of 2.0 mg/cm² and 0.47 mg/cm², enrichments of 99.6% and 95.3%, respectively). Moreover, the ^{117,119}Sn isotopes were recently remeasured with inelastically scattered protons to make use of the improved excitation and γ-ray energy resolutions with OSCAR and SiRi. The most relevant information on all of the performed experiments is summarised in Table 3.1.

The typical energy resolution achieved in the experiments with ^{3}He with the older setup is $\approx 250 - 350$ keV FWHM, estimated from the fit to the elastic peaks in the (^{3}He,^{3}He$'$) and (^{3}He,α) reaction channels. For the same experimental conditions, SiRi allowed to reduce it to $\approx 150 - 200$ keV in the experiments on ^{121,122}Sn. With the 11.5 MeV d and 20 MeV p beams, it was limited to ≈ 300 keV, chiefly due to the large thickness of the ^{112}Sn target. The best resolution ≈ 100 keV was achieved in all the experiments with 16 MeV protons. In addition to such factors as the intrinsic resolution of Si detectors, target thickness, and beam energy, the beam energy resolution also contributed to these values.

The E and ΔE spectra were calibrated with linear functions applied to centroids of elastic peaks, first excited states within the channels of inelastically scattered particles, ground-state and first-excited-state peaks observed in transfer reaction channels, combined with known energies deposited in each of the 64 ΔE-E telescope combinations. An example of the observed (p,p'), (p,d), and (p,t) reaction channels for the ^{120}Sn target is presented in Fig. 3.3(a). Here, the red solid line shows a graphical cut applied to single out the (p,p') reaction channel of interest. Additionally, an energy-dependent gate on the time difference (after alignment) between the front and back detectors was applied to ensure the exclusion of coincidence events from the neighboring beam pulses. With the known reaction kinematics, the energy deposited to the E and ΔE layers by ejectiles was converted into the initial excitation energy of the nuclei of interest prior to γ-ray emission.

The linear calibration of NaI(Tl) detectors of CACTUS was performed with ^{12}C and ^{28}Si

Table 3.1: Characteristics of the experiments on Sn isotopes performed at the OCL. The given angles refer to the particle scattering angles with respect to the beam direction.

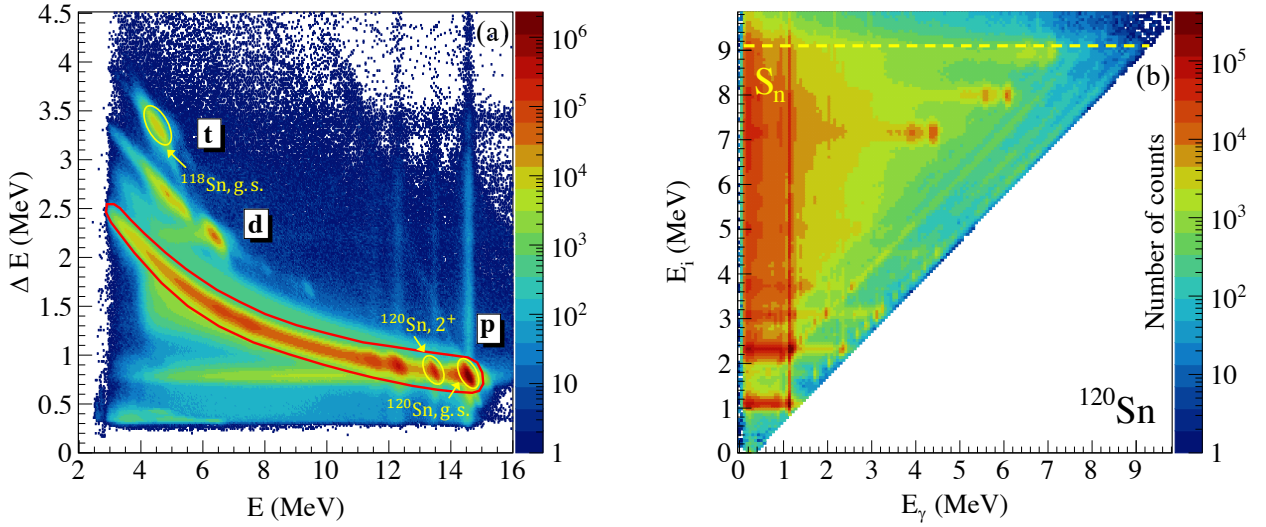| Target	Thickness (mg/cm^2)	Enrichment (%)	Reaction	Beam energy (MeV)	Beam intensity (nA)	Angles ($^\circ$)	Year	Setup
^{112}Sn	4.0	99.8	$(p,d\gamma)$	25.0	≈ 1.0–1.5	126-140	2013	SiRi+CACTUS
			$(p,p'\gamma)$	16.0	≈ 1.0–1.5	126-140	2013	SiRi+CACTUS
			$(d,p\gamma)$	11.5	≈ 0.5–0.7	126-140	2014	SiRi+CACTUS
^{117}Sn	2.1	92.0	$(^{3}\text{He},\alpha\gamma)$	38	≈ 1.5	$\approx 42.5 - 47.5$	2003	Stand. Si + CACTUS
			$(^{3}\text{He},^{3}\text{He}\gamma)^{a}$	38	≈ 1.5	$\approx 42.5 - 47.5$	2003	Stand. Si + CACTUS
			$(p,p'\gamma)^{b}$	16	≈ 2.8	126-140	2019	SiRi + OSCAR
^{119}Sn	1.6	93.2	$(^{3}\text{He},\alpha\gamma)$	38	≈ 1.5	$\approx 42.5 - 47.5$	2008	Stand. Si + CACTUS
			$(^{3}\text{He},^{3}\text{He}\gamma)^{a}$	38	≈ 1.5	$\approx 42.5 - 47.5$	2008	Stand. Si + CACTUS
			$(p,p'\gamma)^{b}$	16	$\approx 0.6 - 0.8$	126-140	2022	SiRi + OSCAR
^{120}Sn	2.0	99.6	$(p,p'\gamma)$	16	$\approx 3.0 - 4.0$	126-140	2019	SiRi + OSCAR
^{122}Sn	1.43	94.0	$(^{3}\text{He},\alpha\gamma)$	38	≈ 0.2	40-54	2010	SiRi+CACTUS
			$(^{3}\text{He},^{3}\text{He}\gamma)$	38	≈ 0.2	40-54	2010	SiRi+CACTUS
^{124}Sn	0.47	95.3	$(p,p'\gamma)$	16	$\approx 3.0 - 4.0$	126-140	2019	SiRi + OSCAR

[a]Not used in the present work.
[b]Remeasured.

Figure 3.3: (a) Experimental $\Delta E - E$ spectrum measured for the ^{120}Sn isotope. The proton channel used for the data analysis is marked with the red solid line. The ground and first excited states of ^{120}Sn in the proton channel and the ground state of ^{118}Sn in the triton channel, used for the linear calibration of the particle telescope, are marked with yellow circles. (b) Raw p-γ coincidence matrix for ^{120}Sn. The data below the neutron threshold (yellow dashed line) are shown.

calibration targets. Even though the large-volume $\varnothing 3.5''\times 8''$ LaBr$_3$(Ce) were shown to provide good linearity of the energy response in tests with the same type of PMT and voltage divider up to 17-18 MeV [215], a minor non-linearity of the 30 OSCAR detectors was accounted for by applying a second-order polynomial fit to centroids of peaks of calibration transitions using the same ^{12}C ($\approx$1 mg/cm^2) and ^{28}Si ($\approx$4 mg/cm^2) targets. Graphical cuts (similar to the one shown in Fig. 3.3(a)) are applied to the energy and time spectra of ΔE and E detectors to limit the analysis to the reaction channel of interest. Further, the data within the gate on the prompt peak in the spectrum of time differences between the signals in the reference E and scintillator detectors are selected. The events obtained by gating on one of the off-prompt peaks, which correspond to random particle-γ coincidences for events from different beam pulses, were subtracted from the selected data to extract the true coincidences for the further analysis. For example, in the most recent experiments on ^{120}Sn and ^{124}Sn, approximately 5.3×10^7 and 1.3×10^7 p-γ coincidence events, respectively, remained below the neutron threshold for the further analysis after the background subtraction.

Selected particle-γ coincidence data were grouped in form of a two-dimensional E_γ-E_i *raw coincidence matrix*, combining γ-ray spectra resulting from γ decays of states with initial excitation energies E_i. An example of such a matrix for the ^{120}Sn isotope is presented in Fig. 3.3(b). The diagonal line with $E_\gamma = E_i$ and other visible neighboring parallel lines correspond to the direct decay to the ground and the first excited states. The experimental resolution allows for a clear separation of the ground state and the first vibrational 2^+ state in all the studied even-even isotopes, while at higher energies or in odd-even isotopes the separation is strongly hindered by a narrow spacing of the low-lying states. The yrast

transitions are usually clearly seen in form of strong vertical lines (e.g. a vertical red line at 1.2 MeV in ^{120}Sn in Fig. 3.3(b)), covering a large range of initial excitation energies up to the neutron threshold. Above S_n, the number of counts is significantly reduced due to the formation of a $^{Z}_{N-1}A$ nucleus and the population of its first excited states. Since the used setup is not optimized for the discrimination of neutrons in coincidence with other particles and photons, the whole subsequent analysis is usually limited to the maximum initial excitation energy $E_i = S_n$. The low-lying transitions between the states within the discrete region were used to check the E_γ and E_i calibrations in each case. The ^{16}O and ^{12}C (6.1 MeV and 7.1 MeV transitions in ^{16}O and a 4.4 MeV transition in ^{12}C in Fig. 3.3(b)) contaminants were present in all data sets and, unless the data within the chosen energy limits were unaffected, were removed at the later stages of the analysis by interpolating the counts from the bins in the immediate vicinity. In most of the cases, the contaminants were successfully removed, leaving a smooth region at relatively high excitation energies below S_n largely unaffected. Any remaining leftover counts have little to no impact on the final results.

3.3 The Oslo method

The information stored in a two-dimensional excitation and γ-ray energy distribution of primary transitions might provide an access to the density of nuclear levels and the distribution of γ-decay probabilities. This was the initial idea behind the first attempts to extract primary transition distributions and NLDs in light-particle-induced reactions by the Oslo group in 1990s, described in the earliest works by Guttormsen *et al.* [33] and Henden *et al.* [219]. This research was to a large extent inspired by particle evaporation experiments, being the main source of information on the NLD as a function of excitation energy outside the discrete region at the time. Attaining a compound-like structure by a nucleus prior to particle or γ emission is the core prerequisite of the analysis. This condition, however, is expected to be better fulfilled for a much slower deexcitation via photon emission.

The idea behind the Oslo method, formulated at the beginning of the 2000s, remains the same. It generalizes and expands the first attempts to access the statistical characteristics of excited nuclei, presenting a rather robust technique to extract the NLD and the GSF from the primary matrix in four key steps: unfolding of experimental spectra, extraction of primary transitions, extraction of functional forms of the NLD and the GSF, and normalization. All these steps applied to the studied Sn isotopes are discussed in detail in the following sections.

3.3.1 Unfolding

As the first step of the analysis with the Oslo method, the measured γ-ray spectra collected at each E_i bin below S_n have to be corrected for the CACTUS or OSCAR detector response in the deconvolution, or unfolding, procedure to reconstruct the true emitted γ-ray spectrum. It relies on the knowledge of a response function of the detecting system, accounting for any interactions of photons within the detector volume or any surrounding materials, and thus a detailed geometry and type of materials used in the array, as well as the statistical nature of scintillation photon emission, the non-uniformity of their collection, and the impact of the PMT and processing electronics, contributing to the final energy resolution. Since Rayleigh
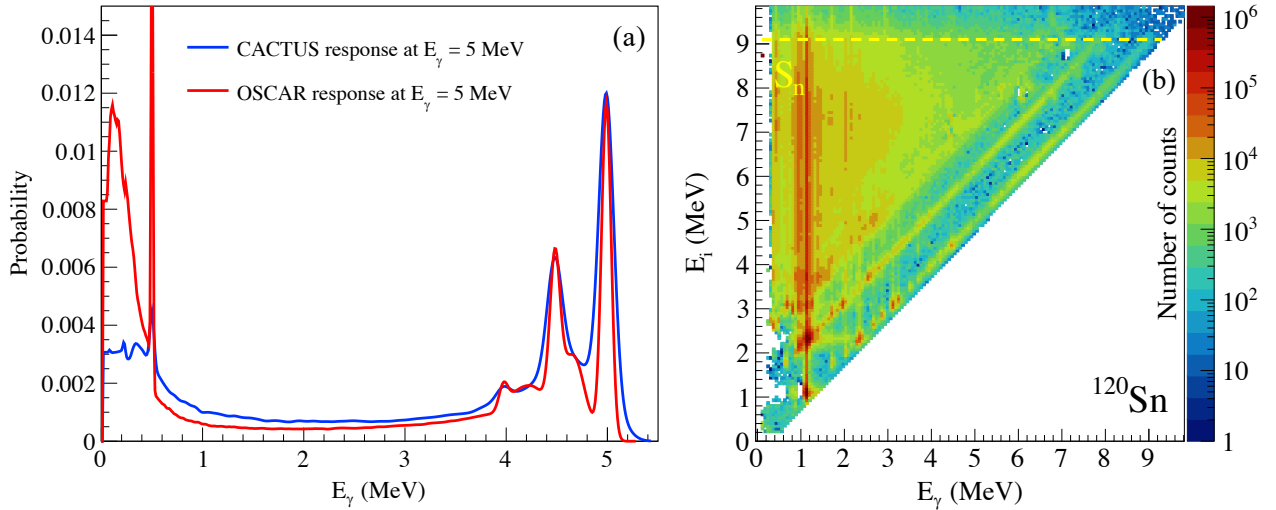
Figure 3.4: (a) Response of CACTUS (blue line) and OSCAR (red line) at E_γ = 5 MeV. The used relative resolution at E_γ = 1.33 MeV is 6% for CACTUS and 3% for OSCAR. (b) Unfolded matrix for ^{120}Sn obtained in the $(p, p'\gamma)$ experiment. All contaminants have been removed. Yellow dashed line indicates the neutron separation energy. The bin size is 64 keV×64 keV.

scattering of very low-energy photons does not result in any measurable effect in the scintillators, the main interaction mechanisms forming the shape of the detector response are the photoelectric effect, Compton scattering, and pair production. The full deposition of a photon energy in the detector volume results in a full energy peak in the spectrum, while any partial energy loss due to Compton scattered photons forms a broad band of the Compton background. Moreover, photons scattered though large angles in the surrounding (e.g. shielding) elements and picked up in the closest scintillator contribute to a broad backscatter peak in the low-energy part of the spectrum (~ 200 keV). For photons with energies E_γ > 1.022 MeV, the pair production process becomes one more mechanism of energy redistribution through a formed electron-positron pair. On its trajectory though the detector (or surrounding) material, a positron annihilates with an atomic electron, forming two 511-keV photons. Both or only one of them may leave the crystal, resulting in the so-called single and double escape peaks, respectively. Alternatively, they might be registered in one of the scintillators, producing a sharp annihilation peak at 511 keV in the spectrum.

In a general case, the response of the detector is presented by a function (or a matrix in a discrete case) $R(E, E_\gamma)$ determining the probability to detect an incident photon of E_γ energy as a signal with energy E. For CACTUS, the response function was determined based on 10 monoenergetic spectra for γ-ray energies from $\approx$ 100 keV to $\approx$ 15 MeV from several radioactive sources and for in-beam experiments [34]. This, however, provides a response limited to these monoenergetic transitions only, whereas a more fine grid of γ energies is generally required. To interpolate between the measured spectra, the full-energy, single and double escape, and annihilation peaks were removed, and the Compton background was interpolated along the channels corresponding to the same scattering angles, forming a fan of interpolation curves.

Hence, for an arbitrary γ energy, the total response is provided by a Compton background reconstructed in this manner and all the peaks added at their corresponding energies, scaled and smoothed with the corresponding intensities and resolutions. For the OSCAR array, the response function [220] was modeled with the GEometry ANd Tracking 4 (GEANT4) library [221–223] for a large grid of incident photon energies, considering the complete geometry of the setup (the OSCAR detectors, support frame, target chamber, SiRi, beam line, target holders, and frame). The simulations were performed for isotropic mono-energetic sources with multiplicity 1. The detailed modeling of the scintillation process was omitted to keep the optimal computation time. To account for this and the response of the signal processing electronics, all peaks were corrected for the experimental resolution. The simulations were verified against measured ^{60}Co, ^{133}Ba, ^{137}Cs, ^{152}Eu source spectra and in-beam spectra and were found to provide a reliable response matrix down to $E_\gamma \lesssim 200$ keV, well below the energies considered in the analysis and the experimental energy threshold. An example of responses of CACTUS and OSCAR at $E_\gamma = 5$ MeV are shown Fig. 3.4(a).

With the response function $R(E, E_\gamma)$, the observed experimental spectrum is provided by the convolution transform of the "true" (unfolded) γ spectrum:

$$R(E) = \int R(E, E_\gamma) U(E_\gamma) dE_\gamma. \tag{3.2}$$

For the recorded spectra discretized by binning, this relation can be rewritten in a matrix form:

$$\mathbf{f} = \mathbf{R}\mathbf{u}, \tag{3.3}$$

with $\mathbf{R}$ representing the discrete probability distribution, replacing the conditional probability density in the previous equation. The vectors $\mathbf{f}$ and $\mathbf{u}$ represent the measured and the true spectra, respectively.

The most straightforward way to restore the unfolded spectrum $\mathbf{u}$ would be solving an inverted matrix equation. However, the response matrix might be ill-conditioned, and any small changes in the measured spectrum might result in large artificial oscillations of the unfolded solution. To avoid such instabilities, an easily performed and not computationally demanding direct folding procedure can be used instead to approximate the unfolded spectrum in an iterative procedure. This technique, called the *folding iteration method*, is used (see e.g. [34, 35]) to deconvolute the measured data from experiments as a part of the analysis with the Oslo method an can be summarized in the following steps:

1. The measured spectrum $\mathbf{f}$ is chosen as a zeroth-order approximation (trial function) of the unfolded spectrum $\mathbf{f}$:

$$\mathbf{u}_0 = \mathbf{f}. \tag{3.4}$$

2. The trial spectrum is folded:

$$\mathbf{f}_0 = \mathbf{R}\mathbf{u}_0. \tag{3.5}$$

3. The next approximation to the unfolded spectrum is constructed from the previous trial function and the difference between the observed and the first folded trial function as:

$$\mathbf{u}_1 = \mathbf{u}_0 + (\mathbf{f} - \mathbf{f}_0). \tag{3.6}$$

4. This process continues until the difference $\mathbf{f} - \mathbf{f}_i$ becomes comparable with the fluctuations in the i-th trial function $\mathbf{u}_i$, *i.e.* $\mathbf{f}_i$ and $\mathbf{f}$ are comparable within the uncertainties.

Large numbers of iterations might result in strong oscillations making the the obtained unfolded spectrum similar to the solution with the response matrix inversion. In most of the Oslo method works performed with the CACTUS array, the recommended number of iterations was limited to $10-50$ iterations. However, with the response matrix of OSCAR, this number of iterations was found to be insufficient when handling strong artificial oscillations in the spectrum linked to the present contaminants. Larger numbers (up to several hundreds) are recommended to reduce such artifacts without creating any strong additional fluctuations. Moreover, as noted in Ref. [224], the quality of the obtained unfolded spectra are also affected by the widths (smoothing) of all structures in the response matrix. Applying the experimental resolution of 1 FWHM might potentially lead to large oscillations around observed peaks. The optimal widths were suggested to be reduced to 50% of the experimental FWHM values. This was confirmed in Ref. [34] for the response matrix of CACTUS and implemented in the unfolding procedure of the Oslo method software. For OSCAR, the response FWHM was further reduced to 10% of the experimental value.

Further refinement of the unfolded spectrum $\mathbf{u}$ obtained in the previous procedure is provided with the so-called Compton subtraction method [34]. The core idea of this last step is to obtain the final unfolded solution having experimental fluctuations of the observed spectrum $\mathbf{f}$, rather than preserving fluctuations introduced with the folding iteration method. Using the unfolded spectrum $\mathbf{u}$ as a starting point, the procedure can be outlined as follows:

1. Provided that the probabilities of counts to be attributed to the full-energy (p_{fe}), single escape (p_{se}), double escape (p_{de}), and annihilation peaks (p_a) were estimated when creating the response matrix, a new spectrum comprising the peak structures only is defined:

$$\mathbf{v} = \mathbf{u}_{fe} + \mathbf{w}, \tag{3.7}$$

where $\mathbf{w} = \mathbf{u}_{se} + \mathbf{u}_{de} + \mathbf{u}_a$, $\mathbf{u}_{fe}(i) = p_{fe}(i)\mathbf{u}(i)$, $\mathbf{u}_{se}(i - i_{511}) = p_{se}(i)\mathbf{u}(i)$, $\mathbf{u}_{de}(i - i_{1022}) = p_{de}(i)\mathbf{u}(i)$, $\mathbf{u}_a(i_{511}) = \sum_i p_a(i)\mathbf{u}(i)$, and i indicates a bin number (i_{511}, i_{1022} are the bins for the energies of 511 keV and 1022 keV, respectively).

2. Each peak is smoothed to match the experimental energy resolution of 1 FWHM.

3. The Compton background is extracted from the folded (raw) spectrum:

$$\mathbf{c} = \mathbf{f} - \mathbf{v}, \tag{3.8}$$

inherently containing strong fluctuations of the unfolded spectrum. The latter can removed by applying a 1 FWHM smoothing to $\mathbf{c}$, since the Compton background is expected to be a slowly varying function of energy.

4. Finally, the final unfolded spectrum preserving the experimentally observed fluctuations is obtained by subtracting the smoothed components from the observed spectrum f:

$$\tilde{\mathbf{u}} = \mathbf{f} - \mathbf{w} - \mathbf{c}. \tag{3.9}$$

Further, this spectrum is corrected for the full-energy peak probability and the total detector efficiency.

The combination of the folding iteration and the Compton subtraction methods has been repeatedly shown to be quite robust and provide reliable results in numerous previous works (see Ref. [35] and references therein). An example of the unfolded matrix produced for ^{120}Sn is shown in Fig. 3.4(b).

3.3.2 Extraction of primary γ-rays

Accessing both the GSF and the NLD from the statistical decay of states in the quasi-continuum requires information on the distribution of branching ratios for the γ decay of states within each initial excitation energy bin. It can be obtained by singling out first-generation, or primary, transitions, by separating them from any secondary, tertiary, and other generations of transitions in all cascades of γ decays contained in the emitted spectra. Within the Oslo method framework, this is done with the so-called *first-generation method* [33], an iterative subtraction technique applied to γ spectra of the unfolded matrix (Fig. 3.4(b)).

To provide an overview of this procedure, let us consider an unfolded spectrum u_i for an initial excitation energy bin i, which contains all possible cascades of photons produced in the deexcitation of a nucleus in excited states within the i-th bin. Naturally, in the statistical region, the level spacing limits us to the analysis of ensembles of excited states within excitation energy bins rather than separate states. If the acquired statistics allow, typical bin widths are usually chosen to be $10 - 100$ keV. Assuming that the decay pattern of these states is independent of the mechanism of their formation (via direct population in a reaction or decay of higher-lying states), the spectra in the lower-lying bins j are expected to include the same γ transitions as in the bin i, excluding all primary transitions stemming directly from the bin i. This is the core assumption of the method, and it is expected to hold well within the chosen E_i and E_γ energy limits [33, 35, 219]. Considering that a typical γ-decay lifetime within the quasi-continuum region is of order $\sim 10^{-15}$ s, comparatively longer than $\sim 10^{-18}$ s required to reach an equilibrium, a nucleus might indeed be expected to attain a compound-like state prior to the observed γ decays. This allows us to express the primary spectrum p_i as a difference of the unfolded spectrum for the bin i and a weighted sum of contributions from the lower-lying bins j:

$$p_i = u_i - \sum_{j<i} n_{ij} w_{ij} u_j. \tag{3.10}$$

Here, the weighting coefficients w_{ij} are normalized ($\sum_j w_{ij} = 1$) and present the distribution of decay probabilities from the states i to the states j, or branching ratios. The coefficients n_{ij} are introduced to account for the difference in cross sections of populating states in the bins i and j.

The correction for the cross-section n_{ij} is determined so that the area of $n_{ij}u_j$ for each j corresponds to the same number of cascades as in the initial spectrum u_i. It can be obtained by comparing numbers of counts N^s in the singles spectra for the bins i and j (singles normalization). Due to the proportionality of the singles-particle cross sections to the numbers of eventual cascades, the coefficients n_{ij} can be written as:

$$n_{ij} = \frac{N_i^s}{N_j^s}. \tag{3.11}$$

Alternatively, they can be deduced through an average γ-ray multiplicity $\langle M \rangle$ for the cascades in the bins i and j (multiplicity normalization). Denoting the numbers of counts in the spectra u_i and u_j as N_i^u and N_j^u, respectively, the coefficients take the following form:

$$n_{ij} = \frac{N_i^u}{\langle M_i \rangle} \frac{\langle M_j \rangle}{N_j^u}, \tag{3.12}$$

where the average multiplicity can be extracted from the average γ-ray energy corresponding to the deexcitation of a nucleus at excitation energy E_x:

$$\langle M \rangle = \frac{E_x}{\langle E_\gamma \rangle}. \tag{3.13}$$

Considering the weighting coefficients w_{ij} are introduced to account for the branching ratio distribution, they correspond directly to the primary spectrum p_i after providing the latter with the same energy calibration as in w_{ij} and normalizing its area to unity. This relation suggests an iterative procedure to obtain the primary spectrum through the series of consecutive approximations of the unknown w_{ij} weights for the considered bins i and $j < i$. As the first step, an arbitrary trial function w_{ij} is adopted. It is used to approximate the primary spectrum p_i from Eq. (3.10), which can be further normalized to 1 and recalibrated to match the energy calibration of w_{ij} in order provide a new, updated function w_{ij}. This process is repeated until the updated coefficients w_{ij} are approximately equal to those from the previous iteration.

To have a better control over this procedure, an area consistency check can be performed at each iteration for the cases with well-determined average multiplicities. Let us denote the subtracted sum in Eq. (3.10) as g_i and multiply the number of counts in it by an additional factor α, so that the areas under the spectra p_i, g_i, and u_i provided by the corresponding numbers of counts N_i^p, N_i^g, and N_i^u are related by

$$N_i^p = N_i^u - \alpha N_i^g. \tag{3.14}$$

The correction α is assumed to be close to 1. The number of primary photons in the spectrum p_i is supposed to be equal to the number of possible cascades, and thus the number of counts in the primary spectrum N_i^p can be linked to the number of counts in the original spectrum u_i and the average γ-ray multiplicity as:

$$N_i^p = \frac{N_i^u}{\langle M_i \rangle}, \tag{3.15}$$

and the correction α from Eq. 3.14 becomes then

$$\alpha = \left(1 - \frac{1}{\langle M_i \rangle}\right) \frac{N_i^u}{N_i^g}. \tag{3.16}$$

Such correction is performed for each excitation energy bin at each iteration and, as a rule of thumb, should not exceed $\approx 15\%$. For larger deviations, a new trial function w_{ij} should be considered. However, in most of the cases analyzed with the Oslo method, including all the
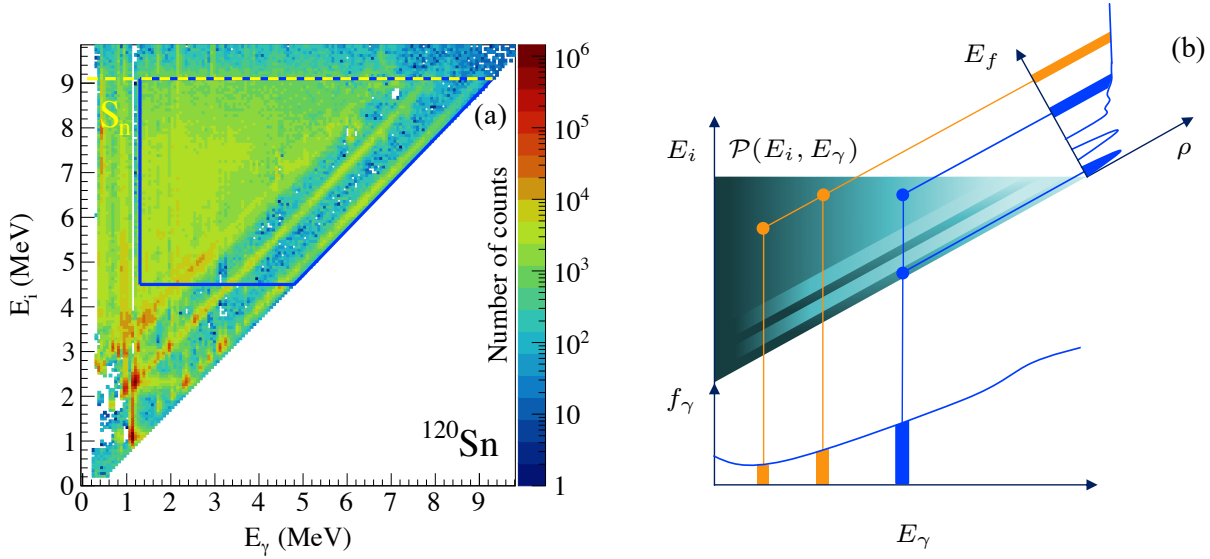
Figure 3.5: Primary matrix for ^{120}Sn obtained in the $(p, p'\gamma)$ experiment. Yellow dashed line indicates the neutron separation energy, and blue solid lines indicate the areas of the primary matrices used further in the Oslo method. The bin size is 64 keV×64 keV . (b) Schematic representation of the decomposition of the primary matrix into the NLD and the GSF.

studied Sn isotopes, α is approximately equal to 1 at relatively high excitation energies below the neutron threshold and only moderately deviates from this value towards the discrete excitation energy region. The procedure has been shown to be essentially insensitive to the initial choice of the trial function w_{ij} (the unfolded spectrum is taken by default), and the choice between the singles and the multiplicity (chosen here) normalizations, providing results well in agreement within the uncertainties. The procedure converges quite well already after a few iterations for simulated spectra, as was shown in Ref. [33]. However, for experimental spectra, including those for all the studied Sn isotopes, $\approx 10 - 20$ iterations are usually performed to ensure a good convergence. An example of a primary matrix obtained with the first-generation method is shown in Fig. 3.5(a).

The area correction check can be used as one of the benchmarks limiting the range of initial excitation energies to a certain $E_i^{\min}$. Moreover, the reliability of the first-generation method is limited at low excitation energies and low γ-ray energies due to the reduced configuration mixing and thus an apparent failure of the adopted hypothesis regarding the independence of decay patterns of a population mechanism. This hypothesis has been discussed in detail in Ref. [35] and put into test in calculations [225]. As mentioned earlier, thermalization of a nucleus at higher excitation energies is justified by the typical time frame required to form a compound nucleus versus that required for a de-excitation via γ decay. The typical spectra of such thermalized states can be expected to be rather smooth and similar in shape, which is indeed the case for the experimental unfolded and primary spectra in the quasi-continuum. The deviations form this pattern tend to occur closer to the discrete state region. Here, it might be observed that some of the states are more likely to be populated directly in a reaction rather than fed via γ decay of above-lying states, or vice versa. This results in a strong over-subtraction or an under-subtraction of counts, respectively, at the same γ-ray

Table 3.2: Minimum and maximum limits for the initial excitation energy ($E_i^{\min}$ and $E_i^{\max} \approx S_n$) and minimum γ-ray energy $E_\gamma^{\min}$ limits applied to the primary matrices of $^{111-113,116-122,124}$Sn. All energies are provided in MeV.

Isotope	^{111}Sn	^{112}Sn	^{113}Sn	^{116}Sn	^{117}Sn	^{118}Sn	^{119}Sn	^{120}Sn	^{121}Sn	^{122}Sn	^{124}Sn
$E_\gamma^{\min}$	1.0	1.5	1.5	1.6	1.4	1.5	1.8	1.3	1.7	1.8	1.6
$E_i^{\min}$	3.0	4.0	5.5	4.0	3.4	4.9	4.0	4.5	3.5	4.5	5.0
$E_i^{\max}$	8.2	10.8	7.7	9.6	6.9	9.2	6.5	9.1	6.2	8.8	8.5

energy in the higher-lying excitation energy bins. An example of such an over-subtraction is clearly seen in Fig. 3.5(a) below ≈ 1.2 MeV. This effect commonly limits the γ-ray energy to a certain $E_\gamma^{\min}$ in each case. For this reason, the extracted GSFs in the studied Sn isotopes reach only down to $\approx 1-2$ MeV.

Another factor that might distort decay patterns towards higher excitation energies is a gradual change of the spin distribution with population of higher-spin states[1]. The experimental spin distribution as a function of excitation energy has been previously addressed in Refs. [219, 226] for the case of ^{162}Dy by studying the ground band side-feeding probability at different excitation energies. The results suggest the spin distribution to be almost constant within the quasi-continuum region. An overall similarity of the populated (unfolded) spectra throughout the quasi-continuum region in the Sn isotopes also support this conclusion.

To test the influence of different reaction mechanisms and thus potentially different populated spin ranges, decay patterns of the same nucleus produced in the pick-up and inelastic scattering reactions have been studied in Refs. [227–229]. A similar test can be provided by a comparison of the results from inelastic scattering of protons, ^{3}He, and α particles on the same target (e.g. ^{117}Sn in the present work). A good agreement of NLDs and GSFs obtained with different reactions within the uncertainty bands supports the assumptions behind the first-generation method.

Based on all the above-mentioned limitations, the $E_\gamma^{\min}$ and $E_x^{\min}$ were chosen to limit the statistical excitation energy region of the primary matrix used for the subsequent extraction of the NLDs and GSFs. The limits for all the eleven Sn isotopes are listed in Table 3.2. In principle, with the primary matrix at hand, one might follow two alternative ways to extract the GSF. The first one is a part of the standard Oslo method and presents a decomposition of the distributions of primary transitions from the states in the quasi-continuum to determine both the NLD and the GSF as functions of excitation and γ-ray energies, respectively (see Fig. 3.5(b)). On the other hand, the *shape method* provides an alternative approach to extracting the slope of the GSF by considering intensities of primary decays to the ground and the first excited discrete states. The application of this method to the studied Sn isotopes will be outlined in detail in Sec 3.4.

---

[1]Another factor might also be a disproportionate contribution of states with positive and negative parities in the quasi-continuum. According to HFB plus combinatorial method calculations by Goriely *et al.* [112] and their further improvement by Hilaire *et al.* [113], this should not not have any significant effect at sufficiently high excitation energies below the neutron threshold.

3.3.3   Decomposition of the primary matrix

As mentioned earlier, the extraction of the statistical characteristics of excited nuclei with the Oslo method is largely based on the compound-nucleus picture. Here, we take as a starting point a nucleus in a thermalized state, γ decaying through a certain final channel f, which is fully decoupled from an initial channel c of the compound state formation. The energy distribution N_f of emitted particles would then be determined by the cross section $\sigma(c \to f)$ of going from the channel c to to the final channel f and the density of final states in the residual nucleus f as [89]:

$$dN_f = \sigma(c \to f)\rho_f dE_f. \tag{3.17}$$

Applied to the distribution of primary transitions $\mathcal{P}(E_i, E_\gamma)$ extracted with the first-generation method, this relation can be further modified within the Hauser–Feshbach theory of statistical reactions to obtain the following relation between the γ-ray transmission coefficient for transitions from the states i in the quasi-continuum to the final states f and the density ρ_f:

$$\mathcal{P}(E_\gamma, E_i) \propto \mathcal{T}_{i \to f} \cdot \rho_f. \tag{3.18}$$

A detailed derivation of this relation is presented in Ref. [230] and in Appendix A. One can arrive at the same factorization with somewhat more illustrative Fermi's golden rule [231, 232] taken as a starting point instead [233]:

$$\lambda_{i \to f} = \frac{2\pi}{\hbar} |\langle f|\hat{H}_{\mathrm{int}}|i\rangle|^2 \rho_f, \tag{3.19}$$

where $\lambda_{i \to f}$ is the transition rate between the states i and f, and $\hat{H}_{\mathrm{int}}$ is the interaction Hamiltonian between the external field and the nucleus. Here, the transition rate can be directly related to the first-generation spectra of the primary matrix, after averaging over numerous initial states within excitation energy bins of $\mathcal{P}(E_\gamma, E_i)$. The γ-ray transmission coefficient in Eq. (3.18) characterizes the average decay properties of such states. Similarly to the matrix element in Eq. (3.19), it depends on both initial and final states, or rather ensembles of states in initial and final excitation energy bins. This makes the simultaneous extraction of $\mathcal{T}_{i \to f}$ and ρ_f from the experimental primary matrix impossible. At this point, to resolve this issue, the Brink-Axel hypothesis is introduced in the analysis, reducing the dependence of the γ-ray transmission coefficient on the initial and final states to E_γ as the only argument, i.e. $\mathcal{T}_{i \to f} \to \mathcal{T}(E_\gamma)$. The Brink-Axel hypothesis is one of the key assumptions adopted in the Oslo method, and its applicability in the case of the studied Sn isotopes will be discussed in detail in the next chapter. With this simplification, Eq. (3.18) can be further modified to obtain the principal relation of the Oslo method:

$$\mathcal{P}(E_\gamma, E_i) \propto \mathcal{T}(E_\gamma) \cdot \rho(E_i - E_\gamma). \tag{3.20}$$

With this factorization, functional forms of the NLD and the GSF are obtained by applying an iterative minimization procedure. Here, we present only the key steps leading from the primary matrix to $\rho(E_x)$ and $\mathcal{T}(E_\gamma)$, while the rest of the intermediate derivations can be found in Ref. [234].

As a first step, the primary matrix $\mathcal{P}(E_i, E_\gamma)$ is normalized to unity for each excitation energy bin E_i and γ-ray energies running from the minimum value defined in Sec. 3.3.2 to the value of E_i:

$$\sum_{E_\gamma = E_\gamma^{\min}}^{E_i} \mathcal{P}(E_i, E_\gamma) = 1. \tag{3.21}$$

The principal idea of the procedure is to approximate the experimental matrix $\mathcal{P}(E_i, E_\gamma)$ with a theoretical matrix $\mathcal{P}_{\text{theor}}(E_i, E_\gamma)$, normalized according to Eq. (3.21) and having the following form:

$$\mathcal{P}_{\text{theor}}(E_i, E_\gamma) = \frac{\mathcal{T}(E_\gamma)\rho(E_i - E_\gamma)}{\sum_{E_\gamma = E_\gamma^{\min}}^{E_i} \mathcal{T}(E_\gamma)\rho(E_i - E_\gamma)}, \tag{3.22}$$

with $\mathcal{T}(E_\gamma)$ and $\rho(E_i - E_\gamma)$ corresponding to the desired solutions for the γ-ray transmission coefficient and the NLD. The approximation is done by minimizing χ^2 in the following form:

$$\chi^2 = \frac{1}{N_{\text{free}}} \sum_{E_i = E_i^{\min}}^{E_i^{\max}} \sum_{E_\gamma = E_\gamma^{\min}}^{E_i} \left(\frac{\mathcal{P}_{\text{theor}}(E_i, E_\gamma) - \mathcal{P}(E_i, E_\gamma)}{\Delta\mathcal{P}(E_i, E_\gamma)} \right)^2 \tag{3.23}$$

with $N_{\text{free}} = N_\mathcal{P} - N_\mathcal{T} - N_\rho$ corresponding to the number of degrees of freedom. $N_\mathcal{P}$, $N_\mathcal{T}$, and N_ρ are the numbers of data points in $\mathcal{P}(E_i, E_\gamma)$, $\mathcal{T}(E_\gamma)$, and $\rho(E_i - E_\gamma)$, respectively. $\Delta\mathcal{P}(E_i, E_\gamma)$ is an uncertainty of each bin (E_i, E_γ) in the experimental primary matrix. Strictly speaking, it is defined by the Poisson statistics, but the Gaussian distribution implied by the use of the χ^2 minimization is a sufficiently good approximation.

It can be shown that the form of the theoretical primary matrix provided by Eq. 3.22 implies that one can construct an infinite set of analytical solutions with the following transformations of the original solutions $\rho(E_i - E_\gamma)$ and $\mathcal{T}(E_\gamma)$ from the least χ^2 method (see Ref. [234] for a detailed derivation):

$$\begin{aligned}\tilde{\rho}(E_i - E_\gamma) &= A\rho(E_i - E_\gamma)\exp\big(\alpha(E_i - E_\gamma)\big), \\ \tilde{\mathcal{T}}(E_\gamma) &= B\mathcal{T}(E_\gamma)\exp\big(\alpha E_\gamma\big),\end{aligned} \tag{3.24}$$

with A and B being the scaling parameters, and α being a slope parameter, shared by both the NLD and the γ-ray transmission coefficient.

Considering this, one can start the procedure by obtaining the first-order estimate of $\mathcal{P}(E_i, E_\gamma)$ by setting the corresponding first-order estimate of $\rho_0(E_i - E_\gamma)$ to 1. Summing over the initial excitation energies and taking into account that $E_\gamma \leq E_i$ provides the first-order estimate of the γ-ray transmission coefficient:

$$\mathcal{T}_0(E_\gamma) = \sum_{E_i = \max(E_i^{\min}, E_\gamma)}^{E_i^{\max}} \mathcal{P}(E_i, E_\gamma). \tag{3.25}$$

Further, we minimize the χ^2 function with respect to $\rho(E_i - E_\gamma)$ and $\mathcal{T}(E_\gamma)$ by letting

$$\frac{\partial\chi^2}{\partial\rho(E_i - E_\gamma)} = 0, \qquad \frac{\partial\chi^2}{\partial\mathcal{T}(E_\gamma)} = 0 \tag{3.26}$$
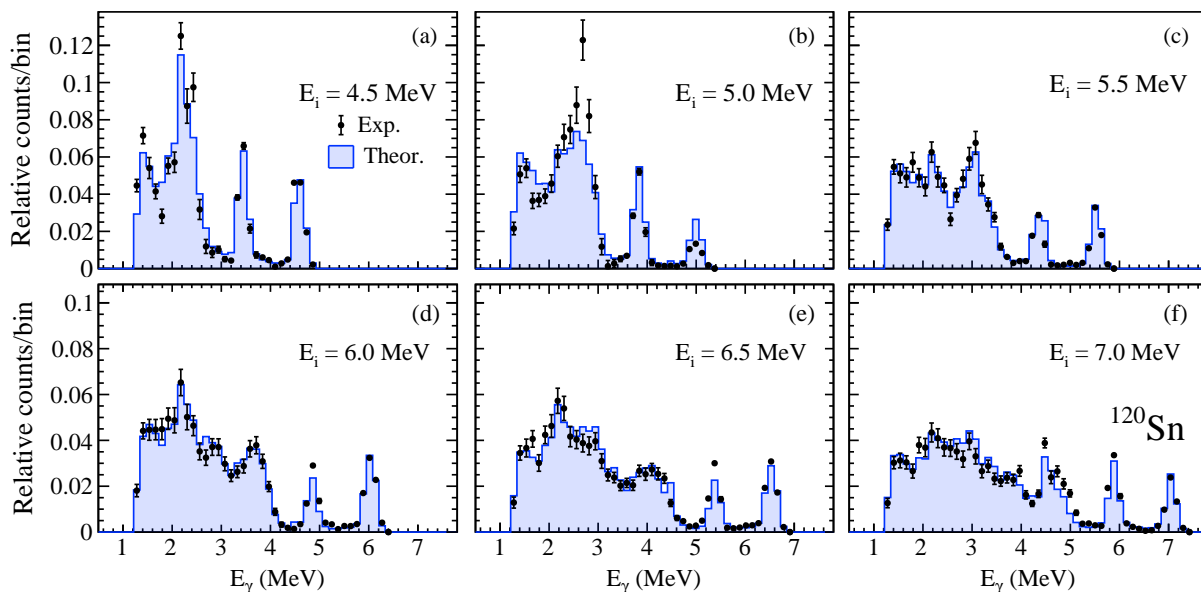
Figure 3.6: Experimental primary spectra of ^{120}Sn at approximately 4.5 MeV (a), 5.0 MeV (b), 5.5 MeV (c), and 6.0 MeV (d), 6.5 MeV (e), 7.0 MeV (f) excitation energy bins compared to the spectra predicted with the derived level density and γ-transmission coefficient (from Eq. (3.22)). The excitation energy bins are 128-keV wide.

for all arguments $E_i - E_\gamma$ and E_γ of these functions. This provides two equations to determine the next-order estimates $\rho_1(E_i - E_\gamma)$ and $\mathcal{T}_1(E_\gamma)$ through the zero-order functions.

In general, this procedure converges fast (within $\approx 30 - 40$ iterations) and well, which was also the case for all the studied Sn isotopes. Some examples of the experimental spectra fitted with the optimized $\mathcal{P}_{\text{theor}}(E_i, E_\gamma)$ for several initial excitation energy bins in ^{120}Sn are shown in Fig. 3.6. The theoretical fitted spectra reproduce all the observed experimental features quite well. To avoid any potential failures due to a too shallow χ^2 minimum, a restriction is imposed on the changes in the NLD and the γ-ray transmission coefficient, obtained in each subsequent iteration. The restricting conditions depend on a parameter varied with the iteration number and chosen to provide a compromise between achieving the minimum possible χ^2 value and maintaining a reasonable execution time.

3.3.4 Normalization of the NLD

As mentioned previously, the χ^2 minimization procedure provides only the functional forms of the NLD and the γ-ray transmission coefficient, which have to be further normalized to available external experimental data to constrain the physical solutions for $\rho(S_n)$ and $\mathcal{T}(E_\gamma)$. The principal goal here is to find the optimal normalization parameters and models based on the most recent experimental and theoretical information available for a consistent description of all the eleven Sn isotopes. The Coulomb excitation (p, p') data serve as an excellent benchmark for both the slope and the absolute values of the GSF, while also indirectly testing the choice of the slope parameter for the NLD.
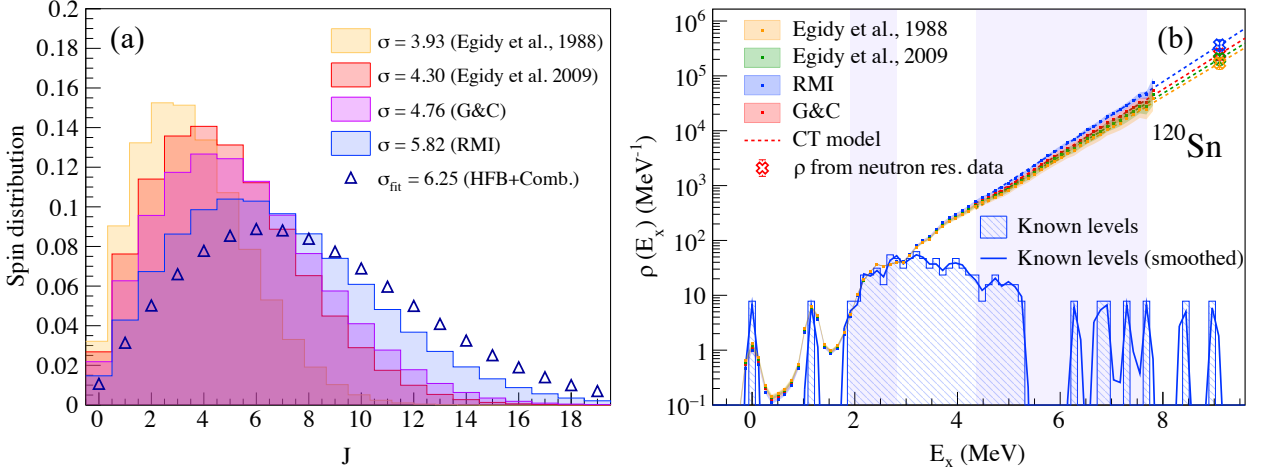
Figure 3.7: (a) Spin distributions at the neutron separation energy in ^{120}Sn modeled within the rigid moment of interta (RMI) [103], Gilbert and Cameron (G&C) [97], Egidy *et al.* (1988) [104] and (2009) [108], and Hartree-Fock-Bogoliubov plus combinatorial (HFB+Comb.) [112] approaches. For the latter, the spin-cutoff fit value obtained by using Eq. (3.28) is shown in the legend. (b) The NLD normalized with different spin cutoff values. The fit ranges at low and high excitation energies are marked with vertical shaded areas.

In the first step, the normalization of the NLD is performed by determining the absolute normalization (scaling) A and the slope α. To do so, the NLD in the form of Eq. 3.24 is fitted to the low-lying discrete states available from the most recent compilation in Ref. [125]. The fit range at low excitation energies is usually chosen from the first closely-spaced discrete states up to the highest energy where the level scheme can still be considered complete (the vertical shaded area in Fig. 3.7). In the present analysis it was chosen to achieve the best match between the experimental NLD, integrated over excitation energy bins within this energy range, and the corresponding NLD provided by the tabulated discrete states. However, in general, the final result for the majority of the studied isotopes does not change in any significant way with the exact choice of low-energy fit limits.

The slope of the NLD and its absolute value at the neutron threshold energy can be determined from the corresponding value of $\rho(S_n)$. The resonance spacings D_0 and D_1 obtained in s-wave and p-wave neutron resonance experiments, respectively, are commonly used to estimate this value. In case of s-wave neutrons incident on a target nucleus with the ground state spin J_t, the *partial* NLD at the neutron separation energy can be linked to the experimental D_0 value as:

$$\frac{1}{D_0} = \frac{1}{2}\big(\rho(S_n, J_t + 1/2) + \rho(S_n, J_t - 1/2)\big), \tag{3.27}$$

where the 1/2 factor is due to an assumption of the parity equipartition, i.e. levels with positive and negative parities contributing equally to the total NLD. This assumption is expected to hold well at sufficiently high excitation energies (in the vicinity of S_n values in the Sn isotopes), which is also confirmed by microscopic NLD calculations within the Hartree-Fock-Bogoliubov plus combinatorial (HFB+Comb.) framework [112].

To access the *total* NLD at the S_n energy, we exploit the fact that the *partial* NLD $\rho(E_x, J)$ can be expressed as a fraction of the *total* NLD $\rho(E_x)$ by applying a certain spin-distribution model $g(E_x, J)$. Here, we adopt the approach of Refs. [95, 97], suggesting the following form of the spin distribution:

$$
\begin{aligned}
g(E_x, J) &= \frac{1}{2\sigma^2(E_x)} \exp\left(-\frac{J^2}{2\sigma^2(E_x)}\right) - \frac{1}{2\sigma^2(E_x)} \exp\left(-\frac{(J+1)^2}{2\sigma^2(E_x)}\right) \\
&\simeq \frac{2J+1}{2\sigma^2(E_x)} \exp\left(-\frac{(J+1/2)^2}{2\sigma^2(E_x)}\right),
\end{aligned}
\tag{3.28}
$$

where $\sigma(E_x)$ is an energy-dependent spin-cutoff parameter. Depending on the choice of the model for the latter, the slope of the NLD might change significantly, thus making it an important source of potential uncertainties in α. Some of the earlier analyses (see e.g. [187]) employed the rigid-body form of $\sigma^2(S_n)$ [98, 103] provided by Eq. (2.13), Eq. (2.11) taken from Refs. [97, 235] (see e.g. [83]), an averaged value from several models [139], or by varying the $\sigma^2(S_n)$ value between several model predictions [36]. Examples of the spin distribution at the neutron threshold in ^{120}Sn obtained with some of the spin cutoffs used in the earlier works are shown in Fig. 3.7(a).

The microscopic calculations by Urenholt *et al.* [236] and Hilaire *et al.* [120] suggest that the pairing correlations might still be sufficiently strong up to relatively high excitation energies in the vicinity of the neutron separation energy to prevent a nucleus from attaining the rigid-body moment of inertia. The recent QRPA plus boson expansion calculations by Hilaire *et al.* [114] also suggest narrower spin distributions (lower σ^2) at energies of $8-12$ MeV in the spherical ^{136}Ba nucleus than those obtained with HFB+Comb. approach [112]. The latter usually provides spin-cutoff values close or slightly larger than the rigid-body estimates in Sn isotopes (see Fig. 3.7(a)). Moreover, a recent experimental study of the spin cutoff in ^{59}Ni provided a reduced estimate for this nucleus as compared to the rigid-body value, highlighting the role of the pairing correlations at relatively high energies. The need for such a reduction is also evident from the Sn Oslo data. For all the studied isotopes, the rigid-body model approach results in systematically steeper slopes of the NLDs and, therefore, the corresponding slopes of the GSFs as compared to the Coulomb excitation data. On the contrary, the slopes of the NLDs obtained with the models proposed in Refs [104, 108] tend to be milder. The search for an optimal spin-cutoff parameter can, for example, be facilitated by the use of the shape method (Sec. 3.4). Unfortunately, experimental limitations (e.g. insufficient statistics) prevent us from obtaining reliable results with the shape method for some of the studied Sn isotopes. Here, instead of introducing an unknown reduction factor applied to the rigid-body estimate, which provides an additional degree of uncertainty, the following form of the spin-cutoff was chosen:

$$
\sigma^2(S_n) = 0.0888a\sqrt{\frac{S_n - E_1}{a}} A^{2/3},
\tag{3.29}
$$

with the level density and the back-shift parameters a and E_1 obtained from the global parameterization of Ref. [103]. The spin-cutoff values provided by this model amount to $\approx 80\%$ of the values based on the rigid-body approach. This choice is additionally supported by an excellent agreement in slopes with the Coulomb excitation data. In cases where no
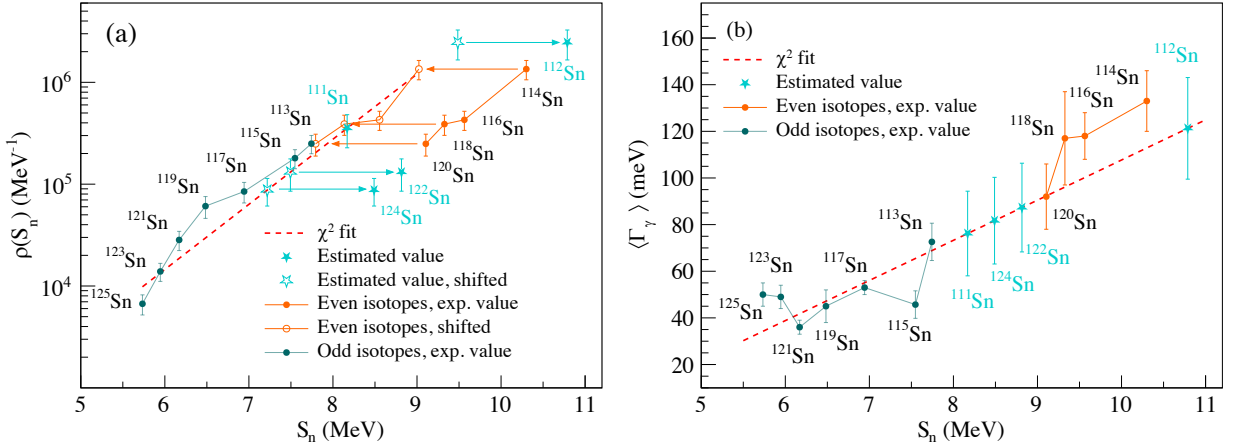
Figure 3.8: (a) Systematics for the $\rho(S_n)$ values extracted from the experimental s-wave neutron resonance spacing D_0 parameters [126]. The even-even and even-odd isotopes are shown as filled orange and teal circles, the shifted values for the even-even isotopes (see text for details) are shown as empty orange circles. The dashed red line corresponds to the χ^2 fit, and the extrapolated and interpolated values for ^{111,112,122,124}Sn as shown as cyan starts. (b) Systematics for the $\langle\Gamma_\gamma\rangle$ values extracted from the experimental s-wave neutron resonance average total radiative widths [126]. All notations are the same as in (a).

experimental data below the threshold are available, one should consider including the spread of the NLD at higher excitation energies due to different spin-cutoff models (Fig. 3.7(b)) into the total final uncertainty. Luckily, the Coulomb excitation data for the Sn isotopes and the shape method allow us to reject some of the models and choose only one approach, consistently used for all nuclei throughout the whole analysis.

Combining Eq. (3.27) and Eq. (3.28), the NLD at the neutron separation energy can be expressed as:

$$\rho(S_n) = \frac{2\sigma^2}{D_0} \frac{1}{(J_t+1)\exp\left(-\frac{(J_t+1)^2}{2\sigma^2}\right) + J_t\exp\left(-\frac{J_t^2}{2\sigma^2}\right)}. \qquad (3.30)$$

The D_0 values available from the compilation in Ref. [126] were used to extract $\rho(S_n)$ in $^{113-121,123,125}$Sn. No experimental data are available for unstable targets ^{110,111,121,123}Sn. To fill these gaps, the systematics of the $\rho(S_n)$ values as a function of S_n were constructed for the Sn isotopes (see Fig. 3.8). The even-odd and even-even nuclei form two separate groups of data points which were combined by shifting the values of $\rho(S_n)$ for the even-even isotopes by the value of a neutron pairing gap Δ_n [237]. The combined data were fitted with a log-linear function to extract the missing $\rho(S_n)$ for ^{111,112,122,124}Sn. The similarity of the slopes of the NLDs in these nuclei with those of their immediate even-even and even-odd neighbors, expected from nuclei with similar structural properties, supports this approach.

Considering the low γ-energy boundary imposed by the first-generation method, extracted NLD data points are usually limited to energies $1.5 - 2.0$ MeV below the neutron threshold. The data thus have to be interpolated between the extracted NLD and the $\rho(S_n)$ value. For this purpose, the constant-temperature (CT) model was employed [96, 97]:

$$\rho_{\mathrm{CT}}(E_x) = \frac{1}{T_{\mathrm{CT}}} \exp\left(\frac{E_x - E_0}{T_{\mathrm{CT}}}\right), \tag{3.31}$$

where the temperature T_{CT} and the energy shift E_0 were treated as free fit parameters. In the earlier Oslo method analyses the back-shifted Fermi gas (BSFG) model was often employed instead (see e.g. [80]). With a relatively small energy gap between the extracted data and the $\rho(S_n)$ value, a particular choice of the interpolation model is of little importance for the final results. In the case of the Sn isotopes, the CT model was chosen over the BSFG approach due to the better χ^2 scores obtained for the fits to the extracted data points at relatively high excitation energies. For the larger energy gaps, a BSFG fit might lead to an additional boost of the NLD values below the neutron threshold, providing a slightly steeper slope of the NLD as compared to the one obtained with the CT approach.

The total uncertainty bands of the extracted NLDs of all the Sn isotopes include the statistical uncertainties of the data propagated through the unfolding and the first-generation procedure as outlined in Ref [234] and the systematic errors due to the input normalization parameters, added in quadrature. Parameter uncertainties were estimated analogously to how it was done in Refs. [186, 238]; the experimental uncertainties of D_0 values were propagated together with an additional assumed 10% error of the spin-cutoff parameter. For the values of $\rho(S_n)$ extracted from the systematics, a 30% symmetrical error was assumed for the extracted D_0 values, corresponding to the doubled maximum uncertainty of the experimentally available D_0 values. The choice of the assumed uncertainty limits is supported by a good comparison with the Coulomb excitation data. The NLDs obtained with some alternative spin-cutoff models fall within this total uncertainty band, as shown in Fig. 3.7(b). All input parameters and the corresponding uncertainties used for the normalization of the NLDs in the studied Sn isotopes are presented in Table C.1.

3.3.5 Normalization of the GSF

The slope parameter α obtained from the normalization of the NLD also determines the slope of the γ-ray transmission coefficient (Eq. (3.24)), and the only unknown to be constrained is the absolute normalization of the GSF, denoted by B in Eq. (3.24). Within the Oslo method, it is done by employing the information on γ decay of neutron resonances. For stable target nuclei, the average total radiative widths $\langle \Gamma_\gamma \rangle$ are available from the compilation in Ref. [126]. The average total radiative width $\langle \Gamma_\gamma(E_x, J, \pi) \rangle$ for decaying resonance states with spin-parities J^π at energies E_x can be expressed in terms of the γ-ray transmission coefficient and the NLD [146]:

$$\langle \Gamma(E_x, J, \pi) \rangle = \frac{1}{2\pi \rho(E_x, J, \pi)} \sum_{XL} \sum_{J_f, \pi_f} \int_{E_\gamma=0}^{E_x} dE_\gamma \times$$
$$\mathcal{T}_{XL}(E_\gamma) \rho(E_x - E_\gamma, J_f, \pi_f). \tag{3.32}$$

Here, XL denotes the radiation type and multipolarity. The γ-ray transmission coefficient entering this relation is considered to be normalized and would correspond to $B\mathcal{T}_{XL}(E_\gamma)$ in the notations of Eq. (3.24) (the correct slope $\exp(\alpha E_\gamma)$ is already included in $\mathcal{T}_{XL}(E_\gamma)$).

Since the transitions of the dipole type $(M1 + E1)$ are expected to dominate within the quasi-continuum, the transmission coefficient can be further substituted with the GSF using the following relation [146]:

$$BT_{XL}(E_\gamma) = 2\pi E_\gamma^{2L+1} f_{XL}(E_\gamma) \approx 2\pi E_\gamma^3 \big(f_{E1}(E_\gamma) + f_{M1}(E_\gamma) \big). \tag{3.33}$$

Neutron resonance experiments provide the $\langle \Gamma_\gamma \rangle$ values at the neutron threshold, corresponding to the decay of sates with spin-parity determined by the target ground state spin and parity $J_t^{\pi_t}$. In case of s-wave neutrons, Eq. (3.32) can be rewritten as:

$$\langle \Gamma_\gamma \rangle = \langle \Gamma(S_n, J_t \pm 1/2, \pi_t) \rangle = \frac{1}{2\rho(S_n, J_t \pm 1/2, \pi_t)} \times$$

$$\int_{E_\gamma=0}^{S_n} dE_\gamma E_\gamma^3 f(E_\gamma) \rho(S_n - E_\gamma) \times$$

$$\sum_{J=-1}^{1} g(S_n - E_\gamma, J_t \pm 1/2 + J). \tag{3.34}$$

Here, we once again assume the parity equpartition and the spin distribution in the form of Eq. (3.28), allowing to account for the final states accessed via dipole radiation. One can easily note that the NLD in the denominator of the first factor is directly related to the resonance spacing value D_0. To account for the lack of extracted data points at very low γ-ray energies due to the imposed $E_\gamma^{\min}$ limit, the γ-ray transmission coefficient is extrapolated to $E_\gamma = 0$ MeV with an exponential function. The contribution of the extrapolated function to the total integral from $E_\gamma = 0$ MeV to S_n does not exceed 10% in the majority of the studied cases, and variations in the fit due to different choices of anchor points for the extrapolation have little to no impact for the Sn isotopes.

The spin distribution $g(E_x, J)$ under the integral sign in Eq. (3.34) runs though a range of excitation energies up to S_n. To account for its energy dependence, the following relation is adopted from Ref. [91]:

$$f(x) = \begin{cases} \sigma^2(E_d), & E_x \le E_d, \\ \sigma_d^2 + \frac{E_x - E_d}{S_n - E_d} \big(\sigma^2(S_n) - \sigma_d^2 \big), & E_d \le E_x \le S_n, \\ \sigma^2(S_n), & E_x \ge S_n, \end{cases} \tag{3.35}$$

where σ_d is a spin-cutoff parameter determined for several levels with a well-defined spin-parity attribution at low excitation energy E_d in the discrete region, where the level scheme can be considered complete. The σ_d and E_d values used for the normalization of the GSF in the Sn isotopes are listed in Table C.1 together with the average total radiative widths $\langle \Gamma_\gamma \rangle$ from s-wave neutron resonance studies.

For ^{111,112,122,124}Sn, no experimental resonance data are available, and the average total radiative widths were extracted from a linear fit to the available values for other Sn isotopes (see Fig. 3.8(b)). A large scatter of the data points in the systematics complicates revealing a certain trend in the $\langle \Gamma_\gamma \rangle$ values. The linear fit, implying the minimum number of assumptions and fit parameters, was found to provide quite reasonable values for the ^{111,122,124}Sn isotopes based on the comparison with the Coulomb excitation data and the Oslo method results for the neighboring nuclei. The uncertainty bands for the extracted values were determined from
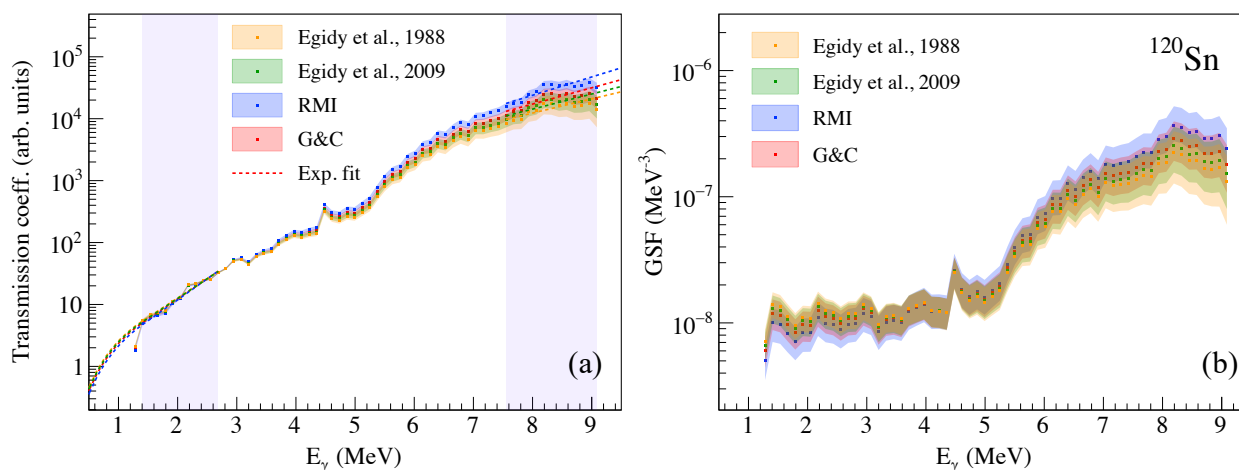
Figure 3.9: (a) γ-ray transmission coefficient for ^{120}Sn obtained with the rigid moment of interta (RMI) [103], Gilbert and Cameron (G&C) [97], and Egidy *et al.* (1988) [104] and (2009) [108] spin-cutoff parameters. The parameter uncertainty component of the total error bands includes only uncertainties due to $\sigma(S_n)$ and D_0. (b) Same for the normalized GSF. The parameter uncertainty component of the total error bands includes also the uncertainty due to $\langle \Gamma_\gamma \rangle$.

the fit. The radiative width extracted from the systematics for ^{112}Sn (shown in Fig. 3.8(b)) was found to result in too large absolute values compared to the Oslo GSFs for ^{111,113}Sn and the Coulomb excitation (p,p') data for ^{112,114}Sn. It was therefore reduced with an additional factor found through a χ^2 minimization of differences between the Oslo and (p,p') strengths for ^{112}Sn in the energy range where the data overlap. The difference between the reduced value and the one obtained from the systematics was assumed to span a symmetric uncertainty for the reduced $\langle \Gamma_\gamma \rangle$ value used in the analysis. Similarly, the $\langle \Gamma_\gamma \rangle$ value for ^{120}Sn from the compilation was additionally revised and modified. The value used for the normalization of the GSF in this isotope was estimated from three s-wave resonances in the energy range between $\approx 455 - 828$ eV [126], while other resonances were excluded either due to being of p nature or having too low resonance width values as compared to the confirmed s-wave resonances in the neighboring Sn isotopes. Substituting the reported $\langle \Gamma_\gamma \rangle$ value for ^{120}Sn with the modified one does not change the χ^2 fit in Fig. 3.8(b) in any significant way. The GSF normalized with the modified value was found to be in excellent agreement with the Coulomb excitation data for the same nucleus. The γ-ray transmission coefficient and the normalized GSF obtained with different spin-cutoff models are shown in Fig. 3.9.

The uncertainty of the average total radiative width is the largest contributor to the total uncertainty band of the GSF, including also the statistical errors propagated through the unfolding and the first generation method and systematic uncertainties from determining the slope parameter α (due to D_0 and $\sigma(S_n)$). Similarly to how it was done for the NLDs, the uncertainties from the unfolding and the primary γ-ray extraction were determined according to Ref [234], and the systematic error due to all the normalization parameters was estimated by varying these parameters by analogy with the earlier works [186, 238]. As it can be seen

in Fig. 3.9(b), the GSFs extracted with different spin-cutoff parameter models fall well within the total uncertainty band of the GSF of ^{120}Sn, presented also in the following chapters.

3.4 The Shape method

For a large number of cases studied with the Oslo method, especially those of interest for astrophysical calculations related to the s and i processes, and all cases studied with the β-Oslo method, no normalization data from neutron resonance experiments are available. One must thus rely on systematics for the isotopes of interest (or the neighboring chains of isotopes). The chain of $Z = 50$ isotopes is one of very few examples, where the number of stable nuclei is sufficient to reveal some trends in the $\rho(S_n)$ and $\langle\Gamma_\gamma\rangle$ values and extrapolate (or interpolate) them to the lighter and heavier isotopes. However, regardless of how complete the systematics are, they yield quite large uncertainties of normalization parameters, further propagated into the NLD and GSF uncertainties. In an endeavor to provide an alternative way to perform the normalization, the shape method has been recently developed [239]. It shares some similar traits with the average resonance [150, 240], ratio [199], and χ^2 [199] methods applied to primary transitions to low-lying states in order to reconstruct the energy dependence of the GSF. The previous studies employing the latter three approaches made use of high-resolution germanium detectors for a more accurate gating on transitions of interest. The shape method, less sensitive to the γ-energy resolution, is an excellent alternative to the above-mentioned techniques to reconstruct the shape of the GSF from Oslo and β-Oslo data, considering a comparatively worse energy resolution of detectors employed to collect them (compared to high-purity Ge detectors). A detailed description of the method and its application to several medium- to heavy-mass nuclei is presented in Ref. [239] and recapped here to provide a better understanding of its application to the Sn data.

The core idea of the shape method is the reconstruction of the shape (slope) of the GSF based on relative intensities of primary transitions to several low-lying discrete states, corresponding to clearly distinguished diagonals in primary matrices from Oslo-type experiments. Depending on a nucleus, such diagonals may contain transitions to only one well-separated discrete state or several closely spaced states clustered together. The number of counts within a diagonal at excitation energy E_i can be written as:

$$N_D \propto \sum_{J_f} \sum_{J_i=J_f-1}^{J_i=J_f+1} \sigma(E_i, J_i)g(E_i, J_i)G(E_i, E_\gamma, J_i, J_f),$$

(3.36)

where $\sigma(E_i, J_i)$ is a population cross section for the initial states J_i within the excitation energy bin E_i, $g(E_i, J_i)$ is the spin distribution in the form of Eq. (3.28), playing the role of a weighting factor, and $G(E_i, E_\gamma, J_i, J_f)$ is a term including the γ-decay widths for the $E_i \to E_f$ transitions. The first sum accounts for the fact that the diagonal may contain several final states, while the second sum excludes transitions of other types than dipole. The γ-decay probability factor can be expressed through the γ-ray transmission coefficient as:

$$G(E_i, E_\gamma, J_i, J_f) \propto \int_{E_\gamma-\Delta/2}^{E_\gamma+\Delta/2} \mathcal{T}(E_i, E'_\gamma, J_i, J_f)\delta(E_i - E'_\gamma, J_f)dE'_\gamma,$$
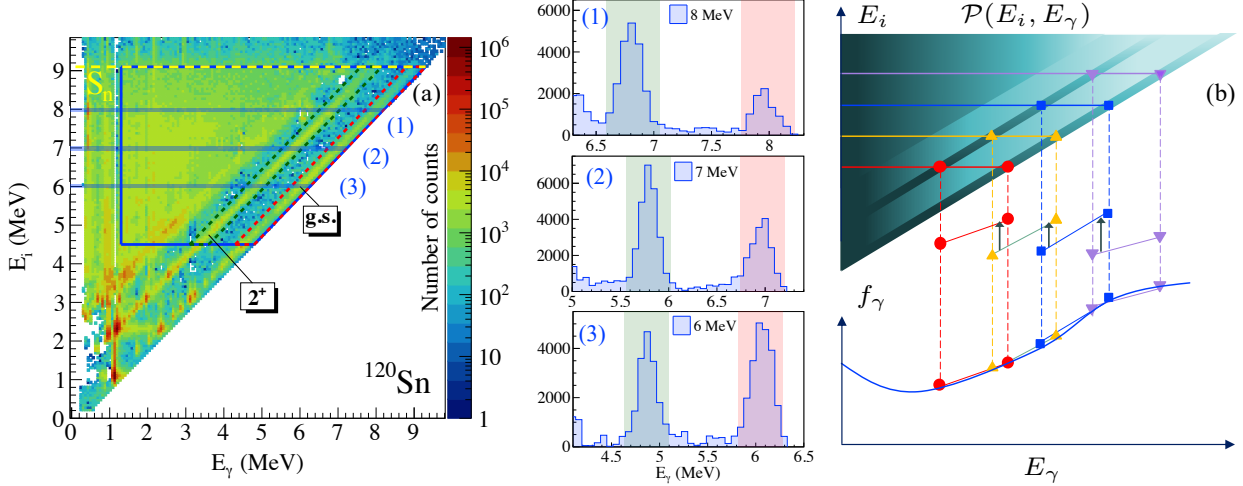
(3.37)

Figure 3.10: (a) Primary matrix for ^{120}Sn. Yellow dashed lines indicate the neutron separation energies, and blue solid lines indicate the areas of the primary matrices used further in the Oslo method. The part of the primary matrix used for the Oslo method is confined within the solid blue lines. The gates on the ground state and the first excited 2$^+$ state are marked with red and green dashed lines, respectively. Projections of 128-keV wide bins at $\approx 6, 7, 8$ MeV with gates on the ground and the 2$^+$ states are shown on the left side of the primary matrix. (b) Schematic description of the sewing technique.

where Δ denotes the γ-energy resolution, and δ controls that only one final state with J_f and $E_f = E_i - E_\gamma$ is included. Assuming that the transmission coefficient does not vary within Δ in the vicinity of $E_\gamma = E_i - E_f$, it can be considered a factor outside the integral sign. Further, assuming the BA hypothesis, its excitation-energy and spin dependence is removed, leaving dependence on E_γ only. Taking the relation from Eq. (3.33) between the γ-ray transmission coefficient and the GSF into account, the initial Eq. (3.36) can be rewritten as:

$$N_D \propto E_\gamma^3 f(E_\gamma) \sum_{J_f} \sum_{J_i=J_f-1}^{J_i=J_f+1} \sigma(E_i, J_i) g(E_i, J_i). \tag{3.38}$$

The population cross section $\sigma(E_i, J_i)$ is essentially unknown, and it is henceforth assumed to be independent of spin. This assumption has been tested for the cases of ^{56}Fe and ^{92}Zr in Ref. [239]. For the former nucleus, two well-separated diagonals corresponding to the same final spins $J_f = 2$ can be distinguished, reducing Eq. (3.38) to solely the proportionality to the GSF corrected for the γ-ray energy. The resulting GSF is in good agreement with the Oslo method strength. However, the GSFs obtained for different diagonals containing spins $J_f = 0, 2, 3, 4, 5$ in ^{92}Zr are also in quite good agreement with the corresponding Oslo method strength, suggesting that the initial assumption regarding $\sigma(E_i, J_i)$ is not the largest contributor to the uncertainty of the result.

In this thesis, the shape method has been applied only to the even-even ^{120,124}Sn isotopes with well-separated transitions to the ground and the first 2$^+$ states, while transitions to the higher-lying 0$^+$, 2$^+$ and 4$^+$ states can no longer be distinguished with the energy resolution of OSCAR. The ranges of initial excitation energies in the primary matrices of both isotopes

were chosen to coincide with those used for the Oslo method. For the two diagonals with $J_f = 0$ (D_1) and $J_f = 2$ (D_2), two values of the GSF can be extracted at excitation energy E_i:

$$f(E_{\gamma 1}) \propto \frac{N_{D_1}}{E_{\gamma 1}^3 g(E_i, 1)}$$

$$f(E_{\gamma 2}) \propto \frac{N_{D_2}}{E_{\gamma 2}^3 \big(g(E_i, 1) + g(E_i, 2) + g(E_i, 3)\big)}. \tag{3.39}$$

The intensities (number of counts) in the diagonals for each excitation energy bin are obtained by applying graphical cuts in a similar way as shown for the ground state (red dashed line) and the 2^+ state (green dashed line) in ^{120}Sn in Fig. 3.10(a). To reconstruct the full slope of the GSF, the pairs of GSF values at consecutive E_i are normalized internally to each other with a so-called sewing technique [199]. To do so, a linear or logarithmic interpolation is applied to fill the data between two values in each pair of extracted points. Further, an average matching point E_γ between the lowest and the highest E_γ of two consecutive pairs is determined. Finally, the interpolated data points for both pairs are scaled to match at the average γ-ray energy. The full shape is obtained by scanning through different excitation energies and scaling each subsequent pair of GSF values to the previous one as shown schematically in Fig. 3.10(b). In such a way, the GSFs corresponding to both the decay to the ground state and the first excited state can be determined and compared with the standard Oslo method result.

This method provides the general shape of the GSF, which has been shown to match well with the shape of the Oslo method strength for most of the cases studied so far [239, 241, 242], but not the absolute normalization. External experimental data below the neutron threshold (e.g. Coulomb excitation or Oslo data) are required to provide the absolute values of the shape method GSF. Despite this limitation, the shape method is an excellent tool to constrain the slope parameter of the GSF and hence the NLD and/or minimize its uncertainty as compared to a value provided by systematics. This might be especially useful for the cases with limited ranges of *populated* spins as compared to theoretically expected *intrinsic* spin distributions. A reduced range of populated spins in the Oslo data has been previously addressed in Refs. [35, 243] and thoroughly studied for the (d, p) reaction on ^{239}Pu in Ref. [244]. In such cases, the primary matrix should be fitted with a product of a reduced NLD and the γ-ray transmission coefficient to provide a correct slope of the GSF. The reduction can be performed by normalizing the NLD to a reduced value $\beta\rho(S_n)$, instead of the total NLD $\rho(S_n)$ from the neutron resonance data or systematics. The reduction β is unknown, but it can be constrained with the shape method by varying this factor until the slopes of the Oslo method and the shape method strengths match. It can also be obtained as a fraction of populated spins provided by the spin distribution from Eq. (3.28), which results in the matching slopes.

Several successful attempts to constrain the slope of the NLDs with the shape method have been performed for ^{76}Ge and ^{88}Kr by Müsher *et al.* [242] and ^{112}Cd by Goriely *et al.* [241]. The GSFs and NLDs available from the β-Oslo and the standard Oslo method for the stable ^{76}Ge and ^{112}Cd nuclei were used to benchmark the shape method results. With all three methods providing results in fairly good agreement with each other, the shape method was further applied to the primary matrix for unstable ^{88}Kr, populated via β-decay of excited ^{88}Br. In this case, the normalization of the partial absolute NLD was performed in essentially a model-independent way, based on the available low-lying discrete states and a slope constrained with

the shape method. Moreover, the uncertainties obtained with the combination of the β-Oslo and the shape method were shown to be comparable with the typical uncertainties of the Oslo method applied to stable nuclei. This result demonstrated a promising potential of the shape method to aid the normalization of GSFs and NLDs far from stability, where systematics can no longer be expected to be reliable.

3.5   The inelastic proton scattering experiment at RCNP

The systematic analysis of the low-lying $E1$ strength in Sn isotopes in this thesis is based on a combined analysis of the Oslo method results and the (p, p') experiments. The idea of the latter was to study the electric and magnetic dipole strength distributions in stable even-even ^{112,114,116,118,120,124}Sn isotopes with a relativistic proton beam via Coulomb excitation, dominating under considered extreme forward angles. The data were obtained in several campaigns in 2015 and 2017 at the Research Center for Nuclear Physics (RCNP), and the results were published in Refs. [42, 77]. All experiments were performed with the high energy resolution magnetic Grand Raiden (GR) Spectrometer and the Large Acceptance Spectrometer (LAS) [29], shown in Fig. 3.11(a). The former includes a series of quadrupole (Q), sextupole (S), multipole (M) magnets (Q-S-Q-D-M-D), combined with a dipole magnet for spin rotation for polarized beam experiments, while LAS consists of a quadrupole and a dipole magnets.

The primary unpolarized beam of protons, produced by a NEOMAFIOS ECR ion source, is accelerated with the Azimuthally Varying Field Cyclotron (AVF) to 54 MeV and injected into the Ring cyclotron to be accelerated to 295 MeV. Further, the beam of relativistic protons is directed towards a target in the scattering chamber (Fig. 3.11(a)). The typical beam intensities were within the 2 – 20 nA range, depending on the spectrometer angle. The scattered protons were measured at central GR spectrometer angles of 0°, 2.5°, and 4.5°.
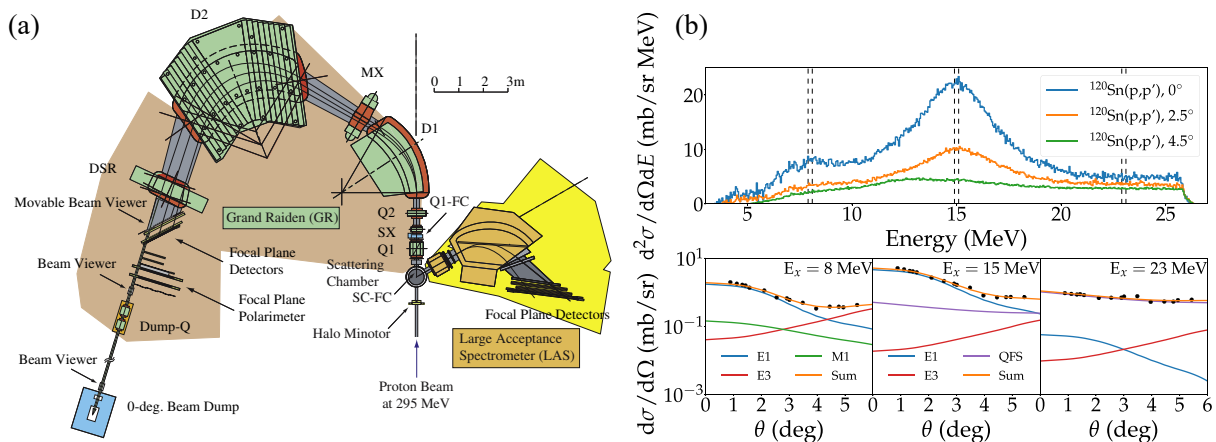

Figure 3.11: (a) Scheme of the Grand Raiden and Large Acceptance spectrometers in the 0° set-up [29]. (b) Double differential cross sections and differential cross sections obtained for excitation energy bins at 8, 15, and 23 MeV (dashed vertical lines in the upper figure), extracted with the MDA for the ^{120}Sn isotope. The figure is taken from Ref. [42].

For 0° measurements, the primary beam is directed through the focal plane detectors to be collected in a Faraday cup downstream, while inelastically scattered protons are deflected more and detected by the focal plane detectors. For other GR spectrometer angles, the whole spectrometer is rotated, and the primary beam is collected in a Faraday cup placed after the first quadrupole magnet. The LAS was used to monitor the vertical beam position, required to achieve a good vertical scattering-angle resolution for the GR and a more precise scattering angle calibration with a ^{58}Ni target. The detector systems of GR and LAS are composed of several vertical drift chambers and plastic scintillators used as trigger detectors. The scattered particles are discriminated with the time of flight (ToF) technique, based on trigger signals generated by the scintillator detectors and the radio frequency of the AVF cyclotron. The typical energy resolution achieved for the Sn isotopes after applying all necessary kinematical and aberration corrections was 30 – 40 keV FWHM.

After performing the tracking efficiency, scattering angle, energy, and Faraday cup calibration, as well as the background subtraction, the cross sections of interest were obtained. The double differential cross sections were extracted from the collected counts per excitation energy bin, information on the used targets, charge collected in the scattering chamber Faraday cup after correction for a beam loss, its efficiency, tracking efficiency of the drift chambers, live time ratio of the data acquisition system, and the spectrometer solid angle. To determine the electric and magnetic dipole cross sections, the data were processed with the multipole decomposition analysis (MDA). Prior to this, the contributions due to the ISGMR and ISGQR in the studied nuclei from (α, α') experiments [245] were subtracted from the experimental spectra. The background due to the quasi-free scattering (QFS) of incident particles off singe nucleons in the target nuclei was also subtracted. The experimental angular distributions were fitted with a linear combination of DWBA-based angular cross sections for different multipolarities at different scattering angles. At each GR spectrometer angle, data for 5 scattering angles were determined by applying gates on different vertical and horizontal angles in the drift chambers. Thus, 15 data points are available per each excitation energy bin for the MDA. An example of the results obtained with the MDA is shown in Fig. 3.11(b). In general, the dipole electric and magnetic contributions dominate the differential cross section at the studied forward scattering angles.

The Coulomb excitation taking place in these experiments can be understood as being due to the absorption of virtual photons, which have the same effect as the same number of real absorbed photons. The *virtual photon method* (see e.g. [246]) exploits this idea to link the extracted double differential cross section of Coulomb excitation to the $E1$ photoabsorption cross-sections. In Ref. [42], this was done by estimating the differential number of virtual photons within the eikonal approximation [246]. The $M1$ strength distributions $B(M1)$ were obtained with the *unit cross-section method* [247], linking the differential $M1$ cross section from the MDA to the dominating isovector spin $M1$ strength. The resulting $E1$ and $M1$ strengths will be compared with the Oslo method results and discussed in the following chapter.

Chapter 4

Testing the Brink-Axel hypothesis for Sn isotopes

In the following chapter, we will consider the main results from Paper I and Paper II, which are relevant for the test of the validity of the BA hypothesis in Sn isotopes. In these articles, similar results were obtained for both ^{120}Sn and ^{124}Sn, as indeed expected for nuclei with similar structural properties. Therefore, in the following, only the results for ^{120}Sn will be presented to illustrate the main points. It is important to note that different spin-cutoff models were adopted in Paper II and Papers I, III, and IV. To avoid any potential confusions between the results presented here and in Paper II, we will follow the results from the latter and discuss the consequences of choosing different spin-cutoff models at the end of this chapter.

4.1   Techniques used for the test

The BA hypothesis, as was already mentioned in the previous chapters, is one of the core assumptions of the Oslo method, and assessing its validity is therefore essential for producing reliable results. In particular, the study of the dependence of the GSF on the initial and final excitation energy windows used in the Oslo method analysis is important for a check of whether this assumption is justified in each particular case. Moreover, the correspondence between the downward Oslo strength and upward strengths, obtained either in NRF or Coulomb excitation experiments, is crucial for the systematic study of the low-lying electric dipole strength and answering the question of to what extent these data can be treated as complementary for extracting its bulk properties.

Oslo method results can not be used alone to provide a comprehensive test of the BA hypothesis. Therefore, several other techniques shown schematically in Fig. 4.1 have been exploited in this thesis. As was mentioned earlier, the Oslo method (Fig. 4.1(a)) combines dipole γ transitions from initial states within a rather broad excitation energy window in the quasi-continuum to lower-lying final states within the quasi-continuum and the discrete region. This implies averaging over a large range of excitation energies, and thus the excitation-energy dependence of the extracted strength might be significantly obscured. To obtain GSFs for different initial and final excitation energy bins, one can use the primary matrix and the Oslo method NLD and limit the analysis to transitions from or to individual excitation energy
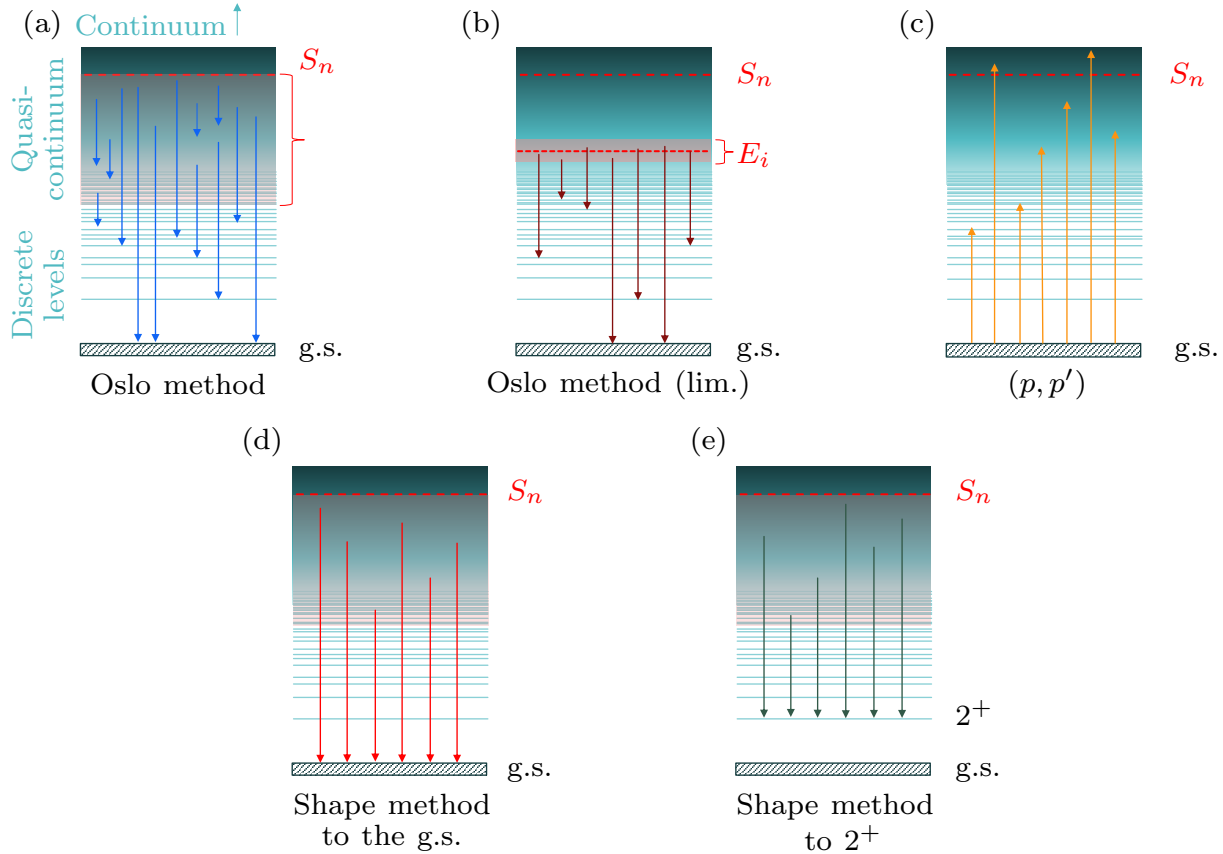
Figure 4.1: Transitions included in the GSF to test the Brink-Axel hypothesis in (a) the Oslo method, (b) the Oslo method limited to specific initial (and, by analogy, final) excitation energy bins, (c) ground-state Coulomb excitation in the (p, p') reaction, (d) the shape method for transitions to the ground state, (e) the shape method for transitions to the first excited 2^+ state.

bins (Fig. 4.1(b)). The Coulomb excitation mechanism in forward-angle inelastic scattering of relativistic protons, from quantum electrodynamical considerations, is equivalent to the ground-state absorption of virtual photons and thus yields an upward GSF, covering both the PDR and the IVGDR energy regions (Fig. 4.1(c)). Moreover, the shape method provides the functional forms of the strengths from a selective decay to the well-resolved ground state and the first excited 2^+ state in even-even Sn isotopes without relying on the NLD from the Oslo method, as shown in Fig. 4.1(d) and (e). An explicit test of the spin dependence of the GSF is generally complicated by the close spacing of states with different spins already in the discrete region. In the case of the even-even Sn isotopes studied in this thesis, this test is possible with the shape method, but limited only to the first $J = 0$ and $J = 2$ states.

4.2 Porter-Thomas fluctuations in ^{120}Sn

Before addressing the excitation-energy dependence of GSFs extracted from primary transitions in Oslo-type experiments, it is useful to provide an estimate of PT fluctuations in each considered case. GSFs for different initial and final excitation energy gates have been demonstrated to be subject to relatively strong fluctuations in medium-mass ^{64,65}Ni [162] and ^{92}Zr [163] and particularly strong fluctuations in the lighter ^{46}Ti isotope [161], as compared to the heavy-mass ^{238}Np case [153]. In the context of studying the applicability of the BA hypothesis, the questions are then the following: How strongly would PT fluctuations be suppressed in the "intermediate" case of Sn isotopes in comparison with the lighter nuclei? How strongly do the individual strengths fluctuate with respect to an "averaged" Oslo method result? And how reliable is the assumption on the excitation energy independence of the GSF in this mass region?

To answer these questions, a prescription from Refs. [162, 163] to estimate the relative deviations from the averaged (or "true") GSF due to PT fluctuations was adopted. Let us assume that they follow the χ^2_ν distribution with the number of degrees of freedom ν determined by the number of contributing transitions between the chosen initial and final excitation energy bins. The relative fluctuations in this case can then be estimated from the fraction of the standard deviation and the mean value, expressed in terms of the number of transitions $n(E_\gamma, E_{i,f})$ as [162, 163]:

$$r(E_\gamma, E_{i,f}) = \sqrt{\frac{2}{n(E_\gamma, E_{i,f})}}. \tag{4.1}$$

The value of $n(E_\gamma, E_{i,f})$ can be estimated from the information on the discrete low-lying states up to the energy where the level scheme can no longer be considered complete and the experimental Oslo method NLD at higher energies. As a minimum excitation energy above which the smooth Oslo NLD will be used and the spin-distribution function from Eq. (3.28) can be assumed to be applicable, the energy corresponding to ≈ 10 levels per excitation energy bin was chosen. In the case of ^{120}Sn, this minimum energy is $E_x^{\min} \approx 3.2$ MeV ($\rho \approx 80$ MeV^{-1}), which coincides with the energy range where the Oslo method NLD starts to diverge from the discrete states from the compilation in Ref. [125]. Furthermore, only the dipole type of transitions within the quasi-continuum and from the quasi-continuum to the discrete states is considered. In terms of the NLD, the number of transitions can then be written as:

$$n(E_\gamma, E_i) = \Delta E^2 \sum_{J\pi} \sum_{L=-1}^{1} \sum_{\pi'} \rho(E_i, J, \pi)\rho(E_i - E_\gamma, J + L, \pi'), \tag{4.2}$$

A similar relation for $n(E_\gamma, E_f)$ is obtained by swapping the corresponding indices in the equation above.

Relative fluctuations in ^{120}Sn as a function of γ-ray energy for different initial and final excitation energy bins are shown in Fig. 4.2. In the left panel (Fig. 4.2(a)), the calculations are limited to transitions within the quasi-continuum from several fixed initial states, i.e. $E_i \geq E_f \geq E_x^{\min} = 3.2$ MeV. The right panel (Fig. 4.2(b)) shows the fluctuations for transitions to several fixed final states within the quasi-continuum ($E_i > E_f \geq E_x^{\min}$) as well as transitions from the quasi-continuum ($E_i \geq E_x^{\min}$) to the low-lying excitation energy bins, including only the ground state, only the first excited 2$^+$ state, and a group of different spin-parity states.
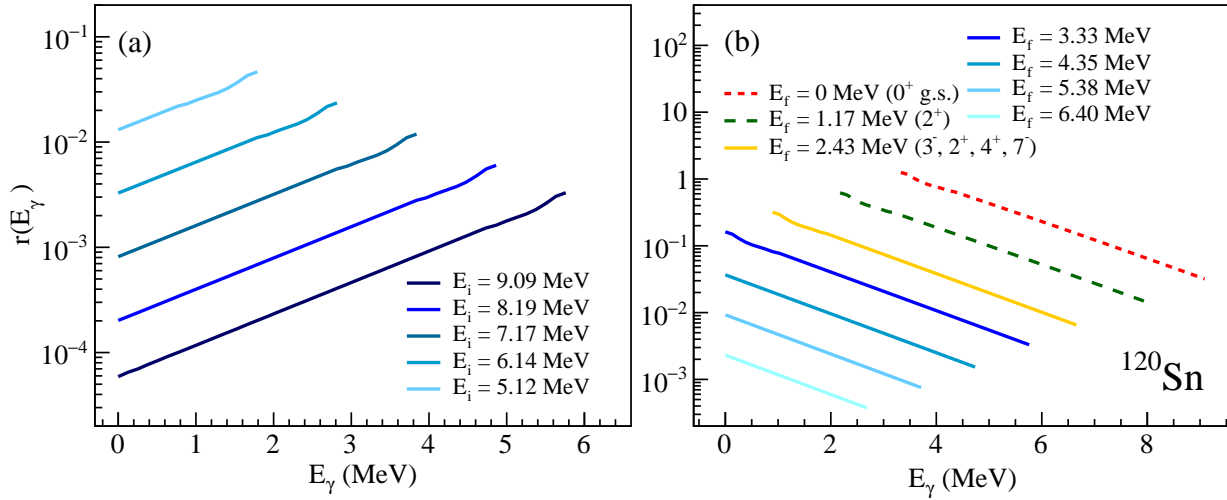
Figure 4.2: Relative fluctuations of the GSF $r(E_\gamma, E_i)$ for different initial (a) and final (b) excitation energies for ^{120}Sn. All initial E_i and final $E_f = E_i - E_\gamma$ energies lie within the quasi-continuum region in (a). The same applies to fluctuations in (b) shown by solid lines of different shades of blue. Here, the red dashed, green dashed, and yellow solid lines correspond to transitions from the quasi-continuum to the ground state, the first 2^+ state, and a group of several low-lying discrete states, respectively. The excitation energy bin is 128 keV. This figure combines results from Figs. 7 and 8 in Paper II.

The relative fluctuations tend to increase exponentially with γ-ray energy for a given E_i bin and decrease with the increasing initial excitation energy. This is evident considering the exponentially increasing NLD with excitation energy and, thus, the increasing number of transitions over which partial radiative widths are averaged in the GSF. For initial energies at the neutron threshold and down to $\approx S_n - 2$ MeV, the fluctuations within the quasi-continuum are significantly suppressed and do not exceed $\approx 1\%$. Moreover, the fluctuations are consistently smaller than for the case of e.g. ^{64}Ni [162], as would indeed be expected provided the higher NLD in ^{120}Sn. For the lower initial excitation energies (6.1 MeV and 5.1 MeV), the fluctuations range from ≈ 0.1–0.3% up to several percent, which is comparable with statistical uncertainties propagated through the unfolding and the first-generation method. It is important to note that including transitions down to the lower-lying discrete states below $E_x^{\min}$, as done in the Oslo method, would further reduce $r(E_\gamma, E_i)$. This effect is, however, quite small due to the lower NLD values in the discrete region as compared to the quasi-continuum.

Similarly, the relative fluctuations $r(E_\gamma, E_f)$ decrease rapidly with increasing E_γ, since more states become available for feeding the selected final states. For the transitions within the quasi-continuum, they are of the same order as in the case of $r(E_\gamma, E_i)$ (up to several percent). However, for individual low-lying states, including the ground state, the fluctuations become especially strong and reach up to several tens of percent, thus exceeding not only the statistical but also the total systematic uncertainties. In the Oslo method GSF, such transitions at a given γ-ray energy are included together with transitions between higher-

lying excited states with the same E_γ, and the ground-state decay strength is thus "blended into" the Oslo method strength. As a consequence, the role of PT fluctuations in the Oslo method is usually negligible, even for light nuclei and relatively narrow excitation energy ranges used for the analysis.

4.3 The GSF as a function of initial and final excitation energies in ^{120}Sn

To investigate a potential excitation-energy dependence of the GSF, a somewhat modified Oslo method analysis can be applied to primary transition distributions, as was first suggested in Ref. [153]. It relies on the same decomposition relation as provided in Eq. (3.18), where an additional normalization factor $N(E_i)^1$ is introduced so that

$$P(E_\gamma, E_i)N(E_i) = \mathcal{T}(E_\gamma)\rho(E_i - E_\gamma). \tag{4.3}$$

The normalization for each excitation energy bin can thus be obtained by integrating the relation above over the whole spectrum, in the range of γ-ray energies from 0 to E_i:

$$N(E_i) = \frac{\int_0^{E_i} \mathcal{T}(E_\gamma)\rho(E_i - E_\gamma)dE_\gamma}{\int_0^{E_i} P(E_\gamma, E_i)dE_\gamma}. \tag{4.4}$$

The idea of the approach from Ref. [153] is to study the γ-ray transmission coefficient, and therefore the GSF, as a function of initial and final excitation energy bins by relying on the experimental primary matrix and the NLD extracted with the Oslo method as:

$$\mathcal{T}(E_\gamma, E_i) = \frac{P(E_\gamma, E_i)N(E_i)}{\rho(E_i - E_\gamma)} \tag{4.5}$$

for initial excitation energy bins and

$$\mathcal{T}(E_\gamma, E_f) = \frac{P(E_\gamma, E_f + E_\gamma)N(E_f + E_\gamma)}{\rho(E_f)} \tag{4.6}$$

for final excitation energies. Any deviations of $f(E_\gamma, E_i)$ and $f(E_\gamma, E_f)$ from the corresponding average values over all studied initial and final excitation energy bins or the Oslo method strength that cannot be explained by PT fluctuations can be a signature for the violation of the BA hypothesis. The averages of $f(E_\gamma, E_i)$ and $f(E_\gamma, E_f)$ agree well within the estimated uncertainties with the Oslo method strength, and therefore all of the individual strength functions will be compared only with the Oslo method strength.

---

[1]As shown in [230, 233] and Appendix A, this factor might have a rather complex dependence on both E_i and E_γ, which complicates this analysis significantly. However, assuming only the excitation-energy dependence seems to be reasonable based on the previous analyses [153, 162, 163]. If there were any strong γ-energy dependence in the normalization factor, it would be manifested, similarly to the violations of the BA hypothesis, in the form of noticeable variations of not only the shape but also the absolute values (scaling) of the GSF, which does not seem to be the case.
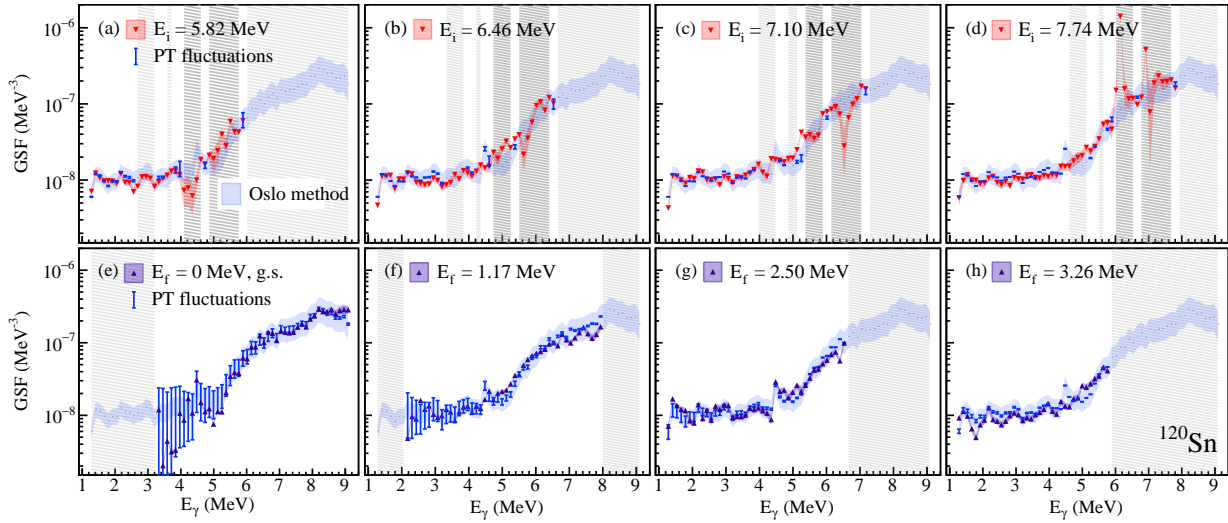
Figure 4.3: GSFs for different excitation energy bins at (a) 5.82 MeV, (b) 6.46 MeV, (c) 7.10 MeV, (d) 7.74 MeV, and final excitation energy bins at (e) the ground state, (f) the first excited 2^+ state, (g) 2.50 MeV, and (h) 3.26 MeV compared with the Oslo method strength. Expected deviations from the latter due to PT fluctuations are shown as blue vertical bars. Light-grey areas correspond to energies where individual strengths or PT fluctuations are not defined, dark-grey areas correspond to the excluded data points (see the text). The excitation energy bin is 128-keV-wide. The figure is taken from Ref. [248].

The GSFs for four different initial and final excitation energy bins are shown in Fig. 4.3. The results are presented with the corresponding statistical uncertainties propagated through the above-mentioned method and the Oslo method strength with the full uncertainty band due to the statistical and systematic errors. Expected deviations due to PT fluctuations from the Oslo method GSF are shown in each case by vertical blue bars. Light-grey shaded areas in the upper panels correspond to energies where the individual strengths are not defined due to the $E_\gamma \leq E_i$ condition and excitation energy bins where PT fluctuations can not be determined due uncertain spin assignments of some of the final states in the discrete region. Here, in contrast to Fig. 4.2(a), transitions to all possible final states in both the quasi-continuum and the discrete region are included when estimating the effect of PT fluctuations. Dark-grey shaded areas correspond to physically impossible transitions to the energy gap between the ground state and the first excited state (with the experimental resolution of 1 FWHM taken into account) and should be excluded from consideration. Extraction of the GSF at these energies is possible due to the leftover counts between the diagonals of the primary matrix and the finite excitation energy resolution, hence the especially large observed fluctuations. Similarly, the light-grey areas in the bottom panels correspond to $E_\gamma < E_i^{\min} - E_f$ and $E_\gamma > S_n - E_f$.

For all the fixed initial excitation energies, the individual strengths agree well within the uncertainties with the Oslo method strength. PT fluctuations are of the same order as the propagated statistical uncertainties of individual strengths at relatively high γ-ray energies and gradually become more suppressed towards low E_γ. For example, for the lowest $E_i = 5.82$ MeV, PT fluctuations are ≈ 6 times larger than the statistical uncertainties at the

highest γ-ray energy, corresponding to the ground-state transition, and drop to $\approx 10\%$ of the statistical uncertainty at the lowest γ-ray energies. For the higher-lying E_i bins, the PT fluctuations are sufficiently suppressed and range from less than 1% to several tens percent of the statistical uncertainties.

In case of the fixed final excitation energies, PT fluctuations become more considerable. At the highest final excitation and γ-ray energies they are negligible and, on average, similar to the estimates for the fixed initial excitation energies. For the ground-state transitions and transitions to the first excited 2^+ state, uncertainties due to PT fluctuations are up to ≈ 10 times larger than the statistical Oslo method uncertainty. All extracted strengths are in good agreement with the Oslo method strength within the above-mentioned errors.

Overall, in all of the considered cases, there are only minor local deviations from the Oslo method strength that can not be explained by PT fluctuations. They still lie within the total uncertainty band of the Oslo method result, except for very few individual E_γ bins. Thus, the assumption regarding the excitation-energy-independent GSF throughout a rather wide excitation energy window below the neutron threshold seems to be well justified in the case of ^{120}Sn and ^{124}Sn, as shown in Ref. [248].

4.3.1 Comparing upward and downward strengths

The procedure described in the previous section provides an internal check of the applicability of the BA hypothesis, and combining these results with other experimental data allows for a more comprehensive test. In addition to the Oslo method GSF, the strengths corresponding to the direct decays to the ground state and the first excited state were extracted with the shape method from the same primary matrix. Both of these strengths are shown separately in Fig. 4.4(a) and (b) with the statistical errors propagated through the unfolding, first-generation method, and the shape method. The ^{120}Sn isotope has previously been studied in two NRF [23, 76] and two Coulomb excitation [42, 77] experiments. A large number of new transitions were observed in the recent NRF experiment [23], whereas both analyses of (p, p') data, despite some differences in the extraction of the photoabsorption cross sections, yield essentially equivalent results. For this reason, only the most recent results from Refs. [23, 42] are shown in Fig. 4.4.

As mentioned in Sec. 3.4, the shape method strengths can only be extracted in arbitrary units and require a normalization. They were therefore scaled to the (p, p') data between 6 MeV and $S_n \approx 9.1$ MeV. Following the analysis in Paper II, the slope of the Oslo method strength was additionally constrained with the shape method. Provided this, we can judge on the agreement (or disagreement) in shapes between the downward and the upward strengths based only on the shape method strength, the (p, p'), and the NRF data. On the other hand, an agreement or disagreement in absolute values can be stated based on the comparison of the Oslo method data with the (p, p') and the NRF strengths.

Overall, the Oslo and the shape method strengths are in excellent agreement with the (p, p') data from the neutron threshold down to 6 MeV. In particular, the shape of the ground- and first-excited-state strengths follows nicely the shape of the (p, p') strength within its uncertainty band. Moreover, the latter agrees quite well with the Oslo method strength in absolute values. The GSF deduced from the continuous spectrum analysis of the NRF data is also shown in Fig. 4.4. Despite a disagreement with the Coulomb excitation data between
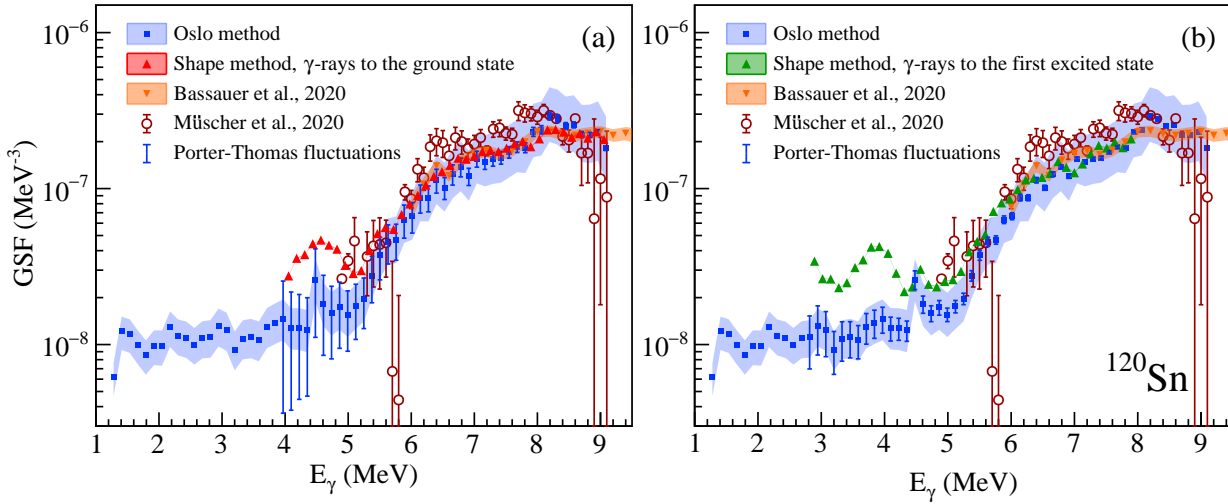
Figure 4.4: Comparison of the Oslo method, (p,p') [42], and NRF [23] GSFs with the shape method strength for transitions to the ground state (a) and the first excited 2^+ state (b). Deviations from the Oslo method strength due to Porter-Thomas fluctuations are shown as vertical blue bars.

$\approx 6 - 8$ MeV, these data still fall within a rather broad uncertainty band of the Oslo strength down to ≈ 5 MeV (except for energies in the immediate vicinity of 6 MeV). Even though the NRF data yield, on average, higher GSF values, the general shape of the strength is quite similar to that of other GSFs. The continuous analysis in Ref. [23] was performed with the CT NLD model, and it was noted to provide by about 6% higher cross-sections as compared to the BSFG model. Altogether, the extraction of this strength is sensitive to the choice of parameters and models used in statistical-model calculations, which might have affected both the absolute values and the shape of the strength. Taking this into account, it is possible to conclude that there is a rather good correspondence between the downward Oslo and shape method strengths and the upward (p,p') and, partly, NRF strengths from about 6 MeV up to the neutron separation energy.

Similarly to the GSFs in Fig. 4.3(e) and (f), the effect of PT fluctuations is expected to be quite strong as compared to the estimated uncertainties of the Oslo and shape method strengths. Expected deviations of the ground-state and the first-excited-state strengths from the Oslo method result due to PT fluctuations are shown in both Fig. 4.4(a) and (b). It can be clearly seen that the upward trend in the shape method strengths, forming a bump-like structure starting from $\approx 5.0 - 5.5$ MeV, cannot be explained by PT fluctuations. No clear structures are present on the diagonals of the primary matrix to cause such artifacts. Most probably, they can be attributed to the violations of the main assumptions in the shape method, namely the symmetric parity distribution of the initial nuclear levels, the pure dipole nature of the involved transitions, and the spin-independent excitation probability in the studied $(p,p'\gamma)$ reaction. Moreover, the PT fluctuations reach up to several tens of percent below ≈ 5.5 MeV, which might impose a lower limit on the initial excitation energy in terms of the appropriate level density for the application of the shape method. Indeed,
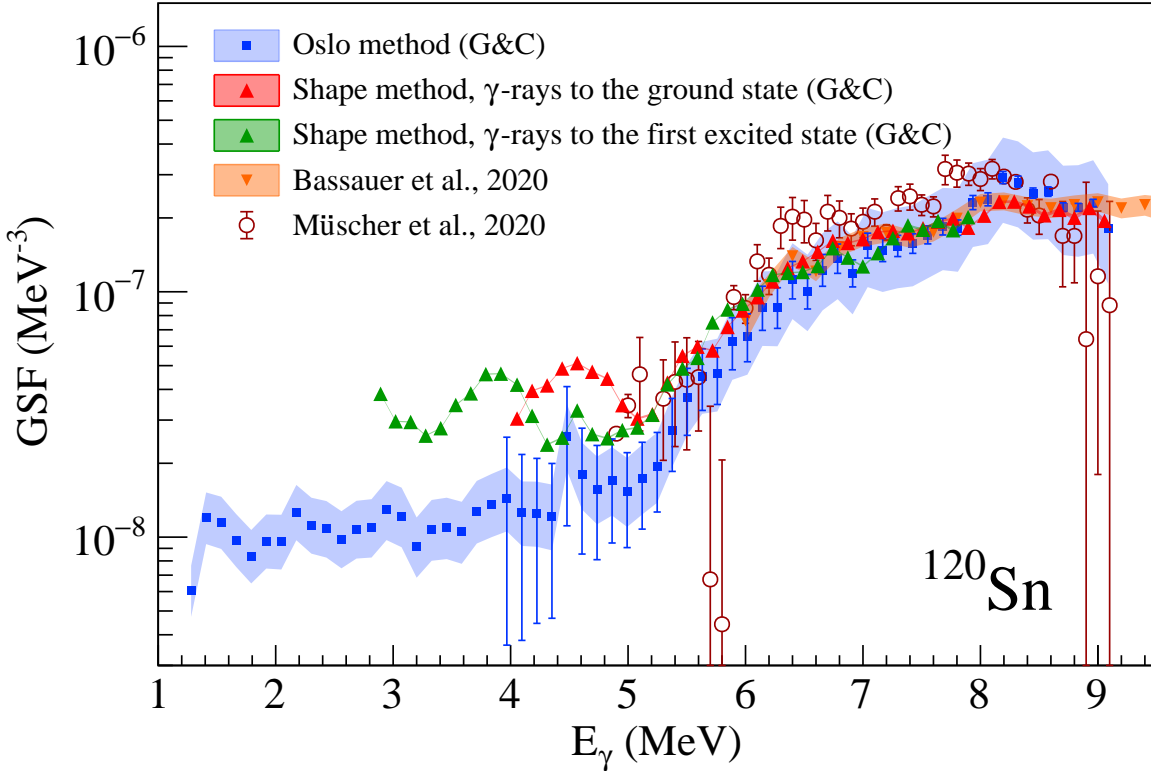
Figure 4.5: Same as in Fig. 4.4, but with the Oslo method and the shape method strengths extracted with the Gilbert and Cameron spin-cutoff model from Eq. (2.11).

the ground-state and the first-excited-state strengths are related by the internal normalization (sewing technique [239]), and large PT fluctuations might affect the reliability of the extracted strengths. Once the density of initial states reaches ~ 1000 MeV^{-1} in ^{120}Sn, deviations of these strengths due to PT fluctuations are reduced to the order of the Oslo method uncertainties. This seems to be an appropriate limit in case of even-even Sn isotopes, but should be estimated in each particular case when the shape method is applied.

Finally, let us discuss the consequences of using different approaches to the spin cutoff in the analysis. In Paper II and all of the results shown in this chapter, the model provided by Eq. (2.13) based on the rigid body moment of inertia (RMI) was used for ^{120,124}Sn, whereas Eq. (2.11) by Gilbert and Cameron (G&C) was exploited in all other articles. The former provides somewhat steeper slopes of NLDs, and the PT fluctuations would thus be larger towards the neutron threshold with the G&C approach. For example, for the highest initial excitation energies in Fig. 4.2, the fluctuations would be about 20-40% larger, while at the lowest initial excitation energies only about 10-20% larger with the G&C spin cutoff used for the normalization of the NLD as compared to the RMI value. In the context of testing the validity of the BA hypothesis and the applicability of the shape method, an approximate order of PT fluctuations is of interest, and, therefore, the spin-cutoff model does not play any critical role.

When it comes to the GSFs obtained with different spin-cutoff models, the results provided by the G&C and the RMI models for both ^{120}Sn and ^{124}Sn are in excellent agreement. The only factor affected in these two cases would be the reduction applied to the slope of the NLD to achieve the matching slope of the GSF with the one from the shape method. With the G&C approach used in Papers I and IV, no additional reduction is required for ^{120}Sn and a smaller reduction is used for ^{124}Sn. In other words, the slope of the Oslo method GSF for ^{120}Sn agrees well with the slopes of the shape method, (p, p'), and NRF strengths without any additional manipulations. Figure 4.5 presents the Oslo method and the shape method strengths extracted using the G&C spin-cutoff mode compared to the other experimental data to illustrate this point.

Based on all of the observations presented in this and the previous section, an assumption on the GSF independent of excitation energy seems to be justified for the analysis of Sn isotopes with the Oslo method. Moreover, the GSF appears to be independent of the studied final spins $J = 0$ and $J = 2$ within the estimated uncertainties, in line with the generalized BA hypothesis. Finally, the upward and downward GSFs obtained with different experimental techniques are in good agreement below the neutron threshold, at least down to $\approx 5 - 6$ MeV. All of them point at a PDR-like enhancement of the strength at $8 - 9$ MeV, which might be of importance for further astrophysical statistical-model calculations.

Chapter 5

Systematics of the low-lying electric dipole strength in Sn isotopes

The GSFs of Sn isotopes extracted with the Oslo method complement the (p, p') and (γ, n) data below the neutron separation energy and can be used to simultaneously constrain the bulk properties of such resonant features as the IVGDR, the PDR, and the scissors mode. Given an ambiguity in the interpretation of the observed features as the PDR, we are going to refer to both the excess $E1$ strength on top of the IVGDR and the total $E1$ strength up to a certain threshold in the vicinity of the neutron separation energy as the low-lying electric dipole response (LEDR). The following chapter provides the main results of the study on the LEDR in the Sn isotopic chain presented in Papers III, IV, and V.

5.1 Nuclear level densities and γ-ray strength functions in Sn isotopes

The NLDs and GSFs of eleven Sn isotopes, $^{111-113,116-122,124}$Sn, were extracted with the Oslo method in accordance with the procedures outlined in Secs. 3.3, 3.3.4, and 3.3.5. The obtained NLDs are shown in Fig. 5.1(a). In general, all of them are quite similar for even-even and even-odd nuclei, which is expected for isotopes with similar structural properties. As was shown in Fig. 2 in Paper IV, the NLDs of even-even isotopes reproduce the low-lying tabulated states quite well up to $E_x \approx 3.0 - 3.5$ MeV and, in case of even-odd isotopes, up to $E_x \approx 2$ MeV. At higher energies, all of the results demonstrate a clear constant-temperature trend, which might be expected to hold up to the neutron thresholds based on the performed fits. They overlap closely within the uncertainty bands, making it difficult to draw any conclusions on a systematic change with increasing neutron number. The NLDs of the lightest ^{111,113}Sn appear to agree well with the results of the neutron evaporation experiment at $\approx 3-6$ MeV (Fig. 4 in Paper III). Moreover, the partial density of 1^- states extracted from the total NLD in ^{124}Sn using the spin distribution from Eq. (3.28) agrees well with the results of the fluctuation analysis of (p, p') data (Fig. 6 in Paper II and Fig. 2 in Paper IV).

In the same manner, the GSFs are quite similar in absolute values and shapes for all the studied isotopes. All of them are in good agreement with the (p, p') data for even-even Sn nuclei down to $E_\gamma \approx 6$ MeV and in reasonable agreement with available (γ, n) data in the
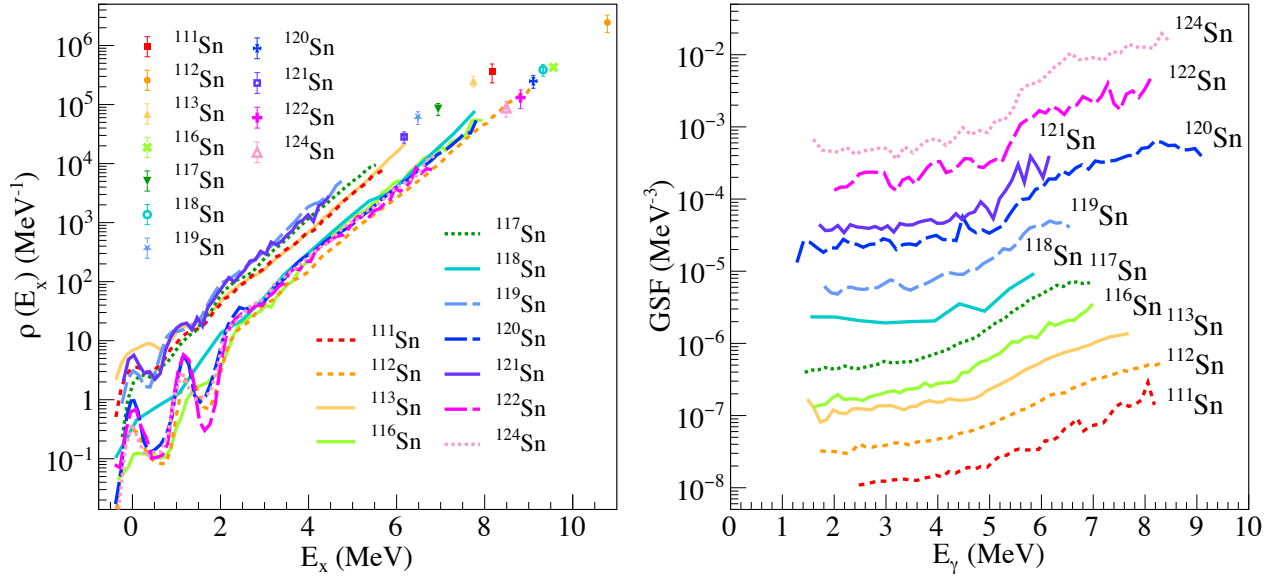
Figure 5.1: The NLDs (a) and GSFs (b) of $^{111-113,116-122,124}$Sn extracted with the Oslo method. The latter are scaled by a factor of 3 with respect to each other (starting from ^{111}Sn) for a more clear visualization.

immediate vicinity of the neutron threshold. As shown in Fig. 5.1(b), the slope of the GSF changes gradually throughout the isotopic chain and becomes steeper towards ^{124}Sn. For the heaviest studied nuclei, a bulk peak-like structure at $6-9$ MeV, which might potentially be interpreted as the PDR, becomes more prominent, whereas the lowest part of the strength remains rather flat and does not demonstrate any clear upbend as was previously seen in some other Oslo data (see e.g. [187]). It is important to note that the observed increase of the slope from ^{111}Sn to ^{124}Sn is small. Based on these data alone, it is already possible to conclude that even if any dependence on the neutron number is present, it should not be expected to be as strong as predicted by theoretical approaches. It is, nevertheless, crucial to extract the LEDR in these nuclei in a model-consistent way prior to comparing it with other experimental estimates and theoretical predictions.

5.2 Decomposition of the dipole strength

As was mentioned in the previous chapters, the Oslo method assumes the dominance of dipole transitions from the quasi-continuum and does not distinguish between the electric and magnetic types of radiation. In an attempt to constrain the LEDR component of the total GSF below the neutron threshold, the latter should be decomposed in terms of the most prominent individual components expected in nearly spherical Sn isotopes, such as the tail of the IVGDR, the LEDR, and the spin-flip $M1$ contribution. In some cases, the upbend feature should also be introduced to account for a flat, as in case of the Sn isotopes, or an increasing trend in the strength at low γ-ray energies.

Since the Oslo data reach only up to the neutron threshold or lower in the studied iso-

topes, they should be complemented by other experimental strengths at higher energies for a more accurate reconstruction of the full LEDR and the IVGDR tail contributions. The total GSFs from the Coulomb excitation (p, p') experiments on even-even ^{112,114,116,118,120,124}Sn nuclei cover the energy range of both the PDR and the IVGDR, from 6 MeV up to 20 MeV. The information on the IVGDR in these and odd-mass stable targets can also be deduced from photoabsorption experiments performed in Saclay [249], Livermore [250], and Moscow [251]. In contrast to these data, typically having quite large errors closer to the neutron threshold, photoabsorption experiments with quasi-monochromatic laser-Compton scattering γ rays on $^{116-120,122,124}$Sn [252, 253] provide the GSFs in the immediate vicinity of S_n in these nuclei with much smaller uncertainties. In general, the (p, p') and (γ, n) strengths agree fairly well within the uncertainties around the peak of the IVGDR [42]. At the left flank of the IVGDR, the strength by Varlamov *et al.* [251] appears to be on average larger than in all other experiments, and all of the (γ, n) data tend to deviate from each other and the (p, p') results closer to the neutron threshold. On the contrary, the GSFs by Utsunomiya *et al.* [252, 253] are in excellent agreement with the (p, p') strengths in all the studied even-even isotopes. Provided a general agreement in the IVGDR region with other experimental results and a significant overlap with the available Oslo method strengths, the LEDR in Sn isotopes in this thesis will be extracted based on the combined Oslo and (p, p') total GSFs.

The Oslo method results for all the eleven studied isotopes are shown together with the (p, p') and (γ, n) strengths in Fig. 5.2. For the cases of the odd nuclei, the Coulomb excitation data for the closest or two neighboring even-even isotopes are shown. The GSFs of ^{111}Sn and ^{121}Sn agree well with the (p, p') strengths of ^{112}Sn and ^{120}Sn, respectively. Similarly, the GSFs of ^{113}Sn, ^{117}Sn, ^{119}Sn are in good agreement with the (p, p') results for both even-even neighboring nuclei in each case. Furthermore, the Oslo method and (p, p') strengths of the even-even ^{112,116,120,124}Sn are in excellent agreement below the threshold within the estimated uncertainties. Due to quite low statistics of the $(^3$He,$\alpha\gamma)$ experiment on ^{119}Sn, the Oslo method GSF of ^{118}Sn is shown only up to $\approx$ 6 MeV, being complementary to the corresponding (p, p') strength. Finally, even though no Coulomb excitation data are available for ^{122}Sn, it is in good agreement with the Oslo method strength for the neighboring even-even and odd nuclei and (p, p') data for ^{120}Sn and ^{124}Sn.

In this thesis, two approaches to the extraction of the LEDR in the Sn isotopes will be applied. The first method is commonly used for the interpretation of experimental strength distributions from Oslo-type and Coulomb excitation experiments with radioactive beams [31, 254] and implies the decomposition of the total GSF in terms of the adopted models for the LEDR and IVGDR. Alternatively, a straightforward integration of the total strength up to a certain energy threshold, without introducing any model-dependent tail of the IVGDR, allows for a more explicit comparison with the theoretical strength distributions in terms of the TRK values.

For the parametrization of the IVGDR (f_{E1}) in Sn isotopes, the GLO model in the form of Eq. (2.24) was chosen. Among other considered approaches, the GFL and hybrid models are not fully able to simultaneously capture the relatively flat low-energy tail of the Oslo strength function and reproduce the left flank of the IVGDR, being more appropriate in cases of less steep GSFs (see e.g. [186]). Despite a great improvement in reproducing the GSF below the neutron threshold as compared to the SLO, the SMLO approach still fails at capturing the relatively steep slope between $3 - 6$ MeV in the studied Sn isotopes. The microscopic calcu-

lations provided by Skyrme-HF BCS [192], Skyrme-HFB [66] and its temperature-dependent extension [255], and Gogny-HFB [256] with QRPA can, in principle, be used to model the IVGDR. However, in the case of Sn isotopes, they require certain modifications (scaling and shift) to be adjusted to fit the IVGDR, which complicates the consistent analysis throughout the whole chain of isotopes. Among all of the above-mentioned approaches, the GLO is sufficiently flexible to reproduce both the IVGDR and the low-energy tail of the GSF and was found to be the most appropriate choice.

The LEDR component on top of the IVGDR was found to be best described by a simple Gaussian function as:

$$f_{E1}^{\text{low}}(E_\gamma) = C_{E1}^{\text{low}} \frac{1}{\sqrt{2\pi}\sigma_{E1}^{\text{low}}} \exp\left(-\frac{(E_\gamma - E_{E1}^{\text{low}})^2}{2(\sigma_{E1}^{\text{low}})^2}\right), \tag{5.1}$$

with centroid E_{E1}^{low}, width σ_{E1}^{low}, and absolute value normalization constant C_{E1}^{low}. A single Lorentzian peak and combinations of several peaks have also been tested in an attempt to reproduce the bump-like structure at $6-9$ MeV in the GSFs and were found to yield significantly worse fit scores.

The experimental information on the $M1$ component in even-even Sn isotopes is available from the MDA of the (p,p') data. It was used to build the systematics for the $M1$ strength in those nuclei where no experimental data are available (see also Appendix C.2). To do so, the $M1$ strength in ^{112,114,116,118,120,124}Sn was fitted with a simple Lorentzian function as:

$$f_{M1}(E_\gamma) = \frac{1}{3\pi^2\hbar^2c^2} \frac{\sigma_{M1}\Gamma_{M1}^2 E_\gamma}{(E_\gamma^2 - E_{M1}^2)^2 + E_\gamma^2\Gamma_{M1}^2} \tag{5.2}$$

with centroid energy E_{M1}, maximum cross section σ_{M1}, and width Γ_{M1}. The systematics of these three parameters were used to reconstruct the $M1$ contribution in the other studied isotopes. It is important to note that the experimental $M1$ strength distribution is somewhat fragmented in all the cases, and the Lorentzian function reproduces only its overall shape and the integrated total $M1$ strength. The detailed fit of the $M1$ strength distribution was found to have a negligible effect on the final results within the estimated uncertainties.

Finally, to account for the flat low-energy tail of the GSF, an upbend should be introduced in some of the cases in accordance with the prescription of Ref. [190]:

$$f_{\text{up}}(E_\gamma) = C_{\text{up}} \exp(-\eta_{\text{up}}E_\gamma), \tag{5.3}$$

with scaling and slope parameters C_{up} and η_{up}. In general, the GSFs of the Sn isotopes do not demonstrate any clear upbends and are limited to γ-ray energies above about 2 MeV. Thus, the upbend $f_{\text{up}}(E_\gamma)$ should be treated solely as an additional feature improving the fit at very low γ-ray energies, which has little to no impact on the extracted LEDR.

To disentangle all of the above-mentioned components in the total GSF provided by the Oslo method and (p,p') data in each case, the strengths were fitted with the combined function $f_{\text{tot}} = f_{E1} + f_{E1}^{\text{low}} + f_{M1} + f_{\text{up}}$, while keeping the parameters of the $M1$ strength fixed. The parameters of the GLO, the Gaussian peak(s), and the upbend were treated as free fit parameters. For the odd isotopes and ^{122}Sn, the (p,p') data of the neighboring even-even isotopes were used for the fit (^{112}Sn for ^{111}Sn, ^{112,114}Sn for ^{113}Sn, ^{116,118}Sn for ^{117}Sn, ^{118,120}Sn for ^{119}Sn,
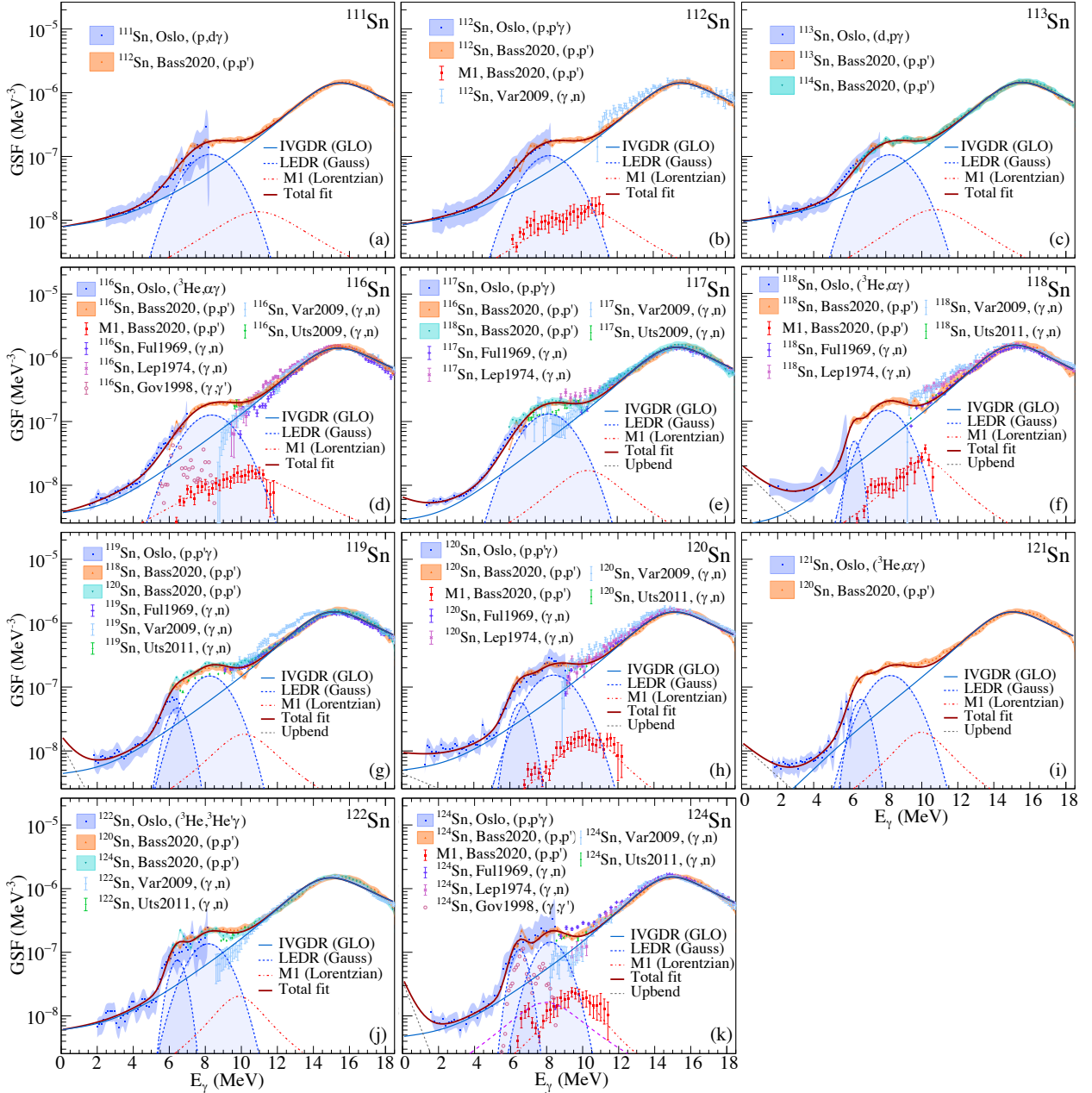
Figure 5.2: Experimental GSFs of ^{111}Sn (a), ^{112}Sn (b), ^{113}Sn (c), ^{116}Sn (d), ^{117}Sn (e), ^{118}Sn (f), ^{119}Sn (g), ^{120}Sn (h), ^{121}Sn (i), ^{122}Sn (j), and ^{124}Sn (k) shown together with the (p,p') data from Ref. [42] (Bass2020) and the (γ,n) experimental data by Varlamov *et al.* [251] (Var2009), Fultz *et al.* [249] (Ful1969), Leprêtre *et al.* [250] (Lep1974), Utsunomiya *et al.* [252, 253] (Uts2009, Uts2011), and Govaert *et al.* [74] (Gov1998). The total fits of the experimental data are shown as solid magenta lines and the fits of the IVGDR as solid blue lines. The low-lying $E1$ components are shown as shaded light-blue areas. The $M1$ data from the Coulomb excitation experiment [42] are shown for ^{112,116,118,120,124}Sn with corresponding Lorentzian fits (dashed red lines).

[120]Sn for [121]Sn, and [120,124]Sn for [122]Sn). Provided that the IVGDR parameters extracted using the Coulomb excitation data demonstrate the same smooth evolution as those from the (γ, n) experiments [42], the sole consequence of preferring the former over the latter for the fit is maintaining a more consistent fit in the vicinity of the neutron threshold. Similarly to the GSFs of the even-even and even-odd isotopes extracted with the Oslo method, the IVGDR is also expected to evolve rather smoothly throughout the isotopic chain.

As was first reported in Refs. [28, 42], the (p, p') data reveal a peak-like structure at $\approx 6.4 - 6.5$ MeV in all the studied even-even isotopes, which appears to become more prominent towards [124]Sn. A hint of a similar structure appears also in the Oslo method strength for [124]Sn. Even though observing such structures in the Oslo data might be complicated due to an overall worse energy resolution, it is still possible to constrain this component based on the combined total Oslo method and (p, p') strength by introducing an additional Gaussian peak in the total fit for isotopes starting from [118]Sn. In this isotope, the peak at $6.4 - 6.5$ MeV becomes sufficiently prominent, and the slope of the Oslo strength becomes sufficiently steep for the additional Gaussian peak to improve an overall fit to the experimental data below the threshold. Different components of the performed fits, including both Gaussian peaks of the LEDR, are shown in Fig. 5.2. All the fit parameters of the IVGDR, the $M1$ response, the LEDR peaks, and the upbend (if included) are collected in Tables C.2 and C.3.

5.3 Discussion of the systematics

To quantify the evolution of the LEDR in the studied Sn isotopes, the energy centroid and the energy-weighted sum of the $E1$ strength in terms of the classical TRK sum rule concentrated in the extracted Gaussian peaks have been estimated. The results obtained for all the studied isotopes are shown in Fig. 5.3. For the isotopes with $A \geq 118$, the centroids of both the larger, higher-lying and the smaller, lower-lying components are shown in Fig. 5.3(a) together with the strength-weighted average centroid of the total LEDR. Similarly, the strengths of both LEDR components are shown together with the total strength in Fig. 5.3(b).

The LEDR in the Sn isotopes is concentrated in the vicinity of $\approx 7.8 - 8.3$ MeV, and its energy centroid appears to remain essentially unchanged throughout the isotopic chain and demonstrates only a mild decrease towards [124]Sn. The higher-lying and the lower-lying components for [118-122,124]Sn are centered around ≈ 8.2 MeV and $6.4 - 6.5$ MeV, respectively. The slight decrease of the average centroid is correlated with the gradual increase of the strength in the lower-lying peak with increasing neutron number. This trend is preserved (within the uncertainties) when using a single-peak for the LEDR fit in [118-122,124]Sn. It is, however, in contradiction with the increase of the centroid in [116-119,121,122]Sn presented in Ref. [83], which is most likely due to large uncertainties in the fits close to the neutron threshold in the latter. The decrease of the centroid has previously been predicted in calculations within the RQRPA and RQTBA [19, 72] and QPM [73] approaches for Sn isotopes and other isotopic chains [19, 257].

As shown in Fig. 5.3(b), the LEDR in the studied Sn isotopes exhausts $\approx 2 - 3\%$ of the TRK sum rule. Except for a local peak in the strength around [120]Sn, no clear increase in the TRK values towards more neutron rich [124]Sn has been observed. The GSFs extracted with the Oslo method are quite similar for the neighboring [118-122,124]Sn isotopes, whereas the (p, p')
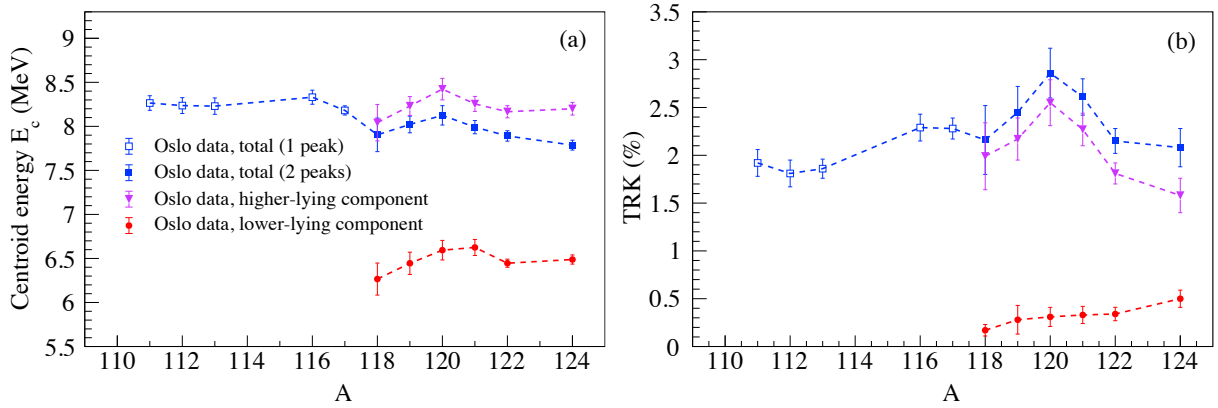
Figure 5.3: TRK values (a) and energy centroids (b) for the total extracted LEDR in Sn
isotopes, its lower-lying, and higher-lying components. Open squares correspond to a single-
Gaussian peak fit, filled squares correspond to the sum (a) and strength-averaged centroids
(b) of two Gaussian peaks.

strength is somewhat larger for ^{120}Sn between $8-10$ MeV than in the neighboring even-even
nuclei, hence the local increase of the TRK value at $A = 120$. A somewhat similar trend
has been obtained with the RPA [56] and RHB plus RQRPA [19] calculations. In the latter
work, the total sum of the energy-weighted dipole strength up to a certain threshold was
shown to have a local maximum around $^{120-124}$Sn, depending on the threshold, and decrease
towards the closed $N = 82$ shell, attributed to the interplay of shell effects and the reduction
of the pairing correlations. On the other hand, the recent study of the isovector and isoscalar
response in Sn isotopes using the TDHF approach [21] suggests that an enhanced isoscalar
and isovector response in the open-shell nucleus ^{120}Sn as compared to doubly-magic ^{100,132}Sn
might be related to a relatively more diffuse isoscalar density profile in the former. It is
important to note that the local increase of the experimental TRK values in the vicinity of
^{120}Sn in Fig. 5.3(b) is quite subtle considering the estimated uncertainties, and a potential
link between its presence in the experimental data and microscopic calculations needs to be
further investigated.

The low-lying component of the LEDR at $6.4-6.5$ MeV exhausts only up to $\approx 0.5\%$ of
the TRK sum rule. Moreover, it appears to increase almost linearly with increasing neutron
number, becoming more prominent in ^{124}Sn. As was mentioned in Sec. 1.3, a concentration
of the isoscalar strength in approximately the same energy range ($5.5-7$ MeV) has been
observed in the $(\alpha, \alpha'\gamma)$ [39, 40] and $(^{17}O, ^{17}O'\gamma)$ [78] experiments. The comparison with the
isovector response obtained with the (γ, γ') and (p, p') experiments suggests that the extracted
lower-lying $E1$ peak can be potentially associated with the isovector component of the PDR.

The majority of the microscopic frameworks, including the RQRPA and RQTBA calcula-
tions of Ref. [72], HFB plus QPM calculations of Ref. [73], and the study based on the Vlasov
equation approach of Ref. [20], suggest a somewhat steady increase of the PDR, or rather
LEDR, strength towards more neutron-rich nuclei in the Sn isotopic chain. A more explicit
comparison of the experimental and theoretical TRK values can be provided by considering
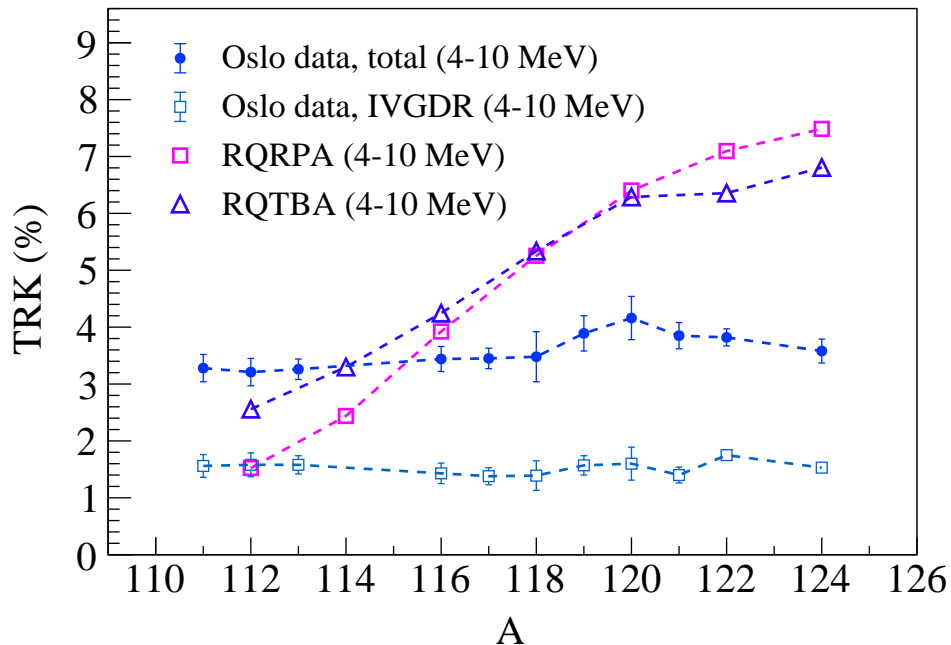an energy-weighted sum of the $E1$ strength up to a certain threshold. The total experimental

Figure 5.4:   Evolution of the energy-weighted electric dipole strength extracted from the RQRPA and RQTBA calculations and the combined experimental Oslo and (p, p') data, integrated from 4 MeV up to 10 MeV.

$E1$ strength (the Lorentzian $M1$ component has been subtracted) including both the IVGDR tail and the LEDR has been integrated from 4 MeV up to 10 MeV. The corresponding TRK values are shown in Fig 5.4 together with the strength concentrated only in the tails of the IVGDR, using the GLO model and the parameters from Table C.2. The latter exhaust an approximately constant fraction of the TRK sum rule ($\approx 1.5\%$) throughout the whole isotopic chain, while the total strength corresponds to $\approx 3 - 4\%$, with a maximum at ^{120}Sn. For comparison, the energy-weighted sums have also been extracted in the range between 4 MeV and 10 MeV for the even-even stable Sn isotopes using the RQRPA and RQTBA calculations introduced in more detail in Paper IV. The results are shown in Fig 5.4. Both approaches demonstrate a monotonic increase in strength from $\approx 1.5 - 2.5$ % to $\approx 6.8 - 7.5$ % of the TRK sum rule. In comparison with the theoretical predictions, the experimental LEDR is essentially constant throughout the isotopic chain, at least up to ^{124}Sn. Despite a great improvement in reproducing the overall shape of the IVGDR and the strength in the PDR region with the RQTBA approach, it still predicts comparatively large concentrations of $E1$ strength in peaks between 6 MeV and 10 MeV, which are not observed experimentally. Future advances in numerical calculations at the next level of complexity, employing $2q \otimes 2$phonon or correlated six-quasiparticle configurations, might be a key to a better reproduction of the experimental results within the valley of stability.

An explicit comparison of TRK values for different nuclei extracted with different experimental techniques (in particular, the Oslo method, NRF, and Coulomb excitation studies) is complicated greatly by the inconsistency in either energy ranges or methods chosen to extract
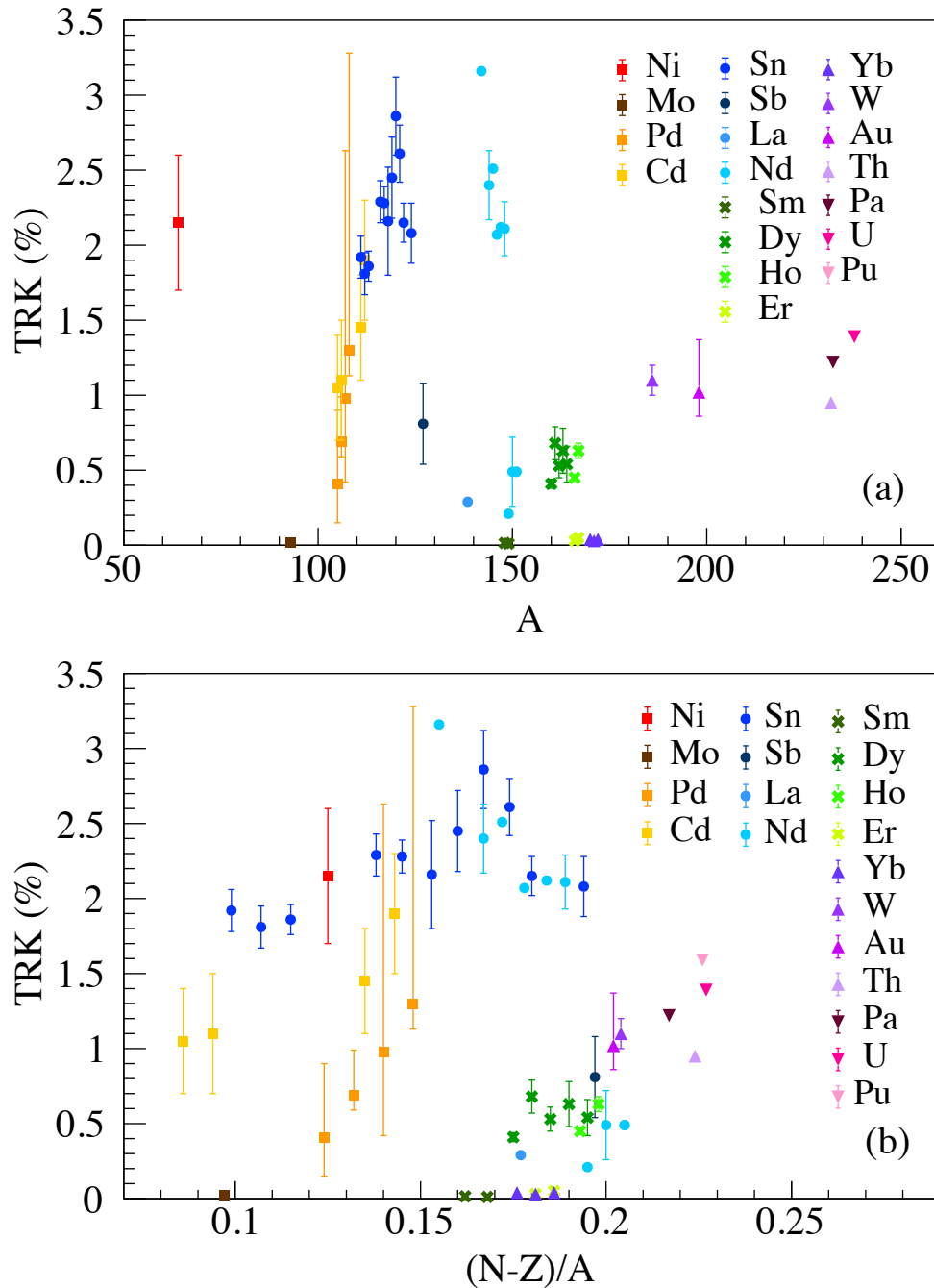
Figure 5.5: TRK values of the low-lying $E1$ response interpreted as the PDR and obtained using the Oslo data versus (a) mass number A, (b) asymmetry parameter $(N - Z)/A$. The values and the parameters used to estimate these values are taken from Refs. [187, 228, 258–269] and the present work.

these values. To put the systematics of the TRK values for the Sn isotopes into a broader context, the TRK values for $^{111-113,116-122,124}$Sn can be compared with the TRK values for other nuclei studied with the Oslo method. These data have been obtained in different experimental campaigns starting from 2001, and the decomposition of the total dipole strength based on the combined Oslo and (γ, n) strengths in an attempt to constrain low-energy features in the GSF (most commonly the scissors mode and the PDR) has been done for the majority of the studied nuclei. Even though these analyses employ different normalization procedures and fit models, the feature interpreted as the PDR has been extracted quite consistently with the cases of the Sn isotopes presented in this thesis. The TRK values reported in these works or estimated based on the reported model parameters are shown for nuclei from Ni to Pu in Fig. 5.5. The TRK value of $\approx 5.5\%$ for the presumable PDR in ^{238}Np [270] was not included in the figure to demonstrate any potential trends in the lighter nuclei more clearly. The upper panel (Fig. 5.5(a)) shows the distribution of the TRK values over the studied mass range $A = 64-243$. Currently, the systematics (more than two values) of the TRK sum rule fractions are available for the isotopic chains of Pd [260], Cd [261], Sn, Nd [187], Dy [264], and Yb [228]. It is clearly seen that different isotopes and nuclei with similar masses are clustered together with respect to the TRK fractions they exhaust. The PDR/LEDR in the studied Pd and Cd isotopes exhausts from $\approx 0.5\%$ to 2% of the TRK sum rule, similarly to $\approx 2\%$ exhausted in the majority of the studied Sn isotopes. The total PDR/LEDR in the lightest Nd isotopes is quite similar to that in the Sn isotopes, whereas for the heaviest ^{150,151,152}Nd it does not exceed the lower-lying LEDR component at $\approx 6.4-6.5$ MeV in Sn, similarly to the studied Dy and Ho isotopes. For a comparison, the PDR/LEDR in Sm, Er, and Yb is vanishingly small, which might be partly related to the used extraction techniques. Finally, for the heaviest nuclei up to Pu, the PDR/LEDR exhausts almost consistently $1-1.5\%$ of the TRK sum rule. When comparing the above-mentioned nuclei, it is important to keep in mind that the majority of the fits have been performed using the (γ, n) data in the vicinity of the neutron threshold, which might have affected the extracted features. If disregarding some individual deviations, there is some trend characterized by the increasing PDR/LEDR strength towards $A \sim 150$, an abrupt drop after $A \sim 150$, and a gradual increase towards $A \sim 250$.

Representing these TRK values as a function of the proton-neutron asymmetry parameter $(N-Z)/A$, as shown in Fig. 5.5(b), might potentially reveal some dependency on the neutron excess in the studied nuclei. Indeed, despite quite large uncertainties, there are some hints of such a dependence in the Pd and Cd isotopic chains and a group of nuclei from Dy to Pu. In the Sn isotopic chain, the gradual increase of the TRK values is interrupted at ^{120}Sn, as was mentioned earlier. Surprisingly, the Nd isotopes demonstrate a sharp decrease of the PDR/LEDR strength towards more neutron-rich isotopes. The fit in this case is significantly complicated by the double-humped IVGDR and the lack of any experimental data in this energy region for ^{147,150,152}Nd.

Chapter 6

Implications for the astrophysical neutron-capture processes

The NLDs and GSFs are two essential input characteristics for Hauser-Feshbach calculations using, for example, the reaction code TALYS. The following chapter is focused on implications of the experimentally extracted NLDs and GSFs of the Sn isotopes for the astrophysical neutron-capture processes. In this thesis, the radiative neutron-capture cross sections and reaction rates have been estimated for $^{113,116-122,124}$Sn using the experimental data as the input in TALYS and compared with the available experimental data and model predictions. The choice of different inputs for the calculations and, in particular, the impact of the LEDR on the estimated cross sections will be addressed for ^{120}Sn in the following sections. Moreover, the importance of the newly constrained ^{121}Sn$(n,\gamma)^{122}$Sn and ^{123}Sn$(n,\gamma)^{124}$Sn reaction rates for the astrophysical i process will be discussed at the end of the chapter.

6.1 Neutron-capture processes in the Sn region

The main formation mechanism of trans-iron nuclides in the universe, including Sn isotopes, is neutron-capture reactions in various astrophysical scenarios. After the seminal works by Burbidge *et al.* [271] and Cameron [272] presenting the first phenomenological formulation of the nucleosynthesis processes in the domain of heavy nuclei, it became common to treat the Solar System abundances in terms of the main contributions of the slow (s) and rapid (r) neutron-capture processes and the so-called p process. Schematically, this allows for splitting the nuclear chart beyond Fe/Ni into nuclei along the bottom part of the stability valley produced in the s process, neutron-rich r-process nuclei, and neutron-deficient nuclei from the p-process. The latter involves a complex interplay of photodisintegrations $((\gamma,p),(\gamma,n),(\gamma,\alpha))$, radiative proton captures (p,γ), and, presumably, some neutron captures and β decays transforming preceding s and r nuclei in the deep O–Ne shells of massive stars exploding as supernovae or while still being in the pre-supernova phase [273]. In comparison with the widely dominating s and r processes, its contribution to the total Solar System abundances is rather humble and does not exceed $0.1-1\%$ of that provided through consecutive neutron captures and β decays in the other two mechanisms [274].

The s process operates under comparatively low neutron densities of $\sim 10^6 - 10^{10}$ cm^{-3}

and requires iron-peak seed nuclei to initiate a chain of neutron captures and β decays [275].
Consecutive neutron captures proceed along the chains of stable isotopes until the first β-unstable nucleus is produced. With the above-mentioned neutron densities, the typical β-decay lifetime is considerably shorter than the time required to capture one more neutron, and
thus the s process proceeds along the stable isotopic chains up to ^{208}Pb and ^{209}Bi. The nuclei
with competing neutron-capture and β-decay rates correspond to the so-called branching
points, whereas those with comparatively low neutron-capture rates act as bottlenecks for the
capture flow and lead to a build-up of stable isotopes with certain mass numbers. Within
the modern picture, the s process is further split into the weak and the main components,
responsible for producing nuclei with $A \lesssim 90$ and $A \gtrsim 90$, respectively. The former is expected
to be mainly powered by the ^{22}Ne$(\alpha, n)^{25}$Mg reaction in the convective core He-burning and,
partly, in C-burning shells in massive stars [276], while the latter is predominantly driven
by the ^{13}C$(\alpha, n)^{16}$O neutron source in intermediate- and low-mass asymptotic giant branch
(AGB) stars [277].

In contrast to the typical time span of thousands of years for the s process, much shorter
timescales are required for the r process (a few seconds) to produce neutron-rich nuclei far
from the valley of stability, provided high neutron densities of $\sim 10^{20}$ cm^{-3} [278]. After
such intense neutron fluxes are exhausted, the produced neutron-rich, unstable nuclei decay
back towards the valley of stability, forming heavy nuclei up to actinides (e. g. U and Th
isotopes). Potential sites able to host neutron captures under such extreme conditions have
for a long time been a matter of numerous debates. In the past two decades, the attention
in these discussions has been shifted from the core collapse supernova scenario to neutron
star mergers as promising hosts of the r process. A recent observation of gravitational wave
signals from the binary neutron star inspiral [54] and its electromagnetic counterpart powered
by the decay of isotopes of heavy elements [279] provided the first observational confirmation
of such an r process site and inspired further large-scale network calculations and simulations
requiring experimental nuclear inputs.

Both the s and r processes are believed to have a contribution of about 50% each to
abundances of elements beyond the Fe peak. Other processes have also been suggested to
contribute to the heavy element nucleosynthesis, in particular the so-called intermediate i
process [275]. The need to introduce an additional neutron-capture process operating under
the neutron densities of $\sim 10^{12} - 10^{16}$ cm^{-3}, somewhat in between the s and r processes, is
related to the discovery of carbon-rich, metal-poor r/s-stars with abundances which can not
be reproduced by the combination of the other two mechanisms (see e.g. [280]). The main
neutron source in this case is expected to be ignited by the ingestion of protons in He-rich
layers, powering the ^{13}C$(\alpha, n)^{16}$O reaction [275]. Numerous sites have been proposed to be
the host of such events, among which the early AGB phase of metal-poor low-mass stars has
been studied thoroughly in the series of recent model calculations in Refs. [87, 275, 281, 282].

Studying isotopic abundances in the Cd-In-Sn-Sb-Te region requires considering an intricate interplay of all the above-mentioned nucleosynthesis processes, as shown in Fig. 6.1.
Both the s- and r-process flows are especially complicated due to the presence of relatively
long-lived, β-decaying isomers, associated with low-energy high-spin proton $g_{9/2}$ and neutron
$h_{11/2}$ orbitals [285]. In particular, a complex branching takes place in ^{113,115}Cd, ^{115}In, and
^{121}Sn. There are several s-only isotopes in the Te isotopic chain (^{122,123,124}Te, with the latter
experiencing the total s-process flow), "shielded" from the series of β decays following the r
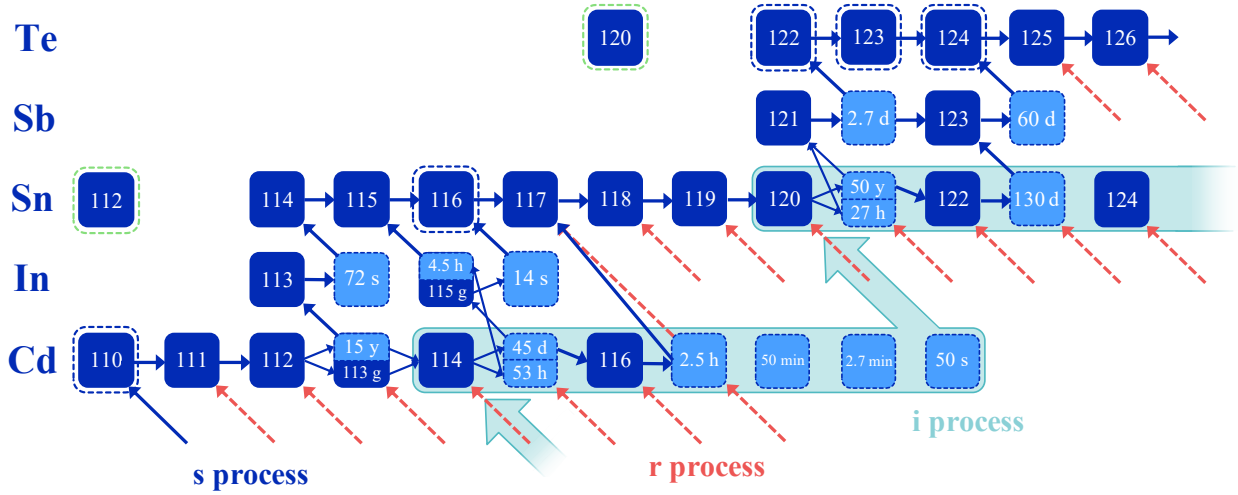
Figure 6.1: Paths of the astrophysical s, r, and i processes in the vicinity of the stable Sn isotopes. The flow of the s process is depicted as solid blue arrows, and the contribution due to the r process through β decays is shown by dashed orange arrows [283, 284]. The i-process path is modeled for a 1 $M_\odot$, [Fe/H]= −2.5 star (see also Sec. 6.4) with the highest neutron density of 5×10^{14} cm^{-3} in Ref. [87]. The s-only and p-only isotopes are shown with the surrounding dashed blue and green boxes, respectively. Stable isotopes correspond to solid blue boxes.

process by stable Sn and Sb isotopes. Accurate measurements of neutron-capture rates over a wide temperature range for these nuclei and the s-only ^{116}Sn isotope are crucial for a correct normalization of the s-process models in this mass region [283]. In contrast to the considered p-only ^{112}Sn isotope, the contribution of different processes to abundances of ^{114,115}Sn has been a highly debated topic in the past few decades [286]. For example, the galactic chemical evolution model computation for low-mass AGB stars by Bisterzo $et\ al.$ [287] suggests the s-process contribution to the origin of these nuclei to be negligible, whereas the r process was found to be a significant contributor to the production of ^{115}Sn together with the p process, which is also the main mechanism of producing ^{114}Sn (see Ref. [288] and references therein). The stable Sn isotopes from ^{117}Sn to ^{120}Sn are produced in the series of s-process neutron captures with a minor feeding through β decays following the r process. The latter is considered the main contributor to the production of the ^{122}Sn and ^{124}Sn (r-only) isotopes [289]. However, the recent low-mass low-metallicity AGB model calculations by Goriely $et\ al.$ [87] demonstrated that the most neutron-rich stable Sn isotopes (^{120,122,124}Sn) might also be involved in the flow of the i process in this mass region. A wealth of experimental data is currently available to provide constraints for the neutron-capture rates on stable Sn isotopes, while the calculations involving ^{121,123}Sn$(n,\gamma)^{122,124}$Sn still have to rely on theoretical model calculations, spanning a wide range of model uncertainties. In light of this, the ^{124}Sn and the newly re-analyzed ^{122}Sn Oslo method data are of particular interest in the i-process modeling in large-scale network calculations, similar to those presented in [87, 275, 281, 282].

6.2 Calculations of radiative neutron-capture cross sections with TALYS

In this thesis, the Oslo method NLDs and GSFs have been used to constrain the radiative neutron-capture cross sections (NCCS or just CS) with the TALYS reaction code of the latest 1.96 version [154, 290]. To do so, the experimental Oslo GSFs have been combined with the (p, p') data at high energies where the Oslo data are not available. The combined total dipole GSF was used to extract the tabulated $E1$ GSF by subtracting the Lorentzian-fitted experimental $M1$ response. The latter was also used to produce the tabulated $M1$ GSFs applied together with the $E1$ strength as inputs for the calculations. In all cases, the phenomenological model of Koning and Delaroche was chosen for the optical model potential [291]. Another alternative available in TALYS is the semi-microscopic Jeukenne-Lejeune-Mahaux (JLM) model renormalized by the Bruyères-le-Châtel group [292]. In case of the Sn isotopes, both of these optical model potentials yield cross sections overlapping closely within the uncertainty bands, and thus the former one was chosen in all the calculations. This, however, is not the case for heavier nuclei, as was shown for ^{185}W in Ref. [186] and ^{165,166}Ho in Ref. [140]. In these cases, the JLM model results in significantly lower cross sections and rates towards lower energies and temperatures, respectively, and should also be included in the total uncertainty band.

The current version of the TALYS code offers several alternative NLD and GSF models for the calculations, which are especially relevant for the nuclei where the Oslo data or some other experimental data below the neutron threshold are not available. The six NLD options in TALYS are the following:

1. The constant-temperature plus Fermi gas model (CT) [97].

2. Back-shifted Fermi gas model (BSFG) [107].

3. Generalized superfluid model (GSM) [293, 294].

4. Hartree–Fock plus Bardeen–Cooper–Schrieffer (HF-BCS) calculations based on the MSk7 Skyrme force [111].

5. Hartree-Fock-Bogoluybov (HFB) plus combinatorial model calculations based on the BSk14 Skyrme force [112].

6. Temperature-dependent HFB plus combinatorial model calculations based on the D1M Gogny force [113].

All of these models are shown in Fig. 6.2(a) for ^{120}Sn together with the Oslo method NLD.

Similarly, the comparison of TALYS $E1$ GSF options with the Oslo method total GSF is shown in Fig. 6.2(b). The nine TALYS models are the following:

1. The Kopecky-Uhl generalized Lorentzian (GLO) [146].

2. The standard Lorentzian (SLO) [85].

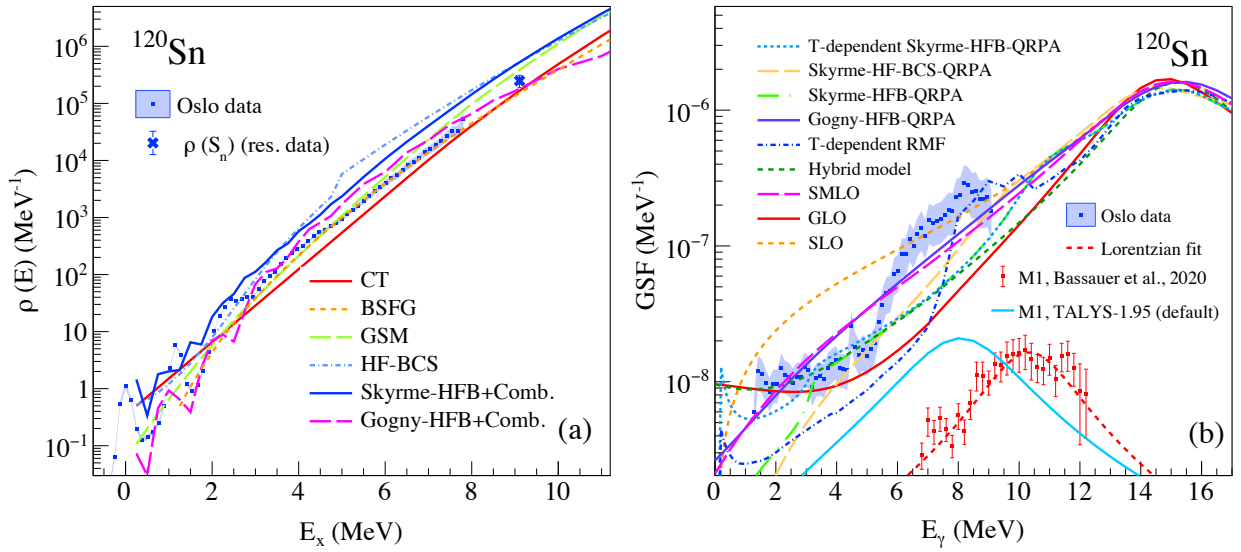3. The HF-BCS plus QRPA calculations using the SLy4 Skyrme force [192].

Figure 6.2:   (a) Comparison of the experimental NLD for ^{120}Sn with the models available in TALYS [154]: constant-temperature model (CT), back-shifted Fermi gas model (BSFG), generalized superfluid model (GSM), HF plus BCS, Skyrme-HFB plus combinatorial, and temperature-dependent Gogny-HFB plus combinatorial model calculations. (b) Comparison of the experimental GSF for ^{120}Sn with the $E1$ and $M1$ models available in TALYS [154]: GLO, SLO, HF-BCS plus QRPA, Skyrme-HFB plus QRPA, hybrid model, temperature-dependent Skyrme-HFB plus QRPA, RMF plus QRPA, Gogny-HFB plus QRPA, SMLO.

4. The HFB plus QRPA calculations using the BSk7 Skyrme force [66].

5. The hybrid model [64].

6. Skyrme (BSk7) HFB plus QRPA with the temperature-dependent width [66].

7. The temperature-dependent relativistic mean field (RMF) plus QRPA calculations [255].

8. HFB plus QRPA calculations using the D1M Gogny force [256].

9. The simplified modified Lorentzian (SMLO) [145].

The latter is also employed for the $M1$ resonance in combination with the parametrized scissors mode and the upbend as a default option in TALYS 1.96 [154]. In the Sn isotopes, the modeled upbend tends to overestimate the experimental data at low γ-ray energies. For this reason, the default $M1$ option of TALYS 1.95 (the SLO $M1$ with the parametrization according to Ref. [290]) was used in the calculations. The corresponding $M1$ GSF is shown in Fig. 6.2(b) together with the experimental (p, p') strength. With the exception of the artificial upbend, all $M1$ options are quite similar for the studied Sn isotopes, and a particular choice of the model has little to no impact on the final calculated results.

As shown in Fig. 6.2(a), the BSFG and GSM NLDs agree quite well with the Oslo method values from ≈ 3 MeV up to the neutron separation energy. The slope of the CT model is

somewhat steeper than the one from the normalization of the experimental data and predicts lower NLD values on average. Among the microscopic calculations, the Gogny-HFB plus combinatorial approach reproduces the experimental NLD best, whereas the HF-BCS and Skyrme-HFB plus combinatorial models tend to overestimate the experimental values quite notably, by a factor of $2 - 3$ on average. On the other hand, none of the available $E1$ GSF options are able to reproduce the experimentally observed LEDR at $6 - 10$ MeV. The temperature-dependent relativistic mean field model predicts a bump-like structure at ≈ 9 MeV resembling the experimental LEDR, which, however, appears to be shifted towards higher energies as compared to the experimental data. Except for the GLO and the hybrid models, the rest of the approaches either overestimate or underestimate the Oslo method GSF significantly at lower energies. Finally, the modeled $M1$ response corresponds to approximately the same amount of strength and peak cross section as provided by the experimental data, but has a centroid shifted towards lower energies by about 2 MeV as compared to the experiment. The same applies to all other $M1$ options in TALYS. The neutron capture proceeding through a compound nucleus formation leaves the compound nucleus at excitation energy $S_n + E_n$ determined by the energy of an incident neutron. In the astrophysical s and r processes, these energies can reach up to several hundred keV, and, therefore, the decay pattern of the compound nucleus in the vicinity of the neutron threshold and several MeV below it can be expected to have the largest impact on calculations of radiative NCCSs. In a recent sensitivity study by Wang *et al.* [295], the radiative neutron-capture rates for stable Sn isotopes have been found to be most sensitive to variations of the $E1$ GSFs in the vicinity of 4 MeV. At these relatively low energies, the spread of the TALYS models, and thus the model uncertainty, reaches its maximum, and constraining the GSF with experimental techniques is especially important.

The NCCSs extracted with the Oslo method inputs are shown in Fig. 6.3 together with the available experimental data and TALYS model uncertainty ranges (beige bands). The TALYS default lines in these figures are extracted using the constant temperature plus Fermi gas NLD model, the SMLO form of the E1 strength, and the Koning and Delaroche global optical model potential. A comparison of these NNCSs with other experimental data even for the case of the lightest ^{113}Sn provides an indirect check of the Oslo data and, in particular, their normalization. Among the shown cases, the reactions on $^{115-122}$Sn nuclei are involved in the s-process flow in the Sn isotopic chain [283], and, as was shown in the recent work by Goriely *et al.* [87], the neutron capture on ^{120,121,123}Sn might also be on the the i process path. No experimental data are available for the unstable targets ^{121}Sn and ^{123}Sn. As shown in Fig. 6.3(g), the Oslo CS for the neutron capture on ^{120}Sn is in excellent agreement with other experimental data, at least above neutron energies of ≈ 20 keV. Similarly, the results for the ^{112,115,118,119}Sn targets were found to agree well within the uncertainty bands with all other available data, as shown in Figs. 6.3(a), (b), (e), (f). This agreement for the ^{116}Sn case (Fig. 6.3(c)) is somewhat worse, and the majority of experimental data points lie closer to the upper part of the uncertainty band of the Oslo result. An opposite situation is observed for ^{117}Sn. Provided a good agreement of the input NLDs and GSFs of the neighboring isotopes, it might be hard to state an exact reason for the observed deviations and whether they are due to the Oslo data alone. In general, different data sets tend to deviate from the Oslo NCCS and each other at low neutron energies $(20 - 30$ keV$)$. It is interesting to note that all the experimental results, including the NCCSs obtained with the Oslo method, lie closer to the
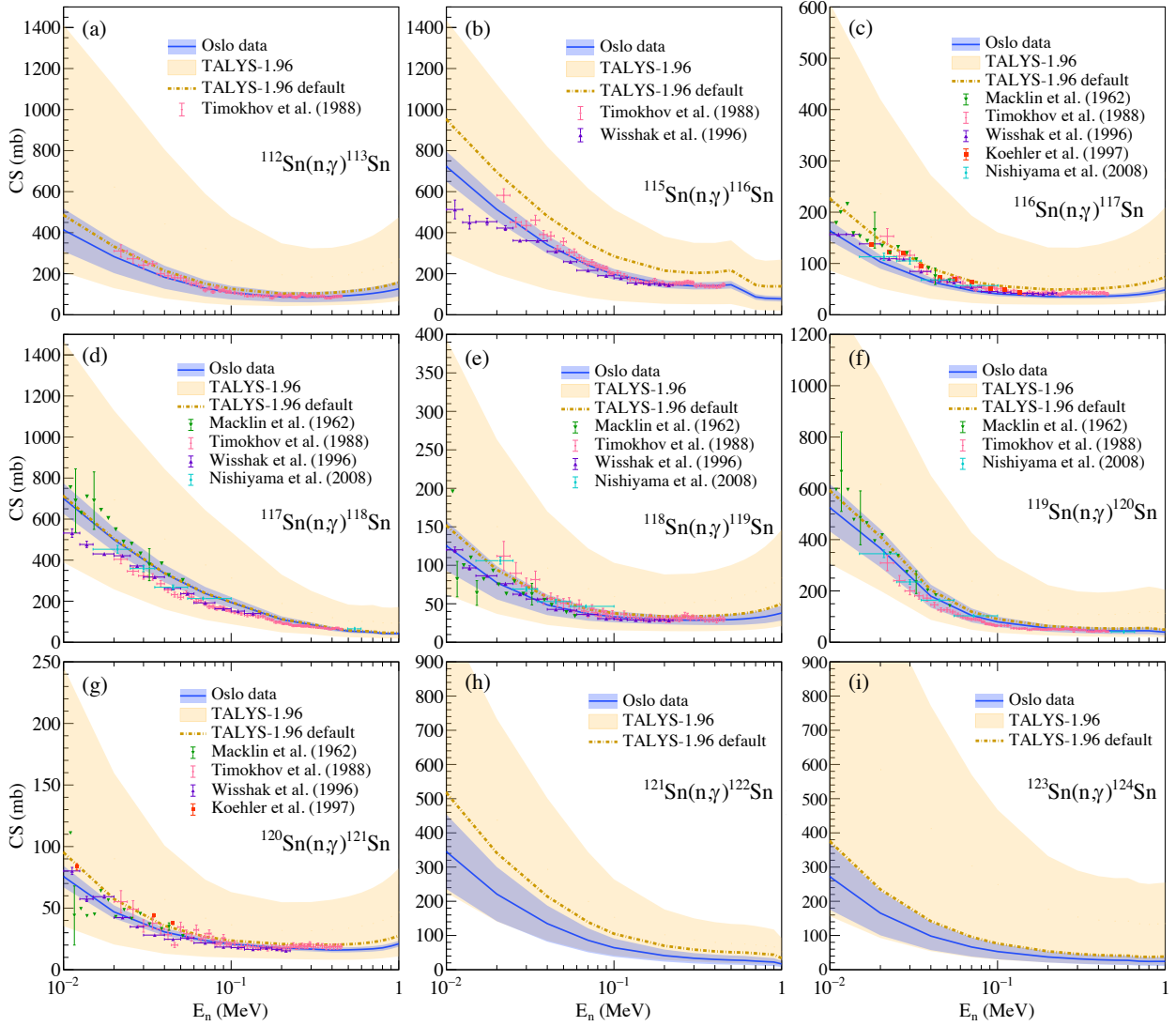
Figure 6.3: Cross sections (CS) for the ^{112}Sn$(n,\gamma)^{113}$Sn (a), ^{115}Sn$(n,\gamma)^{116}$Sn (b), ^{116}Sn$(n,\gamma)^{117}$Sn (c), ^{117}Sn$(n,\gamma)^{118}$Sn (d), ^{118}Sn$(n,\gamma)^{119}$Sn (e), ^{119}Sn$(n,\gamma)^{120}$Sn (f), ^{120}Sn$(n,\gamma)^{121}$Sn (g), ^{121}Sn$(n,\gamma)^{122}$Sn (h), and ^{123}Sn$(n,\gamma)^{124}$Sn (i) reactions. The predictions with the Oslo method inputs (blue bands) are compared with experimental data by Macklin *et al.* [289], Timokhov *et al.* [296], Wisshak *et al.* [284], Koehler *et al.* [283], Nishiyama *et al.* [297], and the TALYS uncertainty range obtained with different available GSFs, NLDs, and optical model potentials (beige band).

bottom part of the TALYS model uncertainty band for the majority of the considered cases. As shown in Fig. 6.2(b), the SLO, SMLO, and Gogny-HFB plus QRPA approaces result in approximately the same or larger amount of strength as compared to the Oslo method GSF, while the rest of the models correspond to much lower amounts of strength. The majority of the NLD models, on the other hand, tend to overestimate the Oslo method values, and the disagreement becomes gradually larger towards more neutron-rich isotopes. Provided that the calculations are essentially insensitive to the choice of the optical model potential, the NLD and the GSF are the main sources of the model uncertainties, and the NLD models are the major reason for the overall larger NCCS estimates with TALYS. It is also important to note that the default $M1$ component (light blue line in Fig. 6.2(b)), despite being by about a factor of 10 suppressed as compared to the $E1$ response, is shifted towards lower energies and tends to increase the calculated cross sections. In the lightest Sn isotopes, the experimental $M1$ component is slightly broader than for the heavier ones and has a larger overlap with the modeled TALYS $M1$ strength. Partly for this reason, the NCCSs for the ^{121,123}Sn targets lie closer to the bottom of the TALYS uncertainty band than those for the lighter targets.

6.3 Maxwellian-averaged cross sections of Sn isotopes

The energy spectra of thermalized neutrons (as well as target nuclei) in the stellar plasma of typical s-process and potential i- and r-process sites can be well described by the Maxwell-Boltzmann distribution. To account for this over a relatively wide range of temperatures for, e.g., a realistic s-process scenario ($k_B T \approx 8 - 90$ keV) involving the majority of the studied Sn isotopes, the radiative NCCS are folded with the Maxwell-Boltzmann distribution to produce the neutron-capture rates [273]:

$$N_A \langle \sigma v \rangle (T) = \left(\frac{8}{\pi \tilde{m}} \right)^{1/2} \frac{N_A}{(k_B T)^{3/2} G(T)} \int_0^\infty \sum_\mu \frac{2 J_t^\mu + 1}{2 J_t^0 + 1} \sigma^\mu(E) E e^{-\frac{E + \epsilon_t^\mu}{k_B T}} \, dE. \tag{6.1}$$

Here, $\tilde{m}$ is the reduced target mass, and N_A and k_B are the Avogadro and Boltzmann constants, respectively. This relation takes into account that the target nucleus in a thermodynamic equilibrium can be present not only in its ground state with spin J_t^0, but also excited states with spins J_t^μ at energies ϵ_t^μ, and the population of these states also obeys the Maxwell-Boltzmann distribution. This is reflected in the sum over the individual cross sections of the neutron capture on the ground and excited states $\sigma^\mu(E)$ and the temperature-dependent normalized partition function $G(T)$ [273]:

$$G(T) = \sum_\mu \frac{2 J_t^\mu + 1}{2 J_t^0 + 1} e^{-\frac{\epsilon_t^\mu}{k_B T}}. \tag{6.2}$$

In case of radiative neutron capture, $N_A \langle \sigma v \rangle (T)$ is also commonly expressed in terms of the Maxwellian-averaged cross section (MACS):

$$N_A \langle \sigma \rangle (T) = \frac{N_A \langle \sigma v \rangle (T)}{v_T}, \tag{6.3}$$

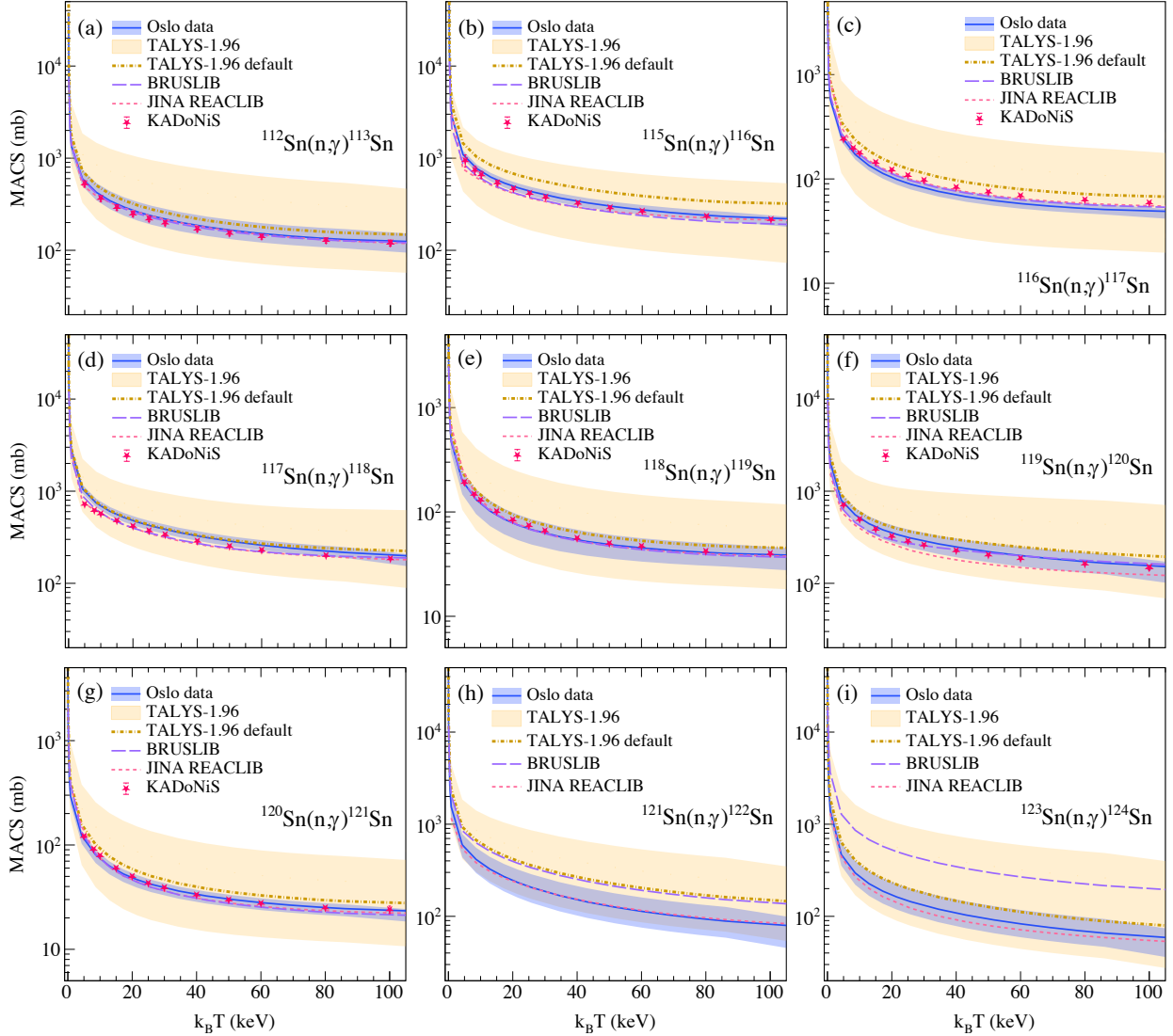where $v_T = \sqrt{2 k_B T / \tilde{m}}$ is the thermal velocity at temperature T.

Figure 6.4: Maxwellian-averaged cross sections (MACS) for the $^{112}\mathrm{Sn}(n,\gamma)^{113}\mathrm{Sn}$ (a), $^{115}\mathrm{Sn}(n,\gamma)^{116}\mathrm{Sn}$ (b), $^{116}\mathrm{Sn}(n,\gamma)^{117}\mathrm{Sn}$ (c), $^{117}\mathrm{Sn}(n,\gamma)^{118}\mathrm{Sn}$ (d), $^{118}\mathrm{Sn}(n,\gamma)^{119}\mathrm{Sn}$ (e), $^{119}\mathrm{Sn}(n,\gamma)^{120}\mathrm{Sn}$ (f), $^{120}\mathrm{Sn}(n,\gamma)^{121}\mathrm{Sn}$ (g), $^{121}\mathrm{Sn}(n,\gamma)^{122}\mathrm{Sn}$ (h), and $^{123}\mathrm{Sn}(n,\gamma)^{124}\mathrm{Sn}$ (i) reactions. The predictions with the Oslo method inputs (blue bands) are compared with recommended values from JINA REACLIB [298], BRUSLIB [299], KADoNiS [300], and the TALYS uncertainty range obtained with different available GSFs, NLDs, and optical model potentials (beige band).

The MACSs extracted with the Oslo method inputs are shown in Fig. 6.4 together with the TALYS uncertainty bands and recommended cross-sections from JINA REACLIB [298] and BRUSLIB [299] libraries. The data points from the KADoNiS database [300] are also available for the $^{112,115-120}$Sn target nuclei. All of the MACSs shown in this figure are stellar cross sections, i.e. they take the target thermalization effect into account. In general, all the MACSs agree well within the Oslo uncertainty band up to k_BT values of about 100 keV. There are systematic shifts of the Oslo data towards lower cross sections in ^{116}Sn and higher cross sections in ^{117}Sn, similar to those observed in Fig. 6.3. Indeed, the recommended KADoNiS values at 30 keV are based on the cross sections of Macklin *et al.* [289], Timokhov *et al.* [296], Wisshak *et al.* [284], Koehler *et al.* [283], Nishiyama *et al.* [297] for the stable-target cases. The values at other energies are presented by the average of evaluations from the ENDF/B-VII.1 [301] and JENDL-4.0 [302] libraries, whereas the uncertainties are often determined by the deviations between these two evaluations. This approach might potentially result in somewhat underestimated uncertainties of KADoNiS values as compared to the Oslo uncertainty bands. The BRUSLIB MACSs are in very good agreement with the Oslo estimates for all the targets up to ^{119}Sn. For the heavier isotopes, these cross sections begin to deviate significantly from the JINA REACLIB and Oslo data. This deviation is primarily due to the Skyrme-HFB plus combinatorial NLD model used for the calculations in BRUSLIB, which reproduces the experimental NLD values quite well for the lighter stable isotopes and tends to overestimate them towards more neutron-rich nuclei.

It is also interesting to note that the LEDR in the studied Sn isotopes extracted as an excess strength on top of the tail of the IVGDR has a noticeable impact on the calculated NCCSs and MACSs. For example, in case of the ^{120}Sn isotope with the LEDR exhausting about 3% of the TRK sum rule, it contributes with $\approx 20\%$ of the total MACS shown in Fig. 6.4(f) at $k_BT \approx 30$ keV. The uncertainty band is relatively large in this case, and a 20% decrease of the MACS still falls within it. Nevertheless, the contribution of the LEDR is notable and becomes even larger when using e.g. RQRPA or RQTBA $E1$ calculations for the input GSF. In cases of neutron-rich ^{130,132}Sn, the structure identified as the PDR exhausts $\approx 4 - 7\%$ of the TRK sum rule [31], but lies above the neutron threshold and thus cannot contribute significantly to the MACSs. It is, however, not clear how the part of the LEDR remaining below the neutron threshold might impact the MACSs in these cases as compared to the stable targets.

6.4 Impact of the ^{121,123}Sn$(n,\gamma)^{122,124}$Sn rates on abundances in the i process

To assess the role of the newly constrained radiative neutron-capture rates (or rather MACSs) in i-process nucleosynthesis, network calculations have been performed by computing a 1 $M_\odot$ low-metallicity ([Fe/H] = −2.5) Asymptotic Giant Branch model with the STAREVOL code [87, 303, 304]. The used network comprises 1160 nuclei, linked through 2123 nuclear reactions (n-, p-, α-captures and α-decays) and weak interactions (electron captures, β-decays). All rates were extracted from the BRUSLIB database, the Nuclear Astrophysics Library of the
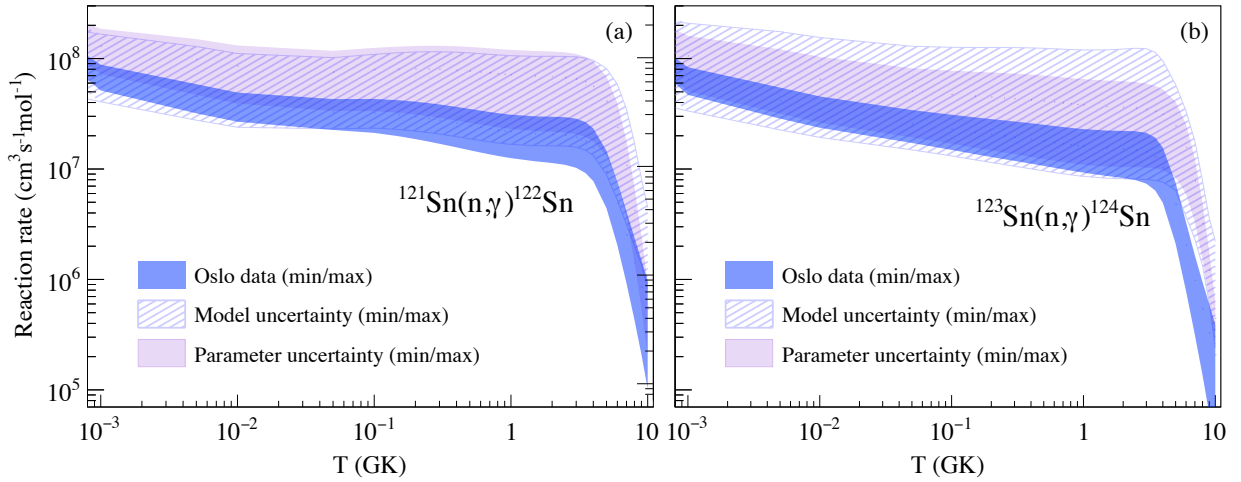
Figure 6.5: Uncertainty bands for the neutron-capture rates in the ^{121}Sn$(n, \gamma)^{122}$Sn (a) and ^{123}Sn$(n, \gamma)^{124}$Sn reaction (b) reactions. The blue band corresponds to the span of experimentally constrained reaction rates due to uncertainties of the input Oslo NLD and GSF. The hatched band denotes the span of TALYS rates for all available GSF, NLD, and optical model potential combinations (model uncertainty). The purple band is due to the variation of the Skyrme-HFB plus combinatorial NLD and D1M Gogny-HFB plus QRPA GSF model parameters according to the procedure of Ref. [282] (parameter uncertainty).

Université Libre de Bruxelles[1][305] and the updated experimental and theoretical rates from the NETGEN interface [299]. All information on the stellar physics inputs, modeling, and nuclear physics involved can be found in Refs. [87, 275, 281]. As was mentioned earlier, among the studied isotopes, the neutron capture on ^{120,121,123}Sn using the Oslo NLD and GSF inputs for ^{121,122,124}Sn might be of potential interest for such calculations. Provided relatively accurate MACSs available for the Sn isotopes up to ^{120}Sn, including the Oslo results for these nuclei in the network calculations would not lead to any significant changes and reduction of the eventual uncertainties. However, for the ^{121,123}Sn isotopes (^{121,122}Sn$(n, \gamma)^{122,124}$Sn reactions) the Oslo method results might potentially help to reduce the model uncertainties.

The radiative neutron-capture rates extracted with the Oslo method for these two cases are shown in Fig. 6.5. For these nuclei, the network calculations can be performed with the rates obtained by varying all available TALYS NLD and GSF models as it was done in the previous sections (beige bands in Fig. 6.3 and Fig. 6.4). The reaction rates obtained in this manner are shown in Fig. 6.5 as pale hatched bands. An alternative source of uncertainties, which should also be considered in large-scale network calculations, is due to the variations of individual parameters entering the used NLD and GSF models (e.g. the temperature and $E0$ parameter in the CT model). This type of uncertainty was studied thoroughly in the recent work by Martinet *et al.* [282]. In this thesis, it was addressed in a similar way by adopting a combination of the Skyrme-HFB plus combinatorial and D1M Gogny-HFB plus QRPA models for the NLD and GSF (model A in [282]), respectively, and varying artificially introduced parameters modulating the energy shift and temperature in the NLD and the

---

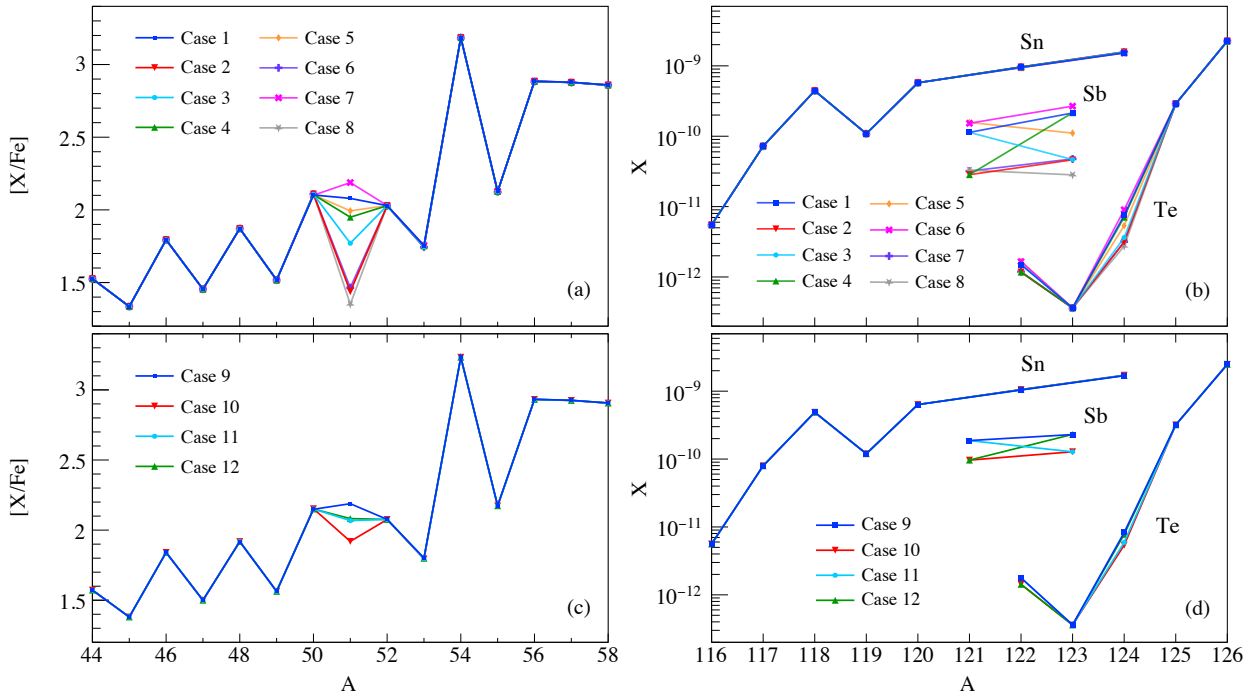[1]Available at http://www.astro.ulb.ac.be/bruslib/

Figure 6.6: Final surface elemental abundances (after decays) of multi-zone AGB stellar models undergoing *i*-process nucleosynthesis, computed with different combinations of $^{121,123}\text{Sn}(n,\gamma)$ rates. Shown are the [X/Fe] ratios. The first and second $\log_{10}$ terms refer to the abundances of the model and the Sun, respectively. (a) Eight theoretical rates combinations are considered. These are theoretical estimates of parameter and model uncertainties affecting TALYS predictions of $^{121}\text{Sn}(n,\gamma)$ and $^{123}\text{Sn}(n,\gamma)$ reaction rates. (c) Same but with the new experimentally constrained rates from this work. (b) and (d) same as (a) and (b), but for the isotopic mass fraction X as a function of the mass number A, around the Sn region.

width and centroid energy in the GSF as prescribed in Ref [282]. The resulting uncertainty is referred to as the parameter uncertainty and shown in Fig. 6.5. In the calculations presented here and in Ref [282], they are assumed to be uncorrelated.

The impact of the above-mentioned sources of uncertainties as compared to the experimental ones was studied using the combinations of the TALYS NLD and GSF models resulting in the minimum rates for the neutron capture on $^{121,123}\text{Sn}$ (case 1), maximum rates for these targets (case 2), minimum rates for ^{121}Sn and maximum rates for ^{122}Sn (case 3), and vice versa (case 4). Similarly, the calculations have been performed with the combinations of parameter modifications in model A resulting in minimum (case 5) and maximum (case 6) rates for ^{121}Sn and unmodified rates for ^{123}Sn, as well as minimum (case 7) and maximum (case 8) rates for ^{123}Sn, combined with unmodified rates for ^{121}Sn. By analogy, the minimum and maximum rates corresponding to the bottom and the top of experimental uncertainty bands were used in different combinations (case 9 is min(^{121}Sn)/min(^{123}Sn), case 10 is max(^{121}Sn)/max(^{123}Sn), case 11 is min(^{121}Sn)/max(^{123}Sn), case 12 is max(^{121}Sn)/min(^{123}Sn)). The resulting final sur-

face elemental abundances (after decays) are shown in terms of $[X/Fe]^2$ in Fig. 6.6(a) and (c). It can be clearly seen that the effect is local and affects predominantly Sb isotopes. Similar figures Fig. 6.6(b) and (d), showing the isotopic mass fraction versus the mass number A, demonstrate clearly that the affected isotopes are ^{121,123}Sb (to a much lesser extent ^{122,124}Te). Naturally, the lower neutron-capture rates on ^{121,123}Sn result in a larger production of ^{121,123}Sb through β decay (blue line) and vice versa (red line). Moreover, the experimentally constrained rates allowed to reduce the uncertainty in abundances by a factor of $\approx 2-3$, down to 0.27 dex from 0.65 dex for parameter and 0.84 dex for model uncertainties. Similar calculations involving Cd isotopes might be one of potential future objectives in the i-process studies employing the Oslo method.

---

[2]The value of $[X/Fe]$ is defined as $[X/Fe] = \log_{10}(N_X/N_{Fe})_\star - \log_{10}(N_X/N_{Fe})_\odot$ with N_X the number density of an element X. The first and second $\log_{10}$ terms refer to the abundances of the model and the Sun.

Chapter 7

Summary, conclusions, and outlook

7.1   Summary of the main results and conclusions

This thesis presents a systematic study on the low-lying electric dipole response (LEDR) in the chain of Sn isotopes, ranging from ^{111}Sn to ^{124}Sn, based on the combined analysis of the Oslo-type and Coulomb excitation experiments [42]. The LEDR below the neutron separation energy in these nuclei was extracted in terms of the dipole γ-ray strength function (GSF) with the Oslo method applied to particle-γ coincidence data collected in proton-, deuteron-, and ^{3}He-induced reactions at the Oslo Cyclotron Laboratory. The overarching objective of this study was to assess the evolution of the LEDR, commonly associated with the pygmy dipole resonance, in stable $^{112,113,116-120,122,124}$Sn and unstable ^{111,121}Sn isotopes with gradually increasing neutron number and compare it with other experimental data and theoretical predictions. This task is closely linked to two other additional objectives covered here: addressing the validity of the generalized Brink-Axel (BA) hypothesis below the neutron threshold and providing the nuclear inputs for statistical-model calculations of radiative neutron-capture cross sections relevant for astrophysical processes.

The validity of the Brink-Axel hypothesis, essential for establishing the correspondence between the NRF, Coulomb excitation, and Oslo method strength distributions and simplifying calculations in statistical-model-based reaction codes, was tested for ^{120,124}Sn isotopes using the Oslo and the shape [239] methods combined with the (p,p') Coulomb excitation data. The shape of the GSFs extracted from the decay to the ground state and the first excited 2^+ state with the shape method was found to be in excellent agreement with that of the (p,p') strength function, at least down to $E_\gamma \approx 6$ MeV, and the results of the continuous spectrum analysis of the NRF data on ^{120}Sn [23] at even lower energies. Moreover, the Oslo method GSF was found to be essentially independent of initial and final excitation energies within the uncertainty bands based on the analysis of primary decays from and to different excitation energy bins. The observed deviations of GSFs for different initial and final excitation energies from the Oslo method strength, especially for transitions to low-lying discrete states, were found to be commensurate with potential deviations due to Porter-Thomas fluctuations and/or systematic uncertainties in each case.

The Oslo method nuclear level densities (NLDs) of $^{111-113,116-122,124}$Sn extracted in a model-consistent way reproduce the low-lying discrete states well and demonstrate a clear constant-temperature behavior below the neutron separation energy. The NLDs of even-even isotopes

are in good agreement with each other, the same is true for the NLDs of even-odd isotopes. An indirect check of the correspondence between the results of the Oslo-type and (p, p') experiments revealed a fair agreement between the Oslo method NLD and results of the fluctuation analysis of the (p, p') data for ^{124}Sn, shown in Ref. [248]. The GSFs of the studied isotopes are in excellent agreement within the uncertainty bands with the (p, p') data for even-even ^{112,114,116,118,120,124}Sn and demonstrate a rather smooth evolution towards more neutron-rich isotopes. These strengths combined reveal a bump-like structure at ≈ 8 MeV in all the studied cases, interpreted as the LEDR. The latter was parametrized in terms of a single or two Gaussian peaks on top of the tail of the modeled IVGDR and extracted through the decomposition of the total dipole strength into different $E1$ and $M1$ components. It was found to exhaust $\approx 2 - 3\%$ of the classical Thomas-Reiche-Kuhn (TRK) sum rule for electric dipole transitions in all the studied isotopes. In contradiction with the majority of theoretical predictions (e.g., RQRPA and RQTBA), the LEDR in the Sn isotopic chain remains relatively constant, with the exception of a local peak in the TRK values close to ^{120}Sn.

Combining the Oslo and the (p, p') strengths allowed for an additional extraction of a peak-like structure at $\approx 6.4 - 6.5$ MeV, clearly seen in the (p, p') data. This lower-lying component of the LEDR was identified for isotopes starting from ^{118}Sn. It appears to become more prominent towards ^{124}Sn, exhausting the TRK values up to $\approx 0.5\%$, and be approximately linearly dependent on the neutron number. Provided the comparison with the strength distributions from experiments with isoscalar (α and ^{17}O) and isovector (γ) probes [40, 78], it is possible to assume that this lower-lying peak in the LEDR can be associated with the isovector component of the PDR. Thus, the interpretation of the total extracted LEDR as the PDR might be unfounded. Moreover, the small fraction of the TRK sum rule exhausted by this feature, in principle, challenges the neutron-skin oscillation picture of the PDR, which implies a certain degree of collectivity. This matter, however, requires further theoretical and experimental investigations.

Finally, the extracted Oslo method NLDs and GSFs were used as the input for Hauser-Feshbach calculations of radiative neutron-capture cross sections with the reaction code TALYS [154]. The cross sections were found to be in good agreement with other experimental data for the target nuclei $^{112,115-120}$Sn and for incident neutron energies above $\approx 20 - 30$ keV. The corresponding Maxwellian-averaged cross sections are also in fair agreement with the recommended cross sections from the JINA REACLIB [298], BRUSLIB [299], and KADoNiS [300] libraries. For the unstable ^{121,123}Sn targets, where no other experimental results are available, the newly constrained cross sections allowed to considerably reduce the TALYS input model uncertainty, by at least a factor of 7 at $k_B T = 30$ keV. Moreover, as was shown in the calculations of the multi-zone AGB stellar models experiencing i-process nucleosynthesis using the STAREVOL code [87, 303, 304], the neutron-capture rates for the ^{121,123}Sn$(n, \gamma)^{122,124}$Sn reactions have a local impact on the i-process flow and affect the production of ^{121,123}Sb isotopes. The first experimental constraints of these reaction rates using the Oslo method presented in this thesis provide the new estimates for the produced abundances of ^{121,123}Sb and notably reduce their model and parameter uncertainties.

7.2   Outlook

In the past decade, a large number of new experimental techniques have been introduced and exploited to unravel the nature of the PDR in nuclei within different mass regions. The task of collecting consistent systematics of its experimental characteristics in different isotopic chains is far from being completed even in the best studied cases. As shown in the present work, the combination of the Oslo method data with the strengths from relativistic Coulomb excitation experiments in forward-angle inelastic proton scattering provides a useful insight into the distribution of the excess low-lying $E1$ strength on top of the IVGDR. Future systematic (p, p') studies, similar to the one presented in Ref. [42], in different isotopic chains are highly desired. The Oslo-type experiments on ^{128,130}Te and some Cd and Sb isotopes of potential interest for the i process are planned to be performed at the OCL in the upcoming years, continuing the effort of studying the LEDR in the $A \approx 110 - 130$ mass region. Recently performed $(p, p'\gamma)$ experiments on ^{112,114}Sn at the Horia Hulubei Institute for Physics and Nuclear Engineering (IFIN-HH) are currently being analyzed, and the preliminary results on ^{114}Sn, provided in Appendix B, fall nicely within the systematics presented in this work.

Another unique source of information on the dipole strength distribution in the PDR energy region is offered by NRF measurements using linearly polarized quasi-monochromatic photon beams at HIγS. Results of a preliminary analysis of such data for ^{120}Sn were recently found to be in excellent agreement with the (p, p') strength distribution[1]. Moreover, this type of data can be used for an ultimate test of the Brink-Axel hypothesis, revealing any potential excitation-energy dependence of the LEDR, and thus complementing the findings for ^{120,124}Sn from this thesis. The ratio method employed in these tests can, in some cases, also be applied to the Oslo particle-γ coincidence data. Such an analysis is currently being performed for ^{120}Sn. For the Oslo-type experiments, the ratio method might provide an alternative, model-independent way to constrain the slope of the GSF, by analogy with the shape method.

Finally, the combination of the shape and β-Oslo methods is another promising direction of future studies, allowing to expand our knowledge on the LEDR towards more neutron-rich nuclei. Here, reliable theoretical approaches for the description of the NLDs and GSFs in both the PDR and IVGDR energy regions are highly desired. The recently developed QRPA plus boson expansion method is a promising step forward towards a more realistic description of NLDs, not only within but also away from the valley of stability [114]. Current efforts on optimizing the numerical $2q \otimes 2$phonon calculations and including the temperature effects in microscopic calculations may enable an improved description of the strength distribution, especially below the neutron threshold, in the near future.

---

[1]J. Isaak, private communication.

Papers

Brief introduction to the papers

In the following, all articles forming the basis of this dissertation will be outlined in brief.

Paper I: Comprehensive Test of the Brink-Axel Hypothesis in the Energy Region of the Pygmy Dipole Resonance

The applicability of the Brink-Axel hypothesis in the pygmy dipole resonance energy range for nuclei with different mass numbers is a matter of great importance for statistical-model calculations. So far, the theoretical and experimental effort directed towards addressing this matter has yielded contradictory or simply inconclusive results. Paper I presents a consolidated attempt to test the validity of the Brink-Axel hypothesis in the immediate vicinity of the neutron threshold in ^{116,120,124}Sn based on the comparison of the GSFs from the analysis of particle-γ coincidence data with the Oslo and shape methods and the multipole decomposition analysis of Coulomb excitation data from forward-angle inelastic proton scattering. The dipole strength functions obtained with all these methods were demonstrated to be in excellent agreement with each other down to $\approx 5.5 - 6.0$ MeV. Moreover, the GSF was shown to be essentially independent of initial excitation energies within the quasi-continuum region as well as of the final excitation energies and spins of the states accessible through the shape method. These observations have an important consequence for subsequent astrophysical Hauser-Feshbach calculations in the Sn mass region, where the downward and upward strength functions can be used interchangeably close to the neutron separation energy, and the Oslo method and (p, p') strengths complement each other to cover a rather wide energy range of the IVGDR and the PDR.

The author of this dissertation was responsible for preparing, planning, and performing the $(p, p'\gamma)$ experiment on ^{120,124}Sn at the OCL in 2019, performing all analyses involving the Oslo data, including the re-analysis of the ^{116}Sn data. The author wrote the manuscript as the sole corresponding author in close collaboration with Prof. A.-C. Larsen, Prof. P. von Neumann-Cosel, and Prof. A. Richter and with input from all other co-authors.

Paper II: Nuclear level densities and γ-ray strength functions in ^{120,124}Sn isotopes: Impact of Porter-Thomas fluctuations

The principal idea of Paper II was to provide a detailed description of the analysis of the particle-γ coincidence data for ^{120,124}Sn, first presented in Paper I, with the main focus on the GSF and the NLD in these nuclei. This work continues the effort to address the Brink-Axel hypothesis in Sn nuclei in more depth and presents one of the first tests of the novel shape

method applied to the Oslo data. The role of Porter-Thomas fluctuations in both of these matters has been investigated using the experimental NLD obtained with the Oslo method. The main questions to be answered were how these fluctuations might affect the comparison of GSFs extracted within limited initial and final excitation energy windows and whether the fluctuations impose any limitations on the applicability of the shape method.

The total extracted NLDs were found to be in good agreement with the earlier published results on other even-even Sn isotopes, and the partial density of 1^- states in ^{124}Sn appears to be in fair agreement with the result of the fluctuation analysis of the Coulomb excitation data. The GSFs of ^{120,124}Sn were shown to be independent within the uncertainties of initial and final excitation energies below the neutron threshold. Moreover, all strong deviations of GSFs extracted for different low-lying final excitation energy bins fall within the expected uncertainties due to strong Porter-Thomas fluctuations. The shape method was tested in application to both ^{120}Sn and ^{124}Sn and was shown to be an excellent tool to constrain the slope of the GSF in the combined analysis with the Oslo method. The shapes of the GSFs from the decay to the ground state and the first excited state were reproduced with this method down to γ-ray energies of ≈ 5 MeV. At even lower energies, the basic assumptions underlying the shape method might be no longer valid, and Porter-Thomas fluctuations become too large to yield reliable results.

The author of this dissertation was responsible for performing all analyses involving the Oslo data. The author wrote the manuscript as the sole corresponding author in close collaboration with Prof. A.-C. Larsen, Prof. P. von Neumann-Cosel, and Dr. J. Isaak and with input from all other coauthors.

Paper III: Nuclear level densities and γ-ray strength functions of ^{111,112,113}Sn isotopes studied with the Oslo method

In this work, the NLDs and the GSFs of the lightest studied at the OCL Sn isotopes, ^{111,112,113}Sn, have been presented for the first time. Particle-γ coincidence data obtained in $(p,d\gamma)$, $(p,p'\gamma)$, and $(d,p\gamma)$ reactions have been analyzed with the Oslo method, and the extracted NLDs and GSFs have been compared with all available Oslo data for other Sn isotopes, the results of the neutron evaporation and the Coulomb excitation experiments. It has also been confirmed that the thermodynamic properties of these nuclei, such as the microcanonical entropy and temperature, are in line with those of the heavier neighboring isotopes, studied earlier. The GSFs of all three isotopes were found to be in excellent agreement in absolute values and slopes with each other. The first assessment of the low-lying electric dipole strength based on the combined Oslo and Coulomb excitation (p,p') data has been performed. The presumable pygmy dipole resonance was found to exhaust $\approx 1.8\%$ of the classical Thomas-Reiche-Kuhn sum rule for electric dipole transitions. This way, the article lays the foundation for a more consistent analysis of the whole isotopic chain in order to study the evolution of the low-lying dipole strength and highlights the need to provide an updated re-analysis of the earlier published data with the newly available auxiliary experimental data for the normalization of the Oslo method results.

The author of this dissertation was responsible for the analysis of all three experiments on ^{112}Sn performed in 2013-2014 to study ^{111,112,113}Sn and writing the manuscript as the sole corresponding author in close collaboration with Prof. A.-C. Larsen and with input from all

other co-authors.

Paper IV: Systematic study of the low-lying electric dipole strength in Sn isotopes and its astrophysical implications

This article presents an attempt to consistently assess the evolution of the low-lying electric dipole strength below the neutron threshold in eleven tin isotopes, $^{111-113,116-122,124}$Sn, studied in various light-ion-induced reactions with the Oslo method. The experiments on ^{117,119}Sn with the newest configuration of the setup at the OCL have been presented for the first time. The objective of the study was twofold: to address the evolution of the low-lying $E1$ strength on top of the IVGDR by combining the Oslo method and (p, p') data, while also putting it into a broader context of other experimental and theoretical studies, and to provide the new constraints for the neutron-capture cross sections and rates of potential interest for the astrophysical i process. The Oslo method and (p, p') strengths have also been compared with the updated RQRPA and RQTBA calculations in terms of the Thomas-Reiche-Kuhn sum rule fraction exhausted by the $E1$ strength below the neutron threshold. Furthermore, the radiative neutron-capture cross sections and Maxwellian-averaged cross sections have been extracted using the reaction code TALYS with the Oslo data as input and compared with cross sections from other experiments and astrophysical rates from different libraries (JINA REACLIB, BRUSLIB, KADoNiS). The Oslo data allowed us to significantly reduce the TALYS model uncertainty, which is especially important for the heaviest studied ^{122,124}Sn, where no other experimental data are available. Moreover, the extracted ^{121,123}Sn$(n, \gamma)^{122,124}$Sn reaction rates were found to impact the production of Sb in the i-process nucleosynthesis in AGB stars based on STAREVOL code calculations.

The author of the dissertation was responsible for a complete re-analysis of all eleven Sn data sets, the analysis of the low-lying $E1$ strength, TALYS calculations and writing the corresponding parts of the manuscript. The RQRPA and RQTBA calculations were performed and provided by Prof. E. Litvinova. STAREVOL calculations were performed by Dr. A. Choplin and S. Martinet. The corresponding parts of the manuscript were prepared in close collaboration with Prof. A.-C. Larsen, Prof. P. von Neumann-Cosel, Prof. E. Litvinova, Dr. A. Choplin, and Prof. S. Goriely and with the contribution of other co-authors.

Paper V: Systematics of the low-energy electric dipole strength in the Sn isotopic chain

This work presents an excerpt from Paper IV with the main focus shifted towards the nuclear structure aspect of the analysis of the low-lying $E1$ strength and a more in-depth discussion of its consequences for the interpretation of the PDR in Sn isotopes.

The manuscript is prepared in close collaboration with Prof. P. von Neumann-Cosel and Prof. E. Litvinova.

Paper I

Comprehensive Test of the Brink-Axel Hypothesis in the Energy Region of the Pygmy Dipole Resonance

Comprehensive Test of the Brink-Axel Hypothesis in the Energy Region of the Pygmy Dipole Resonance

M. Markova,[1,*] P. von Neumann-Cosel,[2,†] A. C. Larsen,[1,‡] S. Bassauer,[2] A. Görgen,[1] M. Guttormsen,[1]
F. L. Bello Garrote,[1] H. C. Berg,[1] M. M. Bjørøen,[1] T. Dahl-Jacobsen,[1] T. K. Eriksen,[1] D. Gjestvang,[1]
J. Isaak,[2] M. Mbabane,[1] W. Paulsen,[1] L. G. Pedersen,[1] N. I. J. Pettersen,[1] A. Richter,[2] E. Sahin,[1] P. Scholz,[3,4]
S. Siem,[1] G. M. Tveten,[1] V. M. Valsdottir,[1] M. Wiedeking,[5,6] and F. Zeiser[1]

[1]*Department of Physics, University of Oslo, N-0316 Oslo, Norway*
[2]*Institut für Kernphysik, Technische Universität Darmstadt, D-64289 Darmstadt, Germany*
[3]*Institut für Kernphysik, Universität zu Köln, D-50937 Köln, Germany*
[4]*Department of Physics, University of Notre Dame, Notre Dame, Indiana 46556-5670, USA*
[5]*Department of Subatomic Physics, iThemba LABS, Somerset West 7129, South Africa*
[6]*School of Physics, University of the Witwatersrand, Johannesburg 2050, South Africa*

The validity of the Brink-Axel hypothesis, which is especially important for numerous astrophysical calculations, is addressed for ^{116,120,124}Sn below the neutron separation energy by means of three independent experimental methods. The γ-ray strength functions (GSFs) extracted from primary γ-decay spectra following charged-particle reactions with the Oslo method and with the shape method demonstrate excellent agreement with those deduced from forward-angle inelastic proton scattering at relativistic beam energies. In addition, the GSFs are shown to be independent of excitation energies and spins of the initial and final states. The results provide a critical test of the generalized Brink-Axel hypothesis in heavy nuclei, demonstrating its applicability in the energy region of the pygmy dipole resonance.

Introduction.—Gamma-ray strength functions (GSFs) describe the average γ decay and absorption probability of nuclei as a function of γ energy. Besides their genuine interest and importance for basic nuclear physics, they are required for applications in astrophysics [1], reactor design [2], and waste transmutation [3] based on the application of the statistical nuclear reaction theory. A particular example is large-scale reaction network calculations of neutron capture reactions in the r-process nucleosynthesis. Accordingly, there are considerable efforts to collect data on the GSF in many nuclei [4] and extract systematic parametrizations [5], which allow extrapolation to unknown, exotic cases.

Although all electromagnetic multipoles can, in principle, contribute, the GSF is dominated by $E1$ radiation with smaller contributions from $M1$ strength. Above particle threshold it is dominated by the isovector giant dipole resonance (IVGDR), but at lower excitation energies the situation is complex. In nuclei with neutron excess, one observes the formation of the pygmy dipole resonance (PDR) [6,7] located on the low-energy tail of the IVGDR. Although the detailed structure of the PDR is under debate, it is commonly believed that its strength is related to the magnitude of neutron excess. As the r process involves nuclei with extreme neutron-to-proton ratios, the impact of low-energy $E1$ strength on the (n, γ) reaction rates and the resulting r-process abundances can be significant [8–11].

The GSFs used in large-scale astrophysical network calculations of the r process [12] are based on model calculations of ground-state photoabsorption. Their application requires the validity of the Brink-Axel (BA) hypothesis [13,14], which in its generalized form states that the GSF is independent of the energies, spins, and parities of the initial and final states and depends on the γ energy only. However, recent theoretical studies [15–17] put that into question, demonstrating that strength functions of collective modes built on excited states generally do show dependence on the excitation energy. Shell-model calculations in light nuclei [16] found $E1$ strength functions approximately independent of excitation energy consistent with the BA hypothesis, but it remains an open question whether this can be generalized for heavier nuclei.

Because of the importance for astrophysical applications, there are many recent experimental studies in the low-energy regime with controversial results, claiming either confirmation [18–21] or violation [22–25] of the BA hypothesis. Possible nonstatistical γ-width distributions observed in s- and p-wave neutron capture experiments [26] would also represent proof against the BA hypothesis [27].

There are two major sources of GSF data [4]. One class of experiments determines the ground-state photoabsorption by measuring the subsequent γ [28] or neutron [29] decay. Alternatively, the primary γ-decay distribution is

extracted in light-ion-induced compound reactions (the so-called Oslo method [30–33]). Experiments measuring particle or γ decay are limited to the excitation-energy region above or below the neutron threshold, respectively. In principle, a comparison of (γ, γ') and Oslo experiments for the same nucleus should provide a test of the validity of the BA hypothesis [34], but is complicated by the assumptions necessary to extract the GSF. For (γ, γ') experiments with broad bremsstrahlung beams, one needs to model the experimentally inaccessible ground-state branching ratios and the significant contributions to the spectra due to atomic scattering. The analysis of Oslo-type data is based on the validity of the BA hypothesis, and assumptions have to be made about the intrinsic spin distribution and the reaction-dependent spin population.

In such comparisons, possible violations of the BA hypothesis have been observed. In heavy deformed nuclei at excitation energies of 2–3 MeV, the GSF is dominated by the orbital $M1$ scissors mode [35]. Larger strengths have been reported in most γ-decay experiments (see, e.g., Refs. [36,37]) than found in the (γ, γ') experiments [38], but the results strongly depend on the assumed form of the $E1$ strength function in this energy range [39]. At even lower energies (< 2 MeV), a general increase of the GSF (called upbend) is seen in Oslo-type experiments [40,41]. No corresponding strength can be present in ground-state absorption experiments on even-even nuclei due to the pairing properties of the nuclear force, which lead to the absence of levels at low excitation energies. In the energy region near neutron threshold, a nonstatistical decay behavior of the PDR has been reported [42,43]. The possible impact of the PDR on the GSF extraction is expected to be largest in magic and semimagic nuclei because of the reduced level density and a shift of part of the IVGDR strength toward lower energies due to K splitting in deformed nuclei.

Here we present a benchmark study allowing a test of the BA hypothesis in the energy region of the PDR taking advantage of recent experimental progress, which overcomes most of the problems discussed above. First, a method for the measurement of $E1$ strength distributions—and thereby the $E1$ part of the GSFs—in nuclei from about 5 to 25 MeV has been developed using relativistic Coulomb excitation in inelastic proton scattering at energies of a few hundred MeV and scattering angles close to 0° [44]. Such data also permit extraction of the $M1$ part of the GSF due to spin-flip excitations [45], which energetically overlaps with the PDR strength. Second, a new system for the measurement of γ emission in Oslo experiments based on large-volume LaBr$_3$(Ce) detectors allows qualitatively new tests of the BA hypothesis, as described below, including resolved coincidence studies of decay to the ground-state and low-lying excited states.

Combining data from the two methods allows for testing the generalized BA hypothesis with respect to the energy and spin independence of initial and final states in the PDR region. Here we present a case study for ^{116,120,124}Sn. The choice is based on the following considerations. (i) Data for $E1$ and $M1$ strength distributions in the stable Sn isotopes from (p, p') experiments at 295 MeV have recently become available [46,47] and found to agree well with the GSF above threshold deduced from the latest (γ, n) experiments by Utsunomiya et al. [48]. (ii) The isotopes have high neutron threshold energies, providing a large overlap region between the GSFs deduced from the (p, p') and the Oslo experiments. (iii) While their low-energy structure is very similar, the GSFs of the Sn isotopes show a distinct dependence on neutron excess in the PDR region [49].

Experimental details and data analysis.—The inelastic proton scattering experiments and the methods to extract the $E1$ and $M1$ contributions to the GSF are described in detail in Ref. [47]. The ^{116}Sn experiment at the Oslo Cyclotron Laboratory (OCL) has previously been reported in Refs. [50,51]. A 38 MeV ^{3}He beam was used to produce ^{116}Sn nuclei via the ^{117}Sn(^{3}He, $\alpha\gamma$) reaction, where the charged particles were measured with eight collimated Si detectors at 45° and the γ rays with the NaI(Tl) array CACTUS [52].

We provide here a brief description of the new ^{120,124}Sn experiments at OCL. A 16-MeV proton beam of intensity $I = 3$–4 nA provided by the MC-35 Scanditronix cyclotron impinged on self-supporting targets of ^{120,124}Sn. The target thicknesses and enrichments were 2.0 mg/cm^2, 99.6% (^{120}Sn) and 0.47 mg/cm^2, 95.3% (^{124}Sn). The reactions of interest were ^{120,124}Sn($p, p'\gamma$). The targets were placed in the center of the Oslo SCintillator ARray (OSCAR) [53,54], consisting of 30 cylindrical LaBr$_3$(Ce) γ-ray detectors of size 3.5×8.5 in. mounted on a truncated icosahedron frame. Charged particles were registered with 64 Si particle $\Delta E - E$ telescopes (SiRi) [55], covering angles $126° - 140°$. The energy resolution of OSCAR is $\approx 2.7\%$ at $E_\gamma = 662$ keV. The front ends of the LaBr$_3$(Ce) crystals were placed 16 cm from the center of the target. Particle-γ coincidences were recorded using XIA digital electronics [56]. Approximately 5.3×10^7 and 1.3×10^7 proton-γ coincidences were measured in the excitation-energy range up to the neutron thresholds for ^{120}Sn and ^{124}Sn, respectively.

The proton energy deposited in the SiRi telescopes was transformed to initial excitation energy E_x in the residual nucleus using the reaction kinematics, and the data were arranged in an E_x vs γ-ray energy matrix. The γ-ray spectra for each E_x bin were unfolded with the technique described in Ref. [30] using the response function of the OSCAR detectors [57]. The distribution of primary γ rays (the first emitted γ rays in the decay cascades) for each E_x bin was obtained through an iterative subtraction method [31]. The resulting primary γ-ray matrix for the example of ^{120}Sn is displayed in Fig. 1.

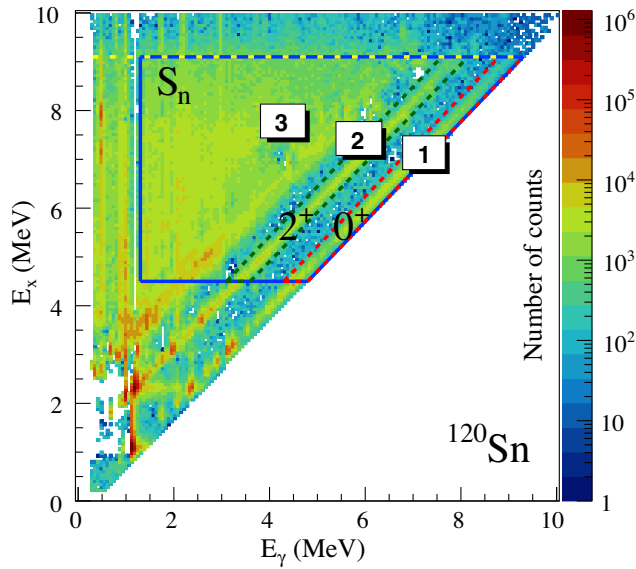With the primary γ-ray matrix $P(E_\gamma, E_x)$ at hand, we can use the ansatz [32]

FIG. 1.   Experimental primary γ-ray matrix $P(E_\gamma, E_x)$ for ^{120}Sn. The yellow dashed line indicates the neutron threshold S_n, while the dashed red and blue lines (regions 1 and 2) confine transitions to the ground state and the first excited $J^\pi = 2^+$ state at $E_x = 1.171$ MeV. The solid blue lines (region 3) mark the region $4.5 \leq E_x \leq 9.1$ MeV, $E_\gamma \geq 1.3$ MeV used for the Oslo method analysis.

$$P(E_\gamma, E_x) \propto \rho(E_f)\mathcal{T}(E_\gamma) \tag{1}$$

to simultaneously extract the level density $\rho(E_f)$ at the final excitation energy $E_f = E_x - E_\gamma$ and the γ-ray transmission

coefficient $\mathcal{T}(E_\gamma)$. For dipole decay, the γ-ray transmission coefficient is connected to the γ-ray strength function $f(E_\gamma)$ through the expression $\mathcal{T}(E_\gamma) = 2\pi E_\gamma^3 f(E_\gamma)$. The application of Eq. (1) assumes that the generalized form of the BA hypothesis holds. Both ρ and $\mathcal{T}$ can be extracted from a χ^2 minimization of a chosen area of the primary γ-ray matrix [32]. For ^{120}Sn, the area confined by the blue lines (area 3) in Fig. 1 was chosen for the decomposition. The minimization yields the functional forms of both the $\rho(E_f)$ and $f(E_\gamma)$, except for the absolute value and the slope (see the Supplemental Material for details [58]). The level density at low excitation energies is normalized using available information on low-lying discrete levels, while the value $\rho(S_n)$, obtained from the s-wave neutron resonance spacing D_0 or from systematics, is used to further constrain the normalization. Finally, the GSF is normalized to the value of the average total radiative width from s-wave neutron resonance experiments. Details of the normalization procedure and a presentation of all parameters, as well as the choice of the primary γ-ray matrix area for ^{116,120,124}Sn can be found in the Supplemental Material [58].

Results and discussion.—Figure 2 compares the GSFs for ^{116,120,124}Sn extracted using the Oslo method (blue) and from inelastic proton scattering [47] (orange). In the energy regions where both results overlap, the two fundamentally different methods yield agreement of the γ-ray energy dependence as well as absolute values within the estimated uncertainty bands for all three nuclei in support of the BA hypothesis.
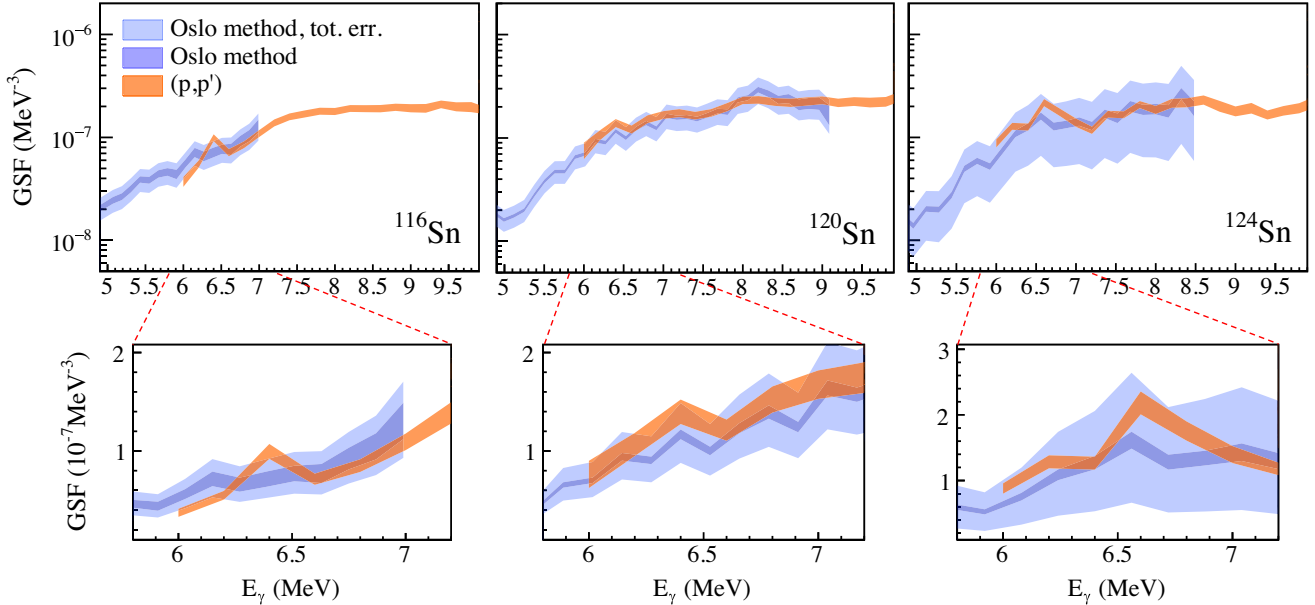

FIG. 2.   Comparison of the GSFs for ^{116,120,124}Sn obtained from the Oslo method (blue) and from the (p, p') experiments [47] (orange). The total error bands for the Oslo method (light blue) are asymmetric and include all uncertainties. The dark blue band represents statistical and systematic uncertainties from the unfolding and the extraction of primary γ rays. The E_γ bin widths are 128 and 200 keV for the Oslo data and the (p, p') measurements respectively.

Peaklike structures at $E_\gamma \approx 6.5$ MeV with a width of about 200 keV (FWHM) are systematically observed in the (p, p') data [47,59] as highlighted in the lower part of Fig. 2. The strength at the peak shows an increase from 1×10^{-7} to 2.2×10^{-7} MeV^{-3} with the increasing neutron number from ^{116}Sn to ^{124}Sn. While the present as well as (γ, γ') data discussed below represent the isovector response, a concentration of isoscalar $E1$ strength has also been found in ^{124}Sn between 6 and 7 MeV [60,61]. The mutual observation in reactions probing the isoscalar and isovector response is considered a signature of the PDR [6,7].

The (γ, γ') data on ^{116,120,124}Sn [62,63] show corresponding peaks at about 6.5 MeV with comparable strength but a rather dramatic suppression at higher excitation energies, reaching an order of magnitude at 8.5 MeV. The differences have been attributed to an increasing complexity of the wave functions of the excited states (as expected for the IVGDR), resulting in small branching ratios to the ground state. Such an interpretation is corroborated by a recent (γ, γ') experiment on ^{120}Sn with improved sensitivity [64]. Applying statistical model corrections of the branching ratios, the deduced photoabsorption cross sections agree within the considerable model dependence of such a procedure discussed above. We note that the recent realization of $(\gamma, \gamma'\gamma'')$ experiments in combination with quasimonoenergetic photon beams from laser Compton backscattering promises a competitive extraction of photoabsorption cross sections below threshold in the future [65].

The possible observation of a peak around 6.5 MeV in the Oslo data is unclear. No such structure is visible for ^{116}Sn. However, the statistics in the high-E_γ range for this older experiment were insufficient to track its existence. A peak at 6.5 MeV can be seen in the GSF of ^{120}Sn, but the fluctuations of data points below and above are of similar size. In ^{124}Sn, where the peak is most pronounced in the ground-state photoabsorption experiments, a potential structure with respect to the uncertainties from the extraction of primary γ-rays is observed. We note that, although systematic uncertainties are large for ^{124}Sn due to the absence of level density information from neutron capture reactions, variations within the total error bars may shift the GSF up or down, but the peak around 6.5 MeV remains.

An alternative way to test the BA hypothesis with Oslo-type data is to study the GSF as a function of the initial and final excitation energy as outlined in Ref. [18]. From the primary γ-ray matrix, we extract the GSF for 256-keV wide excitation-energy bins. This way, we can investigate the possible variation of the GSF as a function of initial excitation energy. The results of applying this procedure to the ^{120}Sn data are illustrated in Fig. 3, where the GSFs for three narrow initial excitation energies are compared to the Oslo-method data extracted from the full E_x range. Each GSF was scaled to the Oslo-method results
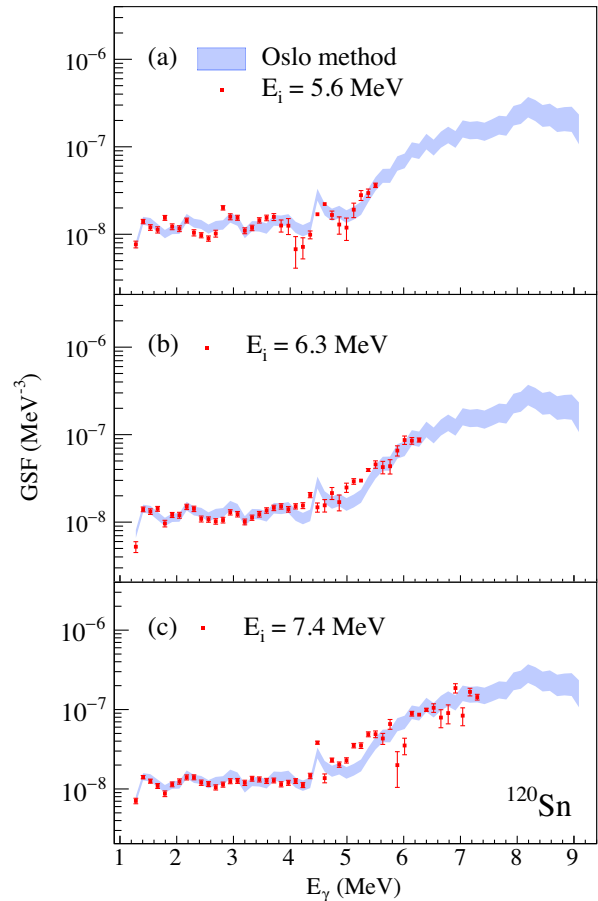

FIG. 3. GSF of ^{120}Sn for narrow initial excitation-energy bins at (a) 5.6 MeV, (b) 6.3 MeV, and (c) 7.4 MeV with a width of 256 keV (red data points) compared to the Oslo method result for the full excitation-energy range $4.5 \leq E_x \leq 9.1$ MeV (blue). For the Oslo method, the total error band is shown. For both approaches, an E_γ bin width of 128 keV is used.

by a χ^2 fit. There is overall good agreement, but the GSFs for the selected initial energy bins exhibit stronger fluctuations compared to the standard Oslo method strength. This can be traced back to the reduced number of levels in the initial-state bins, which lead to an increase of fluctuations of the Porter-Thomas intensity distribution expected for statistical decay [66]. An analog analysis of the final-state energy dependence shows comparable agreement.

Finally, we test the spin independence of the present results by applying a novel approach to extract the energy dependence of the GSF in a largely model-independent way (the so-called "shape method" [67]). Here, we use the capability of the OSCAR array to resolve the decay to the ground state and to the first excited 2^+ state studying again the case of the ^{120}Sn isotope (regions 1 and 2 in Fig. 1). Compared to the much broader spin range contributing to the full Oslo dataset, this defines initial spin windows $J = 1$–3 and $J = 1$ for levels directly feeding the 2^+ state and 0^+ ground state, respectively. As the dipole GSF is given by [68]
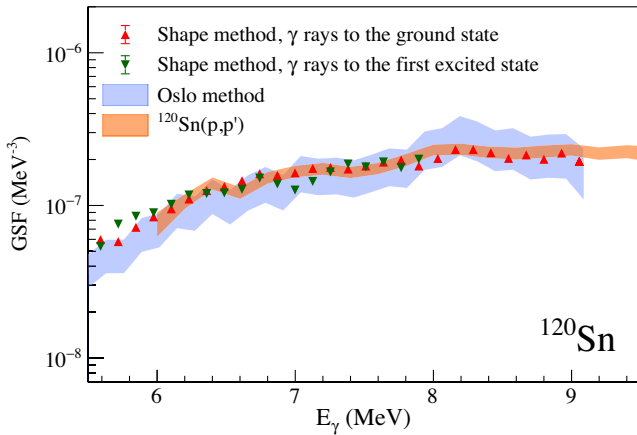
FIG. 4. Comparison of the GSFs for ^{120}Sn extracted with the Oslo method (blue band) from selective decay to the ground state and the first excited 2^+ state utilizing the shape method (red and green triangles) and from the (p, p') data [47] (orange band). The E_γ bin widths are 128 keV for the Oslo and shape-method data and 200 keV for the (p, p') data.

$$f(E_i, E_f, E_\gamma, J_i^\pi) = \frac{\langle \Gamma_\gamma(E_i, E_f, E_\gamma, J_i^\pi)\rangle \rho(E_i, J_i^\pi)}{E_\gamma^3},$$

one can extract information on the shape of the γ strength from the intensities N_D [defined in Eq. (13) of Ref. [67]] proportional to the average, partial radiative width $\langle \Gamma_\gamma(E_i, E_f, E_\gamma, J_i^\pi)\rangle$ in the diagonals.

The GSF deduced from the shape method is shown in Fig. 4 together with those extracted from the Oslo method and from the (p, p') data. Data points from decay to the 0^+ and 2^+ state are shown by red and green triangles, respectively. The error bars include only statistical errors, which are typically smaller than the symbol sizes. Since the shape method does not provide an absolute normalization of the strength, the results were scaled to the (p, p') data by a least-squares fit. The shapes of all three GSFs agree within their uncertainties, demonstrating independence from the particular spin distribution of the initial and final states. The comparison of the GSF from inelastic proton scattering with the shape-method data points from ground-state decay illustrates the direct correspondence between "upward" and "downward" strengths.

Summary and conclusions.—We present a critical test of the generalized BA hypothesis in heavy nuclei in the energy region below the neutron threshold. It is based on a comparison of the GSFs in ^{116,120,124}Sn deduced from relativistic Coulomb excitation in forward-angle inelastic proton scattering [44] and from Oslo-type experiments. The two sets of GSFs agree within experimental uncertainties in the energy region between 6 MeV and the neutron threshold, demonstrating that the generalized BA hypothesis holds for the studied cases in this energy region, and experiments based on ground-state photoabsorption indeed provide the same information on GSFs in nuclei as

Oslo-type experiments. The presence of peaks around 6.5 MeV attributed to the PDR remains unclear in the Oslo data. However, their overall contribution to the GSF—if present—is small. Thus, the assumptions made in the calculations of (n, γ) reactions relevant to r-process nucleosynthesis are verified. Further tests of the BA hypothesis include a demonstration of the independence of the GSFs from the energies and spins of initial and final states. The latter utilizes the novel shape method [67], which allows a largely model-independent extraction of the energy dependence of the GSF from the selective decay to specific final states.

It remains an open question to what extent these results can be generalized. Since we are discussing averaged properties, the most critical parameter is a sufficiently large level density. The examples studied here are semimagic nuclei with correspondingly low-level density values. Thus, we expect that our conclusion on the BA hypothesis may hold, in general, for heavy nuclei with ground-state deformation (and thus higher level densities) [19], except for doubly magic cases [69]. Future comparisons should explore the limits of ground-state photoabsorption experiments to extract the GSF as a function of γ energy, level density, and mass number.

[*]maria.markova@fys.uio.no
[†]vnc@ikp.tu-darmstadt.de
[‡]a.c.larsen@fys.uio.no
[1] M. Arnould and S. Goriely, Prog. Part. Nucl. Phys. **112,** 103766 (2020).
[2] M. B. Chadwick, M. Herman, P. Obložinský, M. E. Dunn, Y. Danon, A. C. Kahler, D. L. Smith, B. Pritychenko, G. Arbanas, R. Arcilla *et al.*, Nucl. Data Sheets **112,** 2887 (2011), Special Issue on ENDF/B-VII.1 Library.

[3] M. Salvatores and G. Palmiotti, Prog. Part. Nucl. Phys. **66,** 144 (2011).

[4] S. Goriely, P. Dimitriou, M. Wiedeking, T. Belgya, R. Firestone, J. Kopecky, M. Krtička, V. Plujko, R. Schwengner, S. Siem *et al.*, Eur. Phys. J. A **55,** 172 (2019).

[5] S. Goriely and V. Plujko, Phys. Rev. C **99,** 014303 (2019).

[6] D. Savran, T. Aumann, and A. Zilges, Prog. Part. Nucl. Phys. **70,** 210 (2013).

[7] A. Bracco, E. Lanza, and A. Tamii, Prog. Part. Nucl. Phys. **106,** 360 (2019).

[8] S. Goriely, Phys. Lett. B **436,** 10 (1998).

[9] S. Goriely, E. Khan, and M. Samyn, Nucl. Phys. **A739,** 331 (2004).

[10] E. Litvinova, H. Loens, K. Langanke, G. Martínez-Pinedo, T. Rauscher, P. Ring, F.-K. Thielemann, and V. Tselyaev, Nucl. Phys. **A823,** 26 (2009).

[11] I. Daoutidis and S. Goriely, Phys. Rev. C **86,** 034328 (2012).

[12] M. Wiescher, F. Käppeler, and K. Langanke, Annu. Rev. Astron. Astrophys. **50,** 165 (2012).

[13] D. M. Brink, Doctoral thesis, University of Oxford, 1955, https://ora.ox.ac.uk/objects/uuid:334ec4a3-8a89-42aa-93f4 -2e54d070ee09.

[14] P. Axel, Phys. Rev. **126,** 671 (1962).

[15] G. W. Misch, G. M. Fuller, and B. A. Brown, Phys. Rev. C **90,** 065808 (2014).

[16] C. W. Johnson, Phys. Lett. B **750,** 72 (2015).

[17] N. Q. Hung, N. D. Dang, and L. T. Quynh Huong, Phys. Rev. Lett. **118,** 022502 (2017).

[18] M. Guttormsen, A. C. Larsen, A. Görgen, T. Renstrøm, S. Siem, T. G. Tornyi, and G. M. Tveten, Phys. Rev. Lett. **116,** 012502 (2016).

[19] D. Martin, P. von Neumann-Cosel, A. Tamii, N. Aoi, S. Bassauer, C. A. Bertulani, J. Carter, L. Donaldson, H. Fujita, Y. Fujita *et al.*, Phys. Rev. Lett. **119,** 182503 (2017).

[20] L. C. Campo, M. Guttormsen, F. L. Bello Garrote, T. K. Eriksen, F. Giacoppo, A. Görgen, K. Hadynska-Klek, M. Klintefjord, A. C. Larsen, T. Renstrøm, E. Sahin, S. Siem, A. Springer, T. G. Tornyi, and G. M. Tveten, Phys. Rev. C **98,** 054303 (2018).

[21] P. Scholz, M. Guttormsen, F. Heim, A. C. Larsen, J. Mayer, D. Savran, M. Spieker, G. M. Tveten, A. V. Voinov, J. Wilhelmy, F. Zeiser, and A. Zilges, Phys. Rev. C **101,** 045806 (2020).

[22] C. T. Angell, S. L. Hammond, H. J. Karwowski, J. H. Kelley, M. Krtička, E. Kwan, A. Makinaga, and G. Rusev, Phys. Rev. C **86,** 051302(R) (2012).

[23] J. Isaak, D. Savran, M. Krticka, M. Ahmed, J. Beller, E. Fiori, J. Glorius, J. Kelley, B. Loher, N. Pietralla *et al.*, Phys. Lett. B **727,** 361 (2013).

[24] L. Netterdon, A. Endres, S. Goriely, J. Mayer, P. Scholz, M. Spieker, and A. Zilges, Phys. Lett. B **744,** 358 (2015).

[25] J. Isaak, D. Savran, B. Löher, T. Beck, M. Bhike, U. Gayer, Krishichayan, N. Pietralla, M. Scheck, W. Tornow, V. Werner, A. Zilges, and M. Zweidinger, Phys. Lett. B **788,** 225 (2019).

[26] P. E. Koehler, A. C. Larsen, M. Guttormsen, S. Siem, and K. H. Guber, Phys. Rev. C **88,** 041305(R) (2013).

[27] P. Fanto, Y. Alhassid, and H. A. Weidenmüller, Phys. Rev. C **101,** 014607 (2020).

[28] N. Pietralla, J. Isaak, and V. Werner, Eur. Phys. J. A **55,** 237 (2019).

[29] B. L. Berman and S. C. Fultz, Rev. Mod. Phys. **47,** 713 (1975).

[30] M. Guttormsen, T. S. Tveter, L. Bergholt, F. Ingebretsen, and J. Rekstad, Nucl. Instrum. Methods Phys. Res., Sect. A **374,** 371 (1996).

[31] M. Guttormsen, T. Ramsøy, and J. Rekstad, Nucl. Instrum. Methods Phys. Res., Sect. A **255,** 518 (1987).

[32] A. Schiller, L. Bergholt, M. Guttormsen, E. Melby, J. Rekstad, and S. Siem, Nucl. Instrum. Methods Phys. Res., Sect. A **447,** 498 (2000).

[33] A. C. Larsen, M. Guttormsen, M. Krtička, E. Běták, A. Bürger, A. Görgen, H. T. Nyhus, J. Rekstad, A. Schiller, S. Siem, H. K. Toft, G. M. Tveten, A. V. Voinov, and K. Wikan, Phys. Rev. C **83,** 034315 (2011).

[34] T. Renstrøm. H.-T. Nyhus, H. Utsunomiya, R. Schwengner, S. Goriely, A. C. Larsen, D. M. Filipescu, I. Gheorghe, L. A. Bernstein, D. L. Bleuel, T. Glodariu *et al.*, Phys. Rev. C **93,** 064302 (2016).

[35] K. Heyde, P. von Neumann-Cosel, and A. Richter, Rev. Mod. Phys. **82,** 2365 (2010).

[36] M. Krtička, F. Bečvář, J. Honzátko, I. Tomandl, M. Heil, F. Käppeler, R. Reifarth, F. Voss, and K. Wisshak, Phys. Rev. Lett. **92,** 172501 (2004).

[37] M. Guttormsen, L. A. Bernstein, A. Bürger, A. Görgen, F. Gunsing, T. W. Hagen, A. C. Larsen, T. Renstrøm, S. Siem, M. Wiedeking, and J. N. Wilson, Phys. Rev. Lett. **109,** 162503 (2012).

[38] J. Enders, P. von Neumann-Cosel, C. Rangacharyulu, and A. Richter, Phys. Rev. C **71,** 014306 (2005).

[39] J. Kroll, B. Baramsai, G. E. Mitchell, U. Agvaanluvsan, F. Becvar, T. A. Bredeweg, A. Chyzh, A. Couture, D. Dashdorj, R. C. Haight *et al.*, Phys. Rev. C **88,** 034317 (2013).

[40] A. Voinov, E. Algin, U. Agvaanluvsan, T. Belgya, R. Chankova, M. Guttormsen, G. E. Mitchell, J. Rekstad, A. Schiller, and S. Siem, Phys. Rev. Lett. **93,** 142504 (2004).

[41] A. C. Larsen, M. Guttormsen, N. Blasi, A. Bracco, F. Camera, L. C. Campo, T. K. Eriksen, A. Görgen, T. W. Hagen, V. W. Ingeberg *et al.*, J. Phys. G **44,** 064005 (2017).

[42] C. Romig, D. Savran, J. Beller, J. Birkhan, A. Endres, M. Fritzsche, J. Glorius, J. Isaak, N. Pietralla, M. Scheck, L. Schnorrenberger, K. Sonnabend, and M. Zweidinger, Phys. Lett. B **744,** 369 (2015).

[43] B. Löher, D. Savran, T. Aumann, J. Beller, M. Bhike, N. Cooper, V. Derya, M. Duchêne, J. Endres, A. Hennig *et al.*, Phys. Lett. B **756,** 72 (2016).

[44] P. von Neumann-Cosel and A. Tamii, Eur. Phys. J. A **55,** 110 (2019).

[45] J. Birkhan, H. Matsubara, P. von Neumann-Cosel, N. Pietralla, V. Y. Ponomarev, A. Richter, A. Tamii, and J. Wambach, Phys. Rev. C **93,** 041302(R) (2016).

[46] S. Bassauer, P. von Neumann-Cosel, P.-G. Reinhard, A. Tamii, S. Adachi, C. A. Bertulani, P. Y. Chan, G. Colò, A. D'Alessio, H. Fujioka *et al.*, Phys. Lett. B **810,** 135804 (2020).

[47] S. Bassauer, P. von Neumann-Cosel, P.-G. Reinhard, A. Tamii, S. Adachi, C. A. Bertulani, P. Y. Chan, A. D'Alessio,

H. Fujioka, H. Fujita *et al.*, Phys. Rev. C **102**, 034327 (2020).

[48] H. Utsunomiya, S. Goriely, M. Kamata, H. Akimune, T. Kondo, O. Itoh, C. Iwamoto, T. Yamagata, H. Toyokawa, Y.-W. Lui, H. Harada, F. Kitatani, S. Goko, S. Hilaire, and A. J. Koning, Phys. Rev. C **84**, 055805 (2011).

[49] S. Bassauer, Doctoral thesis D17, Technische Universität Darmstadt, 2019, http://tuprints.ulb.tu-darmstadt.de/9668.

[50] H. K. Toft, A. C. Larsen, U. Agvaanluvsan, A. Bürger, M. Guttormsen, G. E. Mitchell, H. T. Nyhus, A. Schiller, S. Siem, N. U. H. Syed, and A. Voinov, Phys. Rev. C **81**, 064311 (2010).

[51] H. K. Toft, A. C. Larsen, A. Bürger, M. Guttormsen, A. Görgen, H. T. Nyhus, T. Renstrøm, S. Siem, G. M. Tveten, and A. Voinov, Phys. Rev. C **83**, 044320 (2011).

[52] M. Guttormsen, A. Atac, G. Løvhøiden, S. Messelt, T. Ramsøy, J. Rekstad, T. Thorsteinsen, T. Tveter, and Z. Zelazny, Phys. Scr. **T32**, 54 (1990).

[53] V. W. Ingeberg *et al.* (to be published).

[54] F. Zeiser, G. M. Tveten, F. L. B. Garrote, M. Guttormsen, A. C. Larsen, V. W. Ingeberg, A. Görgen, and S. Siem, Nucl. Instrum. Methods Phys. Res., Sect. A **985**, 164678 (2021).

[55] M. Guttormsen, A. Bürger, T. E. Hansen, and N. Lietaer, Nucl. Instrum. Methods Phys. Res., Sect. A **648**, 168 (2011).

[56] Pixie-16 User Manual, Version 3.06, XIA 2019, https://xia .com/wp-content/uploads/2018/04/Pixie16_UserManual .pdf.

[57] F. Zeiser and G. M. Tveten, oslocyclotronlab/ocl_geant4: GEANT4 model of OSCAR, https://doi.org/10.5281/zen-odo.1342610 (2018).

[58] See Supplemental Material at http://link.aps.org/supplemental/10.1103/PhysRevLett.127.182501 for detailed description of the extraction and normalization of level densities and γ-ray strength functions for the ^{120,124}Sn experiments with the Oslo method.

[59] A. M. Krumbholz, P. von Neumann-Cosel, T. Hashimoto, A. Tamii, T. Adachi, C. A. Bertulani, H. Fujita, Y. Fujita, E. Ganioglu, K. Hatanaka *et al.*, Phys. Lett. B **744**, 7 (2015).

[60] J. Endres, D. Savran, P. A. Butler, M. N. Harakeh, S. Harissopulos, R.-D. Herzberg, R. Krucken, A. Lagoyannis, E. Litvinova, N. Pietralla *et al.*, Phys. Rev. C **85**, 064331 (2012).

[61] L. Pellegri, A. Bracco, F. C. L. Crespi, S. Leoni, F. Camera, E. G. Lanza, M. Kmiecik, A. Maj, R. Avigo, G. Benzoni *et al.*, Phys. Lett. B **738**, 519 (2014).

[62] K. Govaert, F. Bauwens, J. Bryssinck, D. De Frenne, E. Jacobs, W. Mondelaers, L. Govor, and V. Y. Ponomarev, Phys. Rev. C **57**, 2229 (1998).

[63] B. Özel-Tashenov, J. Enders, H. Lenske, A. M. Krumbholz, E. Litvinova, P. von Neumann-Cosel, I. Poltoratska, A. Richter, G. Rusev, D. Savran, and N. Tsoneva, Phys. Rev. C **90**, 024304 (2014).

[64] M. Müscher, J. Wilhelmy, R. Massarczyk, R. Schwengner, M. Grieger, J. Isaak, A. R. Junghans, T. Kögler, F. Ludwig, D. Savran, D. Symochko, M. P. Takács, M. Tamkas, A. Wagner, and A. Zilges, Phys. Rev. C **102**, 014317 (2020).

[65] J. Isaak, D. Savran, B. Löher, T. Beck, U. Friman-Gayer, Krishichayan, N. Pietralla, V. Y. Ponomarev, M. Scheck, W. Tornow, V. Werner, A. Zilges, and M. Zweidinger, Phys. Rev. C **103**, 044317 (2021).

[66] C. E. Porter and R. G. Thomas, Phys. Rev. **104**, 483 (1956).

[67] M. Wiedeking, M. Guttormsen, A. C. Larsen, F. Zeiser, A. Görgen, S. N. Liddick, D. Mücher, S. Siem, and A. Spyrou, Phys. Rev. C **104**, 014311 (2021).

[68] G. A. Bartholomew, E. D. Earle, A. J. Ferguson, J. W. Knowles, and M. A. Lone, Adv. Nucl. Phys. **7**, 229 (1973).

[69] S. Bassauer, P. von Neumann-Cosel, and A. Tamii, Phys. Rev. C **94**, 054313 (2016).

Paper II

Nuclear level densities and γ-ray strength functions in ^{120,124}Sn isotopes: Impact of Porter-Thomas fluctuations

II

Nuclear level densities and γ-ray strength functions in ^{120,124}Sn isotopes: Impact of Porter-Thomas fluctuations

M. Markova [1,*] A. C. Larsen [1,†] P. von Neumann-Cosel,[2] S. Bassauer,[2] A. Görgen [1] M. Guttormsen [1]
F. L. Bello Garrote [1] H. C. Berg [1] M. M. Bjørøen,[1] T. K. Eriksen,[1] D. Gjestvang,[1] J. Isaak [2] M. Mbabane,[1] W. Paulsen,[1]
L. G. Pedersen,[1] N. I. J. Pettersen,[1] A. Richter [2] E. Sahin,[1] P. Scholz [3,4] S. Siem,[1] G. M. Tveten,[1]
V. M. Valsdottir,[1] and M. Wiedeking [5,6]

[1]*Department of Physics, University of Oslo, N-0316 Oslo, Norway*
[2]*Institut für Kernphysik, Technische Universität Darmstadt, D-64289 Darmstadt, Germany*
[3]*Institut für Kernphysik, Universität zu Köln, D-50937 Köln, Germany*
[4]*Department of Physics, University of Notre Dame, Indiana 46556-5670, USA*
[5]*Deptartment of Subatomic Physics to SSC Laboratory, iThemba LABS, Somerset West 7129, South Africa*
[6]*School of Physics, University of the Witwatersrand, Johannesburg 2050, South Africa*

Nuclear level densities (NLDs) and γ-ray strength functions (GSFs) of ^{120,124}Sn have been extracted with the Oslo method from proton-γ coincidences in the $(p, p'\gamma)$ reaction. The functional forms of the GSFs and NLDs have been further constrained with the Shape method by studying primary γ-transitions to the ground and first excited states. The NLDs demonstrate good agreement with the NLDs of ^{116,118,122}Sn isotopes measured previously. Moreover, the extracted partial NLD of 1^- levels in ^{124}Sn is shown to be in fair agreement with those deduced from spectra of relativistic Coulomb excitation in forward-angle inelastic proton scattering. The experimental NLDs have been applied to estimate the magnitude of the Porter-Thomas (PT) fluctuations. Within the PT fluctuations, we conclude that the GSFs for both isotopes can be considered to be independent of initial and final excitation energies, in accordance with the generalized Brink-Axel hypothesis. Particularly large fluctuations observed in the Shape-method GSFs present a considerable contribution to the uncertainty of the method and may be one of the reasons for deviations from the Oslo-method strength at low γ-ray energies and low values of the NLD (below $\approx 1 \times 10^3$–2×10^3 MeV^{-1}).

I. INTRODUCTION

Numerous experimental and theoretical efforts have been dedicated to the study of γ-decay processes in atomic nuclei. The decay properties of excited nuclei are not only pivotal for the basic nuclear physics research, but also are the core ingredients for large-scale calculations of nucleosynthesis and element abundances in the universe [1,2].

While gradually moving from the lowest to higher excitation energies of a nucleus, the spacing between individual excited states becomes smaller, and the sensitivity of experimental techniques might be no longer sufficient to resolve them separately. Here, the nucleus enters the quasicontinuum regime and the concept of the nuclear level density (NLD), i.e., the number of nuclear states per excitation energy unit, becomes an indispensable tool for a statistical description of nuclei. By analogy, the γ-ray strength function (GSF), or the average, reduced γ-transition probability, becomes more suitable to describe the numerous γ transitions. The statistical model as formulated by Hauser and Feshbach [3] with ingre-

dients such as the NLD and GSF provides the main framework for modeling nuclear reactions and calculating their cross sections for astrophysical purposes (see, e.g., Ref. [2]), the design of nuclear reactors [4], and the transmutation of nuclear waste [5].

Among all experimental techniques used for the extraction of GSFs [6], the Oslo method has been widely used to obtain the dipole strength below the neutron threshold by studying the γ decay of residual nuclei formed in light-ion-induced reactions [7–9]. The main advantage of the method is a simultaneous extraction of the NLD and GSF from primary γ-decay spectra at excitation energies below the neutron separation energy S_n. The GSFs for many nuclei obtained by employing different experimental techniques have previously been reported to provide a rather good agreement in absolute values and/or general shapes with the Oslo method strengths [10–12]. A few cases of large discrepancies have also been reported (e.g., the comparison of the Oslo and (γ, γ') data for ^{89}Y and ^{139}La presented in Ref. [6]).

A large fraction of theoretical and experimental techniques focusing on calculating or measuring the GSF, including the Oslo method, rely on the validity of the generalized Brink-Axel (gBA) hypothesis [13,14]. In its most general form, the hypothesis states that the GSF is independent of excitation

*maria.markova@fys.uio.no
†a.c.larsen@fys.uio.no

energies, spins and parities of initial and final states and depends solely on the γ-ray energy of involved transitions. This is often used as a necessary approximation and simplification in many methods and allows us to set a direct correspondence between strengths extracted from the γ decay and photoexcitation processes [13,15]. Even though this hypothesis is experimentally established at high energies, i.e., in the vicinity of the giant dipole resonance, its validity below the neutron threshold still triggers quite some debate. For example, several theoretical studies suggest the need of a modification of the hypothesis [16–20], while experimental studies range from claims of a violation [21–24] to a validity [12,15,25–27]. The question regarding the validity is a rather difficult one, partially depending on what degree of violation is considered acceptable in different experimental and theoretical applications.

A crucial point to be considered when addressing the applicability of the gBA hypothesis is the presence of fluctuations of partial radiative widths, or the so-called Porter-Thomas (PT) fluctuations [28]. The partial radiative widths are proportional to the corresponding reduced transition strengths [$B(XL)$ values where X is the electromagnetic character and L the angular momentum of the γ ray]. At sufficiently high excitation energies and high NLD values, the nuclear wave functions are quite complex with many components. In this region, according to random-matrix theory [29], the partial widths follow a χ_ν^2 behavior with $\nu = 1$ degree of freedom, while the total widths are more narrowly distributed with the variance inversely proportional to the number of independently contributing partial widths.

Such a variation of partial widths is directly reflected in the variation of the GSF, which may mask the excitation energy independence of the strength, and thus a test of the gBA hypothesis might become especially difficult. Indeed, for relatively light nuclei, e.g., ^{64,65}Ni [26] and ^{46}Ti [30], the NLDs are rather low, and tests of the gBA hypothesis are limited. On the other hand, the ^{238}Np nucleus [25] with a particularly high NLD makes a perfect case for studying the GSF as a function of initial and final excitation energies, as fluctuations of the strength are strongly suppressed. The Sn isotopes investigated here present an intermediate case for studying to what degree the PT fluctuations are expected to distort excitation energy dependence of the GSF.

Moving away from the valley of stability opens up new perspectives for studying exotic, neutron-rich nuclei, with applications to heavy-element nucleosynthesis [31], using for example, the β-Oslo method [32] and the Oslo method in inverse kinematics [33]. However, this leads to additional complications, such as the lack of neutron-resonance data for normalizing the NLD and GSF from the Oslo-method data. Moreover, some of the light-ion-induced reactions may lead to a population of a limited spin range, which might introduce additional assumptions and uncertainties when extracting the shapes of the NLD and GSF.

A novel technique, the Shape method [34], has recently been proposed to mend this problem. Applied to the primary γ transitions to several low-lying discrete states at consecutive excitation energy bins, it allows for an independent determination of the shape of the GSF. Thus, the shape of the

strength and the interlinked slope of the NLD extracted with the Oslo method can be additionally constrained by the Shape method. However, as the latter is using data on direct decays to low-lying discrete states only, the PT fluctuations of the involved partial widths are expected to be significantly larger than for the Oslo-method GSF.

In this work, the potential role of PT fluctuations in establishing the validity of the gBA hypothesis as well as the application of the Shape method are addressed for ^{120}Sn and ^{124}Sn. Both the Oslo method and the Shape method have been applied to the same data sets. Experimental NLDs have been used to estimate fluctuations of the strengths for different specific initial and final excitation energies and compared with previous Oslo-method NLDs for even-even isotopes [35–37]. In Sec. II the details of the experimental procedure, the application of the Oslo method (Sec. II A) and the Shape method (Sec. II B) are presented. Section III focuses on the NLDs for ^{120,124}Sn and the comparison with other experimental and theoretical results. In Sec. IV the procedure of estimating fluctuations of the strengths is presented together with the Shape method results, and the study of fluctuations and GSFs as functions of initial and final excitation energies. Finally, the main conclusions are summarized in Sec. V.

II. DETAILS OF THE EXPERIMENT AND DATA ANALYSIS

Experiments on both ^{120}Sn and ^{124}Sn were performed in February 2019 at the Oslo Cyclotron Laboratory (OCL). The isotopes were studied through the inelastic scattering reactions ^{120,124}Sn$(p, p'\gamma)$ with a proton beam of energy 16 MeV and intensity $I \approx 3$–4 nA provided by the MC-35 Scanditronix cyclotron. Both targets used in the experiment were self-supporting with thicknesses and enrichments of 2.0 mg/cm^2, 99.6% for ^{120}Sn and 0.47 mg/cm^2, 95.3% for ^{124}Sn, respectively. The ^{120}Sn target was placed in the beam for approximately 24 hours, while the whole run on ^{124}Sn lasted approximately 17 hours. A self-supporting ^{28}Si target (natural Si, 92.2% ^{28}Si) with thickness of 4 mg/cm^2 was placed in the same proton beam for ≈ 1.5 hours at the end of the experiment for the energy calibration of the γ detectors.

The experimental setup at the OCL comprises of the target chamber surrounded by 30 cylindrical large-volume LaBr$_3$(Ce) detectors (Oslo Scintillator Array, OSCAR for short) [33,38], and 64 Si particle ΔE-E telescopes (SiRi) [39]. The LaBr$_3$(Ce) scintillator detectors with $\phi 3.5'' \times 8''$ crystals were mounted on a truncated icosahedron frame with all front-ends fixed at a distance of 16.3 cm from the center of the target chamber, thus covering $\approx 57\%$ of the total solid angle. The full-energy peak efficiency and energy resolution of OSCAR have been measured to be $\approx 20\%$ and $\approx 2.7\%$, respectively, at $E_\gamma = 662$ keV for the ^{137}Cs calibration source placed at the same distance from the front-ends of the detectors.

The $(p, p'\gamma)$ reaction on ^{120,124}Sn was one of the first in the series of experiments performed with OSCAR, installed in 2018 at the OCL. As compared with the previously used array CACTUS, consisting of 28 5$'' \times 5''$ NaI(Tl) detectors [40], OSCAR provides greatly improved timing and γ-energy resolution. All the scintillator crystals in the OSCAR array
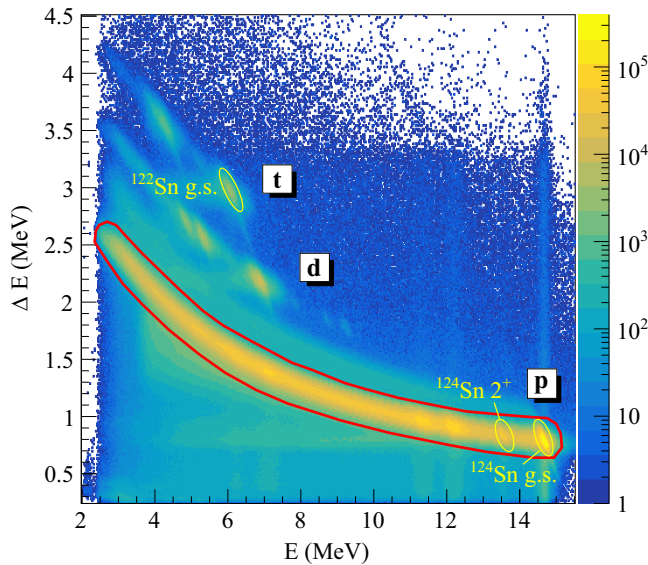
FIG. 1. Experimental E-ΔE spectrum measured for the ^{124}Sn isotope. The proton channel used for the data analysis is marked with the red solid line. The ground and first excited states of ^{124}Sn in the proton channel and the ground state of ^{122}Sn in the triton channel, used for the calibration of the particle telescope, are marked with yellow circles.

are coupled to Hamamatsu R10233-100 photomultiplier tubes with active voltage dividers (LABRVD) [41].

In these experiments, the SiRi particle-telescope array was placed in backward angles with respect to the beam direction, covering a rather narrow range of angles from 126° to 140° and making up $\approx$6% of the total solid-angle coverage. SiRi consists of eight trapezoidal-shaped ΔE-E telescopes with a thick E detector and a thinner ΔE detector with thicknesses of 1550 and 130 μm, respectively. Each of the eight ΔE detectors is segmented into eight curved pads, amounting to 2° of particle scattering angle per pad, yielding an angular resolution of 2°. For the ^{120,124}Sn$(p, p'\gamma)$ experiment, the full width at half maximum (FWHM) for SiRi was estimated to be $\approx$100–120 keV from a Gaussian fit to the elastically scattered protons. All particle-γ coincidences in the experiment were recorded using XIA digital electronics [42].

SiRi enables the exploitation of the ΔE-E technique to differentiate between the various observed reaction channels, as shown in Fig. 1. The elastic peak in the proton channel and the ground-state peak in the triton channel, combined with the known energy deposition in each of the 64 ΔE-E pads, were used to perform a linear calibration of the SiRi detectors for both targets. The kinematics of the reactions were used to convert the proton energies deposited in the SiRi detectors into the corresponding excitation energies of the target nucleus.

As previously shown for $\phi 3.5'' \times 8''$ LaBr$_3$(Ce) detectors coupled to the same type of photomultiplier and voltage divider, the energy response of the detector remains rather linear up to $\approx$17–18 MeV [43]. However, to account for minor nonlinearity effects, a quadratic calibration was applied to all 30 OSCAR detectors. Prominent γ transitions in ^{28}Si ranging from 1.78 to 7.93 MeV were used for this purpose. Further-

more, by applying graphical energy (see Fig. 1) and timing cuts on the studied proton channel, putting gates on the prompt timing peak and subtracting background for particle and γ detection in SiRi and OSCAR, a so-called raw coincidence matrix was constructed for both studied nuclei. The raw matrices are shown in Figs. 2(a) and 2(d) for ^{120}Sn and ^{124}Sn, respectively. Consecutive diagonals indicate direct transitions to the ground and first excited states. For excitation energies between 7 and 9 MeV, peaks that are due to minor ^{12}C and ^{16}O contaminants in the targets are observed. At further stages of the analysis these peaks were removed[1] to minimize the effect of these contaminants and any related artifacts on the final results. Approximately 5.3×10^7 and 1.3×10^7 p-γ events in the excitation-energy range up to the neutron separation energy were collected for ^{120}Sn and ^{124}Sn, respectively.

The γ spectra for each excitation-energy bin of the coincidence matrices were further unfolded according to the procedure outlined in Ref. [7], using the most recent response function of the OSCAR detectors [44] simulated with the GEANT4 simulation tool [45–47]. This procedure has been applied to a large number of Oslo-type data published throughout the past two decades and has been repeatedly shown to provide valuable results. A great advantage of the method is the preservation of statistical fluctuations of the raw coincidence spectrum into the unfolded one by using the so-called Compton subtraction method [7]. This technique strongly suppresses additional, artificial fluctuations. The unfolded matrices for ^{120}Sn and ^{124}Sn are shown in Figs. 2(b) and 2(e).

The main objective of the analysis is to extract the statistical nuclear properties, namely, the NLD and GSF, by exploiting their proportionality to the decay probability at each specific excitation energy and γ energy. Information regarding this decay probability can be obtained by isolating the first γ rays in a cascade emitted by the nucleus at a certain excitation energy, i.e., primary γ rays originating directly from the nucleus decaying from this excited state, or the so-called first-generation γ rays. The unfolded matrix contains all possible generations of γ rays emitted in every cascade from all excitation energies up to the neutron separation energy. The γ-ray spectra for each excitation-energy bin in the unfolded matrix are expected to contain the same γ rays as in the lower-lying bins, in addition to the γ rays originating from the excited states confined by this energy bin. This fact is the key for the iterative subtraction technique, the so-called first-generation method, applied to both unfolded matrices for ^{120}Sn and ^{124}Sn. This technique relies on the assumption that γ decay is independent of whether states were populated directly in a reaction or via decays from higher-lying states. The details of the procedure are outlined in Ref. [8]. The primary matrices obtained after 23 iterations for both nuclei are shown in Figs. 2(c) and 2(f).

---

[1]The contaminants were removed after unfolding of the γ spectra. A narrow graphical gate is put on each Gaussian-like contaminant peak in the unfolded matrix, and the parts of the spectra within the gate are obtained by interpolating the neighboring regions of the matrix.
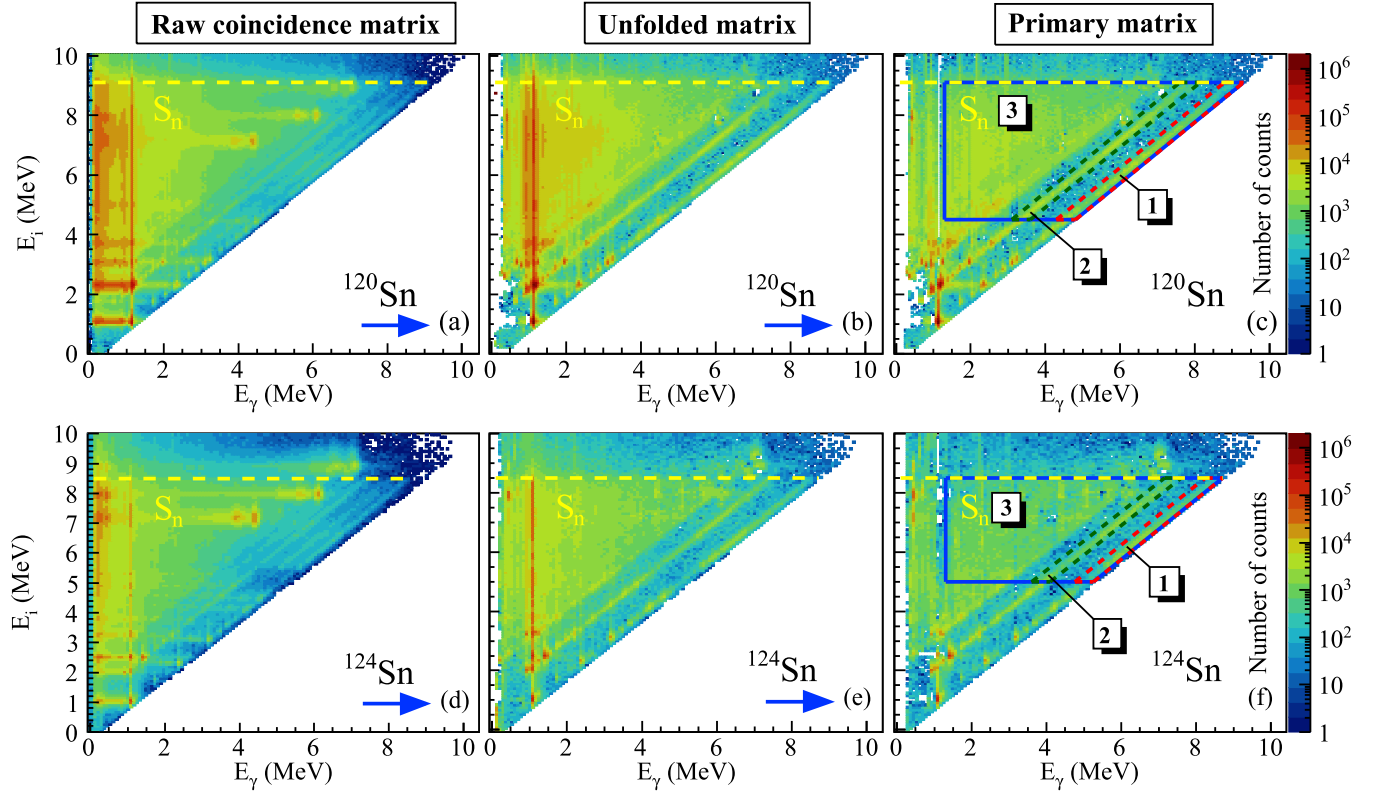
FIG. 2. (a), (d) Experimental raw p-γ coincidence, (b), (e) unfolded and (c), (f) primary matrices for ^{120,124}Sn obtained in the $(p, p'\gamma)$ experiments. Yellow dashed lines indicate the neutron separation energies. Red and green dashed lines in panels (c) and (f) confine transitions to the ground (region 1) and the first excited $J^\pi = 2^+$ (region 2) states. Blue solid lines (region 3) indicate the areas of the primary matrices used further in the Oslo method. Bin sizes are 64 keV $\times$ 64 keV and 80 keV $\times$ 80 keV for ^{120}Sn and ^{124}Sn, respectively. Blue arrows mark the sequence of the analysis steps.

At this stage, two alternative methods can be used in order to extract the GSF from the primary matrix, namely the Oslo method and the Shape method. The former is a well-developed procedure primarily used to extract nuclear properties from the OCL data and it has been in use for more than two decades (see, e.g., Ref. [48]). In addition to the GSF, it provides the simultaneous extraction of the NLD, which are the main characteristics of interest in this article. The latter procedure, the Shape method, has been recently presented and published in Ref. [34]. The two methods are expected to complement each other and a combined analysis yields an improved normalization of the GSF and, therefore, the NLD. All details of these procedures applied to the ^{120,124}Sn isotopes are provided in the subsequent sections.

A. Analysis with the Oslo method

As already mentioned, the primary matrix is proportional to the decay probability from a set of initial excited states i within a chosen bin E_i to final states f confined within a bin E_f of the same size with γ rays of energy $E_\gamma = E_i - E_f$. The first step of the Oslo-type of analysis is the decomposition of the primary matrix into the density of final states ρ_f and the γ-ray transmission coefficient $\mathcal{T}_{i \to f}$:

$$P(E_\gamma, E_i) \propto \mathcal{T}_{i \to f} \rho_f. \qquad (1)$$

Here, $\mathcal{T}_{i \to f}$, the transmission coefficient, is a function of γ-ray energy depending on both the initial and final state. The thorough derivations of this decomposition using Fermi's golden rule and the Hauser-Feshbach theory of statistical reactions as starting points can be found in Refs. [49] and [50], correspondingly. This relation is expected to hold for relatively high excitation energies below the neutron threshold, corresponding to the compound states and their decay [48]. This energy range essentially coincides with the range of applicability of the first-generation method.

This form of dependence on E_i, E_f, and E_γ, however, does not allow a simultaneous extraction of the transmission coefficient and NLD. To enable such an extraction, the gBA hypothesis is adopted as one of the central assumptions in the Oslo method [13,14]. As mentioned previously, the gBA hypothesis suggests an independence of the GSF (and, therefore, the transmission coefficient) of spins, parities, and energies of initial and final states, leading to a dependence on γ-ray energy only. This significantly simplifies the form of the relation given in Eq. (1): $\mathcal{T}_{i \to f} \to \mathcal{T}(E_\gamma)$ and $\rho_f = \rho(E_f) = \rho(E_i - E_\gamma)$.

In earlier applications of the Oslo method, the gBA hypothesis has been found to be adequate for the relatively low-temperature regimes studied ($T \approx 0.7$–1.5 MeV) [30]. However, as the Oslo method relies on the gBA hypothesis,

it cannot be used alone to test its validity. To investigate the validity of the hypothesis, either comparisons of independent experimental methods [15] or additional tests suggested in, e.g., Refs. [25,26] are required. This matter is of particular importance and will be discussed in more detail in Sec. IV.

The next step of the Oslo method includes an iterative χ^2-minimization procedure between the experimental first-generation matrix $P(E_\gamma, E_i)$ normalized to unity for each E_i bin and the theoretical $P_{th}(E_\gamma, E_i)$ given by the following expression [9]:

$$P_{th}(E_\gamma, E_i) = \frac{\mathcal{T}(E_\gamma)\rho(E_i - E_\gamma)}{\sum_{E_\gamma = E_\gamma^{\min}}^{E_i} \mathcal{T}(E_\gamma)\rho(E_i - E_\gamma)}. \quad (2)$$

This χ^2 fit of the transmission coefficient and NLD normally gives a very good agreement with the experimental matrix $P(E_\gamma, E_i)$ when applied to the statistical region of excitation energies. The step-by-step description of the minimization procedure is provided in Ref. [9]. To ensure the applicability of the statistical assumptions, minimum excitation energies of $E_i^{\min} = 4.5$ MeV for ^{120}Sn and 5.0 MeV for ^{124}Sn were chosen. Sufficient statistics at higher energies allows us to set $E_i^{\max}$ to the neutron separation energy for each isotope, $S_n = 9.1$ and 8.5 MeV for ^{120}Sn and ^{124}Sn, respectively. To exclude regions where counts have been over-subtracted in the first-generation procedure, minimum γ-ray energies $E_\gamma^{\min} = 1.3$ and 1.6 MeV were set accordingly for ^{120}Sn and ^{124}Sn. The resulting areas where the Oslo method was applied in this work are marked by the blue lines in Figs. 2(c) and 2(f).

The global χ^2 fit yields only functional forms of the transmission coefficient $\mathcal{T}(E_\gamma)$ and NLD $\rho(E_i - E_\gamma)$. It can be shown mathematically that one can construct an infinite set of $\mathcal{T}(E_\gamma)$ and $\rho(E_i - E_\gamma)$ combinations corresponding to the obtained fit and given by the forms [9]

$$\begin{aligned}\tilde{\rho}(E_i - E_\gamma) &= A\rho(E_i - E_\gamma)\exp{[\alpha(E_i - E_\gamma)]}, \\ \tilde{\mathcal{T}}(E_\gamma) &= B\mathcal{T}(E_\gamma)\exp{(\alpha E_\gamma)},\end{aligned} \quad (3)$$

where ρ and $\mathcal{T}$ are two fixed solutions, A and B are the scaling parameters, and α is the slope parameter shared by both the transmission coefficient and NLD. For each studied nucleus this ambiguity must be removed via determining unique normalization parameters A, B, and α from external experimental data. If available, low-lying discrete states and neutron-resonance data are the main input parameters, combined with models for the spin distribution and for extrapolations where there is a lack of experimental data.

The first step of the normalization procedure is to determine the unique NLD solution $\rho(E_i - E_\gamma)$. The parameters A and α can be constrained by fitting the NLD to low-lying discrete states [51] in the excitation-energy range where the level scheme can be considered complete. At the neutron separation energy, the NLD can be normalized to the total NLD calculated from neutron-resonance spacings [52]. These data also provide the average, total radiative width $\langle\Gamma_\gamma\rangle$ used to determine the scaling parameter B for the transmission coefficient. All details of the normalization procedure for ^{120}Sn and ^{124}Sn have been presented in the Supplemental Material of Ref. [15]. However, some minor changes were introduced

in this work to improve the normalization and the estimated uncertainties. We would like to stress that these changes do not affect the results presented in Ref. [15] in any significant way and do not undermine any of the presented conclusions. To avoid any confusion regarding the normalization parameters, we provide the updated and complete description of this procedure in the following.

The most recent compilation of the discrete states [51] was used to anchor the NLD for ^{120,124}Sn at low excitation energies. As compared with the compilation from 2003 used in the previous analysis, some changes in the number and the excitation energies of low-lying states appear and give a slightly different slope of the NLD. The anchor point at the neutron separation energy, $\rho(S_n)$, is usually extracted from the neutron resonance spacing D_0 for s-wave neutrons or D_1 for p-wave neutrons. As ^{123}Sn is an unstable target nucleus ($T_{1/2} = 129.2$ d [51]), no neutron resonance data are available, and we used other means to estimate $\rho(S_n)$ and $\langle\Gamma_\gamma\rangle$ for ^{124}Sn.

The normalization procedure for ^{120}Sn is rather straightforward, in accordance with the steps outlined in Ref. [48], due to the available s-wave neutron capture data. The target spin of ^{119}Sn is $I_t^\pi = 1/2^+$, thus spins 0^+ and 1^+ of the compound nucleus ^{120}Sn are populated in s-wave capture. Assuming that both positive and negative parities contribute equally to $\rho(S_n)$, the average s-wave neutron resonance spacing D_0 can be written as [48]

$$\frac{1}{D_0} = \frac{1}{2}[\rho(S_n, I_t + 1/2) + \rho(S_n, I_t - 1/2)]. \quad (4)$$

A transformation of the *partial* NLD for specific spins into the *total* NLD can be performed by adopting the backshifted Fermi gas model (BSFG) for the NLD $\rho(E_x, J) = \rho(E_x)g(E_x, J)$ (E_x here stands for the excitation energy variable) with the spin distribution function given by [53,54]

$$g(E_x, J) \simeq \frac{2J + 1}{2\sigma^2}\exp\left[-\frac{(J + 1/2)^2}{2\sigma^2}\right], \quad (5)$$

where σ is the spin-cutoff parameter. Given this distribution function, Eq. (5) can be rewritten for the total NLD at the neutron separation energy as a function of the experimental resonance spacing D_0 (taken from Ref. [52]) and the target nucleus spin [48]:

$$\rho(S_n) = \frac{2\sigma^2}{D_0}\frac{1}{(I_t + 1)\exp\left(-\frac{(I_t+1)^2}{2\sigma^2}\right) + I_t\exp\left(-\frac{I_t^2}{2\sigma^2}\right)}. \quad (6)$$

Note that the spin-cutoff parameter is an excitation-energy-dependent function. The form of the spin-cutoff parameter at S_n of Ref. [55] was chosen for ^{120,124}Sn

$$\sigma^2(S_n) = 0.0146A^{5/3}\frac{1 + \sqrt{1 + 4a(S_n - E_1)}}{2a}. \quad (7)$$

Here, a and E_1 are the level-density parameter and the backshift parameter for the BSFG model taken from Ref. [55].

In the Oslo method, the measured level densities do not reach up to $E_x = S_n$ due to the nonzero minimum γ-ray energy limit in the extraction of $\rho(E_i - E_\gamma)$. To use the $\rho(S_n)$ value as an anchor point for the normalization, the experimental Oslo data were extrapolated using the constant temperature
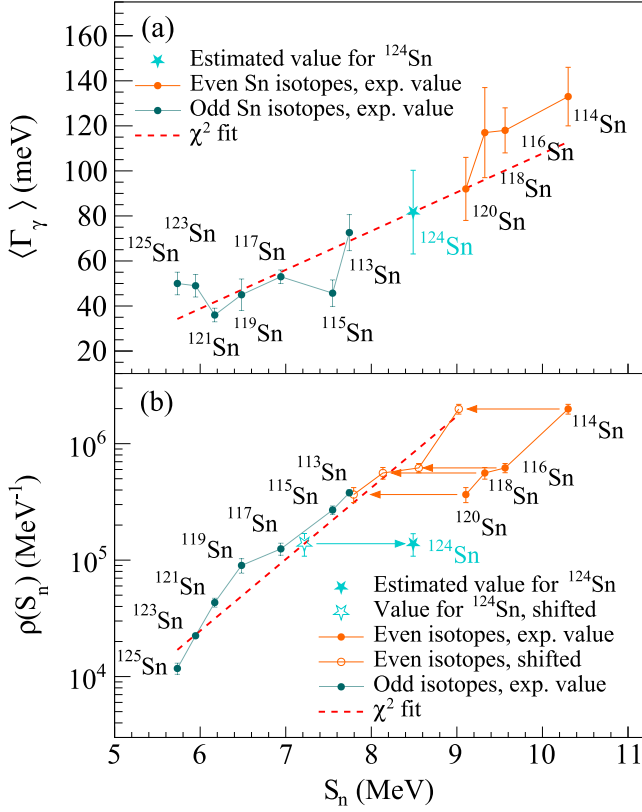
FIG. 3. (a) Experimental systematics for the average total radiative width for Sn isotopes. (b) Experimental systematics for the NLD at the neutron separation energy. The estimated values of $\langle \Gamma_\gamma \rangle$ and $\rho(S_n)$ for ^{124}Sn are marked with stars, the experimental $\langle \Gamma_\gamma \rangle$ values are taken from Ref. [52], and the level densities are obtained from the D_0 values given in Ref. [52]. Arrows mark $\rho(S_n)$ values shifted by the neutron pair-gap values for the χ^2 fit.

(CT) level density model [54–56]:

$$\rho_{CT}(E_x) = \frac{1}{T_{CT}} \exp\left(\frac{E_x - E_0}{T_{CT}}\right), \qquad (8)$$

characterized by the temperature (T_{CT}) and shift energy (E_0) parameters. Earlier Oslo-method analyses exploited the BSFG model as an alternative for the interpolation procedure [48], however, the choice between these two alternatives is defined by the fit quality in each particular case (see Sec. III).

As the experimental information on the *s*-wave neutron-resonance spacing is available for ^{120}Sn, Eq. (6) was used directly to transform the D_0 value into $\rho(S_n)$. For ^{124}Sn, this value was estimated from the systematics for even-even and even-odd Sn isotopes in the following way: The $\rho(S_n)$ values were estimated for each Sn isotope with available neutron-resonance spacing D_0 using Eq. (6). The resulting systematics for the $\rho(S_n)$ values are shown in the lower panel of Fig. 3. The values of $\rho(S_n)$ for even-even isotopes were shifted by the corresponding values of the neutron pairing gaps calculated from the AME 2003 mass evaluation [57] using Eq. (1) of Ref. [58]. Finally, the value of $\rho(S_n)$ for ^{124}Sn was calculated from a log-linear fit through the data points for even-odd and

shifted even-even isotopes as shown by the red dashed line in Fig. 3(b).

The second step after constraining the A and α parameters for the NLD is to normalize the transmission coefficient (and thus the GSF). As the slope α is already determined by the NLD normalization, the scaling parameter B is the only parameter that remains to be estimated. The starting point for normalizing the γ-transmission coefficient is the following relation [59]:

$$\langle \Gamma(E_x, J, \pi) \rangle = \frac{1}{2\pi \rho(E_x, J, \pi)} \sum_{XL} \sum_{J_f, \pi_f} \int_{E_\gamma = 0}^{E_x} dE_\gamma \qquad (9)$$
$$\times \mathcal{T}_{XL}(E_\gamma) \rho(E_x - E_\gamma, J, \pi),$$

where $\langle \Gamma(E_x, J, \pi) \rangle$ is the average radiative width for states with spin J, parity π at excitation energy E_x, and X and L indicate the electromagnetic character and multipolarity, respectively. The GSF, $f_{XL}(E_\gamma)$, is connected to the transmission coefficient by [60]

$$\mathcal{T}_{XL}(E_\gamma) = 2\pi E_\gamma^{(2L+1)} f_{XL}(E_\gamma). \qquad (10)$$

At high excitation energies, there is experimental evidence that the dipole radiation is dominant ($L = 1$) (see e.g., Ref. [59]). The Oslo-type of experiments and analysis does not allow for distinguishing between different types of radiation, and, thus, the strength extracted with the Oslo method is presented by the total contribution of both electric and magnetic types of dipole transitions, $E1$ and $M1$.

Insertion into Eq. (9) links the experimental dipole GSF $f(E_\gamma)$ to the value of the total average radiative width $\langle \Gamma_\gamma \rangle$ obtained from *s*-wave neutron capture [52]. For a target nucleus with ground state spin I_t and parity π_t, Eq. (9) can be rewritten as

$$\langle \Gamma_\gamma \rangle = \langle \Gamma(S_n, I_t \pm 1/2, \pi_t) \rangle = \frac{1}{2\rho(S_n, I_t \pm 1/2, \pi_t)}$$
$$\times \int_{E_\gamma = 0}^{S_n} dE_\gamma E_\gamma^3 f(E_\gamma) \rho(S_n - E_\gamma)$$
$$\times \sum_{J=-1}^{1} g(S_n - E_\gamma, I_t \pm 1/2 + J). \qquad (11)$$

Here, we adopt again the assumption on an equal contribution of states with positive and negative parities and apply the spin distribution function of Eq. (5). It can be easily seen that the $1/\rho(S_n, I_t \pm 1/2, \pi_t)$ term equals the D_0 value. For the spin-cutoff parameter dependence on the excitation energy, we follow the procedure outlined in Ref. [61]:

$$\sigma^2(E_x) = \sigma_d^2 + \frac{E_x - E_d}{S_n - E_d}\left[\sigma^2(S_n) - \sigma_d^2\right], \qquad (12)$$

where σ_d is estimated from the discrete lower-lying states at $E_x \approx E_d$ [51] (see Table I).

In the case of ^{120}Sn, the average total radiative width $\langle \Gamma_\gamma \rangle$ was estimated as an average of three *s*-wave neutron resonances with energies in the range of ≈ 455–828 eV [52]. The remaining two resonances presented in Ref. [52] were excluded due to either being possibly of *p*-wave nature, or having a significantly lower value as compared with values for

TABLE I. Parameters used for the normalization of the nuclear LD and GSF for ^{120,124}Sn

Nucleus	S_n (MeV)	D_0 (eV)	a (MeV^{-1})	E_1 (MeV)	E_d (MeV)	σ_d	$\sigma(S_n)$	$\rho(S_n)$ (10^5 MeV^{-1})	T (MeV)	E_0 (MeV)	β	$\langle\Gamma_\gamma\rangle$ (meV)
^{120}Sn	9.105	95(14)	13.92	1.12	2.53(4)	3.4(5)	5.82	3.66(54)	0.72^{+1}_{-2}	0.19^{+9}_{-4}	0.70	121(25)[b]
^{124}Sn	8.489		12.92	1.03	2.77(3)	3.3(5)	6.00	1.38(30)[a]	0.75^{+2}_{-2}	-0.11^{+11}_{-6}	0.20	82(19)[a]

[a]From systematics.
[b]Modified with respect to the value published in Ref. [52].

confirmed *s*-wave resonances found in the neighboring Sn isotopes. In the case of ^{124}Sn, we performed a linear fit through all values of $\langle\Gamma_\gamma\rangle$ available for other Sn isotopes as shown in Fig. 3(a) to estimate the $\langle\Gamma_\gamma\rangle$ value for ^{124}Sn. Ideally, the fit of the NLD to the low-lying discrete levels and the $\rho(S_n)$ value are sufficient to constrain the slope parameter α for the GSF and NLD. However, the latter can be influenced by the range of experimentally populated spins, which might be narrower than the *intrinsic*[2] spin distribution. This issue was previously discussed in Refs. [62,63]. An analysis of the observed transitions in the unfolded matrices below $E_i \approx 4$–5 MeV and their relative intensities can aid to reveal the populated spins of the ^{120,124}Sn nuclei populated in the ($p, p'\gamma$) reaction. However, this method has a large uncertainty in the determination of the exact maximum spin populated in the reaction. Alternatively, one can make use of the new Shape method [34] to obtain the NLD slope that corresponds to the experimental spin range. This is of particular importance for ^{124}Sn with no available neutron-resonance parameters. The application of the Shape method will be discussed in detail in Sec. II B. From the Shape method we obtained a reduction factor β for $\rho(S_n)$, representing a certain fraction of the total spin distribution from Eq. (5), corresponding to the reduced spin range from $J = 0$ to a certain maximum spin. This was done by requesting optimally matching slopes of the Oslo method and the Shape method GSFs above $E_\gamma \approx 5$ MeV. A rather strong reduction of the level density in ^{124}Sn at the neutron separation energy might reflect some maximum limit of the experimental spin range. However, it is important to note that using experimental systematics of the $\rho(S_n)$ and $\langle\Gamma_\gamma\rangle$ might have large uncertainties. In the case of ^{124}Sn, it is quite probable that such a large reduction factor is needed due to, e.g., an overestimated $\rho(S_n)$ from the χ^2 fit of the systematics. The simultaneous use of the Oslo and Shape methods can therefore significantly reduce systematic uncertainties for the slopes of extracted strengths and level densities. All parameters used in the normalization procedure for ^{120,124}Sn are listed in Table I. The resulting NLDs for ^{120}Sn and ^{124}Sn with their estimated error bands are shown in Fig. 4.

We note that the errors in Table I and the resulting error bands for the NLD and the GSF presented in Secs. III and IV combine statistical and systematic components. The latter includes uncertainties introduced by the unfolding and the first-generation procedures for both ^{120,124}Sn isotopes. These are propagated through the Oslo method according to the

procedure outlined in Ref. [9]. In addition, systematic uncertainties due to the normalization parameters are included. For the ^{120}Sn isotope, the experimental uncertainty (1 standard deviation) of the D_0 value was propagated to estimate the error for the NLD at the neutron separation energy. The experimental uncertainties of the radiative widths in ^{120}Sn [52] were used to estimate the error of the average, total radiative width $\langle\Gamma_\gamma\rangle$, contributing to the uncertainty of the scaling factor B. In the case of the ^{124}Sn isotope, the errors of the $\rho(S_n)$ and $\langle\Gamma_\gamma\rangle$ were calculated from the uncertainties of the χ^2 fit parameters and propagated into the total uncertainties of the NLD and GSF. In the previously published result on ^{124}Sn [15], a 50%
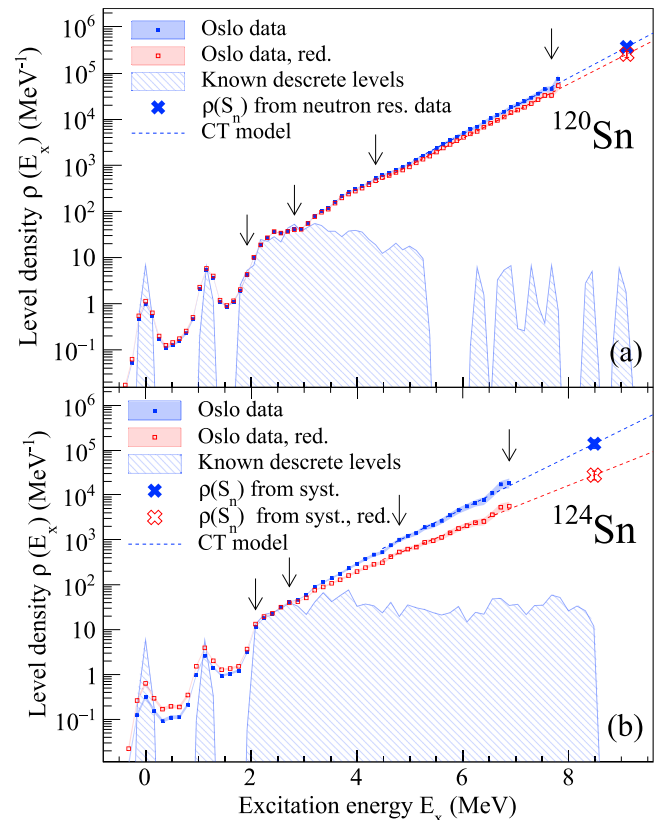

FIG. 4. Experimental nuclear level densities for (a) ^{120}Sn and (b) ^{124}Sn. The NLDs at S_n are marked with crosses, discrete states are shown as shaded areas. For the ^{124}Sn isotope both the total and reduced NLDs are shown. The first two vertical arrows at lower E_x energies on each figure constrain the lower excitation energy fit region, while the last two arrows at higher E_x energies mark the lower and upper limits for the higher excitation energy fit region.

---

[2]All existing spins possible for a given nucleus at a given excitation energy.

uncertainty of $\rho(S_n)$ was assumed to account for presumably underestimated errors from the χ^2 fit. However, the excellent agreement within the estimated error bands of the slopes of the GSFs obtained with the Oslo and Shape method allows us to apply a more modest error band as presented in this work. All errors of the normalization parameters described above are summarized in Table I.

B. Analysis with the Shape method

Quite often, nuclei with no available neutron resonance data and/or a restricted experimental spin range are encountered. One possible way to overcome this is the use of isotopic systematics comprising of nuclei with stable neighboring $A - 1$ isotopes as applied in the present case for ^{124}Sn. However, this is often not possible in other isotopic chains due to the lack of data (e.g., ^{127}Sb [64]). Moreover, the question on whether systematics from neighboring isotopic chains can be used for a given nucleus, and to what extent one can rely on these systematics, is still open. Hence, an alternative way to constrain the normalization parameters is required. The novel Shape method [34] provides a way to determine the slope parameter α for the NLD and the GSF without making use of neutron resonance data.

The starting point for the method is extracting experimental intensities of first generation γ transitions to specific final states with spins and parities J^π at final excitation energies E_f, represented by diagonals in the primary matrix. The intensities (related to the branching ratios) of these γ transitions are proportional to the number of counts N_D in the diagonals. The selection of which diagonals are to be used depends on a particular nucleus, the spacing between the final states, and whether the resolution is sufficient to distinguish between different diagonals. The main concept behind the Shape method is that the intensities of the γ transitions are proportional to the partial widths and hence to the GSF. By taking intensities of transitions in successive excitation energy bins, the functional form of the GSF can be obtained.

In the case of ^{120,124}Sn, the only two diagonals clearly seen in the primary matrices are the ground state diagonal D_1 and the diagonal D_2 corresponding to the first excited state [marked accordingly as regions 1 and 2 in Figs. 2(c) and 2(f)]. For given initial excitation-energy bins E_i (horizontal line) they define the direct decay to the final excitation energy E_f at the ground state with $J^\pi = 0^+$ and the first excited state with $J^\pi = 2^+$ with γ-ray energies $E_\gamma = E_i - E_f$.

The Shape method adopts the same form of the spin distribution, given by Eq. (5), as used in the Oslo method, and assumes γ transitions to be of predominantly dipole nature (this has been confirmed by measuring angular distributions). According to Eq. (13) in Ref. [34], the number of counts in a chosen diagonal N_D corresponding to the final energy E_f is proportional to the population cross-section of initial states E_i with $J_i = J_f - 1, J_f, J_f + 1$, spin distribution function $g(E_i, J_i)$ and the partial γ-decay width. For the case of ^{120,124}Sn with the ground and first-excited-state diagonals D_1

and D_2, the following relations can be written:

$$f(E_{\gamma 1}) \propto \frac{N_{D_1}}{E_{\gamma 1}^3 g(E_i, 1)},$$

$$f(E_{\gamma 2}) \propto \frac{N_{D_2}}{E_{\gamma 2}^3 [g(E_i, 1) + g(E_i, 2) + g(E_i, 3)]}. \quad (13)$$

By varying E_i, one obtains corresponding pairs of values $f(E_\gamma = E_i)$ and $f(E_\gamma = E_i - E_x(2^+))$. As Eqs. (13) only give the proportionality with the GSF, these pairs are not normalized in absolute value.

First, the consecutive pairs of values are normalized internally, as shown and described in Fig. 2 of Ref. [34], to reconstruct the functional shape of the GSF. Thus, one can extract two GSFs, corresponding to decays to the ground state and decays to the first excited state. Second, the general shape of both GSF must be scaled to match any available strength below the neutron separation energy, i.e., normalizing to external experimental data. This is the main limitation of the method because it provides only a slope or a shape of the strength but not the absolute GSF and therefore requires some additional experimental information. For the ^{120,124}Sn isotopes, the GSFs extracted from relativistic Coulomb excitation in forward-angle inelastic proton scattering below the neutron separation energy [65] were used to scale the GSF points obtained for both diagonals separately [15].

The upper excitation energy limit for the application of the Shape method can, in principle, be extended to S_n, while the definition of the lower limit is rather arbitrary. The applicability of Eqs. (13) is restricted to the statistical excitation energy region where the spin distribution function $g(E_x, J)$ can be trusted. There is no clear criterion for the minimum level density which can be considered high enough to assume this is fulfilled. In this work, we require that the level density must be at least 10 levels per excitation energy bin for the spin distribution $g(E_x, J)$ to be applied.

III. NUCLEAR LEVEL DENSITIES

The experimental NLDs of ^{120,124}Sn displayed in Fig. 4 follow nicely the discrete low-lying states up to ≈ 3 MeV for ^{120}Sn and ≈ 2.7 MeV for ^{124}Sn. At higher energies, the NLDs increase rapidly and reach an exponential, constant-temperature behavior. This suggests that the level schemes used for the normalization of the NLDs can be considered complete up to ≈ 3 and 2.7 MeV for ^{120}Sn and ^{124}Sn, respectively. The energy resolution is sufficient to distinguish the ground state and the first excited states, presented by two bumps at 0 and ≈ 1.1–1.2 MeV for both nuclei. The presence of the data points between the ground and first excited states can be explained by the finite excitation energy resolution of order 100 keV and the presence of the leftover counts between the diagonals in the primary matrices after the background subtraction procedure. At higher excitation energies, the experimental points are following the CT model prediction, starting from ≈ 4 MeV. The normalization of the NLDs was found to be rather insensitive to the exact choice of the two upper normalization limits (the two arrows at higher excitation
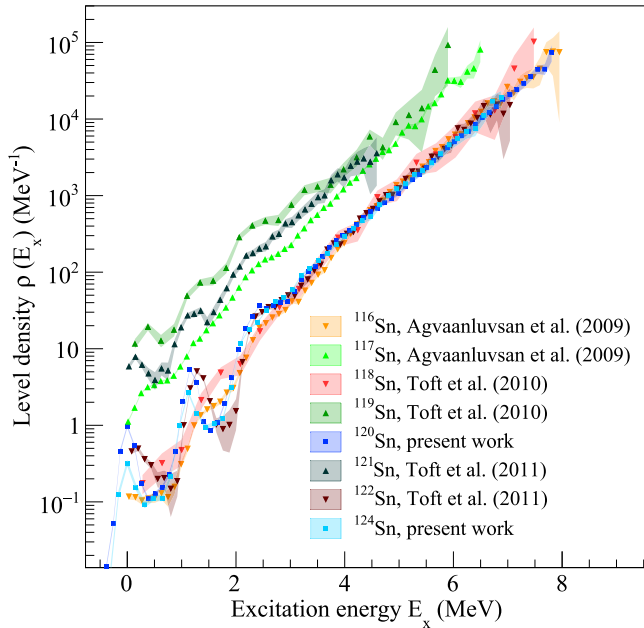
FIG. 5. Experimental total nuclear level densities for ^{116}Sn [35], ^{117}Sn [35], ^{118}Sn [36], ^{118}Sn [36], ^{120}Sn, ^{121}Sn [37], ^{122}Sn [37], ^{124}Sn.

FIG. 6. Experimental nuclear level densities for $1^{\pm}$ states for ^{124}Sn obtained with the Oslo method (blue data points) and the (p, p') data [65] (orange data points). The prediction of the CT model used for the normalization of the Oslo method data is shown by the dashed blue line. A fit with the BSFG through all data and with the composite formula [54] are shown by the dashed magenta and solid cyan lines. Predictions of the microscopic Hartree-Fock-BCS method [67] and Hartree-Fock-Bogolyubov + Gogny force calculations [68] are marked by the dashed light and dark-gray lines, respectively.

energies in Fig. 4), due to the smooth behavior of the NLDs at higher excitation energies.

In Fig. 5 we show a comparison of the total NLDs for Sn isotopes extracted with the Oslo method, including the present results for ^{120,124}Sn. The ^{116,117,118,119,121,122}Sn isotopes were previously studied with a 38-MeV beam of ^{3}He using the $(^3\text{He}, \alpha\gamma)$ and $(^3\text{He}, {}^3\text{He } \gamma)$ reaction channels and reported in Refs. [35–37]. The slopes of the NLDs for ^{120,124}Sn are quite similar to each other ($T = 0.72$ and 0.75 MeV, see Table I) and those of other even-mass isotopes. All NLDs of even-mass nuclei agree quite well within the estimated error bands below the neutron separation energy. However, it is important to note some differences in the normalization procedures in the newest analysis of ^{120,124}Sn and the older analyses of even-mass isotopes. First, all previous analyses exploited the BSFG for the extrapolation of the highest experimental NLD points to the $\rho(S_n)$ values instead of the CT model. As was previously shown in Ref. [66] and confirmed for ^{120,124}Sn, the CT model results in a better χ^2 fit value. For example, between ≈ 4.8 and 6.8 MeV in ^{124}Sn, the reduced χ^2 value is a factor of four smaller for the CT model than for the BSFG model. This factor becomes larger and might exceed 10 if lower excitation energy points above ≈ 3 MeV are included. Second, the different form of the spin-cutoff parameter taken from Ref. [54] was used in the older analyses. The immediate consequence of this choice is slightly less steep slopes of the NLDs if the CT extrapolation is used. However, in combination with the BSFG extrapolation model, the resulting slopes of the NLDs in ^{116,118,122}Sn are expected to be close to those obtained for ^{120,124}Sn, as can also be observed in Fig. 5.

In general, the NLDs of odd-mass Sn isotopes are by a factor of seven to eight higher than for the even-mass isotopes, primarily due to the unpaired valence neutron [69]. As
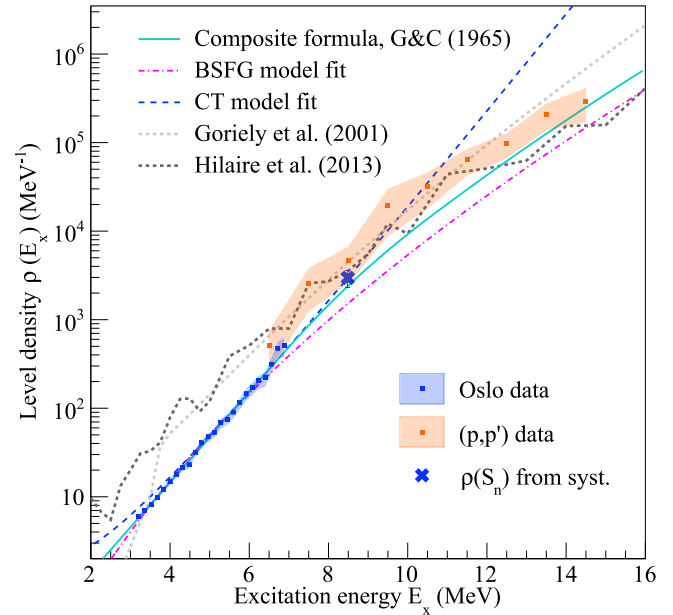
compared with other even-mass isotopes, ^{120,124}Sn demonstrate essentially the same features, such as the well-defined bumps at the ground and the first excited state and a step-like structure right below 3 MeV excitation energy. Earlier studies exploiting microscopic calculations based on the seniority model link the latter feature to breaking of consecutive nucleon Cooper pairs [70]. Due to the closed proton shell, $Z = 50$, the breaking of proton Cooper pairs is suppressed until higher excitation energies are reached. Thus, these step-like structures are likely to be correlated with the breaking of neutron pairs at energies exceeding $2\Delta_n = 2.6$ and 2.5 MeV [58] for ^{120}Sn and ^{124}Sn, respectively. For higher excitation energies, where a continuous "melting" of Cooper pairs sets in, the NLDs follow a smooth trend with no distinctive structures, as previously observed for ^{116,118,122}Sn [35–37].

The inelastic proton scattering data [65], used for the absolute normalization of the Shape method GSFs, can also provide information on the partial NLD. The NLD of 1^- states in ^{124}Sn was extracted for the excitation-energy range ≈ 4.5–14.5 MeV by means of the fluctuation analysis [71], applying procedures analog to those used in Refs. [11,72]. All details of the extraction procedure can be found in Ref. [73]. To compare with the Oslo data, we apply the spin distribution function in Eq. (5) to the total NLD of ^{124}Sn to reduce it to the density of $J = 1$ levels for excitation energies above ≈ 3.2 MeV, where this function can be assumed to be applicable. Furthermore, applying the assumption on equal

contribution of positive- and negative-parity states [74,75], the density of $J = 1$ states was obtained. In contrast with the previously published results on ^{96}Mo [12] and ^{208}Pb [11], there is in fact a region of overlap between the two data sets, as shown in Fig. 6. The Oslo data, as well as the CT model used in the normalization procedure (blue dashed line), lie within, but closer to the lower edge of the error band for the inelastic proton scattering data up to $\approx$10.5 MeV. This provides support of the spin-cutoff model adopted in the Oslo-method normalization. A model predicting a higher spin-cutoff value than presented in Table I would imply a wider spin distribution and, therefore, a significantly lower fraction of $J = 1$ states leading to a larger discrepancy between the Oslo and the (p, p') data in the overlapping area. Thus, we can conclude that the spin-cutoff estimate provided by Eq. (7) is reasonable, and probably lies closer to the upper limit in the range of acceptable spin-cutoff values that would make the two experimental NLDs agree with each other.

The constant-temperature regime, characterized by the pair-breaking process, continues at least up to the neutron separation energy or higher, where the temperature begins to rise and the Fermi gas behavior of nucleons sets in. As shown in Fig. 6, the CT model begins to deviate quite drastically from the (p, p') data at higher excitation energies, well above the S_n value. For this reason, the BSFG model is expected to provide a more accurate description of the NLD at high excitation energies, although it is not an appropriate model at lower excitation energies. The global fit of all data with the BSFG model only indeed fails to reproduce the regime of increasing nuclear temperature between $\approx$6.5–14 MeV, especially in the vicinity of the neutron separation energy and slightly above. The composite NLD formula, introduced by Gilbert and Cameron in Ref. [54] (denoted G&C), combines the CT model at lower excitation energies and the BSFG model at higher energies and appears to be more suitable for the simultaneous description of the Oslo and (p, p') data. From the result of the fit with the composite NLD formula, the constant-temperature regime holds up to $\approx$8.5 MeV, i.e., in the vicinity of the neutron separation energy. Even though this formula reproduces the general trend and performs better than the BSFG, it is still not able to completely describe the NLD above the neutron separation limit.

Microscopic spin-dependent NLD calculations based on the Hartree-Fock-BCS method [67] deviate from both the Oslo and the (p, p') data at low and high excitation energies correspondingly (up to $\approx$6.5 and from 12.5 MeV), being higher by a factor of 2–2.5 on average. Between $\approx$6.5 and 12.5 MeV it agrees quite well with the (p, p') data. Similarly, the spin- and parity-dependent NLD calculated within the temperature-dependent Hartree-Fock-Bogolyubov approach with the Gogny force [68] follows the (p, p') data and the composite formula prediction nicely from $\approx$6.5 MeV excitation energy and above, while still being about a factor of 3 higher than the Oslo-method NLD. For the case of the total NLD, this deviation might reach up to one order of magnitude. We conclude that although microscopic models are appealing, as they should in principle grasp the underlying physics in contrast to simple analytical formulae, they are at this point

not able to describe experimental data well enough over a wide excitation-energy range.

IV. PORTER-THOMAS FLUCTUATIONS AND γ-RAY STRENGTH FUNCTIONS

The experimental GSFs extracted with the Oslo method result from averaging γ transitions over relatively wide excitation-energy windows, $\approx$4.6 for ^{120}Sn and 3.5 MeV for ^{124}Sn [region 3 in Fig. 2(c) and 2(f)]. Therefore, any variations of the strength due to PT fluctuations are expected to be strongly suppressed, lying well within the estimated error bands. As such, PT fluctuations play a minor role and have little influence on the overall shapes of the GSFs. However, to test the gBA hypothesis, it is necessary to investigate how the GSF varies as a function of excitation energy (and also, in principle, spin and parity of the initial and final states). Then, a complication arises because the action of narrowing down the averaging interval to study the GSF for different specific initial and final excitation energies will inevitably introduce larger uncertainties due to increased PT fluctuations of the partial radiative widths.

Oslo-method data have previously been used to study the shapes of the GSFs as functions of initial and final excitation energies to address the question on the validity of the gBA hypothesis [25,26,30,76]. With the exception of Ref. [26], which presents a detailed discussion and estimates of the PT fluctuations for the case of ^{64,65}Ni, the role of these fluctuations are approached mostly in a qualitative way. Due to the particularly high density of initial and accessible final states in ^{238}Np, studied in Ref. [25], reaching up to $\approx$4.3 $\times$ 10^6 states at $S_n = 5.488$ MeV, the PT fluctuations are expected to be negligible for the comparison of individual GSFs for different individual initial and final excitation energies with the Oslo-method strength. An excellent agreement of all strengths was found, and this indeed serves as a strong argument for the validity of the gBA hypothesis [25]. Such a comparison, however, is much more difficult in the case of lighter nuclei such as ^{46}Ti [30], ^{64,65}Ni [26], and ^{92}Zr [34]. For example, the density of levels at $S_n = 9.658$ MeV in ^{64}Ni is only $\approx$2.6 $\times$ 10^3 MeV^{-1}, and variations on the strengths for specific excitation energies might reach some tens of percent of the absolute value [26]. In this regard, the nuclei studied in this work present an intermediate case between the heavy ^{238}Np and relatively light ^{64,65}Ni nuclei, with the total NLDs of $\approx$2.5 $\times$ 10^5 MeV^{-1} at $S_n = 9.104$ MeV for ^{120}Sn and $\approx$8.8 $\times$ 10^4 MeV^{-1} at $S_n = 8.489$ MeV for ^{124}Sn.

To study the variation in the GSFs of ^{120,124}Sn, we follow the procedure outlined in Refs. [26,76], assuming that the fluctuations of the GSF follow a χ_ν^2 distribution with the number of degrees of freedom corresponding to the number of γ-ray transitions $n(E_\gamma)$ at a given transition energy E_γ. Relative fluctuations of the GSF are given by the ratio between the deviation σ_{PT} and average μ, or $r = \sigma_{PT}/\mu = \sqrt{2/\nu}$, of the χ_ν^2 distribution [28].

The number of transitions (i.e., the number of partial widths, or primary transitions) n can be calculated for each E_γ for specific initial and final excitation energies, allowing to study how the fluctuations evolve with γ-ray and excitation
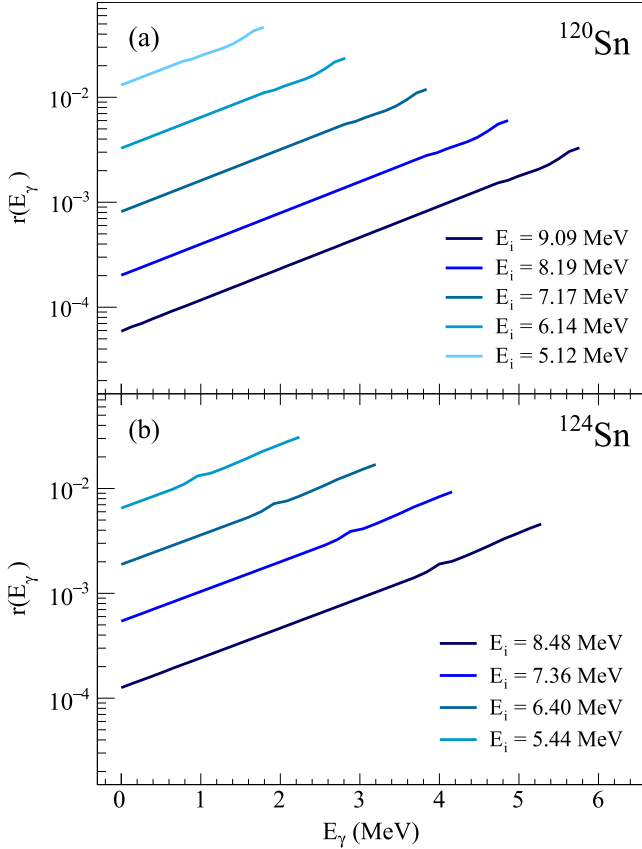
FIG. 7. Relative fluctuations of the GSF $r(E_\gamma, E_i)$ for different initial excitation energies for (a) ^{120}Sn and (b) ^{124}Sn. All initial E_i and final energies $E_i - E_\gamma$ lie within the quasicontinuum region. The excitation and γ-ray energy bins are 128 keV for ^{120}Sn and 160 keV for ^{124}Sn.

FIG. 8. Relative fluctuations of the GSF $r(E_\gamma, E_f)$ for different final excitation energies for (a) ^{120}Sn and (b) ^{124}Sn. All initial energies $E_i - E_\gamma$ lie within the quasicontinuum region. The same applies to the different final energies E_f represented by blue lines. The red dashed line corresponds to the ground state as the final state, the green one corresponds to the first excited 2^+ state as the final state, and the yellow one corresponds to several discrete final low-lying states. The excitation-energy bins and γ-ray energy bins are 128 keV for ^{120}Sn and 160 keV for ^{124}Sn.

energy. We adopt the following relation from Refs. [26,76] to estimate the number of transitions $n(E_\gamma, E_i)$:

$$n(E_\gamma, E_i) = \Delta E^2 \sum_{J\pi} \sum_{L=-1}^{1} \sum_{\pi'} \rho(E_i, J, \pi)$$
$$\times \rho(E_i - E_\gamma, J + L, \pi'), \quad (14)$$

where we consider dipole transitions only, and ΔE is the excitation-energy bin width. By substituting E_i with E_f and $E_i - E_\gamma$ with $E_f + E_\gamma$, it is also possible to obtain the number of transitions as a function of E_γ and final excitation energy.

We limit ourselves to two types of cases in estimating the GSF fluctuations. First, we study the case when the initial E_i and final E_f excitation energies both lie within the quasicontinuum region, for which the spin distribution of Eq. (5) is considered applicable. This allows us to apply this distribution to account for the spin dependence of the NLDs in Eq. (14). Furthermore, it is assumed again an equal contribution of positive- and negative-parity states within the quasicontinuum. We also require a minimum level density of 10 levels per bin, corresponding to $E_f \approx 3.2$ MeV in ^{120}Sn and $E_f \approx 3.0$ MeV in ^{124}Sn. Note that this is a rather crude estimate that should be taken with some caution. However, since we want
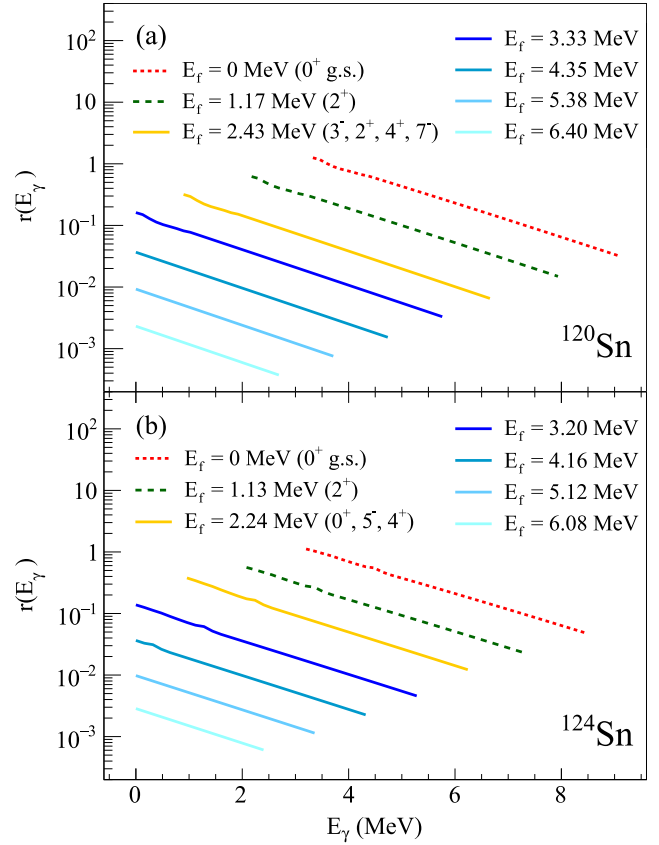
to obtain an approximate magnitude of the fluctuations, small deviations from the spin distribution formula are not expected to impact the results. Second, we consider initial excited states within the quasicontinuum and final states with known parities and spins within the discrete region. Here, the level density at the final excitation energy can be calculated directly using the known states from Ref. [51].

Figure 7 shows the relative GSF fluctuations $r(E_\gamma, E_i) = \sqrt{2/n(E_\gamma, E_i)}$ as functions of E_γ for transitions from different initial excitation-energy bins within the quasicontinuum for ^{120}Sn and ^{124}Sn. The data are shown for $E_f \geqslant 3.2$ MeV for ^{120}Sn and $E_f \geqslant 3.0$ MeV for ^{124}Sn, so that the final excitation energies of the included transitions lie within the quasicontinuum. The experimental level densities were used for the calculation. Similar to the results for ^{64,65}Ni [26], the fluctuations increase exponentially with γ-ray energy for a given E_i, as well as from the lowest to the highest initial excitation energy at a given E_γ. This behavior can easily be explained by the decreasing number of possible transitions for

consecutively lower excitation energies, given the exponentially decreasing density of accessible levels.

The magnitudes of the fluctuations in both nuclei are quite similar due to the similar values of the total NLDs, and all minor differences stem primarily from a slight difference in the bin width. At the neutron separation energy, fluctuations in both nuclei range from $\approx 10^{-2}$ to 4–$5 \times 10^{-1}\%$, while for the lower excitation energy they reach up to ≈ 3–6%. Fluctuations of these orders of magnitude are indeed expected for the relatively heavy ^{120,124}Sn nuclei. For example, based on the NLD of ^{64}Ni [26] and ^{120}Sn, the number of transitions at $E_i \approx 7.7$ MeV at $E_\gamma \approx 2.3$ MeV in ^{120}Sn is roughly a factor of 1000 larger than in ^{64}Ni, which indeed yields larger fluctuations in ^{64}Ni by approximately a factor of 30.

The relative GSF fluctuations calculated from the transitions to specific final excitation energies demonstrate the opposite trend, exponentially decreasing with γ-ray energies, as shown in Fig. 8. These trends are displayed with an approximately equal spacing for several final excitation energy bins within the quasicontinuum, as well as the bins containing the ground state, the first excited state, and several known low-lying excited states. In contrast with the lowest initial excitation energies, fluctuations at final excitation energies below $E_f \approx 3$ MeV reach up to tens of percent and might become a considerable contribution to the total uncertainty of the GSF.

The estimates of the PT fluctuations can be further put into the context of testing the gBA hypothesis for ^{120,124}Sn. By analogy with the ^{238}Np results from Ref. [25], the experimental data obtained for ^{120,124}Sn can be readily used to test whether the transmission coefficients, and, therefore, the GSFs, are dependent on the initial and final excitation energies. Equation (1) can be rewritten in the form [25]

$$P(E_\gamma, E_i)N(E_i) = \mathcal{T}(E_\gamma)\rho(E_i - E_\gamma), \quad (15)$$

where we introduce an additional energy-dependent factor $N(E_i)$ given by

$$N(E_i) = \frac{\int_0^{E_i} \mathcal{T}(E_\gamma)\rho(E_i - E_\gamma)dE_\gamma}{\int_0^{E_i} P(E_\gamma, E_i)dE_\gamma}. \quad (16)$$

Here, we make use of the transmission coefficient extracted from the Oslo method, and hence averaged over a wide range of excitation energies. We can deduce the transmission coefficient as a function of excitation energy and γ energy through

$$\mathcal{T}(E_\gamma, E_i) = \frac{P(E_\gamma, E_i)N(E_i)}{\rho(E_i - E_\gamma)}. \quad (17)$$

A similar relation can be obtained for the final excitation energy by substituting E_i with $E_f + E_\gamma$.

The GSFs for several initial excitation energies in the case of ^{120}Sn were previously published in Ref. [15], where they were compared with the strength extracted with the Oslo method. In this work, we present the comparison of the individual GSFs for different initial and final excitation energy bins for both ^{120}Sn and ^{124}Sn with the corresponding Oslo-method results. Individual strengths are shown together with the error band due to the statistical uncertainty propa-

gated through the method, denoted by statistical for short. As the Oslo-method GSF is an averaged strength with heavily suppressed PT fluctuations, it is shown with the total error band as well as additional error bars, denoting the expected PT fluctuations, or rather expected deviations of the individual strengths due to PT fluctuations. The latter is essential to assess whether there is an agreement or not between the strengths extracted for various excitation-energy bins and the Oslo-method strengths.

The results for ^{120}Sn at four initial excitation energies are shown in the upper row of Fig. 9. The dark-gray shaded areas indicate regions of potential infinite fluctuations due to the expected zero values of the NLD at the final excitation energies in the energy gaps between the first few discrete states. As can be seen from Fig. 4, the experimental NLD has small nonzero values between the ground state and the first and second excited states at ≈ 1.171 and 1.875 MeV due to the experimental resolution and the presence of some residual counts in the raw matrix after the background subtraction. The analysis applied to each individual excitation energy E_i generates a continuous data set for the GSF from the highest possible γ-ray energy at $E_\gamma = E_i$ downward to γ-ray energies below 2 MeV shown for ^{120}Sn in Figs. 9(a)–(d). The GSF values in the dark-gray region at higher gamma energies belong to hypothetical primary γ-ray transitions in the energy range between the ground state and 1.171 MeV, while the dark-gray region at lower energies belongs to decays into the energy range from 1.171 to 1.875 MeV. However, it should be mentioned that direct gamma decays to those final excitation energy regions are physically not possible and that the corresponding data points are artifacts of the continuous analysis. It is, however, interesting to observe that the PT fluctuation analysis reveals those regions by unusually large PT fluctuations

In case of fixed initial excitation energies, light-gray shaded areas correspond to energy bins where the fluctuations cannot be estimated, either due to $E_\gamma > E_i$ or unambiguous spins of some final excited states. In the latter case it is no longer possible to define what spins of initial states within the quasicontinuum yielding dipole transitions must be included to the sum in Eq. (14). For the rest of the experimental points, the fluctuations were estimated and shown in Fig. 9 as vertical error bars. The values of these errors exceed or are of the same magnitude as the statistical uncertainties for high E_γ for all of the presented cases. For the highest initial excitation energies in Fig. 9, $E_i = 7.74$ and 7.10 MeV, they become increasingly suppressed, as compared with the statistical errors, by roughly a factor of 10 at $E_\gamma \approx 4.5$ MeV, gradually increasing to $\approx 10^2$ toward $E_\gamma \approx 1$ MeV. For lower initial excitation energies, this factors are of order 1 and 10. Except for the strong deviations in the areas with expected large fluctuations (dark-gray areas), all strengths are in fairly good agreement with the Oslo-method result within its error band.

Similar results with an excitation energy bin width of 160 keV are shown for ^{124}Sn in the upper row of Fig. 10. Since the range of populated spins might be limited in this case, using the total NLD provides a lower estimate of the PT fluctuations, and they might be slightly larger than shown in the figure. By analogy with the case of ^{120}Sn, the GSFs for different initial
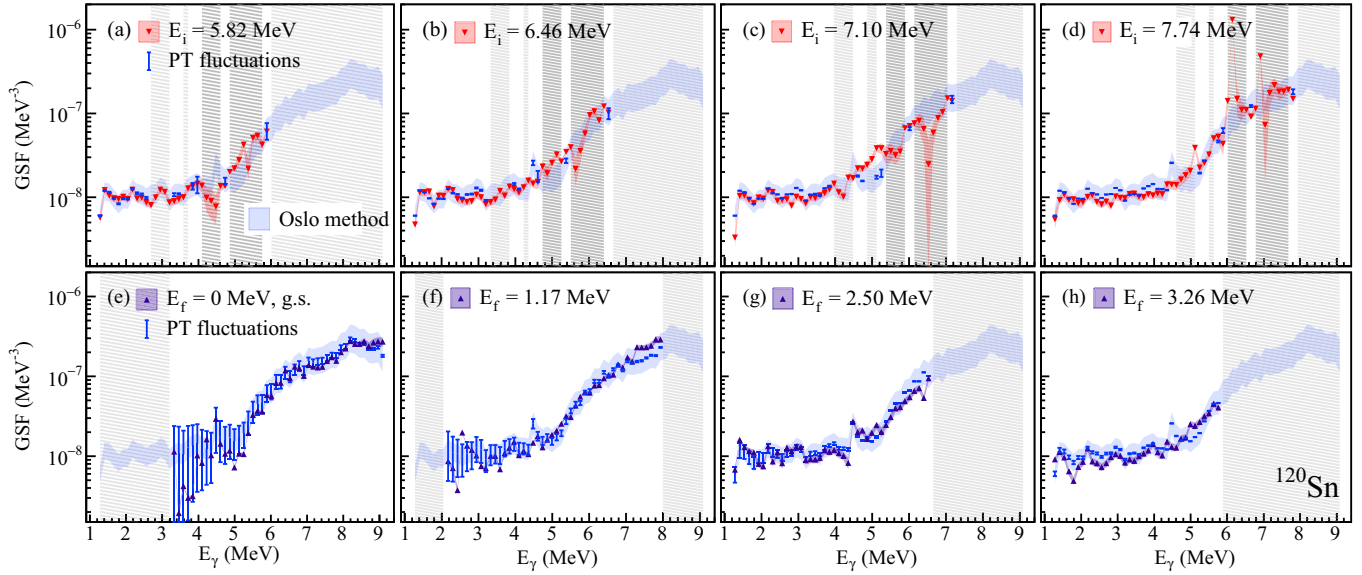
FIG. 9. GSFs for ^{120}Sn at initial excitation energies (a) 5.82 MeV, (b) 6.46 MeV, (c) 7.10 MeV, (d) 7.74 MeV and final excitation energies (e) ground state, (f) first excited state, (g) 2.50 MeV, (h) 3.26 MeV compared with the Oslo method strength (blue shaded band). For each strength the statistical error band is shown together with the error due to the PT fluctuations. Dark gray regions correspond to the areas of expected infinite PT fluctuations, light gray area marks energies for which the fluctuations of the strength were not determined. The γ-ray and excitation energy bin widths are both 128 keV.

excitation energies are in rather good agreement with the Oslo-method strength within the shown error bands and areas of expected finite PT fluctuations. These results for both the ^{120,124}Sn isotopes further support the GSF being independent of the initial excitation energy, in accordance with the gBA hypothesis. At lower excitation energies, the uncertainty due to PT fluctuations is expected to gradually outweigh the sta-

tistical error bar. This effect becomes especially apparent for the GSFs extracted for specific final excitation-energy bins. The GSF for the ground state and the first excited state at 1.171 MeV in ^{120}Sn are demonstrated in comparison with the Oslo-method GSF in Figs. 9(e) and 9(f). The data are shown for $E_f + E_\gamma \geqslant 3.2$ MeV. The area below this energy and the area corresponding to $E_f + E_\gamma > S_n$ are shaded. The
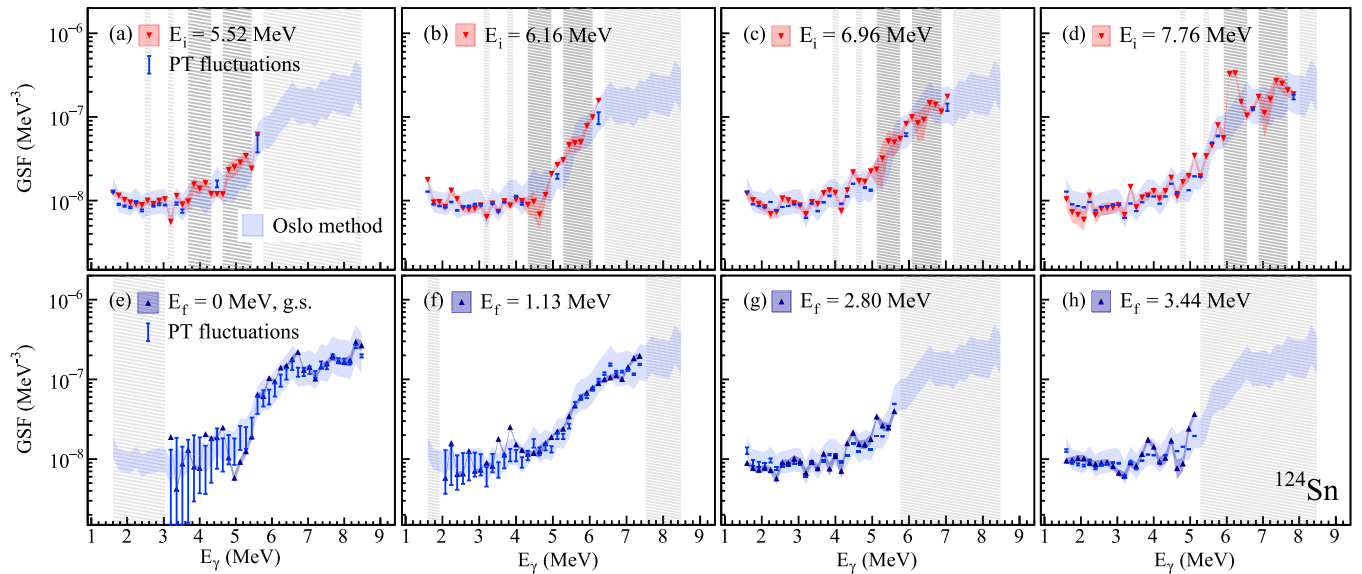

FIG. 10. GSFs for ^{124}Sn at initial excitation energies (a) 5.52 MeV, (b) 6.16 MeV, (c) 6.96 MeV, (d) 7.76 MeV and final excitation energies (e) ground state, (f) first excited state, (g) 2.80 MeV, (h) 3.44 MeV compared with the Oslo method strength (blue shaded band). For each strength the statistical error band is shown together with the error due to the PT fluctuations. Dark gray regions correspond to the areas of expected infinite PT fluctuations, light gray area marks energies for which the fluctuations of the strength were not determined. The γ-ray and excitation energy bin widths are both 160 keV.
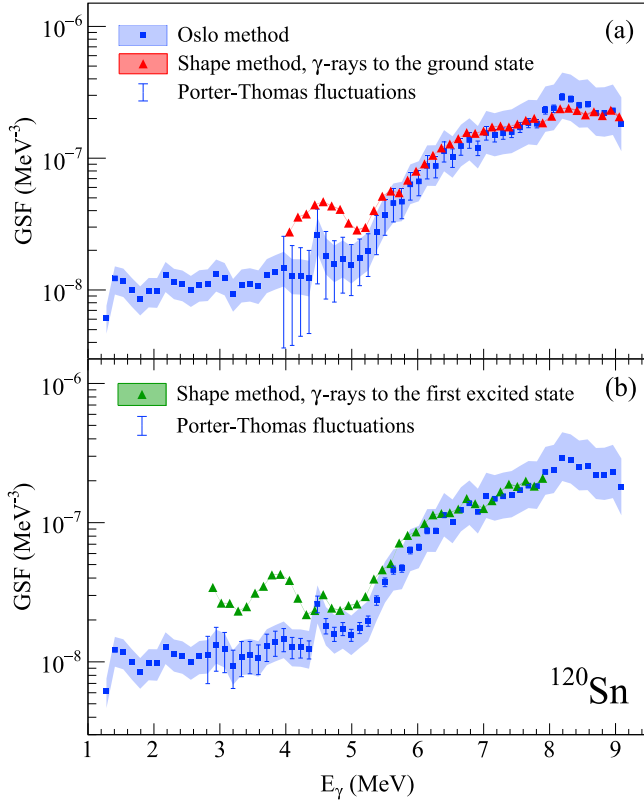
FIG. 11. Shape-method GSFs of ^{120}Sn for γ rays (a) feeding the ground state and (b) the first excited state compared with the Oslo method result (blue band). The Shape method results are shown together with the statistical error propagated through the method, shown as a band (significantly smaller in width than the size of the data points), and the error bars due to the PT fluctuations. The Oslo method GSF is shown with the total (stat.+syst.) error band.

fluctuations of the ground-state strength are large below ≈ 5 MeV, where they reach $\approx 40\%$ of the absolute value. Between $E_\gamma \approx 3.3$ and 5 MeV, the fluctuations of the strength are $\approx 60\%$ on average and reach up to 90% toward the lowest γ energy. The latter case corresponds to only 1–3 possible dipole transitions at this E_γ. Applying the χ_ν^2 distribution for fluctuations of so few transition widths is not justified because it is valid solely in the statistical regime. Thus, the estimation procedure should be taken with great care when $r(E_\gamma)$ approaches values of 1.

Below ≈ 5 MeV, some strong deviations of the ground-state strength from the Oslo-method result are observed. Besides the strong PT fluctuations at these γ-ray energies, there might be some quadrupole transitions that cause methodical problems in this region. As the extraction of the GSF relies on dipole radiation being dominant, quadrupole transitions from numerous low-lying 2^+ states to the ground state could distort the strength as the factor of E_γ^5 should be used instead of E_γ^3. At higher γ-ray energies, the ground-state strength reproduces the slope of the Oslo method strength, lying well within the Oslo-method error band. Similar effects can be seen for the ^{124}Sn [in Fig. 10(e), $E_f + E_\gamma \geqslant 3.0$ MeV], where the fluctuations were again estimated with the total
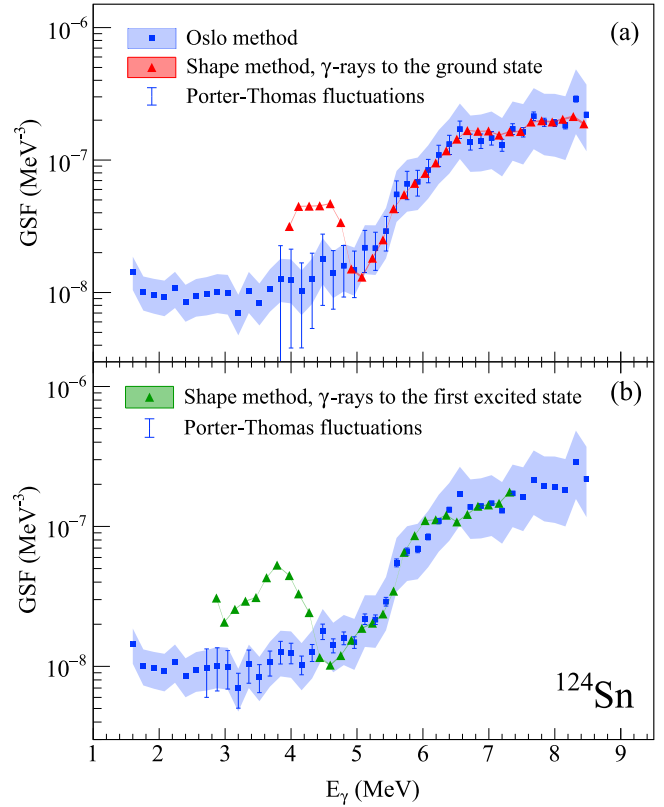

FIG. 12. Same as Fig. 11, but for ^{124}Sn.

NLD and, therefore, should be considered lower-limit estimates.

High PT fluctuations of 10%–60% are observed also for the GSF to the first excited states in both isotopes, as shown in Figs. 9(f) and 10(f). For both nuclei these strengths reproduce the slopes of the Oslo method GSF in the region between 5 and 6.5 MeV quite well. For the higher final excitation energies, the fluctuations of the strengths are at most by one order of magnitude larger than the statistical uncertainties at low γ-ray energies, while at higher γ-ray energies they are by one order of magnitude smaller. For these strengths it is challenging to argue for an *exact* agreement with the Oslo method result. If taking a general agreement of the strengths within the error bars as a criterion, it can be possible to claim an overall independence of the strengths of final excitation energy for ^{120,124}Sn.

As the PT fluctuations become more significant at lower final excitation energies, they are expected to make a considerable contribution to the total error band of the Shape-method results. In Figs. 11 and 12, the GSFs for γ rays feeding the ground state and the first excited 2^+ state are shown for ^{120}Sn and ^{124}Sn, respectively, together with the corresponding Oslo-method strengths. To test what a reasonable minimum excitation-energy limit would be for the application of the Shape method, we choose $E_i = 4$ MeV in both nuclei as a starting point. The Shape method results are presented with their statistical uncertainties, propagated through the unfolding and the first generation method. The Oslo-method strength is shown with the total error band and

the expected variations of the corresponding ground-state or first-excited-state strengths due to the PT fluctuations. Both of these strengths for ^{120}Sn follow the shape of the Oslo-method strength quite well from the neutron separation energy and down to ≈ 5.5–6 MeV. Here, they start deviating gradually for lower γ-ray energies. In ^{124}Sn, the agreement between the GSFs is quite good from $E_\gamma \approx 5$ MeV and higher.

Remarkably, the ground-state strengths and the first-excited-state strengths for ^{120,124}Sn demonstrate quite significant enhancements between 3 and 5 MeV, which cannot be attributed to any real features of the strength. Moreover, there are no noticeable structures on the diagonals at $4 < E_i < 5$ MeV that might have induced these features. No similar effect was previously reported for even-even isotopes [34]. The appearance of these bumps might partly arise from the failure of the internal normalization technique at relatively low γ-ray energies where large fluctuations of the strengths are observed. The fluctuations of the ground-state strength in ^{120,124}Sn range from $\approx 30\%$ to 70% below 5.5 MeV, and from $\approx 15\%$–35% below 4.3 MeV for the GSF corresponding to the first excited state. Since the pairs of data points for the two diagonals at each excitation energy are normalized internally to each other (see Ref. [34]), large variations of the strengths could lead to an erratic internal normalization at relatively low γ-ray energies. When reaching densities of 1×10^3–2×10^3 levels per MeV, the distorting effect due to the PT fluctuations becomes smaller, and the Shape-method results follow nicely the Oslo-method strength in both cases. This potential problem should be considered in future studies performed with the Shape method. When approaching the neutron separation energies in ^{120,124}Sn, fluctuations of the strengths do not exceed a few percent, which is comparable to the statistical error bands shown in Figs. 11 and 12, while for the rest of the energy range, the PT fluctuations make a noticeable contribution to the uncertainties.

Additional explanations for the smooth bump-like structures observed in the GSF might come from the failure of some basic assumptions in the Shape method such as a symmetric parity distribution of the initial nuclear levels, pure dipole transitions of the involved γ-ray decays, and a spin-independent excitation probability in the $(p, p'\gamma)$ reaction at 16 MeV. The lower the excitation energy, the less the assumption of a symmetric parity distribution might be justified, especially in the magic Sn isotopes, so this may lead to deviations when using the Shape method at excitation energies below 5–6 MeV. Furthermore, similar to the discussion of the Oslo method, potential contributions of quadrupole transitions can distort the analysis procedure due to the different energy factor of E_γ^5 as compared with E_γ^3 for dipole transitions. In particular, the excited 2^+ states will most likely decay (on average) preferably to the first 2^+ instead to the ground state. Within the Shape method, this can lead to the fact that the value of the GSF for the ground state γ decay is (on average) smaller than for the decay into the first 2^+ state. Thus the value pair in the Shape method has an increasing course towards low γ energies due to $f_{\text{to }2^+}[E_i - E_x(2^+)] > f_{\text{to g.s.}}[E_i - E_x(\text{g.s.})]$ and might explain the increasing bump-like trend of the GSF. It remains an open question as to why the deviation of the

strengths is systematically upward (always an increase) and whether the PT fluctuations, asymmetric parity distributions or the specific decay behavior of 2^+ states at low excitation energies are the main cause of the observed deviation

V. CONCLUSIONS

The nuclear level densities and γ-ray strength functions of ^{120,124}Sn were extracted using the Oslo method, and the slopes of the strengths were additionally constrained with the Shape method. The NLDs were found to be in good agreement with previously deduced NLDs for ^{116,118,122}Sn, with slight deviations primarily due to some differences in the normalization procedures. The Oslo-method NLD for 1^- states in ^{124}Sn is in fairly good agreement within the estimated error bands with the result obtained from the fluctuation analysis of high-resolution inelastic proton scattering spectra above 6 MeV. Given the model-independence of the (p, p') result, this agreement supports the choice of the spin distribution function and the spin-cutoff parameter employed in the Oslo method. The combined results covering excitation energies up to 14 MeV clearly demonstrate the transition between the constant temperature and the Fermi gas regimes at ≈ 8.5 MeV.

The experimental NLDs were used to estimate the role of the Porter-Thomas fluctuations in assessing the generalized Brink-Axel hypothesis below the neutron separation energy in ^{120,124}Sn, as well as the applicability of the Shape method. Most of the deviations of the GSFs for different initial and final excitation energies from the Oslo-method strength can be explained by strong PT fluctuations due to very few γ transitions. For the ground-state and the first excited state strengths, this effect is especially apparent, with the PT fluctuations reaching up to 90%–100% at low γ-ray energies. Despite some local discrepancies, the individual GSFs are in overall good agreement with the Oslo-method strength within the error bands, suggesting an independence of initial and final excitation energies in support of the generalized Brink-Axel hypothesis within uncertainties of the Oslo method.

Strong PT fluctuations were found to play a noticeable role in the extraction of the GSFs with the Shape method, as they might contribute to considerable deviations from the Oslo-method result at low γ-ray energies. The reliability of the Shape method applied to ^{120,124}Sn is under question for values of the NLDs below 1×10^3–2×10^3 levels per MeV, but quite satisfactory above this limit in both nuclei. Further investigations are needed to understand why the Shape method seemingly leads to an overestimate of the low-energy strength in the region where the PT fluctuations are large.

[1] S. Goriely, Phys. Lett. B **436**, 10 (1998).

[2] M. Arnould, S. Goriely, and K. Takahashi, Phys. Rep. **450**, 97 (2007).

[3] W. Hauser and H. Feshbach, Phys. Rev. **87**, 366 (1952).

[4] M. B. Chadwick, M. Herman, P. Oblozinský, M. E. Dunn, Y. Danon, A. C. Kahler, D. L. Smith, B. Pritychenko, G. Arbanas, R. Arcilla *et al.*, Nucl. Data Sheets **112**, 2887 (2011).

[5] M. Salvatores and G. Palmiotti, Prog. Part. Nucl. Phys. **66**, 144 (2011).

[6] S. Goriely, P. Dimitriou, M. Wiedeking, T. Belgya, R. Firestone, J. Kopecky, M. Krtička, V. Plujko, R. Schwengner, S. Siem *et al.*, Eur. Phys. J. A **55**, 172 (2019).

[7] M. Guttormsen, T. S. Tveter, L. Bergholt, F. Ingebretsen, and J. Rekstad, Nucl. Instrum. Methods Phys. Res., Sect. A **374**, 371 (1996).

[8] M. Guttormsen, T. Ramsøy, and J. Rekstad, Nucl. Instrum. Methods Phys. Res., Sect. A **255**, 518 (1987).

[9] A. Schiller, L. Bergholt, M. Guttormsen, E. Melby, J. Rekstad, and S. Siem, Nucl. Instrum. Methods Phys. Res., Sect. A **447**, 498 (2000).

[10] M. Wiedeking, L. A. Bernstein, M. Krticka, D. L. Bleuel, J. M. Allmond, M. S. Basunia, J. T. Harke, P. Fallon, R. B. Firestone, B. L. Goldblum, R. Hatarik, P. T. Lake, I. Y. Lee, S. R. Lesher, S. Paschalis, M. Petri, L. Phair, and N. D. Scielzo, Phys. Rev. Lett. **108**, 162503 (2012).

[11] S. Bassauer, P. von Neumann-Cosel, and A. Tamii, Phys. Rev. C **94**, 054313 (2016).

[12] D. Martin, P. von Neumann-Cosel, A. Tamii, N. Aoi, S. Bassauer, C. A. Bertulani, J. Carter, L. Donaldson, H. Fujita, Y. Fujita *et al.*, Phys. Rev. Lett. **119**, 182503 (2017).

[13] D. M. Brink, Ph.D. thesis, Oxford University, 1955 (unpublished).

[14] P. Axel, Phys. Rev. **126**, 671 (1962).

[15] M. Markova, P. von Neumann-Cosel, A. C. Larsen, S. Bassauer, A. Görgen, M. Guttormsen, F. L. Bello Garrote, H. C. Berg, M. M. Bjørøen, T. Dahl-Jacobsen *et al.*, Phys. Rev. Lett. **127**, 182501 (2021).

[16] B. A. Brown and A. C. Larsen, Phys. Rev. Lett. **113**, 252502 (2014).

[17] G. W. Misch, G. M. Fuller, and B. A. Brown, Phys. Rev. C **90**, 065808 (2014).

[18] C. W. Johnson, Phys. Lett. B **750**, 72 (2015).

[19] N. Q. Hung, N. D. Dang, and L. T. Q. Huong, Phys. Rev. Lett. **118**, 022502 (2017).

[20] R. A. Herrera, C. W. Johnson, and G. M. Fuller, Phys. Rev. C **105**, 015801 (2022).

[21] C. T. Angell, S. L. Hammond, H. J. Karwowski, J. H. Kelley, M. Krtička, E. Kwan, A. Makinaga, and G. Rusev, Phys. Rev. C **86**, 051302(R) (2012).

[22] J. Isaak, D. Savran, M. Krtička, M. W. Ahmed, J. Beller, E. Fiori, J. Glorius, J. H. Kelley, B. Löher, N. Pietralla *et al.*, Phys. Lett. B **727**, 361 (2013).

[23] L. Netterdon, A. Endres, S. Goriely, J. Mayer, P. Scholz, M. Spieker, and A. Zilges, Phys. Lett. B **744**, 358 (2015).

[24] J. Isaak, D. Savran, B. Löher, T. Beck, M. Bhike, U. Gayer, Krishichayan, N. Pietralla, M. Scheck, W. Tornow *et al.*, Phys. Lett. B **788**, 225 (2019).

[25] M. Guttormsen, A. C. Larsen, A. Görgen, T. Renstrøm, S. Siem, T. G. Tornyi, and G. M. Tveten, Phys. Rev. Lett. **116**, 012502 (2016).

[26] L. C. Campo, M. Guttormsen, F. L. Garrote, T. K. Eriksen, F. Giacoppo, A. Gorgen, K. Hadynska-Klek, M. Klintefjord, A. C. Larsen, T. Renstrom, E. Sahin, S. Siem, A. Springer, T. G. Tornyi, and G. M. Tveten, Phys. Rev. C **98**, 054303 (2018).

[27] P. Scholz, M. Guttormsen, F. Heim, A. C. Larsen, J. Mayer, D. Savran, M. Spieker, G. M. Tveten, A. V. Voinov, J. Wilhelmy, F. Zeiser, and A. Zilges, Phys. Rev. C **101**, 045806 (2020).

[28] C. E. Porter and R. G. Thomas, Phys. Rev. **104**, 483 (1956).

[29] H. A. Weidenmüller and G. E. Mitchell, Rev. Mod. Phys. **81**, 539 (2009).

[30] M. Guttormsen, A. C. Larsen, A. Bürger, A. Görgen, S. Harissopulos, M. Kmiecik, T. Konstantinopoulos, M. Krtička, A. Lagoyannis, T. Lönnroth *et al.*, Phys. Rev. C **83**, 014312 (2011).

[31] A. C. Larsen, A. Spyrou, S. Liddick, and M. Guttormsen, Prog. Part. Nucl. Phys. **107**, 69 (2019).

[32] A. Spyrou, S. N. Liddick, A. C. Larsen, M. Guttormsen, K. Cooper, A. C. Dombos, D. J. Morrissey, F. Naqvi, G. Perdikakis, S. J. Quinn *et al.*, Phys. Rev. Lett. **113**, 232502 (2014).

[33] V. W. Ingeberg, S. Siem, M. Wiedeking, K. Sieja, D. L. Bleuel, C. P. Brits, T. D. Bucher, T. S. Dinoko, J. L. Easton, A. Görgen *et al.*, Eur. Phys. J. A **56**, 68 (2020).

[34] M. Wiedeking, M. Guttormsen, A. C. Larsen, F. Zeiser, A. Görgen, S. N. Liddick, D. Mücher, S. Siem, and A. Spyrou, Phys. Rev. C **104**, 014311 (2021).

[35] U. Agvaanluvsan, A. C. Larsen, M. Guttormsen, R. Chankova, G. E. Mitchell, A. Schiller, S. Siem, and A. Voinov, Phys. Rev. C **79**, 014320 (2009).

[36] H. K. Toft, A. C. Larsen, U. Agvaanluvsan, A. Bürger, M. Guttormsen, G. E. Mitchell, H. T. Nyhus, A. Schiller, S. Siem, N. U. H. Syed, and A. Voinov, Phys. Rev. C **81**, 064311 (2010).

[37] H. K. Toft, A. C. Larsen, A. Bürger, M. Guttormsen, A. Görgen, H. T. Nyhus, T. Renstrøm, S. Siem, G. M. Tveten, and A. Voinov, Phys. Rev. C **83**, 044320 (2011).

[38] F. Zeiser, G. M. Tveten, F. L. B. Garrote, M. Guttormsen, A. C. Larsen, V. W. Ingeberg, A. Görgen, and S. Siem, Nucl. Instrum. Methods Phys. Res., Sect. A **985**, 164678 (2021).

[39] M. Guttormsen, A. Bürger, T. E. Hansen, and N. Lietaer, Nucl. Instrum. Methods Phys. Res., Sect. A **648**, 168 (2011).

[40] M. Guttormsen, A. Ataç, K. Klungland, S. Messelt, T. Ramsøy, J. Rekstad, T. Tveter, and Z. Zelazny, Nucl. Phys. A **531**, 370 (1991).

[41] S. Riboldi, F. Camera, N. Blasi, S. Brambilla, C. Boiano, F. C. Crespi, A. Giaz, B. Million, R. Nicolini, L. Pellegri, and O. Wieland, in *2011 IEEE Nuclear Science Symposium Conference Record* (IEEE, Piscataway, NJ, 2011), pp. 776–778.

[42] Pixie-16 User Manual, Version 3.06, XIA (2019).

[43] A. Giaz, L. Pellegri, S. Riboldi, F. Camera, N. Blasi, C. Boiano, A. Bracco, S. Brambilla, S. Ceruti, S. Coelli *et al.*, Nucl. Instrum. Methods Phys. Res., Sect. A **729**, 910 (2013).

[44] F. Zeiser and G. M. Tveten, oslocyclotronlab/ocl_geant4: Geant4 model of OSCAR (2018).

[45] S. Agostinelli, J. Allison, K. Amako, J. Apostolakis, H. Araujo, P. Arce, M. Asai, D. Axen, S. Banerjee, G. Barrand *et al.*, Nucl. Instrum. Methods Phys. Res., Sect. A **506**, 250 (2003).

[46] J. Allison, K. Amako, J. Apostolakis, H. Araujo, P. Arce Dubois, M. Asai, G. Barrand, R. Capra, S. Chauvie, R. Chytracek *et al.*, IEEE Trans. Nucl. Sci. **53**, 270 (2006).

[47] J. Allison, K. Amako, J. Apostolakis, P. Arce, M. Asai, T. Aso, E. Bagli, A. Bagulya, S. Banerjee, G. Barrand *et al.*, Nucl. Instrum. Methods Phys. Res., Sect. A **835**, 186 (2016).

[48] A. C. Larsen, M. Guttormsen, M. Krtička, E. Běták, A. Bürger, A. Görgen, H. T. Nyhus, J. Rekstad, A. Schiller, S. Siem *et al.*, Phys. Rev. C **83**, 034315 (2011).

[49] J. E. Midtbø, Ph.D. thesis, University of Oslo, 2019 (unpublished).

[50] J. E. Midtbø, F. Zeiser, E. Lima, A.-C. Larsen, G. M. Tveten, M. Guttormsen, F. L. Bello Garrote, A. Kvellestad, and T. Renstrøm, Comput. Phys. Commun. **262**, 107795 (2021).

[51] Data taken from the ENSDF database of the NNDC online data service, https://www.nndc.bnl.gov/ensdf/. Last accessed: January 19, 2022.

[52] S. Mughabghab, *Atlas of Neutron Resonances*, 6th ed. (Elsevier, Amsterdam, 2018).

[53] T. Ericson and V. Strutinski, Nucl. Phys. **8**, 284 (1958).

[54] A. Gilbert and A. G. W. Cameron, Can. J. Phys. **43**, 1446 (1965).

[55] T. von Egidy and D. Bucurescu, Phys. Rev. C **72**, 044311 (2005).

[56] T. Ericson, Nucl. Phys. **11**, 481 (1959).

[57] G. Audi, A. Wapstra, and C. Thibault, Nucl. Phys. A **729**, 337 (2003).

[58] J. Dobaczewski, P. Magierski, W. Nazarewicz, W. Satuła, and Z. Szymański, Phys. Rev. C **63**, 024308 (2001).

[59] J. Kopecky and M. Uhl, Phys. Rev. C **41**, 1941 (1990).

[60] *Handbook for Calculations of Nuclear Reaction Data, RIPL-2*, TECDOC Series No. 1506 (International Atomic Energy Agency, Vienna, 2006).

[61] R. Capote, M. Herman, P. Obložinský, P. Young, S. Goriely, T. Belgya, A. Ignatyuk, A. Koning, S. Hilaire, V. Plujko *et al.*, Nucl. Data Sheets **110**, 3107 (2009).

[62] F. Zeiser, G. Potel, G. M. Tveten, A. C. Larsen, M. Guttormsen, T. A. Laplace, S. Siem, D. L. Bleuel, B. L. Goldblum, L. A. Bernstein *et al.*, Springer Proc. Phys. **254**, 195 (2020).

[63] F. Zeiser, G. M. Tveten, G. Potel, A. C. Larsen, M. Guttormsen, T. A. Laplace, S. Siem, D. L. Bleuel, B. L. Goldblum, L. A. Bernstein *et al.*, Phys. Rev. C **100**, 024305 (2019).

[64] F. Pogliano, A. C. Larsen, F. L. Bello Garrote, M. M. Bjørøen, T. K. Eriksen, D. Gjestvang, A. Görgen, M. Guttormsen, K. C. W. Li, M. Markova *et al.*, Phys. Rev. C **106**, 015804 (2022).

[65] S. Bassauer, P. von Neumann-Cosel, P.-G. Reinhard, A. Tamii, S. Adachi, C. A. Bertulani, P. Y. Chan, A. D'Alessio, H. Fujioka, H. Fujita *et al.*, Phys. Rev. C **102**, 034327 (2020).

[66] M. Guttormsen, M. Aiche, F. L. Bello Garrote, L. A. Bernstein, D. L. Bleuel, Y. Byun, Q. Ducasse, T. K. Eriksen, F. Giacoppo, A. Görgen *et al.*, Eur. Phys. J. A **51**, 170 (2015).

[67] S. Goriely, F. Tondeur, and J. M. Pearson, Atom. Data Nucl. Data Tables **77**, 311 (2001).

[68] S. Hilaire, M. Girod, S. Goriely, and A. J. Koning, Phys. Rev. C **86**, 064317 (2012).

[69] M. Guttormsen, A. Bagheri, R. Chankova, J. Rekstad, S. Siem, A. Schiller, and A. Voinov, Phys. Rev. C **68**, 064306 (2003).

[70] A. Schiller, E. Algin, L. A. Bernstein, P. E. Garrett, M. Guttormsen, M. Hjorth-Jensen, C. W. Johnson, G. E. Mitchell, J. Rekstad, S. Siem *et al.*, Phys. Rev. C **68**, 054326 (2003).

[71] P. O. Hansen, B. Jonson, and A. Richter, Nucl. Phys. A **518**, 13 (1990).

[72] I. Poltoratska, R. W. Fearick, A. M. Krumbholz, E. Litvinova, H. Matsubara, P. von Neumann-Cosel, V. Y. Ponomarev, A. Richter, and A. Tamii, Phys. Rev. C **89**, 054322 (2014).

[73] S. Bassauer, Ph.D. thesis, Universität Darmstadt, 2019 (unpublished).

[74] S. J. Lokitz, G. E. Mitchell, and J. F. Shriner, Jr., Phys. Lett. B **599**, 223 (2004).

[75] Y. Kalmykov, C. Özen, K. Langanke, G. Martínez-Pinedo, P. von Neumann-Cosel, and A. Richter, Phys. Rev. Lett. **99**, 202502 (2007).

[76] M. Guttormsen, A.-C. Larsen, A. Görgen, T. Renstrøm, S. Siem, T. Tornyi, and G. M. Tveten, PoS **INPC2016**, 062 (2017).

Paper III

Nuclear level densities and γ-ray strength functions of ^{111,112,113}Sn isotopes studied with the Oslo method

III

Nuclear level densities and γ-ray strength functions of ^{111,112,113}Sn isotopes studied with the Oslo method

M. Markova[1,*] A. C. Larsen[1,†] G. M. Tveten[1,2] P. von Neumann-Cosel[3] T. K. Eriksen[1]
F. L. Bello Garrote[1] L. Crespo Campo[1] F. Giacoppo[4] A. Görgen[1] M. Guttormsen[1]
K. Hadynska-Klek[5] M. Klintefjord[1] T. Renstrøm[1,2] E. Sahin[1] S. Siem[1] and T. G. Tornyi[1]

[1]*Department of Physics, University of Oslo, N-0316 Oslo, Norway*
[2]*Expert Analytics AS, N-0179 Oslo, Norway*
[3]*Institut für Kernphysik, Technische Universität Darmstadt, D-64289 Darmstadt, Germany*
[4]*GSI Helmholtzzentrum für Schwerionenforschung, Planckstraße 1, 64291 Darmstadt, Germany*
[5]*Heavy Ion Laboratory, University of Warsaw, Ludwika Pasteura 5A, 05-077 Warszawa, Poland*

The ^{111,112,113}Sn isotopes have been studied with $(p, d\gamma)$, $(p, p'\gamma)$, and $(d, p\gamma)$ reactions to extract the nuclear level densities (NLDs) and γ-ray strength functions (GSFs) of these nuclei below the neutron separation energy by means of the Oslo method. The experimental NLDs for all three nuclei demonstrate a trend compatible with the constant-temperature model below the neutron separation energy while also being in good agreement with the NLDs of neighboring Sn isotopes, obtained previously with the Oslo-type and neutron evaporation experiments. The extracted microcanonical entropies yield $\approx 1.5\ k_B$ entropy of a valence neutron in both ^{111}Sn and ^{113}Sn. Moreover, the deduced microcanonical temperatures indeed suggest a clear constant-temperature behavior above ≈ 3 MeV in ^{111,113}Sn and above ≈ 4.5 MeV in ^{112}Sn. We observe signatures for the first broken neutron pairs between 2 and 4 MeV in all three nuclei. The GSFs obtained with the Oslo method are found to be in good agreement below the neutron threshold with the strengths of ^{112,114}Sn extracted in the (p, p') Coulomb excitation experiments.

I. INTRODUCTION

The statistical approach to the description of excited nuclei has always been an integral part of reaction theory since its first introduction and application in 1952 by Hauser and Feshbach [1]. This remains true today, and the statistical model has grown into an indispensable tool for modeling nuclear reactions for astrophysics [2], reactor design and waste transmutation [3,4], and medical isotope production [5]. Two key inputs needed for the statistical-model calculations are the nuclear level density (NLD) and, in the case of reactions involving photons, the γ-ray strength function (GSF). The NLD $\rho(E_x)$ provides a measure of a number of quantum-mechanical levels available at a given excitation energy E_x, whereas the GSF $f(E_\gamma)$ characterizes an average, reduced γ-transition probability as a function of the γ-ray energy E_γ. Besides their importance for reaction cross sections and rate estimations, both of these average nuclear characteristics provide a critical insight into nuclei as complex many-body systems and into their structure and decay properties in the quasicontinuum and continuum excitation energy regimes.

At relatively low excitation energies, within the discrete region, the NLD can be straightforwardly found through counting known discrete levels (e.g., available in compilations such as those provided in Ref. [6]) with conventional spectroscopy. After the onset of Cooper pair breaking at higher excitation energies, the NLD increases exponentially, and experimental spectroscopic data tend to underestimate its values drastically. In this energy range, the experimental information on NLDs can be obtained from, for example, particle evaporation spectra [7] or by a fluctuation analysis of fine structures of giant resonances studied in high-energy light-ion reactions at extreme forward angles [8,9]. Nuclear resonance fluorescence, inelastic relativistic proton scattering, discrete resonance capture, and other experimental techniques reviewed in detail in Ref. [10] provide an access to the GSFs below and above the neutron separation energy. In this work, we make use of the Oslo method [11–13], an experimental technique where the NLD and the GSF are simultaneously extracted for excitation energies below the neutron threshold. This method has been used for addressing numerous key questions, such as the validity of the Brink-Axel hypothesis [14,15], study of thermal properties of excited nuclei [16,17], constraining the radiative neutron capture cross sections relevant for astrophysical s and r processes [18,19],[1] and more.

---

*maria.markova@fys.uio.no
†a.c.larsen@fys.uio.no

[1]Ref. [19] exploits the Oslo method combined with β-decay measurements, or the so-called β-Oslo method.

From the perspective of investigating statistical properties, Sn isotopes provide us with excellent study cases, where the Oslo-method NLDs and GSFs can be directly compared to numerous experimental results and theoretical predictions. Moreover, it becomes possible to combine these cases in a broader systematic study of statistical properties of nuclei with an increasing neutron number performed with the same method. At the moment, the NLDs and GSFs have been reported for the Oslo-type studies of ^{116,117}Sn [16,20], ^{118,119}Sn [21], ^{121,122}Sn [22], and ^{120,124}Sn [23]. The measurements for the latter two isotopes were performed with the new scintillator detector array OSCAR [24,25], currently available at the Oslo Cyclotron Laboratory (OCL).

Additional studies with the Oslo method on lighter Sn isotopes are highly desired to complete this sort of a systematic review. Constraining the statistical properties and putting them into the context of systematics for neutron-deficient Sn isotopes might also be of further interest to shed new light on the rapid proton-capture process that can take place on accreting neutron stars (e.g., Ref. [26]). This work presents the NLDs and GSFs for ^{111,112,113}Sn nuclei obtained from particle-γ coincidence data by means of the Oslo method. In Sec. II we present the details regarding the experimental setup at the OCL and some of the most important steps of the data processing. Section III covers the details of the Oslo-method implementation for the extraction of NLDs (Sec. III A) and GSFs (Sec. III B). The main results on the NLDs in ^{111,112,113}Sn and their thermal properties as well as the GSFs are presented in Secs. IV and V, respectively. Finally, the main conclusions are outlined in Sec. VI.

II. EXPERIMENTAL SETUP AND DATA PROCESSING

The ^{111,112,113}Sn isotopes were studied at the OCL in ^{112}Sn$(p, p'\gamma)^{112}$Sn, ^{112}Sn$(p, d\gamma)^{111}$Sn, and ^{112}Sn$(d, p\gamma)^{113}$Sn reactions performed on a self-supporting 99.8% enriched ^{112}Sn foil target of 4 mg/cm^2 in thickness. Proton beams with energies of 25 and 16 MeV provided by the MC-35 Scanditronix cyclotron were used to investigate ^{111}Sn and ^{112}Sn in $(p, p'\gamma)$ and $(p, d\gamma)$ reactions, respectively. Beam intensities were kept at $I \approx 1.0$–1.5 nA in both cases. The ^{113}Sn nucleus was studied with a 11.5-MeV deuteron beam with intensities of $I \approx 0.5$–0.7 nA.

The energies and angles (relative to the beam direction) of emitted particles were recorded by the silicon particle telescope SiRi [27], consisting of eight 1550-μm-thick trapezoidal-shaped back E detectors and 130-μm-thick front ΔE detectors. Each front part is additionally segmented into eight strips with $\approx 2°$ angular coverage, thus making up 64 $\Delta E-E$ combinations in total. SiRi was placed in a backward position with respect to the beam direction, covering angles from 126° to 140°. This was primarily done to enhance the contribution from compound reactions relative to direct transfer reactions while also ensuring a larger transfer of angular momentum. Each SiRi detector had an $\approx 10.5-\mu$m Al foil in front to reduce the number of δ electrons. The energy resolution of the particle spectra depends primarily on the reaction channel, the beam-spot size, the target thickness, and the intrinsic energy resolution of SiRi. For the (p, p') channel,

the full width at half maximum resolution was estimated from a Gaussian fit to elastically scattered protons to be ≈ 200 keV, while using the first excited and ground states of ^{111}Sn and ^{113}Sn in the (p, d) and (d, p) channels yields the resolutions of ≈ 320 and 300 keV, respectively.

To record γ events, the target chamber was surrounded by the scintillator detector array CACTUS [28], consisting of 28 spherically distributed $5'' \times 5''$ NaI(Tl) scintillator γ-ray detectors. All of them were shielded with conical lead collimators to reduce the Compton contribution to the γ-ray spectra and to improve the peak-to-total ratio. The total efficiency of CACTUS was measured with a ^{60}Co source to be 15.2(1)% ($E_\gamma = 1332$ keV). The energy resolution of the NaI detectors at this γ-ray energy was $\approx 6.8\%$. The signals from the back detectors of SiRi were used as triggers for the data acquisition, and the times of the NaI signals were recorded relative to the particle signals within a time window of ≈ 1 μs.

The particle spectra were calibrated to known levels in the Sn isotopes populated in all three runs, whereas the spectra obtained for a 4-mg/cm^2-thick natural Si target were used to calibrate γ spectra. The reaction channels of interest were further selected with the $\Delta E-E$ technique. The kinematics of the studied reactions were used to convert particle energies within the selected channels into the corresponding excitation energies of ^{111,112,113}Sn. By gating on the prompt time peak and subtracting background, we selected the desired particle-γ events for the further analysis. These events are presented in the form of a raw-data coincidence matrix shown in Fig. 1(a) for the case of ^{112}Sn.

The γ-ray spectra were further corrected for the response functions of the CACTUS array [12]. The Compton subtraction method incorporated in the unfolding procedure allows for preserving the statistical fluctuations of the raw spectra in the resulting unfolded spectra without introducing any artificial features. Details of the procedure are outlined in Ref. [12]. The unfolded matrix for ^{112}Sn is shown in Fig. 1(b).

To extract the NLD and the GSF from the coincidence data, the first-generation γ rays from all possible cascades, i.e., stemming directly from each given initial excitation energy bin, were singled out to form a so-called primary matrix [see Fig. 1(c)]. This was done by means of the first-generation method described in detail in Ref. [11]. This method exploits the assumption that γ-decay patterns of excited levels are independent of the way of their formation, either through a direct population in a reaction or via decays of higher-lying excited states. It is expected to hold well for comparatively high excitation energy bins below the neutron threshold [11]. The distribution of primary γ rays for each excitation energy bin is, thus, determined by subtracting a weighted sum of the spectra corresponding to the lower-lying excitation energy bins. This procedure has been shown to be quite robust and to provide reliable results [29]. The primary matrix obtained in this way serves as the main input for the Oslo method.

Prior to extracting the NLD and the GSF from the first-generation spectra, we set a minimum limit, $E_i^{\min}$, for excitation energies to ensure including the region of statistical decay only, while the upper limit is provided by the neutron separation energy S_n (the outgoing neutrons were not measured). To exclude the low γ-ray energy regions affected by
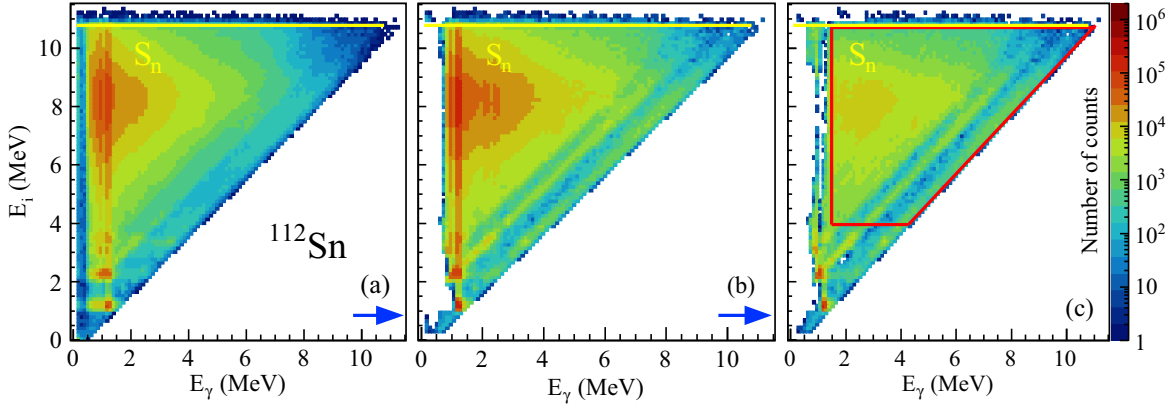
FIG. 1. Experimental raw $p-\gamma$ coincidence (a), unfolded (b), and primary (c) matrices for ^{112}Sn obtained in the $(p, p'\gamma)$ reaction. Yellow lines indicate the neutron separation energy of ^{112}Sn. Red solid lines indicate the area of the primary matrix used in the Oslo method. The bin width is 124 keV for both axes. Blue arrows mark the sequence of the analysis steps.

over- and undersubtraction of counts in the first-generation procedure, we also introduce an $E_\gamma^{\min}$ limit. The regions used in this work for the further processing are given by $3.0 \leqslant E_i \leqslant 8.2$ MeV and $E_\gamma \geqslant 1.0$ MeV for ^{111}Sn, $4.0 \leqslant E_i \leqslant 10.8$ MeV and $E_\gamma \geqslant 1.5$ MeV for ^{112}Sn, and $5.5 \leqslant E_i \leqslant 7.7$ MeV and $E_\gamma \geqslant 1.5$ MeV for ^{113}Sn.

III. ANALYSIS WITH THE OSLO METHOD

The core idea of the Oslo method lies in the decomposition of the primary matrix $P(E_\gamma, E_i)$ into the NLD $\rho_f = \rho(E_i - E_\gamma)$ and the γ-transmission coefficient $\mathcal{T}_{i \to f}$:

$$P(E_\gamma, E_i) \propto \rho_f \mathcal{T}_{i \to f}. \qquad (1)$$

This relation is based on the fact that the primary matrix is proportional to the probability of γ decay of states within each initial excitation energy bin E_i to the states of a final bin E_f with γ-ray energies of $E_\gamma = E_i - E_f$. Both Fermi's golden rule and the Hauser-Feshbach theory of statistical reactions can be used to provide the derivation of Eq. (1) (Refs. [30,31], respectively). This decomposition holds in the same range of compound states as the first generation method. The dependence of the transmission coefficient on E_i, E_f, and E_γ in Eq. (1) significantly complicates factorization of two functions, ρ_f and $\mathcal{T}$. To proceed with the decomposition, validity of the Brink-Axel hypothesis must be assumed [32,33]. The generalized, most frequently used form of this hypothesis suggests the GSF to be solely a function of γ-ray energy, i.e., to be independent of spins, parities, and excitation energies of initial and final states. This effectively removes the excitation energy dependence of the γ-transmission coefficient $\mathcal{T}_{i \to f} \to \mathcal{T}(E_\gamma)$. The applicability of this hypothesis has been previously discussed, e.g., in Refs. [14,15,29,34].

The NLDs and the γ-transmission coefficients are obtained through an iterative χ^2 procedure of fitting the experimental primary matrix (normalized to unity for each E_i) with a theoretical primary matrix given by

$$P_{\text{th}}(E_\gamma, E_i) = \frac{\mathcal{T}(E_\gamma)\rho(E_i - E_\gamma)}{\sum_{E_\gamma = E_\gamma^{\min}}^{E_i} \mathcal{T}(E_\gamma)\rho(E_i - E_\gamma)}. \qquad (2)$$

All the details of this procedure and the error propagation are described in Ref. [13]. The obtained fit provides a very good agreement with the experimental primary matrix, as demonstrated for a few selected excitation energies in the case of ^{112}Sn in Fig. 2. The theoretical function $P_{\text{th}}(E_\gamma, E_i)$ reproduces all experimental features quite well within a large interval of excitation energies below the neutron threshold.

The fit given by Eq. (2) yields the functional forms of the NLD and the γ-transmission coefficient, i.e., their excitation energy and γ-ray energy dependencies, respectively. The general solutions $\tilde{\rho}(E_i - E_\gamma)$ and $\tilde{\mathcal{T}}(E_\gamma)$ for both functions have the following forms [13]:

$$\tilde{\rho}(E_i - E_\gamma) = A\rho(E_i - E_\gamma)\exp[\alpha(E_i - E_\gamma)],$$
$$\tilde{\mathcal{T}}(E_\gamma) = B\mathcal{T}(E_\gamma)\exp(\alpha E_\gamma), \qquad (3)$$

where $\rho(E_i - E_\gamma)$ and $\mathcal{T}(E_\gamma)$ are two fixed solutions, A and B denote scaling coefficients, and α is a slope shared by
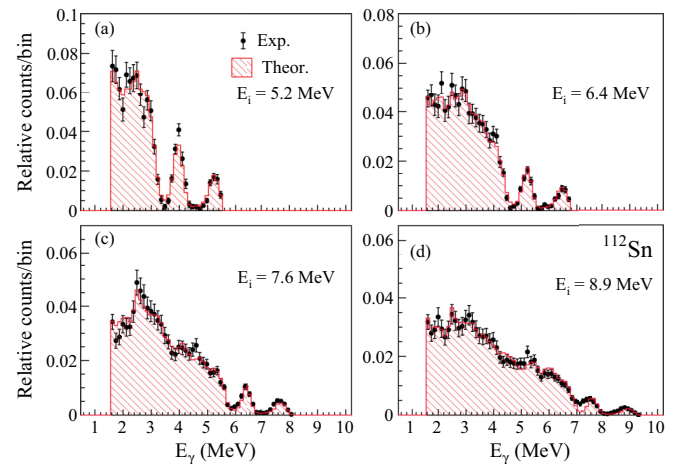

FIG. 2. Experimental primary spectra for 5.2 MeV (a), 6.4 MeV (b), 7.6 MeV (c), and 8.9 MeV (d) excitation energy bins compared to the spectra predicted with the derived level density and γ-transmission coefficient [from Eq. (1)]. The excitation energy bins are 124 keV wide.

$\rho(E_i - E_\gamma)$ and $\mathcal{T}(E_\gamma)$. To determine the physical solutions of the NLDs and γ-transmission coefficients, one must apply external experimental information and model assumptions, as discussed in the following sections.

A. Normalization of the level densities

The key ingredients to determine the absolute value and the slope of the NLD are the discrete low-lying levels and the value of the NLD at the neutron threshold, $\rho(S_n)$. The most recent compilation of discrete levels [6] was used for all three isotopes. The neutron resonance spacings D_0 for *s*-wave neutrons or D_1 for *p*-wave neutrons from neutron resonance experiments are commonly used to estimate the $\rho(S_n)$ values. Among three isotopes studied in this work, only ^{112}Sn is a stable nucleus with ground-state spin and parity $J_t^{\pi_t} = 0^+$ and can be used as a target in neutron resonance studies. For this reason, only ^{113}Sn has readily available data on the resonance spacings [35]. For the case of *s*-wave neutrons, levels of spin and parity $1/2^+$ of the residual ^{113}Sn nucleus are populated, with the partial level density

$$\frac{1}{D_0} = \frac{1}{2}\rho(S_n, J_t + 1/2). \tag{4}$$

Here, we utilize the procedure described in detail in Ref. [29]. Equal positive- and negative-parity contributions at S_n are assumed, which is shown to be a reliable assumption at sufficiently high excitation energies (see, e.g., Refs. [21,29]). The spin and excitation energy dependencies (denoted by J and E_x, respectively) of the NLD are introduced through adopting the back-shifted Fermi gas (BSFG) form of the NLD from Ref. [36], $\rho(E_x, J) = \rho(E_x)g(E_x, J)$. The spin distribution $g(E_x, J)$ is expressed as a function of the energy-dependent spin-cutoff parameter $\sigma(E_x)$ [36,37]:

$$g(E_x, J) \simeq \frac{2J + 1}{2\sigma^2(E_x)} \exp\left[-\frac{(J + 1/2)^2}{2\sigma^2(E_x)}\right]. \tag{5}$$

This allows for transforming Eq. (4) into the relation for $\rho(S_n)$:

$$\rho(S_n) = \frac{2\sigma^2}{D_0} \frac{1}{(J_t + 1)\exp\left(-\frac{(J_t+1)^2}{2\sigma^2(E_x)}\right)}. \tag{6}$$

We chose the form of the spin-cutoff parameter at S_n as given by Ref. [36]:

$$\sigma^2(S_n) = 0.0888a\sqrt{\frac{S_n - E_1}{a}}A^{2/3}, \tag{7}$$

where a and E_1 are the level-density and back-shift parameters for the BSFG model taken from global parametrizations of Ref. [38]. This choice of the spin-cutoff parameter is primarily motivated by observations made for the previously studied tin isotopes. Namely, the rigid-body form of the spin-cutoff parameter provides somewhat larger, overestimated values of $\rho(S_n)$ and, thus, the slopes of the experimental NLDs [relative to Eq. (7)]. Indeed, the effect of pairing correlations is expected to effectively reduce the moment of inertia as compared to the rigid-body model [39]. The abovementioned overestimation can be accounted for by using the shape

method [40] to constrain the true slope of the NLDs (see, e.g., Ref. [23]). The limited experimental resolution of CACTUS for ^{111,113}Sn and a too narrow range of useful shape method data for ^{112}Sn, however, prevent us from extracting reliable results with this method in these cases. Alternatively, a reduction factor can be applied to the rigid-body spin-cutoff parameter. To avoid introducing any additional parameters, we chose the form of $\sigma(S_n)$ given by Eq. (7), corresponding to $\approx 80\%$ of the rigid-body estimate. This choice is additionally supported by the previous analysis of ^{116,120,124}Sn (see Ref. [34]), where the slopes of NLDs were obtained in a similar way and the respective slopes of GSFs were found to be in excellent agreement with the Coulomb excitation data [41]. This is also accounted for by an additional 10% uncertainty we introduce for $\sigma(S_n)$ in this work.

Due to the lower limit of γ-ray energies mentioned in the previous section, the experimental NLDs do not reach the neutron threshold, but rather stop at energies ≈ 1–2 MeV below S_n. To constrain the slope of the NLD, the experimental values have to be extrapolated to $\rho(S_n)$. Here, we use the constant-temperature model [36,38,42]:

$$\rho_{\text{CT}}(E_x) = \frac{1}{T_{\text{CT}}} \exp\left(\frac{E_x - E_0}{T_{\text{CT}}}\right), \tag{8}$$

with the temperature (T_{CT}) and shift energy (E_0) treated as free parameters. This model was favored over the BSFG trend in the present cases based on the observed excitation energy dependencies and the quality of the χ^2 fit to the experimental data. When the energy gap is relatively small (≈ 1–2 MeV), the choice of the extrapolation model is not expected to play any significant role as compared to other sources of uncertainties.

As mentioned previously, both ^{110}Sn and ^{111}Sn are unstable isotopes, and no experimental information on neutron resonance spacings is available for ^{111}Sn and ^{112}Sn. Hence, the values of the NLD at S_n were obtained from the systematics available for stable Sn isotopes in the same way as described in Ref. [23] with the spin-cutoff parameter given by Eq. (7). We additionally include the abovementioned 10% error for $\sigma(E_x)$ in the total errors of $\rho(S_n)$ for each isotope in the systematics together with the experimental uncertainties of D_0.

The obtained error bands of the NLDs include statistical errors combined with the systematic errors from the unfolding and the first-generation method, and are calculated according to the procedure from Ref. [13]. For ^{113}Sn, the 10% error of the spin-cutoff parameter is propagated together with the experimental error of D_0 into the NLD uncertainty at the neutron separation energy and also included in the systematic error band as was done previously in Ref. [18]. We note that if we would use the predictions from systematics for ^{113}Sn rather than the neutron resonance data, the normalization parameters would be slightly lower but well within the error bars reported here. The D_0 values for ^{111,112}Sn were estimated from the $\rho(S_n)$ values extracted from the systematics. We assume a 30% error of D_0 in both cases, which is approximately twice as large as the largest experimental error of D_0 available for other Sn isotopes. A good agreement, well within the estimated error bands, between the slopes of the obtained

TABLE I. Parameters used for the normalization of the NLDs and GSFs for ^{111,112,113}Sn.

Nucleus	S_n (MeV)	D_0 (eV)	a (MeV^{-1})	E_1 (MeV)	E_d (MeV)	σ_d	$\sigma(S_n)$	$\rho(S_n)$ (10^5 MeV^{-1})	T (MeV)	E_0 (MeV)	$\langle\Gamma_\gamma\rangle$ (meV)
^{111}Sn	8.169	120(36)[a]	12.05	-0.29	1.08(7)	2.7(4)	4.6(5)	3.5(13)[a]	$0.67^{+0.03}_{-0.02}$	$-0.06^{+0.04}_{-0.11}$	76(18)[a]
^{112}Sn	10.788	3(1)[a]	12.53	1.12	2.83(4)	2.8(4)	4.8(5)	24.6(8)[a]	$0.71^{+0.02}_{-0.02}$	$0.66^{+0.09}_{-0.08}$	87(34)[b]
^{113}Sn	7.744	172(10)	12.77	-0.27	1.88(2)	3.5(7)	4.6(5)	2.5(5)	$0.63^{+0.01}_{-0.01}$	$0.20^{+0.04}_{-0.04}$	73(8)

[a]From systematics.
[b]Modified (see text).

GSFs with the (p, p') Coulomb excitation data (see Sec. V) also supports this choice. These errors were combined with the $\sigma(E_x)$ uncertainties and propagated in the total systematic error bands for the NLDs of ^{111,112}Sn. All parameters for the NLD normalization used in this work are presented in Table I.

B. Normalization of the γ-ray strength functions

The slope of the γ-transmission coefficient, also defined by the parameter α (see previous sections), is automatically determined through normalizing the NLD. The only parameter left to be constrained is B, i.e., the absolute value of $\mathcal{T}(E_\gamma)$. To extract this parameter, we utilize the expression for the average radiative width $\langle\Gamma(E_x, J, \pi)\rangle$ for the levels of spin-parity J^π at the excitation energy E_x [43]:

$$\langle\Gamma(E_x, J, \pi)\rangle = \frac{1}{2\pi\rho(E_x, J, \pi)} \sum_{XL}\sum_{J_f,\pi_f}\int_{E_\gamma=0}^{E_x} dE_\gamma$$
$$\times \mathcal{T}_{XL}(E_\gamma)\rho(E_x - E_\gamma, J, \pi), \qquad (9)$$

with X and L being the electromagnetic character and multipolarity of the γ radiation. The latter can be safely assumed to be of dipole nature in our case ($E1 + M1$; see, e.g., Ref. [43]). The GSF $f(E_\gamma)$ is then directly obtained from the γ-transmission coefficient by the relation $B\mathcal{T}(E_\gamma) = 2\pi E^3 f(E_\gamma)$ [44].

The total average radiative width $\langle\Gamma_\gamma\rangle$ obtained from s-wave neutron capture experiments [corresponds to $\langle\Gamma(S_n, J_t, \pi_t)\rangle$ in Eq. (9)] can be used to find the scaling parameter B. We adopt the prescription of Ref. [45] and use the following excitation energy dependence of the spin-cutoff parameter:

$$\sigma^2(E_x) = \sigma_d^2 + \frac{E_x - E_d}{S_n - E_d}\big[\sigma^2(S_n) - \sigma_d^2\big], \qquad (10)$$

with σ_d estimated from the discrete lower-lying levels at $E_x \approx E_d$ [6].

For ^{113}Sn, the $\langle\Gamma_\gamma\rangle$ value at S_n is available from s-wave neutron resonance studies [35]. For ^{111}Sn and ^{112}Sn, however, these values have to be constrained from the systematics for other Sn isotopes as it was done for ^{124}Sn in Ref. [23]. The value of $\langle\Gamma_\gamma\rangle = 76(18)$ meV obtained in this way for ^{111}Sn seems to be quite satisfactory based on the comparison with the (p, p') Coulomb excitation data, while the $\langle\Gamma_\gamma\rangle = 121(22)$ meV value for ^{112}Sn yields a significantly overestimated GSF. Given the good agreement of the Oslo data with the (p, p') Coulomb excitation strengths for other even-even

Sn isotopes (see Ref. [34]), we chose to apply an additional reduction factor to the $\langle\Gamma_\gamma\rangle$ value for ^{112}Sn extracted from the systematics. This factor is obtained through a χ^2 minimization with our GSF and the (p, p') data below the neutron threshold. The $\langle\Gamma_\gamma\rangle$ value from the systematics is set to be the maximum value, spanning a symmetrical error bar for $\langle\Gamma_\gamma\rangle$ in ^{112}Sn. For the ^{111}Sn nucleus this error is provided by the fit error from the systematics.

The error bands shown for the GSFs in Sec. V comprise the statistical errors, systematic errors of the unfolding and the first-generation procedure, and the propagated errors due to the D_0, $\langle\Gamma_\gamma\rangle$, $\sigma(S_n)$, σ_d, and E_d values. All parameters and their uncertainties used in the normalization of the GSFs are listed in Table I.

IV. NUCLEAR LEVEL DENSITIES AND THERMAL PROPERTIES

The NLDs of ^{111,112,113}Sn extracted with the Oslo method are presented in Fig. 3. All NLDs follow nicely a number of low-lying excited states up to $\approx$2.2 MeV for ^{111}Sn, 3.5 MeV for ^{112}Sn, and 2.7 MeV for ^{113}Sn. Up to these energies the level schemes can be, thus, considered complete. As compared to ^{113}Sn, the result for ^{111}Sn slightly underestimates the experimental NLD below $\approx$1 MeV, most likely due to the difference in the reaction mechanism and energy, favoring higher momentum transfer in the (p, d) reaction [46]. With the typical resolution of $\approx$200–300 keV, only the ground state and the first excited state of ^{112}Sn are clearly separated. The nonzero values of the NLD between these states are due to the abovementioned experimental resolution and some left-over counts remaining between the diagonals of the primary matrix after the background subtraction and unfolding. The lowest-lying levels in odd-even isotopes are seen as a single bump below $E_x \approx 500$ keV in ^{111}Sn and 700 keV in ^{113}Sn. At energies above $E_x \approx 4$ MeV, all nuclei demonstrate a steep exponential increase toward the neutron threshold, following a constant-temperature trend. For this reason, the normalization fit needed to constrain the CT model parameters for the extrapolation of the NLDs was found to be quite insensitive to the exact choice of the normalization limits (marked as shaded gray areas in Fig. 3).

The comparison of the experimental results for ^{111,112,113}Sn with other neighboring Sn isotopes is shown in Fig. 4. Here, we include the NLDs of ^{115}Sn, studied in a neutron evaporation experiment [47], and ^{116,117}Sn, studied with the Oslo method in (^{3}He, ^{3}He γ) and (^{3}He, ^{4}He γ) experiments [16].
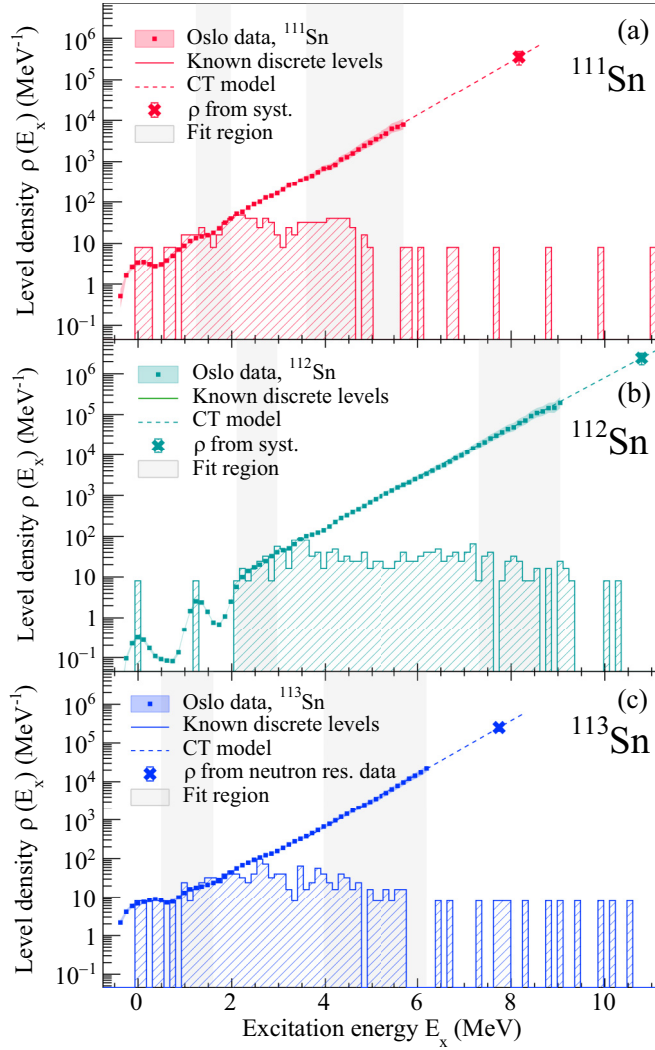
FIG. 3. Experimental NLDs of ^{111}Sn (a), ^{112}Sn (b), and ^{113}Sn (c). The $\rho(S_n)$ values are marked as crosses, and discrete levels are presented as hatched histograms. The gray-shaded areas mark the lower and higher excitation energy normalization regions.

FIG. 4. Comparison of the experimental nuclear level densities for ^{115}Sn [47], ^{116}Sn [16], and ^{117}Sn [16], shown together with the $\rho(S_n)$ values, and the present data for ^{111,112,113}Sn.

The level densities of all shown odd-even isotopes are by a factor of 5–9 higher than those of the even-even isotopes, as expected due to the presence of an uncoupled valence neutron in the odd-even nuclei. The NLDs of ^{111}Sn and ^{113}Sn agree quite well within the estimated error bands with each other above ≈ 2 MeV. Moreover, their slopes and absolute values agree above ≈ 3.5 MeV with those of the NLD in ^{115}Sn [47]. Similarly, the corresponding $\rho(S_n)$ estimates lie well within the error band of the neutron evaporation experiment. The same is true for the $\rho(S_n)$ value of ^{117}Sn, which, however, appears to be higher in absolute values below the neutron threshold than all other odd-even isotopes. As no considerable structural changes in these odd-even isotopes are predicted, we do not expect any significant change in the observed slopes. The NLD of ^{117}Sn being slightly higher might be indeed due some minor systematic evolution of the NLD with an increasing neutron number. However, it is important to mention that the BSFG model was used for the extrapolation

in the case of ^{117}Sn. It usually tends to slightly increase the NLD values when approaching the neutron threshold (see Ref. [16] and Fig. 8 in Ref. [48]). In many studied cases, including ^{111,112,113}Sn, the BSFG yields a poorer χ^2 score for the fit at high excitation energies, while the CT model provides a rather good fit in the same energy range and reproduces the NLD quite well below these energies. For example, within an energy range between 8 and 9 MeV in ^{112}Sn, the fit provided by the BSFG results in a χ^2 score that is a factor of 6 worse than the one obtained with the CT model. The different approach for the extrapolation of the NLD to $\rho(S_n)$ might also be the main explanation for the difference in absolute values of the NLDs in ^{116}Sn and ^{112}Sn. This is additionally supported by the $\rho(S_n)$ value from Ref. [16], which seems to agree well with the CT slope predicted for ^{112}Sn. Otherwise, the two NLDs follow the same trend below ≈ 3.5 MeV. As an older version of the particle telescope with a worse energy resolution was used in the earlier experiments (see Ref. [16]), the ground state and the first excited state at 1.293 MeV of ^{116}Sn are rather seen as two consecutive bumps around the ground state and the 1.256-MeV state of ^{112}Sn. Overall, the NLDs of ^{111,112,113}Sn are considerably smoother and more featureless than those of ^{116,117}Sn at relatively high excitation energies, which is most likely due to the better statistics of the newer experiments.

To study possible structural features present in the NLDs, we extract the entropies S and the temperatures T, similar to how it was done in Refs. [16,17,47]. Here, we have chosen to assume that these nuclei, given the experimental conditions, can be described within the microcanonical approach. By definition, the microcanonical entropy $S(E_x)$ is defined by the number of different ways a system can be arranged and, thus,

can be derived through the corresponding partition function, namely, the multiplicity of the populated states Ω_s:

$$S(E_x) = k_B \ln \Omega_s(E_x), \qquad (11)$$

where k_B is the Boltzmann constant. To link this to the experimental NLD, one has to have an access to the distribution of the populated spins at each excitation energy or, as in Ref. [16,17], introduce an averaged factor so that

$$\Omega_s(E_x) = [2\langle J(E_x)\rangle + 1]\Omega_l, \qquad (12)$$

where $\langle J \rangle$ is the average populated spin and Ω_l is the multiplicity of levels. As the exact spin distribution is quite uncertain and because we are interested in the excitation energy dependence of $S(E_x)$ rather than its absolute values, we omit the spin-dependent factor. Additionally, we introduce a parameter ρ_0 so that

$$\Omega_l(E_x) = \frac{\rho(E_x)}{\rho_0} \qquad (13)$$

and the entropy of the even-even ^{112}Sn at the ground state equates to zero, as expected. In the earlier works, the ρ_0 value was chosen such that the entropy at the excitation energy bin around 0 MeV yields $S \approx 0\ k_B$ [16,17]. As the experimental NLD underestimates the theoretical one at the ground state, we chose ρ_0 to be the average of the ground state and the first 2^+ state densities, $\rho_0 = 1.431\ \mathrm{MeV}^{-1}$. The same value was taken for the odd-even isotopes as well. This choice does not affect the main trends of interest in the excitation energy dependence of $S(E_x)$ [16,17,47].

The experimental entropies of ^{111,112,113}Sn are shown in Fig. 5(a). As $S(E_x)$ is not defined for excitation energy bins with no discrete states, we disregard the excitation energy ranges below 1 MeV for ^{111,113}Sn (dark-gray area) and below 2 MeV for ^{112}Sn (light-gray area), including all such bins. Following Ref. [49], we apply an assumption that the change in entropy between systems with an unpaired valence neutron (^{111,113}Sn) and a system with only paired neutrons (^{112}Sn) can be described with a constant shift as a function of excitation energy. The entropy differences $\Delta S = S(^{111,113}\mathrm{Sn}) - S(^{112}\mathrm{Sn})$ above 2 MeV are shown in Fig. 5(b). Both differences are quite similar, except for a slight increase closer to 6 MeV in case of ^{113}Sn. Between ≈ 2.7 and 5.5–6.0 MeV both differences can be considered almost constant within the estimated error bands, with the average values of $\Delta S = 1.48^{+0.04}_{-0.02}\ k_B$ and $1.47^{+0.02}_{-0.02}\ k_B$ for ^{111}Sn and ^{113}Sn, respectively. These values are slightly lower than those obtained for ^{116,117}Sn ($\approx 1.6\ k_B$) [16] and ^{118,119}Sn [1.7(2) k_B] [21]. The estimate presented in the latter study should be treated with care due to quite poor statistics of the experiments. Both works compare the ΔS values with the semiempirical study on entropies of midshell nuclei in the rare-earth region, providing an averaged value of $\Delta S \approx 1.7\ k_B$ [49]. This study, however, does not include such light isotopes of Sn as ^{111,112}Sn. Overall, the entropy differences of nuclei in the vicinity of $Z = 50$ demonstrate quite a large spread in values, from ≈ 1 to 2 k_B, and, therefore, the estimates we obtained for ^{111,112,113}Sn are in accordance with this study as well as with the earlier works on $^{116-119}$Sn.
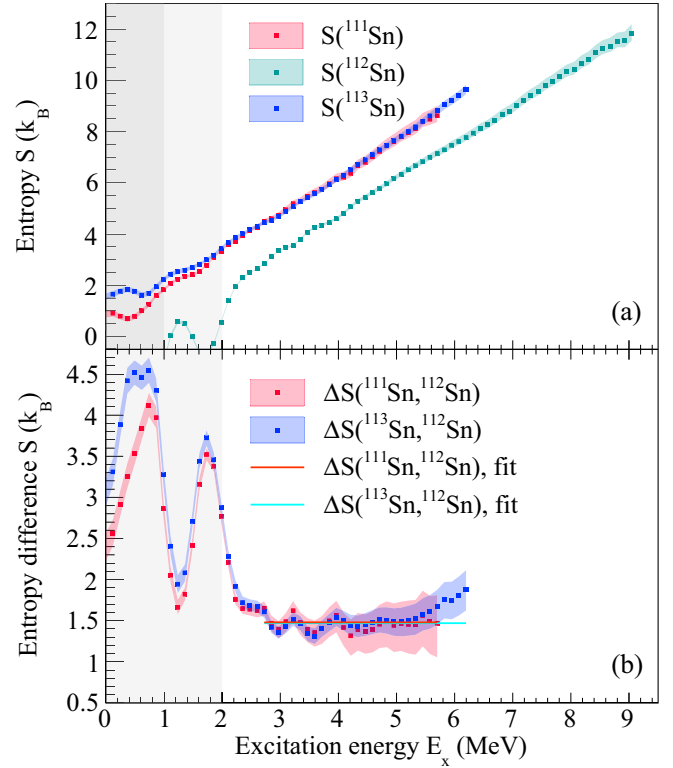
FIG. 5. Experimental entropies for ^{111,112,113}Sn (a) and entropy differences $\Delta S(^{111}\mathrm{Sn}-^{112}\mathrm{Sn})$ and $\Delta S(^{113}\mathrm{Sn}-^{112}\mathrm{Sn})$ (b). Light and darker gray-shaded areas below 2 and 1 MeV indicate the areas where the entropies for ^{112}Sn and ^{111,113}Sn, respectively, are disregarded. Horizontal lines correspond to χ^2 fits with constant functions.

The experimental entropies might potentially be used to shed some light on the process of Cooper pair breaking, contributing to the formation of levels in the NLD. According to the microscopic calculations with seniority-conserving and nonconserving interactions, this process is seen as step-like structures of the NLDs, experimentally observed for ^{56,57}Fe and ^{96,97}Mo [50]. Similar structures are clearly seen in $^{116-119}$Sn [16,21], where the features at relatively high excitation energies should be considered with care due to very large experimental error bars. A few quite clear features are seen in the entropy of ^{115}Sn at ≈ 2–3 and 4–5 MeV [47].

To amplify and study all subtle variations of the entropy, it is convenient to extract the microcanonical temperature $T(E_x)$:

$$T(E_x) = \left(\frac{\partial S(E_x)}{\partial E_x}\right)^{-1}. \qquad (14)$$

The resulting temperatures for all three isotopes are displayed in Fig. 6. The gray-shaded areas below 1 MeV in ^{111,113}Sn and 2 MeV in ^{112}Sn correspond to the disregarded ranges of entropies, similarly to those presented in Fig. 5. For all cases, the first bumps at ≈ 1.0–1.8 MeV in the temperatures reflect the change of the NLD and entropy slope with the onset of a large amount of states above 1 MeV. These states are expected to be of a predominantly single-particle (also

FIG. 6. Experimental temperatures for ^{111}Sn (a), ^{112}Sn (b), and ^{113}Sn (c). The gray-shaded areas below 2 in ^{112}Sn and below 1 MeV in ^{111,113}Sn indicate the areas where temperatures are not defined. Red solid lines denote the constant-temperature fits in each case.

FIG. 7. The experimental GSFs for ^{111,112,113}Sn, shown together with the (p, p') Coulomb excitation data for ^{112,114}Sn [41].

featuring an uncoupled neutron) nature and a collective nature. A similar effect of the collective states can be seen as a bump between 2 and 3 MeV in ^{112}Sn. The ne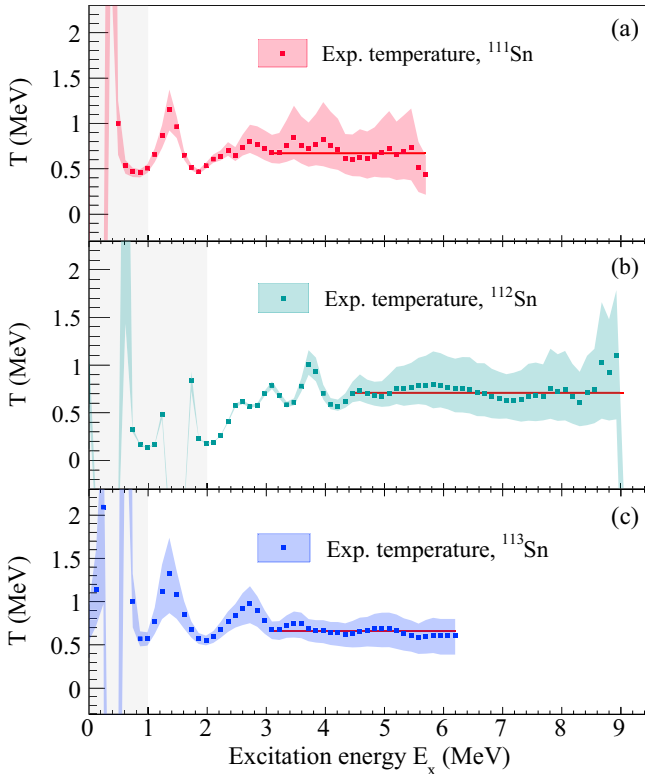xt clear feature in ^{113}Sn is at $\approx$2.6–3.0 MeV. This energy is quite close to the double-neutron pair-gap energy of $\approx$2.6 MeV, and this bump can be a candidate for the first broken neutron Cooper pair. An analogous peak in the same energy range of ^{111}Sn is somewhat less prominent, primarily due to the poorer statistics of the $(p, d\gamma)$ experiment. Similarly, in ^{115}Sn this feature is quite clear in the temperature profile [47]. However, the peak at 4–5 MeV in ^{115}Sn is seen neither in ^{111}Sn nor in ^{113}Sn. Instead, these nuclei demonstrate almost constant-temperature regimes already above $\approx$3 MeV with the average temperature of $T = 0.67^{+0.06}_{-0.04}$ MeV for ^{111}Sn and $T = 0.66^{+0.03}_{-0.03}$ MeV for ^{113}Sn, well in agreement with the corresponding temperatures from the CT extrapolation in Table I. This might be partly due to the experimental resolution, which smears subtle features of the NLD, no longer visible in the temperature profile. In addition, the process of Cooper pair breaking becomes more continuous at higher excitation energies, resulting in the constant-temperature behavior. As the proton $Z = 50$ shell is closed, the contribution of breaking proton pairs is expected to begin at higher energies, above $\approx$4 MeV.

For the case of ^{112}Sn, the temperature profile is quite similar to the odd nuclei. The most prominent feature is a peak at 3.6–4.0 MeV, which might again correspond to the first broken neutron pair ($2\Delta_n \approx 3.0$ MeV), given an extra

energy needed to form a new configuration with the unpaired neutrons. The constant-temperature regime sets in above $\approx$4.5 MeV with the average value $T = 0.71^{+0.04}_{-0.03}$, which is in accordance with the fit temperature from Table I. In general, all of the abovementioned trends are quite consistent with the previously published works on $^{115-119}$Sn, supporting the interpretation of the most-prominent features of the NLDs in $^{111-113}$Sn.

V. γ-RAY STRENGTH FUNCTIONS

The experimental dipole GSFs of ^{111,112,113}Sn extracted with the Oslo method are displayed in Fig. 7. The GSF of ^{112}Sn above 8.3 MeV is not shown due to very poor statistics in the primary matrix at high γ-ray energies. All strengths agree well within the estimated error bands not only in slopes but also in absolute values, demonstrating similar trends for the shown energy range. Even though the data points of ^{111}Sn suffer from relatively low statistics above $\approx$6 MeV, they still remain in good agreement with the GSFs of ^{112,113}Sn up to the neutron threshold. This behavior is expected due to the similar structural properties of the studied isotopes.

The earlier published cases [20–22] have been primarily compared to each other and various (γ, n) data above the neutron separation energy. The recent series of Coulomb excitation experiments through the (p, p') reaction performed on even-even ^{112,114,116,118,120,124}Sn [41] provide us with GSFs below and above the neutron threshold and, thus, an excellent opportunity to compare and benchmark the slopes and absolute values of our GSFs below S_n. Figure 7 displays the comparison of our results with the GSFs extracted from the (p, p') spectra for ^{112,114}Sn. The peaklike feature at $\approx$6.4 MeV in the (p, p') data is not seen in the Oslo strengths, likely due to the significantly worse experimental resolution.

An excellent agreement within the error bars of the Oslo-method GSF for ^{113}Sn with those for ^{112,114}Sn above 6 MeV supports the assumptions made to normalize this strength. A similar agreement for ^{111}Sn further supports the approach to assess the missing normalization parameters $\rho(S_n)$ and $\langle\Gamma_\gamma\rangle$ from the systematics. As previously mentioned, the latter parameter for ^{112}Sn was estimated by scaling the Oslo-method GSF to the (p, p') data. A good agreement of all strengths in slopes suggests that such scaling is needed due to, most probably, the systematics failing to reproduce a reasonable value of $\langle\Gamma_\gamma\rangle$ for ^{112}Sn.

Due to the overlap with the (p, p') data, covering also the energy range above the neutron threshold including the isovector giant dipole resonance (IVGDR), we are able to quantify the low-lying $E1$ strength in ^{111,112,113}Sn, similarly to how it was done in Refs. [20,22]. In the earlier publications this strength was referred to as the pygmy dipole resonance. However, due to the lack of experimental information on the isovector or/and the isoscalar nature of this strength in the present cases we prefer to use a more general term of a low-lying $E1$ strength.

Given the similarities in nuclear structure of $^{111-114}$Sn, we choose the (p, p') data on ^{112}Sn to represent the region above the neutron threshold for all three isotopes, ^{111,112,113}Sn. Following Refs. [20,22], the IVGDR part of the GSF is parametrized with the generalized Lorentzian function (we exploit the same notations for all parameters):

$$f_{E1}(E_\gamma) = \frac{1}{3\pi^2\hbar^2c^2}\sigma_{E1}\Gamma_{E1}$$
$$\times \left[E_\gamma \frac{\Gamma_{\mathrm{KMF}}(E_\gamma, T_f)}{\left(E_\gamma^2 - E_{E1}^2\right)^2 + E_\gamma^2\Gamma_{\mathrm{KMF}}^2(E_\gamma, T_f)} \right.$$
$$\left. + 0.7\frac{\Gamma_{\mathrm{KMF}}(E_\gamma = 0, T_f)}{E_{E1}^3} \right], \qquad (15)$$

where E_{E1}, Γ_{E1}, and σ_{E1} are the IVGDR centroid energy, width, and cross section, respectively. The Γ_{KMF} parameter denotes a temperature-dependent (T_f) width, proposed within the Kadmenskii-Markushev-Furman approach [51]:

$$\Gamma_{\mathrm{KMF}}(E_\gamma, T_f) = \frac{\Gamma_{E1}}{E_\gamma^2}\left(E_\gamma^2 + 4\pi^2 T_f^2\right). \qquad (16)$$

The low-lying excess $E1$ strength superimposed on the low-energy tail of the IVGDR was found to be best described by a Gaussian-like peak:

$$f_{\mathrm{low}}(E_\gamma) = C_{\mathrm{low}}\frac{1}{\sqrt{2\pi}\sigma_{\mathrm{low}}}\exp\left[-\frac{(E_\gamma - E_{\mathrm{low}})^2}{2\sigma_{\mathrm{low}}}\right], \qquad (17)$$

with C_{low}, σ_{low}, and E_{low} representing the absolute value, width, and centroid parameters, correspondingly. The experimental Oslo and Coulomb excitation data are shown together with the fitted IVGDR and the low-lying dipole strength in Fig. 8 for all three isotopes.

Because the Oslo method yields the combined $E1 + M1$ dipole strength, a parametrization of the $M1$ spin-flip resonance is needed to constrain the low-lying $E1$ component. Previously, no experimental data on the $M1$ strength were available, and the model of Ref. [44] was used in the earlier
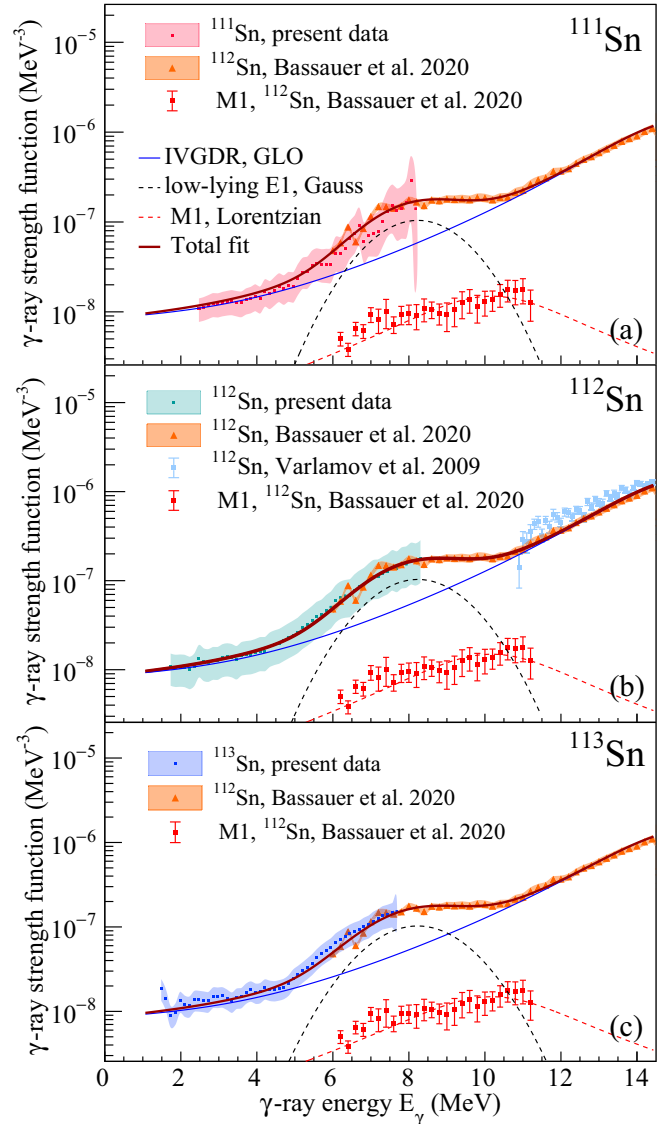
FIG. 8. The experimental GSFs for ^{111}Sn (a), ^{112}Sn (b), and ^{113}Sn (c) shown together with the (p, p') [41] and (γ, n) [53] data for ^{112}Sn. The total fits of the experimental data are shown as solid magenta lines and the fits of the IVGDR are marked as solid blue lines. The low-lying $E1$ and $M1$ components are shown as dashed black and red lines, respectively.

works [21,22]. However, the new (p, p') Coulomb excitation data provide both the $E1$ and $M1$ cross sections through a multipole decomposition analysis [41]. The $M1$ cross sections can be converted to $B(M1)$ strengths with the method described in Ref. [52]. The $M1$ strength appears to be quite fragmented in all of the cases [41]. For ^{111,112,113}Sn, we use the $M1$ component provided by Ref. [41] for ^{112}Sn and fit it with a Lorentzian function to reproduce its overall shape:

$$f_{M1}(E_\gamma) = \frac{1}{3\pi^2\hbar^2c^2}\frac{\sigma_{M1}\Gamma_{M1}^2 E_\gamma}{\left(E_\gamma^2 - E_{M1}^2\right)^2 + E_\gamma^2\Gamma_{M1}^2}, \qquad (18)$$

TABLE II. Parameters used for the description of the IVGDR and the $M1$ strength in ^{112}Sn.

Nucl.	E_{E1} (MeV)	Γ_{E1} (MeV)	σ_{E1} (mb)	T_f (MeV)	E_{M1} (MeV)	Γ_{M1} (MeV)	σ_{M1} (mb)
^{112}Sn	16.1(1)	5.5(3)	266.9(95)	0.70(5)	10.5(4)	4.8(5)	1.8(2)

TABLE III. Parameters used for the description of the low-lying $E1$ strengths in ^{111,112,113}Sn, the integrated low-lying $E1$ strengths, and the corresponding exhausted fractions of the TRK sum rule.

Nucl.	E_{low} (MeV)	Γ_{low} (MeV)	C_{low} (10^{-7} MeV^{-2})	Integrated (MeV mb)	TRK (%)
^{111}Sn	8.24(8)	1.19(6)	3.12(23)	29.6(15)	1.80(10)
^{112}Sn	8.24(9)	1.22(8)	3.17(24)	30.1(22)	1.81(15)
^{113}Sn	8.23(8)	1.25(7)	3.21(17)	30.5(16)	1.82(9)

with the maximum cross section σ_{M1}, width Γ_{M1}, and centroid E_{M1}. The experimental $M1$ data points are shown together with the corresponding Lorentzian fits in Fig. 8.

The fitting approach to disentangle the $M1$ and $E1$ strengths in ^{111,112,113}Sn is similar to that in Ref. [22]. First, the $M1$ strength of ^{112}Sn was fitted with Eq. (18). The obtained fit parameters are listed in Table II. Further, they were kept constant while fitting the total $E1 + M1$ strength of ^{112}Sn with the combined $f_{E1} + f_{\text{low}} + f_{M1}$ function. All of the IVGDR and the low-lying $E1$ strength parameters were kept free. Finally, the parametrization of the IVGDR for ^{112}Sn (see Table II) was applied to constrain the low-lying $E1$ strengths in ^{111}Sn and ^{113}Sn. The characteristics of all low-lying $E1$ strengths listed in Table III were also used to estimate the integrated low-lying $E1$ strengths and the corresponding exhausted fractions of the classical Thomas-Reiche-Kuhn (TRK) sum rule for each isotope. By using the IVGDR and the $M1$ strength of ^{112}Sn for the fit in the cases of ^{111,113}Sn, the integrated low-lying strengths of all three isotopes yield almost the same amount of $\approx 1.8\%$ of the TRK sum rule. This estimate as well as the centroids E_{low} are quite close to those obtained for $^{116-119,121,122}$Sn in Ref. [22], despite a slightly different approach to extract the low-lying $E1$ strength and the normalization.

The new experimental information on the GSFs of Sn isotopes below the neutron separation energy as well as the $M1$ strengths [41] calls for a systematic revision of all Sn isotopes studied at the OCL with a more uniform approach to the normalization of NLDs and GSFs. This might potentially affect the previously published parameters of the low-lying $E1$ strengths [22] and reveal new trends in the evolution of the low-lying strength from the lightest studied ^{111}Sn to the heaviest ^{124}Sn.

The need for a systematic reanalysis of the earlier published experiments is clearly demonstrated in Fig. 9, presenting a comparison of the GSFs for even-even Sn isotopes, namely, ^{112}Sn from the present work and already published results on ^{116,118,120,122,124}Sn. The low-energy part of the strength is quite similar for ^{112}Sn and the most recent results on ^{120,124}Sn, while a clear change of the slope suggests some evolution of the strength with an increasing neutron number. The GSFs of ^{116,118,122}Sn seem to be lower in absolute values than those of ^{112,120,124}Sn at relatively low E_γ energies. Renormalizing these isotopes using the same models as for ^{112,120,124}Sn and the most updated normalization information would further reveal whether this trend is due to the difference in the normalization procedures or some structural effects. For example, the spin-cutoff excitation energy dependence provided by Eq. (10), supported by studies from Ref. [54], was chosen over other alternatives in this work as well as

many other recent OCL publications (e.g., Refs. [55,56]). This model might potentially affect the low-energy part of the GSF, lifting it slightly up as compared to the model used in Refs. [21,22]. Since the time of the earlier publications (Refs. [16,20–22]) the new experimental information on s-wave neutron resonances became available for ^{116}Sn. Even though it yields values of $\rho(S_n)$ and $\langle\Gamma_\gamma\rangle$ quite similar to those obtained from the systematics in Ref. [21], the systematic uncertainty band of the updated result would be considerably reduced. In addition, some issues in the normalization code that might have affected the GSF of ^{118}Sn have been detected and fixed in the subsequent years. This appears to lead to a slightly higher GSF of ^{118}Sn throughout the whole shown energy range. With the new neutron resonance data on ^{116}Sn the systematics become more complete and yield new normalization parameters for ^{122}Sn. These values are quite similar within estimated uncertainties to those in Ref. [22] and are not expected to change the GSF in any considerable way. However, revisiting the energy calibration of this data set seems to yield a better fit of the NLD to the low-lying discrete states, which further shifts the
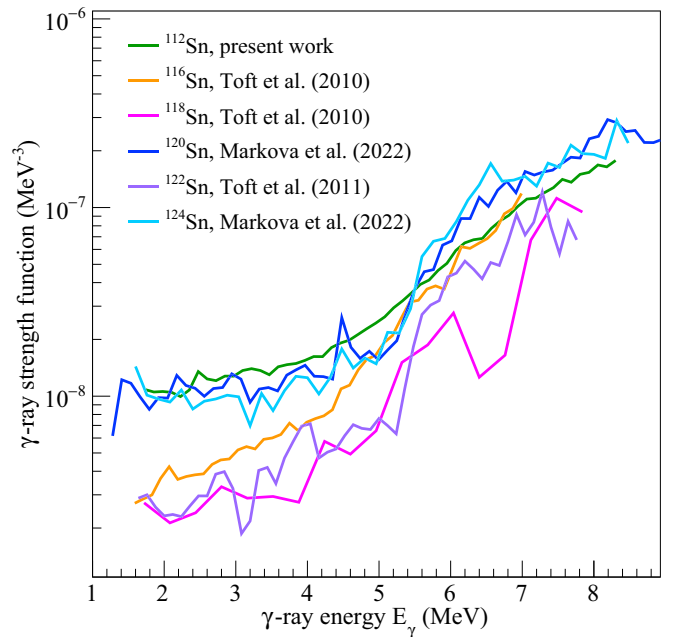

FIG. 9. Comparison of experimental GSFs for ^{112}Sn, ^{116}Sn [21], ^{118}Sn [21], ^{120}Sn [23], ^{122}Sn [22], and ^{124}Sn [23]. All uncertainty bands are omitted for clarity of the figure.

updated GSF up, reaching a good agreement with the ^{120,124}Sn GSFs as well the Coulomb excitation data. Overall, such revision of not only the even-even ^{116,118,122}Sn but also the odd ^{117,119,121}Sn isotopes appears to result in a better agreement in shapes and absolute values with the recently obtained Oslo-method results on $^{111-113,120,124}$Sn, the Coulomb excitation experiments [41], and available (γ, n) data for all studied nuclei.

VI. CONCLUSIONS AND OUTLOOK

In this work, the Oslo method was used to extract the NLDs and GSFs of ^{111,112,113}Sn from particle-γ coincidence events obtained in the $(p, p'\gamma)$, $(p, d\gamma)$, and $(d, p\gamma)$ reactions, respectively. The resulting NLDs of ^{111}Sn and ^{113}Sn are in good agreement with each other and the neutron evaporation data for ^{115}Sn. The NLDs were used to estimate the microcanonical entropies of all three nuclei, and the entropy differences suggest an entropy of ≈ 1.5 k_B carried by valence neutrons in ^{111}Sn and ^{113}Sn. All three nuclei demonstrate a clear constant-temperature trend above 3 MeV in ^{111,113}Sn and above 4.5 MeV in ^{112}Sn, supported by the extracted microcanonical temperatures. Signatures of the first neutron pair breaking can be seen at ≈ 2.6–3 MeV in ^{111,113}Sn and ≈ 3.6–4 MeV in ^{112}Sn. Overall, the temperatures of these nuclei are quite similar to those of the neighboring ^{115,116,117}Sn isotopes.

The GSFs extracted with the Oslo method demonstrate similar slopes for ^{111,112,113}Sn, well in agreement within the estimated error bands with the (p, p') strengths for ^{112,114}Sn above 6 MeV. The total low-lying $E1$ strengths in these nuclei amount to $\approx 1.8\%$ of the TRK sum rule, similar to previously published results on ^{116,117}Sn. The comparison with the new experimental information on the electric and magnetic dipole strengths from the Coulomb excitation experiments calls for a systematic revision of the earlier published $^{116-119,121,122}$Sn information. This further suggests a consistent study of the evolution of the low-lying electric dipole strength with an increasing neutron number in these isotopes. A work along these lines is in progress.

[1] W. Hauser and H. Feshbach, Phys. Rev. **87**, 366 (1952).

[2] M. Arnould, S. Goriely, and K. Takahashi, Phys. Rep. **450**, 97 (2007).

[3] M. B. Chadwick, M. Herman, P. Obložinský, M. E. Dunn, Y. Danon, A. C. Kahler, D. L. Smith, B. Pritychenko, G. Arbanas, R. Arcilla *et al.*, Nucl. Data Sheets **112**, 2887 (2011), special issue on ENDF/B-VII.1 Library.

[4] M. Salvatores and G. Palmiotti, Prog. Part. Nucl. Phys. **66**, 144 (2011).

[5] A. K. M. R. Rahman and A. Awal, J. Radiol. Nucl. Chem. **323**, 731 (2020).

[6] Data taken from the ENSDF database of the NNDC online data service (accessed 19 January 2023), https://www.nndc.bnl.gov/ensdf/ .

[7] H. K. Vonach and J. R. Huizenga, Phys. Rev. **149**, 844 (1966).

[8] D. Martin, P. von Neumann-Cosel, A. Tamii, N. Aoi, S. Bassauer, C. A. Bertulani, J. Carter, L. Donaldson, H. Fujita, Y. Fujita *et al.*, Phys. Rev. Lett. **119**, 182503 (2017).

[9] Y. Kalmykov, C. Özen, K. Langanke, G. Martínez-Pinedo, P. von Neumann-Cosel, and A. Richter, Phys. Rev. Lett. **99**, 202502 (2007).

[10] S. Goriely, P. Dimitriou, M. Wiedeking, T. Belgya, R. Firestone, J. Kopecky, M. Krtička, V. Plujko, R. Schwengner, S. Siem *et al.*, Eur. Phys. J. A **55**, 172 (2019).

[11] M. Guttormsen, T. Ramsøy, and J. Rekstad, Nucl. Instrum. Methods Phys. Res., Sect. A **255**, 518 (1987).

[12] M. Guttormsen, T. S. Tveter, L. Bergholt, F. Ingebretsen, and J. Rekstad, Nucl. Instrum. Methods Phys. Res., Sect. A **374**, 371 (1996).

[13] A. Schiller, L. Bergholt, M. Guttormsen, E. Melby, J. Rekstad, and S. Siem, Nucl. Instrum. Methods Phys. Res., Sect. A **447**, 498 (2000).

[14] M. Guttormsen, A. C. Larsen, A. Görgen, T. Renstrøm, S. Siem, T. G. Tornyi, and G. M. Tveten, Phys. Rev. Lett. **116**, 012502 (2016).

[15] L. C. Campo, M. Guttormsen, F. L. Bello Garrote, T. K. Eriksen, F. Giacoppo, A. Görgen, K. Hadynska-Klek, M. Klintefjord, A. C. Larsen, T. Renstrøm, E. Sahin, S. Siem, A. Springer, T. G. Tornyi, and G. M. Tveten, Phys. Rev. C **98**, 054303 (2018).

[16] U. Agvaanluvsan, A. C. Larsen, M. Guttormsen, R. Chankova, G. E. Mitchell, A. Schiller, S. Siem, and A. Voinov, Phys. Rev. C **79**, 014320 (2009).

[17] H. T. Nyhus, S. Siem, M. Guttormsen, A. C. Larsen, A. Bürger, N. U. H. Syed, H. K. Toft, G. M. Tveten, and A. Voinov, Phys. Rev. C **85**, 014323 (2012).

[18] I. K. B. Kullmann, A. C. Larsen, T. Renstrøm, K. S. Beckmann, F. L. Bello Garrote, L. C. Campo, A. Görgen, M. Guttormsen, J. E. Midtbø, E. Sahin, S. Siem, G. M. Tveten, and F. Zeiser, Phys. Rev. C **99**, 065806 (2019).

[19] A. Spyrou, S. N. Liddick, A. C. Larsen, M. Guttormsen, K. Cooper, A. C. Dombos, D. J. Morrissey, F. Naqvi,

G. Perdikakis, S. J. Quinn *et al.*, Phys. Rev. Lett. **113**, 232502 (2014).

[20] U. Agvaanluvsan, A. C. Larsen, R. Chankova, M. Guttormsen, G. E. Mitchell, A. Schiller, S. Siem, and A. Voinov, Phys. Rev. Lett. **102**, 162504 (2009).

[21] H. K. Toft, A. C. Larsen, U. Agvaanluvsan, A. Bürger, M. Guttormsen, G. E. Mitchell, H. T. Nyhus, A. Schiller, S. Siem, N. U. H. Syed, and A. Voinov, Phys. Rev. C **81**, 064311 (2010).

[22] H. K. Toft, A. C. Larsen, A. Bürger, M. Guttormsen, A. Görgen, H. T. Nyhus, T. Renstrøm, S. Siem, G. M. Tveten, and A. Voinov, Phys. Rev. C **83**, 044320 (2011).

[23] M. Markova, A. C. Larsen, P. von Neumann-Cosel, S. Bassauer, A. Gorgen, M. Guttormsen, F. L. Bello Garrote, H. C. Berg, M. M. Bjoroen, T. K. Eriksen, D. Gjestvang, J. Isaak, M. Mbabane, W. Paulsen, L. G. Pedersen, N. I. J. Pettersen, A. Richter, E. Sahin, P. Scholz, S. Siem *et al.*, Phys. Rev. C **106**, 034322 (2022).

[24] V. W. Ingeberg, S. Siem, M. Wiedeking, K. Sieja, D. L. Bleuel, C. P. Brits, T. D. Bucher, T. S. Dinoko, J. L. Easton, A. Görgen *et al.*, Eur. Phys. J. A **56**, 68 (2020).

[25] F. Zeiser, G. M. Tveten, F. L. B. Garrote, M. Guttormsen, A. C. Larsen, V. W. Ingeberg, A. Görgen, and S. Siem, Nucl. Instrum. Methods Phys. Res., Sect. A **985**, 164678 (2021).

[26] H. Schatz, A. Aprahamian, V. Barnard, L. Bildsten, A. Cumming, M. Ouellette, T. Rauscher, F.-K. Thielemann, and M. Wiescher, Phys. Rev. Lett. **86**, 3471 (2001).

[27] M. Guttormsen, A. Bürger, T. E. Hansen, and N. Lietaer, Nucl. Instrum. Methods Phys. Res., Sect. A **648**, 168 (2011).

[28] M. Guttormsen, A. Ataç, G. Løvhøiden, S. Messelt, T. Ramsøy, J. Rekstad, T. F. Thorsteinsen, T. S. Tveter, and Z. Zelazny, Phys. Scr. **T32**, 54 (1990).

[29] A. C. Larsen, M. Guttormsen, M. Krtička, E. Běták, A. Bürger, A. Görgen, H. T. Nyhus, J. Rekstad, A. Schiller, S. Siem *et al.*, Phys. Rev. C **83**, 034315 (2011).

[30] J. E. Midtbø, Ph.D. thesis, University of Oslo, 2019.

[31] J. E. Midtbø, F. Zeiser, E. Lima, A.-C. Larsen, G. M. Tveten, M. Guttormsen, F. L. Bello Garrote, A. Kvellestad, and T. Renstrøm, Comput. Phys. Commun. **262**, 107795 (2021).

[32] D. M. Brink, Doctoral thesis, Oxford University, 1955.

[33] P. Axel, Phys. Rev. **126**, 671 (1962).

[34] M. Markova, P. von Neumann-Cosel, A. C. Larsen, S. Bassauer, A. Görgen, M. Guttormsen, F. L. Bello Garrote, H. C. Berg, M. M. Bjørøen, T. Dahl-Jacobsen *et al.*, Phys. Rev. Lett. **127**, 182501 (2021).

[35] S. Mughabghab, *Atlas of Neutron Resonances*, 6th ed. (Elsevier, Amsterdam, 2018).

[36] A. Gilbert and A. G. W. Cameron, Can. J. Phys. **43**, 1446 (1965).

[37] T. Ericson and V. Strutinski, Nucl. Phys. **8**, 284 (1958).

[38] T. v. Egidy and D. Bucurescu, Phys. Rev. C **72**, 044311 (2005).

[39] S. Hilaire, J. P. Delaroche, and M. Girod, Eur. Phys. J A **12**, 169 (2001).

[40] M. Wiedeking, M. Guttormsen, A. C. Larsen, F. Zeiser, A. Görgen, S. N. Liddick, D. Mücher, S. Siem, and A. Spyrou, Phys. Rev. C **104**, 014311 (2021).

[41] S. Bassauer, P. von Neumann-Cosel, P.-G. Reinhard, A. Tamii, S. Adachi, C. A. Bertulani, P. Y. Chan, A. D'Alessio, H. Fujioka, H. Fujita *et al.*, Phys. Rev. C **102**, 034327 (2020).

[42] T. Ericson, Nucl. Phys. **11**, 481 (1959).

[43] J. Kopecky and M. Uhl, Phys. Rev. C **41**, 1941 (1990).

[44] *Handbook for Calculations of Nuclear Reaction Data, RIPL-2*, TECDOC Series No. 1506 (International Atomic Energy Agency, Vienna, 2006).

[45] R. Capote, M. Herman, P. Obložinský, P. Young, S. Goriely, T. Belgya, A. Ignatyuk, A. Koning, S. Hilaire, V. Plujko *et al.*, Nucl. Data Sheets **110**, 3107 (2009).

[46] P. Blankert, H. Blok, and J. Blok, Nucl. Phys. A **356**, 74 (1981).

[47] P. Roy, K. Banerjee, T. K. Rana, S. Kundu, D. Pandit, N. Q. Hung, T. K. Ghosh, S. Mukhopadhyay, D. Mondal, G. Mukherjee *et al.*, Eur. Phys. J. A **57**, 48 (2021).

[48] M. Guttormsen, M. Aiche, F. L. Bello Garrote, L. A. Bernstein, D. L. Bleuel, Y. Byun, Q. Ducasse, T. K. Eriksen, F. Giacoppo, A. Görgen *et al.*, Eur. Phys. J. A **51**, 170 (2015).

[49] M. Guttormsen, M. Hjorth-Jensen, E. Melby, J. Rekstad, A. Schiller, and S. Siem, Phys. Rev. C **63**, 044301 (2001).

[50] A. Schiller, E. Algin, L. A. Bernstein, P. E. Garrett, M. Guttormsen, M. Hjorth-Jensen, C. W. Johnson, G. E. Mitchell, J. Rekstad, S. Siem *et al.*, Phys. Rev. C **68**, 054326 (2003).

[51] S. G. Kadmenskii, V. P. Markushev, and V. I. Furman, Sov. J. Nucl. Phys. **37**, 345 (1983).

[52] J. Birkhan, H. Matsubara, P. von Neumann-Cosel, N. Pietralla, V. Y. Ponomarev, A. Richter, A. Tamii, and J. Wambach, Phys. Rev. C **93**, 041302(R) (2016).

[53] V. V. Varlamov, B. S. Ishkhanov, V. N. Orlin, and V. A. Chetvertkova, Bull. Russ. Acad. Sci. Phys. **74**, 833 (2010).

[54] H. Uhrenholt, S. Åberg, A. Dobrowolski, Th. Døssing, T. Ichikawa, and P. Möller, Nucl. Phys. A **913**, 127 (2013).

[55] M. Guttormsen, K. O. Ay, M. Ozgur, E. Algin, A. C. Larsen, F. L. Bello Garrote, H. C. Berg, L. Crespo Campo, T. Dahl-Jacobsen, F. W. Furmyr *et al.*, Phys. Rev. C **106**, 034314 (2022).

[56] V. W. Ingeberg, P. Jones, L. Msebi, S. Siem, M. Wiedeking, A. A. Avaa, M. V. Chisapi, E. A. Lawrie, K. L. Malatji, L. Makhathini *et al.*, Phys. Rev. C **106**, 054315 (2022).

Paper IV

Systematic study of the low-lying electric dipole strength in Sn isotopes and its astrophysical implications

IV

Systematic study of the low-lying electric dipole strength in Sn isotopes and its astrophysical implications

M. Markova,[1, *] A. C. Larsen,[1, †] P. von Neumann-Cosel,[2] E. Litvinova,[3, 4, 5] A. Choplin,[6]
S. Goriely,[6] S. Martinet,[6] L. Siess,[6] M. Guttormsen,[1] F. Pogliano,[1] and S. Siem[1]

[1]*Department of Physics, University of Oslo, N-0316 Oslo, Norway*
[2]*Institut für Kernphysik, Technische Universität Darmstadt, D-64289 Darmstadt, Germany*
[3]*Department of Physics, Western Michigan University, Kalamazoo, Michigan 49008, USA*
[4]*National Superconducting Cyclotron Laboratory, Michigan State University, East Lansing, Michigan 48824, USA*
[5]*GANIL, CEA/DRF-CNRS/IN2P3, F-14076 Caen, France*
[6]*Institut d'Astronomie et d'Astrophysique, Université Libre de Bruxelles, CP 226, B-1050 Brussels, Belgium*
(Dated: May 4, 2024)

The γ-ray strength functions (GSF) and nuclear level densities (NLD) below the neutron threshold have been extracted for $^{111-113,116-122,124}$Sn from particle-γ coincidence data with the Oslo method. The evolution of bulk properties of the low-lying electric dipole response has been investigated on the basis of the Oslo GSF data and results of a recent systematic study of electric and magnetic dipole strengths in even-even Sn isotopes with relativistic Coulomb excitation. The obtained GSFs reveal a resonance-like peak on top of the tail of the isovector giant dipole resonance, centered at ≈ 8 MeV and exhausting $\approx 2\%$ of the classical Thomas-Reiche-Kuhn (TRK) sum. For mass numbers ≥ 118 the data suggest also a second peak centered at ≈ 6.5 MeV. It corresponds to 0.1-0.5% of the TRK sum rule and shows an approximate linear increase with the mass number. In contrast to predictions of the relativistic quasiparticle random-phase and time-blocking approximation calculations (RQRPA and RQTBA), no monotonous increase in the total low-lying $E1$ strength was observed in the experimental data from ^{111}Sn to ^{124}Sn, demonstrating rather similar strength distributions in these nuclei. The Oslo GSFs and NLDs were further used as inputs to constrain the cross sections and Maxwellian-averaged cross sections of (n,γ) reactions in the Sn isotopic chain using TALYS. The obtained results agree well with other available experimental data and the recommended values from the JINA REACLIB, BRUSLIB, and KADoNiS libraries. Despite relatively small exhausted fractions of the TRK sum rule, the low-lying electric dipole strength makes a noticeable impact on the radiative neutron-capture cross sections in stable Sn isotopes. Moreover, the experimental Oslo inputs for the ^{121,123}Sn$(n,\gamma)^{122,124}$Sn reactions were found to affect the production of Sb in the astrophysical i-process, providing new constraints on the uncertainties of the resulting chemical abundances from multi-zone low-metallicity Asymptotic Giant Branch stellar models.

I. INTRODUCTION

The study of the multipole electromagnetic response of atomic nuclei has always been an ultimate testing ground for unraveling a plethora of complex collective and single-particle excitation modes, their interplay, and driving physical mechanisms of nuclear interaction. Historically, one of the most well-studied modes of collective motion is the isovector giant dipole resonance (IVGDR), and the experimental and theoretical systematics on the IVGDR and its bulk properties are currently available for a wide range of mass numbers [1–3]. Within a macroscopic picture, this prominent feature is interpreted as a signature of out-of-phase dipole oscillations of all protons against all neutrons in the nucleus [4].

In contrast to the IVGDR located at $10-20$ MeV in heavy nuclei, the concentration of a weaker electric dipole strength in the vicinity of the neutron threshold, often referred to as the pygmy dipole resonance (PDR), is far less

understood and keeps posing new questions regarding its origin and properties [5–8]. A macroscopic interpretation of the PDR emerging from oscillations of excess neutrons, or a neutron skin, versus an isospin-saturated core [9] has been frequently adopted in publications since the 1970s, shifting the main focus of the experimental efforts in the past few decades to heavier, more neutron rich nuclei to test this interpretation [10–12]. However, this collective surface-motion picture and the degree of collectivity of involved transitions have been a matter of intense debates [5, 7, 8, 13–15]. Some studies suggest the physical mechanism behind the PDR to be a toroidal electric dipole mode instead of a neutron-skin oscillation[16–19].

Another intensively discussed matter related to the PDR energy region is the isovector and/or isoscalar nature of observed structures [14, 20]. The isospin splitting of the low-lying electric dipole response (LEDR) was, indeed, experimentally confirmed in complementary studies with isoscalar and isovector probes in ^{124}Sn, ^{138}Ba, and ^{140}Ce [21–25]. Combined with self-consistent relativistic quasiparticle time-blocking approximation (RQTBA) and quasiparticle-phonon model (QPM) calculations, these experiments point towards the presence

* maria.markova@fys.uio.no
† a.c.larsen@fys.uio.no

of two groups of transitions below the neutron threshold [22, 25]. The lower-lying group of states reveals a signature of a strong neutron contribution on the surface, whereas the higher-lying states are of more isovector nature, corresponding rather to the tail of the IVGDR. Furthermore, recent experiments on ^{208}Pb [26] and ^{120}Sn [27] with a deuteron probe combined with a QPM analysis provided insight into the one-particle-one-hole structure of the LEDR in these nuclei, revealing a similar structural splitting based on the contributing particle-hole configurations. In general, an extensive investigation of the PDR region with complementary isoscalar and isovector probes in various inelastic scattering reactions as well as single-nucleon transfer reactions is pivotal to break down the complex LEDR structure of nuclei within different mass regions.

The tin isotopic chain is probably one of the best studied cases both experimentally and theoretically (see, e.g., the review articles in [6, 8]). For the tin isotopes, the LEDR is available from nuclear resonance fluorescence (NRF) studies [28–30], experiments with α [22], ^{17}O [23], and deuteron [27] probes, Coulomb dissociation [10, 31] and Coulomb excitation [32, 33] experiments. A first attempt to extract the systematics of the PDR observed in the GSFs of $^{116-119,121,122}$Sn measured with the Oslo method was presented in Ref. [34]. With new experimental information available on ^{120,124}Sn [35, 36] and $^{111-113}$Sn [37], a combination of the Oslo data and the recently published strengths for even-even Sn isotopes from Coulomb excitation experiments [33] permits a consistent extensive study on the evolution of the LEDR, covering eleven Sn isotopes from ^{111}Sn to ^{124}Sn.

The connection of the PDR strength to the neutron-skin thickness in neutron-rich nuclei, suggested by the neutron oscillation picture, triggered attempts to provide experimental constraints on the symmetry-energy term in the equation of state [31, 38–40], with implications for the characteristics of neutron stars [41, 42]. While this connection is under debate [15, 43], influence of the enhanced $E1$ strength close to neutron threshold on the astrophysical radiative neutron-capture rates is less ambiguous [13, 44]. An increased probability of radiative neutron capture due to the boosted GSF within the PDR region might impact the element production in the rapid neutron-capture process (r process), responsible for creating $\approx 50\%$ of elements heavier than Fe in the universe. However, assessing the importance of the PDR in the r-process nucleosynthesis is difficult due to a lack of experimental constraints for very neutron-rich nuclei and a large spread in theoretical predictions of the PDR strength. To provide radiative neutron-capture rates for r-process reaction network calculations, the statistical Hauser–Feshbach model is employed [45–47]. This model calls for consistently extracted experimental data on the nuclear level densities (NLD) and γ-ray strength functions (GSF), or average reduced γ-transition probability, for experimentally accessible cases to constrain the available theoretical models.

In addition to investigating the impact of the PDR on the r process, dipole strength distributions below the neutron threshold in stable isotopes are of general interest for the slow (s) neutron-capture process. The majority of the stable Sn isotopes originate predominantly from the s process [48–50], with ^{121}Sn and ^{123}Sn being potential candidates for the s-process branching point nuclei (see Refs. [51, 52], respectively). Moreover, isotopes heavier than ^{120}Sn might be involved in the main flow of the intermediate (i) neutron-capture process, as discussed by Goriely *et al.* [53]. The Oslo method enables the extraction of both key nuclear inputs, the NLDs and GSFs, for statistical calculations within the Hauser–Feshbach framework. Therefore, the method provides experimental constraints on the radiative neutron-capture reaction rates of interest for all the three above-mentioned nucleosynthesis processes.

The paper is outlined as follows. Section II describes the details of experiments on the Sn isotopes performed at the Oslo Cyclotron Laboratory (II A) and the Oslo method (II B). In Sec. III, the extracted NLDs (III A), GSFs, and the systematics of the bulk properties of the low-lying $E1$ strength (III B) are presented. Sec. IV focuses on the comparison of this systematics with model predictions. The neutron-capture cross sections and Maxwellian-averaged cross sections are presented and discussed together with the potential role of the LEDR in Sec. V. In Sec. VI, i-process calculations in Asymptotic Giant Branch (AGB) stars are presented, and the impact of the new experimentally constrained rates on the production of the elements in the Sn region is discussed. Finally, the main findings of this work are summarized in Sec. VII.

II. DATA AND METHODOLOGY

A. Setup and experimental details

Eleven tin isotopes, $^{111-113,116-122,124}$Sn, were studied in nine experimental campaigns taking place at the Oslo Cyclotron Laboratory (OCL) in the period from 2003 to 2022. All nuclei were studied in light-particle-induced reactions with p, d, and ^{3}He beams delivered by the MC-35 Scanditronix cyclotron with the main objective of extracting particle-γ coincidence events for a further analysis with the Oslo method. In all cases, the configuration of the setup involved a scintillator γ-ray detector array surrounding the target chamber and a Si particle-telescope system placed either in forward or backward angles with respect to the beam direction.

The first experiments on ^{117}Sn and ^{119}Sn, aiming at studying ^{116,117}Sn and ^{118,119}Sn, respectively, utilized the $(^3$He,$\alpha\gamma)$ and $(^3$He,^{3}He$'\gamma)$ reactions. These experiments were performed with 38-MeV ^{3}He beams and exploited eight standard $\Delta E - E$ Si telescopes with $\approx$140-μm-thick ΔE and 1500-μm-thick E counters. The telescopes were placed within the target chamber at 45° with respect to

TABLE I. Characteristics of the experiments on Sn isotopes performed at the OCL. The given angles refer to the particle scattering angles with respect to the beam direction.

Target	Thickness (mg/cm^2)	Enrichment (%)	Reaction	Beam energy (MeV)	Beam intensity (nA)	Angles (°)	Year	Setup
^{112}Sn	4.0	99.8	$(p,d\gamma)$	25.0	$\approx$ 1.0–1.5	126-140	2013	SiRi+CACTUS
			$(p,p'\gamma)$	16.0	$\approx$ 1.0–1.5	126-140	2013	SiRi+CACTUS
			$(d,p\gamma)$	11.5	$\approx$ 0.5–0.7	126-140	2014	SiRi+CACTUS
^{117}Sn	2.1	92.0	$(^3\text{He},\alpha\gamma)$	38	$\approx$ 1.5	$\approx 42.5 - 47.5$	2003	Stand. Si + CACTUS
			$(^3\text{He},^3\text{He}\gamma)$[a]	38	$\approx$ 1.5	$\approx 42.5 - 47.5$	2003	Stand. Si + CACTUS
			$(p,p'\gamma)$[b]	16	$\approx$ 2.8	126-140	2019	SiRi + OSCAR
^{119}Sn	1.6	93.2	$(^3\text{He},\alpha\gamma)$	38	$\approx$ 1.5	$\approx 42.5 - 47.5$	2008	Stand. Si + CACTUS
			$(^3\text{He},^3\text{He}\gamma)$[a]	38	$\approx$ 1.5	$\approx 42.5 - 47.5$	2008	Stand. Si + CACTUS
			$(p,p'\gamma)$[b]	16	$\approx 0.6 - 0.8$	126-140	2022	SiRi + OSCAR
^{120}Sn	2.0	99.6	$(p,p'\gamma)$	16	$\approx 3.0 - 4.0$	126-140	2019	SiRi + OSCAR
^{122}Sn	1.43	94	$(^3\text{He},\alpha\gamma)$	38	$\approx$ 0.2	40-54	2010	SiRi+CACTUS
			$(^3\text{He},^3\text{He}\gamma)$	38	$\approx$ 0.2	40-54	2010	SiRi+CACTUS
^{124}Sn	0.47	95.3	$(p,p'\gamma)$	16	$\approx 3.0 - 4.0$	126-140	2019	SiRi + OSCAR

[a] Not used in the present work.

[b] Remeasured.

the beam direction, as a compromise between reducing the contribution from elastic scattering and still having sufficiently large cross sections for the reactions of interest. Collimators were placed in front of the Si detectors to reduce the uncertainty in the scattering angle. This collimation led to a significantly reduced solid-angle coverage of $\approx$0.72% of 4π and $\approx$1.5% of 4π for the collimators with circular (^{117}Sn) and squared openings (^{119}Sn), respectively.

To improve the solid-angle coverage while maintaining a reasonable angular resolution, a custom-designed Si telescope ring (SiRi) was installed in 2011 [54]. The SiRi system was used in the experimental campaigns to study $^{120-122,124}$Sn as well as remeasuring ^{117,119}Sn in $2019 - 2022$ in the $(p,p'\gamma)$ and ^{121,122}Sn in $(^3\text{He},\alpha\gamma)$ and $(^3\text{He},^3\text{He}'\gamma)$ reactions. SiRi is comprised of eight trapezoidal-shaped ΔE-E modules with 130-μm-thick ΔE layers and 1550-μm-thick E layers. The former are additionally segmented into eight curved pads. The coverage of scattering angles in SiRi is either $40 - 54°$ in the forward or $126 - 140°$ in the backward position of the detector array, with a $2°$ polar angle window per each pad. With SiRi, the solid-angle coverage increased approximately 10 times as compared to the previous telescope system, while keeping a sufficient energy resolution.

Both the older Si detector system and SiRi make use of the ΔE-E technique to differentiate between the observed reaction channels. The typical energy resolution for the experiments with the 38-MeV ^{3}He beam performed with the older setup was $\approx 250 - 350$ keV Full Width at Half Maximum (FWHM), determined from the fit to the elastic peaks in the $(^3\text{He},^3\text{He}')$ and $(^3\text{He},\alpha)$ channels. With SiRi, the energy resolution is $\approx 150 - 200$

keV for the same experimental conditions, and ≈ 300 keV for the 11.5-MeV deuteron and 20-MeV proton beams in the (d,p) and (p,d) channels, respectively (due to the large thickness of the ^{112}Sn target). The best resolution of ≈ 100 keV was achieved in the experiments using 16-MeV protons with SiRi. Besides the reaction channel, the beam energy, and intrinsic resolution of the $E - \Delta E$ modules, the excitation-energy resolution was also affected by the beam-energy resolution (the beam-spot size varied significantly in the experiments).

All the $(^3\text{He},^3\text{He}'\gamma)$ and $(^3\text{He},\alpha\gamma)$ experiments on ^{117,119,122}Sn as well as the $(p,p'\gamma)$, $(p,d\gamma)$, and $(d,p\gamma)$ experiments on ^{112}Sn were performed with the detector array CACTUS [55]. CACTUS consisted of 28 spherically distributed cylindrical $5'' \times 5''$ NaI(Tl) detectors, where each detector was additionally collimated with conical Pb collimators. Using a ^{60}Co source, the total efficiency of CACTUS and its energy resolution at $E_\gamma = 1332$ keV were estimated to be 15.2(1)% and $\approx 6.8\%$, respectively.

In 2019, the CACTUS detectors were replaced by OS-CAR (Oslo SCintillator ARray), a γ-ray detector array of 30 cylindrical large-volume $3.5'' \times 8''$ LaBr$_3$(Ce) crystals [56, 57]. OSCAR provides a significantly improved energy resolution and excellent timing properties for selecting particle-γ events. The total efficiency in the most recent experiments is $\approx 40\%$, with the energy resolution of $\approx 2.2\%$ at $E_\gamma = 1332$ keV.

In the period between 2003 and 2022, ^{117}Sn and ^{119}Sn were measured twice; first, with the $(^3\text{He},^3\text{He}'\gamma)$ reaction using the old setup configuration (standard Si telescopes + CACTUS), and later with SiRi and OSCAR using the $(p,p'\gamma)$ reactions. Due to a fairly good agreement between the new and the old data sets, and considering

the improved energy resolution and timing with the new setup, we choose to show only the $(p, p'\gamma)$ data for ^{117}Sn and ^{119}Sn in the present work. The data processing before the application of the Oslo method for these two experiments is identical to the one described in detail for ^{120,124}Sn in Ref. [36]. All relevant parameters for the above-mentioned experiments are outlined in Table I.

Using the known kinematics of the studied reactions, the energy deposited in the particle Si detectors was converted into the initial excitation energy E_i of the residual nucleus. By applying proper gates on the outgoing particle species and the time spectra, the background-subtracted particle-γ coincidence events were extracted. A more in-depth discussion of the experimental details, calibration, and event selection in each case is presented in Refs. [37] for $^{111-113}$Sn, Refs. [58, 59] for ^{116}Sn, Ref. [60] for ^{118}Sn, Ref. [36] for ^{120,124}Sn, and Ref. [34] for ^{121,122}Sn. Calibrations of the excitation and γ-ray energies for the ^{121,122}Sn data sets were revised and improved compared to the earlier published results [34].

In the next step, the recorded γ-ray spectra are corrected using the detector response functions of either CACTUS or OSCAR to obtain the unfolded spectra. For all cases, the unfolding was done with the same iterative technique described in detail in Ref. [61]. The method is based on a consecutive correction of the trial function for the unfolded spectra, until they match with the original raw spectra within the experimental uncertainties. To avoid introducing any strong artificial fluctuations while still preserving the original statistical fluctuations, the Compton subtraction technique was also applied in each case. The details of this procedure are presented in Refs. [61, 62].

The last step prior to the extraction of the NLD and GSF is to determine the distribution of first-generation γ rays for each excitation-energy bin, i.e., γ rays stemming directly from a nucleus decaying with an initial excitation energy E_i. The distribution $P(E_\gamma, E_i)$ of such first-generation – or primary – γ rays, is proportional to the probability of γ decay from initial excitation energies E_i to the final levels $E_f = E_i - E_\gamma$, i.e., to the corresponding average branching ratios of the levels within the excitation-energy bin E_i. An important assumption for the extraction of the primary γ rays is that the decay pattern of the excited levels within the E_i bin is independent of the way they were populated (either directly through the reactions or via the decay of higher-lying states). Then, the γ cascades at each initial excitation-energy bin E_i are expected to contain the same transitions as those in the bins below, except for the primary γ transitions. By use of the iterative first-generation method (see Ref. [63] for details), the non-primary γ transitions are successively removed from each initial excitation-energy bin below the neutron threshold. The above-mentioned assumption is expected to hold for relatively high excitation energies where the spin distribution is approximately equal for neighboring E_i bins. This imposes a lower limit on the initial excitation energy for the fur-
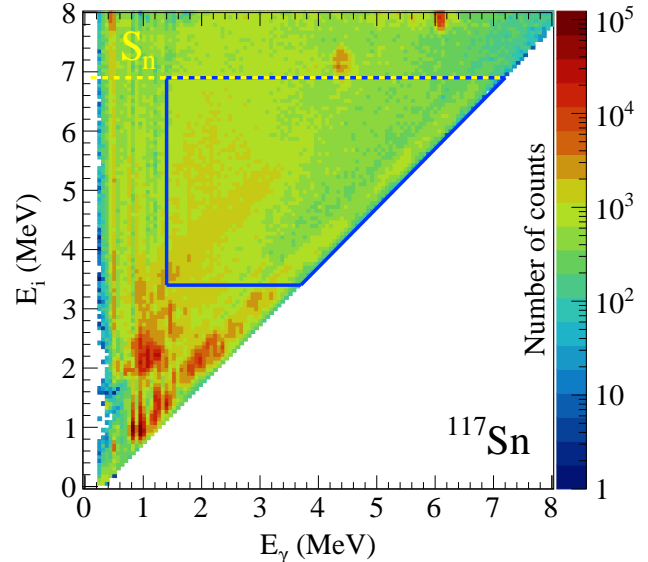
FIG. 1. The first-generation matrix for ^{117}Sn extracted in the $(p, p'\gamma)$ experiment. The yellow dashed line corresponds to the neutron separation energy, while the blue solid lines confine the area used for the Oslo method. The bin size is 64 keV×64 keV.

ther data analysis with the Oslo method, while an upper limit is set by the neutron separation energy S_n in each case. In addition, an over-subtraction of γ transitions at low γ energies seen in all data sets limits γ-ray energy to $E_\gamma \gtrsim 1-2$ MeV. A thorough discussion of the application of the first-generation method and its limitations is presented in Ref. [62]. For the most recent experiments on ^{117}Sn and ^{119}Sn, these limits were set to $3.4 \lesssim E_i \lesssim 6.9$ MeV, $E_\gamma \gtrsim 1.4$ MeV and $4.0 \lesssim E_i \lesssim 6.5$ MeV, $E_\gamma \gtrsim 1.8$ MeV, respectively. Discussions of the chosen E_i and E_γ limits for the subsequent Oslo method analysis of other Sn isotopes can be found in Refs. [34, 36, 37, 58–60].

B. Extraction of NLDs and GSFs

As mentioned in the previous section, the first-generation matrix reflects a distribution of decay probabilities from the levels within each initial excitation-energy bin E_i to the final levels E_f via γ transitions with energies $E_\gamma = E_i - E_f$. The Oslo method exploits this fact to perform a decomposition of the primary matrix $P(E_\gamma, E_i)$ into the γ transmission coefficient $\mathcal{T}_{i \to f}$ and the density of final levels ρ_f:

$$P(E_\gamma, E_i) \propto \mathcal{T}_{i \to f} \cdot \rho_f. \qquad (1)$$

This decomposition is supported by both Fermi's golden rule and the Hauser-Feshbach theory of statistical reactions (see Ref. [64] and Ref. [65], respectively, for

detailed derivations). Being valid only for the compound excited states, this relation is expected to hold well for the chosen excitation-energy ranges.

The transmission coefficient in Eq. (1) depends on both the initial and the final excitation energy, making it practically impossible to disentangle $\mathcal{T}_{i \to f}$ and ρ_f in the factorized first-generation matrix. For this reason, the generalized Brink-Axel hypothesis [66, 67] needs to be employed in the Oslo method to reduce the dependence of the transmission coefficient on the initial and final excitation energy to a dependence on E_γ only ($\mathcal{T}_{i \to f} \to \mathcal{T}(E_\gamma)$). In its most commonly used, generalized form, this hypothesis states that the GSF (and, thus, the γ transmission coefficient proportional to it) is independent of excitation energy, spin, and parity of the initial and final levels. Even though the Brink-Axel hypothesis was originally formulated for the IVGDR region, it is commonly applied also in the PDR region at lower excitation energies, as it significantly simplifies any calculations involving photon absorption and emission [68]. Even though the discussion around the applicability of the Brink-Axel hypothesis in this region involves cases where it holds well (e.g. [69, 70]) as well as cases where it seems questionable (e.g., Refs. [71, 72]), it has been shown that for the Oslo method analysis of nuclei in different mass regions (including Sn isotopes) it is a reasonable assumption [35, 36, 62, 69, 73].

To extract the NLD $\rho_f = \rho(E_i - E_\gamma)$ and the γ transmission coefficient $\mathcal{T}(E_\gamma)$, the first-generation matrix $P(E_\gamma, E_i)$ is approximated in an iterative χ^2-fit procedure with the following "theoretical" matrix [74]:

$$P_{th}(E_\gamma, E_i) = \frac{\mathcal{T}(E_\gamma)\rho(E_i - E_\gamma)}{\sum_{E_\gamma = E_\gamma^{min}}^{E_i} \mathcal{T}(E_\gamma)\rho(E_i - E_\gamma)}. \quad (2)$$

Prior to this step, the first-generation spectra are normalized to unity for each E_i bin. The details of this procedure and the propagation of statistical, unfolding, and first-generation method uncertainties are outlined in Ref. [74]. It has been repeatedly shown to converge well in each case [37, 75, 76], and the resulting matrix $P_{th}(E_\gamma, E_i)$ reproduces the experimental spectrum quite well for each excitation-energy bin within the chosen limits.

The obtained functions $\rho(E_i - E_\gamma)$ and $\mathcal{T}(E_\gamma)$ of $P_{th}(E_\gamma, E_i)$ provide the best fit of the experimental spectra and represent the solutions for the experimental NLD and the γ transmission coefficient. However, as shown in Ref. [74], although the variation of individual data points with respect to their neighboring points is uniquely determined by the fit, the solutions can be modified with arbitrary chosen scaling parameters A and B and a slope parameter α, providing an equally good fit to the experimental primary spectra through the following transformations:

$$\begin{aligned} \tilde{\rho}(E_i - E_\gamma) &= A\rho(E_i - E_\gamma)\exp[\alpha(E_i - E_\gamma)], \\ \tilde{\mathcal{T}}(E_\gamma) &= B\mathcal{T}(E_\gamma)\exp[\alpha E_\gamma]. \end{aligned} \quad (3)$$

To extract the "true" physical NLD and the γ transmission coefficient, the parameters A, B, and α must be constrained with external experimental data by following normalization procedures as presented in the two subsequent sections.

To ensure a fully consistent normalization procedure, all the Sn nuclei considered here were revisited and renormalized using the most updated experimental information and the same model approaches for the normalization. The main objective of this part of the analysis was not only to make use of the updated external data, but also to apply a consistent model approach for the spin distribution, supported by the most recent experimental and theoretical works [77, 78]. As was shown in the earlier publications, the latter yields a reasonable agreement of the Oslo method NLDs and GSFs with other experimental results [35, 37]. Also, a comparison with the inelastic relativistic proton scattering data [(p,p′) for short] [33] providing the GSFs for the even-even ^{112,114,116,118,120,124}Sn isotopes serves as a benchmark for the slope parameter α shared by the NLD and GSF as well as the absolute normalization of the strength.

1. Normalization of the NLDs

To determine the slope α and the absolute value A, the NLD solutions from Eq. (3) are anchored to known low-lying excited states and the NLD at the neutron separation energy $\rho(S_n)$. We follow the same normalization procedure as presented in the latest publication on $^{111-113}$Sn [37]. The most recent compilation of discrete states [79] was used for all isotopes. To estimate the total NLD at the neutron separation energy, $\rho(S_n)$, the average neutron-resonance spacing D_0 (s-wave neutrons) or D_1 (p-wave neutrons) from neutron resonance experiments can be used. For seven out of eleven studied isotopes, namely $^{113,116-121}$Sn, such data on neutron resonances are available [80]. For s-wave resonances, the D_0 value for a target with non-zero spin can be written as:

$$\frac{1}{D_0} = \rho(S_n, J_t + 1/2, \pi_t) + \rho(S_n, J_t - 1/2, \pi_t), \quad (4)$$

where J_t and π_t are the ground-state spin and parity of the target (sample) in the neutron resonance experiments, respectively. A similar relation for a zero-spin target includes only the first term of this equation. The parity dependence in Eq. (4) is further reduced to the factor of $1/2$ applied to the energy- and spin-dependent level densities due to the assumption that levels with positive and negative parities contribute equally to the NLD in the vicinity of S_n [62, 74]. This assumption was shown to hold well for this excitation-energy region [60, 62]. To calculate the *total* NLD $\rho(S_n)$, we exploit that the *partial* NLD for a given spin J can be found through the relation $\rho(E_x, J) = g(E_x, J)\rho(E_x)$, where $g(E_x, J)$ is the

spin distribution from Refs. [81, 82]:

$$g(E_x, J) \simeq \frac{2J+1}{2\sigma^2(E_x)} \exp\left[-\frac{(J+1/2)^2}{2\sigma^2(E_x)}\right]. \quad (5)$$

Here, $\sigma(E_x)$ is the excitation-energy dependent spin-cutoff parameter. Following the same line of arguments as in Ref. [36], we choose the form of $\sigma(E_x)$ provided by Ref. [82]:

$$\sigma^2(S_n) = 0.0888a\sqrt{\frac{S_n - E_1}{a}}A^{2/3}, \quad (6)$$

with the level density and back-shift parameters a and E_1 obtained from the global parameterization of Ref. [83]. In line with the previously published results on $^{111-113,116,120,124}$Sn [35, 37], the slopes of the NLDs and, therefore, the slopes of the GSFs obtained with this spin-cutoff parameter are in good agreement with the Coulomb excitation data for all isotopes [33]. Moreover, recent calculations by Hilaire *et al.* [78] within the quasi-particle random-phase approximation plus boson expansion reveal a smaller spin cutoff parameter than obtained, e.g., in the rigid-body moment of inertia approximation [83], which further supports the use of $\sigma(E_x)$ in Eq. (6).

Combining Eq. (4) and Eq. (5), $\rho(S_n)$ takes the following form:

$$\rho(S_n) = \frac{2\sigma^2}{D_0} \frac{1}{(J_t+1)\exp\left(-\frac{(J_t+1)^2}{2\sigma^2}\right) + J_t \exp\left(-\frac{J_t^2}{2\sigma^2}\right)}. \quad (7)$$

For ^{111,112,122,124}Sn no neutron resonance data are available, and the $\rho(S_n)$ values were estimated from systematics in the same way as it was done in Ref. [37]. The slopes of the NLDs in ^{120,124}Sn were additionally constrained with the shape method [84] as described in Refs. [35, 36].

The low E_γ boundary employed in the Oslo method analysis limits the experimental NLDs to energies $\approx 1-2$ MeV below the neutron threshold. To be able to connect the experimental NLD fixed to low-lying discrete states and the $\rho(S_n)$ data point, the experimental data were extrapolated with the constant-temperature model [81, 82, 85]:

$$\rho_{CT}(E_x) = \frac{1}{T_{CT}} \exp\left(\frac{E_x - E_0}{T_{CT}}\right), \quad (8)$$

with the temperature T and excitation-energy shift E_0 used as free fit parameters. As discussed earlier in Ref. [86], as well as in Refs. [36, 37] specifically for the Sn isotopes, this model provides the best χ^2 fit to the experimental data above ≈ 3 MeV in the odd nuclei and ≈ 4 MeV in the even-even nuclei.

The uncertainty bands for the experimental NLDs comprise the statistical errors and systematic uncertainties due to the unfolding and the first-generation method, as outlined in Ref. [74]. Analogous to the analysis of

$^{111-113}$Sn [37], the experimental errors of D_0 were propagated together with the assumed additional 10% errors for the $\sigma(S_n)$ parameter and added to the total uncertainty band in each case as described in Refs. [76, 87]. Following Ref. [37], for the cases where the normalization input parameters are obtained from the systematics, a symmetric 30% error for the extracted D_0 parameters was assumed and propagated in the total uncertainty bands. The choices of the errors for $\sigma(S_n)$ and D_0 extracted from the systematics are supported in all the studied cases by a good agreement of the slopes of the Oslo method GSFs with those extracted from the Coulomb excitation data [33]. All input values used for the normalization of the NLDs for $^{111-113,116-122,124}$Sn are provided in Table II.

2. Normalization of the GSFs

The only remaining normalization parameter to be determined after the NLD normalization is the scaling B of the experimental GSF. It can be obtained from the average total radiative width $\langle\Gamma_\gamma\rangle$ extracted in neutron-resonance studies [80]. In general, the average total radiative width for excited states with spin J and parity π at excitation energy E_x can be written as [88]:

$$\langle\Gamma(E_x, J, \pi)\rangle = \frac{1}{2\pi\rho(E_x, J, \pi)} \sum_{XL} \sum_{J_f, \pi_f} \int_{E_\gamma=0}^{E_x} dE_\gamma \times$$
$$\times \mathcal{T}_{XL}(E_\gamma)\rho(E_x - E_\gamma, J_f, \pi_f), \quad (9)$$

where the γ-ray transmission coefficient $T_{XL}(E_\gamma)$ governs γ decays of these states to final states with spins and parities $J_f^{\pi_f}$ with photons of type X (E and M for the electric and magnetic character, respectively) and multipolarity L. Further, the transmission coefficient is linked to the GSF, $f_{XL}(E_\gamma)$, by the relation [88]

$$T_{XL}(E_\gamma) = 2\pi E_\gamma^{2L+1} f_{XL}(E_\gamma). \quad (10)$$

Within the limits of excitation and γ-ray energies chosen for the Oslo method analysis, the γ decay is expected to be dominated by dipole transitions of mixed $E1+M1$ nature (see e.g. [88, 89]). Specifically, for the case of s-wave neutron capture on a target nucleus with ground-state spin-parity $J_t^{\pi_t}$ (where $J_t \neq 0$), Eq. (9) takes the following form:

$$\langle\Gamma_\gamma\rangle = \langle\Gamma(S_n, J_t \pm 1/2, \pi_t)\rangle = \frac{1}{2\rho(S_n, J_t \pm 1/2, \pi_t)} \times$$
$$\times \int_{E_\gamma=0}^{S_n} dE_\gamma E_\gamma^3 f(E_\gamma)\rho(S_n - E_\gamma) \times$$
$$\times \sum_{J=-1}^{1} g(S_n - E_\gamma, J_t \pm 1/2 + J) \quad (11)$$

with $1/\rho(S_n, J_t \pm 1/2, \pi_t) = D_0$ and $g(E_x, J)$ is given by Eq. (5). By analogy with Refs. [35–37], the

TABLE II. Parameters used for the normalization of the NLDs and GSFs for $^{111-113,116-122,124}$Sn.

Nucleus	S_n (MeV)	D_0 (eV)	a (MeV^{-1})	E_1 (MeV)	E_d (MeV)	σ_d	$\sigma(S_n)$	$\rho(S_n)$ (10^5 MeV^{-1})	T (MeV)	E_0 (MeV)	$\langle\Gamma_\gamma\rangle$ (meV)
^{111}Sn	8.169	120(36)[a]	12.05	-0.29	1.08(7)	2.7(4)	4.6(5)	3.54(127)[a]	$0.67^{+0.03}_{-0.02}$	$-0.06^{+0.04}_{-0.11}$	76(18)[a]
^{112}Sn	10.788	3(1)[a]	12.53	1.12	2.83(4)	2.8(4)	4.8(5)	24.61(80)[a]	$0.71^{+0.02}_{-0.02}$	$0.66^{+0.09}_{-0.08}$	87(34)[b]
^{113}Sn	7.744	172(10)	12.77	-0.27	1.88(2)	3.5(7)	4.6(5)	2.50(51)	$0.63^{+0.01}_{-0.01}$	$0.20^{+0.04}_{-0.04}$	73(8)
^{116}Sn	9.563	55(5)	13.66	1.13	2.27(6)	2.7(5)	4.8(5)	4.28(91)	$0.79^{+0.02}_{-0.02}$	$-0.50^{+0.09}_{-0.04}$	118(10)
^{117}Sn	6.943	507(60)	13.62	-0.21	1.11(11)	2.5(2)	4.6(5)	0.85(19)	$0.69^{+0.02}_{-0.02}$	$-0.57^{+0.07}_{-0.05}$	53(3)
^{118}Sn	9.326	61(7)	13.94	1.14	2.48(4)	2.7(5)	4.8(5)	3.89(87)	$0.76^{+0.02}_{-0.02}$	$-0.18^{+0.08}_{-0.13}$	117(20)
^{119}Sn	6.483	700(100)	13.80	-0.30	1.32(2)	3.7(10)	4.6(5)	0.61(15)	$0.69^{+0.02}_{-0.02}$	$-0.80^{+0.05}_{-0.12}$	45(7)
^{120}Sn	9.105	95(14)	13.92	1.12	2.53(4)	3.7(5)	4.8(5)	2.49(60)	$0.75^{+0.02}_{-0.02}$	$0.07^{+0.05}_{-0.05}$	121(25)[c]
^{121}Sn	6.170	1485(130)	13.63	-0.39	1.26(5)	4.0(8)	4.5(5)	0.28(6)	$0.70^{+0.02}_{-0.02}$	$-0.70^{+0.10}_{-0.09}$	36(3)
^{122}Sn	8.815	95(28)[a]	13.58	1.07	2.75(2)	4.2(8)	4.7(5)	1.31(46)[a]	$0.76^{+0.03}_{-0.04}$	$0.07^{+0.19}_{-0.06}$	87(19)[a]
^{124}Sn	8.489	96(27)[a]	12.92	1.03	2.77(3)	3.3(5)	4.7(5)	0.87(26)[a]	$0.79^{+0.02}_{-0.04}$	$-0.31^{+0.16}_{-0.09}$	82(19)[a]

[a] From systematics.
[b] Modified (see Ref. [37]).
[c] Modified (see Ref. [36]).

excitation-energy dependence of the spin-cutoff parameter is adopted from Ref. [68]:

$$\sigma^2(E_x) = \sigma_d^2 + \frac{E_x - E_d}{S_n - E_d}[\sigma^2(S_n) - \sigma_d^2], \qquad (12)$$

which is additionally supported by microscopic calculations (see e.g. [90]). Here, σ_d is the spin-cutoff determined at excitation energy E_d from low-lying discrete states with definite spin and parity assignment, within the energy range where the level scheme can be considered complete.

The average total radiative widths are available from neutron resonance experiments for most of the studied nuclei. For the lightest ^{111,112}Sn isotopes, the values of $\langle\Gamma_\gamma\rangle$ and the corresponding uncertainties were extracted from the systematics in the same way as in Ref. [37]. For ^{124}Sn and ^{122}Sn, the $\langle\Gamma_\gamma\rangle$ values and their uncertainties were extracted from the same systematics according to the procedure described in Refs. [35, 36].

The total experimental uncertainty bands for the GSFs in all the studied Sn isotopes include the statistical errors, systematic uncertainties of the unfolding and the first-generation method combined with the propagated uncertainties due to the normalization input parameters D_0, $\sigma(S_n)$, σ_d, E_d, and $\langle\Gamma_\gamma\rangle$. All of the discussed parameters and uncertainties are presented in Table II.

III. EXPERIMENTAL RESULTS

A. Nuclear level densities of Sn isotopes

The experimental NLDs of $^{111-113,116-122,124}$Sn extracted with the Oslo method are shown in Fig. 2 together with the corresponding constant-temperature

model fits and the $\rho(S_n)$ values. In all cases, the low-lying discrete states are well reproduced by the experimental results up to $\approx 2.5-3.5$ MeV in even-even and $\approx 1.5-2.5$ MeV in even-odd isotopes. Above these energies, the level schemes can no longer be considered complete, failing to follow the exponential increase observed in the Oslo data. For the experiments performed with the oldest configuration of the setup (^{116,118}Sn) the excitation-energy resolution is noticeably worse than in the most recent experiments with SiRi, and the ground and the first excited states are seen as broad bumps rather than well defined peaks as in, e.g., ^{120,124}Sn. The ground state is somewhat underestimated in most of the cases as compared to the first excited state(s), which appears to be a commonly observed feature in OCL experiments (see e.g. the case of ^{46}Ti [54]). This might be linked to the reaction mechanism favoring slightly higher spins of populated states [37] or the structure of the states involved, hindering direct transitions from the quasi-continuum to the ground state. This issue will be addressed in more detail in a forthcoming publication on ^{64}Zn.

At higher excitation energies, all NLDs are well described by the constant-temperature model. Even though the data are available only up to excitation energies $\approx 1-2$ MeV below S_n in each case due to the limitations of the first-generation method (see Secs. II A and II B 1), this trend may be assumed to continue up to the neutron threshold. The new $(p,p'\gamma)$ data on ^{117}Sn perfectly reproduce the earlier published result using a ^{3}He beam [58], while the new $(p,p'\gamma)$ data on ^{119}Sn do not seem to reveal the same step-like structures below ≈ 4 MeV as seen in the previous experiment [60]. The present result is more consistent with the NLDs of the neighboring ^{117,121}Sn and reveals only one clear step-like structure in the vicinity of ≈ 2.6 MeV. This fea-
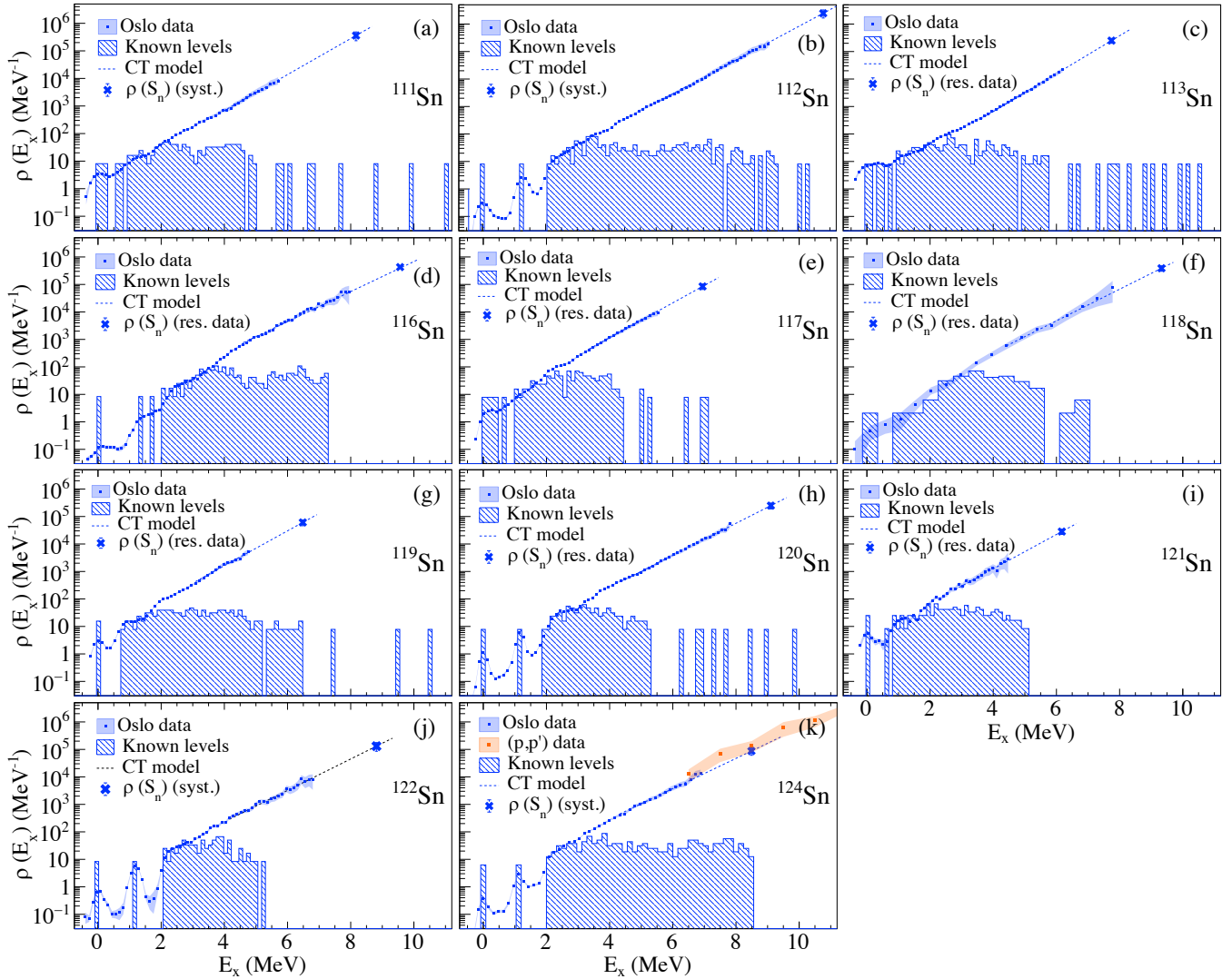
FIG. 2. Experimental NLDs for $^{111-113,116-122,124}$Sn obtained with the Oslo method shown together with the $\rho(S_n)$ values and the constant-temperature fits. The orange band indicates the NLD of for ^{124}Sn from the fluctuation analysis of the Coulomb excitation data [33].

ture is also seen in ^{117}Sn (present work and Ref. [58]) and ^{113}Sn (Ref. [37]) and might be potentially linked to the first broken neutron pair. The features reported in the older experiment should be treated with care, considering the poor statistics of the ^{119}Sn(^{3}He,$\alpha\gamma$)^{118}Sn and ^{119}Sn(^{3}He,^{3}He$'\gamma$)^{119}Sn experiments.

A comparison of the NLDs for ^{111,113}Sn with the NLD for ^{115}Sn from neutron-evaporation experiments [91] has already been discussed in Ref. [37]. The density of 1^- states for ^{124}Sn from a fluctuation analysis of the Coulomb excitation data on ^{124}Sn [33] was compared to the corresponding density from the Oslo data in Ref. [36]. In contrast to the present work, the latter publication presents the data normalized using a spin-cutoff parameter based on the rigid-body moment of inertia [83], providing slightly steeper slopes of the NLDs (lower temperatures). When applied to all the studied isotopes, the

slopes of the corresponding GSFs appear to be steeper than those from the Coulomb excitation data, unless corrected with the shape method [36, 75]. Due to difficulties with the application of the shape method (such as insufficient statistics to provide reliable results at relatively high γ-ray energies), a consistent correction of the NLD slopes in the studied Sn nuclei is complicated. The spin-cutoff parameter from Eq. (6) was found to provide the most consistent description of the NLDs and GSFs in all isotopes, supported by the good agreement with the Coulomb excitation data.

It is important to check if the agreement of the fluctuation-analysis result and the Oslo data for ^{124}Sn presented in Ref. [37] still holds for the new normalization approach. The spin distribution from Eq. (9) was applied to the density of 1^- states obtained with the fluctuation analysis, assuming an equal contribution of
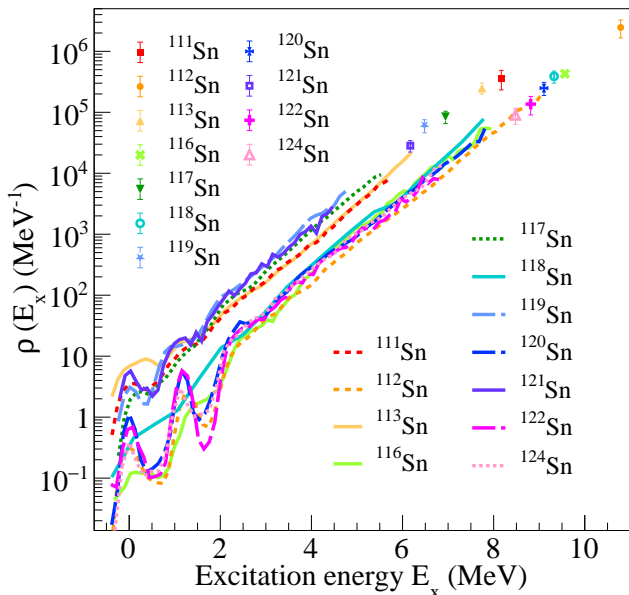
FIG. 3. Experimental NLDs for $^{111-113,116-122,124}$Sn obtained with the Oslo method. The uncertainty bands are omitted for enhancing the clarity of the figure.

states with negative and positive parities above the lower limit of the analysis at $E_x \approx 6.5$ MeV. The resulting total NLD for the ^{124}Sn isotope is shown together with the Oslo data in Fig. 2(k). This comparison of the total NLDs is almost identical to that for the 1^- states from Ref. [36]. Indeed, the rigid-body spin-cutoff parameter provides a broader spin distribution, predicting slightly steeper slopes of the total NLDs and, accordingly, smaller fractions of 1^- states. These two effects compensate each other as seen in the analogous figure of Ref. [36]. With the normalization approach of the present work, the total NLD obtained with the Oslo data lies closer to the bottom of the error band of the fluctuation-analysis data, staying within the band together with the $\rho(S_n)$ value. Hence, when applying the normalization procedure from Sec. II B 1 for a consistent description of all isotopes in the present work, the main conclusions of Ref. [36] still hold.

The NLDs of all the studied isotopes are shown together in Fig. 3. With the same approach to the normalization, the slopes of all NLDs appear to be very similar, corresponding to temperatures of $T \approx 0.6 - 0.8$ MeV. For the even-even nuclei, the NLDs show a good agreement in absolute values, well within the uncertainty bands from ≈ 2 MeV up to the neutron separation energies. This is expected for the even-even Sn isotopes considering their similar structural properties. A much better agreement between the NLDs of the even-odd nuclei from ≈ 1.5 MeV to ≈ 4 MeV is achieved with the present consistent normalization approach, in contrast to the comparison with the earlier published data presented in Ref. [36]. As expected, the level densities of the odd nuclei are system-

atically higher than those of the even-even ones due to the unpaired neutron. The NLDs of the lightest ^{112}Sn and ^{111,113}Sn are slightly lower when compared to the heavier even-even and even-odd isotopes, respectively. This is similar to a pattern observed for the lightest Ni isotopes in Ref. [92]. However, the NLDs of the heavier Sn isotopes display a smaller spread than the heaviest studied Ni isotopes in [92], and the trend of the NLD increasing with neutron number as discussed in [92] is not apparent in the Sn data.

B. Experimental low-lying electric dipole strength in Sn isotopes and its evolution

The GSFs normalized as described in section II B 2 are shown together with the (p, p') and (γ, n) data in Fig. 4. The Coulomb excitation strengths are available only for the even-even ^{112,114,116,118,120,124}Sn isotopes, while photoabsorption data from experiments performed in Saclay [93], Livermore [94], and Moscow [95] are also available for the even-odd stable Sn targets. The photoabsorption cross sections provided by these experiments cover a wide range above the neutron threshold. Overall, these data agree quite well with the (p, p') data in the vicinity of the IVGDR peak at ≈ 15 MeV (for a more detailed discussion see Ref. [33]). The largest deviations of the (γ, n) data from each other and the (p, p') experiments occur in the vicinity of the neutron threshold, which makes a consistent comparison with the Oslo data difficult. Because the Coulomb excitation strengths are available for lower energies (down to ≈ 6 MeV), there is a sufficient overlap with the Oslo method GSFs in most cases. Therefore, we put greater emphasis on the (p, p') data when comparing with the Oslo method results than the (γ, n) data. In contrast to the above-mentioned (γ, n) experiments with quite large uncertainties close to the S_n energy, the most recent (γ, n) experiments on $^{116-120,122,124}$Sn using quasi-monoenergetic photon beams from laser Compton backscattering demonstrate a very good agreement with the (p, p') strengths where the data overlap ($\approx 6 - 12$ MeV).

In Fig. 4(a,b,c), the extracted GSFs for $^{112-113}$Sn are shown together with the (p, p') strength of ^{112}Sn. In all three cases, the strengths agree well within the uncertainty bands as previously discussed in Ref. [37]. The (p, p') strength of ^{114}Sn is in good agreement in slope and absolute value with both the Oslo method GSF of ^{113}Sn and the (p, p') strength of ^{112}Sn. This is also the case for ^{117}Sn and ^{119}Sn, shown together with the (p, p') strengths of the closest neighboring even-even ^{116,118}Sn and ^{118,120}Sn, respectively. The Oslo strengths of ^{116,120,124}Sn agree exceptionally well within the uncertainty bands with the corresponding (p, p') strengths, as reported in Ref. [35]. Due to some minor updates in the response functions used for the unfolding since the time of the latter publication, the slope of the ^{124}Sn is slightly steeper than the one reported in [35], while still
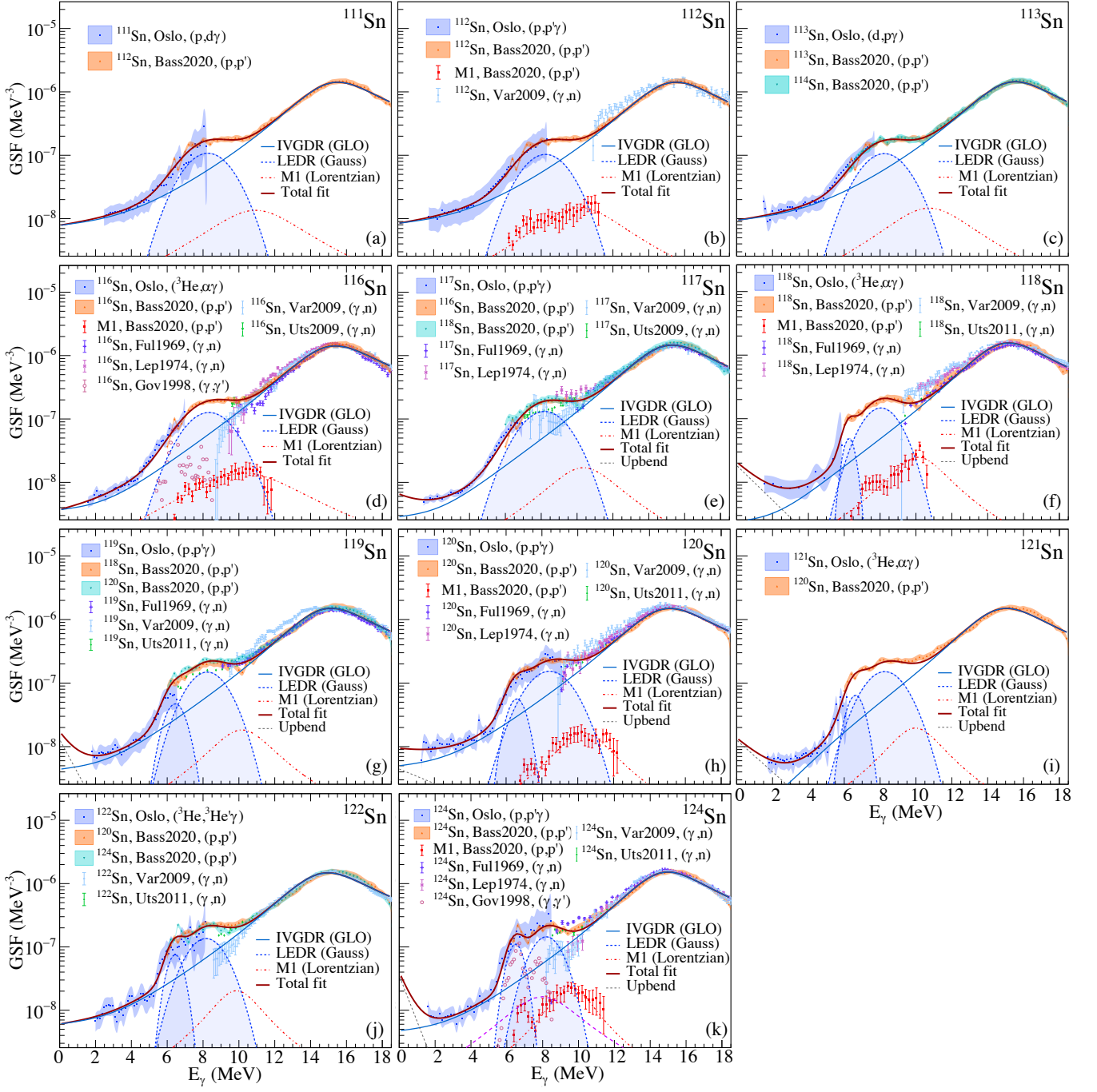
FIG. 4. Experimental GSFs of ^{111}Sn (a), ^{112}Sn (b), ^{113}Sn (c), ^{116}Sn (d), ^{117}Sn (e), ^{118}Sn (f), ^{119}Sn (g), ^{120}Sn (h), ^{121}Sn (i), ^{122}Sn (j), and ^{124}Sn (k) shown together with the (p, p') data from Ref. [33] (Bass2020) and the (γ, n) experimental data by Varlamov *et al.* [95] (Var2009), Fultz *et al.* [93] (Ful1969), Leprêtre *et al.* [94] (Lep1974), Utsunomiya *et al.* [96, 97] (Uts2009 and Uts2011), and Govaert *et al.* [28] (Gov1998). The total fits of the experimental data are shown as solid magenta lines and the fits of the IVGDR as solid blue lines. The low-lying $E1$ components (LEDR), obtained from fits with Eq. (17), are shown as shaded light-blue areas. The $M1$ data from the Coulomb excitation experiment [33] are shown for ^{112,116,118,120,124}Sn with corresponding Lorentzian fits (dashed red lines).

being well within both systematic and statistical uncertainty bands of the earlier published strength. Thus, the conclusions of [35] remain unchanged with the updated version of the GSF for ^{124}Sn.

Above ≈ 6 MeV, the statistics of the older experiment on ^{118}Sn are insufficient to draw any reliable conclusions on the low-lying dipole strength at these energies based on the Oslo data alone. For this reason, the Oslo method GSF of ^{118}Sn is shown only up to ≈ 6 MeV with the (p,p') strength being complementary at higher energies. The Oslo strength in this case agrees fairly well with the strengths of the neighboring even-even isotopes. Similarly, the ^{122}Sn strength is shown up to ≈ 8 MeV, being in good agreement with the (p,p') GSFs of ^{120}Sn and ^{124}Sn. No experimental data on ^{121}Sn above the neutron threshold are available. Assuming a smooth evolution of the IVGDR strength with increasing neutron number as demonstrated by the Coulomb excitation results and the (γ,n) data, the Oslo strength was compared with the (p,p') GSF of the closest even-even ^{120}Sn in Fig. 4(i). Similarly to ^{118}Sn, both GSFs are in fair agreement in absolute values. Overall, the Oslo data reveal a smooth evolution of the low-lying dipole strength below the neutron threshold, with neighboring isotopes having similar shapes of the GSF, consistent with the observed strength in the IVGDR region.

C. Empirical model fits to the data

To address the evolution of the low-lying $E1$ strength with neutron number, it should be consistently extracted from the total dipole response in the studied nuclei. As mentioned earlier, the Oslo method does not distinguish between $E1$ and $M1$ components. Therefore, other experimental constraints on the $M1$ spin-flip resonance are highly desired. In the case of the Sn isotopes, the experimental magnetic dipole strengths are available from the multipole decomposition analysis of the Coulomb excitation data for even-even Sn isotopes [33]. These data provide sufficient information to extract systematics, which allow us to estimate the $M1$ component in the neighboring nuclei. To determine the contribution of the LEDR (or PDR in other works, e.g. [34]), the low-energy tail of the IVGDR has to be subtracted from the remaining total $E1$ response. Unfortunately, there is no common approach to predict the PDR strength distribution in nuclei, nor any consensus on how to separate it from the IVGDR strength. The experimental strength distributions obtained with complementary probes for the same nucleus, albeit being insightful from a nuclear-structure perspective, do not suggest any consistent, quantitative answer to this problem. One of the frequently adopted approaches to extract the LEDR is to assume a model for the IVGDR and estimate the remaining LEDR by subtracting the tail of the modeled IVGDR from the total $E1$ response. Alternatively, a model is assumed to reproduce the general shape of the LEDR yielding the best fit

to the experimental data. This technique is often used for the interpretation of experimental strength distributions in neutron-rich nuclei [10, 98] or analyses featuring Oslo-type experiments (see e.g. [75, 76]). Furthermore, the total theoretical or experimental $E1$ strength can be summed up to a chosen threshold, or within a certain energy range with no assumptions made regarding the tail of the IVGDR and its contribution (see, e.g., [5, 28, 30, 32]).

In this section, we exploit the first of the two abovementioned methods, with as few assumptions as possible, to quantify the evolution of the LEDR in the Sn isotopes from the Oslo results and Coulomb excitation data within the $\simeq 2-18$ MeV γ energy range. In accordance with Ref. [37], we choose the enhanced Generalized Lorentzian model (GLO) to describe the IVGDR data [68]:

$$f_{E1}(E_\gamma) = \frac{1}{3\pi^2\hbar^2c^2}\sigma_{E1}\Gamma_{E1}\times$$
$$\times \left[E_\gamma \frac{\Gamma_{\text{KMF}}(E_\gamma, T_f)}{(E_\gamma^2 - E_{E1}^2)^2 + E_\gamma^2\Gamma_{\text{KMF}}^2(E_\gamma, T_f)} + \right.$$
$$\left. + 0.7\frac{\Gamma_{\text{KMF}}(E_\gamma = 0, T_f)}{E_{E1}^3} \right],$$
(13)

with E_{E1}, Γ_{E1}, σ_{E1} being the IVGDR centroid energy, width, and cross section, respectively. The Γ_{KMF} width corresponds to a temperature-dependent width in the Kadmenskii-Markushev-Furman model [99]:

$$\Gamma_{\text{KMF}}(E_\gamma, T_f) = \frac{\Gamma_{E1}}{E_{E1}^2}(E_\gamma^2 + 4\pi^2 T_f^2), \qquad (14)$$

where T_f is the temperature of the final states.

The standard Lorentzian function, commonly used to fit the photo-neutron cross section above the neutron threshold (see e.g. [32]), is known to overshoot the low-energy flank of the strength and is, therefore, excluded from consideration here. Among other phenomenological models, the Generalized Fermi Liquid model by Mughabghab [100] and the Hybrid model by Goriely [101] are either able to capture the strength distribution at low energies ($\approx 2-4$ MeV) and fail to follow the left flank of the IVGDR or vice versa, being more appropriate in cases with a less steep GSF below S_n (e.g. [76]). The Simplified Modified Lorentzian function (SMLO) [102] results in a milder overshoot below the threshold energy as compared to the standard Lorentzian, while still failing to reproduce the low-energy tail of the Oslo data. Microscopic strength distributions provided by calculations within Skyrme-Hartree-Fock with Bardeen-Cooper-Schrieffer pairing [103], Skyrme-Hartree-Fock-Bogoliubov [44], its temperature-dependent extension [104], and Gogny-Hartree-Fock-Bogoliubov [105] with the quasiparticle random-phase approximation (QRPA) require certain modifications (scaling of the absolute value or width, and often an energy shift) to be able to reproduce the IVGDR part. Even with these modifications, the microscopic calculations still can not be used

TABLE III. Parameters used for the description of the IVGDR and the $M1$ strength in the studied Sn isotopes.

Nucl.	E_{E1} (MeV)	Γ_{E1} (MeV)	σ_{E1} (mb)	T_f (MeV)	E_{M1} (MeV)	Γ_{M1} (MeV)	σ_{M1} (mb)	$C_{\rm up}$ (10^{-8} MeV^{-3})	$\eta_{\rm up}$ (MeV^{-1})
^{111}Sn	16.15(9)	5.49(31)	264.5(93)	0.67(4)	11.22(24)[a]	5.15(39)[a]	1.73(15)[a]	–	–
^{112}Sn	16.14(9)	5.46(31)	265.9(95)	0.70(5)	10.45(43)	4.77(53)	1.77(21)	–	–
^{113}Sn	16.14(6)	5.25(23)	274.4(74)	0.75(3)	10.99(20)[a]	4.72(32)[a]	1.84(11)[a]	–	–
^{116}Sn	16.09(10)	6.03(35)	251.3(91)	0.43(2)	10.79(41)	6.28(96)	1.70(13)	–	–
^{117}Sn	15.98(7)	5.84(26)	257.1(74)	0.38(6)	10.54(12)[a]	3.86(20)[a]	2.05(7)[a]	0.38(10)	0.59(9)
^{118}Sn	15.78(10)	5.50(47)	270.0(153)	0.35(7)	10.26(19)	3.21(34)	2.90(24)	1.84(56)	0.63(8)
^{119}Sn	15.82(6)	5.77(22)	264.0(69)	0.45(9)	10.31(9)[a]	3.44(16)[a]	2.16(8)[a]	1.29(15)	1.20(31)
^{120}Sn	15.82(9)	5.79(39)	262.8(111)	0.48(14)	10.45(18)	3.13(33)	1.97(16)	0.45(7)	0.27(8)
^{121}Sn	15.72(6)	5.86(24)	255.3(66)	0.22(12)	10.08(9)[a]	3.01(14)[a]	2.27(11)[a]	1.27(63)	0.58(22)
^{122}Sn	15.67(3)	5.85(11)	258.7(24)	0.52(3)	9.97(10)[a]	2.79(15)[a]	2.32(13)[a]	–	–
^{124}Sn	15.59(7)	5.37(28)	266.8(90)	0.49(4)	9.66(14)	2.42(20)	2.61(16)	3.52(115)	1.67(40)

[a] From systematics.

to extract the LEDR consistently in all the studied Sn isotopes due to an overshoot at low γ energies in some cases. However, the GLO model is sufficiently flexible within a relatively wide energy range to obtain simultaneously a satisfactory fit of the IVGDR peak and the tail of the strength at $\approx 2-4$ MeV.

For a consistent modeling of the $M1$ part in all Sn isotopes, we assume a simple Lorentzian shape of the spin-flip resonance:

$$f_{M1}(E_\gamma) = \frac{1}{3\pi^2\hbar^2c^2}\frac{\sigma_{M1}\Gamma_{M1}^2E_\gamma}{(E_\gamma^2-E_{M1}^2)^2+E_\gamma^2\Gamma_{M1}^2} \quad (15)$$

with centroid energy E_{M1}, maximum cross section σ_{M1}, and width Γ_{M1}. The experimental $M1$ strengths from the (p,p') experiments on even-even Sn isotopes are quite fragmented, and the Lorentzian function merely reproduces the overall shapes and total integrated $M1$ strengths. As the contribution of this component to the total GSF is less than 10% at the maximum, the details of this fit are of little influence on the final results.

The LEDR component was parameterized with Gaussian peaks:

$$f_{E1}^{\rm low}(E_\gamma) = C_{E1}^{\rm low}\frac{1}{\sqrt{2\pi}\sigma_{E1}^{\rm low}}\exp\left[-\frac{(E_\gamma-E_{E1}^{\rm low})^2}{2(\sigma_{E1}^{\rm low})^2}\right], \quad (16)$$

with centroid $E_{E1}^{\rm low}$, width $\sigma_{E1}^{\rm low}$, and absolute value $C_{E1}^{\rm low}$. The choice of this fit function is not immediately obvious, and for more moderate slopes of the GSFs, the LEDR is also well reproduced by one or a combination of several Lorentzian peaks [75]. For the Sn isotopes having steep slopes at $E_\gamma \approx 4-6$ MeV and relatively flat strength distributions at lower energies, the best fits to the experimental data in the energy range up to S_n are achieved using Gaussian peaks. The Gaussian model was also applied to reproduce the LEDR in very neutron-rich nuclei [10, 98].

To account for the flat low-energy tails of the GSF, we follow the prescription of Ref. [106] suggesting an exponential form of the upbend feature based on the comparison of shell-model calculations and experimental data on Zr and Mo isotopes:

$$f_{\rm up}(E_\gamma) = C_{\rm up}\exp(-\eta_{\rm up}E_\gamma), \quad (17)$$

with scaling and slope parameters $C_{\rm up}$ and $\eta_{\rm up}$. The Oslo data on the Sn isotopes reveal no clear sign of a strong upbend at low E_γ, but show rather flat strength distributions. Since the data are restricted to $E_\gamma \gtrsim 2$ MeV, we do not have sufficient information to reveal any reliable systematics on the upbend as was done recently for the Nd isotopes [75]. In the present work, the upbend is treated solely as a fit component at low γ-ray energies, having negligible impact on the extracted LEDR.

To disentangle the $E1$ and $M1$ components of the total GSF, we first fit the $M1$ strength distributions for ^{112,114,116,118,120,124}Sn and build the systematics for the parameters of the Lorentzian functions to reconstruct the $M1$ part in the even-odd isotopes and ^{122}Sn. The strength distribution in the neighboring even-odd nuclei can be expected to be even more fragmented, but the total amount of the $M1$ strength should still be close to that in the even-even neighbors. Further, the total $E1 + M1$ strength is fitted with the combined function $f_{tot} = f_{E1}+f_{E1}^{\rm low}+f_{M1}+f_{\rm up}$, where the parameters of f_{M1} are kept constant. This corresponds to a simultaneous fit of all $E1$ features of the total strength. Alternatively, the IVGDR region can be fitted first with the f_{E1} function (e.g. see Refs. [37, 107]), then keeping its parameters constant while constraining the remaining LEDR component. The latter method yields slightly larger χ^2 values than the simultaneous fit. Since both methods provide integrated strengths well in agreement within the error bars, we are limiting the analysis to the simultaneous fit

TABLE IV. Parameters used for the description of the low-lying $E1$ strengths, integrated low-lying $E1$ strengths, and the corresponding exhausted fractions of the TRK sum rule in the studied Sn isotopes.

Nucl.	Peak 1			Peak 2			Integrated strength (MeV mb)	TRK (%)
	E_{E1}^{low} (MeV)	$\sigma_{E1}^{\mathrm{low}}$ (MeV)	C_{E1}^{low} $(10^{-7}\ \mathrm{MeV}^{-2})$	E_{E1}^{low} (MeV)	σ_{E1}^{low} (MeV)	C_{E1}^{low} $(10^{-7}\ \mathrm{MeV}^{-2})$		
^{111}Sn	–	–	–	8.26(9)	1.23(7)	3.32(23)	31.6(25)	1.92(14)
^{112}Sn	–	–	–	8.24(9)	1.22(8)	3.17(24)	30.1(25)	1.81(14)
^{113}Sn	–	–	–	8.23(6)	1.23(6)	3.27(17)	31.1(18)	1.86(10)
^{116}Sn	–	–	–	8.33(8)	1.29(6)	4.08(25)	39.2(28)	2.29(14)
^{117}Sn	–	–	–	8.18(6)	1.26(5)	4.15(19)	39.2(20)	2.28(11)
^{118}Sn	6.27(18)	0.33(10)	0.40(15)	8.04(21)	1.00(20)	3.71(65)	37.3(55)	2.16(36)
^{119}Sn	6.44(13)	0.56(11)	0.67(35)	8.23(11)	1.06(11)	3.97(41)	42.7(40)	2.45(27)
^{120}Sn	6.59(11)	0.50(9)	0.71(22)	8.42(12)	1.19(10)	4.60(43)	50.1(47)	2.86(26)
^{121}Sn	6.62(9)	0.48(7)	0.77(20)	8.25(9)	1.11(7)	4.20(31)	45.9(33)	2.61(19)
^{122}Sn	6.45(5)	0.43(5)	0.82(16)	8.17(7)	1.00(7)	3.40(20)	38.1(21)	2.15(13)
^{124}Sn	6.49(5)	0.43(5)	1.20(22)	8.20(7)	0.83(12)	2.99(34)	37.3(36)	2.08(20)

of the total $E1$ strength with f_{tot}. The data to be fitted are the Oslo method GSFs and the corresponding (p, p') strengths for even-even ^{112,116,118,120,124}Sn. For ^{122}Sn and the odd isotopes ^{111,113,117,119,121}Sn, the Coulomb excitation data for the closest even-even isotopes were used (^{120,124}Sn, ^{112}Sn, ^{112,114}Sn, ^{116,118}Sn, ^{118,120}Sn, and ^{120}Sn, respectively). As the (p, p') data demonstrate the same smooth evolution of the IVGDR with increasing neutron number as the (γ, n) data, while also being more consistent in the vicinity of S_n, they were preferred over the (γ, n) strengths for all the considered odd isotopes.

The (p, p') data have been reported to reveal a peak-like structure at $\approx 6.4 - 6.5$ MeV in all studied even-even isotopes [33]. This feature becomes especially prominent in ^{124}Sn. The lack of data points at energies below ≈ 6 MeV did not allow to perform a fit of this feature by using the Coulomb excitation data alone. In general, the energy resolution in Oslo-type of experiments and relatively large systematic uncertainties make it difficult to observe such features in the Oslo data. However, there are some hints of a peak-like feature at $\approx 6.4 - 6.5$ MeV in the ^{124}Sn Oslo strength. Also, the Oslo method GSFs become gradually steeper for heavier Sn isotopes, allowing for introducing an additional Gaussian peak to the fit of the LEDR of the heavier isotopes starting from ^{118}Sn. Indeed, a double-peaked LEDR yields an improved fit of the experimental data between ≈ 5 and 11 MeV for these isotopes as compared to a single Gaussian peak. For the lighter Sn isotopes, the second peak is not well defined and, therefore, was not included in the total fit. All the above-mentioned fit parameters of the IVGDR, the $M1$, and the upbend functions are presented in Table III. The characteristics of the extracted LEDR components are shown in Table IV.

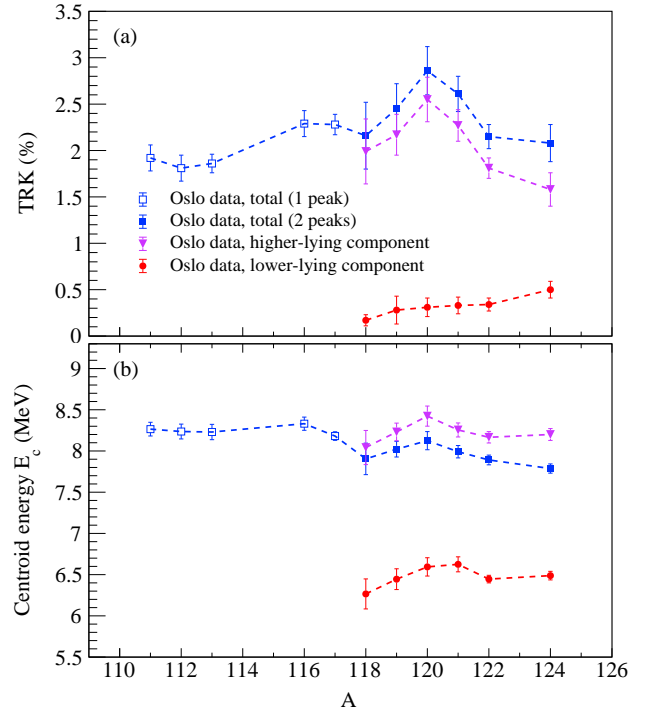The systematics of the total integrated strength of

FIG. 5. TRK values (a) and energy centroids (b) for the total extracted LEDR in Sn isotopes, its lower-lying, and higher-lying components. Hollow squares correspond to a single Gaussian peak fit, filled squares correspond to the sum (a) and strength-averaged centroids (b) of two Gaussian peaks.

the LEDR in the studied Sn isotopes in terms of the exhausted fraction of the TRK sum rule [108–110] are shown in Fig. 5(a). For the isotopes fitted with double

peaks, this fraction is also shown for the smaller, low-lying and the larger, higher-lying components separately. The LEDR extracted according to the above-mentioned procedure appears to correspond to $\approx 2-3\%$ of the TRK sum rule for all the Sn nuclei considered here. No clear systematic increase of the total strength with increasing neutron number is observed. On the contrary, the energy-weighted integrated strengths are quite similar for all the studied nuclei within the uncertainties, peaking around ^{120}Sn ($\approx 3\%$ of the TRK sum rule). The Oslo GSF for ^{120}Sn (normalized independently of the Coulomb excitation data) is quite close within the uncertainty bands to the GSFs of the neighboring isotopes. The appearance of the local maximum is mainly driven by the (p,p') data which show slightly larger absolute values in the energy range from 8 to 10 MeV than in the other isotopes.

Considering that the GSFs of the even-even isotopes were used for constraining the LEDR in the even-odd isotopes, all of them, as expected, reveal a somewhat averaged behavior with respect to the even-even neighbors. This is additionally supported by the Oslo GSFs, demonstrating no clear odd-even effects and showing a smooth trend from the lightest to the heaviest nuclei.

D. Discussion and comparison with theoretical predictions in the literature

Most of the theoretical approaches predict that the low-lying $E1$ strength should increase with the proton-neutron asymmetry parameter, while also not being a function of the neutron excess alone. How steep and monotonous this trend is strongly depends on the theoretical framework and the criteria applied to identify the potential PDR (or LEDR in general) strength. Specifically for the Sn isotopes, the microscopic relativistic quasiparticle random-phase approximation (RQRPA) and relativistic quasiparticle time-blocking approximation (RQTBA) calculations of Ref. [13], Hartree–Fock–Bogoliubov plus quasiparticle phonon model (QPM) calculations of Ref. [111], and the study based on the Vlasov equation approach of Ref. [112] demonstrate a smooth general increase of the LEDR strength with increasing neutron excess. Provided the experimental constraints shown in Fig. 5(a), no claims on any strong dependence of the integrated strength on increasing neutron number between ^{111}Sn and ^{124}Sn can be made. A weak dependence, if present, is obscured by a local peak in strength around ^{120}Sn. Exploiting a single-peak fit for $^{118-122,124}$Sn affects neither the general trend nor the absolute values of the integrated strength within the limits of the estimated uncertainties. The choice of the fit for the $M1$ component was also found to have negligible impact on the obtained values. For example, a more detailed fit of the $M1$ strength with three and two Lorentzian functions for ^{120}Sn and ^{124}Sn, respectively, results only in $\approx 1\%$ reduction of the values shown in Fig. 5(a).

A similar local maximum of the integrated strength in the vicinity of ^{120}Sn has previously been observed within the random-phase approximation (RPA) approach [38], interrupting an almost linear correlation of the integrated PDR strength and the neutron skin thickness. This effect was related to a gradual filling of the $1h_{11/2}$ neutron orbital in the heavier isotopes, suppressing transitions of low multipolarity within the PDR region. Furthermore, pairing correlation effects were included in relativistic Hartree–Bogoliubov (RHB) plus RQRPA calculations [5], which revealed a somewhat similar local peak at $^{120-124}$Sn in the strength evolution. This was attributed to an interplay between reduced pairing correlations and shell effects when approaching the $N = 82$ shell closure. A similar pattern emerges in calculations from a relatively recent study on the isovector and isoscalar response in Sn nuclei within the time-dependent Hartree-Fock (TDHF) approach [113]. The open-shell nucleus ^{120}Sn was shown to have a larger fraction of the energy-weighted sum rule exhausted within the PDR region in both the isoscalar and isovector channels, as compared to the doubly magic ^{100}Sn and ^{132}Sn. Among the studied TDHF density profiles, ^{120}Sn appears to exhibit a slightly more diffuse surface, potentially correlated with the enhancement of the strength in this nucleus. All of these studies employ an upper limit for the extraction of the total integrated strength, which complicates a direct quantitative comparison with the present experimental results. We note that the local maximum of the strength at ^{120}Sn is a subtle feature considering the uncertainties in the data. However, a theoretical interpretation would still be important, in particular whether it presents a local feature based on shell structure or a general phenomenon in nuclei with sufficient neutron excess. A possible link to the explanations offered in Refs. [5, 113] requires further investigations.

It is interesting to note that the energy-weighted integrated strength of the smaller, low-lying component in $^{118-122,124}$Sn increases approximately linear with neutron number [see Fig. 5(a)]. As mentioned earlier, the feature at ≈ 6.5 MeV appearing in the (p,p') strength in all the studied Sn isotopes has, indeed, been noted to become more prominent toward ^{124}Sn [114]. Nevertheless, this trend is quite subtle, and the total exhausted strength of this peak-like structure is limited to only 0.1-0.5% of the TRK sum rule. A similar concentration of the isoscalar strength between 5.5 and 7 MeV has been observed earlier in the studies of ^{124}Sn with the $(\alpha, \alpha'\gamma)$ [22] and $(^{17}\text{O},^{17}\text{O}'\gamma)$ reactions [23]. Combined with the (p,p') and (γ,γ') data, they provide experimental evidence of a structural splitting of the LEDR in this nucleus into a group of lower-lying states of mixed isovector-isoscalar nature, observed in all the mentioned probes, and higher-lying states of isovector nature, seen only in the (p,p') and (γ,γ') experiments. The correspondence with the isoscalar probes and large ground state branching ratios observed in (γ,γ') experiments suggest that the lower-energy peak represents the isovector response

of the PDR. The implications of this result will be further discussed in Ref. [115].

The employed Gaussian fit allows to easily access the evolution of the centroid of the LEDR with increasing neutron number, presented in Fig. 5(b). For $^{118-122,124}$Sn, the centroids of both components are shown together with the strength-weighted average centroid for the total LEDR. The strength in all the studied isotopes is concentrated at $\approx 7.8 - 8.3$ MeV, while the lower and the higher peaks in $^{118-122,124}$Sn show almost constant centroid energies of $\approx 6.4 - 6.5$ and ≈ 8.2 MeV, respectively. Provided that the centroids of the lower and higher components are almost unchanged, a mild decrease of the total LEDR centroid reflects the same strength redistribution as in Fig. 5(a), with gradually more strength grouped at $\approx 6.4 - 6.5$ MeV toward ^{124}Sn. The decrease of the LEDR/PDR centroid is reproduced in RQRPA [5, 13] and QPM [111] calculations for Sn isotopes, appearing also in isotopic chains of other elements [5, 116]. The observed experimental trend of Fig. 5(b) contradicts the previously extracted Oslo systematics of the LEDR centroids in Ref. [34]. This is mainly due to the great inconsistency of the photoabsorption data close to the neutron threshold, which the previous fits in Ref. [34] heavily relied on.

IV. COMPARISON WITH AB INITIO-BASED MODEL CALCULATIONS

Nuclear response theory is the most practical tool to quantify the nuclear strength functions for a wide energy range. At the simplest level, the response theory is confined by the RPA or its superfluid extension, QRPA. Using Feynman diagrams, (Q)RPA is represented by a one-loop diagram of the two-fermion in-medium propagator, while in the most fundamental *ab initio* equation-of-motion (EOM) framework [117, 118], QRPA is obtained by neglecting two-particle-two-hole ($2p2h$) and higher-rank correlations in the interaction kernel. In the EOM of Rowe [119], (Q)RPA is associated with the simplest one-particle-one-hole (two-quasiparticle) $1p1h$ ($2q$) excitation operator, which generates the excited states by its action on a Hartree-Fock (Hartree-Fock-Bogoliubov) ground state. (Q)RPA is known to reproduce the basic properties of giant resonances and soft modes; however, it fails at describing fine spectral details. More accurate solutions involve higher complexity ($npnh$) correlations in both the excited states and the ground state of the nucleus.

All approximations beyond (Q)RPA are derivable from the *ab initio* EOM for the two-fermion response function [120, 121] by retaining more complex correlations, in particular, in the dynamical kernel. The leading approximation beyond (Q)RPA contains the quasiparticle-vibration coupling (qPVC) in the minimal coupling scheme, which includes $2q \otimes$ phonon configurations in the intermediate two-fermion propagator. The vibrations

(phonons) emerge naturally as correlated $2q$ pairs, with the qPVC vertices as the new order parameters. This approach admits realistic implementations that employ effective interactions adjusted in the framework of density functional theory. With such interactions, reasonable phonons can be obtained already within (Q)RPA, and the qPVC can then be combined with subtraction restoring the self-consistency of the *ab initio* framework [122].

The first self-consistent microscopic approach, which includes qPVC in terms of $2q \otimes$ phonon configurations, was presented in Ref. [123] and applied to the dipole response of medium-heavy nuclei. This implementation was a major step toward as a universal theory of nuclear structure rooted in particle physics, named relativistic nuclear field theory, and used the effective meson-exchange interaction [124, 125]. The approach [123] to the response function was based on a phenomenological assumption about the leading role of $2q \otimes$ phonon configurations and the time-blocking technique [126]; thus identified as the relativistic quasiparticle time-blocking approximation (RQTBA). In Refs. [120, 121] the complete response theory was obtained via *ab initio* EOMs, where both the phenomenological qPVC and time blocking are ruled out as unnecessary ingredients. The relativistic EOM confined by the $2q \otimes$ phonon (REOM^2) configurations with the QRPA phonons was shown to be essentially equivalent to RQTBA. However, in contrast to the phenomenological approach, REOM is an *ab initio* theory extendable to configurations of arbitrary complexity. An example of such an extension was presented as REOM^3 accommodating $2q \otimes 2$phonon configurations in Refs. [120, 127].

In this work, REOM^2-RQTBA was applied to calculations of the dipole response of the Sn isotopes under study in a broad energy range up to 25 MeV. The obtained strength distributions are compared to those of relativistic QRPA (RQRPA), which is used as a reference case, and to experimental data, as displayed in Figs. 6 and 7. The NL3* meson-exchange interaction [125] was employed in both approaches and the subtraction [122] is implemented in REOM^2. In the latter, natural-parity phonons up to 15 MeV with $J = [1, 6]$ and reduced transition probabilities above 5% of the maximal one for each multipolarity were comprised in the intermediate $2q \otimes$ phonon propagators. The $2q$ configurations were included up to 100 MeV, while the $2q \otimes$ phonon ones were accommodated up to 25 MeV. Calculations with two values of the smearing parameter Δ, which is defined below, $\Delta = 20$ keV and $\Delta = 200$ keV are presented.

It is clearly seen from Figs. 6 and 7 that adding $2q \otimes$ phonon configurations in RQTBA significantly changes the strength distribution, as compared to RQRPA. Overall, the gross structures of the strength become fragmented and a significant portion moves toward lower transition energies. In particular, the PDR region below 10 MeV manifests considerable structural differences between the RQTBA and RQRPA approaches. Thus,
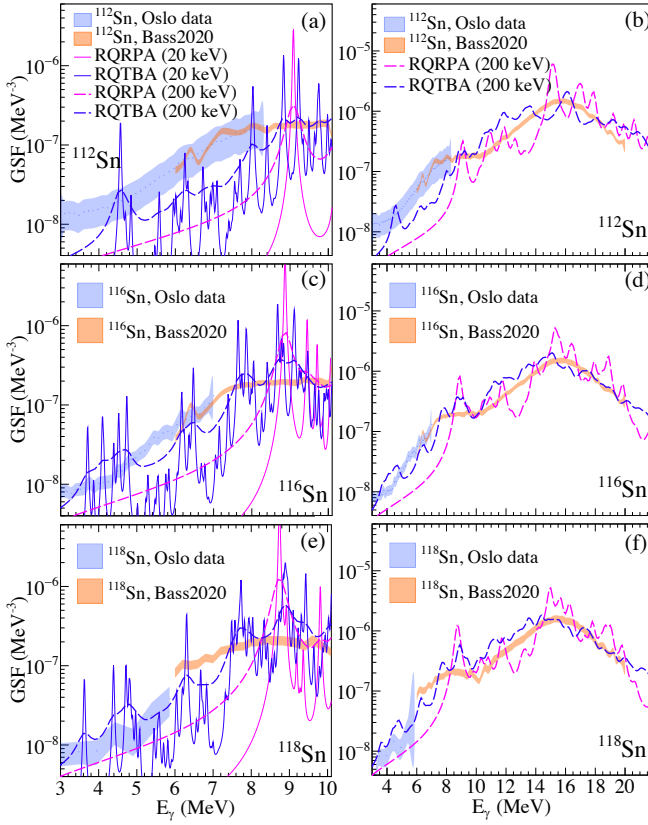
FIG. 6. Calculated dipole strengths for ^{112,116,118}Sn. The low-lying $E1$ transitions computed with the 20-keV (thin solid line) and 200-keV (thick dashed line) artificial widths are shown up to 10 MeV (a, c, e). The strengths computed with the 200-keV artificial width are also shown up to 22 MeV in (b, d, f). The blue and orange bands indicate the corresponding Oslo and (p, p') data (Bass2020). Calculations within the RQRPA and the RQTBA are shown with magenta and violet lines, respectively.

the spreading of the IVGDR and the PDR structure occur mainly due to these configurations. In the paradigm of a self-consistent covariant many-body theory, its only input is the local meson-exchange interaction between two nucleons, while all the in-medium many-body correlations are included without changing the parameters of this interaction, or introducing new ones. Within this paradigm, the RQTBA strength distribution is a result of the fragmentation of the RQRPA modes.

This can be understood from the general model-independent relationships, where the strength function $S(\omega)$ for a given energy (or frequency) ω is defined by Fermi's golden rule:

$$S(\omega) = \sum_{\nu>0}\Big[|\langle\nu|F^\dagger|0\rangle|^2\delta(\omega-\omega_\nu) - |\langle\nu|F|0\rangle|^2\delta(\omega+\omega_\nu)\Big],$$

(18)

where the summation is performed over all excited states $|\nu\rangle$ with transition energy $\omega_\nu = E_\nu - E_0$ with E_0 being
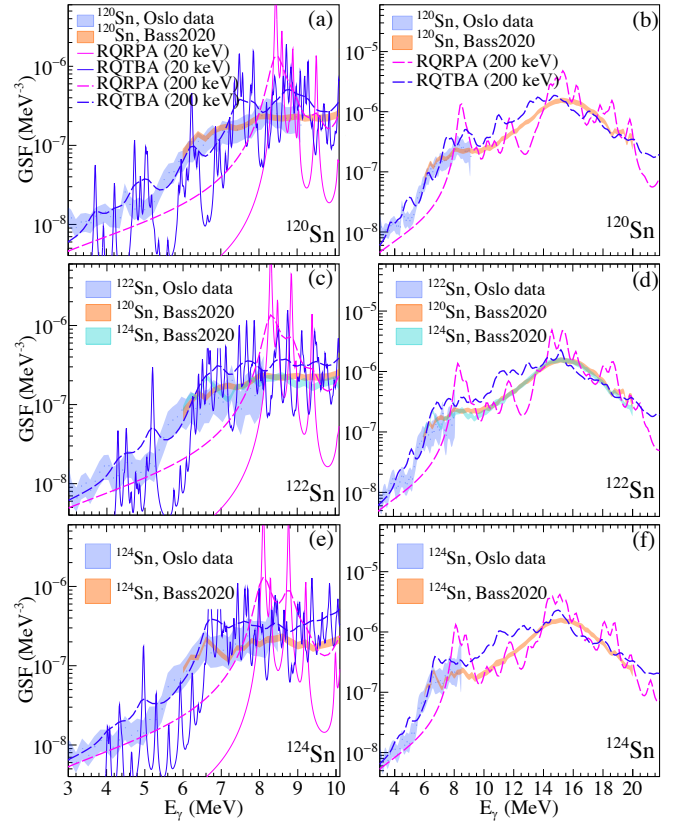
FIG. 7. Same as in Fig. 6, but for ^{120,122,124}Sn. For ^{122}Sn, both ^{120}Sn and ^{124}Sn (p, p') data are shown.

the ground-state energy. The transition matrix element $\langle\nu|F^\dagger|0\rangle$ for the typical one-body external field operator

$$\langle\nu|F^\dagger|0\rangle = \sum_{12}\langle\nu|F_{12}^*\psi_2^\dagger\psi_1|0\rangle = \sum_{12}F_{12}^*\rho_{21}^{\nu*},$$

(19)

is expressed via the transition densities

$$\rho_{12}^\nu = \langle0|\psi_2^\dagger\psi_1|\nu\rangle,$$

(20)

which are the weights of the pure particle-hole configurations $\psi_2^\dagger\psi_1$ in the single-particle basis $\{1\}$, on top of the ground state $|0\rangle$, in the excited states $|\nu\rangle$, and ψ_1 and $\psi_1^\dagger$ are the nucleonic field operators. Conventionally, the δ functions in Eq. (18) are represented by the Lorentz distribution

$$\delta(\omega - \omega_\nu) = \frac{1}{\pi}\lim_{\Delta\to0}\frac{\Delta}{(\omega-\omega_\nu)^2+\Delta^2},$$

(21)

so that

$$S(\omega) = -\frac{1}{\pi}\lim_{\Delta\to0}\mathrm{Im}\Pi(\omega+i\Delta),$$

(22)

where $\Pi(\omega)$ is the polarizability of the nucleus:

$$\Pi(\omega) = \sum_\nu\Big[\frac{B_\nu}{\omega-\omega_\nu} - \frac{\bar{B}_\nu}{\omega+\omega_\nu}\Big]$$

(23)

related to the transition probabilities B_ν and $\bar{B}_\nu$ of absorption and emission, respectively:

$$B_\nu = |\langle\nu|F^\dagger|0\rangle|^2 \qquad \bar{B}_\nu = |\langle\nu|F|0\rangle|^2. \qquad (24)$$

Therefore, the strength function that quantifies the nuclear response to the given external field operator F reads:

$$S_F(\omega) = -\frac{1}{\pi} \lim_{\Delta\to 0} \text{Im} \sum_{121'2'} F_{12} R_{12,1'2'}(\omega + i\Delta) F^*_{1'2'},$$
$$(25)$$

where the central role in characterizing the nuclear structure is played by the response function $R_{12,1'2'}(\omega)$, whose spectral representation is:

$$R_{12,1'2'}(\omega) = \sum_{\nu > 0} \Big[\frac{\rho^\nu_{21}\rho^{\nu*}_{2'1'}}{\omega - \omega_\nu + i\delta} - \frac{\rho^{\nu*}_{12}\rho^\nu_{1'2'}}{\omega + \omega_\nu - i\delta} \Big]. \quad (26)$$

The poles of $R_{12,1'2'}(\omega)$ are at the energies $\omega_\nu = E_\nu - E_0$ of the excited states with respect to the ground state energy and $\delta \to +0$.

Eq. (26) is the Fourier transform of the particle-hole propagator in a correlated medium:

$$R_{12,1'2'}(t - t') = -i\langle T\psi^\dagger(1)\psi(2)\psi^\dagger(2')\psi(1')\rangle, \quad (27)$$

where $\langle...\rangle$ is a shorthand notation for the expectation value in the ground state and $\psi(1), \psi^\dagger(1)$ are the fermionic field operators in the Heisenberg picture:

$$\psi(1) \equiv \psi_1(t_1) \equiv e^{iHt_1}\psi_1 e^{-iHt_1}$$
$$\psi^\dagger(1) \equiv \psi^\dagger_1(t_1) \equiv e^{iHt_1}\psi^\dagger_1 e^{-iHt_1}. \qquad (28)$$

where $t_1 = t_2 = t$, $t_{1'} = t_{2'} = t'$, and the fermionic Hamiltonian

$$H = \sum_{12} h_{12}\psi^\dagger_1\psi_2 + \frac{1}{4}\sum_{1234} \bar{v}_{1234}\psi^\dagger_1\psi^\dagger_2\psi_4\psi_3 \qquad (29)$$

is specified by its one-body h_{12} and two-body $\bar{v}_{1234}$ matrix elements.

The strength distribution for the given external field operator, which, in this work, is the electric dipole operator (μ denotes the magnetic substate)

$$F^{(E1)}_{1\mu} = \frac{eN}{A}\sum_{i=1}^{Z} r_i Y_{1\mu}(\hat{\mathbf{r}}_i) - \frac{eZ}{A}\sum_{i=1}^{N} r_i Y_{1\mu}(\hat{\mathbf{r}}_i),$$
$$(30)$$

is completely determined by the response function given by Eq. (26). The number of peaks in the resulting spectrum is equal to the number of terms in Eq. (26), and this number as well as the locations of the poles and transition densities are determined by the correlation content of the theory. The response function can be found from the Bethe-Salpeter-Dyson equation (BSDE), that is, in the operator form,

$$R(\omega) = R^0(\omega) + R^0(\omega)\Big(K^0 + K^r(\omega)\Big)R(\omega), \qquad (31)$$

where $R^0(\omega)$ is the non-interacting particle-hole propagator in the mean field and the specific forms of the interaction kernels are given, for instance, in Refs. [121, 123]. For the application discussed in this work, it is essential that the RQRPA strength is obtained by neglecting completely the $K^r(\omega)$ term, which contains the qPVC correlations and is retained in RQTBA.

In the implementations using physical effective interactions, these interactions play the role of the static kernel K^0, which is the only interaction term in the (R)QRPA. In this approach, the dipole spectrum is characterized by two pronounced peaks, one at higher energy and the other at low energy, and a few less prominent structures. The high-energy peak is associated with the IVGDR formed by the out-of-phase oscillations of the proton and neutron Fermi liquids against each other, which follows from the radial behavior of the transition densities for this excitation. The two-quasiparticle content of the transition densities shows a rather high degree of collectivity when many $2q$ configurations contribute coherently to the probabilities from Eq. (24). The low-energy peak, often assigned as the PDR, can be identified by similar means. Within this framework, it shows up as a neutron excess oscillation against the isospin-saturated core, also with some sign of collectivity [5, 20].

In comparison to data, the position of the main IVGDR peak is typically described reasonably well in (R)QRPA, however, this is often not the case for the PDR. The reason becomes evident only when going beyond the simplistic QRPA and including the frequency-dependent kernel $K^r(\omega)$ in the BSDE [Eq. (31)]. The leading $2q \otimes$ phonon configurations included in REOM²-RQTBA induce a similar fragmentation of both major peaks, and the resulting fragments overlap in the energy region between the IVGDR and PDR modes. This further leads to the same problem of separating the PDR contribution from the low-energy tail of the IVGDR as discussed earlier in Sec. III B.

According to Eq. (26), adding $2q \otimes$ phonon configurations produces additional terms in the sum on the right-hand side, i.e., more states in the resulting spectrum than with $2q$ configurations alone. This is reflected in Figs. 6 and 7 for all the isotopes under study. The number of additional states is equal to the number of possible $2q \otimes$ phonon combinations compatible with angular-momentum conservation. Overall, adding complex configurations leads to a better description of the data, in particular, the IVGDR width and the PDR fine structure. The importance of these configurations is especially evident when comparing the strength distributions at low energies shown in the left panels of Figs. 6 and 7 obtained with the different values of the smearing parameter Δ. It can be seen, for instance, that the low-energy portion of the RQRPA strength function is the purely artificial tail of the states located at 8-9 MeV. The finite strength below that energy originates solely from the smearing. Accordingly, the strength varies considerably when varying Δ. In contrast, the RQTBA strength below the neu-
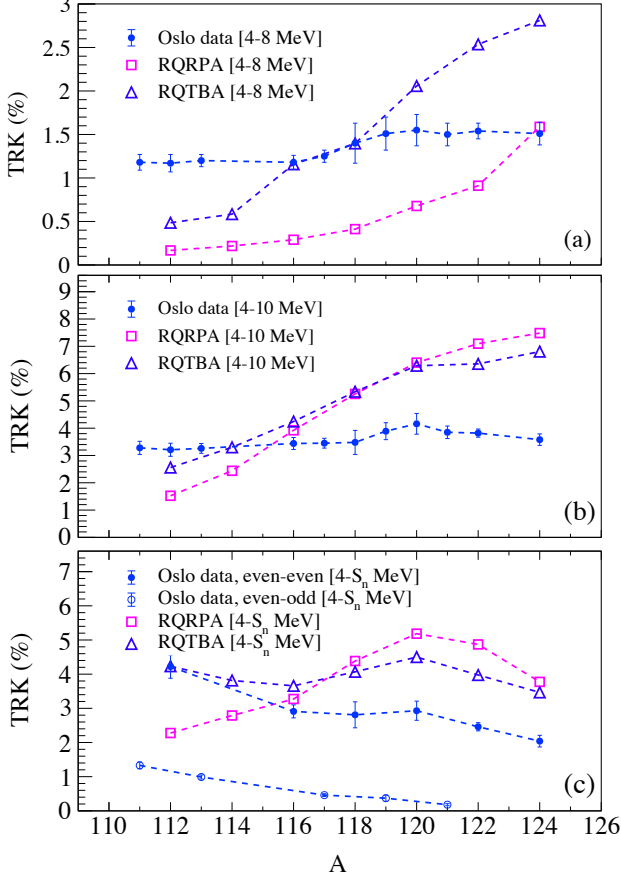
FIG. 8. The evolution of the energy-weighted electric dipole strength extracted from the RQRPA and RQTBA calculations and the combined experimental Oslo and (p,p'), integrated from 4 MeV up to 8 MeV (a), 10 MeV (b), and S_n (c).

tron threshold is essentially physical and the choice of the smearing parameter plays a minor role. This choice in the low level-density regime is stipulated by the experimental energy resolution, the finite level lifetime and missing higher-complexity configurations. In the context of this work, $\Delta = 200$ keV is an appropriate value, and calculations with $\Delta = 20$ keV are given to illustrate the fine structure of the strength. Nevertheless, the choice of this parameter plays a minor role as long as complex configurations are taken into account, which emphasizes the importance of these configurations for an adequate description of the low-energy nuclear strength functions.

To compare the overall behavior of the RQRPA, RQTBA, and experimental strength distributions on an equal footing, we extract the energy-weighted sums of the total electric dipole strength (the $M1$ component was subtracted from the experimental strength functions) within three energy ranges, namely $4 - 8$ MeV, $4 - 10$ MeV, and $4 - S_n$, similarly to how it was done in Ref. [13]. This procedure corresponds to the second method of quantifying the LEDR contribution mentioned in the pre-

vious section. The extracted fractions of the TRK sum rule exhausted in each case are shown in Fig. 8. As discussed earlier, the experimental LEDR appears to be concentrated in the vicinity of 8 MeV and, naturally, a large fraction of the strength is located above this threshold. The experimental strength between 4 and 8 MeV corresponds to $\approx 1.2 - 1.5\%$ of the TRK sum rule. The monotonous increase of the RQRPA strength in this energy range is solely due to the artificial tails of the states at 8-9 MeV with the applied 200-keV smearing parameter, while the RQTBA strength increases gradually from $\approx 0.5 - 2.7\%$ of the TRK sum rule. Within the energy range up to 10 MeV, including most of the LEDR in the studied nuclei, the experimental strength exhausts $\approx 3 - 4\%$ of the TRK sum rule (here the IVGDR tail is included in the sum), in contrast to both RQRPA and RQTBA predicting a steady, monotonous increase of strength up to $\approx 7\%$ in ^{124}Sn. Indeed, both approaches result in larger concentrations of strength in the immediate vicinity of 8-10 MeV as compared to the experimental strength distribution, gradually increasing with neutron number. Moreover, as clearly shown in Fig. 8(c), RQRPA and RQTBA yield on average more strength below the neutron threshold in comparison to the experimental data, demonstrating steadily decreasing TRK values toward ^{124}Sn in the even-even isotopes.

The agreement of RQTBA to experimental data, although improved compared to RQRPA, is still imperfect. This indicates that some mechanisms of the strength formation are still missing to achieve spectroscopic accuracy. A complete response theory should take into account the continuum, including the multiparticle escape, a more complete set of phonons (in particular, those of unnatural parity and isospin-flip), complex ground state correlations, and in principle higher-complexity configurations.

The single-particle continuum effect above the particle emission threshold can be taken into account by the smearing parameter, as it mainly causes uniform broadening of the individual peaks. This was quantified by direct calculations in Ref. [130] that give a 100-200 keV width to characterize such a broadening, which is considerably smaller than the spreading width. The two-fermionic cluster decomposition of the fully correlated dynamical kernel of the response function [120] suggests that the next-level complexity non-perturbative approximation is the $2q \otimes 2$phonon or correlated six-quasiparticle configurations in the intermediate propagators. The implementation of such configurations is becoming gradually possible with the increasing computational capabilities [120, 127]; however, systematic calculations for long isotopic chains of medium-heavy nuclei are still computationally demanding. Current efforts on optimizing the numerical $2q \otimes 2$phonon approach may enable such calculations in the near future.
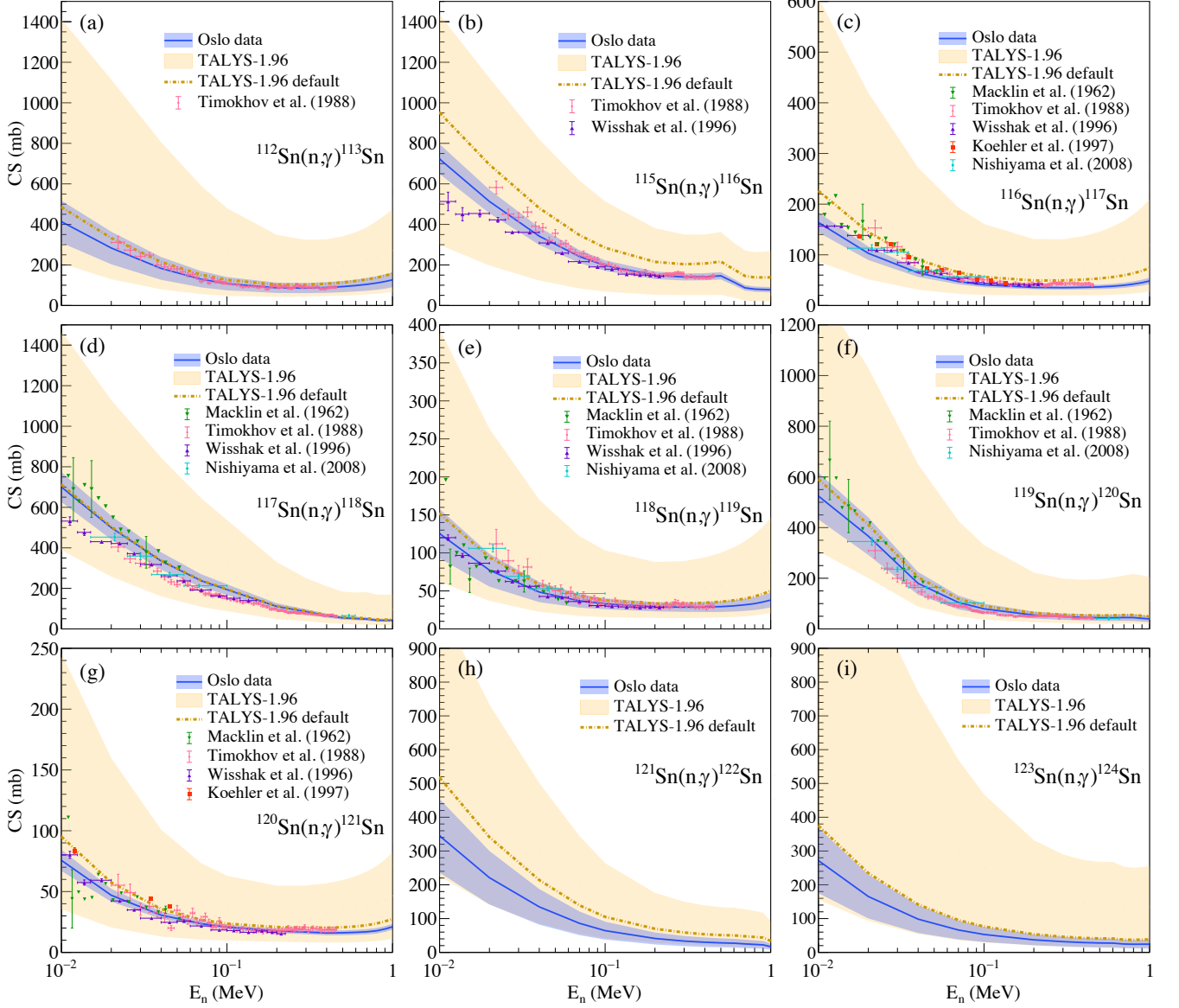
FIG. 9. Cross sections (CS) for the ^{112}Sn$(n,\gamma)^{113}$Sn (a), ^{115}Sn$(n,\gamma)^{116}$Sn (b), ^{116}Sn$(n,\gamma)^{117}$Sn (c), ^{117}Sn$(n,\gamma)^{118}$Sn (d), ^{118}Sn$(n,\gamma)^{119}$Sn (e), ^{119}Sn$(n,\gamma)^{120}$Sn (f), ^{120}Sn$(n,\gamma)^{121}$Sn (g), ^{121}Sn$(n,\gamma)^{122}$Sn (h), and ^{123}Sn$(n,\gamma)^{124}$Sn (i) reactions. The predictions with the Oslo method inputs (blue bands) are compared with experimental data by Macklin *et al.* [48], Timokhov *et al.* [128], Wisshak *et al.* [49], Koehler *et al.* [50], Nishiyama *et al.* [129], and the TALYS uncertainty range obtained with different available GSFs, NLDs, and optical model potentials (beige band).

V. NEUTRON CAPTURE CROSS SECTIONS

The experimental values of the NLD and GSF extracted with the Oslo method can further be used to estimate the radiative neutron-capture cross sections (n,γ) (NCCS) and reaction rates of interest for the astrophysical neutron capture processes. This was done within the statistical Hauser-Feshbach framework [45] with the TALYS reaction code (version 1.96) [47, 134]. The experimental Oslo method GSFs were combined with the

(p,p') data at energies above their range to produce the tabulated $E1$ strengths used as input functions. For the $M1$ input strength function, the (p,p') $M1$ data were chosen. For the optical model potential we use the phenomenological model of Koning and Delaroche [135]. An alternative option provided by TALYS is the semimicroscopic Jeukenne-Lejeune-Mahaux model renormalized by the Bruyères-le-Châtel group [136]. In contrast to the earlier published cases of ^{165,166}Ho [137] and ^{185}W [76], the results obtained with both optical model potentials agree well within the uncertainty bands. Therefore, only
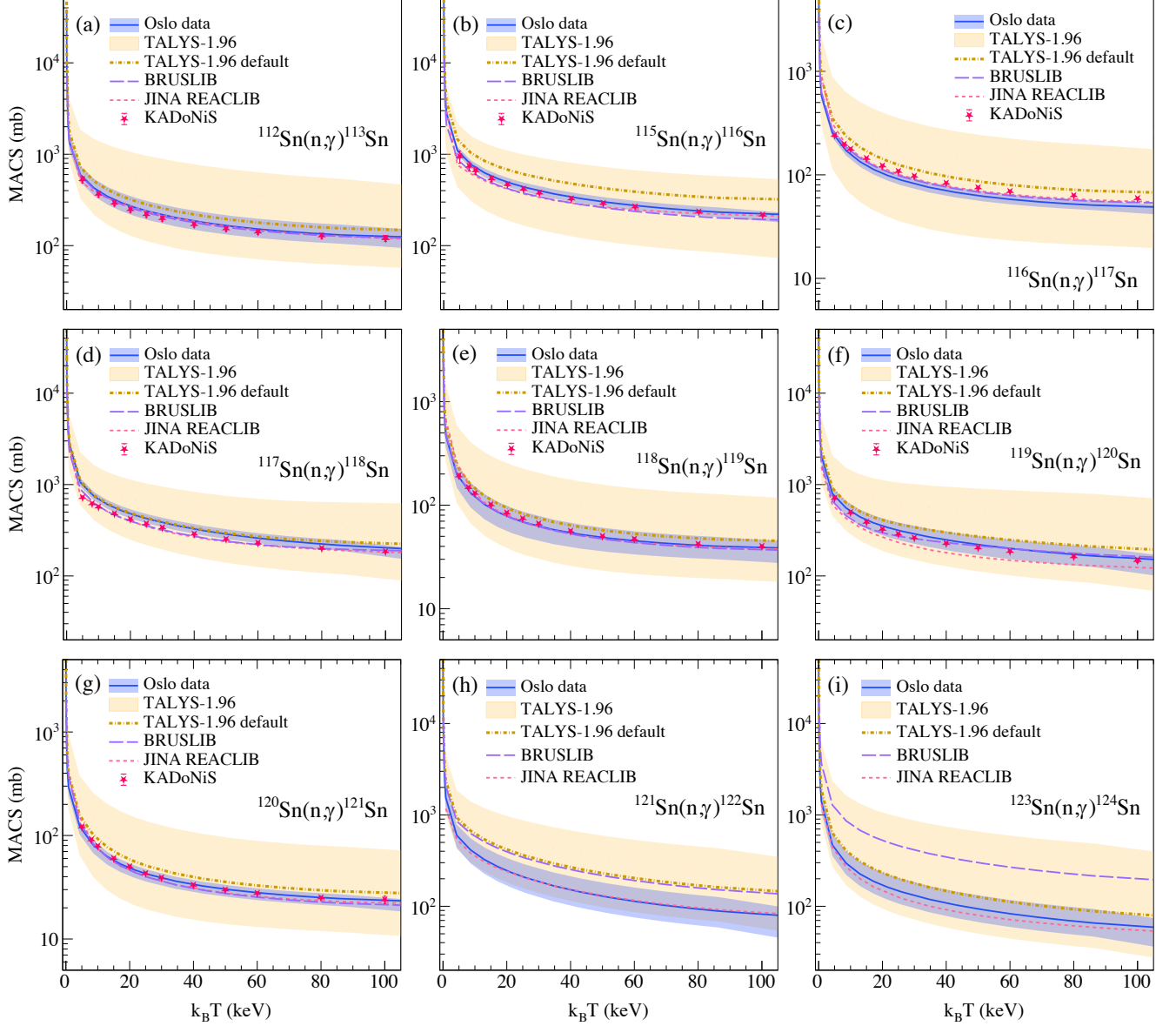
FIG. 10. Maxwellian-averaged cross sections (MACS) for the ^{112}Sn$(n,\gamma)^{113}$Sn (a), ^{115}Sn$(n,\gamma)^{116}$Sn (b), ^{116}Sn$(n,\gamma)^{117}$Sn (c), ^{117}Sn$(n,\gamma)^{118}$Sn (d), ^{118}Sn$(n,\gamma)^{119}$Sn (e), ^{119}Sn$(n,\gamma)^{120}$Sn (f), ^{120}Sn$(n,\gamma)^{121}$Sn (g), ^{121}Sn$(n,\gamma)^{122}$Sn (h), and ^{123}Sn$(n,\gamma)^{124}$Sn (i) reactions. The predictions with the Oslo method inputs (blue bands) are compared with recommended values from JINA REACLIB [131], BRUSLIB [132], KADoNiS [133], and the TALYS uncertainty range obtained with different available GSFs, NLDs, and optical model potentials (beige band).

calculations performed with the former model are presented in this work. The resulting NCCSs are shown in Fig. 9. The uncertainties due to the normalization parameters are included in the total uncertainty bands. The Oslo NCCSs (blue bands) are shown together with the span of TALYS cross sections, obtained by varying available GSFs, NLDs, and optical model potentials. In case of the Sn isotopes, since the radiative NCCS is rather insensitive to the optical potential and the experimental masses are adopted in each case, the former two are the major contributors to the wide spread of TALYS predic-

tions, describing the overall discrepancies between NLD and GSF options available in TALYS [47, 137]. The cross section obtained with the default combination of models (constant temperature plus Fermi gas NLD model, SMLO form of the $E1$ strength, Koning and Delaroche global optical model potential) is also shown for each isotope in Fig. 9.

Even though the ^{112}Sn$(n,\gamma)^{113}$Sn reaction is of no potential interest for the astrophysical s process, the comparison of the Oslo results with experimental (n,γ) cross sections from a comprehensive study by Timokhov et

al. [128] is still valuable. Other experimental data in the keV region are also available for the neutron capture on the $^{115-120}$Sn targets [see Figs. 9(b)-(g)], covering almost all Sn isotopes involved in the s process [50]. As was shown recently by Goriely et al [53], the (n, γ) reactions on ^{120,121,123}Sn [Figs. 9(g)-(i)] might be of interest for the intermediate neutron capture process (i process). All experimental cross sections in Fig. 9 were obtained with the time-of-flight method with neutrons produced in the ^{7}Li$(p, n)^7$Be reaction. The cross sections of Timokhov et al. appear to be in excellent agreement with the Oslo cross sections for the (n, γ) reaction on ^{112}Sn, ^{115}Sn, ^{118}Sn, ^{119}Sn, and ^{120}Sn. The Oslo NCCS is systematically lower for the ^{116}Sn and systematically higher for the ^{117}Sn targets compared to the data by Timokhov et al., while still agreeing within the uncertainty bands with the cross sections by Wisshak et al. [49]. In particular, a good agreement is achieved with the cross sections by Nishiyama et al. for the neutron capture on $^{116-119}$Sn [129, 138]. Overall, the Oslo results tend to agree within the uncertainty margins with all other experimental NCCS above neutron energies of $\approx 20 - 30$ keV. At lower energies, the experimental uncertainties increase, and different data sets demonstrate a wide spread of cross sections (of the order of ≈ 100 mb). For the ^{121,123}Sn targets no experimental data are available and, similarly to the lighter isotopes, the Oslo results are closer to the bottom part of the range of TALYS cross sections.

With the radiative NCCS at hand, the corresponding Maxwellian-averaged cross sections (MACS) can be estimated. The MACS values for the same target nuclei obtained with the experimental Oslo data are shown in Fig. 10 together with the span covered by available combinations of TALYS input models and the TALYS default MACSs. We also compare our results to the cross sections from the JINA REACLIB [131] and BRUSLIB [132] libraries, commonly used for astrophysical network calculations. The available data points from the KADoNiS database [133] are also shown in Fig. 10. It is important to note that all cross sections shown in Fig. 10 are stellar MACSs. For the ^{119}Sn and ^{121}Sn target nuclei the discrepancy between the stellar and laboratory MACSs might reach up to $\approx 56\%$ and 20%, respectively, below the thermal energy of 100 keV [133].

In the majority of considered cases, the recommended MACSs from the libraries fall well within the uncertainty bands of the Oslo results. The BRUSLIB MACSs for the ^{121}Sn and ^{123}Sn targets appear to be on average ≈ 1.2 and ≈ 2.2 times higher, respectively, compared to the Oslo MACSs for the thermal energies between 10 and 100 keV. This disagreement stems primarily from the combinations of the NLD model (Skyrme-Hartree-Fock-Bogoluybov plus Combinatorial NLDs [139]) and GSF model (Gogny-Hartree-Fock-Bogoliubov plus QRPA GSF [44]) employed in BRUS-LIB. The latter model tends to underestimate the $E1$ strength distribution in the immediate vicinity of S_n. In
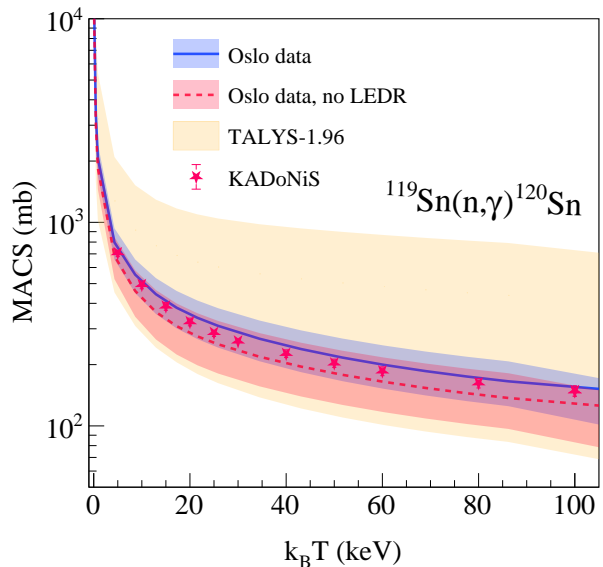

FIG. 11. MACS for the ^{119}Sn$(n, \gamma)^{120}$Sn reaction with and without the low-lying electric dipole strength included. The Oslo results with the LEDR (blue band) and without (red band) are compared with the TALYS uncertainty range (beige band) and recommended values from KADoNiS [133].

general, the Skyrme-HFB plus combinatorial model reproduces the Oslo method NLDs quite well for the lighter Sn nuclei (e.g. ^{116}Sn) and begins to overestimate the Oslo NLD values quite significantly toward more neutron-rich isotopes. Despite the model GSF being, on average, lower than the experimental strength, the net effect of these models combined together leads to the disagreement visible in Figs. 10(h) and (i).

The Oslo MACSs agree quite well within the estimated uncertainties with the values provided by the KADoNiS database. Some systematic deviations are observed for the ^{116}Sn and ^{117}Sn targets, similarly to those in the NCCSs. The source of these deviations in both cases is not immediately obvious based on the used Oslo input data. The recommended KADoNiS values at 30 keV for Sn isotopes are largely based on the cross sections of Macklin et al. [48], Timokhov et al., Wisshak et al., Koehler et al. [50], Nishiyama et al., and are often presented at other k_BT values by the average of evaluations from the ENDF/B-VII.1 [140] and JENDL-4.0 [141] libraries. The uncertainties of these values, estimated for the majority of Sn isotopes from the deviations of these two evaluations, might be underestimating the KADoNiS systematic errors. The error bands of the Oslo MACSs, including all uncertainties due to the normalization of the nuclear inputs (NLD and GSF), provide far more conservative spans of the cross sections, nevertheless, considerably constraining the TALYS uncertainty range.

As mentioned earlier, correct theoretical reproduction of the LEDR is of importance for astrophysical applications, in particular involving neutron-rich nuclei. Albeit

the LEDR in the studied stable isotopes exhausts only $\approx 2 - 3\%$ of the TRK sum rule, it might still noticeably contribute to the radiative neutron capture rates and cross sections. To estimate the contribution of the observed LEDR in the Sn isotopes to the MACS, we performed TALYS calculations for the $^{119}\text{Sn}(n,\gamma)^{120}\text{Sn}$ reaction with the Oslo input GSF of ^{120}Sn with an artificially subtracted LEDR, extracted according to the procedure in Sec. III B (see Table IV for the Gaussian peak parameters). This MACS is compared to the MACS extracted with the original Oslo GSF of ^{120}Sn in Fig. 11. The MACS obtained with no LEDR is consistently lower and, on average, it amounts to $\approx 80\%$ of the full MACS in the vicinity of 30 keV. Even though the cross sections overlap within the estimated uncertainty bands, the 20% decrease is considerable for the relatively small exhausted fraction of the TRK sum rule ($\approx 3\%$). With the current status of available theoretical frameworks a consistent quantitative assessment of the role of the LEDR in astrophysical simulations remains a complex, non-trivial task, encouraging further advances in theoretical approaches and experimental studies of nuclei beyond the valley of stability.

VI. ASTROPHYSICAL IMPLICATIONS

To illustrate the impact of the newly determined reaction rates on some astrophysical applications, we consider the i-process nucleosynthesis in Asymptotic Giant Branch (AGB) stars. The AGB phase corresponds to the last evolutionary stage of $\approx 1 - 8\ M_\odot$ stars [e.g. 142]. During this stage, hydrogen can be engulfed by one of the recurrent convective thermal pulses, leading to a proton ingestion event (PIE, e.g. [143–146]). During a PIE, protons are transported downwards in a timescale of about 1 hr and quickly burnt by the $^{12}\text{C}(p,\gamma)^{13}\text{N}$ reaction. The

TABLE V. Cases considered for the rates of the $^{121}\text{Sn}(n,\gamma)^{122}\text{Sn}$ and $^{123}\text{Sn}(n,\gamma)^{124}\text{Sn}$ reactions for the multizone stellar calculations.

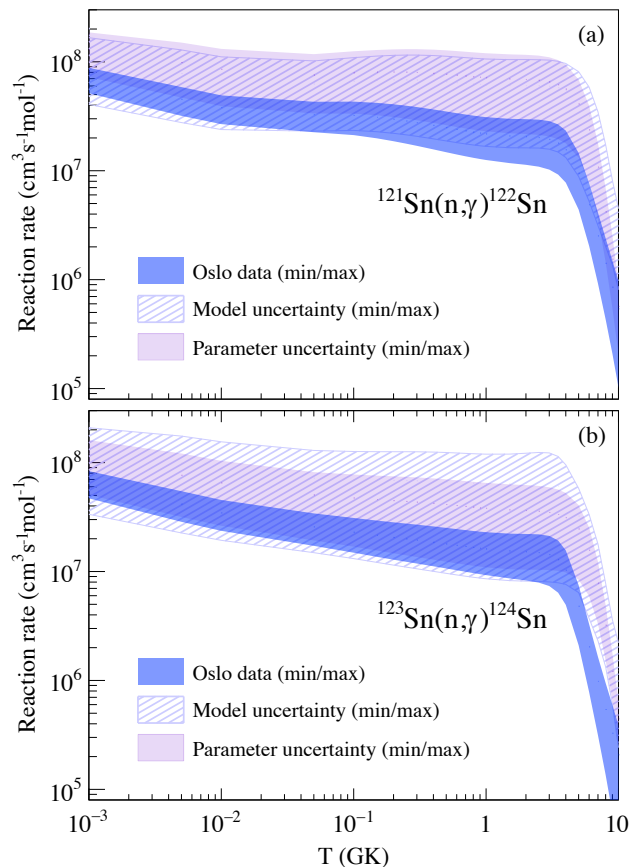|	$^{121}\text{Sn}(n,\gamma)^{122}\text{Sn}$	$^{123}\text{Sn}(n,\gamma)^{124}\text{Sn}$
TALYS parameter uncertainties		
case 1	min	min
case 2	max	max
case 3	min	max
case 4	max	min
TALYS model uncertainties		
case 5	min	–
case 6	max	–
case 7	–	min
case 8	–	max
Experiment (this work)		
case 9	min	min
case 10	max	max
case 11	min	max
case 12	max	min

FIG. 12. Uncertainty bands for the neutron capture rates in the $^{121}\text{Sn}(n,\gamma)^{122}\text{Sn}$ (a) and $^{123}\text{Sn}(n,\gamma)^{124}\text{Sn}$ reaction (b) reactions. The blue band corresponds to the span of experimentally constrained reaction rates due to uncertainties of the input Oslo NLD and GSF. The hatched band denotes the span of TALYS rates for all available GSF, NLD, and optical model potential combinations (model uncertainty). The purple band is due to the variation of the HFB+Combinatorial NLD and D1M+QRPA GSF model parameters according to the procedure of Ref. [152] (parameter uncertainty).

^{13}N isotope decays to ^{13}C in a timescale of about 10 min. Then, the reaction $^{13}\text{C}(\alpha,n)^{16}\text{O}$ is activated, mostly at the bottom of the pulse, where $T \simeq 250$ MK. The neutron density goes up to about 10^{15} cm^{-3} which leads to an i-process nucleosynthesis [e.g. 147–151]. The i-process material is later dredged up to the stellar surface and expelled through stellar winds.

Here, we investigated the impact of our new experimentally constrained $^{121,123}\text{Sn}(n,\gamma)^{122,124}\text{Sn}$ reaction rates and corresponding uncertainties on the i-process nucleosynthesis in a 1 $M_\odot$ low-metallicity ([Fe/H] = -2.5) AGB model computed with the STAREVOL code [53, 153, 154]. The network considered comprises 1160 nuclei, linked through 2123 nuclear reactions (n-, p-, α-captures and α-decays) and weak interactions (electron captures, β-decays). The rates were extracted from the BRUSLIB database, the Nuclear Astrophysics Library of
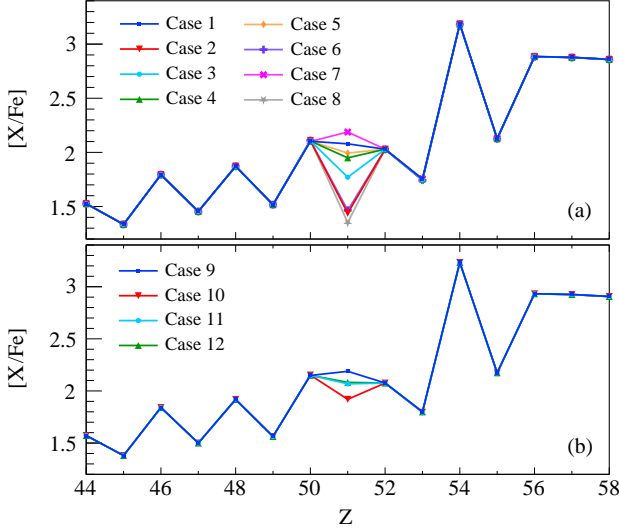
FIG. 13. Final surface elemental abundances (after decays) of multi-zone AGB stellar models experiencing i-process nucleosynthesis, computed with different combinations of ^{121,123}Sn(n,γ) rates. Shown are the [X/Fe] ratios defined as $[X/Fe] = \log_{10}(N_X/N_{Fe})_\star - \log_{10}(N_X/N_{Fe})_\odot$ with N_X the number density of an element X. The first and second $\log_{10}$ terms refer to the abundances of the model and the Sun, respectively. (a) Eight theoretical rates combinations are considered. These are theoretical estimates of parameter and model uncertainties affecting TALYS predictions of ^{121}Sn(n,γ) and ^{123}Sn(n,γ) reaction rates. (b) Same but with the new experimentally constrained rates from this work.

the Université Libre de Bruxelles[1][155] and the updated experimental and theoretical rates from the NETGEN interface [132]. Additional information on the stellar physics ingredients, modeling, and nuclear physics can be found in Refs. [53, 149, 150].

Since relatively accurate MACS have been previously measured for stable Sn isotopes, we only consider here the uncertainties affecting ^{121}Sn(n,γ) and ^{123}Sn(n,γ) reaction rates. To do so, we first considered their theoretical TALYS predictions and associated uncertainties. The latter include both parameter and models uncertainties, as extensively discussed in Ref. [152]. The impact of uncorrelated parameter uncertainties has been estimated considering four cases (cases 1–4 in Table V) obtained on the basis of the HFB+Combinatorial NLD and D1M+QRPA GSF models (note that similar parameter uncertainties are obtained for different NLD or GSF models, as discussed in Ref. [152]). The four cases correspond to the different minimum / maximum possible combinations for both rates. The impact of correlated nuclear model uncertainties was investigated by considering the NLD and GSF models leading to the lower or upper limits
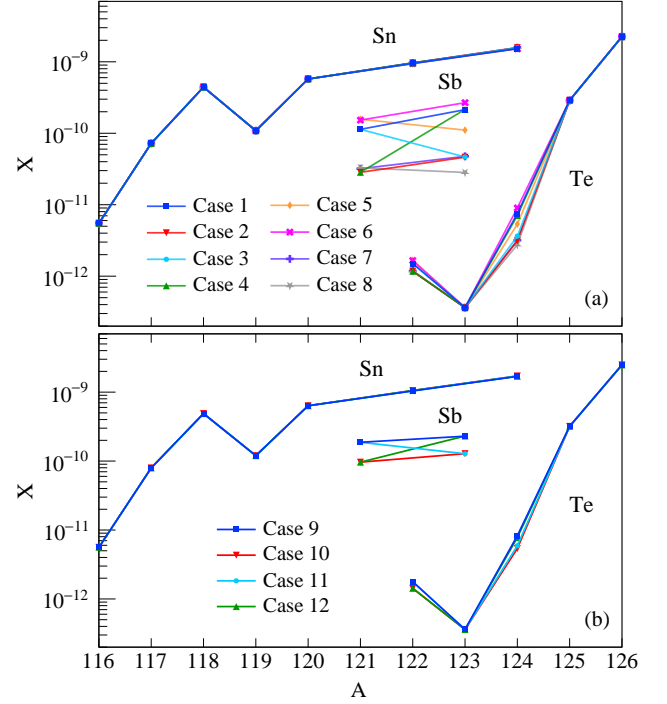
———————

FIG. 14. Same as Fig. 13 but for the isotopic mass fraction X as a function of the mass number A, around the Sn region.

of the TALYS MACSs [beige bands in Fig. 10(h) and (i)] and, thus, the respective reaction rates; these correspond to cases 5 to 8 in Table V. Finally, the new experimentally constrained rates are considered (cases 9 to 12) and assumed to be uncorrelated. In total, 12 AGB simulations experiencing a PIE were computed with these different rate combinations. The associated uncertainty bands are shown in Fig. 12.

As seen in Fig. 13, the impact of ^{121,123}Sn(n,γ) rate uncertainties on the i-process nucleosynthesis is local, arising at $Z = 51$ (Sb). This is in line with recent results from [152] where the relevant reactions for i-process nucleosynthesis in AGB stars were shown to mainly have a local impact on the resulting chemical abundances. In particular, the ^{121,123}Sn(n,γ) reactions appear in their Table 1, listing the key uncertain reactions affecting i-process predictions. The impacted element, Sb ($Z = 51$), is produced in different quantities depending on the strength of the ^{121,123}Sn(n,γ) reactions, the latter competing with β-decay (with half-lives of 27 hr and 129 days, respectively). A minimal rate for both ^{121,123}Sn(n,γ) reactions favors the production of ^{121,123}Sb through β-decay (blue pattern in Fig. 14). By contrast, if the (n,γ) rates are maximal, the flow favours the production of ^{122,124}Sn and less of ^{121,123}Sb, which results in lower ^{121,123}Sb abundances (red pattern in Fig. 14). Globally, TALYS theoretical uncertainties lead to an uncertainty of 0.84 dex in the final surface Sb abundance (the uncertainty is 0.65 dex for parameter uncertainties and 0.84 dex for model

uncertainties). It is decreased to 0.27 dex when considering the new experimentally constrained rates (Fig. 13). As shown in Fig. 14, for the ^{121}Sb (^{123}Sb) isotope, the overall uncertainty is reduced from 0.75 (0.98) to 0.29 (0.26) dex.

VII. CONCLUSIONS AND OUTLOOK

In this work, a consistent analysis of the $^{111-113,116-122,124}$Sn isotopes with the Oslo method applied to light-particle-induced reaction data has been presented. The extracted NLDs demonstrate a clear constant-temperature trend below the neutron separation energy. They appear to be in good agreement with each other and reproduce the low-lying discrete states up to $\approx 2-3$ MeV quite well. The Oslo GSFs are fully compatible with the available Coulomb excitation (p, p') data for even-even isotopes ^{112,116,118,120,124}Sn within the uncertainty bands and demonstrate a smooth evolution of the low-lying dipole strength with a slight increase of the GSF slope toward the heaviest studied ^{124}Sn isotope.

Based on the Oslo method and (p, p') strength distributions, the low-lying $E1$ strength on top of the IVGDR was found to be located at $\approx 7.8-8.3$ MeV and exhaust $\approx 2-3\%$ of the TRK sum rule for all the studied nuclei. The observed trend does not reveal any strong dependence on neutron number, and suggests a local maximum of strength at ^{120}Sn. The 6.4-MeV component of the LEDR extracted in $^{118-122,124}$Sn demonstrates an approximate dependence on neutron excess and might potentially be related to a similar concentration of strength observed in this energy region in earlier works [22, 23], where it was interpreted as the PDR.

The experimental results have been compared to calculations of the LEDR in the even-even Sn isotopes within the RQRPA and RQTBA frameworks. Despite a greatly improved agreement with the experimental strength distribution within the PDR and IVGDR regions as compared to the RQRPA approach, the RQTBA calculations do not reproduce the experimental TRK values extracted within the same energy regions. Both the RQRPA and RQTBA predict a clear linear increase in strength at $\approx 8-10$ MeV toward ^{124}Sn, in contrast to the experimental estimates that are approximately constant throughout the whole chain of the investigated isotopes.

The Oslo method NLDs and GSFs were further used to constrain the radiative neutron-capture cross sections and Maxwellian-averaged cross sections with the reaction code TALYS. Overall, the obtained values are in good agreement with available experimental data and Maxwellian-averaged cross sections and reaction rates reported in the JINA REACLIB, BRUSLIB, and KADoNiS libraries. The ^{121,123}Sn(n, γ) reaction rates obtained with the Oslo input NLDs and GSFs were found to locally impact the production of ^{121,123}Sb in the i-process nucleosynthesis in AGB stars and significantly reduce the available model and parameter uncertainties for the estimated final surface Sb abundance.

Despite the relatively small fractions of the TRK sum rule exhausted in the studied stable Sn isotopes, the low-lying dipole strength in these nuclei has a noticeable impact on the estimated reaction cross sections and rates. Further improvements in the microscopic calculations of $E1$ and $M1$ strength distributions close to the neutron threshold, especially in neutron-rich nuclei beyond the valley of stability, are highly desirable for future astrophysical calculations involving the i- and r-process nucleosynthesis. Moreover, from a nuclear-structure point of view, further detailed studies of the underlying structure of the states contributing to the LEDR strength are called for. In the near future, high-resolution experiments utilizing $(d, p\gamma)$ and $(p, d\gamma)$ reactions to populate the same even-even nucleus ^{118}Sn are envisaged to shed new light on this very intriguing issue.

ACKNOWLEDGMENTS

[1] R. Eramzhyan, B. Ishkhanov, I. Kapitonov, and V. Neudatchin, Phys. Rep. **136**, 229 (1986).

[2] D. Kusnezov, Y. Alhassid, and K. Snover, Nucl. Phys. A **649**, 193 (1999).

[3] W. Kleinig, V. O. Nesterenko, J. Kvasil, P.-G. Reinhard, and P. Vesely, Phys. Rev. C **78**, 044313 (2008).

[4] A. Migdal, J. Phys. Acad. Sci. USSR **8**, 331 (1944).

[5] N. Paar, D. Vretenar, E. Khan, and G. Coló, Rep. Prog. Phys. **70**, 671 (2007).

[6] D. Savran, T. Aumann, and A. Zilges, Prog. Part. Nucl. Phys. **70**, 210 (2013).

[7] A. Bracco, E. Lanza, and A. Tamii, Prog. Part. Nucl. Phys. **106**, 360 (2019).

[8] E. Lanza, L. Pellegri, A. Vitturi, and M. Andrés, Prog. Part. Nucl. Phys. **129**, 104006 (2023).

[9] R. Mohan, M. Danos, and L. C. Biedenharn, Phys. Rev. C **3**, 1740 (1971).

[10] P. Adrich, A. Klimkiewicz, M. Fallot, K. Boretzky, T. Aumann, D. Cortina-Gil, U. D. Pramanik, T. W. Elze, H. Emling, *et al.* (LAND-FRS Collaboration), Phys. Rev. Lett. **95**, 132501 (2005).

[11] O. Wieland, A. Bracco, F. Camera, G. Benzoni, N. Blasi, S. Brambilla, F. C. L. Crespi, S. Leoni, B. Million, R. Nicolini, *et al.*, Phys. Rev. Lett. **102**, 092502 (2009).

[12] O. Wieland, A. Bracco, F. Camera, R. Avigo, H. Baba, N. Nakatsuka, T. Aumann, S. R. Banerjee, G. Benzoni, K. Boretzky, *et al.*, Phys. Rev. C **98**, 064313 (2018).

[13] E. Litvinova, P. Ring, V. Tselyaev, and K. Langanke, Phys. Rev. C **79**, 054312 (2009).

[14] X. Roca-Maza, G. Pozzi, M. Brenna, K. Mizuyama, and G. Coló, Phys. Rev. C **85**, 024601 (2012).

[15] P.-G. Reinhard and W. Nazarewicz, Phys. Rev. C **87**, 014324 (2013).

[16] P. Papakonstantinou, V. Y. Ponomarev, R. Roth, and J. Wambach, Eur. Phys. J. A **47**, 14 (2011).

[17] A. Repko, P.-G. Reinhard, V. O. Nesterenko, and J. Kvasil, Phys. Rev. C **87**, 024305 (2013).

[18] V. Derya, D. Savran, J. Endres, M. Harakeh, H. Hergert, J. Kelley, P. Papakonstantinou, N. Pietralla, V. Ponomarev, R. Roth, *et al.*, Phys. Lett. B **730**, 288 (2014).

[19] P. von Neumann-Cosel, V. O. Nesterenko, I. Brandherm, P. I. Vishnevskiy, P. G. Reinhard, J. Kvasil, H. Matsubara, A. Repko, A. Richter, M. Scheck, and A. Tamii, arXiv:2310.04736 (2023).

[20] D. Vretenar, Y. F. Niu, N. Paar, and J. Meng, Phys. Rev. C **85**, 044317 (2012).

[21] J. Endres, D. Savran, A. M. v. d. Berg, P. Dendooven, M. Fritzsche, M. N. Harakeh, J. Hasper, H. J. Wörtche, and A. Zilges, Phys. Rev. C **80**, 034302 (2009).

[22] J. Endres, D. Savran, P. A. Butler, M. N. Harakeh, S. Harissopulos, R.-D. Herzberg, R. Krücken, A. Lagoyannis, E. Litvinova, N. Pietralla, *et al.*, Phys. Rev. C **85**, 064331 (2012).

[23] L. Pellegri, A. Bracco, F. Crespi, S. Leoni, F. Camera, E. Lanza, M. Kmiecik, A. Maj, R. Avigo, G. Benzoni, *et al.*, Phys. Lett. B **738**, 519 (2014).

[24] M. Krzysiek, M. Kmiecik, A. Maj, P. Bednarczyk, A. Bracco, F. C. L. Crespi, E. G. Lanza, E. Litvinova, N. Paar, R. Avigo, *et al.*, Phys. Rev. C **93**, 044330 (2016).

[25] D. Savran, V. Derya, S. Bagchi, J. Endres, M. Harakeh, J. Isaak, N. Kalantar-Nayestanaki, E. Lanza, B. Löher, A. Najafi, *et al.*, Phys. Lett. B **786**, 16 (2018).

[26] M. Spieker, A. Heusler, B. A. Brown, T. Faestermann, R. Hertenberger, G. Potel, M. Scheck, N. Tsoneva, M. Weinert, H.-F. Wirth, and A. Zilges, Phys. Rev. Lett. **125**, 102503 (2020).

[27] M. Weinert, M. Spieker, G. Potel, N. Tsoneva, M. Müscher, J. Wilhelmy, and A. Zilges, Phys. Rev. Lett. **127**, 242501 (2021).

[28] K. Govaert, F. Bauwens, J. Bryssinck, D. De Frenne, E. Jacobs, W. Mondelaers, L. Govor, and V. Y. Ponomarev, Phys. Rev. C **57**, 2229 (1998).

[29] B. Özel-Tashenov, J. Enders, H. Lenske, A. M. Krumbholz, E. Litvinova, P. von Neumann-Cosel, I. Poltoratska, A. Richter, G. Rusev, D. Savran, and N. Tsoneva, Phys. Rev. C **90**, 024304 (2014).

[30] M. Müscher, J. Wilhelmy, R. Massarczyk, R. Schwengner, M. Grieger, J. Isaak, A. R. Junghans, T. Kögler, F. Ludwig, D. Savran, *et al.*, Phys. Rev. C **102**, 014317 (2020).

[31] A. Klimkiewicz, N. Paar, P. Adrich, M. Fallot, K. Boretzky, T. Aumann, D. Cortina-Gil, U. D. Pramanik, T. W. Elze, *et al.* (LAND Collaboration), Phys. Rev. C **76**, 051603 (2007).

[32] A. Krumbholz, P. von Neumann-Cosel, T. Hashimoto, A. Tamii, T. Adachi, C. Bertulani, H. Fujita, Y. Fujita, E. Ganioglu, K. Hatanaka, *et al.*, Phys. Lett. B **744**, 7 (2015).

[33] S. Bassauer, P. von Neumann-Cosel, P.-G. Reinhard, A. Tamii, S. Adachi, C. A. Bertulani, P. Y. Chan, A. D'Alessio, H. Fujioka, H. Fujita, *et al.*, Phys. Rev. C **102**, 034327 (2020).

[34] H. K. Toft, A. C. Larsen, A. Bürger, M. Guttormsen, A. Görgen, H. T. Nyhus, T. Renstrøm, S. Siem, G. M. Tveten, and A. Voinov, Phys. Rev. C **83**, 044320 (2011).

[35] M. Markova, P. von Neumann-Cosel, A. C. Larsen, S. Bassauer, A. Görgen, M. Guttormsen, F. L. Bello Garrote, H. C. Berg, M. M. Bjørøen, T. Dahl-Jacobsen, *et al.*, Phys. Rev. Lett. **127**, 182501 (2021).

[36] M. Markova, A. C. Larsen, P. von Neumann-Cosel, S. Bassauer, A. Görgen, M. Guttormsen, F. L. B. Garrote, H. C. Berg, M. M. Bjørøen, T. K. Eriksen, *et al.*, Phys. Rev. C **106**, 034322 (2022).

[37] M. Markova, A. C. Larsen, G. M. Tveten, P. von Neumann-Cosel, T. K. Eriksen, F. L. Bello Garrote, L. Crespo Campo, F. Giacoppo, A. Görgen, M. Guttormsen, *et al.*, Phys. Rev. C **108**, 014315 (2023).

[38] J. Piekarewicz, Phys. Rev. C **73**, 044325 (2006).

[39] J. Piekarewicz, Phys. Rev. C **83**, 034319 (2011).

[40] X. Roca-Maza, M. Centelles, X. Viñas, and M. Warda, Phys. Rev. Lett. **106**, 252501 (2011).

[41] C. J. Horowitz and J. Piekarewicz, Phys. Rev. Lett. **86**, 5647 (2001).

[42] F. J. Fattoyev and J. Piekarewicz, Phys. Rev. C **86**, 015802 (2012).

[43] P.-G. Reinhard, V. O. Nesterenko, A. Repko, and J. Kvasil, Phys. Rev. C **89**, 024321 (2014).

[44] S. Goriely, E. Khan, and M. Samyn, Nucl. Phys. A **739**, 331 (2004).

[45] W. Hauser and H. Feshbach, Phys. Rev. **87**, 366 (1952).

[46] T. Rauscher and F.-K. Thielemann, At. Data Nucl. Data Tables **75**, 1 (2000).

[47] A. Koning, S. Hilaire, and S. Goriely, Eur. Phys. J. **59**, 131 (2023).

[48] R. L. Macklin, T. Inada, and J. H. Gibbons, Nature **194**, 1272 (1962).

[49] K. Wisshak, F. Voss, C. Theis, F. Käppeler, K. Guber, L. Kazakov, N. Kornilov, and G. Reffo, Phys. Rev. C

54, 1451 (1996).

[50] P. E. Koehler, J. A. Harvey, R. R. Winters, K. H. Guber, and R. R. Spencer, Phys. Rev. C **64**, 065802 (2001).

[51] F. Käppeler, W. Schanz, K. Wisshak, and G. Reffo, ApJ **410**, 370 (1993).

[52] R. Diehl, D. H. Hartmann, and N. Prantzos, Distributed radioactivities, in *Astrophysics with Radioactive Isotopes*, edited by R. Diehl, D. H. Hartmann, and N. Prantzos (Springer International Publishing, Cham, 2018) pp. 427–497.

[53] S. Goriely, L. Siess, and A. Choplin, A&A **654**, A129 (2021).

[54] M. Guttormsen, A. Bürger, T. E. Hansen, and N. Lietaer, Nucl. Instrum. Methods Phys. Res. A **648**, 168 (2011).

[55] M. Guttormsen, A. Ataç, G. Løvhøiden, S. Messelt, T. Ramsøy, J. Rekstad, T. F. Thorsteinsen, T. S. Tveter, and Z. Zelazny, Phys. Scr. **1990**, 54 (1990).

[56] V. W. Ingeberg, S. Siem, M. Wiedeking, K. Sieja, D. L. Bleuel, C. P. Brits, T. D. Bucher, T. S. Dinoko, J. L. Easton, A. Görgen, *et al.*, Eur. Phys. J. A **56**, 68 (2020).

[57] F. Zeiser, G. M. Tveten, F. L. B. Garrote, M. Guttormsen, A. C. Larsen, V. W. Ingeberg, A. Görgen, and S. Siem, Nucl. Instrum. Methods Phys. Res. A **985**, 164678 (2021).

[58] U. Agvaanluvsan, A. C. Larsen, M. Guttormsen, R. Chankova, G. E. Mitchell, A. Schiller, S. Siem, and A. Voinov, Phys. Rev. C **79**, 014320 (2009).

[59] U. Agvaanluvsan, A. C. Larsen, R. Chankova, M. Guttormsen, G. E. Mitchell, A. Schiller, S. Siem, and A. Voinov, Phys. Rev. Lett. **102**, 162504 (2009).

[60] H. K. Toft, A. C. Larsen, U. Agvaanluvsan, A. Bürger, M. Guttormsen, G. E. Mitchell, H. T. Nyhus, A. Schiller, S. Siem, N. U. H. Syed, and A. Voinov, Phys. Rev. C **81**, 064311 (2010).

[61] M. Guttormsen, T. S. Tveter, L. Bergholt, F. Ingebretsen, and J. Rekstad, Nucl. Instrum. Methods Phys. Res. A **374**, 371 (1996).

[62] A. C. Larsen, M. Guttormsen, M. Krtička, E. Běták, A. Bürger, A. Görgen, H. T. Nyhus, J. Rekstad, A. Schiller, S. Siem, *et al.*, Phys. Rev. C **83**, 034315 (2011).

[63] M. Guttormsen, T. Ramsøy, and J. Rekstad, Nucl. Instrum. Methods Phys. Res. A **255**, 518 (1987).

[64] J. E. Midtbø, Ph.D. thesis, University of Oslo (2019).

[65] J. E. Midtbø, F. Zeiser, E. Lima, A.-C. Larsen, G. M. Tveten, M. Guttormsen, F. L. Bello Garrote, A. Kvellestad, and T. Renstrøm, Comput. Phys. Commun. **262**, 107795 (2021).

[66] D. M. Brink, (1955), doctoral thesis, Oxford University.

[67] P. Axel, Phys. Rev. **126**, 671 (1962).

[68] R. Capote, M. Herman, P. Obložinský, P. Young, S. Goriely, T. Belgya, A. Ignatyuk, A. Koning, S. Hilaire, V. Plujko, *et al.*, Nucl. Data Sheets **110**, 3107 (2009).

[69] M. Guttormsen, A. C. Larsen, A. Görgen, T. Renstrøm, S. Siem, T. G. Tornyi, and G. M. Tveten, Phys. Rev. Lett. **116**, 012502 (2016).

[70] D. Martin, P. von Neumann-Cosel, A. Tamii, N. Aoi, S. Bassauer, C. A. Bertulani, J. Carter, L. Donaldson, H. Fujita, Y. Fujita, *et al.*, Phys. Rev. Lett. **119**, 182503 (2017).

[71] J. Isaak, D. Savran, M. Krtička, M. Ahmed, J. Beller, E. Fiori, J. Glorius, J. Kelley, B. Löher, N. Pietralla,

[72] K. Sieja, Eur. Phys. J. A **59**, 147 (2023).

[73] L. C. Campo, M. Guttormsen, F. L. B. Garrote, T. K. Eriksen, F. Giacoppo, A. Görgen, K. Hadynska-Klek, M. Klintefjord, A. C. Larsen, T. Renstrøm, *et al.*, Phys. Rev. C **98**, 054303 (2018).

[74] A. Schiller, L. Bergholt, M. Guttormsen, E. Melby, J. Rekstad, and S. Siem, Nucl. Instrum. Methods Phys. Res. A **447**, 498 (2000).

[75] M. Guttormsen, K. O. Ay, M. Ozgur, E. Algin, A. C. Larsen, F. L. Bello Garrote, H. C. Berg, L. Crespo Campo, T. Dahl-Jacobsen, F. W. Furmyr, *et al.*, Phys. Rev. C **106**, 034314 (2022).

[76] A. C. Larsen, G. M. Tveten, T. Renstrøm, H. Utsunomiya, E. Algin, T. Ari-izumi, K. O. Ay, F. L. Bello Garrote, L. Crespo Campo, F. Furmyr, *et al.*, Phys. Rev. C **108**, 025804 (2023).

[77] A. V. Voinov, N. Alanazi, S. Akhtar, S. Dhakal, C. R. Brune, S. M. Grimes, T. N. Massey, Z. Meisel, C. E. Parker, and A. L. Richard, Phys. Rev. C **108**, 034302 (2023).

[78] S. Hilaire, S. Goriely, S. Péru, and G. Gosselin, Physics Letters B **843**, 137989 (2023).

[79] Data taken from the ENSDF database of the NNDC online data service, https://www.nndc.bnl.gov/ensdf/. Last accessed: October 5, 2023.

[80] S. Mughabghab, *Atlas of neutron resonances; 6th ed.* (Elsevier, Amsterdam, 2018).

[81] T. Ericson and V. Strutinski, Nucl. Phys. **8**, 284 (1958).

[82] A. Gilbert and A. G. W. Cameron, Can. J. Phys. **43**, 1446 (1965).

[83] T. von Egidy and D. Bucurescu, Phys. Rev. C **72**, 044311 (2005).

[84] M. Wiedeking, M. Guttormsen, A. C. Larsen, F. Zeiser, A. Görgen, S. N. Liddick, D. Mücher, S. Siem, and A. Spyrou, Phys. Rev. C **104**, 014311 (2021).

[85] T. Ericson, Nucl. Phys. **11**, 481 (1959).

[86] M. Guttormsen, M. Aiche, F. L. Bello Garrote, L. A. Bernstein, D. L. Bleuel, Y. Byun, Q. Ducasse, T. K. Eriksen, F. Giacoppo, A. Görgen, *et al.*, Eur. Phys. J. A **51**, 170 (2015).

[87] I. K. B. Kullmann, A. C. Larsen, T. Renstrøm, K. S. Beckmann, F. L. B. Garrote, L. C. Campo, A. Görgen, Guttormsen, J. E. Midtbø, E. Sahin, *et al.*, Phys. Rev. C **99**, 065806 (2019).

[88] J. Kopecky and M. Uhl, Phys. Rev. C **41**, 1941 (1990).

[89] A. C. Larsen, N. Blasi, A. Bracco, F. Camera, T. K. Eriksen, A. Görgen, M. Guttormsen, T. W. Hagen, S. Leoni, B. Million, *et al.*, Phys. Rev. Lett. **111**, 242504 (2013).

[90] H. Uhrenholt, S. A. berg, A. Dobrowolski, T. D. ssing, T. Ichikawa, and P. Möller, Nucl. Phys. A **913**, 127 (2013).

[91] P. Roy, K. Banerjee, T. K. Rana, S. Kundu, D. Pandit, N. Q. Hung, T. K. Ghosh, S. Mukhopadhyay, D. Mondal, G. Mukherjee, *et al.*, Eur. Phys. J. A **57**, 48 (2021).

[92] V. W. Ingeberg, P. Jones, L. Msebi, S. Siem, M. Wiedeking, A. A. Avaa, M. V. Chisapi, E. A. Lawrie, K. L. Malatji, L. Makhathini, *et al.*, Phys. Rev. C **106**, 054315 (2022).

[93] S. C. Fultz, B. L. Berman, J. T. Caldwell, R. L. Bramblett, and M. A. Kelly, Phys. Rev. **186**, 1255 (1969).

[94] A. Leprêtre, H. Beil, R. Bergère, P. Carlos, A. De Miniac, A. Veyssière, and K. Kernbach, Nucl. Phys. A

219, 39 (1974).

[95] V. V. Varlamov, B. S. Ishkhanov, V. N. Orlin, and V. A. Chetvertkova, Bull. Russ. Acad. Sci.: Phys. **74**, 833 (2010).

[96] H. Utsunomiya, S. Goriely, M. Kamata, T. Kondo, O. Itoh, H. Akimune, T. Yamagata, H. Toyokawa, Y. W. Lui, S. Hilaire, and A. J. Koning, Phys. Rev. C **80**, 055806 (2009).

[97] H. Utsunomiya, S. Goriely, M. Kamata, H. Akimune, T. Kondo, O. Itoh, C. Iwamoto, T. Yamagata, H. Toyokawa, Y.-W. Lui, *et al.*, Phys. Rev. C **84**, 055805 (2011).

[98] D. M. Rossi, P. Adrich, F. Aksouh, H. Alvarez-Pol, T. Aumann, J. Benlliure, M. Böhmer, K. Boretzky, E. Casarejos, M. Chartier, *et al.*, Phys. Rev. Lett. **111**, 242503 (2013).

[99] S. Kadmenskii, V. Markushev, and V. Furman, Sov. J. Nucl. Phys. **37**, 345 (1983).

[100] S. Mughabghab and C. Dunford, Phys. Lett. B **487**, 155 (2000).

[101] S. Goriely, Phys. Lett. B **436**, 10 (1998).

[102] V. A. Plujko, S. Ezhov, M. Kavatsyuk, A. Grebenyuk, and R. Yermolenko, J. Nucl. Sci. Technol. **39**, 811 (2002).

[103] S. Goriely and E. Khan, Nucl. Phys. A **706**, 217 (2002).

[104] I. Daoutidis and S. Goriely, Phys. Rev. C **86**, 034328 (2012).

[105] S. Goriely, S. Hilaire, S. Péru, and K. Sieja, Phys. Rev. C **98**, 014327 (2018).

[106] R. Schwengner, S. Frauendorf, and A. C. Larsen, Phys. Rev. Lett. **111**, 232504 (2013).

[107] F. Pogliano, F. L. Bello Garrote, A. C. Larsen, H. C. Berg, D. Gjestvang, A. Görgen, M. Guttormsen, V. W. Ingeberg, T. W. Johansen, K. L. Malatji, *et al.*, Phys. Rev. C **107**, 034605 (2023).

[108] W. Thomas, Sci. Nat. **13**, 627 (1925).

[109] F. Reiche and W. Thomas, Z. Phys. **34**, 510 (1925).

[110] W. Kuhn, Z. Phys. **33**, 408 (1925).

[111] N. Tsoneva and H. Lenske, Phys. Rev. C **77**, 024321 (2008).

[112] V. Baran, M. Colonna, M. Di Toro, B. Frecus, A. Croitoru, and D. Dumitru, Eur. Phys. J. D **68**, 356 (2014).

[113] S. Burrello, M. Colonna, G. Colò, D. Lacroix, X. Roca-Maza, G. Scamps, and H. Zheng, Phys. Rev. C **99**, 054314 (2019).

[114] S. Bassauer, Doctoral thesis D17, Technische Universität Darmstadt (2019); http://tuprints.ulb.tu-darmstadt.de/9668.

[115] M. Markova *et al.*, To be published.

[116] G. Tertychny, V. Tselyaev, S. Kamerdzhiev, F. Grümmer, S. Krewald, J. Speth, A. Avdeenkov, and E. Litvinova, Phys. Lett. B **647**, 104 (2007).

[117] S. Adachi and P. Schuck, Nucl. Phys. **A496**, 485 (1989).

[118] J. Dukelsky, G. Röpke, and P. Schuck, Nucl. Phys. **A628**, 17 (1998).

[119] D. J. Rowe, Rev. Mod. Phys. **40**, 153 (1968).

[120] E. Litvinova and P. Schuck, Phys. Rev. C **100**, 064320 (2019).

[121] E. Litvinova and Y. Zhang, Phys. Rev. C **106**, 064316 (2022).

[122] V. I. Tselyaev, Phys. Rev. C **88**, 054301 (2013).

[123] E. Litvinova, P. Ring, and V. Tselyaev, Phys. Rev. C **78**, 014312 (2008).

[124] G. A. Lalazissis, J. König, and P. Ring, Phys. Rev. C **55**, 540 (1997).

[125] G. Lalazissis, S. Karatzikos, R. Fossion, D. P. Arteaga, A. Afanasjev, and P. Ring, Phys. Lett. B **671**, 36 (2009).

[126] V. Tselyaev, Sov. J. Nucl. Phys. **50**, 780 (1989).

[127] E. Litvinova, arXiv:2308.07574 (2023).

[128] V. M. Timokhov, M. V. Bokhovko, A. G. Isakov, L. E. Kazakov, V. N. Kononov, G. N. Manturov, E. D. Poletaev, and V. G. Pronyaev, Sov. J. Nucl. Phys. **50**, 375 (1989).

[129] J. Nishiyama, M. Igashira, T. Ohsaki, G. Kim, W.-C. Chung, and T.-I. Ro, J. Nucl. Sci. Technol. **45**, 352 (2008).

[130] S. Kamerdzhiev, R. J. Liotta, E. Litvinova, and V. Tselyaev, Phys. Rev. C **58**, 172 (1998).

[131] R. H. Cyburt, A. M. Amthor, R. Ferguson, Z. Meisel, K. Smith, S. Warren, A. Heger, R. D. Hoffman, T. Rauscher, and A. Sakharuk, ApJS **189**, 240 (2010).

[132] Y. Xu, S. Goriely, A. Jorissen, G. Chen, and M. Arnould, A&A **549**, 10 (2013), A106.

[133] I. Dillmann, R. Plag, F. Käppeler, and T. Rauscher, data extracted using the KADoNiS on-line data service, https://exp-astro.de/kadonis1.0/index.php. Last accessed: October 1, 2023.

[134] A. Koning, D. Rochman, J.-C. Sublet, N. Dzysiuk, M. Fleming, and S. van der Marck, Nucl. Data Sheets **155**, 1 (2019), special Issue on Nuclear Reaction Data.

[135] A. Koning and J. Delaroche, Nucl. Phys. A **713**, 231 (2003).

[136] E. Bauge, J. P. Delaroche, and M. Girod, Phys. Rev. C **63**, 024607 (2001).

[137] F. Pogliano, A. C. Larsen, S. Goriely, L. Siess, M. Markova, A. Görgen, J. Heines, V. W. Ingeberg, R. G. Kjus, J. E. L. Larsson, *et al.*, Phys. Rev. C **107**, 064614 (2023).

[138] N. Otuka, E. Dupont, V. Semkova, B. Pritychenko, A. Blokhin, M. Aikawa, S. Babykina, M. Bossant, G. Chen, S. Dunaeva, *et al.*, Nucl. Data Sheets **120**, 272 (2014).

[139] S. Goriely, S. Hilaire, and A. J. Koning, Phys. Rev. C **78**, 064307 (2008).

[140] M. B. Chadwick, M. Herman, P. Obložinsk'y, M. Dunn, Y. Danon, A. Kahler, D. Smith, B. Pritychenko, G. Arbanas, R. Arcilla, *et al.*, Nucl. Data Sheets **112**, 2887 (2011), special Issue on ENDF/B-VII.1 Library.

[141] K. Shibata, O. Iwamoto, T. Nakagawa, N. Iwamoto, A. Ichihara, S. Kunieda, S. Chiba, K. Furutaka, N. Otuka, T. Ohsawa, *et al.*, J. Nucl. Sci. Technol. **48**, 1 (2011).

[142] A. I. Karakas and J. C. Lattanzio, Publ. Astron. Soc. Aust. **31**, e030 (2014).

[143] M. Y. Fujimoto, Y. Ikeda, and I. Iben, Jr., ApJ **529**, L25 (2000).

[144] N. Iwamoto, T. Kajino, G. J. Mathews, M. Y. Fujimoto, and W. Aoki, ApJ **602**, 377 (2004).

[145] T. Suda and M. Y. Fujimoto, Mon. Notices Royal Astron. Soc. **405**, 177 (2010).

[146] R. J. Stancliffe, D. S. P. Dearborn, J. C. Lattanzio, S. A. Heap, and S. W. Campbell, ApJ **742**, 121 (2011).

[147] S. Cristallo, L. Piersanti, O. Straniero, R. Gallino, I. Domínguez, and F. Käppeler, Publ. Astron. Soc. Aust. **26**, 139 (2009).

[148] S. Cristallo, D. Karinkuzhi, A. Goswami, L. Piersanti, and D. Gobrecht, ApJ **833**, 181 (2016).

[149] A. Choplin, L. Siess, and S. Goriely, A&A **648**, A119 (2021).

[150] A. Choplin, L. Siess, and S. Goriely, A&A **667**, A155 (2022).

[151] A. Choplin, S. Goriely, and L. Siess, A&A **667**, L13 (2022).

[152] S. Martinet, A. Choplin, S. Goriely, and L. Siess, arXiv:2310.08694 (2023).

[153] L. Siess, E. Dufour, and M. Forestini, A&A **358**, 593 (2000).

[154] L. Siess, A&A **448**, 717 (2006).

[155] M. Arnould and S. Goriely, Nuclear Physics A **777**, 157 (2006), special Isseu on Nuclear Astrophysics.

Paper V

Systematics of the low-energy electric dipole strength in the Sn isotopic chain

Appendices

Appendix A

Derivation of the Oslo method decomposition equation

To provide a derivation of the decomposition of the primary matrix into the NLD and the GSF (Eq. (3.18)), let us start with a residual nucleus Y in a compound excited state C below the neutron threshold, produced in a light-ion-induced reaction $X(a,b)Y$. Here, we follow closely the notations of Blatt and Weisskopf ([90], p.342-345). The experimentally extracted primary matrix contains information on the subsequent γ decay of this compound state, and instead of focusing on the energy distribution of particles b, we consider the decay products of the compound state C. According to the assumption of Bohr, the cross section of the formation of the compound state C through an entrance channel α with a subsequent decay though an exit channel β can be factorized as:

$$\sigma(\alpha,\beta) = \sigma_C(\alpha)G_C(\beta), \tag{A.1}$$

with the entrance and exit channels being decoupled from one another. The first factor is the cross section for the formation of the compound state though the channel α, and the last factor corresponds to the decay probability through a specific exit channel β, or the branching ratio. It can be expressed in terms of the decay rates $\Gamma/\hbar$ (Γ is further referred to as the level width):

$$G_C(\beta) = \frac{\Gamma_C(\beta)}{\sum_\beta \Gamma_C(\beta)} = \frac{\Gamma_C(\beta)}{\Gamma_C}, \tag{A.2}$$

where $\Gamma_C(\beta)$ determines a decay rate of C through β, and Γ_C is the total width, accounting for all decay channels β. We shall keep in mind that for the compound state C below the neutron threshold, these widths correspond solely to the γ decay (radiative widths).

The energy spectrum of emitted photons can be written as:

$$dN_\gamma(\epsilon) \propto I_\gamma(\epsilon)d\epsilon = \sum_{\epsilon<\epsilon_\beta<\epsilon+d\epsilon} \sigma(\alpha,\beta) = \sigma_C(\alpha) \sum_{\epsilon<\epsilon_\beta<\epsilon+d\epsilon} G_C(\beta)$$

$$= \sigma_C(\alpha) \sum_{\epsilon<\epsilon_\beta<\epsilon+d\epsilon} \frac{\Gamma_C(\beta)}{\Gamma_C} = \frac{\sigma_C(\alpha)}{\Gamma_C} \sum_{\epsilon<\epsilon_\beta<\epsilon+d\epsilon} \Gamma_C(\beta). \tag{A.3}$$

Here $I_\gamma(\epsilon)d\epsilon$ is proportional to the number of emitted photons with energies from ϵ to $\epsilon + d\epsilon$, which can be simply expressed as a sum of cross sections with energies of emitted photons

falling within this interval. The proportionality factor is constant, depends on the properties of the target nucleus and a flux of incident particles, and will be canceled out in the subsequent steps. The intensity $I_\gamma(\epsilon)$ represents the number of particles with energies $\epsilon - \epsilon d\epsilon$ per energy interval $d\epsilon$. Moreover, in Eq. (A.3) we take into account that the total width and the cross section $\sigma_C(\alpha)$ depend only on the properties of the compound state C.

At this point, let us change the notations in the equations above to match the notations from the main part the thesis. The compound state would correspond to the initial state i, decaying to the final state f by emitting photons with energy E_γ. The previous equation can then be rewritten as:

$$
\begin{aligned}
I_\gamma(i \to f)dE_\gamma &= \frac{\sigma_C(i)}{\Gamma_C(i)} \sum_{E_\gamma < E_\gamma(i \to f) < E_\gamma + dE_\gamma} \Gamma_C(i \to f) \\
&\overset{(1)}{=} \frac{\sigma_C(i)}{\Gamma_C(i)} \sum_{XL} \langle \Gamma_\gamma(i \to f) \rangle \rho_{XL}^{av}(f) dE_\gamma.
\end{aligned}
\tag{A.4}
$$

In (1) we take into account that the decay can proceed via photons of different type X and multipolarity L, and that the number of terms in the sum is determined by the number of available final states $\rho_{XL}^{av}(f)dE_\gamma$, accessible through the radiation of type XL. The partial radiative widths are averaged over all possible transitions of type XL from the state i to the states f with energies ranging from $E_i - E_\gamma - dE_\gamma$ up to $E_i - E_\gamma$.

To be able to use this relation, we should note that the experimental matrix contains such transitions grouped in excitation energy bins E_i and E_γ, and we thus work with ensembles of transitions from states within the initial excitation energy bin E_i to states with final excitation energies, determined by the width of the corresponding γ-energy bin. For such bins, Eq. (A.4) can be written as:

$$
\begin{aligned}
I_\gamma(E_i, J_i, \pi_i, E_\gamma) &= \frac{\sigma_C(i)}{\Gamma_\gamma(i)} \sum_{XL} \langle \Gamma_{\gamma XL}(i \to f) \rangle \rho_{XL}^{av}(f) \\
&= \frac{\sigma_C(i)}{\Gamma_\gamma(i)} \sum_{XL} \frac{f_{XL}(i \to f) E_\gamma^{2L+1}}{\rho(i)} \rho_{XL}^{av}(f) \\
&\overset{BA}{=} \frac{\sigma_C(i)}{\Gamma_\gamma(i)\rho(i)} \sum_{XL} \frac{f_{XL}(E_\gamma) E_\gamma^{2L+1}}{\rho(i)} \rho_{XL}^{av}(f).
\end{aligned}
\tag{A.5}
$$

Here $I_\gamma(E_i, J_i, \pi_i, E_\gamma)$ determines the number of decays of the states with spin-parity $J_i^{\pi_i}$ in the bin E_i with γ energies falling within the γ-ray energy bin in the vicinity of E_γ per γ-ray energy bin width. An explicit dependence on the energy E_i, spin J_i, and parity π_i of the initial states is shortened down to (i) in the cross-section and the total radiative width. By averaging the partial widths we now assume averaging in the vicinity of the above-mentioned bins E_i and E_γ. According to the definition of the GSF [143], they can now be replaced by $f_{XL}(i \to f)$, which can be further simplified to $f_{XL}(E_\gamma)$ using the Brink-Axel hypothesis. The density $\rho(i)$ depends on the energy, spin, and parity of the initial states.

The products of the GSF and the density of the final states are summed over different types of radiation. In the following, we assume that the dipole radiations plays the leading role in the γ decay, and the only decay modes are $E1$ and $M1$. The former one changes the initial parity $\pi_f \to -\pi_i$, while the latter preserves it. Considering this, Eq. (A.5) can be further

APPENDIX A. DERIVATION OF THE OSLO METHOD DECOMPOSITION EQUATION

transformed as:

$$
\begin{aligned}
I_\gamma(E_i, J_i, \pi_i, E_\gamma) &= \frac{\sigma_C(i) E_\gamma^3}{\Gamma_\gamma(i)\rho(i)} \sum_{E1+M1} \frac{f_{X1}(E_\gamma)}{\rho(i)} \rho_{X1}^{av}(f) \\
&= \frac{\sigma_C(i) E_\gamma^3}{\Gamma_\gamma(i)\rho(i)} \Big(f_{E1}(E_\gamma)\rho_{E1}^{av}(f) + f_{M1}(E_\gamma)\rho_{M1}^{av}(f) \Big) \\
&= \frac{\sigma_C(i) E_\gamma^3}{\Gamma_\gamma(i)\rho(i)} \Big(f_{E1}(E_\gamma) \sum_{J_f=J_i-1}^{J_i+1} \rho(E_f, J_f, -\pi_i) + f_{M1}(E_\gamma) \sum_{J_f=J_i-1}^{J_i+1} \rho(E_f, J_f, \pi_i) \Big) \quad \text{(A.6)} \\
&\stackrel{(2)}{=} \frac{\sigma_C(i) E_\gamma^3}{\Gamma_\gamma(i)\rho(i)} \left(\frac{f_{E1}(E_\gamma)}{2} \sum_{J_f=J_i-1}^{J_i+1} \rho(E_f, J_f) + \frac{f_{M1}(E_\gamma)}{2} \sum_{J_f=J_i-1}^{J_i+1} \rho(E_f, J_f) \right) \\
&\stackrel{(3)}{=} \frac{\sigma_C(i) E_\gamma^3 \rho(E_f)}{\Gamma_\gamma(i)\rho(i)} \left(\frac{f_{E1}(E_\gamma)}{2} \sum_{J_f=J_i-1}^{J_i+1} g(E_f, J_f) + \frac{f_{M1}(E_\gamma)}{2} \sum_{J_f=J_i-1}^{J_i+1} g(E_f, J_f) \right).
\end{aligned}
$$

In (2), the parity equipartition is taken into account, hence the 1/2 factor. In step (3), we also adopt the expression for the partial NLD $\rho(E_x, J)$ through the spin distribution $g(E_x, J)$ and the total NLD $\rho(E_x)$ [95, 97].

With the dipole radiation, the angular momentum either remains unchanged or changes by one unit, so the sum of $g(E_f, J_i - 1) + g(E_f, J_i) + g(E_f, J_i + 1)$ can be approximated by the value of $3g(E_f, J_i)$. Strictly speaking, the factor of three should be smaller due to the initial states with $J_i = 0$ and $1/2$. This correction is, however, quite small and assumed to be negligible. Taking this approximation into account:

$$
\begin{aligned}
I_\gamma(E_i, J_i, \pi_i, E_\gamma) &\approx \frac{3\sigma_C(i) E_\gamma^3 \rho(E_f) g(E_f, J_i)}{2\Gamma_\gamma(i)\rho(i)} \big(f_{E1}(E_\gamma) + f_{M1}(E_\gamma) \big) \\
&= \frac{3\sigma_C(i) E_\gamma^3 \rho(E_f) g(E_f, J_i) f(E_\gamma)}{2\Gamma_\gamma(i)\rho(i)}.
\end{aligned}
\quad \text{(A.7)}
$$

The intensity can now be presented in the following form:

$$
I_\gamma(E_i, J_i, \pi_i, E_\gamma) = A(i)\rho(E_i - E_\gamma) f(E_\gamma) E_\gamma^3 g(E_i - E_\gamma, J_i), \quad \text{(A.8)}
$$

where $A(i)$ includes the cross section of the population of the initial compound states, density of these states, and the corresponding total radiative width and thus depends on the energy, spin, and parity of the initial state. The probability of decay of these states with a certain E_γ can be expressed through a normalized intensity as:

$$
P_\gamma(E_i, J_i, \pi_i, E_\gamma) = \frac{I_\gamma(E_i, J_i, \pi_i, E_\gamma)}{\sum_{E_\gamma} I_\gamma(E_i, J_i, \pi_i, E_\gamma)} = B(E_i, J_i)\rho(E_i - E_\gamma) f(E_\gamma) E_\gamma^3 g(E_i - E_\gamma, J_i), \quad \text{(A.9)}
$$

where summation in the denominator runs over all γ-ray energy bins in the experimental spectra. Here, the factor $A(i)$ in the numerator and the denominator, depending on the properties of the initial states, is canceled out. The remaining normalization factor

$$
B(E_i, J_i) = \frac{1}{\sum_{E_\gamma=0}^{E_i} \rho(E_i - E_\gamma) f(E_\gamma) E_\gamma^3 g(E_i - E_\gamma, J_i)} \quad \text{(A.10)}
$$

depends on the initial excitation energy and spin only. We can notice that the inverted normalization factor $B(E_i, J_i)$ resembles the average total radiative width, provided by Eq. (2.11) in [143], multiplied by the density of initial states $\rho(i)$.

The γ-ray spectra, corresponding to a certain excitation energy bin in the primary matrix, can be expressed as a weighted sum of normalized intensities for the decay of states with different spins and parities. The weights would be proportional to a populated spin distribution $g_{\mathrm{pop}}(E_x, J, \pi)$, which might be different from the initially adopted intrinsic spin distribution $g(E_x, J)$. Taking this into account, the primary spectrum takes the following form:

$$
\begin{aligned}
P_\gamma(E_i, E_\gamma) &= \sum_{J_i, \pi_i} g_{\mathrm{pop}}(E_i, J_i, \pi_i) P_\gamma(E_i, J_i, \pi_i, E_\gamma) \\
&= \sum_{J_i, \pi_i} g_{\mathrm{pop}}(E_i, J_i, \pi_i) B(E_i, J_i) \rho(E_i - E_\gamma) f(E_\gamma) E_\gamma^3 g(E_i - E_\gamma, J_i) \\
&= \rho(E_i - E_\gamma) f(E_\gamma) E_\gamma^3 \sum_{J_i, \pi_i} B(E_i, J_i) g_{\mathrm{pop}}(E_i, J_i, \pi_i) g(E_i - E_\gamma, J_i) \\
&= C(E_i, E_\gamma) \rho(E_i - E_\gamma) f(E_\gamma) E_\gamma^3.
\end{aligned}
\tag{A.11}
$$

The remaining normalization factor C depends on both the γ-ray and the initial excitation energy. In principle, it also depends on the parity π_i (due to g_{pop}), which was omitted in C due to a presumably small impact.

Within the Oslo method, this factor is assumed to be approximately constant, leading to the decomposition relation in the form of Eq. (3.18):

$$
P_\gamma(E_i, E_\gamma) \propto \rho(E_i - E_\gamma) f(E_\gamma) E_\gamma^3.
\tag{A.12}
$$

The omitted normalization factor is a potential source of an additional systematic uncertainty, which is believed to have little impact on the final NLD and the GSF within the estimated total uncertainty bands. For a large number of cases of stable nuclei, a good agreement between the Oslo and other experimental data supports this belief. The impact of the normalization $C(E_i, E_\gamma)$ with the factor $B(E_i, J_i)$ assumed to be constant was studied in Ref. [233]. It was shown to affect the coupling between the NLD and the GSF in such a way that, for different ranges of populated spins, the low-energy tail of the GSF might vary significantly. The largest deviation from the case where the normalization factor was assumed to be constant (standard Oslo method) was observed for a narrow range of high populated spins. In other cases, the correction is quite small and might indeed be expected to be well accounted for by the total uncertainty band. Nevertheless, it should be considered in the studies with limited ranges of populated spins, in particular, when focusing on the low-lying part of the strength (e.g. systematics of the upbend [187], comparison with shell-model calculations [306]). For the studied Sn isotopes, this factor is expected to have little to no impact on the main trend in the systematics of the low-lying $E1$ strength.

Appendix B

Preliminary analysis of the ^{114}Sn data

Two $(p, p'\gamma)$ experiments have been recently performed at the Horia Hulubei Institute for Physics and Nuclear Engineering (IFIN-HH) in order to study the ^{112,114}Sn isotopes with the Oslo method. The work on the analysis and preparation of a manuscript is currently in progress. One of the main objectives of this study is to address the transitions in the PDR region in terms of QPM calculations in comparison with the experimental data and thermodynamic properties, by analogy with Paper III and the earlier publications of the Oslo group.

The experiments have been performed with the 9 MV Tandem accelerator at IFIN-HH, using a special version of the ROmanian array for SPectroscopy in HEavy ion REactions
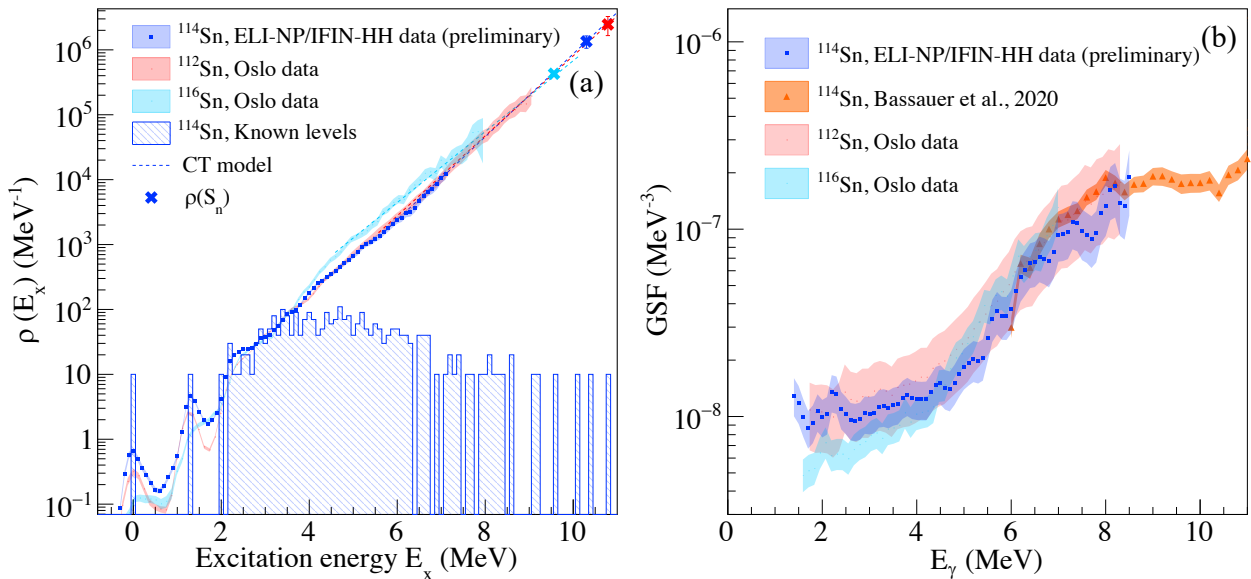

Figure B.1: The preliminary experimental NLD (a) and GSF (b) of ^{114}Sn. The low-lying discrete states are shown as a blue-shaded histogram, the $\rho(S_n)$ value and the constant-temperature fit are shown as a blue cross and a blue dashed line, respectively. The GSF is compared with the (p, p') data for the same isotope [42] and the GSFs of ^{112,116}Sn from this thesis.
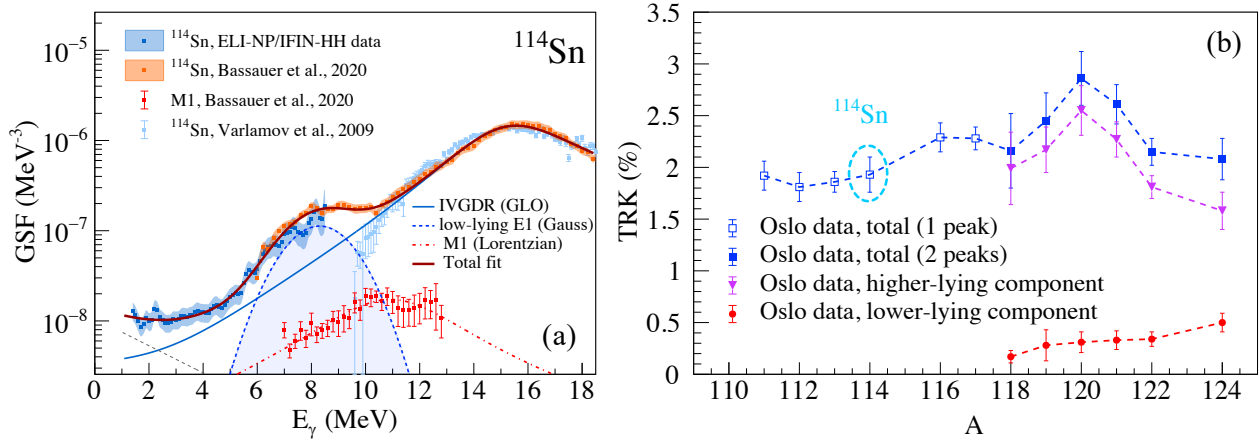
Figure B.2: (a) Decomposition of the ELI-NP/IFIH-HH and the (p, p') GSFs into the IVGDR, $M1$, and LEDR shown together with the (n, γ) data by Varlamov *et al.* [251]. The notations are the same as in Fig. 5.2. (b) Systematics of the LEDR (same as Fig. 5.3), but including the preliminary TRK value for ^{114}Sn.

(ROSPHERE) setup [307]. The latter consists of 21 LaBr$_3$:Ce and CeBr$_3$ detectors from ELI-NP with the total solid-angle coverage of 11.95% of 4π (see Ref. [308] for more details). The setup also includes a particle telescope consisting of two annular double-sided silicon strip detectors placed in the backward direction and covering polar angles of $120° - 136°$ with respect to the beam line. The experiment was performed with a 12.7-MeV proton beam with an average beam current of ≈ 0.5 nA. Further details regarding the experiment and the data analysis will be presented in the upcoming publication [309].

To assess the LEDR in the ^{114}Sn isotope, a preliminary analysis of p-γ data has been performed by analogy with the analyses presented in this thesis. The normalization coefficients used in this case are provided in Table C.1. The NLD and the GSF extracted with these coefficients in accordance with the procedures from Secs. 3.3.4 and 3.3.5 are shown in Fig. B.1. The extracted NLD is in excellent agreement with that of ^{112}Sn over the whole studied range of excitation energies and somewhat lower than in ^{116}Sn between $4 - 7$ MeV. Similarly to the neighboring even-even isotopes, the extracted GSF is in good agreement within the uncertainty bands with the corresponding (p, p') data.

To extract the fraction of the TRK sum rule exhausted in this case, the decomposition of the ELI-NP/IFIN-HH and the (p, p') strengths was performed in accordance with the procedure from Sec. 5.2. Similarly to $^{111-113}$Sn and ^{116,117}Sn, the best fit to the experimental data below the neutron threshold was achieved using a single Gaussian peak for the LEDR in the decomposition of the total GSF, as shown in Fig. B.2(a). The parameters for each component of the fit (IVGDR, LEDR, $M1$ response, upbend) are presented in Table C.2. The LEDR in this nucleus exhausts $\approx 1.9\%$ of the TRK sum rule, which appears to be perfectly in line with the systematics presented in this thesis, as demonstrated in Fig. B.2(b).

Appendix C

Results, normalization and fit parameters

C.1 Tables

This section contains all input parameters used for the normalization of the NLDs and the GSFs of $^{111-113,116-122,124}$Sn, the fit parameters of the GLO for the IVGDR, the SLO for the $M1$ response, the Gaussian function for the LEDR, and the integrated strengths for each isotope. The preliminary normalization and fit parameters for ^{114}Sn are also included.

Table C.1: Parameters used for the normalization of the NLDs and the GSFs for $^{111-113,116-122,124}$Sn. Preliminary normalization parameters for ^{114}Sn are also included.

Nucleus	S_n (MeV)	D_0 (eV)	a (MeV^{-1})	E_1 (MeV)	E_d (MeV)	σ_d	$\sigma(S_n)$	$\rho(S_n)$ (10^5 MeV^{-1})	T (MeV)	E_0 (MeV)	$\langle\Gamma_\gamma\rangle$ (meV)
^{111}Sn	8.169	120(36)[a]	12.05	-0.29	1.08(7)	2.7(4)	4.6(5)	3.54(127)[a]	$0.67^{+0.03}_{-0.02}$	$-0.06^{+0.04}_{-0.11}$	76(18)[a]
^{112}Sn	10.788	3(1)[a]	12.53	1.12	2.83(4)	2.8(4)	4.8(5)	24.61(80)[a]	$0.71^{+0.02}_{-0.02}$	$0.66^{+0.09}_{-0.08}$	87(34)[b]
^{113}Sn	7.744	172(10)	12.77	-0.27	1.88(2)	3.5(7)	4.6(5)	2.50(51)	$0.63^{+0.01}_{-0.01}$	$0.20^{+0.04}_{-0.04}$	73(8)
^{114}Sn^c	10.300	18(2)	13.17	1.09	2.28(7)	1.8(4)	4.8(5)	13.49(290)	$0.68^{+0.01}_{-0.01}$	$0.97^{+0.01}_{-0.02}$	106(7)[b]
^{116}Sn	9.563	55(5)	13.66	1.13	2.27(6)	2.7(5)	4.8(5)	4.28(91)	$0.79^{+0.02}_{-0.02}$	$-0.50^{+0.09}_{-0.04}$	118(10)
^{117}Sn	6.943	507(60)	13.62	-0.21	1.11(11)	2.5(2)	4.6(5)	0.85(19)	$0.69^{+0.02}_{-0.02}$	$-0.57^{+0.07}_{-0.05}$	53(3)
^{118}Sn	9.326	61(7)	13.94	1.14	2.48(4)	2.7(5)	4.8(5)	3.89(87)	$0.76^{+0.02}_{-0.02}$	$-0.18^{+0.08}_{-0.13}$	117(20)
^{119}Sn	6.483	700(100)	13.80	-0.30	1.32(2)	3.7(10)	4.6(5)	0.61(15)	$0.69^{+0.02}_{-0.02}$	$-0.80^{+0.05}_{-0.12}$	45(7)
^{120}Sn	9.105	95(14)	13.92	1.12	2.53(4)	3.7(5)	4.8(5)	2.49(60)	$0.75^{+0.02}_{-0.02}$	$0.07^{+0.10}_{-0.05}$	121(25)[b]
^{121}Sn	6.170	1485(130)	13.63	-0.39	1.26(5)	4.0(8)	4.5(5)	0.28(6)	$0.70^{+0.02}_{-0.02}$	$-0.70^{+0.10}_{-0.09}$	36(3)
^{122}Sn	8.815	95(28)[a]	13.58	1.07	2.75(2)	4.2(8)	4.7(5)	1.31(46)[a]	$0.76^{+0.03}_{-0.04}$	$0.07^{+0.19}_{-0.06}$	87(19)[a]
^{124}Sn	8.489	96(27)[a]	12.92	1.03	2.77(3)	3.3(5)	4.7(5)	0.87(26)[a]	$0.79^{+0.02}_{-0.04}$	$-0.31^{+0.16}_{-0.09}$	82(19)[a]

[a]From systematics.
[b]Modified (see text).
[c]Not included in the main part of the thesis and publications.

Table C.2: Parameters used for the description of the IVGDR and the $M1$ strength in the studied Sn isotopes. Preliminary parameters for ^{114}Sn are also included.

Nucl.	E_{E1} (MeV)	Γ_{E1} (MeV)	σ_{E1} (mb)	T_f (MeV)	E_{M1} (MeV)	Γ_{M1} (MeV)	σ_{M1} (mb)	C_{up} (10^{-8} MeV^{-3})	η_{up} (MeV^{-1})
^{111}Sn	16.15(9)	5.49(31)	264.5(93)	0.67(4)	11.22(24)[a]	5.15(39)[a]	1.73(15)[a]	—	—
^{112}Sn	16.14(9)	5.46(31)	265.9(95)	0.70(5)	10.45(43)	4.77(53)	1.77(21)	—	—
^{113}Sn	16.14(6)	5.25(23)	274.4(74)	0.75(3)	10.99(20)[a]	4.72(32)[a]	1.84(11)[a]	—	—
^{114}Sn[b]	16.21(10)	5.71(47)	262.5(134)	0.43(23)	11.22(33)	5.14(69)	2.21(18)	1.06(34)	0.35(17)
^{116}Sn	16.09(10)	6.03(35)	251.3(91)	0.43(2)	10.79(41)	6.28(96)	1.70(13)	—	—
^{117}Sn	15.98(7)	5.84(26)	257.1(74)	0.38(6)	10.54(12)[a]	3.86(20)[a]	2.05(7)[a]	0.38(10)	0.59(9)
^{118}Sn	15.78(10)	5.50(47)	270.0(153)	0.35(7)	10.26(19)	3.21(34)	2.90(24)	1.84(56)	0.63(8)
^{119}Sn	15.82(6)	5.77(22)	264.0(69)	0.45(9)	10.31(9)[a]	3.44(16)[a]	2.16(8)[a]	1.29(15)	1.20(31)
^{120}Sn	15.82(9)	5.79(39)	262.8(111)	0.48(14)	10.45(18)	3.13(33)	1.97(16)	0.45(7)	0.27(8)
^{121}Sn	15.72(6)	5.86(24)	255.3(66)	0.22(12)	10.08(9)[a]	3.01(14)[a]	2.27(11)[a]	1.27(63)	0.58(22)
^{122}Sn	15.67(3)	5.85(11)	258.7(24)	0.52(3)	9.97(10)[a]	2.79(15)[a]	2.32(13)[a]	—	—
^{124}Sn	15.59(7)	5.37(28)	266.8(90)	0.49(4)	9.66(14)	2.42(20)	2.61(16)	3.52(115)	1.67(40)

[a] From systematics.
[b] Not included in the main part of the thesis and Paper IV.

213

Table C.3: Parameters used for the description of the low-lying $E1$ strengths, integrated low-lying $E1$ strengths, and the corresponding exhausted fractions of the TRK sum rule in the studied Sn isotopes. Preliminary parameters for ^{114}Sn are also included.

Nucl.	Peak 1			Peak 2			Integrated strength	TRK
	E_{E1}^{low} (MeV)	σ_{E1}^{low} (MeV)	C_{E1}^{low} (10^{-7} MeV^{-2})	E_{E1}^{low} (MeV)	σ_{E1}^{low} (MeV)	C_{E1}^{low} (10^{-7} MeV^{-2})	(MeV mb)	(%)
^{111}Sn	—	—	—	8.26(9)	1.23(7)	3.32(23)	31.6(23)	1.92(14)
^{112}Sn	—	—	—	8.24(9)	1.22(8)	3.17(24)	30.1(23)	1.81(14)
^{113}Sn	—	—	—	8.23(6)	1.23(6)	3.27(17)	31.1(16)	1.86(10)
^{114}Sn^a	—	—	—	8.30(9)	1.20(7)	3.40(29)	32.5(28)	1.93(17)
^{116}Sn	—	—	—	8.33(8)	1.29(6)	4.08(25)	39.2(25)	2.29(14)
^{117}Sn	—	—	—	8.18(6)	1.26(5)	4.15(19)	39.2(19)	2.28(11)
^{118}Sn	6.27(18)	0.33(10)	0.40(15)	8.04(21)	1.00(20)	3.71(65)	37.3(62)	2.16(36)
^{119}Sn	6.44(13)	0.56(11)	0.67(35)	8.23(11)	1.06(11)	3.97(41)	42.7(47)	2.45(27)
^{120}Sn	6.59(11)	0.50(9)	0.71(22)	8.42(12)	1.19(10)	4.60(43)	50.1(46)	2.86(26)
^{121}Sn	6.62(9)	0.48(7)	0.77(20)	8.25(9)	1.11(7)	4.20(31)	45.9(34)	2.61(19)
^{122}Sn	6.45(5)	0.43(5)	0.82(16)	8.17(7)	1.00(7)	3.40(20)	38.1(23)	2.15(13)
^{124}Sn	6.49(5)	0.43(5)	1.20(22)	8.20(7)	0.83(12)	2.99(34)	37.3(36)	2.08(20)

^{a}Not included in the main part of the thesis and Paper IV.

C.2 Systematics of the Lorentzian parameters for the description of the $M1$ spin-flip resonance
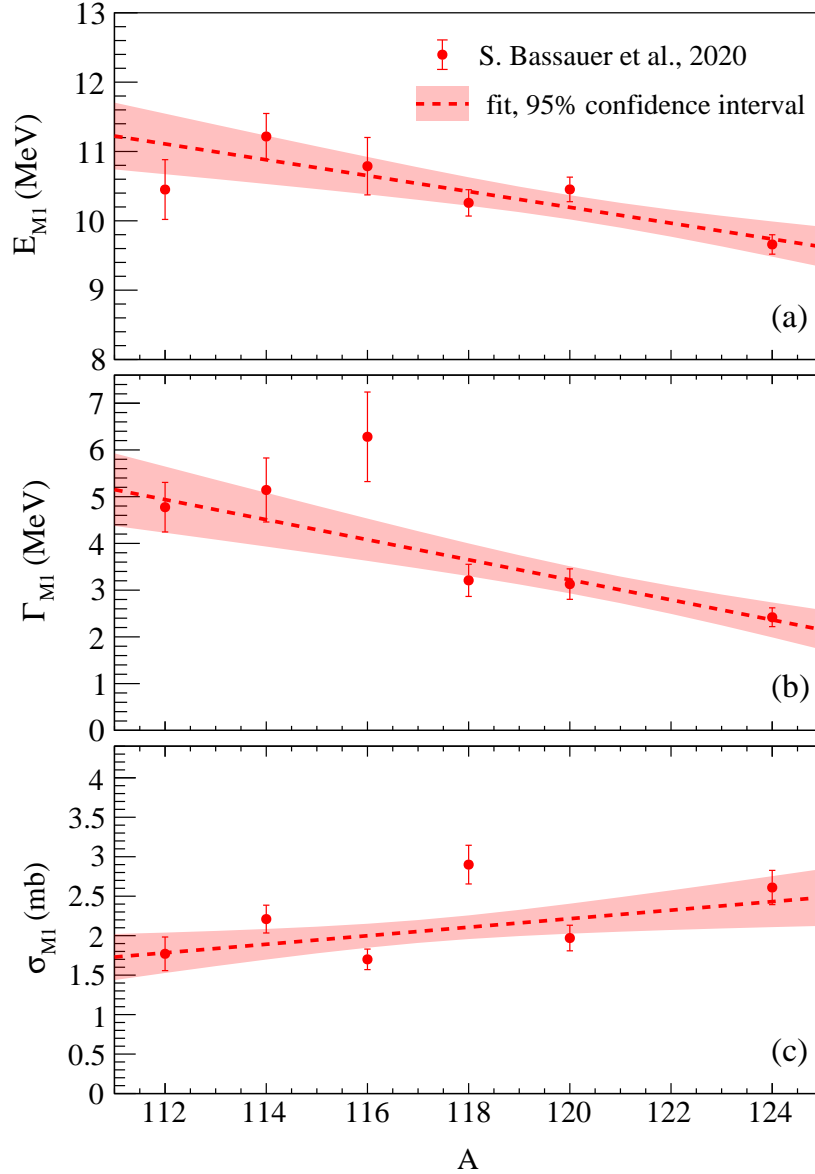

Figure C.1: Systematics of the energy centroid E_{M1} (a), the width Γ_{M1} (b), and the peak cross section σ_{M1} (c) from the fit of the experimental $M1$ data from Ref. [42] with the SLO. The linear fit (red dashed line) is used to extract the parameters for the $M1$ resonance in ^{111,113,117,119,121,122}Sn.

Bibliography

Bibliography

[1] W. Bothe and W. Gentner, Z. Phys. **106**, 236 (1937).

[2] A. Migdal, J. Phys. Acad. Sci. USSR **8**, 331 (1944).

[3] G. C. Baldwin and G. S. Klaiber, Phys. Rev. **71**, 3 (1947).

[4] G. C. Baldwin and G. S. Klaiber, Phys. Rev. **73**, 1156 (1948).

[5] M. Goldhaber and E. Teller, Phys. Rev. **74**, 1046 (1948).

[6] H. Steinwedel, J. H. D. Jensen, and P. Jensen, Phys. Rev. **79**, 1019 (1950).

[7] M. N. Harakeh and A. van der Woude, *Giant Resonances: Fundamental High-Frequency Modes of Nuclear Excitation,* (Clarendon Press, Oxford, 2001) pp. 1 – 155.

[8] G. A. Bartholomew, Annu. Rev. Nucl. Sci. **11**, 259 (1961).

[9] N. Starfelt, Nucl. Phys. **53**, 397 (1964).

[10] J. S. Brzosko, E. Gierlik, A. Soltan Jr., and Z. Wilhelmi, Can. J. Phys. **47**, 2849 (1969).

[11] W. Thomas, Sci. Nat. **13**, 627 (1925).

[12] F. Reiche and W. Thomas, Z. Phys. **34**, 510 (1925).

[13] W. Kuhn, Z. Phys. **33**, 408 (1925).

[14] D. Savran, T. Aumann, and A. Zilges, Prog. Part. Nucl. Phys. **70**, 210 (2013).

[15] E. Lanza, L. Pellegri, A. Vitturi, and M. Andrés, Prog. Part. Nucl. Phys. **129**, 104006 (2023).

[16] R. Mohan, M. Danos, and L. C. Biedenharn, Phys. Rev. C **3**, 1740 (1971).

[17] Y. Suzuki, K. Ikeda, and H. Sato, Prog. Theor. Phys. **83**, 180 (1990).

[18] S. Bastrukov, I. Molodtsova, D. Podgainy, Ş. Mişicu, and H.-K. Chang, Phys. Lett. B **664**, 258 (2008).

[19] N. Paar, D. Vretenar, E. Khan, and G. Coló, Rep. Prog. Phys. **70**, 671 (2007).

[20] V. Baran, M. Colonna, M. Di Toro, B. Frecus, A. Croitoru, and D. Dumitru, Eur. Phys. J. D **68**, 356 (2014).

[21] S. Burrello, M. Colonna, G. Colò, D. Lacroix, X. Roca-Maza, G. Scamps, and H. Zheng, Phys. Rev. C **99**, 054314 (2019).

[22] A. Zilges and D. Savran, "Pygmy dipole resonance: Experimental studies by different probes," in *Handbook of Nuclear Physics*, edited by I. Tanihata, H. Toki, and T. Kajino (Springer Nature Singapore, Singapore, 2020) pp. 1–28.

[23] M. Müscher, J. Wilhelmy, R. Massarczyk, R. Schwengner, M. Grieger, J. Isaak, A. R. Junghans, T. Kögler, F. Ludwig, D. Savran, *et al.*, Phys. Rev. C **102**, 014317 (2020).

[24] J. Isaak, D. Savran, M. Fritzsche, D. Galaviz, T. Hartmann, S. Kamerdzhiev, J. H. Kelley, E. Kwan, N. Pietralla, C. Romig, *et al.*, Phys. Rev. C **83**, 034304 (2011).

[25] R. Schwengner, R. Beyer, F. Dönau, E. Grosse, A. Hartmann, A. Junghans, S. Mallion, G. Rusev, K. Schilling, W. Schulze, and A. Wagner, Nucl. Instrum. Methods Phys. Res. A **555**, 211 (2005).

[26] D. Savran, K. Lindenberg, J. Glorius, B. Löher, S. Müller, N. Pietralla, L. Schnorrenberger, V. Simon, K. Sonnabend, C. Wälzlein, *et al.*, Nucl. Instrum. Methods Phys. Res. A **613**, 232 (2010).

[27] H. R. Weller, M. W. Ahmed, H. Gao, W. Tornow, Y. K. Wu, M. Gai, and R. Miskimen, Prog. in Part. and Nucl. Phys. **62**, 257 (2009).

[28] S. Bassauer, Doctoral thesis D17, Technische Universität Darmstadt (2019).

[29] A. Tamii, Y. Fujita, H. Matsubara, T. Adachi, J. Carter, M. Dozono, H. Fujita, K. Fujita, H. Hashimoto, K. Hatanaka, *et al.*, Nucl. Instrum. Methods Phys. Res. A **605**, 326 (2009).

[30] R. Neveling, H. Fujita, F. Smit, T. Adachi, G. Berg, E. Buthelezi, J. Carter, J. Conradie, M. Couder, R. Fearick, *et al.*, Nucl. Instrum. Methods Phys. Res. A **654**, 29 (2011).

[31] P. Adrich, A. Klimkiewicz, M. Fallot, K. Boretzky, T. Aumann, D. Cortina-Gil, U. D. Pramanik, T. W. Elze, H. Emling, H. Geissel, *et al.* (LAND-FRS Collaboration), Phys. Rev. Lett. **95**, 132501 (2005).

[32] D. Savran, V. Derya, S. Bagchi, J. Endres, M. Harakeh, J. Isaak, N. Kalantar-Nayestanaki, E. Lanza, B. Löher, A. Najafi, *et al.*, Phys. Lett. B **786**, 16 (2018).

[33] M. Guttormsen, T. Ramsøy, and J. Rekstad, Nucl. Instrum. Methods Phys. Res. A **255**, 518 (1987).

[34] M. Guttormsen, T. S. Tveter, L. Bergholt, F. Ingebretsen, and J. Rekstad, Nucl. Instrum. Methods Phys. Res. A **374**, 371 (1996).

[35] A. C. Larsen, M. Guttormsen, M. Krtička, E. Běták, A. Bürger, A. Görgen, H. T. Nyhus, J. Rekstad, A. Schiller, S. Siem, *et al.*, Phys. Rev. C **83**, 034315 (2011).

[36] F. Pogliano, F. L. Bello Garrote, A. C. Larsen, H. C. Berg, D. Gjestvang, A. Görgen, M. Guttormsen, V. W. Ingeberg, T. W. Johansen, K. L. Malatji, *et al.*, Phys. Rev. C **107**, 034605 (2023).

[37] A. Voinov, E. Algin, U. Agvaanluvsan, T. Belgya, R. Chankova, M. Guttormsen, G. E. Mitchell, J. Rekstad, A. Schiller, and S. Siem, Phys. Rev. Lett. **93**, 142504 (2004).

[38] D. Savran, M. Babilon, A. M. van den Berg, M. N. Harakeh, J. Hasper, A. Matic, H. J. Wörtche, and A. Zilges, Phys. Rev. Lett. **97**, 172502 (2006).

[39] J. Endres, D. Savran, A. M. v. d. Berg, P. Dendooven, M. Fritzsche, M. N. Harakeh, J. Hasper, H. J. Wörtche, and A. Zilges, Phys. Rev. C **80**, 034302 (2009).

[40] J. Endres, D. Savran, P. A. Butler, M. N. Harakeh, S. Harissopulos, R.-D. Herzberg, R. Krücken, A. Lagoyannis, E. Litvinova, N. Pietralla, *et al.*, Phys. Rev. C **85**, 064331 (2012).

[41] F. Crespi, A. Bracco, E. Lanza, A. Tamii, N. Blasi, F. Camera, O. Wieland, N. Aoi, D. Balabanski, S. Bassauer, *et al.*, Phys. Lett. B **816**, 136210 (2021).

[42] S. Bassauer, P. von Neumann-Cosel, P.-G. Reinhard, A. Tamii, S. Adachi, C. A. Bertulani, P. Y. Chan, A. D'Alessio, H. Fujioka, H. Fujita, *et al.*, Phys. Rev. C **102**, 034327 (2020).

[43] P.-G. Reinhard and W. Nazarewicz, Phys. Rev. C **87**, 014324 (2013).

[44] M. Spieker, A. Heusler, B. A. Brown, T. Faestermann, R. Hertenberger, G. Potel, M. Scheck, N. Tsoneva, M. Weinert, H.-F. Wirth, and A. Zilges, Phys. Rev. Lett. **125**, 102503 (2020).

[45] N. Paar, J. Phys. G Nucl. Part. Phys. **37**, 064014 (2010).

[46] D. Vretenar, N. Paar, P. Ring, and T. Nikšić, Phys. Rev. C **65**, 021301 (2002).

[47] A. Repko, P.-G. Reinhard, V. O. Nesterenko, and J. Kvasil, Phys. Rev. C **87**, 024305 (2013).

[48] B. Alex Brown, Phys. Rev. Lett. **85**, 5296 (2000).

[49] C. J. Horowitz and J. Piekarewicz, Phys. Rev. Lett. **86**, 5647 (2001).

[50] B. T. Reed, F. J. Fattoyev, C. J. Horowitz, and J. Piekarewicz, Phys. Rev. Lett. **126**, 172503 (2021).

[51] C. J. Horowitz and J. Piekarewicz, Phys. Rev. Lett. **86**, 5647 (2001).

[52] F. J. Fattoyev and J. Piekarewicz, Phys. Rev. C **86**, 015802 (2012).

[53] F. J. Fattoyev and J. Piekarewicz, Phys. Rev. Lett. **111**, 162501 (2013).

[54] B. P. Abbott, R. Abbott, T. D. Abbott, F. Acernese, K. Ackley, C. Adams, T. Adams, P. Addesso, R. X. Adhikari, V. B. Adya, *et al.*, Astrophys. J. Lett. **848**, L12 (2017).

[55] F. J. Fattoyev, J. Piekarewicz, and C. J. Horowitz, Phys. Rev. Lett. **120**, 172702 (2018).

[56] J. Piekarewicz, Phys. Rev. C **73**, 044325 (2006).

[57] P.-G. Reinhard and W. Nazarewicz, Phys. Rev. C **81**, 051303 (2010).

[58] O. Bohigas, N. Van Giai, and D. Vautherin, Phys. Lett. B **102**, 105 (1981).

[59] J. Piekarewicz, Phys. Rev. C **83**, 034319 (2011).

[60] X. Roca-Maza, N. Paar, and G. Colò, J. Phys. G Nucl. Part. Phys. **42**, 034033 (2015).

[61] A. Klimkiewicz, N. Paar, P. Adrich, M. Fallot, K. Boretzky, T. Aumann, D. Cortina-Gil, U. D. Pramanik, T. W. Elze, H. Emling, *et al.* (LAND Collaboration), Phys. Rev. C **76**, 051603 (2007).

[62] A. Carbone, G. Coló, A. Bracco, L.-G. Cao, P. F. Bortignon, F. Camera, and O. Wieland, Phys. Rev. C **81**, 041301 (2010).

[63] X. Roca-Maza and N. Paar, Prog. Part. Nucl. **101**, 96 (2018).

[64] S. Goriely, Phys. Lett. B **436**, 10 (1998).

[65] A. Tonchev, N. Tsoneva, C. Bhatia, C. Arnold, S. Goriely, S. Hammond, J. Kelley, E. Kwan, H. Lenske, J. Piekarewicz, R. Raut, G. Rusev, T. Shizuma, and W. Tornow, Phys. Lett. B **773**, 20 (2017).

[66] S. Goriely, E. Khan, and M. Samyn, Nucl. Phys. A **739**, 331 (2004).

[67] E. Litvinova, H. Loens, K. Langanke, G. Martínez-Pinedo, T. Rauscher, P. Ring, F.-K. Thielemann, and V. Tselyaev, Nucl. Phys. A **823**, 26 (2009).

[68] W. Hauser and H. Feshbach, Phys. Rev. **87**, 366 (1952).

[69] L. Wolfenstein, Phys. Rev. **82**, 690 (1951).

[70] F. Giacoppo, F. L. B. Garrote, T. K. Eriksen, A. Görgen, M. Guttormsen, T. W. Hagen, A. C. Larsen, B. V. Kheswa, M. Klintefjord, P. E. Koehler, *et al.*, arXiv:1402.2451 (2014).

[71] A. Avdeenkov, S. Goriely, S. Kamerdzhiev, and S. Krewald, Phys. Rev. C **83**, 064316 (2011).

[72] E. Litvinova, P. Ring, V. Tselyaev, and K. Langanke, Phys. Rev. C **79**, 054312 (2009).

[73] N. Tsoneva and H. Lenske, Phys. Rev. C **77**, 024321 (2008).

BIBLIOGRAPHY

[74] K. Govaert, F. Bauwens, J. Bryssinck, D. De Frenne, E. Jacobs, W. Mondelaers, L. Govor, and V. Y. Ponomarev, Phys. Rev. C **57**, 2229 (1998).

[75] P. Axel, K. K. Min, and D. C. Sutton, Phys. Rev. C **2**, 689 (1970).

[76] B. Özel-Tashenov, J. Enders, H. Lenske, A. M. Krumbholz, E. Litvinova, P. von Neumann-Cosel, I. Poltoratska, A. Richter, G. Rusev, D. Savran, and N. Tsoneva, Phys. Rev. C **90**, 024304 (2014).

[77] A. Krumbholz, P. von Neumann-Cosel, T. Hashimoto, A. Tamii, T. Adachi, C. Bertulani, H. Fujita, Y. Fujita, E. Ganioglu, K. Hatanaka, *et al.*, Phys. Lett. B **744**, 7 (2015).

[78] L. Pellegri, A. Bracco, F. Crespi, S. Leoni, F. Camera, E. Lanza, M. Kmiecik, A. Maj, R. Avigo, G. Benzoni, *et al.*, Phys. Lett. B **738**, 519 (2014).

[79] M. Weinert, M. Spieker, G. Potel, N. Tsoneva, M. Müscher, J. Wilhelmy, and A. Zilges, Phys. Rev. Lett. **127**, 242501 (2021).

[80] U. Agvaanluvsan, A. C. Larsen, M. Guttormsen, R. Chankova, G. E. Mitchell, A. Schiller, S. Siem, and A. Voinov, Phys. Rev. C **79**, 014320 (2009).

[81] U. Agvaanluvsan, A. C. Larsen, R. Chankova, M. Guttormsen, G. E. Mitchell, A. Schiller, S. Siem, and A. Voinov, Phys. Rev. Lett. **102**, 162504 (2009).

[82] H. K. Toft, A. C. Larsen, U. Agvaanluvsan, A. Bürger, M. Guttormsen, G. E. Mitchell, H. T. Nyhus, A. Schiller, S. Siem, N. U. H. Syed, and A. Voinov, Phys. Rev. C **81**, 064311 (2010).

[83] H. K. Toft, A. C. Larsen, A. Bürger, M. Guttormsen, A. Görgen, H. T. Nyhus, T. Renstrøm, S. Siem, G. M. Tveten, and A. Voinov, Phys. Rev. C **83**, 044320 (2011).

[84] P. Van Isacker, M. A. Nagarajan, and D. D. Warner, Phys. Rev. C **45**, R13 (1992).

[85] D. M. Brink, (1955), Doctoral thesis, Oxford University.

[86] P. Axel, Phys. Rev. **126**, 671 (1962).

[87] S. Goriely, L. Siess, and A. Choplin, Astron. Astrophys. **654**, A129 (2021).

[88] N. Bohr, Nature **137**, 344 (1936).

[89] A. Bohr and B. R. Mottelson, *Nuclear Structure*, Vol. Volume I: Single-particle motion (World Scientific, Singapore, 1998) pp. 183 – 186.

[90] J. M. Blatt and W. V. F., *Theoretical Nuclear Physics* (Springer New York, NY, New York, 1979) pp. 340 – 345, 365 –379.

[91] R. Capote, M. Herman, P. Obložinský, P. Young, S. Goriely, T. Belgya, A. Ignatyuk, A. Koning, S. Hilaire, V. Plujko, *et al.*, Nucl. Data Sheets **110**, 3107 (2009).

[92] H. Bethe, Z. Phys. **76**, 293 (1936).

[93] H. A. Bethe, Phys. Rev. **50**, 332 (1936).

[94] H. A. Bethe, Rev. Mod. Phys. **9**, 69 (1937).

[95] T. Ericson and V. Strutinski, Nucl. Phys. **8**, 284 (1958).

[96] T. Ericson, Nucl. Phys. **11**, 481 (1959).

[97] A. Gilbert and A. G. W. Cameron, Can. J. Phys. **43**, 1446 (1965).

[98] T. Ericson, Adv. Phys. **9**, 425 (1960).

[99] A. Mengoni and Y. Nakajima, J. Nucl. Med. Technol. **31**, 151 (1994).

[100] T. D. Newton, Can. J. Phys. **34**, 804 (1956).

[101] P.-l. Huang, S. M. Grimes, and T. N. Massey, Phys. Rev. C **62**, 024002 (2000).

[102] S. M. Grimes, J Nucl. Sci. Technol. **39**, 709 (2002).

[103] T. von Egidy and D. Bucurescu, Phys. Rev. C **72**, 044311 (2005).

[104] T. Von Egidy, H. Schmidt, and A. Behkami, Nucl. Phys. A **481**, 189 (1988).

[105] J. H. D. Jensen and J. M. Luttinger, Phys. Rev. **86**, 907 (1952).

[106] S. M. Grimes, J. D. Anderson, J. W. McClure, B. A. Pohl, and C. Wong, Phys. Rev. C **10**, 2373 (1974).

[107] W. Dilg, W. Schantl, H. Vonach, and M. Uhl, Nucl. Phys. A **217**, 269 (1973).

[108] T. von Egidy and D. Bucurescu, Phys. Rev. C **80**, 054310 (2009).

[109] M. Guttormsen, M. Aiche, F. L. Bello Garrote, L. A. Bernstein, D. L. Bleuel, Y. Byun, Q. Ducasse, T. K. Eriksen, F. Giacoppo, A. Görgen, *et al.*, Eur. Phys. J. A **51**, 170 (2015).

[110] A. V. Ignatyuk, *Statistical properties of excited atomic nuclei* (Energoatomizdat, USSR, 1983) p. 176.

[111] S. Goriely, F. Tondeur, and J. M. Pearson, At. Data Nucl. Data Tables **77**, 311 (2001).

[112] S. Goriely, S. Hilaire, and A. J. Koning, Phys. Rev. C **78**, 064307 (2008).

[113] S. Hilaire, M. Girod, S. Goriely, and A. J. Koning, Phys. Rev. C **86**, 064317 (2012).

[114] S. Hilaire, S. Goriely, S. Péru, and G. Gosselin, Phys. Lett. B **843**, 137989 (2023).

[115] T. Renstrøm, H.-T. Nyhus, H. Utsunomiya, R. Schwengner, S. Goriely, A. C. Larsen, D. M. Filipescu, I. Gheorghe, L. A. Bernstein, D. L. Bleuel, *et al.*, Phys. Rev. C **93**, 064302 (2016).

[116] R. Chankova, A. Schiller, U. Agvaanluvsan, E. Algin, L. A. Bernstein, M. Guttormsen, F. Ingebretsen, T. Lönnroth, S. Messelt, G. E. Mitchell, *et al.*, Phys. Rev. C **73**, 034311 (2006).

[117] A. Schiller, A. Bjerve, M. Guttormsen, M. Hjorth-Jensen, F. Ingebretsen, E. Melby, S. Messelt, J. Rekstad, S. Siem, and S. W. Ødegård, Phys. Rev. C **63**, 021306 (2001).

[118] S. Goriely, Nucl. Phys. A **605**, 28 (1996).

[119] P. Demetriou and S. Goriely, Nucl. Phys. A **695**, 95 (2001).

[120] S. Hilaire, J. P. Delaroche, and M. Girod, Eur. Phys. J. A **12**, 169 (2001).

[121] Y. Alhassid, Nucl. Phys. A **690**, 163 (2001).

[122] Y. Alhassid, L. Fang, and H. Nakada, J. Phys. Conf. **267**, 012033 (2011).

[123] Y. Alhassid, Eur. Phys. J. **51**, 171 (2015).

[124] N. Shimizu, T. Mizusaki, Y. Utsuno, and Y. Tsunoda, Comput. Phys. Commun. **244**, 372 (2019).

[125] Data taken from the ENSDF database of the NNDC online data service, `https://www.nndc.bnl.gov/ensdf/`. Last accessed: October 5, 2023.

[126] S. Mughabghab, *Atlas of neutron resonances; 6th ed.* (Elsevier, Amsterdam, 2018).

[127] H. K. Vonach and J. R. Huizenga, Phys. Rev. **149**, 844 (1966).

[128] D. R. Chakrabarty, V. M. Datar, S. Kumar, E. T. Mirgule, H. H. Oza, and U. K. Pal, Phys. Rev. C **51**, 2942 (1995).

[129] T. Rauscher, F.-K. Thielemann, and K.-L. Kratz, Phys. Rev. C **56**, 1613 (1997).

[130] D. Martin, P. von Neumann-Cosel, A. Tamii, N. Aoi, S. Bassauer, C. A. Bertulani, J. Carter, L. Donaldson, H. Fujita, Y. Fujita, *et al.*, Phys. Rev. Lett. **119**, 182503 (2017).

[131] T. Ericson, Phys. Rev. Lett. **5**, 430 (1960).

[132] V. Mishra, N. Boukharouba, S. M. Grimes, K. Doctor, R. S. Pedroni, and R. C. Haight, Phys. Rev. C **44**, 2419 (1991).

[133] F. B. Bateman, S. M. Grimes, N. Boukharouba, V. Mishra, C. E. Brient, R. S. Pedroni, T. N. Massey, and R. C. Haight, Phys. Rev. C **55**, 133 (1997).

[134] W. P. Abfalterer, R. W. Finlay, and S. M. Grimes, Phys. Rev. C **62**, 064312 (2000).

[135] Y. Kalmykov, T. Adachi, G. P. A. Berg, H. Fujita, K. Fujita, Y. Fujita, K. Hatanaka, J. Kamiya, K. Nakanishi, P. von Neumann-Cosel, *et al.*, Phys. Rev. Lett. **96**, 012502 (2006).

[136] Y. Kalmykov, C. Özen, K. Langanke, G. Martínez-Pinedo, P. von Neumann-Cosel, and A. Richter, Phys. Rev. Lett. **99**, 202502 (2007).

[137] I. Poltoratska, R. W. Fearick, A. M. Krumbholz, E. Litvinova, H. Matsubara, P. von Neumann-Cosel, V. Y. Ponomarev, A. Richter, and A. Tamii, Phys. Rev. C **89**, 054322 (2014).

[138] S. Bassauer, P. von Neumann-Cosel, and A. Tamii, Phys. Rev. C **94**, 054313 (2016).

[139] V. W. Ingeberg, P. Jones, L. Msebi, S. Siem, M. Wiedeking, A. A. Avaa, M. V. Chisapi, E. A. Lawrie, K. L. Malatji, L. Makhathini, *et al.*, Phys. Rev. C **106**, 054315 (2022).

[140] F. Pogliano, A. C. Larsen, S. Goriely, L. Siess, M. Markova, A. Görgen, J. Heines, V. W. Ingeberg, R. G. Kjus, J. E. L. Larsson, *et al.*, Phys. Rev. C **107**, 064614 (2023).

[141] A. Spyrou, S. N. Liddick, A. C. Larsen, M. Guttormsen, K. Cooper, A. C. Dombos, D. J. Morrissey, F. Naqvi, G. Perdikakis, S. J. Quinn, *et al.*, Phys. Rev. Lett. **113**, 232502 (2014).

[142] V. W. Ingeberg, S. Siem, M. Wiedeking, K. Sieja, D. L. Bleuel, C. P. Brits, T. D. Bucher, T. S. Dinoko, J. L. Easton, A. Görgen, *et al.*, Eur. Phys. J. A **56**, 68 (2020).

[143] G. A. Bartholomew, E. D. Earle, A. J. Ferguson, J. W. Knowles, and M. A. Lone, Adv. Nucl. Phys. **7**, 229 (1973).

[144] P. Axel, in *Proceedings of International Symposium on Nuclear Structure*, Vol. 189 (1969) p. 299.

[145] S. Goriely, P. Dimitriou, M. Wiedeking, T. Belgya, R. Firestone, J. Kopecky, M. Krtička, V. Plujko, R. Schwengner, S. Siem, *et al.*, Eur. Phys. J. **55**, 172 (2019).

[146] J. Kopecky and M. Uhl, Phys. Rev. C **41**, 1941 (1990).

[147] C. E. Porter and R. G. Thomas, Phys. Rev. **104**, 483 (1956).

[148] D. J. Hughes and J. A. Harvey, Phys. Rev. **99**, 1032 (1955).

[149] L. M. Bollinger, R. E. Coté, R. T. Carpenter, and J. P. Marion, Phys. Rev. **132**, 1640 (1963).

[150] L. M. Bollinger and G. E. Thomas, Phys. Rev. C **2**, 1951 (1970).

[151] S. Goriely, Phys. Lett. B **436**, 10 (1998).

[152] F. Käppeler, R. Gallino, S. Bisterzo, and W. Aoki, Rev. Mod. Phys. **83**, 157 (2011).

[153] M. Guttormsen, A. C. Larsen, A. Görgen, T. Renstrøm, S. Siem, T. G. Tornyi, and G. M. Tveten, Phys. Rev. Lett. **116**, 012502 (2016).

[154] A. Koning, S. Hilaire, and S. Goriely, Eur. Phys. J. **59**, 131 (2023).

BIBLIOGRAPHY

[155] M. Herman, R. Capote, B. Carlson, P. Obložinský, M. Sin, A. Trkov, H. Wienke, and V. Zerkin, Nucl. Data Sheets **108**, 2655 (2007).

[156] A. F. Fantina, E. Khan, G. Colò, N. Paar, and D. Vretenar, Phys. Rev. C **86**, 035805 (2012).

[157] R. A. Herrera, C. W. Johnson, and G. M. Fuller, Phys. Rev. C **105**, 015801 (2022).

[158] P. F. Bortignon, A. Bracco, and R. A. Broglia, *Giant Resonances: Nuclear Structure at Finite Temperature* (Harwood Academic, Amsterdam, 1998).

[159] P. Scholz, M. Guttormsen, F. Heim, A. C. Larsen, J. Mayer, D. Savran, M. Spieker, G. M. Tveten, A. V. Voinov, J. Wilhelmy, F. Zeiser, and A. Zilges, Phys. Rev. C **101**, 045806 (2020).

[160] M. Krtička, F. Bečvář, J. Honzátko, I. Tomandl, M. Heil, F. Käppeler, R. Reifarth, F. Voss, and K. Wisshak, Phys. Rev. Lett. **92**, 172501 (2004).

[161] M. Guttormsen, A. C. Larsen, A. Bürger, A. Görgen, S. Harissopulos, M. Kmiecik, T. Konstantinopoulos, M. Krtička, A. Lagoyannis, T. Lönnroth, *et al.*, Phys. Rev. C **83**, 014312 (2011).

[162] L. C. Campo, M. Guttormsen, F. L. B. Garrote, T. K. Eriksen, F. Giacoppo, A. Görgen, K. Hadynska-Klek, M. Klintefjord, A. C. Larsen, T. Renstrøm, *et al.*, Phys. Rev. C **98**, 054303 (2018).

[163] M. Guttormsen, A. C. Larsen, A. G. Görgen, T. Renstrøm, S. Siem, T. G. Tornyi, and G. M. Tveten, Proc. Sci. **INPC2016**, 062 (2017).

[164] C. T. Angell, S. L. Hammond, H. J. Karwowski, J. H. Kelley, M. Krtička, E. Kwan, A. Makinaga, and G. Rusev, Phys. Rev. C **86**, 051302 (2012).

[165] C. Romig, J. Beller, J. Glorius, J. Isaak, J. H. Kelley, E. Kwan, N. Pietralla, V. Y. Ponomarev, A. Sauerwein, D. Savran, *et al.*, Phys. Rev. C **88**, 044331 (2013).

[166] J. Isaak, D. Savran, M. Krtička, M. Ahmed, J. Beller, E. Fiori, J. Glorius, J. Kelley, B. Löher, N. Pietralla, *et al.*, Phys. Lett. B **727**, 361 (2013).

[167] L. Netterdon, A. Endres, S. Goriely, J. Mayer, P. Scholz, M. Spieker, and A. Zilges, Phys. Lett. B **744**, 358 (2015).

[168] J. Isaak, D. Savran, B. Löher, T. Beck, M. Bhike, U. Gayer, Krishichayan, N. Pietralla, M. Scheck, W. Tornow, *et al.*, Phys. Lett. B **788**, 225 (2019).

[169] K. Sieja, Eur. Phys. J. A **59**, 147 (2023).

[170] E. Litvinova and N. Belov, Phys. Rev. C **88**, 031302 (2013).

[171] N. Q. Hung, N. D. Dang, and L. T. Q. Huong, Phys. Rev. Lett. **118**, 022502 (2017).

[172] K. Sieja, Phys. Rev. Lett. **119**, 052502 (2017).

[173] H. P. Loens, K. Langanke, G. Martínez-Pinedo, and K. Sieja, Eur. Phys. J. **48**, 34 (2012).

[174] C. W. Johnson, Phys. Lett. B **750**, 72 (2015).

[175] V. F. Weisskopf, Phys. Rev. **83**, 1073 (1951).

[176] C. M. McCullagh, M. L. Stelts, and R. E. Chrien, Phys. Rev. C **23**, 1394 (1981).

[177] S. Kadmenskii, V. Markushev, and V. Furman, Sov. J. Nucl. Phys. **37**, 345 (1983).

[178] J. Kopecky and R. Chrien, Nucl. Phys. A **468**, 285 (1987).

[179] J. Kopecky, M. Uhl, and R. E. Chrien, Phys. Rev. C **47**, 312 (1993).

[180] *Handbook for Calculations of Nuclear Reaction Data, RIPL-2*, TECDOC Series No. 1506 (International Atomic Energy Agency, Vienna, 2006).

[181] V. Plujko, Nucl. Phys. A **649**, 209 (1999), giant Resonances.

[182] V. Plujko, Acta Phys. Pol. B **31**, 435 (2000).

[183] V. A. Plujko, S. Ezhov, M. Kavatsyuk, A. Grebenyuk, and R. Yermolenko, J. Nucl. Sci. Technol. **39**, 811 (2002).

[184] V. A. Plujko, I. M. Kadenko, O. M. Gorbachenko, and E. V. Kulich, Int. J. Mod. Phys. E **17**, 240 (2008).

[185] S. Mughabghab and C. Dunford, Phys. Lett. B **487**, 155 (2000).

[186] A. C. Larsen, G. M. Tveten, T. Renstrøm, H. Utsunomiya, E. Algin, T. Ari-izumi, K. O. Ay, F. L. Bello Garrote, L. Crespo Campo, F. Furmyr, *et al.*, Phys. Rev. C **108**, 025804 (2023).

[187] M. Guttormsen, K. O. Ay, M. Ozgur, E. Algin, A. C. Larsen, F. L. Bello Garrote, H. C. Berg, L. Crespo Campo, T. Dahl-Jacobsen, F. W. Furmyr, *et al.*, Phys. Rev. C **106**, 034314 (2022).

[188] O. Iwamoto, N. Iwamoto, S. Kunieda, F. Minato, S. Nakayama, Y. Abe, K. Tsubakihara, S. Okumura, C. Ishizuka, T. Yoshida, *et al.*, J. Nucl. Med. Technol. **60**, 1 (2023).

[189] T. Togashi, T. Otsuka, N. Shimizu, and Y. Utsuno, JPS Conf. Proc. **23**, 012031 (2018).

[190] R. Schwengner, S. Frauendorf, and A. C. Larsen, Phys. Rev. Lett. **111**, 232504 (2013).

[191] S. N. Liddick, A. C. Larsen, M. Guttormsen, A. Spyrou, B. P. Crider, F. Naqvi, J. E. Midtbø, F. L. Bello Garrote, D. L. Bleuel, L. Crespo Campo, *et al.*, Phys. Rev. C **100**, 024624 (2019).

[192] S. Goriely and E. Khan, Nucl. Phys. A **706**, 217 (2002).

[193] S. Goriely, S. Hilaire, M. Girod, and S. Péru, Phys. Rev. Lett. **102**, 242501 (2009).

[194] S. Hilaire, S. Goriely, S. Péru, F. Lechaftois, I. Deloncle, and M. Martini, EPJ Web Conf. **146**, 05013 (2017).

[195] F. Andreozzi, F. Knapp, N. L. Iudice, A. Porrino, and J. Kvasil, Phys. Rev. C **75**, 044312 (2007).

[196] V. I. Tselyaev, Phys. Rev. C **75**, 024306 (2007).

[197] T. Kawano, Y. Cho, P. Dimitriou, D. Filipescu, N. Iwamoto, V. Plujko, X. Tao, H. Utsunomiya, V. Varlamov, R. Xu, *et al.*, Nuc. Data Sheets **163**, 109 (2020).

[198] N. Pietralla, Nucl. Phys. News **28**, 4 (2018).

[199] M. Wiedeking, L. A. Bernstein, M. Krtička, D. L. Bleuel, J. M. Allmond, M. S. Basunia, J. T. Harke, P. Fallon, R. B. Firestone, B. L. Goldblum, *et al.*, Phys. Rev. Lett. **108**, 162503 (2012).

[200] N. Otuka, E. Dupont, V. Semkova, B. Pritychenko, A. Blokhin, M. Aikawa, S. Babykina, M. Bossant, G. Chen, S. Dunaeva, *et al.*, Nucl. Data Sheets **120**, 272 (2014).

[201] J. Kopecky, *Revision and Update of experimental Gamma-Ray Strength Functions Derived from the Discrete Neutron Resonance Capture*, Tech. Rep. INDC(NDS)–0772 (International Atomic Energy Agency (IAEA), 2018).

[202] J. Kopecky and S. Goriely, *Strength Functions Derived from The Discrete And Average Neutron Resonance Capture*, Tech. Rep. INDC(NDS)–0790 (International Atomic Energy Agency (IAEA), 2019).

[203] J. Kopecky, *Photon Strength Functions in Thermal Neutron Capture*, Tech. Rep. INDC(NDS)–0799 (International Atomic Energy Agency (IAEA), 2022).

[204] J. Kopecky and F. Bečvář, *Comparison of Photon Strength Functions from the Oslo Method with Neutron Capture Systematics*, Tech. Rep. INDC(NDS)–0868 (International Atomic Energy Agency (IAEA), 2022).

[205] T. Belgya, L. Szentmiklósi, R. Massarczyk, R. Schwengner, A. R. Junghans, and E. Grosse, EPJ Web Conf. **146**, 05009 (2017).

[206] F. Bečvář, P. Cejnar, R. E. Chrien, and J. Kopecký, Phys. Rev. C **46**, 1276 (1992).

[207] A. Voinov, S. M. Grimes, C. R. Brune, M. Guttormsen, A. C. Larsen, T. N. Massey, A. Schiller, and S. Siem, Phys. Rev. C **81**, 024319 (2010).

[208] S. A. Sheets, U. Agvaanluvsan, J. A. Becker, F. Bečvář, T. A. Bredeweg, R. C. Haight, M. Krtička, M. Jandel, G. E. Mitchell, J. M. O'Donnell, *et al.*, Phys. Rev. C **76**, 064317 (2007).

[209] S. Valenta, B. Baramsai, T. A. Bredeweg, A. Couture, A. Chyzh, M. Jandel, J. Kroll, M. Krtička, G. E. Mitchell, J. M. O'Donnell, *et al.*, Phys. Rev. C **96**, 054315 (2017).

[210] M. Krtička, S. Goriely, S. Hilaire, S. Péru, and S. Valenta, Phys. Rev. C **99**, 044308 (2019).

[211] C. Iliadis, *Nuclear Physics of Stars* (Wiley-VCH, Weinheim, 2015) pp. 133 – 137.

[212] M. Guttormsen, A. Ataç, G. Løvhøiden, S. Messelt, T. Ramsøy, J. Rekstad, T. F. Thorsteinsen, T. S. Tveter, and Z. Zelazny, Phys. Scr. **1990**, 54 (1990).

[213] F. Zeiser, G. M. Tveten, F. L. B. Garrote, M. Guttormsen, A. C. Larsen, V. W. Ingeberg, A. Görgen, and S. Siem, Nucl. Instrum. Methods Phys. Res. A **985**, 164678 (2021).

[214] S. Riboldi, F. Camera, N. Blasi, S. Brambilla, C. Boiano, F. C. Crespi, A. Giaz, B. Million, R. Nicolini, L. Pellegri, and O. Wieland, in *2011 IEEE Nuclear Science Symposium Conference Record* (2011) pp. 776–778.

[215] A. Giaz, L. Pellegri, S. Riboldi, F. Camera, N. Blasi, C. Boiano, A. Bracco, S. Brambilla, S. Ceruti, S. Coelli, *et al.*, Nucl. Instrum. Methods Phys. Res. A **729**, 910 (2013).

[216] M. Guttormsen, A. Bürger, T. E. Hansen, and N. Lietaer, Nucl. Instrum. Methods Phys. Res. A **648**, 168 (2011).

[217] F. Bloch, Ann. Phys. **408**, 285.

[218] *Pixie-16 User Manual, Version 3.06*, XIA (2019).

[219] L. Henden, L. Bergholt, M. Guttormsen, J. Rekstad, and T. Tveter, Nucl. Phys. A **589**, 249 (1995).

[220] F. Zeiser and G. M. Tveten, "oslocyclotronlab/ocl_geant4: Geant4 model of OSCAR," (2018).

[221] S. Agostinelli, J. Allison, K. Amako, J. Apostolakis, H. Araujo, P. Arce, M. Asai, D. Axen, S. Banerjee, G. Barrand, *et al.*, Nucl. Instrum. Methods Phys. Res. A **506**, 250 (2003).

[222] J. Allison, K. Amako, J. Apostolakis, H. Araujo, P. Arce Dubois, M. Asai, G. Barrand, R. Capra, S. Chauvie, R. Chytracek, *et al.*, IEEE Trans. Nucl. Sci. **53**, 270 (2006).

[223] J. Allison, K. Amako, J. Apostolakis, P. Arce, M. Asai, T. Aso, E. Bagli, A. Bagulya, S. Banerjee, G. Barrand, *et al.*, Nucl. Instrum. Methods Phys. Res. A **835**, 186 (2016).

[224] C. Sükösd, W. Galster, I. Licot, and M. Simonart, Nucl. Instr. Meth. Phys. Res. A **355**, 552 (1995).

[225] Běták, E., EPJ Web Conf. **2**, 11002 (2010).

[226] M. Guttormsen, L. Bergholt, F. Ingebretsen, G. Løvhøiden, S. Messelt, J. Rekstad, T. Tveter, H. Helstrup, and T. Thorsteinsen, Nucl. Phys. A **573**, 130 (1994).

[227] M. Guttormsen, A. Bagheri, R. Chankova, J. Rekstad, S. Siem, A. Schiller, and A. Voinov, Phys. Rev. C **68**, 064306 (2003).

[228] U. Agvaanluvsan, A. Schiller, J. A. Becker, L. A. Bernstein, P. E. Garrett, M. Guttormsen, G. E. Mitchell, J. Rekstad, S. Siem, A. Voinov, and W. Younes, Phys. Rev. C **70**, 054611 (2004).

[229] M. Guttormsen, R. Chankova, U. Agvaanluvsan, E. Algin, L. A. Bernstein, F. Ingebretsen, T. Lönnroth, S. Messelt, G. E. Mitchell, J. Rekstad, *et al.*, Phys. Rev. C **71**, 044307 (2005).

[230] J. E. Midtbø, Ph.D. thesis, University of Oslo (2019).

[231] P. A. M. Dirac, Proc. R. Soc. Lond. **114**, 141 – 143 (1927).

[232] E. Fermi, *Nuclear Physics* (University of Chicago Press, Chicago, 1950) pp. 183 – 186.

[233] J. E. Midtbø, F. Zeiser, E. Lima, A.-C. Larsen, G. M. Tveten, M. Guttormsen, F. L. Bello Garrote, A. Kvellestad, and T. Renstrøm, Comput. Phys. Commun. **262**, 107795 (2021).

[234] A. Schiller, L. Bergholt, M. Guttormsen, E. Melby, J. Rekstad, and S. Siem, Nucl. Instrum. Methods Phys. Res. A **447**, 498 (2000).

[235] J. H. D. Jensen and J. M. Luttinger, Phys. Rev. **86**, 907 (1952).

[236] H. Uhrenholt, S. A. berg, A. Dobrowolski, T. D. ssing, T. Ichikawa, and P. Möller, Nucl. Phys. A **913**, 127 (2013).

[237] J. Dobaczewski, P. Magierski, W. Nazarewicz, W. Satuła, and Z. Szymański, Phys. Rev. C **63**, 024308 (2001).

[238] I. K. B. Kullmann, A. C. Larsen, T. Renstrøm, K. S. Beckmann, F. L. B. Garrote, L. C. Campo, A. Görgen, Guttormsen, J. E. Midtbø, E. Sahin, *et al.*, Phys. Rev. C **99**, 065806 (2019).

[239] M. Wiedeking, M. Guttormsen, A. C. Larsen, F. Zeiser, A. Görgen, S. N. Liddick, D. Mücher, S. Siem, and A. Spyrou, Phys. Rev. C **104**, 014311 (2021).

[240] J. Kopecky, S. Goriely, S. Péru, S. Hilaire, and M. Martini, Phys. Rev. C **95**, 054317 (2017).

[241] S. Goriely, A.-C. Larsen, and D. Mücher, Phys. Rev. C **106**, 044315 (2022).

[242] D. Mücher, A. Spyrou, M. Wiedeking, M. Guttormsen, A. C. Larsen, F. Zeiser, C. Harris, A. L. Richard, M. K. Smith, A. Görgen, *et al.*, Phys. Rev. C **107**, L011602 (2023).

[243] J. E. Midtbø, F. Zeiser, E. Lima, A.-C. Larsen, G. M. Tveten, M. Guttormsen, F. L. Bello Garrote, A. Kvellestad, and T. Renstrøm, Comput. Phys. Commun. **262**, 107795 (2021).

[244] F. Zeiser, G. M. Tveten, G. Potel, A. C. Larsen, M. Guttormsen, T. A. Laplace, S. Siem, D. L. Bleuel, B. L. Goldblum, L. A. Bernstein, *et al.*, Phys. Rev. C **100**, 024305 (2019).

[245] T. Li, U. Garg, Y. Liu, R. Marks, B. K. Nayak, P. V. M. Rao, M. Fujiwara, H. Hashimoto, K. Kawase, *et al.*, Phys. Rev. Lett. **99**, 162503 (2007).

[246] C. A. Bertulani and G. Baur, Phys. Rep. **163**, 299 (1988).

[247] J. Birkhan, H. Matsubara, P. von Neumann-Cosel, N. Pietralla, V. Y. Ponomarev, A. Richter, A. Tamii, and J. Wambach, Phys. Rev. C **93**, 041302 (2016).

[248] M. Markova, A. C. Larsen, P. von Neumann-Cosel, S. Bassauer, A. Görgen, M. Guttormsen, F. L. B. Garrote, H. C. Berg, M. M. Bjørøen, T. K. Eriksen, *et al.*, Phys. Rev. C **106**, 034322 (2022).

[249] S. C. Fultz, B. L. Berman, J. T. Caldwell, R. L. Bramblett, and M. A. Kelly, Phys. Rev. **186**, 1255 (1969).

[250] A. Leprêtre, H. Beil, R. Bergère, P. Carlos, A. De Miniac, A. Veyssière, and K. Kernbach, Nucl. Phys. A **219**, 39 (1974).

[251] V. V. Varlamov, B. S. Ishkhanov, V. N. Orlin, and V. A. Chetvertkova, Bull. Russ. Acad. Sci.: Phys. **74**, 833 (2010).

[252] H. Utsunomiya, S. Goriely, M. Kamata, T. Kondo, O. Itoh, H. Akimune, T. Yamagata, H. Toyokawa, Y. W. Lui, S. Hilaire, and A. J. Koning, Phys. Rev. C **80**, 055806 (2009).

[253] H. Utsunomiya, S. Goriely, M. Kamata, H. Akimune, T. Kondo, O. Itoh, C. Iwamoto, T. Yamagata, H. Toyokawa, Y.-W. Lui, *et al.*, Phys. Rev. C **84**, 055805 (2011).

[254] D. M. Rossi, P. Adrich, F. Aksouh, H. Alvarez-Pol, T. Aumann, J. Benlliure, M. Böhmer, K. Boretzky, E. Casarejos, M. Chartier, *et al.*, Phys. Rev. Lett. **111**, 242503 (2013).

[255] I. Daoutidis and S. Goriely, Phys. Rev. C **86**, 034328 (2012).

[256] S. Goriely, S. Hilaire, S. Péru, and K. Sieja, Phys. Rev. C **98**, 014327 (2018).

[257] G. Tertychny, V. Tselyaev, S. Kamerdzhiev, F. Grümmer, S. Krewald, J. Speth, A. Avdeenkov, and E. Litvinova, Phys. Lett. B **647**, 104 (2007).

[258] L. Crespo Campo, F. L. Bello Garrote, T. K. Eriksen, A. Görgen, M. Guttormsen, K. Hadynska-Klek, M. Klintefjord, A. C. Larsen, T. Renstrøm, E. Sahin, *et al.*, Phys. Rev. C **94**, 044321 (2016).

[259] G. M. Tveten, A. Spyrou, R. Schwengner, F. Naqvi, A. C. Larsen, T. K. Eriksen, F. L. Bello Garrote, L. A. Bernstein, D. L. Bleuel, L. Crespo Campo, *et al.*, Phys. Rev. C **94**, 025804 (2016).

[260] T. K. Eriksen, H. T. Nyhus, M. Guttormsen, A. Görgen, A. C. Larsen, T. Renstrøm, I. E. Ruud, S. Siem, H. K. Toft, G. M. Tveten, and J. N. Wilson, Phys. Rev. C **90**, 044311 (2014).

[261] A. C. Larsen, N. Blasi, A. Bracco, F. Camera, T. K. Eriksen, A. Görgen, M. Guttormsen, T. W. Hagen, S. Leoni, B. Million, *et al.*, Phys. Rev. Lett. **111**, 242504 (2013).

[262] F. Pogliano, A. C. Larsen, F. L. Bello Garrote, M. M. Bjørøen, T. K. Eriksen, D. Gjestvang, A. Görgen, M. Guttormsen, K. C. W. Li, M. Markova, E. F. Matthews, *et al.*, Phys. Rev. C **106**, 015804 (2022).

[263] B. V. Kheswa, M. Wiedeking, F. Giacoppo, S. Goriely, M. Guttormsen, A. C. Larsen, F. L. Bello Garrote, T. K. Eriksen, A. Görgenrgen, T. Hagen, *et al.*, Phys. Lett. B **744**, 268 (2015).

[264] T. Renstrøm, H. Utsunomiya, H. T. Nyhus, A. C. Larsen, M. Guttormsen, G. M. Tveten, D. M. Filipescu, I. Gheorghe, S. Goriely, S. Hilaire, *et al.*, Phys. Rev. C **98**, 054310 (2018).

[265] S. Siem, M. Guttormsen, K. Ingeberg, E. Melby, J. Rekstad, A. Schiller, and A. Voinov, Phys. Rev. C **65**, 044318 (2002).

[266] E. Melby, M. Guttormsen, J. Rekstad, A. Schiller, S. Siem, and A. Voinov, Phys. Rev. C **63**, 044309 (2001).

[267] F. Giacoppo, F. L. Bello Garrote, L. A. Bernstein, D. L. Bleuel, R. B. Firestone, A. Görgen, M. Guttormsen, T. W. Hagen, M. Klintefjord, P. E. Koehler, *et al.*, Phys. Rev. C **91**, 054327 (2015).

[268] M. Guttormsen, L. A. Bernstein, A. Görgen, B. Jurado, S. Siem, M. Aiche, Q. Ducasse, F. Giacoppo, F. Gunsing, T. W. Hagen, *et al.*, Phys. Rev. C **89**, 014302 (2014).

[269] T. A. Laplace, F. Zeiser, M. Guttormsen, A. C. Larsen, D. L. Bleuel, L. A. Bernstein, B. L. Goldblum, S. Siem, F. L. Bello Garrote, J. A. Brown, *et al.*, Phys. Rev. C **93**, 014323 (2016).

[270] T. G. Tornyi, M. Guttormsen, T. K. Eriksen, A. Görgen, F. Giacoppo, T. W. Hagen, A. Krasznahorkay, A. C. Larsen, T. Renstrøm, S. J. Rose, *et al.*, Phys. Rev. C **89**, 044323 (2014).

[271] E. M. Burbidge, G. R. Burbidge, W. A. Fowler, and F. Hoyle, Rev. Mod. Phys. **29**, 547 (1957).

[272] A. G. W. Cameron, Pub. Astron. Soc. Pac. **69**, 201 (1957).

[273] M. Arnould and S. Goriely, Phys. Rep. **384**, 1 (2003).

[274] M. Arnould and S. Goriely, Prog. Part. Nucl. Phys. **112**, 103766 (2020).

[275] A. Choplin, L. Siess, and S. Goriely, Astron. Astrophys. **648**, A119 (2021).

[276] C. Travaglio, R. Gallino, A. E., J. Cowan, F. Jordan, and S. C., Astrophys. J. **601**, 864 (2004).

[277] S. Bisterzo, R. Gallino, F. Käppeler, M. Wiescher, G. Imbriani, O. Straniero, S. Cristallo, J. Görres, and R. J. deBoer, Mon. Notices Royal Astron. Soc. **449**, 506 (2015).

[278] A. Larsen, A. Spyrou, S. Liddick, and M. Guttormsen, Prog. Part. Nucl. **107**, 69 (2019).

[279] D. Kasen, B. Metzger, J. Barnes, E. Quataert, and E. Ramirez-Ruiz, Nature **551**, 80 (2017).

[280] U. Roederer and P. M. H. F. Karakas, A.I., Astrophys. J. **821**, 37 (2016).

[281] A. Choplin, L. Siess, and S. Goriely, Astron. Astrophys. **667**, A155 (2022).

[282] S. Martinet, A. Choplin, S. Goriely, and L. Siess, arXiv:2310.08694 (2023).

[283] P. E. Koehler, J. A. Harvey, R. R. Winters, K. H. Guber, and R. R. Spencer, Phys. Rev. C **64**, 065802 (2001).

[284] K. Wisshak, F. Voss, C. Theis, F. Käppeler, K. Guber, L. Kazakov, N. Kornilov, and G. Reffo, Phys. Rev. C **54**, 1451 (1996).

[285] Z. Nemeth, F. Käppeler, C. Theis, T. Belgya, and S. W. Yates, Astrophys. J. **426**, 357 (1994).

[286] C. Theis, F. Käppeler, K. Wisshak, and F. Voss, Astrophys. J. **500**, 1039 (1998).

[287] S. Bisterzo, C. Travaglio, R. Gallino, M. Wiescher, and F. Käppeler, Astrophys. J. **787**, 10 (2014).

[288] L. Roberti, M. Pignatari, A. Psaltis, A. Sieverding, P. Mohr, Z. Fülöp, and M. Lugaro, Astron. Astrophys. **677**, A22 (2023).

[289] R. L. Macklin, T. Inada, and J. H. Gibbons, Nature **194**, 1272 (1962).

[290] A. Koning, D. Rochman, J.-C. Sublet, N. Dzysiuk, M. Fleming, and S. van der Marck, Nucl. Data Sheets **155**, 1 (2019), Special Issue on Nuclear Reaction Data.

[291] A. Koning and J. Delaroche, Nucl. Phys. A **713**, 231 (2003).

[292] E. Bauge, J. P. Delaroche, and M. Girod, Phys. Rev. C **63**, 024607 (2001).

[293] A. V. Ignatyuk, K. K. Istekov, and G. N. Smirenkin, Sov. J. Nucl. Phys. **29(4)**, 875 (1979).

[294] A. V. Ignatyuk, J. L. Weil, S. Raman, and S. Kahane, Phys. Rev. C **47**, 1504 (1993).

[295] B. Wang, Y. Xu, and X. Tang, Phys. Rev. C **108**, 065805 (2023).

[296] V. M. Timokhov, M. V. Bokhovko, A. G. Isakov, L. E. Kazakov, V. N. Kononov, G. N. Manturov, E. D. Poletaev, and V. G. Pronyaev, Sov. J. Nucl. Phys. **50**, 375 (1989).

[297] J. Nishiyama, M. Igashira, T. Ohsaki, G. Kim, W.-C. Chung, and T.-I. Ro, J. Nucl. Sci. Technol. **45**, 352 (2008).

[298] R. H. Cyburt, A. M. Amthor, R. Ferguson, Z. Meisel, K. Smith, S. Warren, A. Heger, R. D. Hoffman, T. Rauscher, and A. Sakharuk, Astrophys. J., Suppl. Ser. **189**, 240 (2010).

[299] Y. Xu, S. Goriely, A. Jorissen, G. Chen, and M. Arnould, Astron. Astrophys. **549**, A106 (2013).

[300] I. Dillmann, R. Plag, F. Käppeler, and T. Rauscher, data extracted using the KADoNiS on-line data service, `https://exp-astro.de/kadonis1.0/index.php`. Last accessed: January 5, 2024.

[301] M. B. Chadwick, M. Herman, P. Obložinsk'y, M. Dunn, Y. Danon, A. Kahler, D. Smith, B. Pritychenko, G. Arbanas, R. Arcilla, *et al.*, Nucl. Data Sheets **112**, 2887 (2011), Special Issue on ENDF/B-VII.1 Library.

[302] K. Shibata, O. Iwamoto, T. Nakagawa, N. Iwamoto, A. Ichihara, S. Kunieda, S. Chiba, K. Furitaka, N. Otuka, T. Ohsawa, *et al.*, J. Nucl. Sci. Technol. **48**, 1 (2011).

[303] L. Siess, E. Dufour, and M. Forestini, Astron. Astrophys. **358**, 593 (2000).

[304] L. Siess, Astron. Astrophys. **448**, 717 (2006).

[305] M. Arnould and S. Goriely, Nucl. Phys. A **777**, 157 (2006), Special Issue on Nuclear Astrophysics.

[306] A. C. Larsen, J. E. Midtbø, M. Guttormsen, T. Renstrøm, S. N. Liddick, A. Spyrou, S. Karampagia, B. A. Brown, O. Achakovskiy, S. Kamerdzhiev, *et al.*, Phys. Rev. C **97**, 054329 (2018).

[307] D. Bucurescu, I. Căta-Danil, G. Ciocan, C. Costache, D. Deleanu, R. Dima, D. Filipescu, N. Florea, D. Ghiţă, T. Glodariu, *et al.*, Nucl. Instrum. Methods Phys. Res. A **837**, 1 (2016).

[308] S. Aogaki, D. Balabanski, R. Borcea, P. Constantin, C. Costache, M. Cuciuc, A. Kuşoğlu, C. Mihai, R. Mihai, L. Stan, *et al.*, Nucl. Instrum. Methods Phys. Res. A **1056**, 168628 (2023).

[309] P.-A. Söderström *et al.*, To be published.